ASME
SETTING THE STANDARD

# Journal of Engineering for Gas Turbines and Power

Published Bimonthly by ASME

VOLUME 131 • NUMBER 6 • NOVEMBER 2009



**Transactions of the ASME, Journal of Engineering for Gas Turbines and Power** (ISSN 0742-4795) is published bimonthly (Jan., Mar., May, July, Sep, Nov.) by The American Society of Mechanical Engineers, Three Park Avenue, New York, NY 10016. Periodicals postage paid at New York, NY and additional mailing offices. POSTMASTER: Send address changes to Transactions of the ASME, Journal of Engineering for Gas Turbines and Power, c/o THE AMERICAN SOCIETY OF MECHANICAL ENGINEERS, 22 Law Drive, Box 2300, Fairfield, NJ 07007-2300.
**CHANGES OF ADDRESS** must be received at Society headquarters seven weeks before they are to be effective. Please send old label and new address.
**STATEMENT from By-Laws.** The Society shall not be responsible for statements or opinions advanced in papers or ... printed in its publications (B7.1, par. 3).


## RESEARCH PAPERS



(Contents continued on inside back cover)

This journal is printed on acid-free paper, which exceeds the ANSI Z39.48-1992 specification for permanence of paper and library materials. ♾™
♻ 85% recycled content, including 10% post-consumer fibers.

Journal of Engineering for Gas Turbines and Power NOVEMBER 2009

Volume 131, Number 6



The ASME Journal of Engineering for Gas Turbines and Power is abstracted and indexed in the following:

*AESIS (Australia's Geoscience, Minerals, & Petroleum Database), Applied Science & Technology Index, Aquatic Sciences and Fisheries Abstracts, Civil Engineering Abstracts, Compendex (The electronic equivalent of Engineering Index), Computer & Information Systems Abstracts, Corrosion Abstracts, Current Contents, Engineered Materials Abstracts, Engineering Index, Enviroline (The electronic equivalent of Environment Abstracts), Environment Abstracts, Environmental Science and Pollution Management, Fluidex, INSPEC, Mechanical & Transportation Engineering Abstracts, Mechanical Engineering Abstracts, METADEX (The electronic equivalent of Metals Abstracts and Alloys Index), Pollution Abstracts, Referativnyi Zhurnal, Science Citation Index, SciSearch (The electronic equivalent of Science Citation Index), Shock and Vibration Digest*

# Energy and Economic Analyses of Integrated Biogas-Fed Energy Systems

**R. Bettocchi**
**M. Cadorin**
**G. Cenci**
**M. Morini**
**M. Pinelli**
**P. R. Spina**
**M. Venturini**

Department of Engineering (ENDIF),
University of Ferrara,
Via Saragat 1,
44100 Ferrara, Italy

*The process, which includes production, collection, carriage, and transformation of biomass into renewable fuels and then into energy (both electrical and thermal), involves a large number of decisions to select the most efficient plant layout. In order to identify the optimal solutions, models, which simulate the whole process, represent a useful and practical tool. In this paper, the energy and economic analysis of the entire process from biomass to energy production is presented. Among the different transformation processes, the thermophilic batch anaerobic digestion is considered in this paper. The analyses performed allow the comparison of the results for different scenarios characterized by different types of biomass (ensiled corn and organic fraction of municipal solid wastes), yearly mass of biomass, anaerobic digestion process parameters (number of yearly batch cycles and number of batch digesters), and type of energy systems (micro gas turbine and internal combustion engine). The results are presented in terms of classical economic indices for the investment and of producible electric and thermal energy. With respect to the economic indices, micro gas turbines allow a higher profitability than internal combustion engines, mainly because internal combustion engines require a scrubbing system to remove hydrogen sulphide from biogas. The contrary occurs with the producible electric and thermal energy. With regard to the digested substance, even if the methane yield is lower for organic fraction of municipal solid wastes than for ensiled corn, the net present values for organic fraction of municipal solid wastes are always higher than those obtained by using ensiled corn, and they are always positive, since municipal waste digestion avoids their disposal costs. The efficiency of the cogeneration process, evaluated in terms of primary energy saving index, usually shows quite high values and confirm the good capability of these systems.* [DOI: 10.1115/1.3078197]

## 1 Introduction

The use of biomass for energy production has progressively increased over the past years, due to an increasing interest both in agricultural and energy policies of many industrialized countries.

At present, the exploitation of biomass resources is considered as a viable addition with respect to the use of fossil fuels and so a great deal of research is directed toward investigating the effective capabilities of such resources [1]. Moreover, biofuels are predictable renewable energy sources. This is very important in distributed grid-connected generation where unpredictable renewable energy sources, such as solar photovoltaic and wind, have proved to be critical for network voltage and frequency stability [2,3].

However, the issue of the sustainability of energy from biomass is still being studied, and therefore the effect on any of the three pilasters (social, economic, and environmental) [4] cannot be clearly stated at present. In fact, the use of food crops for energy purposes has strong social effects, in particular, on low-income people. For instance, the US decision for the progressive gasoline substitution with ethanol has caused a 100% increase in the price of corn and consequently a 60% increase in the price of tortilla [5]. Even from an environmental point of view, the situation is not so clear, since many problems are frequently associated with cultivation of annual crops: degradation of water quality with sediments, nutrients, and pesticides; hydrologic modifications contributing to flooding and groundwater depletion; disruption of terrestrial and aquatic wildlife habitats; degradation of air quality with odors, pesticides, and particulates [6]. Moreover, biofuel utilization could not be the most profitable strategy for mitigation of anthropogenic carbon emission, since the greenhouse gas emission balance is not always equal to zero, due to carbon dioxide emission deriving from cultivation, collection, and other transformation processes [7–9]. Moreover, by taking into account land-use change (i.e., conversion of rainforests, peat lands, savannas, or grasslands to croplands), the net effect of biofuel production could be the increase in carbon dioxide emissions for decades or centuries relative to emissions caused by fossil fuel replacement [10].

Therefore, a great deal of research, also supported by governmental funding provided by many industrialized countries, is concentrated on the evaluation of actual performance of energy systems (ESs) fed by biofuels. One of the main problems encountered in this field is that the whole process, which includes production, collection, carriage, and transformation of biomass into renewable fuels and then into energy (both electrical and thermal), involves a large number of decisions to select the most efficient plant layout.

In order to identify the optimal plant solutions (which imply the fulfillment of environmental issues, economic constraints, reduced impact on population, and high system efficiency) and to carry out an efficient management of the whole plant, an optimization procedure has to be carried out. To do this, a model, which simulates the whole process, is required. Process optimization can be performed according to the maximization of economic indices, such as investment net present value (NPV), internal rate of return, and pay-back period, to the maximization of the producible energy, or to the minimization of environmental impact.

In recent years, a large number of technical papers, which deal with energy production from biomass, have been presented [11–27]. In this context, this paper is aimed at investigating a quite novel aspect, i.e., the energy and economic analysis of energy production from biomass. This is carried out by using a

Manuscript received July 10, 2008; final manuscript received July 24, 2008; published online July 17, 2009. Review conducted by Dilip R. Ballal. Paper presented at the ASME Turbo Expo 2008: Land, Sea and Air (GT2008), Germany, Berlin, June 9–13, 2008.

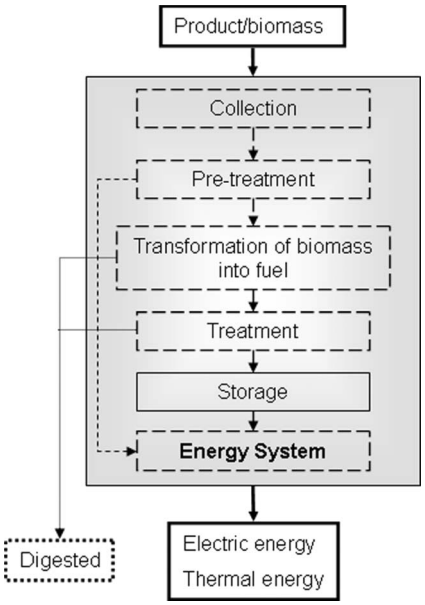


**Fig. 1 Scheme of the model of the complete process**

model for the simulation of the *entire* process, which was developed and implemented in a MATLAB environment by adopting a modular structure in order to reproduce different plant configurations [27]. Such a comprehensive view should allow investors and politicians to be guided in the choice of the most profitable investment for energy production. Few papers with the same aim have been presented in literature [18,19,25,27].

As a case study, energy systems fed by biogas produced through the thermophilic batch anaerobic digestion process were considered. In fact, literature on this topic is not very rich [14,24,27]. In particular, the anaerobic digestion transformation process was considered due to the following reasons.

- Its technology is well established, and relatively cheap, compared to other processes.
- It represents a possible solution for power generation, especially for distributed power generation.
- It represents an additional opportunity for agriculture.
- It allows wastes from agriculture and from the food industry to be exploited, so that disposal costs are decreased or even turned into revenues.
- It represents a viable option for urban waste organic matter with respect to the thermovalorization [28].

The batch digestion process was analyzed in this paper in order to investigate the actual capability of this type of process, since the continuous digestion process is a consolidated technology.

Moreover, even though nowadays most of the anaerobic digestion plants in Italy adopt a mesophilic process, the interest toward thermophilic processes has increased because of its higher values of methane yield, and, therefore, in this paper a thermophilic process is considered. However, it should be noted that the mesophilic process requires a lower thermal power for maintaining the suitable temperature inside the digesters.

## 2 General Model for the Simulation of the Complete Process From Biomass to Energy Production

The target of the model is the simulation of the behavior of the whole integrated system (from raw materials to electric and thermal energy) to optimize investment profitability, by also considering system efficiency and environmental impact.

The model is characterized by a modular structure in order to simulate different plant layouts. In Fig. 1 the main modules composing the model (collection, pretreatment, transformation of biomass into fuel, treatment, storage, and energy system) are highlighted. The main program links the modules and allows the determination of the operating conditions and of the performance indices of the plant as a function of system parameters, which depend on the transformation process, the considered biomass, and energy system configuration.

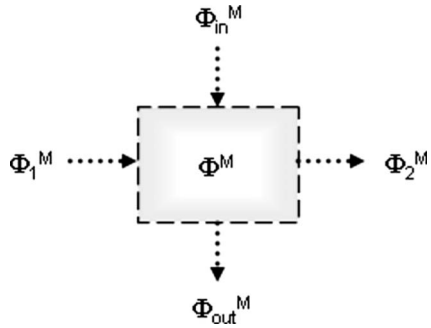


**Fig. 2 Quantity balance**

The main equations used in all modules are general balance equations. According to the scheme reported in Fig. 2, a general balance for each quantity can be written as [27]

$$\Phi^{M} = \Phi_1{}^{M} - \Phi_2{}^{M} + \Phi_{in}{}^{M} - \Phi_{out}{}^{M} \tag{1}$$

where 1 and 2 are the entry and exit sections with respect to the main flow, respectively, and the superscript M stands for the generic module M. The terms $\Phi_{in}{}^{M}$ and $\Phi_{out}{}^{M}$ in Eq. (1) represent the contributions to the balance (positive and negative, respectively) given to the quantity from the outside. For instance, if the considered quantity is mass, $\Phi_{in}{}^{M}$ may represent an additive flow with respect to the main flow, while $\Phi_{out}{}^{M}$ may take into account the subtraction of residuals from the process.

The general balance expressed in Eq. (1) assumes different forms, when applied to a given property, to mass or to energy.

For each typology of transformation process and supplied mixture, different modules are required. Some guidelines about each module are provided below.

*Collection.* This module is used to estimate the total mass (together with its physical characteristic parameters), which will feed the subsequent modules, by also considering different combinations of input substances. This is made by considering a yield $Y_{ij}$ for each specific "field" (whose dimension is $D_{ij}$) from which the biomass is collected and for each substance

$$m_j^C = \sum_{i=1}^{n_{field}} m_{ij}^C = \sum_{i=1}^{n_{field}} Y_{ij}^C D_{ij}, \quad j = 1, \ldots, n_{subst} \tag{2}$$

The term field does not only refer to the agricultural field, but may also include the case of urban waste as biomass. In this case, the field is the urban surface and the yield represents the urban waste rate of production for each inhabitant.

*Pretreatment.* This module is used to simulate the process carried out before the biomass is supplied to the transformation process to be converted into fuel, in order to render the process efficient through a proper treatment of the mixture.

Some of the products of the pretreatment process may be supplied directly to the ES. These are the ones that are already characterized by proper values of lower heating value (LHV) and sulphur content. The rest are supplied to the transformation process.

*Transformation of biomass into fuel.* Biofuels can be obtained in a number of ways, and can be processed to give refined fuels, or, in some cases, can be used directly. Different modules are required for each type of transformation process, in order to determine the following quantities, as a function of the mixture supplied to the process:

- the quantity of biofuel that the process can produce
- the thermal power, which has to be supplied to maintain the desired process temperature
- biofuel temperature
- heat losses due to heat exchange from pipelines and reservoirs
- the quantity of process wastes (digested), which have to be drained or, if possible, alternatively used

*Treatment.* This module is used to simulate the process carried out after the biomass is converted into fuel. This usually consists of fuel refinement and purging so that the fuel can be supplied to the ES.

*Storage.* The storage module is necessary to simulate the fact that a part of the biofuel may be used to feed the ES, while the rest can be stored in a reservoir. Both the filling and the emptying of the reservoir, as a function of the electric and thermal power outputs, are allowed.

*Energy system.* The ES module can be built by adopting two different approaches:

- a systemic approach
- a physics-based modeling approach

The first approach can be adopted independent of the typology of the ES. In this case, it is possible to establish the following power balance equation:

$$P_f = P_{el} + P_{th} + P_l \tag{3}$$

The terms in Eq. (3) can be calculated as $P_f = M_f \mathrm{LHV}$, $P_{el} = \eta_{el} P_f$, $P_{th} = \eta_{th} P_f$, and $P_l = (1 - \eta_{el} - \eta_{th}) P_f$. The values of the two efficiencies $\eta_{el}$ and $\eta_{th}$ depend on the ES under consideration and on ambient and load conditions as well. It should be noticed that the term $P_l$ takes into account both nonrecoverable power losses and self-consumed power (e.g., for plant auxiliaries).

In the case of the physics-based modeling approach, the availability of a model for the considered ES is required to replace the general balance equation (3). This approach allows a more detailed analysis of the behavior of the whole system. For instance, a gas turbine thermodynamic model would allow the estimation of exhaust gas temperature. However, a physics-based model may not always be available and its development could also be time consuming.

## 3 Evaluation of System Profitability

The evaluation of system profitability can be applied either to the whole process from biomass to energy production or only to one of the three main parts into which the process can be divided, i.e., biomass production and collection, biomass conversion into fuel (including pretreatment, transformation, and treatment), or energy conversion through the ESs. The net cash flow can be estimated as

$$R = (R_{Eel} + R_{Eth} + R_{nonfood} + R_d) - C \tag{4}$$

Revenues can be written as

$$\begin{aligned} R_{Eel} &= r_{Eel} \cdot E_{el} \\ R_{Eth} &= r_{Eth} \cdot E_{th} \\ R_{nonfood} &= r_{nonfood} \cdot m_{nonfood} \\ R_d &= r_d \cdot m_d \end{aligned} \tag{5}$$

Two of the products are electric $E_{el}$ and thermal $E_{th}$ energy, while the rest is a mass product (i.e., the amount of nonfood $m_{nonfood}$ and disposal $m_d$ products). In fact, though some sludge may be a source of costs to perform its disposal, a fraction of the sludge may be alternatively used to produce a marketable product (e.g., compost and fertilizer).

**Table 1 Units for specific revenues and costs**

| Quantity | Unit | |
|---|---|---|
| $r_{Eel}$, $r_{Eth}$ | Euro/MJ | Eq. (5) |
| $r_{nonfood}$, $r_d$ | Euro/kg | Eq. (5) |
| $c_E$, $c_d$ | Euro/kg | Eq. (8) |
| $c_{maint}$ | Euro/MJ | Eq. (8) |
| $c_{subst}$ | Euro/kg | Eq. (10) |
| $c^C$, $c^P$, $c^{TR}$, $c^T$, $c^S$ | Euro/kg | Eq. (10) |
| $c_{transp}$ | Euro/km | Eq. (11) |

Total cost is the sum of fixed and variable costs

$$C = C_{fix} + C_{var} \tag{6}$$

The expression for fixed costs is

$$C_{fix} = C_{pers} + C_A \tag{7}$$

where $C_{pers}$ is the annual cost for plant personnel and the term $C_A$ represents the amortization of plant value per year. Thus, the economic analysis performed through Eq. (4) refers to revenues and costs during 1 year. Economic analyses extended to a longer period are performed by calculating proper economic indices, such as the NPV.

Variable costs can be expressed as

$$C_{var} = c_{biomass} m_{biomass} + (c_{maint} + c_E m_E) E_{el} + c_d m_d \tag{8}$$

The overall specific cost $c_{biomass}$ for the different $n_{subst}$ substances can be estimated as

$$c_{biomass} = \sum_{i=1}^{n_{subst}} (c_{biomass})_i \tag{9}$$

Fuel cost for each $i$th single biomass can be then written as

$$(c_{biomass})_i = (c_{subst})_i + \{c^C + c^P + c^{TR} + c^T + c^S\}_i \tag{10}$$

where the cost takes into account the specific purchase cost of each substance and also the cost of the energy, which has to be supplied for the process itself. In particular, the cost for collecting the biomass can be estimated as in Eq. (11), by considering the specific transportation cost, the biomass supply distance (the factor of 2 accounts for the round-trip journey), and the biomass mass per trip

$$c^C = \frac{c_{transp} \cdot 2 \cdot D_{bs}}{m_{trip}} \tag{11}$$

Maintenance costs $c_{maint}$ are obtained as the sum of the costs for all scheduled maintenance actions

$$c_{maint} = \sum_{i=1}^{n_{sma}} (c_{sma})_i \tag{12}$$

The cost for emissions $c_E$ is calculated by taking into account the fact that the total amount of emissions is a function of the produced electric energy. So $m_E$ is the emission per unit of produced electric energy, and $c_E$ is the specific cost per unit of mass of emission.

Finally, the disposal costs are calculated as the disposal specific cost $c_d$ multiplied by the mass $m_d$ of process wastes (e.g., sludge).

Owing to their definition, specific revenues, reported in Eq. (5), and specific costs, reported in Eqs. (8)–(11), have different units, which are summarized in Table 1.

## 4 Application of the Model to the Anaerobic Digestion Through a Batch Process

Biogas can be obtained by means of the anaerobic digestion of a large number of different substances, e.g., municipal solid

wastes (landfill gas), sewage, farm slurry, agricultural products and wastes, and also process wastes [11,14,24,27,29–35].

A description of all the specific modules for a plant, which uses the anaerobic digestion batch process to produce fuel from biomass, is reported below.

*Collection and pretreatment.* This module allows the evaluation of mixture properties, mass, and energy fluxes through equations derived from the general equation (1).

*Property balance.* The value of each module property can be obtained as a weighted averaged sum with respect to the fraction (mass or volume basis depends on the considered property) of each substance (subscript i stands for the ith substance), i.e.,

$$P^{\mathrm{M}} = \sum_{\mathrm{i}=1}^{\mathrm{n}_1} (\chi_1^{\mathrm{M}} P_1^{\mathrm{M}})_{\mathrm{i}} - \sum_{\mathrm{i}=1}^{\mathrm{n}_2} (\chi_2^{\mathrm{M}} P_2^{\mathrm{M}})_{\mathrm{i}} + \sum_{\mathrm{i}=1}^{\mathrm{n}_{\mathrm{in}}} (\chi_{\mathrm{in}}^{\mathrm{M}} P_{\mathrm{in}}^{\mathrm{M}})_{\mathrm{i}} - \sum_{\mathrm{i}=1}^{\mathrm{n}_{\mathrm{out}}} (\chi_{\mathrm{out}}^{\mathrm{M}} P_{\mathrm{out}}^{\mathrm{M}})_{\mathrm{i}} \tag{13}$$

*Mass balance.* The mass balance can be expressed as

$$m^{\mathrm{M}} = \sum_{\mathrm{i}=1}^{\mathrm{n}_1} (m_1^{\mathrm{M}})_{\mathrm{i}} - \sum_{\mathrm{i}=1}^{\mathrm{n}_2} (m_2^{\mathrm{M}})_{\mathrm{i}} + \sum_{\mathrm{i}=1}^{\mathrm{n}_{\mathrm{in}}} (m_{\mathrm{in}}^{\mathrm{M}})_{\mathrm{i}} - \sum_{\mathrm{i}=1}^{\mathrm{n}_{\mathrm{out}}} (m_{\mathrm{out}}^{\mathrm{M}})_{\mathrm{i}} \tag{14}$$

*Energy balance.* The energy balance takes into account module inner and outer energy fluxes, both through the main flow (from Secs. 1 and 2) and through the energy supplied to (subscript "in") or exchanged from (subscript "out") the module

$$m^{\mathrm{M}} h^{\mathrm{M}} = \sum_{\mathrm{i}=1}^{\mathrm{n}_1} (m_1^{\mathrm{M}} h_1^{\mathrm{M}})_{\mathrm{i}} - \sum_{\mathrm{i}=1}^{\mathrm{n}_2} (m_2^{\mathrm{M}} h_2^{\mathrm{M}})_{\mathrm{i}} + \sum_{\mathrm{i}=1}^{\mathrm{n}_{\mathrm{in}}} (q_{\mathrm{in}}^{\mathrm{M}})_{\mathrm{i}} - \sum_{\mathrm{i}=1}^{\mathrm{n}_{\mathrm{out}}} (q_{\mathrm{out}}^{\mathrm{M}})_{\mathrm{i}} \tag{15}$$

The following can be said of Eq. (15).

- Specific enthalpies are evaluated in correspondence to actual temperatures, e.g., $h^{\mathrm{M}}$ is evaluated at module operating temperature.
- ${q_{\mathrm{in}}}^{\mathrm{M}}$ is the energy entering the module and can be modeled through the equation ${q_{\mathrm{in}}}^{\mathrm{M}} = \varepsilon^{\mathrm{M}} {q_{\mathrm{s}}}^{\mathrm{M}} + {q_{\mathrm{l}}}^{\mathrm{M}}$. The first contribution is given by the energy ${q_{\mathrm{s}}}^{\mathrm{M}}$ that has to be supplied to a heat exchanger characterized by the efficiency $\varepsilon^{\mathrm{M}}$. The second contribution is given by possible sources of loss, as for instance frictional losses or mixing losses, and is taken into account through the term ${q_{\mathrm{l}}}^{\mathrm{M}}$.
- ${q_{\mathrm{out}}}^{\mathrm{M}}$ represents thermal power losses toward the outside and can be written as

$$q_{\mathrm{out}}^{\mathrm{M}} = \alpha_{\mathrm{out}}^{\mathrm{M}} S_{\mathrm{out}}^{\mathrm{M}} (T^{\mathrm{M}} - T_{\mathrm{amb}}^{\mathrm{M}}) \tag{16}$$

Ambient temperature ${T_{\mathrm{amb}}}^{\mathrm{M}}$ can be defined by also considering the effect of solar radiation on external wall surface temperature, as in Ref. [18].

Both collection and pretreatment modules allow (i) water to be added to the mixture, so that its density is reduced and thus mixture processability is increased, and (ii) the recirculation of already-digested gas to improve bacteria action. Finally, the model determines the quantity of substance, which is extracted after pretreatment. For all fluxes, the model calculates mass fractions and all characteristic quantities for all components to be passed to the anaerobic digestion module.

*Transformation of biomass into fuel.* The process of biomass conversion into fuel through the anaerobic digestion process mainly depends on the following.

- Process temperature. Processes are usually classified as psychrophilic ($T_{\mathrm{proc}} < 30\,^{\circ}\mathrm{C}$), mesophilic ($T_{\mathrm{proc}} = 30\text{–}45\,^{\circ}\mathrm{C}$), or thermophilic ($T_{\mathrm{proc}} > 45\,^{\circ}\mathrm{C}$) [13].
- Biomass addition strategy: batch or continuous. The former option means that the digestion process takes place while the whole biomass lies inside the digester. Otherwise, biomass continuously flows through the digester.

To model anaerobic digestion processes, empirical correlations are adopted. Such relations express output methane mass as a function of mixture mass and of some coefficients (reported in Eq. (17)), which take into account the specific characteristics of each substance and can be determined experimentally [14]

$$m_{\mathrm{CH_4}}^{\mathrm{D}} = \sum_{\mathrm{k}=1}^{\mathrm{n}_{\mathrm{subst}}} (m_{\mathrm{mixt}}^{\mathrm{D}})_{\mathrm{j}} \mathrm{TS}_{\mathrm{j}} \mathrm{TVS}_{\mathrm{j}} Y_{\mathrm{j}}^{\mathrm{D}} \beta_{\mathrm{j}}^{\mathrm{D}} \tag{17}$$

where

- Total solid fraction (TS): $[m_{\mathrm{dry\_s}}/m_{\mathrm{subst}}]$
- Total volatile solid fraction (TVS): $[m_{\mathrm{org\_s}}/m_{\mathrm{dry\_s}}]$
- $Y$: maximum process yield, i.e., maximum producible methane per unit of mass of total volatile solids
- $\beta$: nondimensional coefficient (values in the range 0–1), which takes into account the dependence of methane yield on the residence time inside the digester.

Coefficients TS and TVS depend on the specific substance under consideration. Some values for municipal solid wastes and for different genera of fruit and vegetables can be found in Ref. [13]. Moreover, parameters $Y$ and $\beta$ do not only depend on the specific substance, but also on process temperature and on substance physical state (for instance, mixture acidity). While $Y$ can be quite easily found in specific literature for a large number of substances (as in Ref. [13]), the dependence of $\beta$ with respect to the residence time inside the digester can be found only for a few substances. Thus, in this paper, the same curve is adopted for all the considered substances. This curve is derived in Ref. [27], where it was assumed that the process of methane production can be modeled by considering the growth and the activity of microorganisms through statistics-based models. So the trend of yield with respect to the residence time was modeled through a noncentral $\chi^2$ distribution, whose parameters could be used to tune the function for the considered substance, for its physical state and type of process.

## 5 Simulation Assumptions

An extensive sensitivity parametric analysis was carried out to evaluate the influence of the following three quantities on the profitability of a system, which produces energy from biomass through a batch anaerobic digestion process:

- total mass of biomass
- number of batch digesters
- retention time, i.e., time spent by the biomass inside each digester, which depends on the number of yearly batch cycles

System profitability was evaluated according to the classical economic indices [36]: net present value, internal rate of return (IRR), and pay-back period (PBP) of the investment.

Due to the very high number of alternatives, the analyses reported in this paper are restricted to the following ESs, biomass types, and biomass yearly masses.

- Micro gas turbine (MGT) and internal combustion engine (ICE).
- Ensiled corn (EC) and organic fraction of municipal solid wastes (OFMSW).
- Biomass mass: yearly biomass (YB) mass was considered in the range 20,000–100,000 t/yr. By assuming a yearly specific production of 60 t/ha of corn (forage corn), this corresponds to a cultivated surface in the range 333–1667 ha (about 1.0–2.3 km in radius). In the case of OFMSW, the

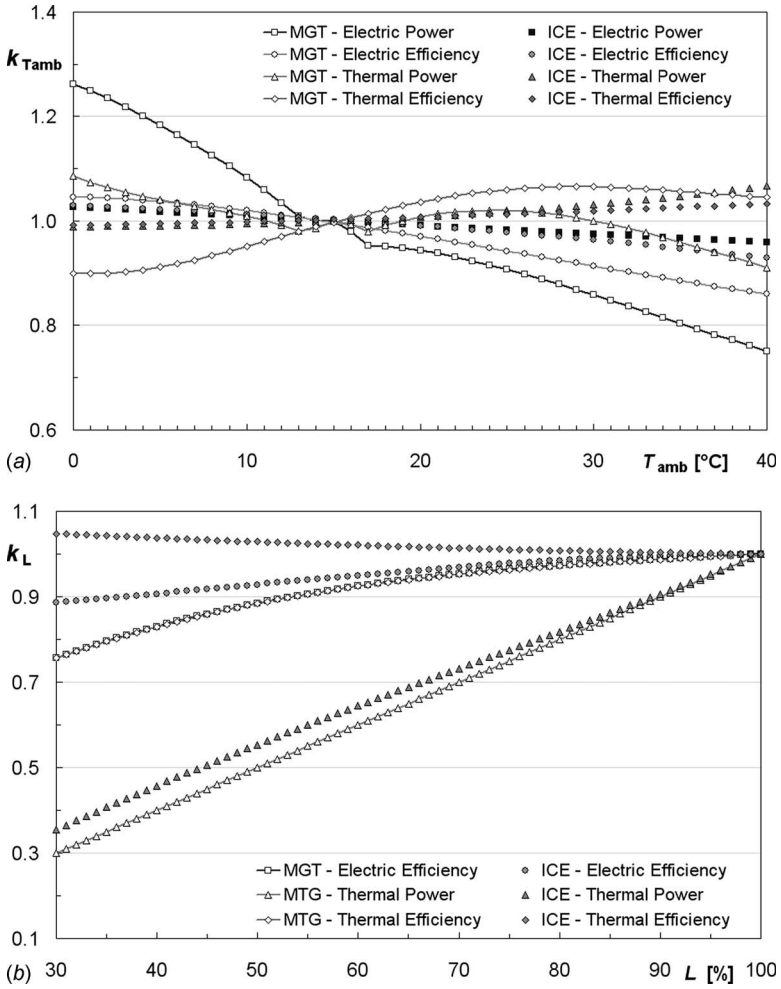


**Fig. 3 (*a*) Correction factor $k_{T_{amb}}$ versus ambient temperature and (*b*) correction factor $k_L$ versus load**

considered values of biomass correspond to a population of 100,000–500,000 inhabitants, by assuming a production of 0.2 t p.c. of OFMSW.

For each case analyzed, the respective specific costs were considered for both plant and ES installation.

*Energy system performance.* The electric and thermal power produced by an ES, as well as electrical and thermal efficiencies, depend on both ambient and load conditions. In the simulations, these effects were accounted by using the correction factors reported in Figs. 3(*a*) and 3(*b*), which show the trends of the correction factors for MGTs and ICEs versus ambient temperature and load, respectively. Correction factors for electric power are not reported in Fig. 3(*b*), since they are equal to the ratio between actual and nominal load. The values and trends of correction factors as a function of ambient temperature and of the load for MGTs and ICEs were derived, as reported in Table 2.

Monthly mean values of the ambient temperature over 1 year derived from Ref. [39] were used in the simulations. In addition to ambient temperature, the average values of wind speed [39] were considered in order to correctly estimate the heat transfer from the digesters and the pipelines toward the outside, according to Eq. (16).

In particular, for the simulations carried out in the paper, the Italian city of Ferrara was considered: monthly average ambient temperature ranges from 1.4°C to 23.9°C, with a yearly average value of 13.1°C [39], while the yearly average value of wind speed is approximately 2.4 m/s.

*Digester costs.* The digester cost was calculated by using the specific investment cost, which depends on digester volume, represented through the continuous line in Fig. 4. This line was obtained by using data from a biogas plant survey conducted in Germany [40]. Since costs in Ref. [40] were reported in German Marks (1999 value), they were converted into Euros and discounted at the 2007 value. Due to scale effect, digester specific cost decreases by increasing digester volume.

*Energy system costs.* The characteristics of the ESs considered

**Table 2 Sources of correction factors**

| ES | Parameter | $k_{Tamb}$ | $k_L$ |
|---|---|---|---|
| MGT | $P_{el}$ | [38] | a |
| | $P_{th}$ | b | [37] |
| | $\eta_{el}$ | [37] | [37] |
| | $\eta_{th}$ | [37] | b |
| ICE | $P_{el}$ | $(T_{amb}/T_{amb\_ref})^{0.5}$ | a |
| | $P_{th}$ | b | b |
| | $\eta_{el}$ | [37] | [37] |
| | $\eta_{th}$ | c | d |

[a]Calculated as a function of the load.
[b]Calculated through the equation $P_{th}=P_f \cdot \eta_{th}$.
[c]Calculated from $\eta_{el}$, $\eta_{th}$=f(load) (see Fig. 3(*b*)).
[d]Manufacturer's data.

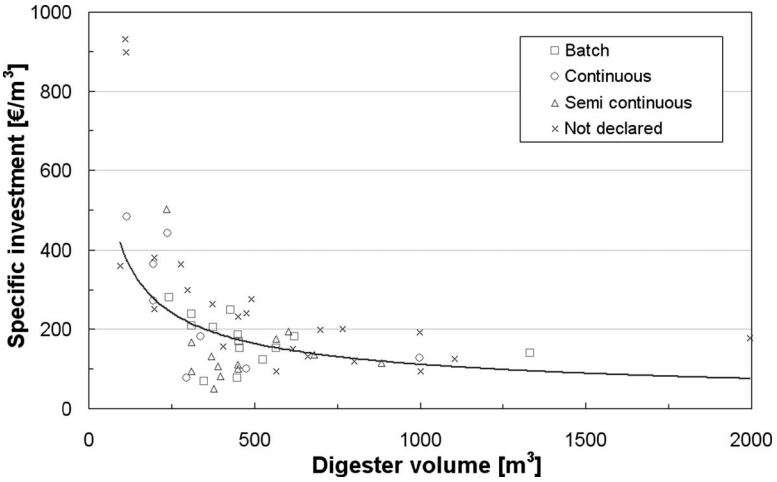


**Fig. 4 Field data [40] and interpolation function for digester specific cost**

for the simulations are shown in Table 3. Four different sizes for both ICEs (from 45 $kW_{el}$ to 232 $kW_{el}$) and MGTs (in the range 30–250 $kW_{el}$) were considered. Values for nominal power output and for electrical and thermal efficiencies were derived from manufacturer design data of commercial units. Specific costs were also derived from manufacturer data. However, the following considerations should be made:

- common experience reveals that specific installation costs for MGTs are still higher than those for ICEs, though in Table 3 they are almost comparable
- specific maintenance costs for MGTs are lower than those for ICEs, as usually happens in practice

With regard to ICEs, a scrubbing system is required to remove hydrogen sulfide from biogas. Thus, the presence of the scrubbing system leads to two additional sources of cost for ICEs: a specific capital cost, derived from manufacturer data and assumed equal to $0.6€/(Nm^3/yr)$ of biogas treated, and a specific operating cost, taken from Ref. [41] and equal to $0.03€/Nm^3$ of biogas treated.

MGTs do not require this system since they have proved to run with a percentage of hydrogen sulfide in the fuel up to 7% [42], and sulfur dioxide emissions from biogas-fed gas turbines are of the order of magnitude of distillated oil fed gas turbines [43]. If restrictions on this emission species are strengthened, a scrubbing system will be an effective sulfur dioxide reduction system and so, it will have to be considered also for MGTs.

As a final remark, the data reported in Table 3 refer to the situation in which flue gas treatment for pollutant abatement is not required. However, if emission regulations should become more strict, as is expected in the near future, costs for ICEs would increase, due to costs required for pollutant reduction systems (mainly $NO_x$), while the increase in MGT costs should be lower, since MGT emissions are usually lower than ICE emissions.

*Energy system configuration.* The identification of ES configuration results from the determination of the number of ESs for each size, once the typology (ICE or MGT) is selected. The main idea is that all ESs should work at 100% of load, with the exception of one of the ESs of minimum size, which instead is allowed to work at part load.

The procedure for the identification of ES configuration is sketched in Fig. 5. Starting from the available quantity of biomass, the yearly methane production can be determined through Eq. (17) and, thus, the available fuel power can also be obtained as the product between the yearly methane mass and methane lower heating value, divided by the yearly working hours (WHs) of the ES.

The number $n_{ES}^{(k)}$ of the ESs of type $k$ ($1 \leq k \leq 4$ in Table 3) is given by the integer part of the ratio between the available power and the power to be supplied to the single ES of type $k$. The power to be supplied through the fuel depends on both electrical effi-

**Table 3 ES characteristics**

| $k$ | 1 | 2 | 3 | 4 |
|---|---|---|---|---|
| Micro gas turbine | $MGT^{(1)}$ | $MGT^{(2)}$ | $MGT^{(3)}$ | $MGT^{(4)}$ |
| Nominal power ($kW_{el}$) | 250.0 | 100.0 | 60.0 | 30.0 |
| Electrical efficiency (%) | 30.0 | 30.0 | 28.0 | 26.0 |
| Thermal efficiency (%) | 46.0 | 48.0 | 54.0 | 50.0 |
| Specific installation cost (€/$kW_{el}$) | 1000 | 1100 | 1150 | 1200 |
| Specific maintenance cost (€/MWh) | 10.0 | 12.5 | 14.0 | 15.0 |
| Internal combustion engine[a] | $ICE^{(1)}$ | $ICE^{(2)}$ | $ICE^{(3)}$ | $ICE^{(4)}$ |
| Nominal power ($kW_{el}$) | 232.0 | 119.0 | 75.0 | 45.5 |
| Electrical efficiency (%) | 34.5 | 34.5 | 27.2 | 28.4 |
| Thermal efficiency (%) | 56.3 | 57.4 | 53.4 | 55.4 |
| Specific installation cost (€/$kW_{el}$) | 1000 | 1050 | 1100 | 1150 |
| Specific maintenance cost (€/MWh) | 11.0 | 14.5 | 15.0 | 15.0 |

[a]A scrubbing system is required for ICEs to remove hydrogen sulfide from biogas. Thus, the presence of the scrubbing system leads to two additional sources of cost for ICEs: a specific capital cost equal to $0.6€/(Nm^3/yr)$ and a specific operating cost equal to $0.03€/Nm^3$.

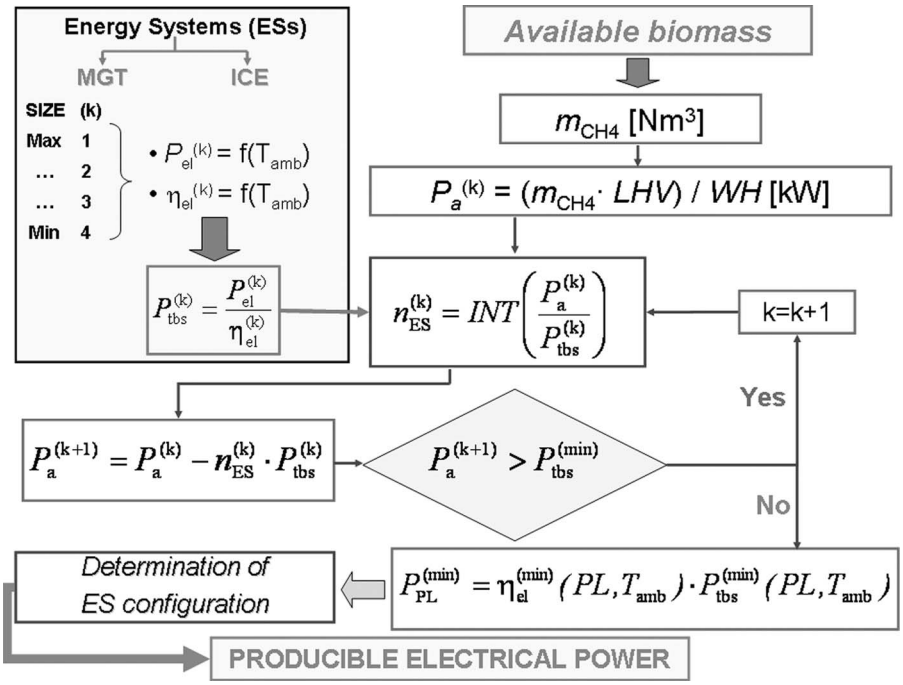


**Fig. 5 Procedure for ES configuration identification**

ciency and load, which in turn depend on ambient temperature. In fact, the values of $P_{el}$ and $\eta_{el}$ are updated as a function of the yearly average temperature in Ferrara.

Then, an iterative procedure starts. If the ESs of type $k$ do not require the whole available power (i.e., $P_a^{(k)} > n_{ES}^{(k)} P_{tbs}^{(k)}$) and the remaining available power $P_a^{(k+1)}$ is higher than the $P_{tbs}$ to the ES of lowest size (i.e., $P_a^{(k+1)} > P_{tbs}^{(min)}$), the model starts a new calculation loop to estimate the number of the ESs of lower size $(k+1)$, which can be supplied with the remaining available power $P_a^{(k+1)}$. Otherwise, if the remaining available power $P_a^{(k+1)}$ is lower than $P_{tbs}^{(min)}$, the model calculates the actual load for the ES of minimum size (power output at part load $P_{PL}$). As anticipated, this ES of minimum size is the only one allowed to work at part load. For this ES, the actual working load is calculated through an iterative procedure and then the load correction factor is determined.

Thus, the composition of ESs is determined and the producible electrical power can be calculated.

*Model input data.* The most significant model input data for the two considered substances (EC and OFMSW) are summarized in Table 4. The following remarks can be made.

- The anaerobic digestion process allows the exploitation of the OFMSW. So a revenue is usually granted, since the exploitation for digestion avoids OFMSW disposal costs. This is the reason why the OFMSW specific purchase cost is "negative" (i.e., −30€/t). In this paper, the economic costs for spreading the digested material are not considered; this analysis is reported in Ref. [44].
- Truck transport is usually applied for relatively short distances. Transport cost consists of a flat kilometer cost, fuel cost, and loading/unloading cost. In the paper, overall transport cost is estimated to be equal to 1.75€/km [45].
- Both pretreatment and digestion temperatures are assumed equal to 50°C. This choice has already been discussed previously in this paper.
- Electrical energy and thermal energy specific revenues were considered constant for all plant life and equal to 70.99€/$MWh_{el}$ and 30.00€/$MWh_{th}$, respectively. These values correspond to average selling prices in Italy in 2007.
- Green certificates are incentives supplied in Italy to plant owners producing electrical energy from renewable sources. The value of the green certificate was assumed equal to 137.49€/MWh (value at 2007), and it is granted for the whole electrical energy production for the first 12 years and only for 60% of the electrical energy production for the following 4 years.
- Economic analysis considers a period of 16 years, according to the duration of the green certificates. So the calculated values of NPV and IRR should be evaluated over a period of 16 years, as the time horizon considered for plant amortization was also 16 years. Instead the investment was supposed to be paid within 5 years.
- Specific plant cost, which has to be added to the cost of the energy system and of the digester, varies significantly from the plant fed by EC to the one fed by OFMSW. In fact, the specific cost is doubled, due to the higher cost of treating OFMSW to make it suitable for the digester. For the same reason, personnel costs are also higher.
- Plant yearly WHs are chosen according to the fact that MGTs usually present lower downtime than ICEs in industrial applications.
- The time for filling and emptying each digester for each cycle is assumed constant (i.e., independent of the number of digesters) and equal to 3 days. This time also takes into account the time required to heat the biomass inside the digesters. This assumption represents the situation in which plant configuration is properly designed to keep this parameter constant. Thus, the retention time (expressed in days) for a batch process can be calculated as follows:

$$\tau = \frac{365 - 3n_b}{n_b} \tag{18}$$

- For all calculations, transport costs are evaluated by considering an average fixed distance between the collection point and the plant equal to 20 km.
- Parasitic electrical energy demand is assumed equal to 18.3 kWh/t for EC [44] and equal to 80.0 kWh/t for

**Table 4 Model input data**

| Quantity | Unit | EC | OFMSW |
|---|---|---|---|
| **Biomass** | | | |
| Density | $t/m^3$ | 0.7 | 0.8 |
| Specific heat | kJ/(kg K) | 1.8 | 2.0 |
| Total solid | % | 34 | 29 |
| Total volatile solid | % | 86 | 76 |
| Yearly specific production | | 60 t/ha | 0.2 t p.c. |
| Specific purchase cost | €/t | 25 | −30 |
| Specific transport cost | €/km | 1.75 | |
| Biomass supply distance | km | 20 | |
| Biomass per trip | t/trip | 20 | |
| **Anaerobic digestion process** | | | |
| Pretreatment temp. | °C | 50 | |
| Digestion temp. | °C | 50 | |
| Biogas yield | $Nm^3/(t_{TVS})$ | 500 | 550 |
| Methane yield | $Nm^3/(t_{TVS})$ | 320 | 350 |
| Biogas LHV | $kJ/Nm^3$ | 21,450 | |
| Time for filling and emptying each digester | day/cycle | 3 | |
| **Economic parameters** | | | |
| Electrical energy specific revenue | $€/MWh_{el}$ | 70.99 | |
| Green certificates value | $€/MWh_{el}$ | 137.49 | |
| Thermal energy specific revenue | $€/MWh_{th}$ | 30.00 | |
| Amortization period | years | 16 | |
| Investment payment time | years | 5 | |
| Loan discount rate | % | 5 | |
| Insurance cost | % | 0.3 | |
| Taxes | % | 50 | |
| Specific plant cost | $k€/m^3$ | 0.6 | 1.2 |
| Personnel costs | k€/yr | 125 | 170 |
| Administration costs | k€/yr | 20 | |
| **Other** | | | |
| Yearly working hours | h/yr | 8500 (MGT) 8200 (ICE) | |
| Parasitic electrical energy | kWh/t | 18.3 | 80.0 |

OFMSW [46]. In fact, the electrical energy demand for OFMSW is higher than for EC because of the specific pretreatment process.

## 6 Sensitivity Analyses on the Profitability of the Energy System

The profitability of the whole system from biomass to energy production was evaluated according to different scenarios. It should be noticed that the electric energy selling price always includes the so-called "green certificates." However, a preliminary analysis showed that investment profitability is never reached by using EC, if these incentives are absent.

*Influence of yearly biomass.* The NPV trend as a function of the YB is shown in Fig. 6. The results refer to the case of 12 yearly batch cycles and 2 digesters.

As can be seen NPVs, evaluated after 16 years, increase as the

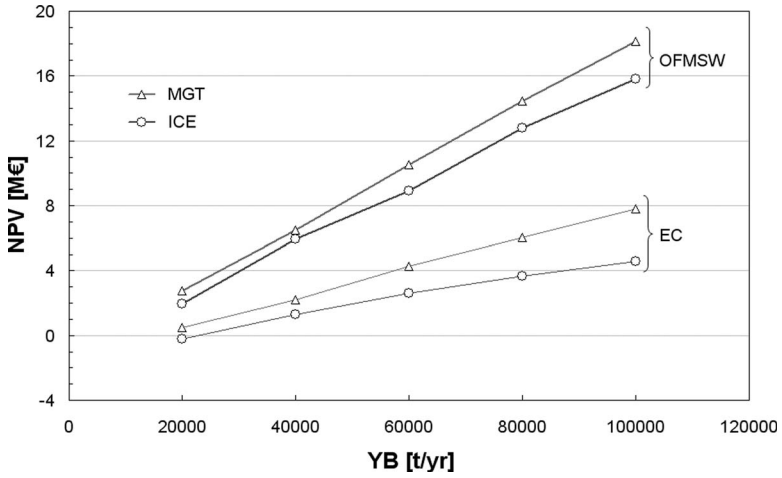


**Fig. 6 NPV trend versus yearly biomass ($n_b$=12 and $n_{dig}$=2)**

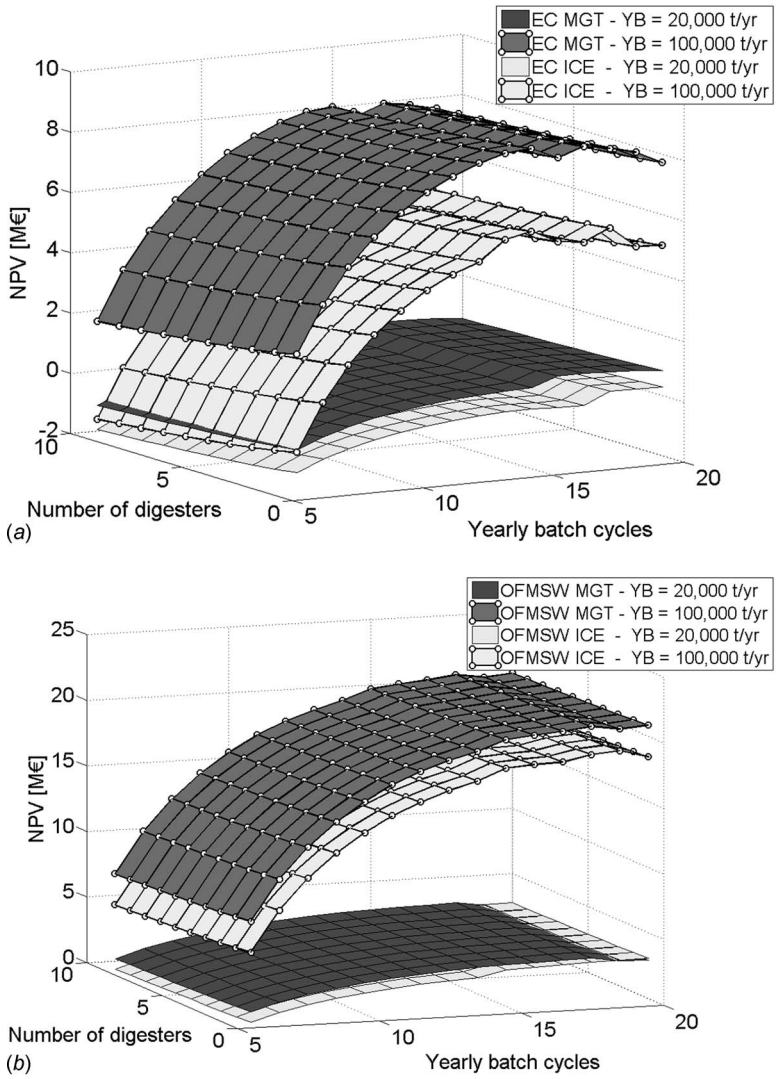


**Fig. 7 (*a*) NPV trend as a function of the number of digesters and the number of yearly batch cycles (biomass=EC, ES=MGT and ICE, YB=20,000 t/yr, and YB=100,000 t/yr) and (*b*) NPV trend as a function of the number of digesters and the number of yearly batch cycles (biomass =OFMSW, ES=MGT and ICE, YB=20,000 t/yr, and YB=100,000 t/yr)**

quantity of YB increases. For the same value of YB and given biomass typology, the NPV for ICE is lower than the NPV for MGT despite the fact that electrical and thermal efficiencies for ICEs are higher than those for MGTs, since ICEs need a scrubbing system, which increases both capital and operating costs.

Moreover, the results of simulations with OFMSW show that the NPVs are always higher than those obtained by using EC. In fact OFMSW specific purchase cost is negative and therefore a revenue is always guaranteed.

*Influence of the number of digesters.* As can be seen in Figs. 7(*a*) and 7(*b*) for the two considered types of biomass, the number of digesters does not significantly influence NPVs. In general, by increasing the number of digesters, NPV slightly decreases because of the increase in the thermal losses in the digesters. This leads to an increase in thermal energy to be used to maintain the digesters at the desired digestion temperature and therefore thermal energy available for sale decreases. Moreover, the specific digester cost decreases by increasing digester volume and by decreasing the number of digesters, according to Fig. 4.

*Influence of the number of yearly batch cycles.* Figures 7(*a*) and 7(*b*) also show the influence of $n_b$ on NPV. The values of $n_b$ analyzed are in the range 6–20 cycles/yr. For both ESs and for both types of biomass, NPV increases up to a value of $n_b$ equal to about 15 cycles/yr. In fact, by increasing the number of yearly batch cycles, the yearly methane production also increases. For $n_b$ higher than 15 cycles/yr, NPV remains, instead, approximately constant or even slightly decreases.

*Influence of the retention time.* In this section, the influence of the retention time on the number of yearly batch cycles, on yearly methane production and on NPV is investigated. The results reported refer to a YB mass equal to 100,000 t/yr and 2 digesters. Thus, the value of the volume of each digester results is equal to 5900 $m^3$ for EC and equal to 5200 $m^3$ for OFMSW. These values are in agreement with digester sizes of most of Italian plants. The results are summarized in Figs. 8(*a*) and 8(*b*) for the two types of considered biomass (EC and OFMSW) and ESs (MGT and ICE).

It can be observed that the yearly number of batch cycles obviously decreases by increasing the retention time.

The yearly methane production can be calculated as the product between the number of yearly batch cycles and the cycle methane production, which is calculated as the cumulative function of $\chi^2$

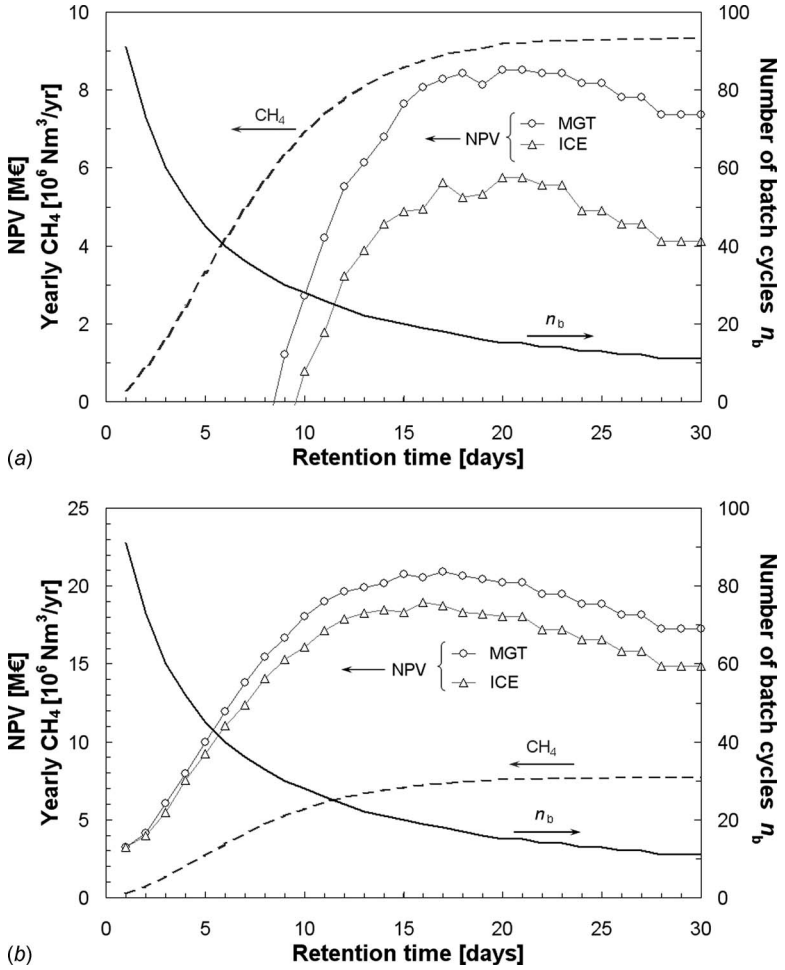


**Fig. 8 (*a*) Influence of biomass retention time (biomass=EC, ES=MGT and ICE, YB=100,000 t/yr, and $n_{dig}=2$) and (*b*) influence of biomass retention time (biomass=OFMSW, ES=MGT and ICE, YB=100,000 t/yr, and $n_{dig}=2$)**

distribution [27]. The adopted $\chi^2$ function considers that methane production starts at the first day of retention, while in practice some days are necessary to start the methanogenic process. However, this process could be accelerated by using special inoculations, which reduce the biochemical reaction start-up time. In any case, it can be observed that the yearly methane production increases by increasing the retention time, though its increase is not remarkable for a retention time higher than 15–20 days.

Figure 8(*a*) shows that NPV in the case of EC has a negative value for a retention time lower than about 10 days for ICE and lower than about 8 days for MGT. Then, its value continues to increase up to a retention time equal to 18–20 days and then it begins to decrease. In fact, after 18–20 days, both methane production and electric and thermal energy increase, but the increase in costs is higher than that of revenues. Moreover, NPV for MGTs is considerably higher than NPV for ICEs.

Figure 8(*b*) shows that the yearly methane production in the case of OFMSW is always slightly lower than that for EC, the difference being due to the different yield according to Eq. (17). However, the use of OFMSW always allows positive NPVs. In fact, even if the methane production process is not completely exploited due to the low retention time, positive revenues are guaranteed by waste disposal. Furthermore, the use of OFMSW also allows revenues, which are approximately twice those obtainable by digesting corn.

*Evaluation of PBP and IRR*. In order to investigate system economic performance further, the values of two additional economic indices, i.e., the PBP and the IRR, are calculated. The results are shown in Figs. 9 and 10, as a function of the number of yearly cycles and of YB mass, respectively.

Figure 9 shows that the PBP decreases with the number of yearly cycles for all the four cases analyzed and so the values of IRR increase. This behavior is due to the fact that plant costs, proportional to the total volume of the digesters, decrease when $n_b$ increases, since the quantity of biomass per cycle decreases. Even though $n_b$ is increased, the revenues decrease as (because of the lower methane production) the investment costs are lower and so PBP decreases.

Otherwise, Figure 10 shows that both PBP and IRR are not strongly influenced by the value of YB. In fact, PBP and IRR are almost constant for YB higher than about 40,000 t/yr. In fact, by increasing YB, both costs and revenues increase so that PBP and IRR remain approximately constant.

In the case of YB equal to 20,000 t/yr, the values of PBP are higher because the reduction in methane production, and so in the amount of electric and thermal energy sold, prevails against the reduction in investment costs.

Figures 9 and 10 show that in the case of EC, the PBP for ICEs is roughly 2–3 years higher than that of MGTs. Also for OFMSW, the values of the PBP for ICE are higher than the values referred to for MGT, but for this kind of biomass, the difference, which is approximately equal to 2 years, is lower. Therefore, in the case of OFMSW, the advantage of MGT against ICE is less significant.

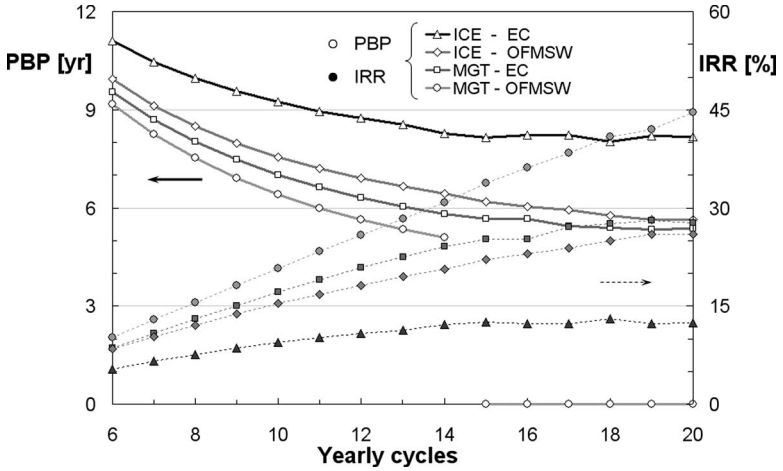


**Fig. 9 PBP and IRR as a function of the number of yearly cycles (YB =100,000 t/yr and $n_{dig}$=2)**

As can also be seen in Fig. 9, PBP for OFMSW and MGT falls to zero for 15 or more yearly cycles. This is due to the fact that the investment payment time is equal to 5 years and annual revenues are almost constant. Thus, if revenues are higher than costs for the first 5 years, PBP is equal to zero; otherwise, PBP is at least 5 years.

Moreover, the values of IRR in Fig. 9 vary between 10% and 30% for EC and MGT, while they are in the range of 5–12% for EC and ICE. Thus, in the case of EC and MGT, the IRR is twice the IRR in the case of EC and ICE. This behavior is also highlighted in the case of OFMSW (10–44% for MGT and 10–26% for ICE).

Figures 9 and 10 also show that in the case of OFMSW, the values of PBP are lower than the values for EC (about 2–3 years lower for ICE and 1–2 years lower for MGT).

*Influence of transport costs.* In this section, the influence of the distance between the biomass collection point and the location of the ES is evaluated. In all the simulations performed up until now, the distance between the biomass collection point and the ES was considered constant and equal to 20 km.

The values of NPV after 16 years as a function of the distance are shown in Fig. 11 for different cases. The simulations refer to the anaerobic digestion of EC (12 yearly batch cycles, 2 digesters, and MGT). Two different YB values (40,000 t/yr and 100,000 t/yr) and two different transport specific costs (1.75€/km and 3.50€/km) are considered.

This calculation gives an estimation of the distance value at which NPV is equal to zero for each value of YB. This value represents the maximum distance beyond which the investment is not profitable. This distance is also influenced by the different transport specific costs. In fact, for a transport specific cost equal to 1.75€/km, the maximum distance can be 40–50 km higher than the case relative to 3.50€/km.

In the analyzed cases, the values of maximum distance are in the range of 40–105 km. Therefore, in order to have an economic profit, a small distance between the collection point and the plant is necessary.

*Electric and thermal energy production.* In this section, the producible electric and thermal energy as a function of YB is evaluated. The values of YB considered for the calculations are included in the range 20,000–100,000 t/yr. Figure 12 shows the resources necessary to produce the considered quantity of YB. The cultivated surface is reported for the EC, while the number of inhabitants is considered for OFMSW. As can be seen from Fig. 12, for the YB values considered in the paper, the cultivated surface is lower than about 1700 ha (maximum radius equal to about 2.3 km) and the maximum number of inhabitants involved is 500,000.

The aim of the present analysis is to determine the electric and thermal energy as a function of the plant size (proportional to YB) and to compare the results obtained for different ESs and types of biomass. The results of the calculations are reported in Fig. 13 in

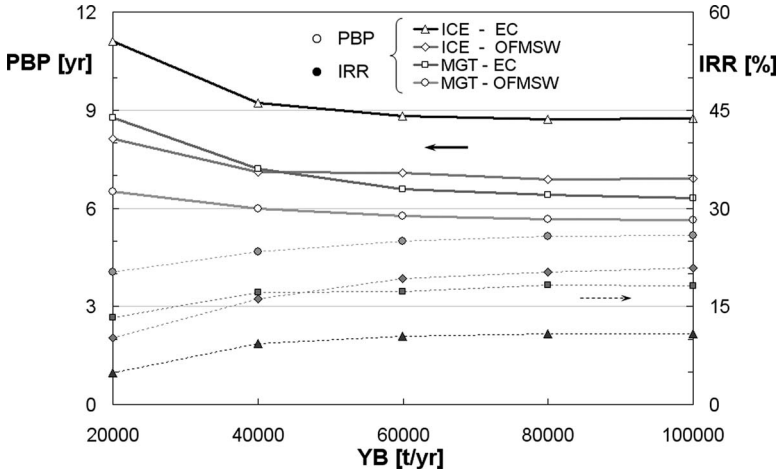


**Fig. 10 PBP and IRR as a function of YB ($n_b$=12 and $n_{dig}$=2)**

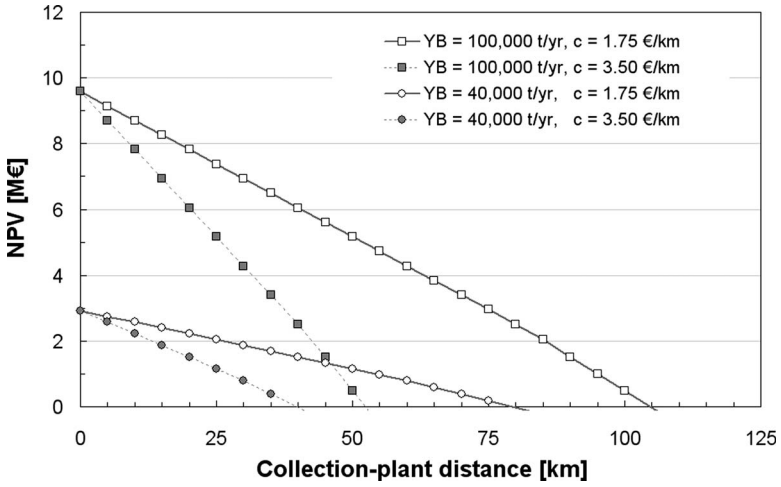


**Fig. 11 NPV trend as a function of distance (biomass=EC and ES=MGT)**

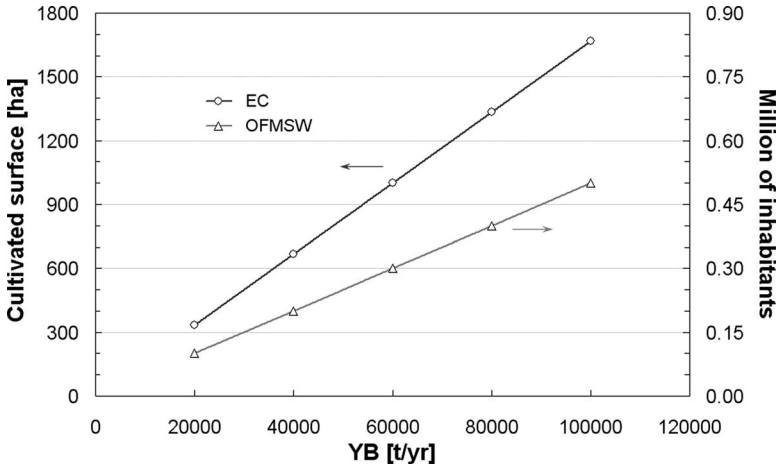


**Fig. 12 EC cultivated surface and number of inhabitants necessary for YB production**

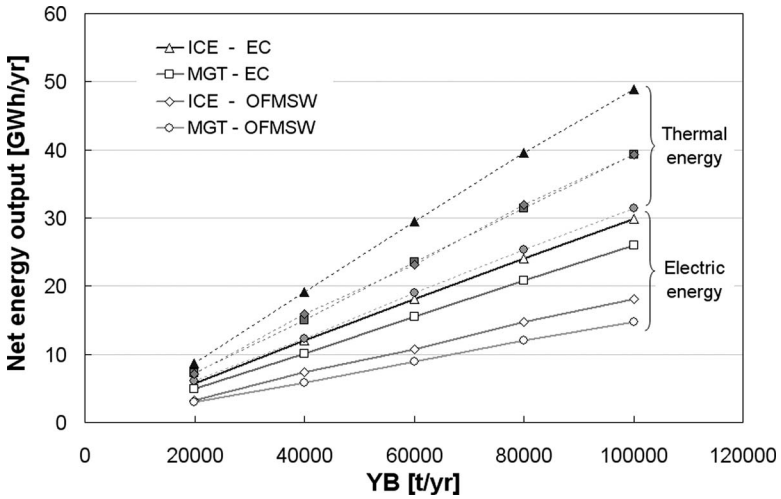


**Fig. 13 Electric and thermal producible energy versus yearly biomass ($n_b$=12 and $n_{dig}$=2)**

**Table 5 Specific producible energy (YB=100,000 t/yr for EC and YB=20,000 t/yr for OFMSW)**

| | | Unit | MGT | ICE |
|---|---|---|---|---|
| EC | Surface | ha | 1,667 | 1,667 |
| | $E_{el}$ | $GWh_{el}$ | 26.0 | 29.6 |
| | $E_{el\ sp}$ | $MWh_{el}$/ha | 15.6 | 17.9 |
| | Inhabitants (demand met) | | 21,620 | 24,793 |
| OFMSW | Inhabitants (waste producers) | | 100,000 | 100,000 |
| | $E_{el}$ | $GWh_{el}$ | 3.0 | 3.3 |
| | $E_{el\ sp}$ | $kWh_{el}$/p.c. | 30 | 33 |
| | Inhabitants (demand met) | | 2,460 | 2,701 |

terms of the net energy output, without considering the energy required for biomass production, collection, and transportation.

For a given value of YB, the electric and thermal energy produced through the EC is higher than the energy produced through the OFMSW. This result is due to the fact that, for the same value of YB, the methane production from EC is higher than that produced from OFMSW.

Moreover, the energy produced by using ICE is higher than the energy produced when using MGT. In fact the values of electric and thermal efficiencies for ICEs are higher than the values of the efficiencies for MGT. Since the thermal efficiency is higher than the electric efficiency for both ESs, the production of thermal energy always exceeds the production of electric energy.

*Evaluation of specific producible energy.* In this section, the calculation of the specific producible electric energy is reported. This represents the electric energy being referred to in 1 ha of cultivated surface in the case of EC and the electric energy per inhabitant for OFMSW. The results relative to a YB of 100,000 t/yr of EC and 20,000 t/yr of OFMSW are reported in Table 5. The cultivated surface and the number of inhabitants (waste producers) are calculated as the ratio between YB and the biomass specific yield (60 t/ha for the EC and 0.2 t p.c. for the OFMSW), according to Table 4.

By considering the yearly demand of electric energy for domestic use per capita in Ferrara equal to 1204 $kWh_{el}$/yr [47], the number of inhabitants, whose yearly electric energy demand is met, can be calculated.

For OFMSW, the ratio between the number of inhabitants whose yearly electric energy demand is met and the number of inhabitants who produced the considered quantity of OFMSW can also be calculated. For example, the electric energy obtained by using the quantity of OFMSW produced by the inhabitants of Ferrara (about 100,000) and equal to 20,000 t/yr, meets the yearly electric energy demand of 2460 inhabitants for MGT and of 2701 for ICE. This ratio is independent of the considered YB and is equal to 2.5% for MGT and 2.7% for ICE. This calculation highlights that this type of biomass should only be considered an additional energy source, and not an alternative energy source.

Table 5 also leads to the conclusion that each hectare cultivated with corn supplies an amount of electrical energy, which satisfies the demand of about 13–15 inhabitants. An alternative use of corn could be the production of food, starting from corn seeds. The corn seed yield can be assumed equal to 10 t/ha, while the yield previously considered in the paper referred to forage corn (yield equal to 60 t/ha, according to Table 4). By assuming a human daily energy need of 10,000 kJ and a corn seed energy content of 15,270 kJ/kg, it results that the same hectare can feed about 40 inhabitants for 1 year. This may lead to consider the use of corn for energy production only in the case of set-aside or marginal fields, and not in competition with alimentary cultivation.

*Primary energy saving evaluation.* An additional aspect to be considered is the determination of the efficiency of the CHP process. One of the methods to evaluate CHP process efficiency consists of the assessment of the primary energy saved with respect to the separate production of the same amount of electrical and thermal energy, by means of reference technologies. In Ref. [48] the primary energy saving (PES) index is defined as

$$\mathrm{PES} = 1 - \frac{\mathrm{E_f}}{\frac{E_{el}}{\eta_{el}^*} + \frac{E_{th}}{\eta_{th}^*}} \tag{19}$$

where $E_f$ represents the primary energy supplied to the system, $E_{el}$ is the produced electric energy, $E_{th}$ is the useful produced thermal energy, $\eta_{el}^*$ and $\eta_{th}^*$ are the harmonized efficiency reference values for separate production of electricity and heat, respectively.

To correctly evaluate the PES index of integrated biogas-fed ESs, the primary energy supplied to the system should be calculated by multiplying the yearly biomass by its LHV. Since the two typologies of biomass taken into account in this paper (EC and OFMSW) are mainly suitable for the digestion process, and not for direct firing, their primary energy contents cannot be clearly evaluated. For this reason, PES was calculated by using for $E_f$ the energy supplied by the biogas, while $E_{el}$ and $E_{th}$ are the electrical and thermal energies produced by the ESs, respectively. The value of $\eta_{el}^*$ referred to the standard ISO condition (15°C ambient temperature, 1.013 bar, and 60% relative humidity) is reported in Ref. [49]. For the present work, the value of $\eta_{el}^*$ is corrected as a function of the yearly average ambient temperature in Ferrara (13.1°C) and it is equal to 39%. This value also takes into account the correction factor for avoided grid losses in case of energy supplied to low-voltage (i.e., <0.4 kV) distribution grid. With regard to the reference thermal efficiency, in the case of biogas and thermal energy used for steam and hot water production, $\eta_{th}^*$ is equal to 70% according to Ref. [49].

Table 6 reports the maximum and minimum PES values, for all the considered plant configurations ($n_{dig}=1-10$, $n_b=6-20$, and YB=20,000–100,000 t). It can be noticed that PES values are always positive and higher in the case of ICEs than in the case of MGTs.

The values reported in Table 6 do not take into account the energy required for biogas production and therefore, they are not representative of the performance of an integrated biogas-fed ESs. Thus, the calculations were also performed by considering, for $E_f$ the energy supplied by the biogas, while, for $E_{el}$ and $E_{th}$, the net

**Table 6 Maximum and minimum PES values (gross produced electric and thermal energy)**

| | | MGT (%) | ICE (%) |
|---|---|---|---|
| EC | Min | 26 | 37 |
| | Max | 30 | 41 |
| OFMSW | Min | 25 | 36 |
| | Max | 30 | 41 |

**Table 7 Maximum and minimum PES values (net produced electric and thermal energy)**

| | | MGT (%) | ICE (%) |
|---|---|---|---|
| EC | Min | 18 | 31 |
| | Max | 26 | 38 |
| OFMSW | Min | −5 | 16 |
| | Max | 10 | 28 |

produced energies were considered. These electrical and thermal energies account for the energy used for biogas production. Results are summarized in Table 7.

Also in this case, the PES index can reach very high values (i.e., 38% by means of ICE), but these values are obviously lower than that in the previous case. Negative PES values may also occur in the case of OFMSW (high value of parasitic electrical energy) and MGT (low electrical efficiency), when a number of yearly batch cycles higher than 18 is adopted. This is due to the fact that a high value of yearly batch cycles corresponds to a low value of retention time and so, to an incomplete digestion of the biomass. This means that the CHP production from biomass can be justified from an energy point of view when a proper design of the plant is carried out. Based on local legislation, this may lead to further economic incentives. In any case, the reduction in primary energy consumption also allows a reduction in plant emissions.

## 7 Conclusions

In this paper, a physics-based model for the simulation of an integrated energy system, which is fed by biogas produced by means of a batch anaerobic digestion process, was applied to evaluate the economic profitability and the producible energy.

The analyses carried out allow the comparison of the results for different scenarios characterized by different types of biomass (ensiled corn and organic fraction of municipal solid wastes), yearly mass of biomass, anaerobic digestion process parameters (number of yearly batch cycles and number of batch digesters), and type of energy systems (micro gas turbine and internal combustion engine). The results are presented in terms of classical economic indices for the investment and of producible electric and thermal energy.

With respect to the economic indices, micro gas turbines allow a higher profitability than internal combustion engines, mainly because internal combustion engines require a scrubbing system to remove hydrogen sulphide from biogas. The contrary occurs with the producible electric and thermal energy because internal combustion engines usually have higher electric and thermal efficiencies.

Even if the methane yield is lower for organic fraction of municipal solid wastes than for ensiled corn, the results for organic fraction of municipal solid wastes show that the NPVs are always higher than those obtained by using ensiled corn and that they are always positive. In fact, waste specific purchase cost is negative and therefore a revenue is always guaranteed. Otherwise, the electric and thermal energies are higher for ensiled corn than for the organic fraction of municipal solid wastes. This result is due to the higher methane yield of the ensiled corn and to a higher electrical energy self-consumption needed for pretreatment of organic fraction of municipal solid waste.

From the evaluation of the efficiency of the CHP process, PES values usually show quite high values and confirm the good capability of these systems.

It should be noted that the numerical results are specific to the data assumed for performing the simulations. However, data were chosen according to present market availability. In any case, the directional results should hold.

## Acknowledgment

The work was carried out with the support of the Italian Ministry of University and Research (MiUR).

The work was also funded by the Emilia-Romagna Region within the framework of the research project "Biogas production for electric and thermal power generation starting from organic municipal wastes."

## Nomenclature

$c$ = specific cost
$C$ = cost
$D$ = field dimension
$D_{bs}$ = biomass supply distance
$E$ = energy
$h$ = specific enthalpy
IRR = internal rate of return
$k$ = index for energy systems, correction factor
$k_l$ = coefficient of power losses
$L$ = load
LHV = lower heating value
$m$ = mass
$M$ = mass flow rate
$n$ = number
NPV = net present value
$P$ = power, property
PBP = pay-back period
p.c. = per capita
PL = part load
$q$ = exchanged thermal power
$r$ = specific revenue
$R$ = revenue
$S$ = surface
$T$ = temperature
TS = total solids
TVS = total volatile solids
$Y$ = yield
YB = yearly biomass
$\alpha$ = overall heat transfer coefficient
$\beta$ = nondimensional coefficient to account for the dependence on time of methane yield
$\chi$ = volume or mass fraction
$\varepsilon$ = heat exchanger efficiency
$\Phi$ = quantity
$\eta$ = efficiency
$\tau$ = retention time

**Subscripts**

1, 2, in, and out = module sections
a = available
A = amortization
amb = ambient
b = yearly batch cycle
biomass = biomass product
$CH_4$ = methane
d = disposal
dig = digester
dry_s = dry substance
E = emissions
Eel = electrical energy
el = electrical
ES = energy system
Eth = thermal energy
f = fuel
field = field
fix = fixed
l = loss
L = load
maint = maintenance
mixt = mixture
nonfood = nonfood
org_s = volatile organic substance
pers = personnel
PL = part load
proc = process
ref = reference
s = supplied
sma = scheduled maintenance action
sp = specific
subst = substance
tbs = to be supplied

th = thermal
transp = transportation
trip = trip
var = variable

**Superscripts**

* = normalized with respect to ISO conditions
C = collection
D = digester
M = module
min = minimum size
P = pretreatment module
S = storage
T = treatment
TR = transformation process

## References


[1] Parikka, M., 2004, "Global Biomass Fuel Resources," Biomass Bioenergy, **27**(6), pp. 613–620.
[2] Akhmatov, V., and Knudsen, H., 2007, "Large Penetration of Wind and Dispersed Generation Into Danish Power Grid," Electr. Power Syst. Res., **77**, pp. 1228–1238.
[3] Paatero, J. V., and Lund, P. D., 2007, "Effects of Large-Scale Photovoltaic Power Integration on Electricity Distribution Networks," Renewable Energy, **32**, pp. 216–234.
[4] Arscott, L., 2004, "Sustainable Development in the Oil & Gas Industry," ASME J. Energy Resour. Technol., **126**, pp. 1–5.
[5] Said, C., 2007, "Nothing Flat About Tortilla Prices," San Francisco Chronicle, p. C-1.
[6] Jordan, N., Boody, G., Broussard, W., Glover, J. D., Keeny, D., McCown, B. H., McIsaac, G., Muller, M., Murray, H., Neal, J., Pansing, C., Turner, R. E., Warner, K., and Wyse, D., 2007, "Sustainable Development of the Agricultural Bio-Economy," Science, **316**, pp. 1570–1571.
[7] Righelato, R., and Spracklen, D. V., 2007, "Carbon Mitigation by Biofuels or by Saving and Restoring Forests?," Science, **317**, p. 902.
[8] MacLean, H. L., and Lave, L. B., 2003, "Evaluating Automobile Fuel/Propulsion System Technologies," Prog. Energy Combust. Sci., **29**, pp. 1–69.
[9] Read, P., 2008, "Biosphere Carbon Stock Management: Addressing the Threat of Abrupt Climate Change in the Next Few Decades: An Editorial Essay," Clim. Change, **87**, pp. 305–320.
[10] Fargione, J., Hill, J., Tilman, D., Polasky, S., and Hawthorne, P., 2008, "Land Clearing and the Biofuel Carbon Debt," Science, **319**, pp. 1235–1238.
[11] Sofer, S. S., and Zaborsky, O. R., 1981, *Biomass Conversion Processes for Energy and Fuels*, Plenum, New York.
[12] Anani, A., Jibrill, Z., and Abu-Allan, F., 1990, "Standardized Charts for Cost-Benefit Analysis of Biogas Systems: Case Study in Jordan," Sol. Wind Technol., **7**, pp. 229–236.
[13] Gunaseelan, V. N., 1997, "Anaerobic Digestion of Biomass for Methane Production: A Review," Biomass Bioenergy, **13**, pp. 83–114.
[14] Zhang, R., and Zhang, Z., 1999, "Biogasification of Rice Straw With an Anaerobic-Phased Solids Digester System," Bioresour. Technol., **68**, pp. 235–245.
[15] McKendry, P., 2002, "Energy Production From Biomass (Part 1): Overview of Biomass," Bioresour. Technol., **83**, pp. 37–46.
[16] Bohn, D., and Lepers, J., 2003, "Effects of Biogas Combustion on the Operation Characteristics and Pollutant Emissions of a Micro Gas Turbine," ASME Paper No. GT2003-38767.
[17] Fantozzi, F., D'Alessandro, B., and Desideri, U., 2003, "IPRP—Integrated Pyrolysis Regenerated Plant—An Efficient and Scalable Concept for Gas Turbine Based Energy Conversion From Biomass and Waste," ASME Paper No. GT2003-38653.
[18] Jurado, F., Cano, A., and Carpio, J., 2003, "Modeling of Combined Cycle Power Plants Using Biomass," Renewable Energy, **28**, pp. 743–753.
[19] Rodrigues, M., Walter, A., and Faaij, A., 2003, "Co-Firing of Natural Gas and Biomass Gas in Biomass Integrated Gasification/Combined Cycle System," Energy, **28**, pp. 1115–1131.
[20] Green, A. E. S., Swanson, G. P., and Najafi, F. T., 2004, "Co-Utilization of Fossil and Renewable Fuel: Biomass Gas/Natural Gas," ASME Paper No. GT2004-54194.
[21] Jurado, F., Cano, A., and Carpio, J., 2004, "Biomass Based Micro-Turbine Plant and Distribution Network Stability," Energy Convers. Manage., **45**, pp. 2713–2727.
[22] Green, A., and Feng, J., 2005, "Assessment of Technologies for Biomass Conversion to Electricity at the Wild Land-Urban Interface," ASME Paper No. GT2005-68294.
[23] Lupandin, V., Thamburaj, R., and Nikolayev, A., 2005, "Test Results of the OGT2500 Gas Turbine Engine Running on Alternative Fuels: Biooil, Ethanol, Biodiesel and Crude Oil," ASME Paper No. GT2005-68488.
[24] Parker, W. J., 2005, "Application of ADM1 Model to Advanced Anaerobic Digestion," Bioresour. Technol., **96**, pp. 1832–1842.
[25] Dornburg, V., Faaij, A. P. C., and Meuleman, B., 2006, "Optimising Waste Treatment Systems—Part A: Methodology and Technological Data for Optimising Energy Production and Economic Performance," Resour. Conserv. Recycling, **49**, pp. 68–88.
[26] Porta, M., Traverso, A., and Marigo, L., 2006, "Thermoeconomic Analysis of a Small-Size Biomass Gasification Plant for Combined Heat and Distributed Power Generation," ASME Paper No. GT2006-90918.
[27] Bettocchi, R., Pinelli, M., Spina, P. R., Venturini, M., Cenci, G., and Morini, M., 2007, "Energy Production From Biomass: Development of a General Model and Application to Anaerobic Digestion," ASME Paper No. GT2007-27039.
[28] Murphy, J. D., and Power, N., 2007, "A Technical, Economic, and Environmental Analysis of Energy Production From Newspaper in Ireland," Waste Manage., **27**, pp. 177–192.
[29] Benefield, L. D., and Randall, C. W., 1985, "Sludge Digestion," *Biological Process Design for Wastewater Treatment*, Ibis, Charlottesville, VA, Chap. 8.
[30] Rittmann, B. E., and McCarty, P. L., 2001, "Anaerobic Treatment by Methanogenesis," *Environmental Biotechnology: Principles and Applications* (Biological Sciences), McGraw-Hill, New York, Chap. 13.
[31] Kalia, V. C., and Joshi, A. P., 1995, "Conversion of Waste Biomass (Pea-Shells) Into Hydrogen and Methane Through Anaerobic Digestion," Bioresour. Technol., **53**, pp. 165–168.
[32] Jeyaseelan, S., 1997, "A Simple Mathematical Model for Anaerobic Digestion Process," Water Sci. Technol., **35**(8), pp. 185–191.
[33] Kiely, G., Tayfur, G., Dolan, C., and Tanji, K., 1997, "Physical and Mathematical Modelling of Anaerobic Digestion of Organic Wastes," Water Sci. Technol., **31**(3), pp. 534–540.
[34] Keshtkar, A., Meyssami, B., Abolhamd, G., Ghaforian, H., and Khalagi Asadi, M., 2003, "Mathematical Modeling of Non-Ideal Mixing Continuous Flow Reactors for Anaerobic Digestion of Cattle Manure," Bioresour. Technol., **87**, pp. 113–124.
[35] Blumensaat, F., and Keller, J., 2005, "Modeling of Two-Stage Anaerobic Digestion Using the IWA Anaerobic Digestion Model No. 1 (ADM1)," Water Res., **39**, pp. 171–183.
[36] Thuesen, G. J., and Fabrycky, W. J., 2000, *Engineering Economy* (International Series in Industrial and Systems Engineering), 9th ed., Prentice-Hall, Englewood Cliffs, NJ.
[37] Macchi, E., Campanari, S., and Silva, P., 2005, *La microgenerazione a gas naturale*, Polipress, Milano, Italy, in Italian.
[38] Thermoflow Inc., 2007, THERMOFLOW 17, Release 1, Sudbury, MA.
[39] 1994, "Heating and Cooling of Buildings. Climatic Data," Italian National Standard, Paper No. UNI 10349, in Italian.
[40] Schafer, W., 2003, "Biogas On-Farm: Energy and Material Flow," Proceedings of the Nordic Association of Agricultural Scientists 22nd Congress, Turku, Finland, Jul. 1–4.
[41] Murphy, J. D., McKeogh, E., and Kiely, G., 2004, "Technical/Economic/Environmental Analysis of Biogas Utilization," Appl. Energy, **77**, pp. 407–427.
[42] Kolanowski, B. F., 2004, *Guide to Microturbines*, Fairmont, Lilburn, GA.
[43] U.S. Environmental Protection Agency (EPA), 2001, "Compilation of Air Pollutant Emission Factors," Report No. AP-42.
[44] Berglund, M., and Börjesson, P., 2006, "Assessment of Energy Performance in the Life-Cycle of Biogas Production," Biomass Bioenergy, **30**, pp. 254–266.
[45] Hamelinck, C. N., Suurs, R. A. A., and Faaij, A. P. C., 2005, "International Bioenergy Transport Costs and Energy Balance," Biomass Bioenergy, **29**, pp. 114–134.
[46] Murphy, J. D., and McCarthy, K., 2005, "The Optimal Production of Biogas for Use as a Transport Fuel in Ireland," Renewable Energy, **30**, pp. 2111–2127.
[47] National Institute of Statistics (Istat), http://www.istat.it/english.html.
[48] Commission of the European Communities, 2004, "Directive 2004/8/EC of the European Parliament and of the Council of 11 February 2004 on the promotion of Cogeneration Based on a Useful Heat Demand in the Internal Energy Market and Amending Directive 92/42/EEC," Official Journal of the European Union, **L52**, pp. 50–60.
[49] Commission of the European Communities, 2007, "Commission Decision of 21 December 2006 Establishing Harmonised Efficiency Reference Values for Separate Production of Electricity and Heat in Application of Directive 2004/8/EC of the European Parliament and of the Council," Official Journal of the European Union, **L32**, pp. 183–188.

# Large Eddy Simulation of Premixed Combustion With a Thickened-Flame Approach

**Ashoke De**
Department of Mechanical Engineering,
Louisiana State University,
Baton Rouge, LA 70803

**Sumanta Acharya**[1]
Professor
Department of Mechanical Engineering and
Turbine Innovation and Energy Research Center,
Louisiana State University,
Baton Rouge, LA 70803
e-mail: acharya@me.lsu.edu

*A thickened-flame (TF) modeling approach is combined with a large eddy simulation (LES) methodology to model premixed combustion, and the accuracy of these model predictions is evaluated by comparing with the piloted premixed stoichiometric methane-air flame data of Chen et al. (1996, "The Detailed Flame Structure of Highly Stretched Turbulent Premixed Methane-Air Flames," Combust. Flame, **107**, pp. 233–244) at a Reynolds number Re = 24,000. In the TF model, the flame front is artificially thickened to resolve it on the computational LES grid and the reaction rates are specified using reduced chemistry. The response of the thickened-flame to turbulence is taken care of by incorporating an efficiency function in the governing equations. The efficiency function depends on the characteristics of the local turbulence and on the characteristics of the premixed flame such as laminar flame speed and thickness. Three variants of the TF model are examined: the original thickened-flame model, the power-law flame-wrinkling model, and the dynamically modified TF model. Reasonable agreement is found when comparing predictions with the experimental data and with computations reported using a probability distribution function modeling approach. The results of the TF model are in better agreement with data when compared with the predictions of the G-equation approach.* [DOI: 10.1115/1.3094021]

*Keywords: thickened-flame, flame-wrinkling, turbulence, gas turbine emission, large eddy simulation*

## 1 Introduction

The majority of the land based gas turbines are operated in a premixed mode due, in part, to environmental regulations for reducing $NO_x$. To properly design premixed combustion systems, accurate predictions of premixed flames are desirable. Since the capability of the classical approach of using Reynolds averaged Navier–Stokes (RANS) equations in conjunction with phenomenological combustion models [1] is limited, numerical simulations of reacting flows based on large eddy simulations (LES) have been pursued since they are well suited to provide accurate and cost-effective predictions. The main philosophy behind LES of a reacting flow is to explicitly simulate the large scales of the flow and reactions, and to model the small scales. Hence, it is capable of capturing the unsteady phenomenon more accurately. The unresolved small scales or subgrid scales must be modeled accurately to include the interaction between the turbulent scales. For premixed combustion, since the typical premixed flame thickness is smaller than the computational grid ($\Delta$), the small-scale or subgrid scale modeling must also take care of the interaction between turbulence and the combustion processes. In the thickened-flame (TF) model [2] the flame is artificially thickened to resolve it on the computational mesh and to enable reaction rates from kinetic models to be specified in the flame region using reduced mechanisms. The influence of turbulence is represented by a parametrized efficiency function. A key advantage of the TF model is that it directly solves the species transport equations and uses the Arrhenius formulation for the evaluation of the reaction rates.

In the present paper, the TF model [2] is used, along with its variants, the power-law flame-wrinkling model [3,4], and the dynamically modified version of these models [5]. A generic premixed combustion configuration is adopted for which experimental data [6] and numerical predictions with other approaches [7,8] are available. These simulations and comparison with the benchmark data will help identify the accuracy of the TF modeling approach. In particular, earlier studies with this approach [2–4] have not provided a comparative assessment of the model and its variants with respect to detailed measurements, nor have the model predictions been compared with those from the more commonly used, but computationally more expensive, probability distribution function (PDF) approach, and the commonly used *G*-equation approach. This paper provides the first detailed comparative assessment (which includes velocity, turbulence kinetic energy, temperature, and major species) of all three modeling approaches and experimental data.

## 2 Flow Modeling Using LES

To model the turbulent flow field, LES is used so that the energetic larger-scale motions are resolved, and only the small-scale fluctuations are modeled. Therefore, the equations solved are the filtered governing equations for the conservation of mass, momentum, energy, and species transport in curvilinear coordinate system [9–11]. The subgrid stress modeling is done using a dynamic Smagorinsky model where the unresolved stresses are related to the resolved velocity field through a gradient approximation

$$\widetilde{u_i u_j} - \tilde{u}_i \tilde{u}_j = -2\nu_t \bar{S}_{ij} \tag{1}$$

$$\text{where} \quad \nu_t = C_s^2(\Delta)^2|\bar{S}| \tag{2}$$

$$\bar{S}_{ik} = \frac{1}{2}\left( (\boldsymbol{a}^m)_k \frac{\partial \bar{u}_i}{\partial \xi_m} + (\boldsymbol{a}^m)_k \frac{\partial \bar{u}_k}{\partial \xi_m} \right) \tag{3}$$

[1]Corresponding author.

Manuscript received October 15, 2008; final manuscript received October 17, 2008; published online July 14, 2009. Review conducted by Dilip R. Ballal. Paper presented at the ASME Turbo Expo 2008: Land, Sea and Air (GT2008), Berlin, Germany, June 9–13, 2008.

$$|\bar{S}| = \sqrt{2\bar{S}_{ik}\bar{S}_{ik}} \tag{4}$$

and $S$ is the mean rate of strain. The coefficient $C_s$ is evaluated dynamically [12,13] and locally averaged.

## 3 Combustion Modeling

Modeling the flame-turbulence interaction in premixed flames requires tracking of the thin flame front on the computational grid. Three major approaches have been used in the combustion modeling community.

(a) *G-equation model.* This approach treats the flame surface as an infinitely propagating surface (flamelet), and hence the flame thickness is treated approximately to zero [14,15]. The propagating surface, which is called the flame front, is tracked using a field variable or isosurface $G_o$. This technique is valid in both the corrugated flamelet regime and the thin reaction zone regime. However, the signed-distance function (which views the scalar $G$ surrounding the front as the signed distance to the front) plays an important role since the $G$-equation only captures the instantaneous flame front. This dependence on the distance function is an inherent drawback of this method.

(b) *PDF approach.* The probability density function (PDF) is a stochastic method, which directly considers the probability distribution of the relevant stochastic quantities in a turbulent reacting flow. This kind of PDF description of turbulent reacting flow has some theoretical benefits, such as the complex chemistry is taken care of without applying any ad hoc assumptions (such as "flamelet" or "fast reaction"). Moreover, it can be applied to nonpremixed, premixed, and partially premixed flames without having much difficulty. Usually, there are two ways that are mainly used to calculate the PDF: one is *presumed* PDF approach, and the other is PDF *transport balance equation* approach. The presumed PDF approach, which essentially assumes the shape of the probability function $P$, is relatively simpler to use; however, it has severe limitations in the context of applicability. On the other hand, the PDF transport balance equation approach solves a transport equation for PDF function, which is applicable for multispecies, mass-weighted probability density function. This method has considerable advantage over any other turbulent combustion model due to its inherent capability of handling any complex reaction mechanism. However, the major drawback of transport PDF approach is its high dimensionality, which essentially makes the implementation of this approach to different numerical techniques, such as finite volume method (FVM) or finite element method (FEM), limited, since their memory requirements increase almost exponentially with dimensionality. Usually, Monte Carlo algorithms, which reduce the memory requirements, are used by Pope [16]. Moreover, a large number of particles need to be present in each grid cell to reduce the statistical error; however, this makes it a very time consuming process. So far, the transport equation method has been only applied to relatively simple situations.

(c) *Thickened-flame model.* In this technique, the flame front is artificially thickened to resolve on computational grid. Corrections are made to ensure that the flame is propagating at the same speed as the unthickened-flame [2,3]. The key benefit of this approach, as noted earlier, rests in the ability to computationally resolve the reaction regions and the chemistry in these regions. More details on this approach are described in Sec. 4.

In the present paper we use the thickened-flame approach due to its ability of using less computational resources, and the model predictions are examined for a methane flame with detailed velocity and temperature data [6] available. As noted earlier, the paper will provide a detailed evaluation of the TF model relative to two other popular choices, the PDF model and the $G$-equation model.

## 4 TF Model

Butler and O'Rourke [17] were the first to propose the idea of capturing a propagating premixed flame on a coarser grid. The basic idea with this approach is that the flame is artificially thickened to include several computational cells and by adjusting the diffusivity to maintain the same laminar flame speed $s_L^0$. It is well known from the simple theories of laminar premixed flames [18,19] that the flame speed and flame thickness can be related through the following relationship:

$$s_L^0 \propto \sqrt{D\bar{B}}, \quad \delta_L^0 \propto \frac{D}{s_L^0} = \sqrt{\frac{D}{\bar{B}}} \tag{5}$$

where $D$ is the molecular diffusivity and $\bar{B}$ is the mean reaction rate. When the flame thickness is increased by a factor $F$, the molecular diffusivity and reaction rate are modified accordingly ($FD$ and $\bar{B}/F$) to maintain the same flame speed. The major advantages associated with thickened-flame modeling are as follows: (i) The thickened-flame front, which is resolved on LES mesh, is usually less than typical premixed flame thickness (around 0.1–1 mm), (ii) quenching and ignition events can be simulated, and (iii) chemical reaction rates are calculated exactly like in a direct numerical simulation (DNS) calculation without any ad hoc submodels so that it can theoretically be extended to incorporate multistep chemistry [2].

In LES framework, the spatially filtered species transport equation can be written as

$$\frac{\partial \bar{\rho}\tilde{Y}_i}{\partial t} + \frac{\partial}{\partial x_j}(\bar{\rho}\tilde{Y}_i\tilde{u}_j) = \frac{\partial}{\partial x_j}\left(\bar{\rho}D_i\frac{\partial \tilde{Y}_i}{\partial x_j}\right) - \frac{\partial}{\partial x_j}[\bar{\rho}(\widetilde{Y_i u_j} - \tilde{Y}_i\tilde{u}_j)] + \bar{\dot{\omega}}_i \tag{6}$$

where the terms on the right-hand side are the filtered diffusion flux, the unresolved transport, and the filtered reaction rate, respectively. In general, the unresolved term is modeled with a gradient diffusion assumption by which the laminar diffusivity is augmented by turbulent eddy diffusivity. However, in the TF model, the "thickening" procedure multiplies the diffusivity term by a factor $F$, which has the effect of augmenting the diffusivity. Therefore, the gradient approximation for the unresolved fluxes is not explicitly used in the closed species transport equations. The corresponding filtered species transport equation in the thickened-flame model becomes

$$\frac{\partial \bar{\rho}\tilde{Y}_i}{\partial t} + \frac{\partial}{\partial x_j}(\bar{\rho}\tilde{Y}_i\tilde{u}_j) = \frac{\partial}{\partial x_j}\left(\bar{\rho}FD_i\frac{\partial \tilde{Y}_i}{\partial x_j}\right) + \frac{\bar{\dot{\omega}}_i}{F} \tag{7}$$

Although the filtered thickened-flame approach looks promising, a number of key issues need to be addressed. The thickening of the flame by a factor of $F$ modifies the interaction between turbulence and chemistry, like the Damköhler number, Da, which is a ratio of the turbulent ($\tau_t$) and chemical ($\tau_c$) time-scales, is decreased by a factor $F$ and becomes Da/$F$, where

$$\mathrm{Da} = \frac{\tau_t}{\tau_c} = \frac{l_t s_L^0}{u' \delta_L^0} \tag{8}$$

As the Da is decreased, the thickened-flame becomes less sensitive to turbulent motions. Therefore, the subgrid scale effects have been incorporated into the thickened-flame model, and parametrized using an efficiency function $E$ derived from DNS results [2,3]. Using the efficiency function, the final form of species transport equation becomes

$$\frac{\partial \bar{\rho}\tilde{Y}_i}{\partial t} + \frac{\partial}{\partial x_j}(\bar{\rho}\tilde{Y}_i\tilde{u}_j) = \frac{\partial}{\partial x_j}\left(\bar{\rho}EFD_i\frac{\partial \tilde{Y}_i}{\partial x_j}\right) + \frac{E\bar{\omega}_i}{F} \tag{9}$$

where the modified diffusivity $ED$, before multiplication by $F$ to thicken the flame front, may be decomposed as $ED=D(E-1)+D$ and corresponds to the sum of molecular diffusivity, $D$, and a turbulent subgrid scale diffusivity, $(E-1)D$. In fact, $(E-1)D$ can be regarded as a turbulent diffusivity used to close the unresolved scalar transport term in the filtered equation.

**4.1 The Original TF Model.** The central ingredient of the TF model is the subgrid scale wrinkling function $E$, which is defined by introducing a dimensionless wrinkling factor $\Xi$. The factor $\Xi$ is the ratio of flame surface to its projection in the direction of propagation. The efficiency function, $E$, is written as a function of the local filter size ($\Delta_e$), local subgrid scale turbulent velocity ($u'_{\Delta_e}$), laminar flame speed ($s_L^0$), and the thickness of the laminar and the artificially thickened-flame ($\delta_L^0, \delta_L^1$). Colin et al. [2] proposed the following expressions for modeling the efficiency function:

$$\Xi = 1 + \beta\frac{u'_{\Delta_e}}{s_L^0}\Gamma\left(\frac{\Delta_e}{\delta_L^0}, \frac{u'_{\Delta_e}}{s_L^0}\right) \tag{10}$$

$$\beta = \frac{2\ln 2}{3c_{\mathrm{ms}}(\mathrm{Re}_t^{1/2} - 1)}, \quad c_{\mathrm{ms}} = 0.28, \quad \mathrm{Re}_t = u' l_t/\nu \tag{11}$$

where $\mathrm{Re}_t$ is the turbulent Reynolds number. The local filter size $\Delta_e$ is related with laminar flame thickness as

$$\Delta_e = \delta_L^1 = F\delta_L^0 \tag{12}$$

The function $\Gamma$ represents the integration of the effective strain rate induced by all scales affected due to artificial thickening, and is estimated as

$$\Gamma\left(\frac{\Delta_e}{\delta_L^0}, \frac{u'_{\Delta_e}}{s_L^0}\right) = 0.75\exp\left[-1.2\left(\frac{u'_{\Delta_e}}{s_L^0}\right)^{-0.3}\right]\left(\frac{\Delta_e}{\delta_L^0}\right)^{2/3} \tag{13}$$

Finally, the efficiency function takes the following form as defined by the ratio between the wrinkling factor, $\Xi$, of laminar flame ($\delta_L = \delta_L^0$) to thickened-flame ($\delta_L = \delta_L^1$):

$$E = \frac{\Xi|_{\delta_L=\delta_L^0}}{\Xi|_{\delta_L=\delta_L^1}} \geq 1 \tag{14}$$

where the subgrid scale turbulent velocity is evaluated as $u'_{\Delta_e} = 2\Delta_x^3|\nabla^2\nabla\times\tilde{u}|$, and $\Delta_x$ is the grid size. This formulation for subgrid scale velocity estimation is free from dilatation. Usually, $\Delta_e$ differs from $\Delta_x$, and it has been suggested that values for $\Delta_e$ be at least $10\Delta_x$ [2].

**4.2 Power-Law Flame-Wrinkling Model.** This model uses a different estimation of efficiency function that was proposed by Charlette et al. [3,4]. This approach basically relates the flame surface area to a cutoff length, which limits wrinkling at the smallest length-scales of the flame. Based on asymptotic analysis, the efficiency function is evaluated using the following relationships:

$$E = \left(1 + \min\left[\frac{\Delta_e}{\delta_L^0}, \Gamma\frac{u'_{\Delta_e}}{s_L^0}\right]\right)^{\alpha} \tag{15}$$

where $\Gamma$ is defined as

$$\Gamma\left(\frac{\Delta_e}{\delta_L^0}, \frac{u'_{\Delta_e}}{s_L^0}, \mathrm{Re}_\Delta\right) = [((f_u^{-a} + f_\Delta^{-a})^{-1/a})^{-b} + f_{\mathrm{Re}}^{-b}]^{-1/b} \tag{16}$$

$$f_u = 4\left(\frac{27C_k}{110}\right)\left(\frac{18C_k}{55}\right)\left(\frac{u'_{\Delta_e}}{s_L^0}\right)^2 \tag{17}$$

$$f_\Delta = \left[\frac{27C_k\pi^{4/3}}{110} \times \left(\left(\frac{\Delta_e}{\delta_L^0}\right)^{4/3} - 1\right)\right]^{1/2} \tag{18}$$

$$f_{\mathrm{Re}} = \left[\frac{9}{55}\exp\left(-\frac{3}{2}C_k\pi^{4/3}\ \mathrm{Re}_\Delta^{-1}\right)\right]^{1/2} \times \mathrm{Re}_\Delta^{1/2} \tag{19}$$

The constants $a$, $b$, and $C_k$ control the sharpness of the transitions between the asymptotic behaviors. The suggested values are $b=1.4$, $C_k=1.5$,

$$a = 0.6 + 0.2\exp[-0.1(u'_{\Delta_e}/s_L^0)] - 0.20\exp[-0.01(\Delta_e/\delta_L^0)]$$

$$\Delta_e = F\delta_L^0, \quad \mathrm{Re}_\Delta = 4\frac{\Delta_e}{\delta_L^0}\frac{u'_{\Delta_e}}{s_L^0} \tag{20}$$

In the present work, $\alpha=0.5$ is used, resulting in the nondynamic formulation for power-law model.

**4.3 Dynamically Modified TF Model.** The major issue associated with TF model is that it modifies the diffusion term (multiplying with a thickening factor $F$) throughout the whole computational domain. This may lead to inaccuracies in the species mass fraction prediction, especially in the case of inhomogeneous premixed or partially premixed combustion. To overcome this disadvantage, a dynamically thickened-flame model has initially been developed at CERFACS [20,21]. Recently, Durand and Polifke [5] came up with a different expression for the diffusivity that is based on the reaction progress variable, and is used in the present work in the following form:

$$F_{\mathrm{loc}} = 1 + (F-1)\Omega(c) \tag{21}$$

$$\Omega(c) = 16[c(1-c)]^2, \quad c = 1 - \frac{Y_F}{Y_F^{\mathrm{st}}} \tag{22}$$

$$D_{i,\mathrm{loc}} = \frac{\mu}{\mathrm{Sc}}EF_{\mathrm{loc}} + (1 - F_{\mathrm{loc}})\frac{\mu_t}{\mathrm{Sc}_t} \tag{23}$$

As seen in the above equation, the global thickening factor $F$ and diffusivity $D$ are both represented in terms of a local function $\Omega(c)$, evaluated based on reaction progress variable. Hence, the species transport equation is also modified and takes the form

$$\frac{\partial \bar{\rho}\tilde{Y}_i}{\partial t} + \frac{\partial}{\partial x_j}(\bar{\rho}\tilde{Y}_i\tilde{u}_j) = \frac{\partial}{\partial x_j}\left(\bar{\rho}EF_{\mathrm{loc}}D_{i,\mathrm{loc}}\frac{\partial \tilde{Y}_i}{\partial x_j}\right) + \frac{E\bar{\omega}_i}{F_{\mathrm{loc}}} \tag{24}$$

All of these afore-mentioned models are used in the present work in conjunction with one- and two-step global Arrhenius chemistries.

## 5 Chemistry Model

As all the species are explicitly resolved on the computational grid, the thickened-flame model is best suited to resolve major species. Intermediate radicals with very short time-scales cannot be resolved. To this end, only simple global chemistry has been used with the thickened-flame model. In the present study, one- and two-step reaction chemistries are explored.

A single-step scheme, which includes five species ($CH_4$, $O_2$, $H_2O$, $CO_2$, and $N_2$), is given by the following expression:

$$CH_4 + 2O_2 \rightarrow CO_2 + 2H_2O$$

where the reaction rate expression is given by

$$q_1 = A \exp(-T_a/T)[CH_4]^a[O_2]^b \quad (25)$$

The activation temperature $T_a$ is 24,358 K, parameters $a=0.2$, $b=1.3$, and pre-exponential factor $A=2.29\times10^{13}$ as given by Kim and Maruta [22].

A two-step chemistry, which includes six species ($CH_4$, $O_2$, $H_2O$, $CO_2$, CO, and $N_2$), is given by the following equation set:

$$CH_4 + 1.5O_2 \rightarrow CO + 2H_2O$$

$$CO + 0.5O_2 \leftrightarrow CO_2$$

The corresponding reaction rate expressions are given by

$$q_1 = A_1 \exp(-E^1{}_a/RT)[CH_4]^{a1}[O_2]^{b1} \quad (26)$$

$$q_2(f) = A_2 \exp(-E^2{}_a/RT)[CO][O_2]^{b2} \quad (27)$$

$$q_2(b) = A_2 \exp(-E^2{}_a/RT)[CO_2] \quad (28)$$

where the activation energy $E^1{}_a=34{,}500$ cal/mol, $E^2{}_a=12{,}000$ cal/mol, $a1=0.9$, $b1=1.1$, $b2=0.5$, and $A_1$ and $A_2$ are $2\times10^{15}$ and $1\times10^9$, respectively, as given by Selle et al. [23]. Properties including density of mixtures are calculated using CHEMKIN-II [24] and TRANFIT [25] depending on the local temperature and the composition of the mixtures at 1 atm.

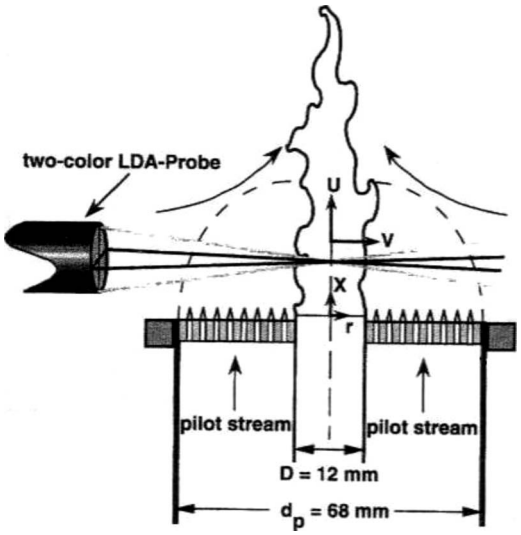


**Fig. 1 Schematic of the Bunsen burner with enlarge pilot flame [6]**

## 6 Solution Procedure

In the present study, a parallel multiblock compressible flow code for an arbitrary number of reacting species, in generalized curvilinear coordinates, is used. Chemical mechanisms and thermodynamic property information of individual species are input in standard CHEMKIN format. Species equations along with momentum and energy equation are solved implicitly in a fully coupled fashion using a low Mach number preconditioning technique, which is used to effectively rescale the acoustics scale to match that of convective scales [26]. An Euler differencing for the pseudotime derivative and second order backward three-point differencing for physical time derivatives are used. A second order low diffusion flux-splitting algorithm is used for the convective terms [27]. However, the viscous terms are discretized using second order central differences. An incomplete lower-upper (ILU) matrix decomposition solver is used. Domain decomposition and load balancing are accomplished using a family of programs for partitioning unstructured graphs and hypergraphs and computing fill-reducing orderings of sparse matrices, METIS. The message communication in distributed computing environments is achieved using message passing interface (MPI). The multiblock structured curvilinear grids presented in this paper are generated using commercial grid generation software GRIDPRO™.

## 7 Flow Configuration

The configuration of interest in the present work is the Bunsen burner geometry investigated by Chen et al. [6], and is shown in Fig. 1. The flame is a stoichiometric premixed methane-air flame, stabilized by an outer pilot. The incoming streams of both the main and pilot jets have the same composition. The main jet nozzle diameter ($D$) is 12 mm. The pilot stream is supplied through a perforated plate (1175 holes of 1 mm in diameter) around the main jet, with an outer diameter of $5.67D$. The Reynolds number used in the present work is Re=24,000 (flame $F3$ in Ref. [6]). Based on the estimated characteristic length- and time-scales given in Ref. [6], $u'/S_L=11.9$, $l/l_f=13.7$, flame $F3$ corresponds to the thin reaction zone regime.

The computational domain extends $20D$ downstream of the fuel-air nozzle exit, $4D$ upstream of the nozzle exit, and $4D$ in the radial direction. Two different LES grids are studied (for cold flow only): one that consists of $300\times94\times64$ grid points downstream of the nozzle exit plus $50\times21\times64$ grid points upstream, and corresponds to approximately $1.88M$ grid points (mesh1: coarse); and the other, the finer mesh, consists of $444\times140\times96$ grid points downstream of the nozzle plus $74\times31\times96$ grid points upstream, and contains approximately $5.91M$ grid points (mesh2: fine).

At the inflow boundary, the instantaneous velocities are computed using a random flow generation technique [28]. Convective boundary conditions [29] are prescribed at the outflow boundary, and stress-free conditions are applied on the lateral boundary in order to allow the entrainment of fluid into domain. The time step used for the computation is $dt=1.0\times10^{-3}$, and the heated pilot temperature chosen is 2005 K. The inlet temperature of the main premixed fuel-air jet and the initial temperature in the calculation domain are specified as 300 K [30].

## 8 Nonreacting Flow Results

In order to validate the flow solver, LES calculation for the nonreacting flow is reported in this section. That ensures that the grid and boundary conditions are properly chosen, and that the subgrid model is able to capture the modeled turbulence adequately.

Figure 2($a$) represents the instantaneous snap shot of the velocity fields. The evolution of three components of velocities is clearly observed and shows that the radial and tangential velocities are of the same order of magnitude, and considerably lower in magnitude relative to the peak axial velocity. The premixed-jet breakup appears to occur about 3–4 jet-diameters downstream of injection.

**8.1 Mean Axial Velocity.** The mean axial velocity profiles in the radial directions at different axial locations are shown in Fig. 3. The time-averaged mean velocity is normalized by the bulk velocity $U_o=30$ m/s. As observed from the experimental data and predictions, the jet shows the expected spreading behavior. The potential core appears to persist up to about $X/D=4.5$, beyond which the centerline mean velocity decreases as the jet expands in the radial direction. These effects are well reproduced by the LES simulations, and the overall predictions are in good agreement with the experimental results. Moreover, the coarse mesh ($1.88M$ grid points) results are in good agreement with the fine mesh ($5.91M$ grid points), and indicate that the $1.88M$ node calculations are grid-independent.

**8.2 Turbulent Kinetic Energy.** The radial profile of the turbulent kinetic energy, normalized by square of the bulk velocity, at different axial locations is shown in Fig. 3. It is evident from the figure that the computed results are reasonably well predicted

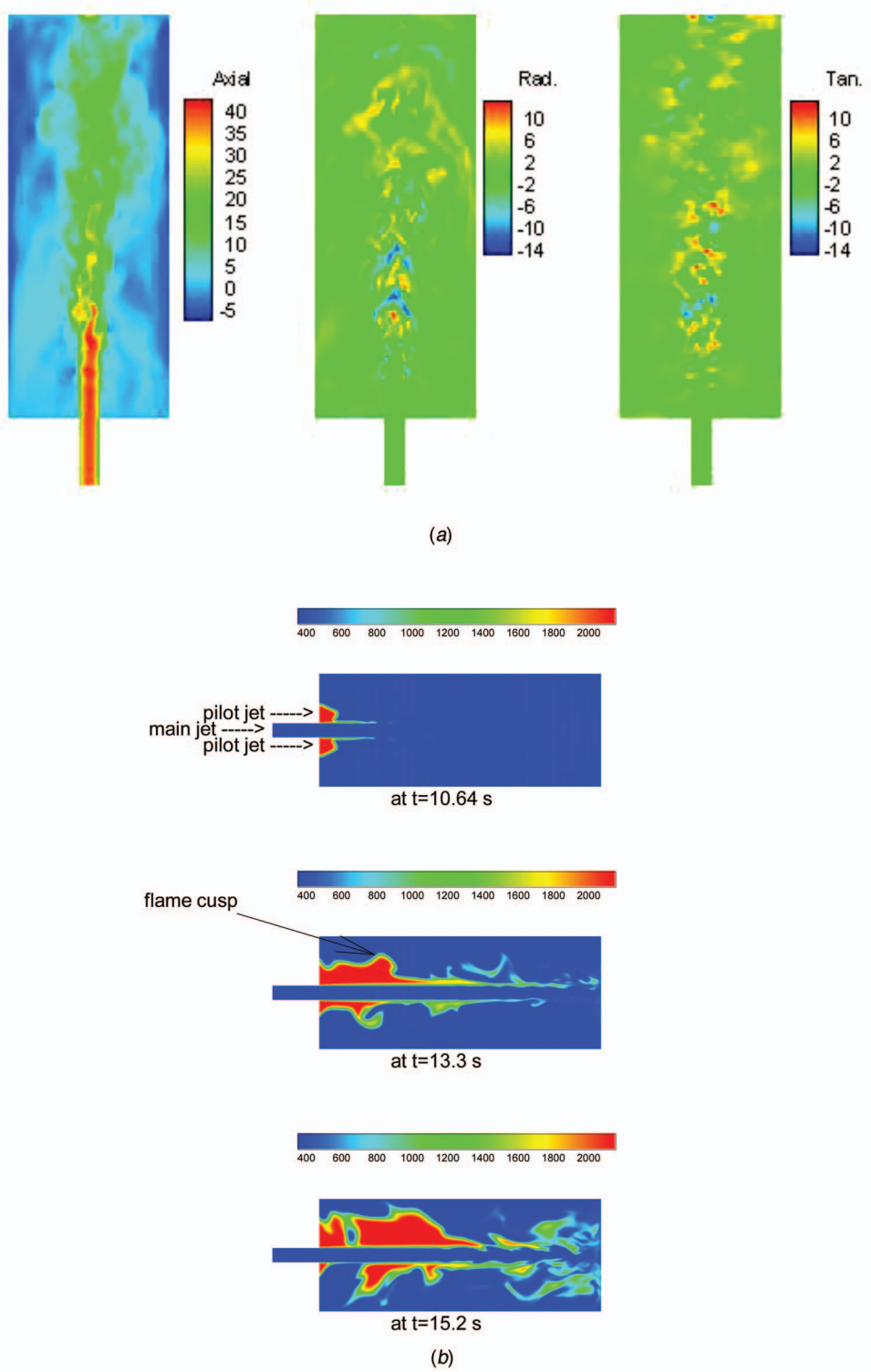


**Fig. 2 Instantaneous flow field. (*a*) Velocity (m/s) and (*b*) temperature (K).**

and compare well with the experimental data set. At $X/D=4.5$, the centerline peak value for the fine mesh is slightly overpredicted, but at $X/D=6.5$ this overprediction is eliminated. The evolution of kinetic energy follows the expected trend and initially shows the kinetic energy peak in the mixing layer formed by the primary-jet and the coaxial air-stream. Further downstream, the mixing layers merge and the kinetic energy peak moves toward the centerline as seen at $X/D=8.5$.

## 9 Reacting Flow Results: Assessment of Model Variants

Figure 2(*b*) shows a typical evolution of instantaneous flame front, which is represented by the temperature field. As time increases the flame front is seen to expand radially and in the downstream directions with the burnt regions having higher flame temperatures, and the unburnt regions (in blue) at lower temperatures.

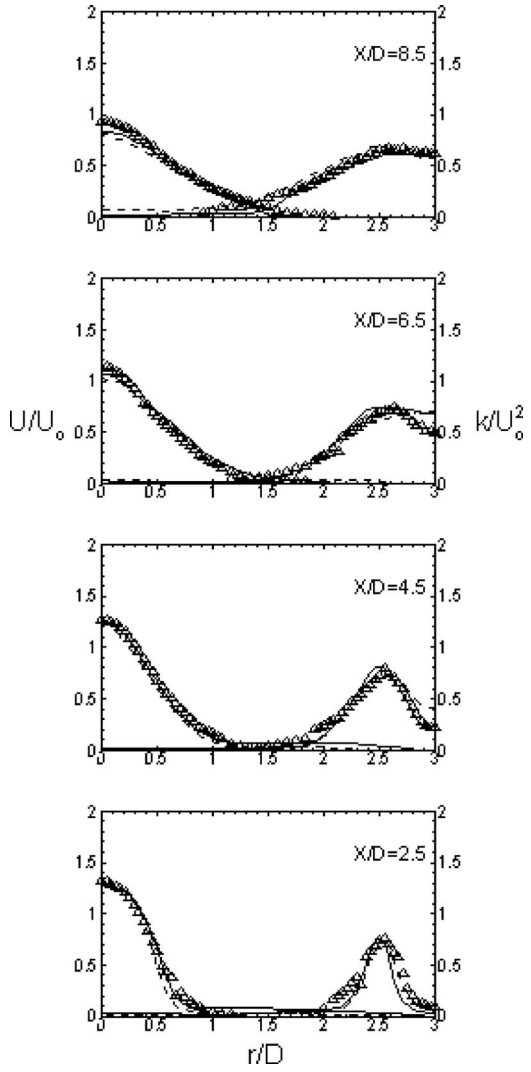


**Fig. 3 Cold flow: mean axial velocity $U/U_o$ and turbulent kinetic energy $k/U_o^2 \times 20$. Experimental data are shown by symbols (△) and lines are LES results: coarse (—) and fine (- - - - -).**

The cusp formation (regions with negative curvature) is clearly observed from the instantaneous field along the boundaries of the burnt (product side) and unburnt (air or premixed fuel-air side) regions. The cusps are usually formed toward the product side, where the flow field is accelerated due to the heat release from the flame. However, the small-scale cusp formation is reduced by thickening the flame front artificially (seen as narrow band in Fig. 2(*b*)), and this reduces the flame-wrinkling as well.

**9.1 Comparison of the TF Model and Its Variants.** Figure 4 shows the predicted results for variants of TF model using two-step and one-step chemistries. It is observed that the various TF model predictions do not show any major differences. The dynamic versions of the models do show some improvements, while the power-law model for the two-step chemistry model also shows an improvement in the prediction of the peak kinetic energy. However, the profiles with all the models are relatively close to each other and no model consistently shows improved prediction over the others at the various $X/D$ locations. Hence, based on this comparison, the original TF model would be an appropriate choice, and therefore, further calculations reported are based on the original TF model. It is also observed that the velocity predictions using the *G*-equation model do not show good agreement with the measurements while both the TF model and the PDF model predictions are in good agreement with the mean velocity data. The turbulent kinetic energy predictions with the PDF model appear to be overpredicted at $X/D=2.5$ at all radial locations, while the TF model tends to underpredict at radial locations close to centerline.

**9.2 Chemistry Model Comparison.** The mean temperature profiles obtained from different chemistry models are presented in Fig. 5. The mean progress variable is defined as $C=(T-T_u)/(T_b-T_u)$, where $T_u=298$ K and $T_b=2248$ K.

It is observed that the two-step chemistry predictions appear to be a significant improvement over one-step chemistry predictions and agree better with experimental data. Moreover, the different variants of the TF model with two-step chemistry produce very comparable predictions. Hence, from this point, we will present original TF model predictions using two-step chemistry. It should be noted that the *G*-equation model predictions generally overpredict the temperature values significantly and appear to perform much worse than the PDF or TF models.

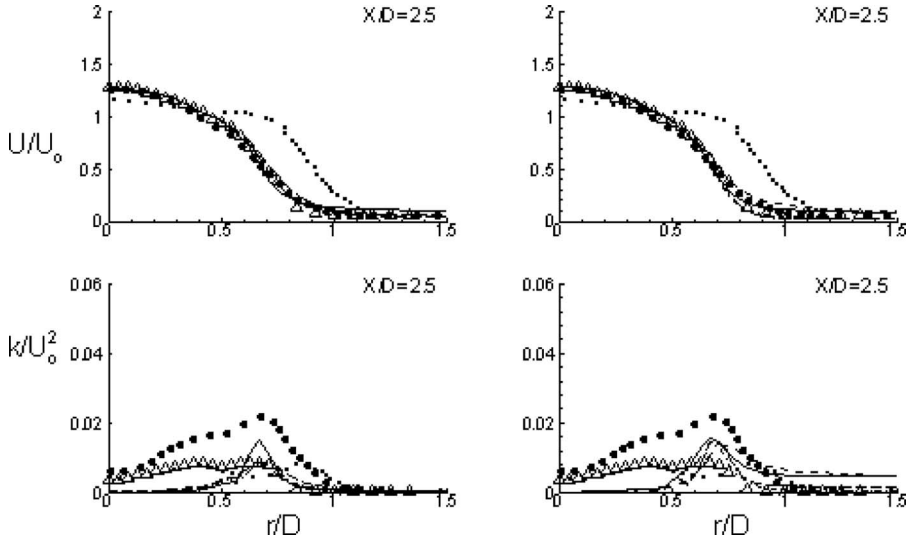


**Fig. 4 Two-step chemistry (left) and one-step chemistry (right): mean axial velocity $U/U_o$ (top) and turbulent kinetic energy $k/U_o^2$ (bottom). Experimental data (△), Lindstedt simulations (●), Duchamp simulations (■), TF model (—), power-law (- - - - -), dynamically modified TF model (–·–·–), and dynamically modified power-law model (—).**

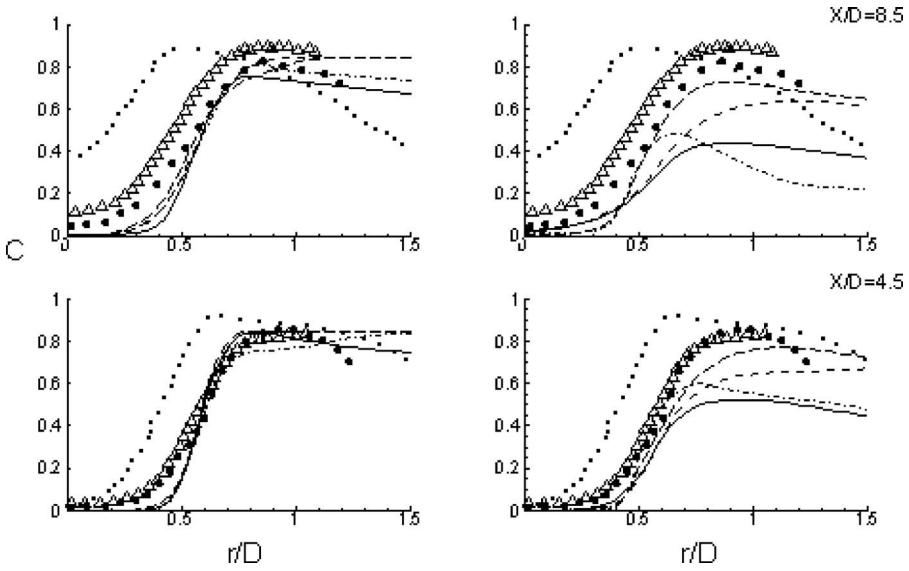


**Fig. 5 Two-step chemistry (left) and one-step chemistry (right): mean temperature C. Legend—see Fig. 4.**

## 10 Original TF Model Results: Detailed Distributions

Based on the observations so far that show improvements with the two-step chemistry calculations, and no clear difference between the variants of the TF models, additional results will be presented only with the original TF model and with the two-step chemistry calculations. In this section, attention will be focused on detailed comparisons of the TF model, the PDF model, the *G*-equation model, and the experimental data for the mean velocity, temperature, kinetic energy, and all major species. This comparison will be presented at several $X/D$ locations (2.5, 4.5, 6.5, and 8.5).

**10.1 Mean Axial Velocity.** Figure 6 shows the mean axial velocity profiles at different axial locations obtained using two-step global chemistry. Also shown are the predictions of Lindstedt and Vaos [7] (used PDF model for their calculations) and Duchamp de La Geneste and Pitsch [8] (used *G*-equation for their simulations).

In evaluating the models, the perspective of computational economy must be kept in mind. A multistep calculation requires the calculation of transport equations for multiple species, and with a PDF modeling approach, the reaction rate expressions require the use of a look-up table with substantial computational input/output (I/O) requirements. In the thickened-flame modeling approach, the reaction rate expressions are computed using Arrhenius law, and computational effort including I/O time is expected to be less. However, we have not undertaken a direct study of the two approaches comparing the computational efforts at this stage.

Figure 6 shows that the mean velocity predictions using the TF modeling approach and these are in reasonably good agreement with experimental data as well as with the PDF model predictions. At the downstream locations, the TF model predictions show higher spreading along the inner edge of the mixing layer (the PDF model shows a similar behavior also). In comparing the models, the *G*-equation shows significant overprediction with the data for $X/D < 6.5$.

The radial profiles of the mean axial velocity show greater radial broadening compared with the nonreacting case (as shown in Fig. 3), due the effect of the flame front, pushing the shear layer outward in the radial direction. Furthermore, it is observed that the peak centerline velocity remains almost constant in the axial di-

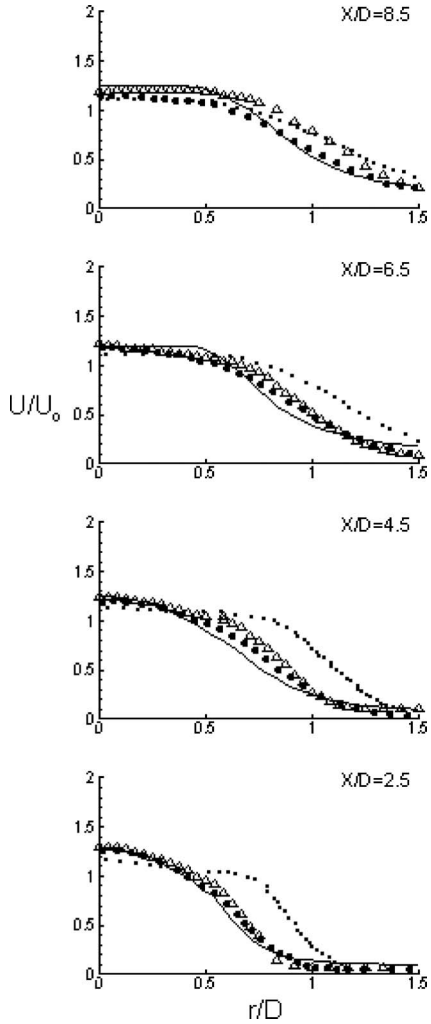


**Fig. 6 Reacting flow: mean axial velocity $U/U_o$. Experimental data (△), Lindstedt simulations (●), Duchamp simulations (■), and TF model (—).**

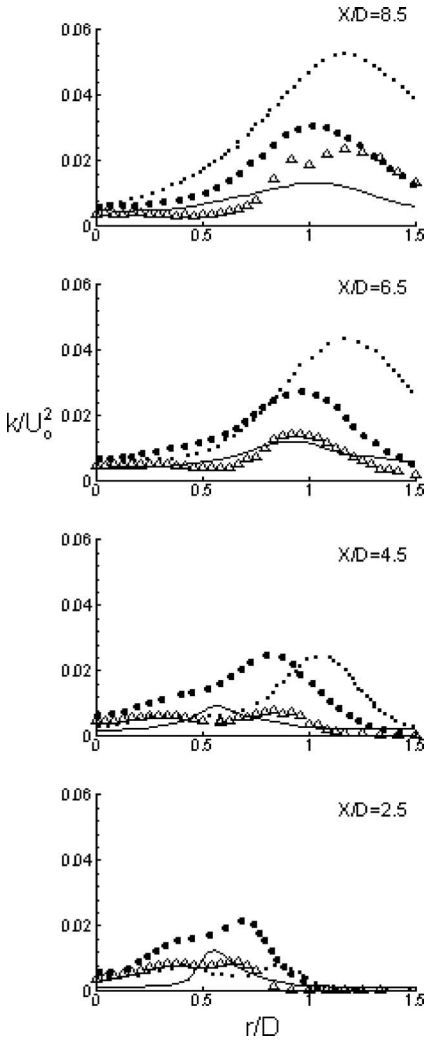


**Fig. 7 Reacting flow: turbulent kinetic energy $k/U_o^2$. Legend—see Fig. 6.**

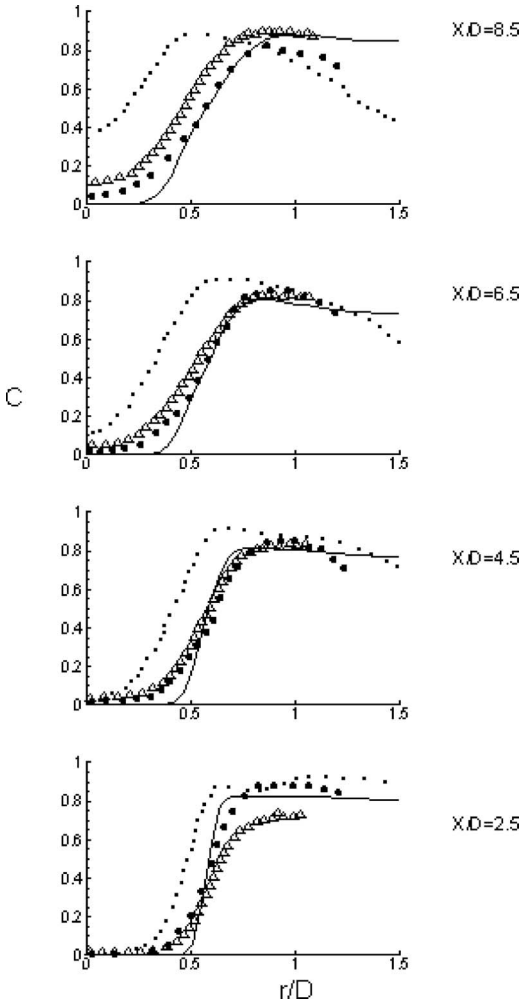


**Fig. 8 Reacting flow: mean temperature C. Legend—see Fig. 6.**

rection, and exhibits a longer potential core compared with the nonreacting case. These effects are reasonably well reproduced by the simulations.

**10.2 Turbulent Kinetic Energy.** Turbulent kinetic energy predictions using the TF modeling approach are shown in Fig. 7. As it is evident from the experimental data there are significant differences observed while compared with the nonreacting case (Fig. 3). The measured turbulent kinetic energy initially increases with axial distance for the reacting case while it decreases for the nonreacting case. Furthermore, for the reacting case, the kinetic energy peak moves away from the centerline (due to radial expansion of the flame front) with increasing axial direction while the peak moves toward the centerline in the nonreacting case due to turbulent diffusion effects.

The predicted kinetic energy shows significant differences between the various models. The TF model shows an initial underprediction close to the centerline (at $X/D=2.5$), but the peak values and the general trend are well predicted by the TF model. At the downstream locations ($X/D=4.5$ and 6.5), the TF model predictions are in reasonably good agreement with the experimental data. The PDF model overpredicts the turbulence levels at all radial locations in the near-field of injection, but appears to be in better agreement with the measured data at $X/D=8.5$. The $G$-equation model generally shows the poorest performance excluding the near-injection location at $X/D=2.5$ where the agreement is reasonable. These discrepancies are linked with the mean temperature predictions and discussed in Sec. 10.3. Clearly, in assessing all $X/D$ locations, the TF model predictions appear to provide the best agreement with the data.

**10.3 Mean Temperature.** Mean temperature profiles are presented in Fig. 8. Immediately downstream of the nozzle exit ($X/D=2.5$), the temperature is overpredicted due to the effect of the two-step chemistry model (as opposed to more complex chemistry schemes) and is likely to overpredict temperature in fuel-rich regions. However, further downstream ($X/D=4.5$, $X/D=6.5$), the peak temperature predictions with the TF model and the PDF models are in better agreement with the data. In particular, the TF model and the PDF model show good agreement, while the $G$-equation consistently shows an overprediction. At $X/D=8.5$ all models excluding the $G$-equation underpredict the measured temperature distribution. With the TF model, it is apparent that the spreading of the temperature shear layer is not being correctly predicted, and that this is likely due to the artificial thickening of the flame front and the scalar diffusivity in the flame region. It can be seen that the centerline mean temperature increases downstream in the experiments, whereas it remains close to the unburnt temperature in the TF simulation. While both the PDF model and the TF model show qualitatively similar behavior, the PDF model does show somewhat better agreement with the temperature data. This is a consequence of the more detailed chemistry calculations

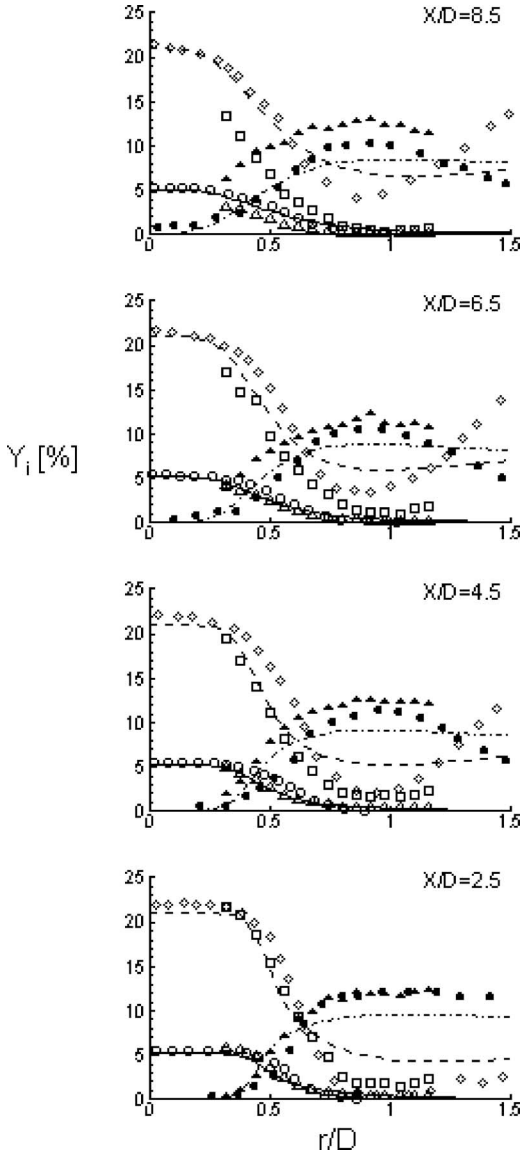


**Fig. 9 Reacting flow: mean $CH_4$ (△, ○, —), $O_2$ (□, ◇, — —), and $H_2O$ (▲, ●, –·–) concentrations. Experimental data (△, □, ▲), Lindstedt simulations (○, ◇, ●), and lines are TF model predictions.**

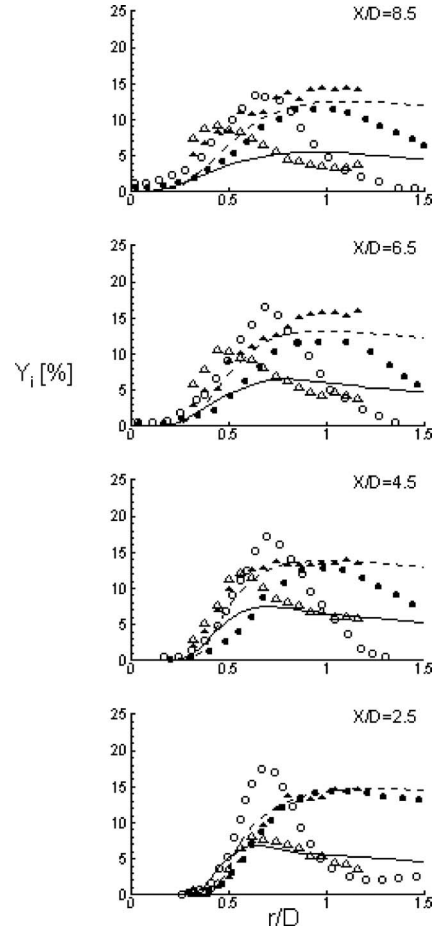


**Fig. 10 Reacting flow: mean CO×10 (△, ○, —) and $CO_2$ (▲, ●, — —) concentrations. Experimental data (△, ▲), Lindstedt simulations (○, ●), and lines are TF model predictions.**

incorporated in their models. Despite this, the poorer predictions of the turbulent kinetic energy with the PDF model, relative to the TF model, are puzzling.

**10.4 Species Mass Fraction.** The radial distributions of the major species mass fractions are presented in Figs. 9 and 10. In presenting these results, the *G*-equation model calculations are not presented here since the detailed data with this model are not available.

Figure 9 shows the mean $CH_4$ distributions at the four radial locations. The profile of the curve clearly shows the premixed unburnt core (plateau region near the centerline), the flame region where methane is consumed (represented by the decay region), and the burnt or outer region where no methane is present. It can be seen that only by $X/D=8.5$ does the flame region start approaching the centerline. The TF model predictions are in excellent agreement with the data, and the level of agreement is even better than that observed with the PDF model. The $O_2$ concentrations are shown in Fig. 9, exhibit distributions similar to the $CH_4$ curve, and the experimental trends are well captured by both the TF model the PDF model. The TF model appears to overpredict oxygen concentrations in the outer regions. This observation leads to an underprediction of $H_2O$ in the outer regions as well (Fig. 9).

$CO_2$ concentrations are also in good agreement with the measurements (Fig. 10) at all $X/D$ locations, while CO predictions (Fig. 10) show excellent agreement at $X/D$ of 2.5 but underpredict at other $X/D$ locations. This may possibly be due to the lower $O_2$ consumption. However, PDF model simulations always significantly overestimate the CO concentrations, and also underestimate $CO_2$ concentrations. At this stage, the discrepancies in CO predictions are not very clear; hence one needs to be more careful in interpreting the data.

**10.5 Turbulent Flame Brush Thickness.** The turbulent flame-brush thickness, which is a characteristic representation of the transition zone between burnt and unburnt gases in premixed flames, is computed as

$$l_{F,t} = \left[\frac{\partial C}{\partial r}\right]^{-1}_{\max} \tag{29}$$

Figure 11 represents the comparison of turbulent flame-brush thickness for TF model, with respect to experiments and other simulations. Overprediction of flame-brush thickness inherently explains the underprediction of mean reaction progress variable *C*, which is evident from Fig. 8. Among all the models, TF model predictions and PDF simulations are in better agreement with the data.

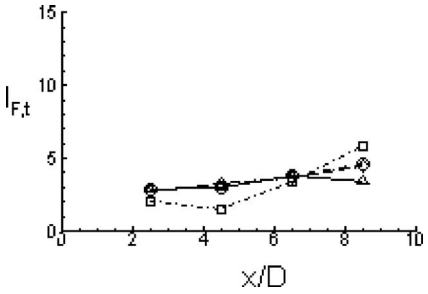


**Fig. 11 Turbulent flame-brush thickness $l_{f,t}$: experimental data (△), Lindstedt simulations (○), Duchamp simulations (■), and TF model (◇)**

## 11 Conclusions

In the present paper, a thickened-flame approach is used to compute the piloted premixed stoichiometric methane-air flame for Reynolds number Re=24,000. The original TF model and its variants including the power-law flame-wrinkling model, and the dynamically modified version of these models in conjunction with two different chemistry models have been implemented and compared. In the first part of the work, the comparison between various TF models and different chemistry models has been presented.

It has been shown that the various variants of TF model produce close agreement with each other using two-step chemistry model. However, they do exhibit some differences while using one-step chemistry. Moreover, the two-step chemistry model appears to perform better over one-step chemistry model. In the second part of the paper the detailed results using the original TF model with two-step chemistry have been reported.

The original TF model predictions with two-step chemistry have been found to be in satisfactory agreement with the experimental data and with the more detailed PDF simulations. The mean reaction progress variable and the mean axial velocity are well predicted in the near-field while showing some discrepancies at the downstream locations. The turbulent kinetic energy is underpredicted in the vicinity of the centerline at axial locations $X/D=2.5$, but matches well at the locations $X/D=4.5-8.5$. The major species mass fraction predictions are also in good agreement with the exception of CO that is underpredicted by the TF model and overpredicted by the PDF model. In general, the TF model and the previously published PDF model predictions are in reasonable agreement with each other and experiments, whereas the *G*-equation model predictions show poor performance.

In comparing the computational resources, the TF model is always been less computationally expensive compared with PDF model where the use of a look-up table takes substantial computational I/O requirements. However, TF model simulations at this stage are restricted to very few number of chemical kinetics (one- or two-step chemistry) while producing reasonably good agreement of the data.

## Acknowledgment

This work was supported by the Clean Power and Energy Research Consortium (CPERC) of Louisiana through a grant from the Louisiana Board of Regents and by the Department of Energy (DOE). Partial support for this work is also provided through Industrial Ties Research Subprogram from the Board of Regents. Simulations are carried out on the computers provided by LONI network at Louisiana[2] and HPC resources at LSU.[3] This support is gratefully acknowledged.

[2]See www.loni.org.
[3]See www.hpc.lsu.edu.

## Nomenclature

$A$ = pre-exponential constant
$a,b$ = $\Gamma$ efficiency model exponents
$c_{\mathrm{ms}}$ = material surface constant $\sim 0.28$
$C_s$ = LES model coefficient
$C$ = mean reaction progress variable
$C'$ = rms of mean reaction progress variable
$D_i$ = molecular diffusivity
$D_{i,\mathrm{loc}}$ = local molecular diffusivity
Da = Damköhler number
$E$ = efficiency function
$E_a$ = activation energy
$F$ = thickening factor
$F_{\mathrm{loc}}$ = local thickening factor
$l_{F,t}$ = flame-brush thickness
$l_t$ = integral length-scale
$\mathrm{Re}_t$ = turbulent Reynolds number
$\mathrm{Re}_\Delta$ = subgrid scale turbulent Reynolds number
$s_L^0$ = laminar flame speed
$S_{ij}$ = mean strain rate tensor
Sc = Schmidt number
$\mathrm{Sc}_t$ = turbulent Schmidt number
$T_a$ = activation temperature
$T_b$ = adiabatic flame temperature
$T_u$ = temperature of unburnt mixtures
$\tilde{u}_i$ = velocity vector
$u'$ = rms turbulence velocity
$u'_{\Delta_e}$ = subgrid scale turbulent velocity
$x_i$ = Cartesian coordinate vector
$\tilde{Y}_i$ = species mass fraction

### Greek Symbols

$\alpha$ = model constant
$\beta$ = model constant
$\delta_L^0$ = laminar flame thickness
$\delta_L^1$ = thickened-flame thickness
$\Delta_x$ = mesh spacing
$\Delta_e$ = local filter size
$\Gamma$ = efficiency function
$\mu_t$ = dynamic turbulent eddy viscosity
$\nu_t$ = kinematic turbulent eddy viscosity
$\bar{\rho}$ = mean density
$\tau_c$ = chemical time-scale
$\tau_i^k$ = subgrid stress tensor
$\tau_t$ = turbulent time-scale
$\omega_i$ = reaction rate
$\Xi$ = wrinkling factor

## References

[1] Poinsot, T., and Veynante, D., 2001, *Theoretical and Numerical Combustion*, Edwards, Ann Arbor, MI.
[2] Colin, O., Ducros, F., Veynante, D., and Poinsot, T., 2000, "A Thickened Flame Model for Large Eddy Simulation of Turbulent Premixed Combustion," Phys. Fluids, **12**(7), pp. 1843–1863.
[3] Charlette, F., Meneveau, C., and Veynante, D., 2002, "A Power-Law Flame Wrinkling Model for LES of Premixed Turbulent Combustion Part I: Non-Dynamic Formulation and Initial Tests," Combust. Flame, **131**, pp. 159–180.
[4] Charlette, F., Meneveau, C., and Veynante, D., 2002, "A Power-Law Flame Wrinkling Model for LES of Premixed Turbulent Combustion Part II: Dynamic Formulation," Combust. Flame, **131**, pp. 181–197.
[5] Durand, L., and Polifke, W., 2007, "Implementation of the Thickened Flame Model for Large Eddy Simulation of Turbulent Premixed Combustion in a Commercial Solver," ASME Paper No. GT2007-28188.
[6] Chen, Y. C., Peters, N., Schneemann, G. A., Wruck, N., Renz, U., and Mansour, M. S., 1996, "The Detailed Flame Structure of Highly Stretched Turbulent Premixed Methane-Air Flames," Combust. Flame, **107**, pp. 233–244.
[7] Lindstedt, R. P., and Vaos, E. M., 2006, "Transported PDF Modeling of High-Reynolds-Number Premixed Turbulent Flames," Combust. Flame, **145**, pp. 495–511.
[8] Duchamp de La Geneste, L., and Pitsch, H., 2000, "A Level-Set Approach to Large-Eddy Simulation of Premixed Turbulent Combustion," *Annual Research*

*Briefs*, CTR, Stanford, pp. 105–116.
[9] Jordan, S. A., 1999, "A Large-Eddy Simulation Methodology in Generalized Curvilinear Coordinates," J. Comput. Phys., **148**, pp. 322–340.
[10] Jordan, S. A., 2001, "Dynamic Subgrid-Scale Modeling for Large-Eddy Simulations in Complex Topologies," ASME J. Fluids Eng., **123**, pp. 619–627.
[11] Tafti, D. K., 2005, "Evaluating the Role of Subgrid Stress Modeling in a Ribbed Duct for the Internal Cooling of Turbine Blades," Int. J. Heat Fluid Flow, **26**, pp. 92–104.
[12] Smagorinsky, J., 1963, "General Circulation Experiments With the Primitive Equations. I. The Basic Experiment," Mon. Weather Rev., **91**, pp. 99–165.
[13] Germano, M., Piomelli, U., Moin, P., and Cabot, W. H., 1991, "A Dynamic Subgrid-Scale Eddy Viscosity Model," Phys. Fluids A, **3**, pp. 1760–1765.
[14] Peters, N., 2000, *Turbulent Combustion*, Cambridge University Press, London.
[15] Pitsch, H., and Duchamp de La Geneste, L., 2002, "Large-Eddy Simulation of a Premixed Turbulent Combustion Using Level-Set Approach," Proc. Combust. Inst., **29**, pp. 2001–2008.
[16] Pope, S. B., 1985, "PDF Methods for Turbulent Reactive Flows," Prog. Energy Combust. Sci., **11**, pp. 119–192.
[17] Butler, T. D., and O'Rourke, P. J., 1977, "A Numerical Method for Two-Dimensional Unsteady Reacting Flows," Proc. Combust. Inst., **16**, pp. 1503–1515.
[18] Kuo, K. K., 2005, *Principles of Combustion*, 2nd ed., Wiley, New York.
[19] Williams, F. A., 1985, *Combustion Theory*, Benjamin/Cummins, Menlo Park, CA.
[20] Legier, J. P., Poinsot, T., and Veynante, D., 2000, "Dynamically Thickened Flame LES Model for Premixed and Non-Premixed Turbulent Combustion," *Summer Program*, Center for Turbulent Research, Stanford University, Stanford, CA, pp. 157–168.
[21] Tuffin, K., Varoquié, B., and Poinsot, T., 2003, "Measurements of Transfer Functions in Reacting Flows Using Large Eddy Simulations," Tenth International Congress on Sound and Vibration, pp. 785–793.
[22] Kim, N. I., and Maruta, K., 2006, "A Numerical Study on Propagation of Premixed Flames in Small Tubes," Combust. Flame, **146**, pp. 283–301.
[23] Selle, L., Lartigue, G., Poinsot, T., Koch, R., Schildmacher, K. U., Krebs, W., Prade, B., Kaufmann, P., and Veynante, D., 2004, "Compressible Large Eddy Simulation of Turbulent Combustion in Complex Geometry on Unstructured Meshes," Combust. Flame, **137**, pp. 489–505.
[24] Kee, R. J., Rupley, F. M., and Miller, J. A., 1989, "Chemkin-II: A Fortran Chemical Kinetics Package for Analysis of Gas-Phase Chemical Kinetics," Sandia National Laboratories, Report No. SAND 89-8009B.
[25] Kee, R. J., Dixon-Lewis, G., Warnatz, J., Coltrin, M. E., and Miller, J. A., 1986, Sandia National Laboratories, Technical Report No. SAND86-8246 (TRANFIT).
[26] Weiss, J. M., and Smith, W. A., 1995, "Preconditioning Applied to Variable and Constant Density Flows," AIAA J., **33**, pp. 2050–2057.
[27] Edwards, J. R., 1997, "A Low-Diffusion Flux-Splitting Scheme for Navier-Stokes Calculations," Comput. Fluids, **26**, pp. 635–659.
[28] Smirnov, A., Shi, S., and Celik, I., 2001, "Random Flow Generation Technique for Large Eddy Simulations and Particle-Dynamics Modeling," ASME J. Fluids Eng., **123**, pp. 359–371.
[29] Akselvoll, K., and Moin, P., 1996, "Large-Eddy Simulation of Turbulent Confined Coannular Jets," J. Fluid Mech., **315**, pp. 387–411.
[30] Herrmann, M., 2006, "Numerical Simulation of Turbulent Bunsen Flames With a Level Set Flamelet Model," Combust. Flame, **145**, pp. 357–375.

**Daren Yu**
Professor
e-mail: yudaren@hcms.hit.edu.cn

**Xiaofeng Liu**
e-mail: lxfryn@gmail.com

**Wen Bao**
Professor
e-mail: baowen@hit.edu.cn

**Zhiqiang Xu**
Associate Professor
e-mail: xuzhiqiang@hit.edu.cn

School of Energy Science and Engineering,
Harbin Institute of Technology,
150001 Heilongjiang, P.R.C.

# Multiobjective Robust Regulating and Protecting Control for Aeroengines

*The multiobjective regulating and protecting control method presented here will enable improved control of multiloop switching control of an aeroengine. The approach is based on switching control theory, the switching performance objectives and the strategy are given, and a family of $H_\infty$ proportional-integral-derivative controllers was designed by using linear matrix inequality optimization algorithm. The simulation shows that using the switching control design method not only can improve the dynamic performance of the engine control system but also can guarantee the stability in some peculiar occasions.*
[DOI: 10.1115/1.2903905]

## 1 Introduction

With the development of advanced aeroengine technology, the control technology plays a more and more important role. Because the aeroengines have become more complex, with more control signals and higher demands on performance and functionality, electronic control systems have been introduced [1]. The experience of development of the aeroengines in the world shows that the performance parameters of aeroengines, such as thrust, specific fuel consumption, stable operation range, etc., can be changed to a certain extent in order to increase aeroengine function, adaptation, and reliability to meet the requirements of different potential users, and can be implemented only by using advanced control modes and control laws almost without changing the aeroengines' hardware.

The aeroengine is a complex nonlinear system that operates in an uncertain environment of limitations: limitations in temperature, air pressure, physical acceleration, etc. Traditionally, aeroengine control systems were designed using linearized engine models at multiple trimmed flight conditions throughout the flight envelope. For each of these operating points a corresponding linear-controller is derived using the well-established linear-based control design methods [2–6]. However, a problem of this approach is that good performance and robustness properties cannot be guaranteed for a highly nonlinear aeroengine. Nonlinear control methods have been developed to overcome the shortcomings of linear design approaches.

Several nonlinear control system design methods have emerged over the past two decades [7–11]. The theoretically established feedback linearization approach is the best known and most widely used of these methods. Feedback linearization is a nonlinear design method that can explicitly handle systems with known nonlinearities. By using nonlinear feedback and exact state transformations rather than linear approximations, the nonlinear system is transformed into a constant linear system. This linear system can in principle be controlled by just a single linear controller [12–14].

Whatever the linear or nonlinear control system design methods, the aeroengine will encounter limitations on some occasions. So the aeroengine control system consists of a family of continuous-time subsystems and switches from one to another depending on various environmental factors (see Fig. 1). When the aeroengine switches from one subcontrol loop to another, the stability of the system is the basic performance that must be considered. The traditional control method is to switch slowly to avoid the dangers. Therefore, there is much space to improve the dynamic performance of the control system.

During the past decade, switched systems have attracted significant attention, because they can model several practical control problems that involve the integration of supervisory logic-based control schemes and feedback control algorithms. The results have been developed for linear [15] and nonlinear systems [16–18]. Concerning output feedback control of switched systems, there are some results. In Ref. [19], by checking the existence of a switched Lyapunov function, linear matrix inequality based sufficient conditions are derived to deal with the switched static output feedback control of discrete-time switched systems under arbitrary switching. Since there exist linear time-invariant systems, which cannot be stabilized via a single static output feedback, research has been dedicated to the study of hybrid static output feedback stabilization of linear time-invariant systems [20–24]. In Ref. [25], the output feedback robust stability problem for uncertain dynamic systems is also considered.

Despite much progress, significant research remains to be done in the direction of nonlinear control of switched systems, especially since the majority of practical switched systems inherently exhibit nonlinear dynamics. In Ref. [26], a hybrid control methodology for a class of switched nonlinear systems with input constraints that accounts for the interactions between the "lower-level" constrained continuous dynamics and the "upper-level" discrete or logical components was developed. The key idea was the integrated synthesis, via multiple Lyapunov functions, of bounded nonlinear continuous controllers and switching laws that orchestrate the transitions between the constituent control modes to guarantee stability of the switched closed-loop system.

The outline of this paper is as follows: First, the aeroengine multiloop control system is described in Sec. 2, the control problems are formulated, and the design contradictions in switching control are detailed. Section 3 is devoted to the theory of the switching control. In Sec. 4, the switching performance objectives are given, and a new control design method based on the pole placement is drawn. A switching strategy is developed to choose the controller, which may take acceptable transient performance objectives from the candidate controllers. Section 5 shows the procedure to design the aeroengine multiloop control system and the simulation results and comparisons. Finally, the conclusion can be obtained in Sec. 6.

Manuscript received August 16, 2007; final manuscript received January 3, 2008; published online July 13, 2009. Review conducted by Allen Volponi.

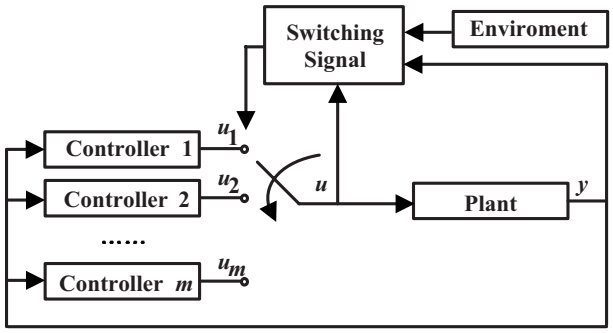


Fig. 1 Architecture of multicontrollers

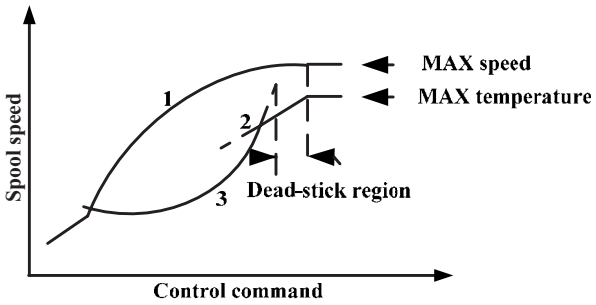


Fig. 4 Illustration of dead-stick conditions and possible method for avoidance

## 2 Aeroengine Multiloop Control System Description

**2.1 Multiobjective With Aeroengines.** For a modern aircraft, in order to achieve high performance flights, an aeroengine control system with high performance is essentially required. However, there are also many limitations during the aeroengine working process. For example, when the aeroengine accelerates from one stable condition to another, compressor surge imposes limits on the aeroengine operation. On the compressor map (see Fig. 2), this limit is represented by the "surge line." The surge line demarcates the regions between the stable and unstable operations of the compressor. If the accelerating line goes through the surge line, the stability of the aeroengine working condition is destroyed. Therefore, the aeroengine control system has to switch to a stable control loop to avoid the unstable surge oscillation.

Also in the accelerating process, more fuel flow can cause the excess air coefficient to go through the "rich blow-out line" (see Fig. 3), resulting in a combustor blow-out event and loss of thrust. So the aeroengine control system has to switch from the accelerating control loop to another stable control loop, such as speed control loop.

If a limitation of turbine temperature is encountered, the remaining command has no effect on an engine. The condition is known as "dead-stick" and is said to be rather disconcerting. Figure 4 shows the phenomenon. The PLA generates a speed governing and a temperature governing characteristic (Curves (1) and (2), respectively). As speed increases along Curve (1), turbine temperature may rise according to Curve (3). If the temperature reaches its permissible limit before speed attains its maximum value, Curve (3) must intersect Curve (2). The principle is obviously applicable to several protection controls; whichever parameter reaches its control line first determines the final mode of control. Therefore, the safe working regions are shown in Fig. 5.

**2.2 Multiloop Controller Regulation and Protection.** In the aeroengine control field, the control requirements of an engine may be classified under three aspects:

(1) performance controls for optimum engine operation
(2) limit controls for mechanical integrity
(3) change-of-state controls, mainly for engine handling

As the engine complexity increases, the number of primary variables increases. It may be necessary to adjust variable geometry within the nozzle. Propulsion nozzle area control is a variable with several uses. In this paper, the variables are $Q_{mf}$ and $A_I$, the effect of which is to vary engine speed and thus engine thrust. Turbine temperature should not exceed a value determined by the properties of constructional materials. To accelerate an engine, fuel flow is increased; a too rapid rate of increase of fuel flow may result in a breakdown of the air-flow conditions within a compressor, leading to engine surge. In order to satisfy the multiobjectives in aeroengine control, the control system setup includes many subcontrol loops, which is shown in Fig. 6. However, during the controller design process, there are many contradictions between the subcontrol loops.

Twin-shaft engines are speed controlled on one shaft only, the other being allowed to find its equilibrium value. Both spools need to be independently protected against overspeed conditions. Figure 7 illustrates a typical complex control requirement. The speed of the high pressure spool is controlled by the PLA. To achieve a compromise between engine handling behavior and fuel consumption, the turbine pressure ratio is shown in Fig. 8. Near to

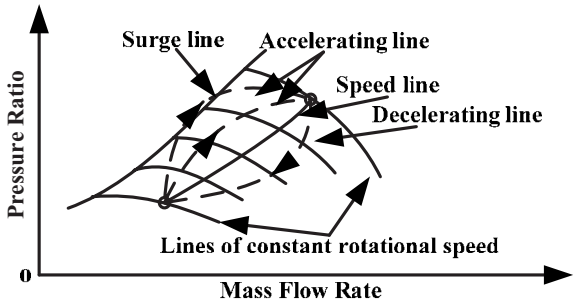


Fig. 2 The aeroengine working characteristics maps

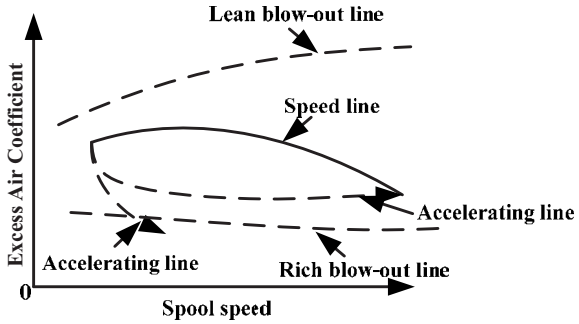


Fig. 3 Variation of excess air coefficient with spool speed

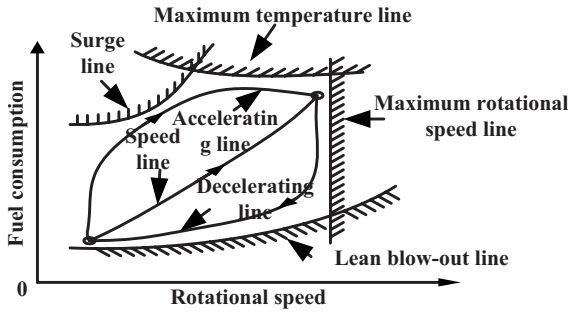


Fig. 5 Limitations of the aeroengine works

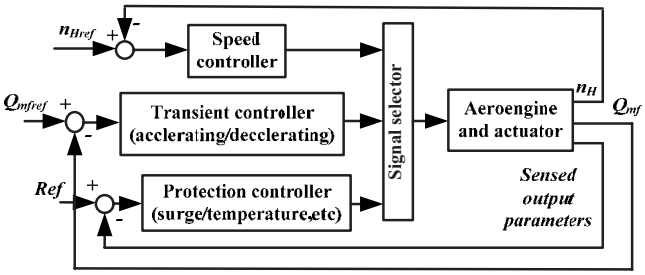


**Fig. 6 Simplified diagram of the aeroengine**

maximum low pressure spool speed, turbine pressure ratio is progressively reduced. For further PLA command, high pressure turbine temperature considerably rises, high pressure spool speed slightly rises, and low pressure spool speed remains almost constant. During this process, in order to avoid the overspeed and overtemperature, the traditional control system makes the aeroengine's acceleration a slow transition.

In accelerating the control loop, it allows independent setting of spool speed and turbine temperature, allowing engine working lines to be more closely "fitted" to surge line, with benefit to specific fuel consumption. The speed of response of a nozzle compared to the accelerating time of engine rotor permits rapid thrust control. However, the surge margin is an important factor that will influence the accelerating progress, which is shown in Fig. 2.

**2.3 Nonlinear Aeroengine Model.** Modeling plays an important role in the development of control systems, which is particularly true for the aeroengine control system because the aeroengine is a very complicated multivariable nonlinear aerothermodynamic process. For high performance and multimission requirements, modern aeroengines are becoming more and more complex in engine cycles and geometries. Such an engine is an inherently nonlinear multivariable system and has numerous variable geometry features, such as variable nozzle, variable guide vanes, etc., to realize the optimum performance. Aeroengine modeling with high fidelity is a task with a high level of sophistication.

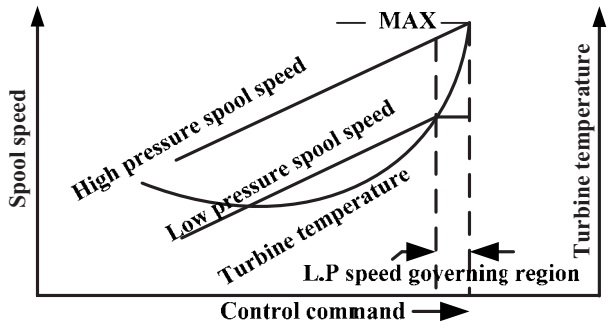


**Fig. 7 Illustration of typical engine control requirements**

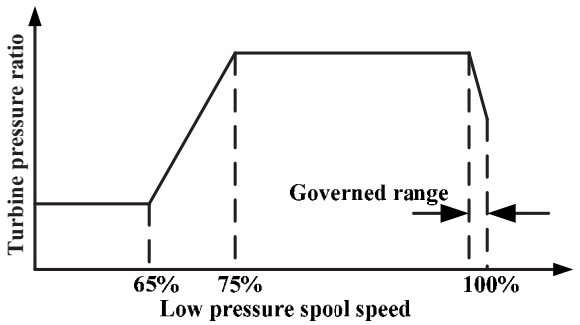


**Fig. 8 Turbine pressure ratio schedule related to the control requirement**

The aeroengine used in this paper is a low bypass ratio, twin spool, separated flow, nonaugmented, and variable nozzle turbofan engine. This turbofan engine has both physical constraints and operational constraints. From the physical standpoint, the maximum low pressure turbine inlet temperature must not exceed 1173 K. Operationally, it is required that all variables can be constrained to their respective operating envelopes and the engine compressor should not surge. This aeroengine model makes use of individual component maps and is therefore able to characterize the inherent dynamical system nonlinearities. The relatively slow temperature heat soaks and the faster volume dynamics are removed from the model, yielding a second-order engine model with the two rotor speeds as the state variables.

In general, the component-level model is defined by two nonlinear vector equations:

$$\dot{\mathbf{x}} = f(x,u,p,H,M_a)$$
$$\mathbf{y} = g(x,u,p,H,M_a) \tag{1}$$

that are functions of a $2\times1$ state vector $(x)$, a $2\times1$ input vector $(\boldsymbol{u})$, a $11\times1$ health parameter vector $(\boldsymbol{p})$, altitude $(H)$, and Mach number $(M_a)$. A $17\times1$ vector of sensor outputs $(y)$ is combined to calculate thrust $(F)$, compressor surge $(SMC)$, etc. These performance parameters form the controlled outputs.

Each of the two inputs $(u)$ is controlled by a separate actuator of a torque motor and servomechanism with saturation limits for position, velocity, and current. The actuators drive the fuel flow $Q_{mf}$ and variable nozzle exit area $A_I$. These actuators' inputs form the control signals.

$$u = [Q_{mf}\ A_I]^T \tag{2}$$

## 3 Output Feedback Stabilization Control of Multiloop Switched System

Switched systems are a class of hybrid systems consisting of several subsystems and a switching rule indicating the active subsystem at each instant of time [27]. Control techniques based on switching between different controllers have been extensively applied in recent years, particularly in the adaptive context, where they have been shown to achieve stability and improve transient response. Among the dynamical systems that exhibit switching behavior, it is possible to cite the electric circuits with electric switches that define the important family of power converters [28], biochemical processes, and all the systems subject to switch control laws [25,29,30]. It is worth mentioning that switching control strategies are important to improve the performance of some systems, to guarantee their robustness, and also to implement some adaptive control schemes [31].

A switched system differs from a conventional dynamical system in that it has not only continuous dynamics but also discrete event dynamics. It is common that discrete event dynamics manifest themselves in subsystem switching. Switching usually takes place when an external event signal is received or an internal condition for the states, inputs, and time evolution is satisfied. In this section, some definitions and theorems are given to describe the switched systems.

We consider the class of switched systems represented by the following state-space description:

$$\dot{x}(t) = f_{\sigma(t)}(x(t)), \quad \sigma(t) \in \{1, \ldots, N\} \tag{3}$$

where $x(t) \in R^n$ denotes the vector of continuous-time state variables, and $\sigma:[0,\infty)$ is the switching signal, which is assumed to be a piecewise continuous (from the right) function of time, i.e., $\sigma(t_k)=\lim_{t\to t_k^+}\sigma(t)$ for all $k$, implying that only a finite number of

switches is allowed on any finite interval of time. The variable $\sigma(t)$ represents a discrete state that indexes the vector field $f(\cdot)$. For each value $\sigma$, the temporal evolution of the continuous state $x$ is governed by a different set of differential equations. Systems of the form of Eq. (3) are therefore referred to as multimodal or of variable structure. They consist of a finite family of $N$ continuous-time nonlinear subsystems (or modes) and some rules for switching between them. These rules define a switching sequence that describes the temporal evolution of the discrete state. Throughout the paper, we use the notations $t_{i_k}$ and $t_{i_k'}$ to denote the $k$th times that the $i$th subsystem is switched in and out, respectively, i.e., $\sigma(t_{i_k}^+)=\sigma(t_{i_k}^-)=i$, for all $k \in Z_+$. With this notation, it is understood that the continuous state evolves according to $\dot{x}=f_i(x)$ for $t_{i_k} \leqslant t < t_{i_k'}$.

Consider the continuous-time switched system,

$$\begin{aligned} \dot{\mathbf{x}} &= A_i x + B_{1i} w + B_{2i} u \\ \mathbf{z} &= C_{1i} x + D_{11i} w + D_{12i} u, \quad i = 1, \ldots, N \\ \mathbf{y} &= C_{2i} x + D_{21i} w + D_{22i} u \end{aligned} \tag{4}$$

where the vector of state variables is $\mathbf{x} \in R^n$, $w \in R^r$ is an exogenous input, $u \in R^{m_i}$ is the control input of subsystem $i$, $z \in R^p$ is the controlled output, $y \in R^r$ is the measured output, and $A_i$, $B_{1i}$, $B_{2i}$, $C_{1i}$, $C_{2i}$, $D_{11i}$, $D_{12i}$, $D_{21i}$, and $D_{22i}$ are the subsystem matrices.

The aim here is to determine a stabilizing switching output feedback control

$$\begin{aligned} \dot{x}_{Ki} &= A_{Ki} x_{Ki} + B_{Ki} y_i \\ u &= C_{Ki} x_{Ki} + D_{Ki} y_i \end{aligned} \tag{5}$$

Such that the closed-loop system

$$\begin{bmatrix} \dot{x}_{cli} \\ z \end{bmatrix} = \begin{bmatrix} A_{cli} & B_{cli} \\ C_{cli} & D_{cli} \end{bmatrix} \begin{bmatrix} x_{cli} \\ w \end{bmatrix} \tag{6}$$

satisfies the bounded real lemma [32], and the linear matrix inequality is

$$\begin{bmatrix} A_{cli}^T P + P A_{cli} & P B_{cli} & C_{cli}^T \\ B_{cli}^T P & -\gamma I & D_{cli}^T \\ C_{cli} & D_{cli} & -\gamma I \end{bmatrix} < 0 \tag{7}$$

where

$$\begin{aligned} A_{cli} &= \begin{bmatrix} A_i + B_{2i} D_{Ki} (I - D_{22i} D_{Ki})^{-1} C_{2i} & B_{2i} [C_{Ki} + D_{Ki} (I - D_{22i} D_{Ki})^{-1} D_{22i} C_{Ki}] \\ B_{Ki} (I - D_{22i} D_{Ki})^{-1} C_{2i} & A_{Ki} + B_{Ki} (I - D_{22i} D_{Ki})^{-1} D_{22i} C_{Ki} \end{bmatrix} \\ B_{cli} &= \begin{bmatrix} B_{1i} + B_{2i} D_{Ki} (I - D_{22i} D_{Ki})^{-1} D_{21i} \\ B_{Ki} (I - D_{22i} D_{Ki})^{-1} D_{21i} \end{bmatrix} \\ C_{cli} &= [C_{1i} + D_{12i} D_{Ki} (I - D_{22i} D_{Ki})^{-1} C_{2i} \quad D_{12i} C_{Ki} + D_{12i} D_{Ki} (I - D_{22i} D_{Ki})^{-1} D_{22i} C_{Ki}] \\ D_{cli} &= D_{11i} + D_{12i} D_{Ki} (I - D_{22i} D_{Ki})^{-1} D_{21i} \end{aligned} \tag{8}$$

The output feedback controllers are obtained from the use of a common Lyapunov function. This approach is appealing because of its numerical simplicity and also by the possibility to express the tests in terms of linear matrix inequalities (LMIs). Another interesting feature is that the fixed Lyapunov function can cope with arbitrarily fast time-varying system, thus encompassing the switched systems.

## 4 Switching Performance Objectives and Strategy in Aeroengine Multiloop System

The method mentioned above is an optimal controller design method, which can generate a set of dynamic output feedback controllers. However, the common Lyapunov function method above could not solve the dynamic performance objectives of the system outputs and the strategy.

In the traditional control mode, the performance objective is only safety. In the case of the instability during the controller switching, minimum signal is selected to control the engine, and the slow switching was required. However, for modern control requirements, the aeroengine's performance is more and more important. The transient performance of the control system is given more attention.

**4.1 Switching Performance Objectives.** Above, we discussed the conservatism of the traditional control mode, and we concluded that the dynamic performance can be improved by using switching control theory. In the aeroengine control system, different subsystems have different performance objectives. In the speed control loop, the performance objectives are to achieve good tracking of $n_H$ command, overshoot less than 4%, zero steady-state error for step command, range of settling time from 1 s to 2 s, and a closed-loop bandwidth of 10 rad/s. In the accelerating control loop, the performance objectives are the same as in the speed control system. In addition, during the accelerating process, *SMC* is not less than 10%. In temperature protection subsystem, the performance objectives are to achieve good transition time that is not greater than 3 s, and steady-state error for step command is zero. During this process, the close-loop's states reach the switching surface, and the temperature controller starts to control the aeroengine. At this moment, the active controller's states cannot match with the engine's states well, and the output of the temperature loop, $T_{35}$, should have a large overshoot, which will take a larger impulse to the system.

The goal of the switching control system in this paper is to achieve a fast thrust response with nonovershoot, zero steady-state error and fast settling time, while maintaining safe temperature limits and surge margins during switching.

**4.2 Switching PID Controller Based on Pole Placement.** In this section, the robust multiloop switching proportional-integral-derivative (PID) controllers are formulated in $H_\infty$ control framework. A method to tune PID controllers for multivariable plants to achieve both robust stability and performance is proposed in Ref. [33].

It is known that the transient response of a linear system is related to the location of its poles. By constraining the poles to lie

in a prescribed region, specific bounds can be ensured a satisfactory transient response. The interesting region for control purposes is the set $S(l,r,\theta)$, as shown in Fig. 9. Consider a linear time-invariant system described by

$$\dot{x} = Ax + B_1 w + B_2 u$$

$$z = C_1 x + D_{11} w + D_{12} u \tag{9}$$

$$y = C_2 x + D_{21} w + D_{22} u$$

DEFINITION. (LMI Regions) *A subset D of the complex plane is called a LMI region if there exists a symmetric matrix* $\mathbf{L} \in \mathbf{R}^{m\times m}$ *and a matrix* $\mathbf{M} \in \mathbf{R}^{m\times m}$, *such that*

$$D = \{s \in C : L + sM + \bar{s}M^T < 0\} \tag{10}$$

with

$$f_D(s) = L + sM + \bar{s}M^T \tag{11}$$

*Note that the characteristic function* $f_D(s)$ *takes values in the space of* $n \times n$ *Hermitian matrices and that* $<0$ *stands for negative definite.* $\bar{s}$ *represents the conjugate of s.*

THEOREM 1. *All the eigenvalues of matrix* $\mathbf{A}$ *lies in the LMI region, if and only if there exists a symmetric positive definite matrix* $\mathbf{X}$, *such that*

$$M_D = (\mathbf{A}, \mathbf{X}) < 0 \tag{12}$$

*where*

$$M_D(A,X) = L \otimes X + M \otimes (AX) + M^T \otimes (AX)^T \tag{13}$$

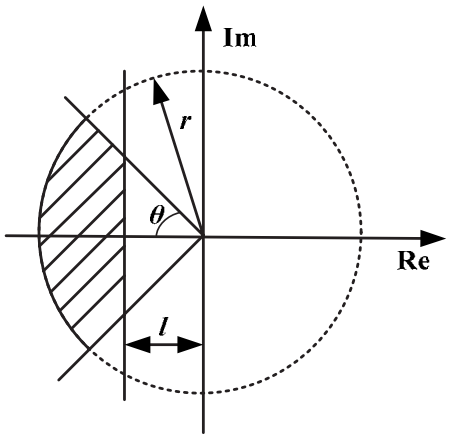


**Fig. 9 Region of $S(l,r,\theta)$**

*and* $\otimes$ *represents the matrices' Kronecker product.*

Note that the LMI region is convex and symmetric with respect to the real axis; in other words, LMI regions cover most practical needs for control purposes. According to the bounded real lemma, the pole placement constraint output feedback controller exists if and only if $\gamma > 0$; there exists the positive definite matrices $\mathbf{R}$ and $\mathbf{S}$, and the matrices $\bar{\mathbf{A}}_K$, $\bar{\mathbf{B}}_K$, $\bar{\mathbf{C}}_K$, $\mathbf{D}_K$, such that

$$\begin{bmatrix} R & I \\ I & S \end{bmatrix} > 0 \tag{14}$$

$$\begin{bmatrix} AR + B_2\bar{C}_K + RA^T + \bar{C}_K^T B_2^T & A + B_2 D_K C_2 + \bar{A}_K^T \\ \bar{A}_K + A^T + C_2^T D_K^T B_2^T & SA + \bar{B}_K C_2 + A^T S + C_2^T \bar{B}_K^T \end{bmatrix} < -2l \begin{bmatrix} R & I \\ I & S \end{bmatrix} \tag{15}$$

$$\begin{bmatrix} -rR & -rI & AR + B_2\bar{C}_K & A + B_2 D_K C_2 \\ -rI & -rS & \bar{A}_K & SA + \bar{B}_K C_2 \\ RA^T + \bar{C}_K^T B_2^T & \bar{A}_K^T & -rR & -rI \\ A^T + C_2^T D_K^T B_2^T & A^T S + C_2^T \bar{B}_K^T & -rI & -rS \end{bmatrix} < 0 \tag{16}$$

$$\begin{bmatrix} \sin\theta(\Phi + \Phi^T) & \cos\theta(\Phi - \Phi^T) \\ \cos\theta(\Phi^T - \Phi) & \sin\theta(\Phi + \Phi^T) \end{bmatrix} < 0 \tag{17}$$

$$\begin{bmatrix} AR + RA^T + B_2\bar{C}_K + \bar{C}_K^T B_2^T & * & * & * \\ \bar{A}_K + A^T + C_2^T D_K^T B_2^T & A^T S + SA + \bar{B}_K C_2 + C_2^T \bar{B}_K^T & * & * \\ B_1^T + D_{21}^T D_K^T B_2^T & B_1^T S + D_{21}^T B_K^T & -\gamma I & * \\ C_1 R + D_{12}\bar{C}_K & C_1 + D_{12} D_K C_2 & D_{11} + D_{12} D_K D_{21} & -\gamma I \end{bmatrix} < 0 \tag{18}$$

where $*$ represents the symmetric sub-blocks of the matrices. $r$, $l$, and $\theta$ are shown in Fig. 9.

$$\Phi = \begin{bmatrix} AR + B_2\bar{C}_K & A + B_2 D_K C_2 \\ \bar{A}_K & SA + \bar{B}_K C_2 \end{bmatrix} \tag{19}$$

Given any solution to this LMI system, a full rank factorization $MN^T = I - RS$ of the matrix $I - RS$ is computed via SVD ($M$ and $N$ are then square invertible).

$$\begin{aligned} D_K &= D_K \\ C_K &= (\bar{C}_K - D_K C_2 R) M^{-T} \\ B_K &= N^{-1}(\bar{B}_K - S B_2 D_K) \\ A_K &= N^{-1}(A_K - N B_K C_2 R - S B_2 C_K M^T - S(A + B_2 D_K C_2) R) M^{-T} \end{aligned} \tag{20}$$

Then $K(s)=D_K+C_K(sI-A_K)^{-1}B_K$ is an $n$th order controller that places the closed poles in the LMI region and such that $\|T_{wz}\|_\infty < \gamma$.

Theorem 1 answers the need for a characterization of stability regions that is affine in the **A** matrix. The convenience of LMI regions for synthesis purposes can be shown.

In fact, the LMI region $D$, which can be concerned in practical application, is the intersection of the basic LMI regions $D_1,\ldots,D_N$. Assuming that the LMI region $D_i$'s characteristic function is

$$f_{D_i}(s) = L_i + sM_i + \bar{s}M_i^T \tag{21}$$

then the intersection $D=D_1\cap\cdots\cap D_N$'s characteristic function is

$$f_D(s) = \mathrm{diag}\{f_{D_1}(s),\ldots,f_{D_N}(s)\} \tag{22}$$

THEOREM 2. *The poles of the control system are assigned in a LMI region $D=D_1\cap\cdots\cap D_N$, if and only if there exists a symmetric positive definite matrix* **X**, *such that*

$$M_D = (A_i,X) < 0, \quad i\in\{1,\ldots,N\} \tag{23}$$

*The characteristic function is*

$$f_D = \mathrm{diag}(D_1\cap\cdots\cap D_N) \tag{24}$$

*Proof*. Simply observe that

$$M_D(A,X) = M_{D_1\cap\cdots\cap D_N}(A,X) = \mathrm{diag}(M_{D_1}(A,X),\ldots,M_{D_N}(A,X)) \tag{25}$$

since $D_1\cap\cdots\cap D_N$ has the characteristic function $\mathrm{diag}(f_{D_1},\ldots,f_{D_N})$. Applying Theorem 1 to $D_1\cap\cdots\cap D_N$ completes the proof.

So, according to both the approach of the pole placement and Theorem 2, the output feedback switching controller of the multiloop control system can be designed.

In this section, we discussed the stability and the controller design methods of the switched systems. However, Theorem 2 is only a sufficient condition to controller design. During the loop switching, the switching strategy is also an important problem that must be solved.

**4.3 Smooth Switching and Switching Strategy in Multiloop Control System.** Obviously, the controllers have abrupt variations at the switched points. As a result, chattering happens during the operating process, which reduces the control accuracy, increasing energy consumption, and sometimes causes destructive impact to the aeroengine system. In order to attenuate the chattering, smooth switching is considered. A natural idea is to let the feedback controller $K_i(s)$ vary gradually from one to another.

How to choose the next controller is a crucial decision that affects the performance of the system. We can systematically switch according to a presorted list. The transient performance, however, might not be acceptable if we have to switch through a long sequence of controllers. A better way is to use on-line information to decide on the next controller. In order to give a switching strategy to the aeroengine control system, we first introduce the concept of the matrix pencil.

DEFINITION 1. *The matrix pencil is a convex combination of matrices, defined as follows*:

$$\zeta[A_1,A_2] = \alpha A_1 + (1-\alpha)A_2, \quad \alpha\in[0,1] \tag{26}$$

Considering a switched system with two subsystems, the closed-loop systems are

$$\begin{aligned} \dot{x}_{cl} &= A_{cli}x_{cl} + B_{cl}w \\ z &= C_{cl}x_{cl} \end{aligned} \quad i=1,2 \tag{27}$$

where $x_{cl}=[x \quad x_K]^T$. Given the constant $\gamma>0$, if there exist $\bar{A}\in\zeta[A_1,A_2]$ and a symmetric positive matrix **P**, satisfying the following Riccati inequality

$$\bar{A}^TP + P\bar{A} + \gamma^{-2}PB_{cl}B_{cl}^TP + C_{cl}^TC_{cl} < 0 \tag{28}$$

then the switched system's $H_\infty$ norm is $\gamma$.

According to Definition 1, we have

$$\bar{A} = \alpha A_1 + (1-\alpha)A_2 \tag{29}$$

We take Eq. (29) to Eq. (28),

$$\begin{aligned} &\alpha(A_{cl1}^TP + PA_{cl1} + \gamma^{-2}PB_{cl}B_{cl}^TP + C_{cl}^TC_{cl}) + (1-\alpha)(A_{cl2}^TP + PA_{cl2} \\ &\quad + \gamma^{-2}PB_{cl}B_{cl}^TP + C_{cl}^TC_{cl}) < 0 \end{aligned} \tag{30}$$

So $\forall x\in R^n$ and $x\neq 0$,

$$\begin{aligned} &\alpha x_{cl}^T(A_{cl1}^TP + PA_{cl1} + \gamma^{-2}PB_{cl}B_{cl}^TP + C_{cl}^TC_{cl})x_{cl} + (1-\alpha)x_{cl}^T(A_{cl2}^TP \\ &\quad + PA_{cl2} + \gamma^{-2}PB_{cl}B_{cl}^TP + C_{cl}^TC_{cl})x_{cl} < 0 \end{aligned} \tag{31}$$

Let

$$\Omega_i = \{x_{cl}|x_{cl}^T(A_{cli}^TP + PA_{cli} + \gamma^{-2}PB_{cl}B_{cl}^TP + C_{cl}^TC_{cl})x_{cl} < 0\} \tag{32}$$

then

$$\Omega_1\cup\Omega_2 = R^n\setminus\{0\} \tag{33}$$

The switching strategy is

$$i = \begin{cases} 1, & x_{cl}\in\Omega_1 \\ 2, & x_{cl}\in\Omega_2 \end{cases} \tag{34}$$

*Proof*. The Lyapunov function $V=x_{cl}^TPx_{cl}$, and $P$ satisfies Eq. (28). If $x_{cl}\in\Omega_i$, $i=1,2$, and $w=0$, according to Eq. (30), there is

$$\dot{V} = x_{cl}^T(A_{cli}^TP + PA_{cli})x_{cl} < 0 \tag{35}$$

So the closed-loop system (27) is asymptotically stable.

## 5 Control Design Procedure and Simulation Results

**5.1 Augmented Aeroengine Model.** In order to analyze the time-domain performance objectives, we draw the linear design model of the form

$$\begin{aligned} \dot{x} &= Ax + Bu \\ y &= Cx + Du \end{aligned} \tag{36}$$

where $x=[n_H \quad n_L]^T$ and $u=[Q_{mf} \quad A_I]^T$. Two first order actuator models are used for $Q_{mf}$ and $A_I$ in the design and evaluation process; the time constants are 0.2 s and 0.3 s. The PID controllers are designed to achieve the following robustness and performance specifications.

In the speed subcontrol loop, the PID controllers are tuned such that steady-state tracking error is zero. The settling time is expected to be within 2 s. The sensitivity weighting function $W_S(s)$ is chosen to be large at low frequency in order to obtain good command tracking at low frequency. The complementary sensitivity weighting function $W_T(s)$ is chosen to be large at high frequency to obtain robustness to unmodeled high frequency dynamics. The sensitivity and complementary sensitivity weighting functions are designed as two parallel first-order lags and leads, respectively, with the low frequency magnitudes and crossover frequencies specified by the user.

Here, $W_S(s)$ should have the characteristic of low-pass frequency and the unity-gain crossover frequencies of 0.4 rad/s. In order to satisfy the bandwidth requirement, $W_T(s)$'s static gain should be adequately small, and it should exhibit a unity-gain crossover frequencies of 100 rad/s. According to the above specifications, the weighting functions are chosen as follows:

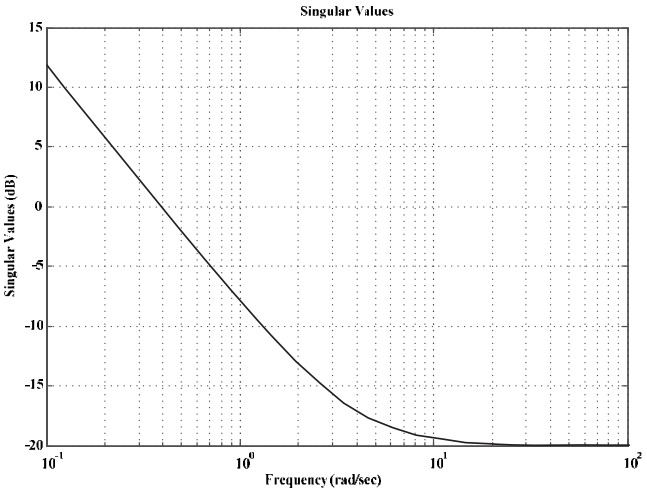


**Fig. 10 Singular value plot of $W_S(s)$ in speed control loop**

$$W_S(s) = \begin{bmatrix} \dfrac{0.02556s + 0.1}{0.2556s + 1e^{-5}} & 0 \\ 0 & \dfrac{0.02556s + 0.1}{0.2556s + 1e^{-5}} \end{bmatrix}$$

$$W_T(s) = \begin{bmatrix} \dfrac{0.01022s + 0.04}{1e^{-5}s + 1} & 0 \\ 0 & \dfrac{0.01022s + 0.04}{1e^{-5}s + 1} \end{bmatrix} \tag{37}$$

The singular value plots of the weighting functions are shown in Figs. 10 and 11.

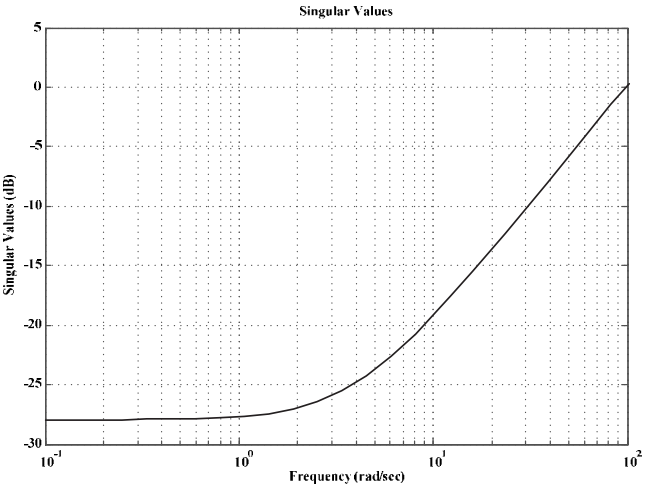


**Fig. 11 Singular value plot of $W_T(s)$ in speed control loop**

In the protection subcontrol loops, the weighting functions are same as the speed subcontrol loop.

**5.2 Switching PID Tuning Procedure With Closed-Loop Dominant Pole Placement.** In this step, the output feedback dynamic controllers are described in Eq. (5), where the $i$ in the subscript denotes different subcontrol loops. We give a procedure to show how to design the switching controllers.

(1) Given data. Matrices of the aeroengine subsystem model (speed, surge protection, and temperature protection):

$$\begin{bmatrix} \dot{n}_H \\ \dot{n}_L \\ \dot{Q}_{mf} \\ \dot{A}_I \end{bmatrix} = \begin{bmatrix} -2.1022 & -0.5281 & 92.4704 & 7410.8640 \\ 1.9240 & -6.2069 & 109.2637 & 74540.8101 \\ 0 & 0 & -5 & 0 \\ 0 & 0 & 0 & -10/3 \end{bmatrix} \times \begin{bmatrix} n_H \\ n_L \\ Q_{mf} \\ A_I \end{bmatrix} + \begin{bmatrix} 0 & 0 \\ 0 & 0 \\ 5 & 0 \\ 0 & 10/3 \end{bmatrix} \begin{bmatrix} u_1 \\ u_2 \end{bmatrix}$$

$$n_H = [1 \quad 0 \quad 0 \quad 0] \begin{bmatrix} n_H \\ n_L \\ Q_{mf} \\ A_I \end{bmatrix} + [0 \quad 0] \begin{bmatrix} u_1 \\ u_2 \end{bmatrix}$$

$$SMC = [0.0015 \quad 0.0017 \quad -0.1655 \quad 5.7838] \begin{bmatrix} n_H \\ n_L \\ Q_{mf} \\ A_I \end{bmatrix} + [0 \quad 0] \begin{bmatrix} u_1 \\ u_2 \end{bmatrix}$$

$$T_{35} = [-0.0097 \quad -0.01730 \quad 2.5657 \quad -74.8948] \times \begin{bmatrix} n_H \\ n_L \\ Q_{mf} \\ A_I \end{bmatrix} + [0 \quad 0] \begin{bmatrix} u_1 \\ u_2 \end{bmatrix}$$

(2) Given data. The pole location $S(l, r, \theta)$ and the performance index $\gamma$.

According to the given switching performance above and Theorem 2, which we proved in this paper, we put the subcontrol loops to have the same closed-loop dominant pole region, then we set $l=5$, $r=15$, $\theta=0.6435$, and $\gamma=1$.

(3) Combining, the sensitivity and complementary sensitivity weighting functions produces the aeroengine augmented state-space realization.

(4) By calculating the LMIs from Eq. (14) to Eq. (20), the subcontrol loops' dynamic controllers are

$$K_1(s) = \begin{bmatrix} 0.2821\left(1 + \dfrac{1}{2.7603s} + 0.2003s\right)\dfrac{1}{0.1s + 1} & 0 \\ 0 & 0.2412\left(1 + \dfrac{1}{3.216s} + 0.4979s\right)\dfrac{1}{s + 1} \end{bmatrix}$$

$$K_2(s) = \begin{bmatrix} 3.9621\left(1 + \frac{1}{0.0275s} + 0.3963s\right)\frac{1}{0.1s+1} & 0 \\ 0 & 4.8768\left(1 + \frac{1}{0.0281s} + 0.3152s\right)\frac{1}{0.1s+1} \end{bmatrix}$$

$$K_3(s) = \begin{bmatrix} 6.1483\left(1 + \frac{1}{2.7906s} + 0.0763s\right)\frac{1}{0.1s+1} & 0 \\ 0 & 0.1143\left(1 + \frac{1}{3.2106s} + 0.0019s\right)\frac{1}{s+1} \end{bmatrix}$$

where the subscript 1 represents the speed subcontrol loop, 2 represents the surge protection subcontrol loop, and 3 represents the temperature subcontrol loop

.

**5.3 Simulation Results.** In this section, we use the PID controllers, which are optimized above to the aeroengine nonlinear component-level model. Meanwhile, the nozzle area $A_I$ is kept as a constant.

Simulation 1. Switching process between speed and *SMC* two subcontrol loops.

In order to show the switching between the two subcontrollers in a harsh condition, the reference input of the fuel flow is given as step signals, which are shown in Fig. 12.

We assume that the *SMC* boundary is as shown in Fig. 13. As speed subcontrol loop fuel flow demand increases, *SMC* approaches the safe limit, and the surge protection controller engages to control the engine (Fig. 14). As expected, there are small glitches during controller switching, and the tracking performance is acceptable.

Simulation 2. Comparing the traditional switching method during switching process between speed subcontrol loop and temperature protection subcontrol loop (Fig. 15).

We give three simulations below:

(1) Using the controllers designed by this paper, switching from the speed subcontrol loop to the temperature protection control loop. During this procedure, the aeroengine's input is step input with $Q_{mf}$.
(2) Using traditional single-loop design method switch for safety and the plant input is the same as in Simulation (1).
(3) Using Simulation (2)'s controllers for safely switching and the plant's input is slope input with $Q_{mf}$.

Figure 16 shows comparison of three switching modes. Curve 1 shows the response of $T_{35}$ using the method of this paper, Curve 2 shows the output with the same condition, and Curve 3 shows the step response of $T_{35}$ for safety. Compared with Curve 3, Curve 2

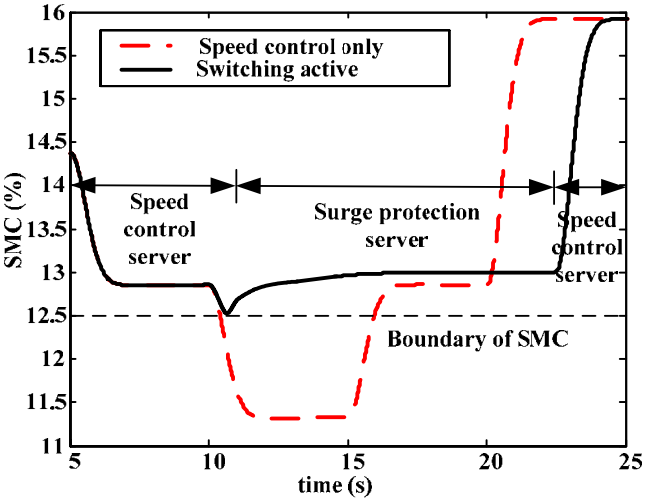


**Fig. 13 Output of *SMC***

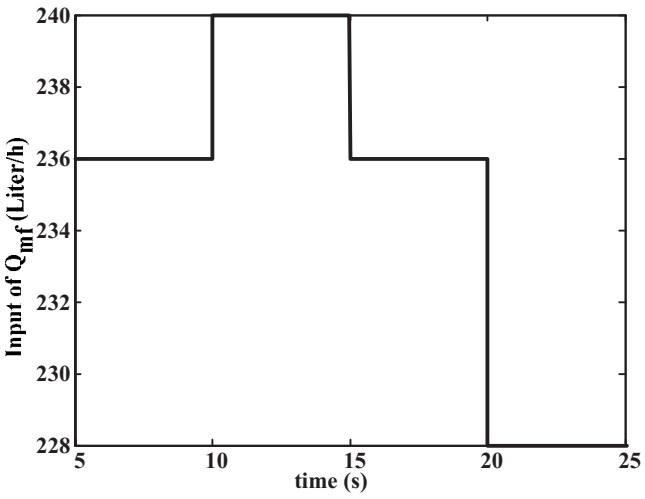


**Fig. 12 Reference input of the fuel flow**

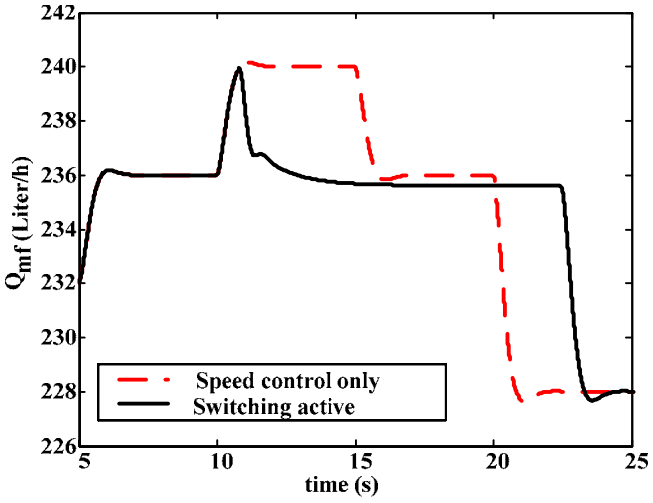


**Fig. 14 Output of fuel flow**

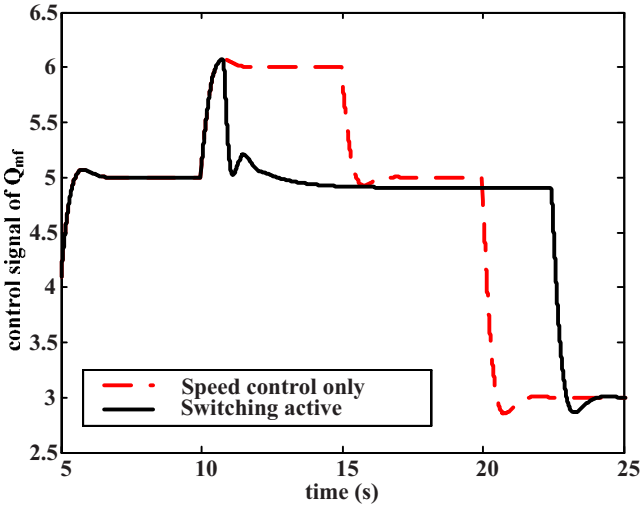


Fig. 15 Control signal output of the switching between speed and *SMC* subcontrol loop

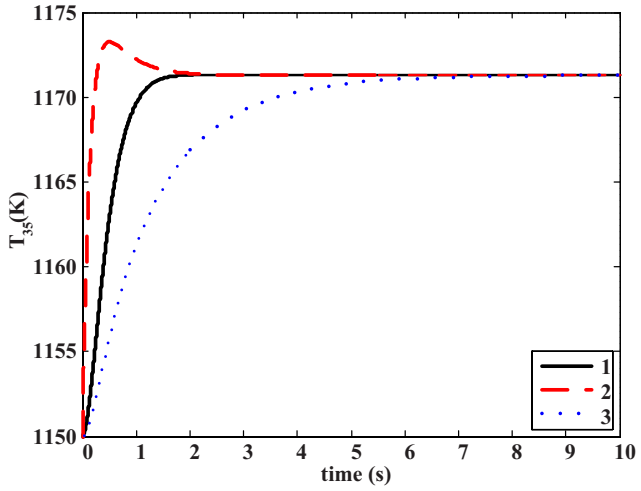


Fig. 16 Step response of $T_{35}$.

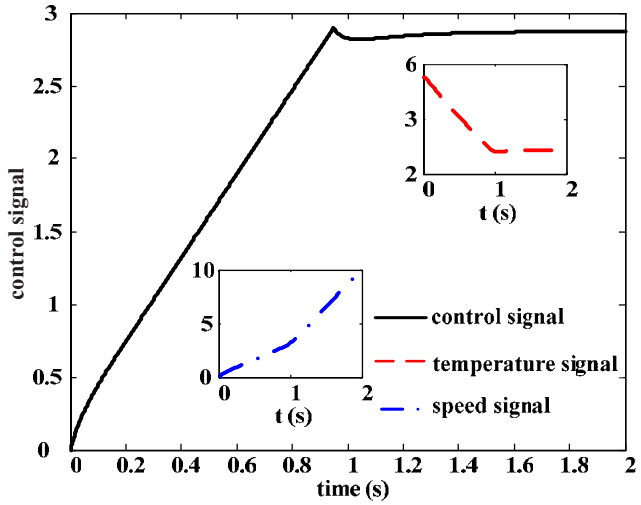


Fig. 17 Control signal output of the switching between speed and temperature subcontrol loop

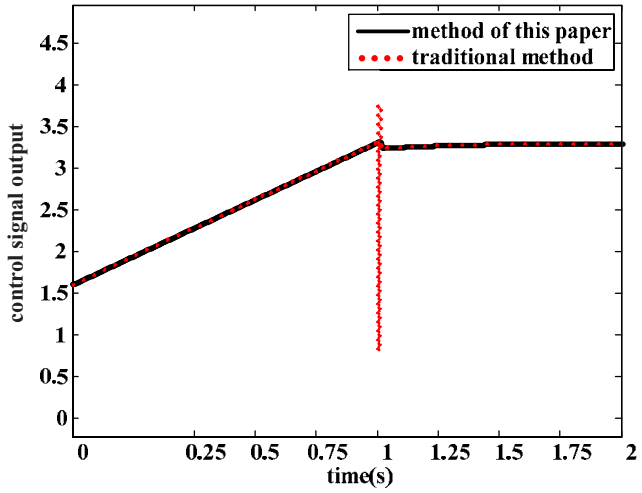


Fig. 18 Control signal output of the switching between speed and temperature subcontrol loop

shows the better dynamic performance, but the overshoot is too high. In the real aeroengine control, it is not allowed. Curve 1 shows the better dynamic performance than Curve 3, and the better stability than Curve 2. Figure 17 shows the control signal during the switching.

The results presented above have shown that the robust multivariable control design approach leads to satisfactory performance for an aeroengine with reasonable PID controllers, which require safe and fast switching during some special working conditions.

Simulation 3. Comparing, the switching strategy with the traditional one.

The dash line denotes the traditional method, and the solid line denotes the switching strategy introduced in this paper. Obviously, under some uncertainties, the traditional method gives a huge impulse to the system during the switching (Fig. 18).

## 6 Conclusions

In this paper, the aeroengine multiloop control system is described in detail and the switching control theory is introduced to solve the regulating and protecting control problems. The contributions of this paper are that the switching performance objectives and the switching strategy are given and a family of $H_\infty$ PID controllers was designed by using the LMI optimization algorithm.

In order to design the regulating and protecting controllers of the aeroengines, there are three steps that should be taken, which are (1) using the switching control theory to calculate the robust suboptimized controller region, (2) using the switching pole placement method to choose the more suitable controllers in the region, and (3) using the switching strategy to control the system.

The simulations show that using the method not only can improve the dynamic performance of the engine control system but also can guarantee the stability in some occasions. With the method, the conservatism is reduced, the dynamic performance is improved, and the multiloop controllers are regulated well.

## Acknowledgment

The authors would like to thank Dr. Allan J. Volponi and the three reviewers for their constructive and insightful suggestions for further improving the quality of this paper. This work is supported by the National Natural Science Foundation of China (Nos. 50606008, 90716012).

## Nomenclature

$n_H$ = high pressure spool speed (rpm)

$n_L$ = low pressure spool speed (rpm)
$SMC$ = compressor surge margin (equal to pressure ratio at stall minus operating pressure ratio)/(operating pressure ratio)
$T_{35}$ = high pressure turbine outlet temperature (K)
$Q_{mf}$ = fuel flow (l/h)
$A_I$ = nozzle area ($m^2$)
$H$ = altitude (m)
$M_a$ = Mach number
PLA = power level angle

## References


[1] Skira, C. A., and Agnello, M., 1992, "Control Systems for the Next Century Engines," ASME J. Eng. Gas Turbines Power, **114**, pp. 749–754.
[2] Blakelock, J. H., 1991, *Automatic Control of Aircraft and Missiles*, 2nd ed., Wiley, New York.
[3] Garg, S., 1993, "Robust Integrated Flight/Propulsion Control Design for a STOVL Aircraft Using $H_\infty$ Control Design Techniques," Automatica, **29**(1), pp. 129–145.
[4] Garg, S., 1996, "A Simplified Scheme for Scheduling Multivariable Controllers and its Application to a Turbofan Engine," ASME International Gas Turbine Institute Expo, Birmingham, UK, June.
[5] Watts, S. R., and Garg, S., 1995, "A Comparison of Multivariable Control Design Techniques for a Turbofan Engine Control," ASME Paper No. 95-GT-258.
[6] Menon, P. K., Iragavarapu, V. R., and Sweriduk, G. D., 1996, "Software for Modern Multivariable Control of Aircraft Engines," Optimal Synthesis Inc, October.
[7] Isidori, A., 1989, *Nonlinear Control Systems: An Introduction*, Springer-Verlag, New York.
[8] da Costa, R. R., Chu, Q. P., and Mulder, J. A., 2003, "Reentry Flight Controller Design Using Nonlinear Dynamic Inversion," J. Spacecr. Rockets, **40**(1), pp. 64–71.
[9] Littleboy, D. M., and Smith, P. R., 1998, "Using Bifurcation Methods to Aid Nonlinear Dynamic Inversion Control Law Design," J. Guid. Control Dyn., **21**(4), pp. 632–638.
[10] Snells, S. A., Enns, D. F., and William, W. L., 1992, "Nonlinear Inversion Flight Control for a Super Maneuverable Aircraft," J. Guid. Control Dyn., **15**(4), pp. 976–984.
[11] Mulgund, S. S., and Stengel, R. F., 1995, "Aircraft Flight Control in Wind Shear Using Sequential Dynamic Inversion," J. Guid. Control Dyn., **18**(5), pp. 1084–1091.
[12] Smar, R., and Postlethwait, I., 1994, "Multivariable Controller Design for a High Performance Aero-Engine," *Proceedings of the IEE Control Conference'94*, pp. 1312–1317.
[13] Frederick, D., Garg, S., and Adibhatla, S., 1996, "Turbofan Engine Control Design Using Robust Multivariable Control Technologies," AIAA Paper No. 96–2587.
[14] Adibhatla, S., Garg, S., Collier, G., and Zhao, X., 1998, "$H_\infty$ Control Design for a Jet Engine," AIAA Paper No. 98-3753.
[15] Peleties, P., DeCarlo, R., 1991, "Asymptotic Stability of m-Switched Systems Using Lyapunov-Like Functions," *Proceedings of American Control Conference'91*, Boston, MA, pp. 1679–1684.
[16] Branicky, M. S., 1998, "Multiple Lyapunov Functions and Other Analysis Tools for Switched and Hybrid Systems," IEEE Trans. Autom. Control, **43**(4), pp. 475–482.
[17] Pettersson, S., and Lennartson, B., 1996, "Stability and Robustness for Hybrid Systems," *IEEE Conference on Decision and Control*, Kobe, Japan, pp. 1202–1207.
[18] Ye, H., Micheal, A. N., and Hou, L., 1998, "Stability Theory for Hybrid Dynamic Systems," IEEE Trans. Autom. Control, **43**(4), pp. 461–474.
[19] Daafouz, J., Riedinger, P., and Iung, C., 2002, "Stability Analysis and Control Synthesis for a Switched System: A Switched Lyapunov Function Approach," IEEE Trans. Autom. Control, **47**(11), pp. 1883–1887.
[20] Hu, B., Zhai, G., and Michel, A. N., 2002, "Hybrid Static Output Feedback Stabilization of Second-Order Linear Time-Invariant Systems," Linear Algebr. Appl., **351**(15), pp. 475–485.
[21] Liberzon, D., 1999, "Stabilizing A Linear Systems With Finite-State Hybrid Output Feedback," *Proceedings of the Seventh IEEE Mediterranean Conference on Control and Automation*, Haifa, Israel, pp. 176–183.
[22] Litsyn, E., Nepomnyashchikh, Y. V., and Ponosov, A., 2000, "Stabilization of Linear Differential Systems via Hybrid Feedback Controls," SIAM J. Control Optim., **38**(5), pp. 1468–1480.
[23] Artstein, Z., 1996, "Examples of Stabilization With Hybrid Feedback," *Hybrid Systems III*, E. Alur et al., eds. Springer-Verlag, Berlin, pp. 173–185.
[24] Zhai, G., and Chen, X., 2002, "Stabilizing Linear Time-Invariant Systems With Finite-State Hybrid Static Output Feedback," *IEEE International Symposium on Circuits and Systems*, Vol. 1, pp. 249–252.
[25] Savkin, A. V., Skafidas, E., and Evans, R. J., 1999, "Robust Output Feedback Stabilizability via Controller Switching," Automatica, **35**, pp. 69–74.
[26] El-Farra, N. H., and Christofides, P. D., 2001, "Switching and Feedback Laws for Control of Constrained Switched Nonlinear Systems," Chem. Eng. Sci., p. 184.
[27] Decarlo, R. A., Branicky, M. S., Pettersson, S., and Lennartson, B., 2000, "Perspectives and Results on the Stability and Stabilizability of Hybrid Systems," Proc. IEEE, **88**(7), pp. 1069–1082.
[28] Kassakian, J. G., Schlecht, M. F., and Verghese, G. C., 1991, *Principles of Power Electronic*, Addison-Wesley, Boston, MA.
[29] Leith, D. J., Shorten, R. N., Leithead, W. E., Mason, O., and Curran, P., 2003, "Issues in the Design of Switched Linear Control System: A Benchmark Study," Int. J. Adapt. Control Signal Process., **17**(2), pp. 103–118.
[30] Skafidas, E., Evans, R. J., Savkin, A. V., and Pertersen, I., 1999, "Stability Results for Switched Controller Systems," Automatica, **35**(4), pp. 553–564.
[31] Hespanha, J. P., Liberzon, D., and Morse, A. S., 2003, "Overcoming the Limitations of Adaptive Control by Means of Logic-Based Switching," Syst. Control Lett., **49**(1), pp. 49–65.
[32] Boyd, S., Ghaoui, L. E., Feron, E., and Balakrishnan, V., 1994, "Linear Matrix Inequalities in System and Control Theory," *SIAM Studies in Applied Mathematics*, SIAM, Philadelphia, PA, Vol. 15.
[33] Bao, J., Forbes, J. F., and McLellan, P. J., 1999, "Robust Multiloop PID Controller Design: A Successive Semidefinite Programming Approach," Ind. Eng. Chem. Res., **38**(9), pp. 3407–3419.

# An Innovative Gas Turbine Cycle With Methanol-Fueled Chemical-Looping Combustion

**Hongguang Jin**
Institute of Engineering Thermophysics,
Chinese Academy of Sciences,
Beijing 100039, China
e-mail: hgjin@mail.etp.ac.cn

**Xiaosong Zhang**
Institute of Engineering Thermophysics,
Chinese Academy of Sciences,
Beijing 100080, China;
Graduate University of the Chinese Academy of Sciences,
Beijing 100080, China

**Hui Hong**

**Wei Han**

Institute of Engineering Thermophysics,
Chinese Academy of Sciences,
Beijing 100080, China

*In this paper, a novel gas turbine cycle integrating methanol decomposition and the chemical-looping combustion (CLC) is proposed. Two types of methanol-fueled power plants, including the new gas turbine cycle with CLC combustion and a chemically intercooled gas turbine cycle, have been investigated with the aid of the T-Q diagram. In the proposed system, methanol fuel is decomposed into syngas mainly containing $H_2$ and CO by recovering low-temperature thermal energy from an intercooler of the air compressor. After the decomposition of methanol, the resulting product of syngas is divided into two parts: the part reacting with $Fe_2O_3$ is sent into the CLC subsystem, and the other part is introduced into a supplement combustor to enhance the inlet temperatures of the gas turbine to 1100–1500°C. As a result, the new methanol-fueled gas turbine cycle with CLC had a breakthrough in thermodynamic and environmental performance. The thermal efficiency of the new system can achieve 60.6% with 70% of $CO_2$ recovery at a gas turbine inlet temperature of 1300°C. It would be expected to be at least about 10.7 percentage points higher than that of the chemically intercooled gas turbine cycle with the same recovery of $CO_2$ and is environmentally superior due to the recovery of $CO_2$. The promising results obtained here indicated that this novel gas turbine cycle with methanol-fueled chemical-looping combustion could provide a promising approach of both effective use of alternative fuel and recovering low-temperature waste heat and offer a technical probability of blending a combination of the chemical-looping combustion and the advanced gas turbine for carbon capture and storage.*
[DOI: 10.1115/1.3098418]

## 1 Introduction

Currently, we face a potentially serious problem of rapid climate change due to anthropogenic emissions of greenhouse gases (e.g., $CO_2$). One of the options to control the greenhouse gas emission is the $CO_2$ capture technologies from flue gases. In a fossil fuel-fired power plant, $CO_2$ capture can be carried out mainly through three available technologies: *precombustion*, *postcombustion*, and *oxyfuel combustion*. The progress in this field has been addressed by Abi-Khader [1]. The main disadvantages of these techniques are both the substantial addition to the cost of power generation and the large amount of energy that is required for the separation of $CO_2$, which means a relative reduction of 15–20% in the overall efficiency of a power plant [2,3]. It is important and urgent to find a new method where $CO_2$ can be separated from the flue gases in the power plant with a small energy penalty.

Chemical-looping combustion (CLC) with inherent separation of $CO_2$ is considered a promising technology proposed by Ishida and Jin in 1994 [4,5]. It is the most attractive energy efficient method for $CO_2$ capture from fuel conversion in the combustion process. Compared with conventional combustion, the chemical-looping combustion involves the use of a metal oxide as an oxygen carrier, which transfers oxygen from the combustion air to the fuel, and the direct contact between fuel and the mixture of fuel and air is avoided. In this way, $CO_2$ and $H_2O$ are inherently separated from the other components of flue gases leading to no energy needed for $CO_2$ separation. It is worth emphasizing that this novel $CO_2$ capture technology simultaneously resolve both energy and environmental problems in combustion processes, since the conversion of fuel-based chemical energy into thermal energy in the traditional combustion not only results in the largest irreversibility in power systems but also gives rise to a serious environmental impact. In recent years, several researchers have investigated and contributed in the development of the chemical-looping combustion technology [6,7]. For example, Mattison and Lyngfelt [8] designed and proposed a 10 kW fluidized-bed boiler with chemical-looping combustion, and Korea has developed a 50 kW chemical-looping combustor for future industrial application [9]. A project for a novel $CO_2$ separation system with CLC has been conducted by the Department of Energy of the United States [10].

In our previous papers [4,11,12], Jin creatively integrated and proposed three kinds of gas turbine thermal cycles coupling different fuels of natural gas, hydrogen, and coal gas with chemical-looping combustion, respectively. The kinetic catalysis and reaction for various kinds of fuel-based chemical-looping combustions have also been investigated [13,14]. With the development of alternative fuels such as methanol or dimethylether (DME), there is a great potential application in the power generation sectors. Especially for China and United States where coal is the main energy resource, methanol or DME is economically produced from the promising coal based polygeneration technology (POLYGEN). However, when alternative fuel is being converted into thermal energy to generate electricity by traditional combustion in the conventional power plant, we have to face a serious issue that there are yet both the largest exergy destruction of chemical energy and the high energy penalty for $CO_2$ removal due to containing carbon. Hence, one of the biggest potential for the development of the next-generation power plant using alternative fuel would be directed toward the new approach of fuel conversion. The chemical-looping combustion can be the promising candidate. In the present paper, the new fuel conversion method of chemical-looping combustion is applied into the methanol-fueled intercooling gas turbine cycle.

Manuscript received November 10, 2008; final manuscript received December 10, 2008; published online July 17, 2009. Review conducted by Dilip R. Ballal. Paper presented at the ASME Turbo Expo 2008: Land, Sea and Air (GT2008), Berlin, Germany, June 9–13, 2008.

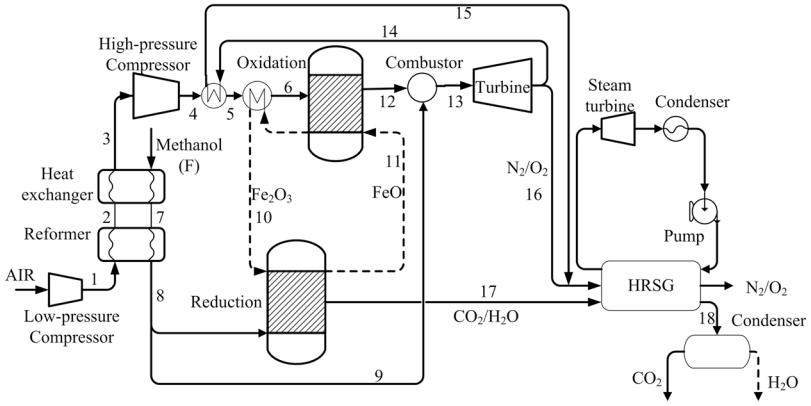


**Fig. 1 The flow diagram of the new system**

The objective of this paper is (i) to propose a new methanol-fueled combined cycle (CC) synergistically integrating chemical-looping combustion, (ii) to identify the feature of the key processes of energy conversion with the aid of the *T-Q* diagram, and (iii) to disclose the potentials for reducing the energy penalty of $CO_2$ separation.

## 2 Description of the Two Methanol-Fueled Power Systems

**2.1 Methanol-Fueled Power Plant With CLC.** Figure 1 shows the plant scheme of the new system. The plant includes three main parts: the methanol decomposition subsystem with the recovery of the low-grade waste thermal energy, the CLC subsystem fired by the syngas, and the $CO_2$ separation subsystem.

*Methanol decomposition subsystem*. Since in the conventional intercooled gas turbine, the heat released from the intercooler with temperature at 200–300°C is wasted, methanol decomposition can be utilized to recover the intercooling heat. The compressed air (stream 1) with low pressure is cooled down to 143°C in an intercooler and is then compressed in the next stage compressor (stream 3) in the methanol decomposition subsystem. The intercooler heat is recovered through methanol decomposition. The intercooler is divided into two segments containing a heat exchanger and a reactor. The liquid methanol as a fuel, at the pressure of 15 bar, is first superheated to methanol vapor at the temperature of 165°C. After that, the superheated methanol then proceeds to an endothermic reaction with a catalyst in the reactor (stream 7). The endothermic reaction path is $CH_3OH \rightarrow CO + 2H_2$ and absorbs the thermal energy of 96 kJ/mol–$CH_3OH$ at 220°C, after which the syngas then enters the CLC subsystem. Because of the use of intercooling, heat recovery should be adopted.

*CLC subsystem*. In the CLC subsystem, two separated reactors—syngas with metal oxide (reduction) and the resulting metal with air (oxidation)—are used. Here a particle of $Fe_2O_3$ is used as a solid metal oxide (i.e., looping material) in the chemical-looping combustion. Oxygen is transferred between the two reactors by means of an oxygen carrier. The syngas is first reacted with the solid $Fe_2O_3$, as shown in reaction (1) in a reduction reactor, producing solid FeO and steam. When 95% of $Fe_2O_3$ is reduced, the equilibrium temperature reaction (1) is about 360°C. To achieve a higher conversion ratio of $Fe_2O_3$, the temperature of the reduction reaction is set at 411°C. In the oxidation reactor, the air is reacted with the solid FeO, as shown in reaction (2), in high-temperature produced from the former reactor yielding $Fe_2O_3$ and high-temperature flue gas through strong exothermic oxidation.

*Supplementary combustor subsystem*. Due to the physical characteristics of FeO, the temperature of oxidation cannot, however, be higher than 1000°C [7]. To reach a higher gas turbine inlet temperature (TIT), a supplementary combustor is adopted. Most of the syngas enters the oxidation reactor, and the rest as fuel is fed into the supplementary combustor after the exiting of the oxidation reactor in order to enhance the inlet temperature of the gas turbine ranging 1100–1500°C. Finally, the gases from the oxidation and reduction reactors can be used as the working fluid to generate power in the gas turbines. Then part of flue gas (stream 14) is drawn out to heat the compressed air and then go back to the dual-pressure heat recovery steam generator (HRSG) as a heat resource with the other part flue gas.

In a reduction reactor,

$$3Fe_2O_3 + CO + 2H_2 \rightarrow 6FeO + CO_2 + 2H_2O, \quad \Delta H^0_{red} = 80 \text{ kJ} \tag{1}$$

In an oxidation reactor,

$$6FeO + 3/2O_2 \rightarrow 3Fe_2O_3, \quad \Delta H^0_{oxd} = -840 \text{ kJ} \tag{2}$$

The $CO_2$ separation subsystem is used to separate $CO_2$ from the mixture of $CO_2/H_2O$. The mixture's temperature is about 150°C, 15 bar from the HRSG, before it is cooled down to 30°C by the condenser. At this temperature, the $H_2O$ turns into its liquid form and the $CO_2$ is separated at 15 bar.

*Reference system*. In the previous paper [15], we have proposed a methanol-fueled chemically-intercooling gas turbine plant with the integration of low-temperature thermal energy and methanol decomposition. Figure 2 shows the flow diagram of the reference system.

The liquid fuel methanol, at the pressure of 15 bar, is first superheated to methanol vapor at the temperature of 220°C. After that, the superheated methanol proceeds to an endothermic reaction with catalyst in the reactor and is decomposed by the intercooler heat. The syngas fuel with primary $H_2$ and CO (stream 8) is

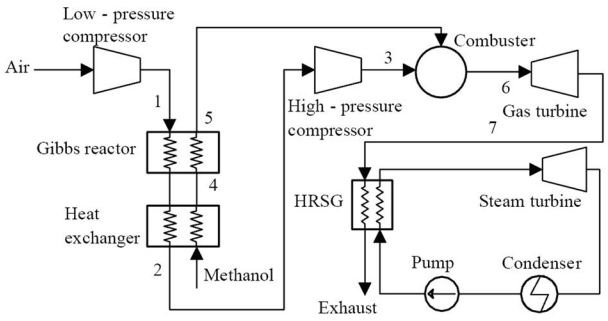


**Fig. 2 A simplified diagram for the chemically intercooled gas turbine combined cycle**

**Table 1 Main assumption for evaluation**

| | Reference system | New system |
|---|---|---|
| Turbine inlet temperature (°C) | 1300 | 1300 |
| Turbine inlet pressure (bar) | 15.00 | 15.00 |
| Reduction temperature (°C) | - | 411 |
| Pressure of the reduction reactor (bar) | - | 15.00 |
| Pressure loss of heat exchangers (%) | 3.00 | 3.00 |
| Isentropic efficiency of air compressor | 0.88 | 0.88 |
| Isentropic efficiency of gas turbine | 0.90 | 0.90 |
| Isentropic efficiency of steam turbine | 0.88 | 0.88 |
| Pinch point in HRSG (°C) | 15 | 15 |
| Pressure loss of HRSG (gas-side) (%) | 3 | 3 |
| Pressure loss of HRSG (steam, water) (%) | 10 | 10 |
| Condensation pressure (bar) | 0.07 | 0.07 |

fed to a combustor of the gas turbine and burned with the compressed air (stream 3). This exothermic reaction is according to $CO+2H_2+1.5O_2 \rightarrow CO_2+2H_2O$ and its heating value of combustion is 772.29 kJ/mol–$CH_3OH$. The flue gas leaving the combustor (stream 6) is expanded in a gas turbine with the inlet temperature of 1300°C. Then the exhaust gas from the gas turbine at 500–600°C (stream 7) drives a steam turbine through dual-pressure HRSG.

## 3 Evaluation of the System Performance

This paper presents an evaluation of the system performance with ASPEN PLUS software. The pressure in the reactors was 15 bar, and the flue gas temperature was 150°C. The cooling air fraction is specified for each cooled stage and the value of the cooling air fraction is about 7% of the air compressor inlet flow. The temperature of water and $CO_2$ existing in the condenser was 25°C, 15 bar. The data of unit operation are specified in Tables 1 and 2.

Based on the analysis of the system model, this system has four important variables: (i) the TIT of the high-temperature gas turbine, (ii) the total pressure ratio ($\pi$) of the compressor, (iii) the temperature ($T_{re}$) of the reduction reactor, and (iv) the pressure ratio ($\pi_1$) of low-pressure compressor.

For a given case of the new system, four variables, namely, TIT, $\pi$, $T_2$, and $\pi_1$, were set at 1300°C, 15.00, 411°C and 7.92, respectively.

**Table 2 Parameters of main points**

| Point | T (°C) | P (bar) | Component | kmol |
|---|---|---|---|---|
| 1 | 295 | 8.03 | $N_2$(79%) $O_2$(21%) | 28.84 |
| 2 | 195 | 8.03 | $N_2$(79%) $O_2$(21%) | 28.84 |
| 3 | 143 | 8.00 | $N_2$(79%) $O_2$(21%) | 28.84 |
| 4 | 234 | 15.20 | $N_2$(79%) $O_2$(21%) | 28.84 |
| 5 | 490 | 15.20 | $N_2$(79%) $O_2$(21%) | 28.84 |
| 6 | 648 | 15.20 | $N_2$(79%) $O_2$(21%) | 28.84 |
| 7 | 165 | 15.20 | $CH_4O$(100%) | 1 |
| 8 | 248 | 15.20 | $CH_4O$(6%) $H_2$(62%) CO(31%) | 2.79 |
| 9 | 248 | 15.20 | $CH_4O$(4%) $H_2$(64%) CO(32%) | 1.09 |
| 10 | 600 | 15.10 | $Fe_2O_3$(100%) | 1.18 |
| 11 | 411 | 15.20 | FeO(100%) | 2.35 |
| 12 | 1000 | 15.10 | $N_2$(82%) $O_2$(18%) | 25.94 |
| 13 | 1300 | 15.00 | $N_2$(81%) $O_2$(13%) $CO_2$(2%) $H_2O$(4%) | 26.56 |
| 14 | 584 | 1.03 | $N_2$(81%) $O_2$(13%) $CO_2$(2%) $H_2O$(4%) | 20.59 |
| 15 | 300 | 1.03 | $N_2$(81%) $O_2$(13%) $CO_2$(2%) $H_2O$(4%) | 20.59 |
| 16 | 584 | 1.03 | $N_2$(81%) $O_2$(13%) $CO_2$(2%) $H_2O$(4%) | 5.97 |
| 17 | 411 | 15.00 | $CO_2$(33%) $H_2O$(66%) | 2.01 |
| 18 | 150 | 1.03 | $CO_2$(33%) $H_2O$(66%) | 2.01 |

**Table 3 Result of exergy analysis**

| Items | The new system | | Chemically intercooled CC | |
|---|---|---|---|---|
| | Exergy (kJ/mol-$CH_4O$) | Ratio (%) | Exergy (kJ/mol-$CH_4O$) | Ratio (%) |
| Lower heating value | 636 | | 636 | |
| Input exergy of fuel (HHV) | 676.92 | 100 | 676.92 | 100 |
| | Exergy destruction | | | |
| HRSG | 13.69 | 2.02 | 15.51 | 2.29 |
| Compressor | 20.75 | 3.06 | 16.22 | 2.4 |
| Gas turbine | 23.60 | 3.49 | 18.48 | 2.73 |
| Combustor | 161.05[a] | 23.79 | 208.1 | 30.74 |
| Decomposition reaction | 6.62 | 0.98 | 8.83 | 1.31 |
| Heat exchanger | 24.64 | 3.64 | 34.46 | 5.09 |
| Exhaust gas loss | 28.98 | 4.28 | 16.59 | 2.45 |
| Total exergy destruction | 279.32 | 41.26 | 318.19 | 47.08 |
| Output exergy (net power) | 387.13 | 57.19 | 356.60 | 52.68 |
| Sum of exergy | 675.10 | 99.88 | 675.09 | 99.76 |
| Thermal efficiency | | 60.60 | | 56.10 |

[a]The sum of reduction and oxidation.

Table 3 shows the exergy destruction in the new system compared with the reference system without $CO_2$ recovery. The gas turbine inlet temperature of the reference system was set at 1300°C, and the approach temperature difference of the heat exchanger and the efficiency of the corresponding assembly are the same as the new system. The results show that the new system provides a higher efficiency than that of the reference system without $CO_2$ separation. At the same time, it may separate 70% of the $CO_2$. Obviously, it can be seen that the thermal efficiency of the new system would be expected to be 60.6%, higher than that of the reference system without $CO_2$ recovery (56.1%). Considering the $CO_2$ separation, when the reference system separates $CO_2$ by conventional physical or chemical absorption, its thermal efficiency would be decreased by 6–8 percentage points with the same ratio of $CO_2$ separation as the new system. This indicates that the thermal efficiency of the new system would be 10–12% higher than that of the reference system with the same ratio of $CO_2$ separation.

## 4 *T-Q* Diagram Analysis of the Key Energy Conversion Processes

Unlike the conventional power system, the proposed system integrates the chemically endothermic reaction and the thermal cycle. In order to disclose the feature of the energy conversion, the *T-Q* diagram is adopted. The heat duties (*x*-coordinate) in Figs. 3–5 are based on the input of 1 kmol methanol.

*Methanol decomposition driven by the low-temperature waste heat*. In the proposed system, the energy conversion of the methanol decomposition process is composed of two sections: methanol evaporation (as shown by F–7 in Fig. 3) and the endothermic reaction of methanol (as shown by 7–8 in Fig. 3). It can be observed that the heat from the upper temperature of the compressed air at around 300°C is released to drive the methanol decomposition, while the rest of the heat is utilized to preheat and evaporate the methanol fuel. During this energy conversion process, the temperature matches between the compressed air and the methanol decomposition is a key factor. From Fig. 3, we may see that the minimal temperature differences in the preheated methanol and the methanol decomposition are fixed at 10°C and 30°C, respectively. This means that the thermal match not only ensures

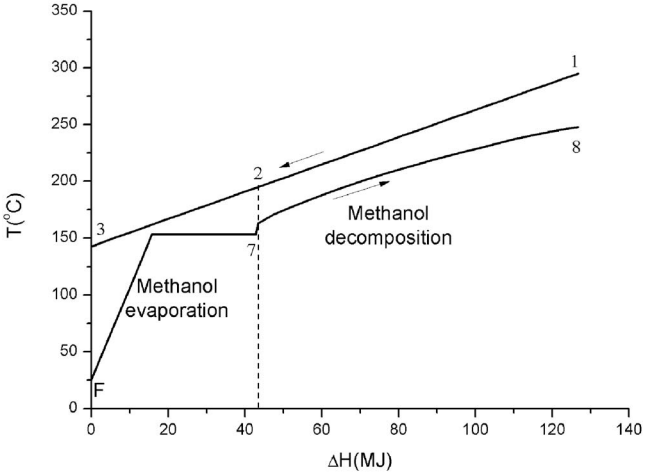


**Fig. 3 *T-Q* diagram of $CH_4O$ evaporation and decomposition**

the energy conversion to proceed easily but also lessens irreversibility.

*Recovery of the middle-temperature waste heat*. Figure 4 illustrates the energy transformation of the middle-temperature waste heat from the $Fe_2O_3$. The minimal temperature difference is fixed at 60°C. The compressed air is first heated to 491°C by the exhaust gas and then is heated to 648°C by $Fe_2O_3$. The use of exhaust gas as part of the heat source can lessen irreversibility than using $Fe_2O_3$ as the entire heat source. The exhaust gas with a temperature decrease from 585°C to 300°C is shown as the left part of the hot side. The right part represents the temperature change in $Fe_2O_3$. After heating the compressed air, the rest heat of $Fe_2O_3$ is used to support the reduction reaction. The recovery heat supported by the exhaust gas and $Fe_2O_3$ is 212 MJ and 135 MJ, respectively.

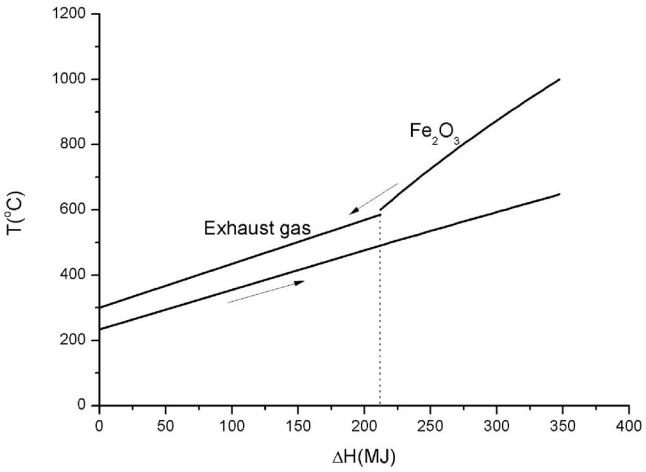


**Fig. 4 *T-Q* diagram of heat recovery**

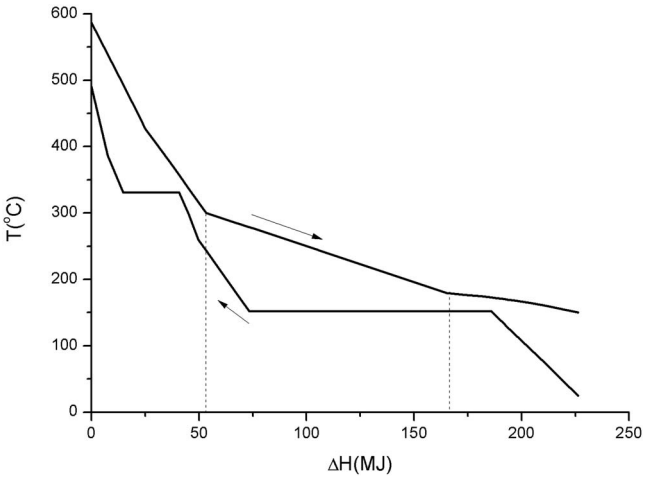


**Fig. 5 *T-Q* diagram of HRSG**

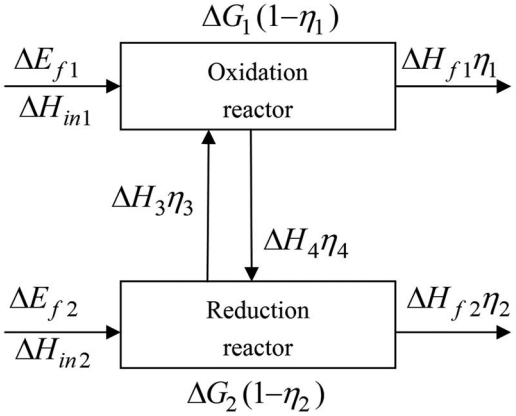


**Fig. 6 Sketch map of the CLC combustion**

In most gas turbine systems, the compressor air could only be heated by exhaust gas form the gas turbine, so the temperature of the compressor air can just reach about 500°C (see the left part of Fig. 4). On the other hand, in the new CLC system, the compressed air is also heated by $Fe_2O_3$ from the oxidation reactor. In this way, the temperature of the compressed air can reach about 650°C due to the higher temperature of $Fe_2O_3$ (right part of Fig. 4). Thus, more waste heat in the system can be recovered, leading to a better thermodynamic performance.

*Heat transfer in HRSG*. Fig. 5 illustrates the energy conversion of the dual-pressure heat recovery steam generation in HRSG.

The minimal temperature difference for the gas/liquid heat transfer in HRSG is fixed at 20°C. The turbine exhaust is 584°C, which is used to produce steam at 490°C. There are two inflexions on the hot side. The first inflexion is caused by the products ($CO_2$ and $H_2O$) from the reduction reactor due to the change in thermal capacity. The inlet of the exhaust gas after heat recovery brings about the second inflexion. The heat duty from the exhaust gas and the products of the reduction reactor are 174 MJ and 52 MJ, respectively.

## 5 Results and Discussion

**5.1 Features of Synergistically Integrating CLC and Methanol Decomposition.** *Significant decrease in exergy destruction in the combustion*. The CLC subsystem is a key process for this new system. We have seen that CLC plays a significant role in decreasing the exergy destruction in the new system. To disclose the characteristic of CLC, we examine the inter-relationship between the reduction and oxidation reactors.

The CLC combustion is presented in Fig. 6. We assumed that the temperature of the oxidation reaction is constant. The parameters of $\Delta H$ and $\Delta E$ represent enthalpy and exergy, respectively. First, the oxidation reaction and reduction reaction is at the equilibrium temperature. $\Delta H_{ox}$ is the exothermic heat of oxidation and $\Delta H_{re}$ is the endothermic heat of reduction at the equilibrium temperature. Since $\Delta H_{ox}$ and $\Delta H_{re}$ are not affected by the reaction temperature so much, thereby in our study, $\Delta H_{ox}$ and $\Delta H_{re}$ can be assumed as the constant. Then the temperature of these two reactions reaches the real reaction temperature.

We assume $\Delta EXL_1$ and $\Delta EXL_2$ as the exergy destruction in the

oxidation and reduction reactions, respectively

Based on the energy and exergy balance, in the oxidation reactor,

$$\Delta H_{f1} = \Delta H_{\text{in1}} + \Delta H_{\text{ox}} + \Delta H_3 - \Delta H_4 \tag{3}$$

where $\Delta H_{f1}$ is the enthalpy output of the oxidation reactor, $\Delta H_{\text{in1}}$ is the enthalpy of air, $\Delta H_3$ is the enthalpy of FeO, and $\Delta H_4$ is the enthalpy of $Fe_2O_3$.

$$\Delta E_{f1} + \Delta H_3 \eta_3 - \Delta H_4 \eta_4 = \Delta H_{f1} \eta_1 + \Delta \text{EXL}_1 \tag{4}$$

where $\Delta E_{f1}$ is the exergy of air, and $\Delta H_3 \eta_3$ and $\Delta H_4 \eta_4$ are the exergies of FeO and $Fe_2O_3$ according to the second law of thermodynamics.

In the reduction reactor,

$$\Delta H_{f2} = \Delta H_{\text{in2}} + \Delta H_{red} - \Delta H_3 + \Delta H_4 \tag{5}$$

where $\Delta H_{f2}$ is the enthalpy output of the reduction reactor, and $\Delta H_{\text{in2}}$ is the enthalpy of fuel.

$$\Delta E_{f2} - \Delta H_3 \eta_3 + \Delta H_4 \eta_4 = \Delta H_{f2} \eta_2 + \Delta \text{EXL}_2 \tag{6}$$

where $\Delta E_{f2}$ is the exergy of fuel.

According to the Appendix [16], the exergy destruction $\Delta \text{EXL}_1$ and $\Delta \text{EXL}_2$ can be shown as

$$\Delta \text{EXL}_1 = \Delta G_1 (1 - \eta_1) \tag{7}$$

$$\Delta \text{EXL}_2 = \Delta G_2 (1 - \eta_2) \tag{8}$$

The total exergy destruction of the two reactors is

$$\Delta \text{EXL} = \Delta \text{EXL}_1 + \Delta \text{EXL}_2 = \Delta G_1 (1 - \eta_1) + \Delta G_2 (1 - \eta_2) \tag{9}$$

The introduction of Eqs. (4) and (6) into Eq. (9) yields

$$\Delta \text{EXL} = \Delta E_{f1} + \Delta E_{f2} - \Delta H_{f1} \eta_1 - \Delta H_{f2} \eta_2 \tag{10}$$

We assume $\Delta H_{\text{ex}} = \Delta H_4 - \Delta H_3$. Hence $\Delta H_{\text{ex}}$ is the heat exchanged between reduction reactor and oxidation reactor. The introduction of Eqs. (3) and (5) into Eq. (10) yields

$$\Delta \text{EXL} = (\Delta E_{f1} + \Delta E_{f2}) - ((\Delta H_{\text{ox}} + \Delta H_{\text{in1}}) \eta_1 + (\Delta H_{\text{re}} + \Delta H_{\text{in2}}) \eta_2) + \Delta H_{\text{ex}} (\eta_1 - \eta_2) \tag{11}$$

The first item in the right side of Eq. (11) is the exergy input of the CLC system, while the second item is mainly related with the type of metal. The third item shows the effect of $\Delta H_3$ on the system performance. $\eta_2$ is a key parameter and depended on the reduction reaction temperature. When $T_{\text{re}}$ decreases, the second and the third items will be increased, thereby reducing the $\Delta$EXL. That is, when the reduction reaction temperature ($T_{\text{re}}$) decreases, the exergy destruction of the CLC system is reduced, thereby resulting in a better thermodynamic performance of the system.

Equation (11) can be rearranged as

$$\Delta \eta_{\text{EXL}} = \frac{\Delta \text{EXL}}{\Delta E_{f1} + \Delta E_{f2}} = 1 - \frac{((\Delta H_{\text{ox}} + \Delta H_{\text{in1}}) \eta_1 + (\Delta H_{\text{re}} + \Delta H_{\text{in2}}) \eta_2) + \Delta H_{\text{ex}} (\eta_1 - \eta_2)}{\Delta E_{f1} + \Delta E_{f2}} = f(T_{\text{re}}, \Delta H_{\text{ex}}) \tag{12}$$

As a function of $T_{\text{re}}$ and $\Delta H_{\text{ex}}$, the $\Delta \eta_{\text{EXL}}$ will be reduced as $T_{\text{re}}$ and $\Delta H_{\text{ex}}$ decreased.

Figure 7 illustrates the overall $\Delta \eta_{\text{EXL}}$ of the system as it varies with the reduction reactor temperature and turbine inlet temperature. It can be seen that its exergy destruction is expected to increase 2% with the reduction temperature from 400°C to 900°C.

**5.2 Upgrading of the Energy Level of Low-Temperature Thermal Energy.** Unlike the traditional approach of heat transfer, the low-grade waste heat in this proposed cycle can be recovered by the chemical processes. An attractive feature is that the low-grade waste heat can be upgraded to the high-grade chemical energy of the solid FeO via reduction reaction. It means that for the intercooling heat at around 300°C from the compressor, it is utilized to drive methanol decomposition where such low-grade thermal energy is first recovered in the products of the syngas and is then converted into the chemical energy of FeO in the reduction reactor. In addition, the middle-temperature heat from the $Fe_2O_3$ at about 600°C can be converted into high-grade chemical energy in the reduction reactor. From the viewpoint of the energy level, there levels of the intercooling heat and the heat of $Fe_2O_3$ may be upgraded from 0.35 and 0.6 to the high-grade chemical energy of FeO (0.89) [17], respectively. This kind of the middle-and-low temperature waste heat is finally released as the form of the high-temperature thermal energy via oxidation reaction of FeO to produce electricity with a high-efficiency Brayton cycle.

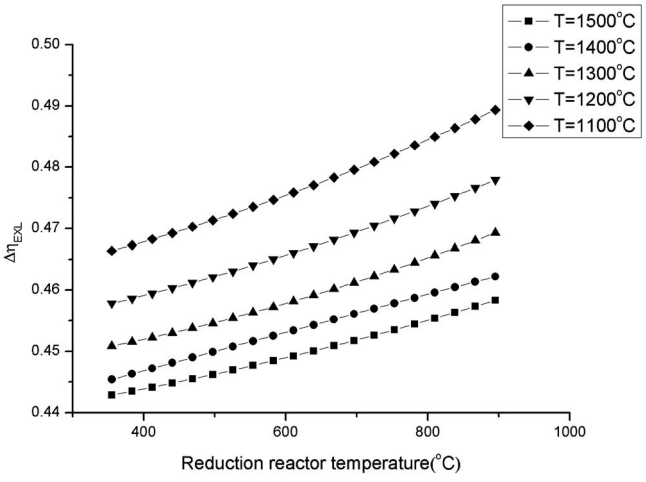


**Fig. 7 Variation in the exergy destruction of the cycle with reduction temperature**

It should be emphasized that this benefit is attributed to the energy-level degradation from methanol combustion to FeO oxidation in the chemical-looping combustion, meaning that this degradation acts as a "driving force" to upgrade the energy level of low-temperature intercooling thermal energy. At the same time, this energy-level degradation has the function of the art combined cycle of the combustion. chemical energy released, decreasing the energy-level difference between chemical energy of fuel and thermal energy at the gas turbine inlet temperature, reducing the irreversibility of the combustion and improving the thermal efficiency. It can be seen from Table 3 that the net thermal efficiency of the proposed cycle could be as high as 60.6% at TIT of 1300°C, competitive with that of the state-of-the art combined cycle.

**5.3 Advanced Thermodynamic Performance.** Figure 8 illustrates the variation in the overall thermal efficiency ($\eta$) of the system with varying TITs and pressure ratios ($\pi$). In addition, for the given $\pi$, $\eta$ will increase with an increase in TIT. For each TIT, there is a $\pi_{\text{opt}}$ to get maximum thermal efficiency, which is similar to that of the conventional combined cycle, with the $\pi_{\text{opt}}$ at about

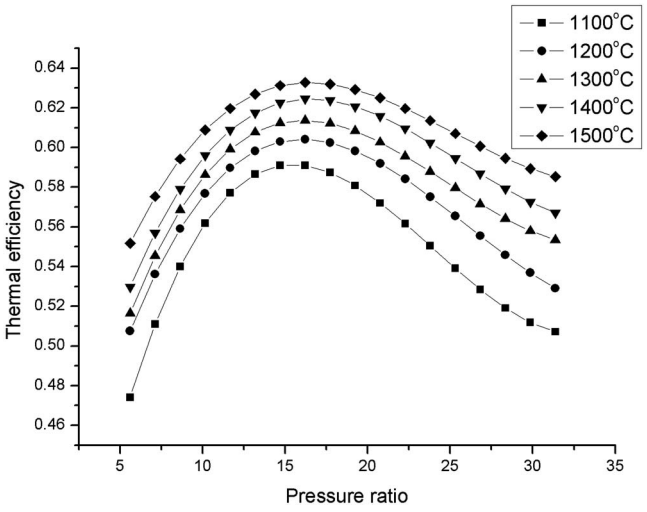


**Fig. 8 Variation of thermal efficiency with TIT and $\pi$**

15–17 bar. This means that the new system has a similar value of $\pi_{opt}$ with the conventional combined cycle. The thermal efficiency is expected to be about 63.2% at the pressure ratio of 16 at a gas turbine inlet temperature of 1500°C.

In the reference system, the $\pi_{opt}$ is about 25–30, which is bigger than the optimize pressure ratio of this new system. It is very difficult to achieve this pressure ratio under the present technology. According to the integration of CLC combustion and methanol decomposition, this new system uses $Fe_2O_3$ (stream 5) to reheat the pressured air (stream 3), so that the $\pi_{opt}$ of the new system is about 15, which is similar to the combined cycle and is easily achievable.

**5.4 Significant Role of Decreasing Energy Penalty for $CO_2$ Capture.** In conventional technology for suppressing environmental impact, it can be easily found that the undesirable substances formed from the upstream process are often removed from the downstream process with various separation processes by dealing with a great amount of exhaust gas and at a high cost of energy consumption [18]. The tendency of the next-generation systems will be toward the elimination of undesirable formation from the upstream process. From this point, we may find that the CLC combustion will be the promising technology to recover $CO_2$. Thus, in a thermal cycle with a CLC combustion scenario, environmental pollution due to greenhouse gas emissions will be eliminated. Similarly, we may find that the product of the reduction reactor in the chemical-looping combustion is also very simple, consisting of only water and $CO_2$.

Table 4 illustrates the comparison of $CO_2$ capture on the three systems (combined cycle, the reference system, and the new system) with and without $CO_2$ compression. The combined cycle is based on Mitsubishi M701F type, whose turbine inlet temperature is 1350°C and pressure ratio is 17. If all these three systems remove 70% of $CO_2$, and because of the characteristics of CLC combustion, the thermal efficiency of the new system will not be reduced, but the thermal efficiencies of the other two systems will be decreased by about 6%. Considering the transportation, the $CO_2$ is generally compressed to 85 bar to be liquefied and transported. From Table 4, it can be seen that the thermal efficiency of the combined cycle and the reference system will be decreased by 1.5%, and the new system will be decreased by 0.8%. This is because the $CO_2/H_2$ from the reduction reactor is 15 bar, a value higher than the exhaust gas of the other systems (1.03 bar).

**Table 4 Comparison of thermal efficiencies with 70% $CO_2$ capture**

| | CC (%) | Reference system (%) | New system (%) |
|---|---|---|---|
| Thermal efficiency (without $CO_2$ compression) | 47.4 | 50.3 | 60.6 |
| Thermal efficiency ($CO_2$ compressed to 85 bar) | 45.9 | 48.8 | 59.5 |

Considering the $CO_2$ capture, the new system has an advanced feature without energy penalty, which is 13.6 percentage points higher than the combined cycle, and 10.7 percentage points higher than reference system.

## 6 Further Consideration of the New System

Chemical-looping combustion is the core technology in the new system. To verify the feasibility of CLC, we have performed several experiments about methanol-fueled and syngas fueled CLC.

**6.1 Experiment of Methanol-Fueled CLC.** The experiment of the reduction reaction between methanol and $Fe_2O_3$ was performed.

The reaction rates of each solid particle were measured by a thermal gravimetrical analysis (TGA) system. The particles were spherical and composed of 60 wt % $Fe_2O_3$ and 40 wt % $Al_2O_3$. The preparation method, the dissolution method, was introduced to improve the kinetic characteristics of particles. The particles were prepared by freeze granulation and sintered at 1300°C for 6 h before they were sieved to a diameter of 1–2 mm.

For the experiment in reduction, the methanol is evaporated and then is transferred to the reactor. The reaction temperature is 300°C. After the $Fe_2O_3$ is reduced to FeO, the temperature of the reactor is heated to 800°C, and the air is injected into the reactor. The FeO is oxidized to $Fe_2O_3$.

By using the scanning electron microscope (SEM), the surface of the particles is investigated. Figure 9 shows the images of two such particles. This SEM magnifies the particles 2000 times. Before the reaction, the surface of the particles is smooth and compact. The surface of the particles becomes coarse after reaction. There are many small particles adhering to the big ones, which bring about lots of irregular porosities. These porosities can make the gas diffuse easily, which is helpful for reaction.

**6.2 Experiment of Syngas Fueled CLC.** We also have experimentally investigated the kinetics of chemical-looping combustion with simulated syngas in an elevated pressure fixed bed reactor [12]. Two kinds of particles—$NiO/NiAl_2O_4$ and CoO–NiO/YSZ particles—were prepared. The particles were shaped in pellet form with 4.0 mm diameter and 1.5 mm in height and were calcined at 1300°C for 6 h in the atmosphere. The weight ratio of the solid reactant to the binder was set at 6:4.

An outstanding finding is that syngas is a suitable fuel for chemical-looping combustion. The looping material ($NiO/NiAl_2O_4$) has higher reduction reactivity with syngas. There was no damage to the samples of solid materials, after more than 10 cycles of reduction and oxidation. The syngas fueled chemical-looping combusting has high reactivity, avoidance of carbon deposition, and regenerability.

Furthermore, the reactivity of syngas with $Fe_2O_3$ will be investigated in more details to develop the chemical-looping combustion and to promote this new power generation system.

## 7 Conclusions

A novel combined cycle based on the integration of methanol decomposition and CLC has been proposed and evaluated by means of exergy analysis and *T-Q* diagram. The system study on two methanol-fueled power plants points out the defects and potential for improvement of the chemically intercooled combined cycle. In the new system, because of the integration of the metha-

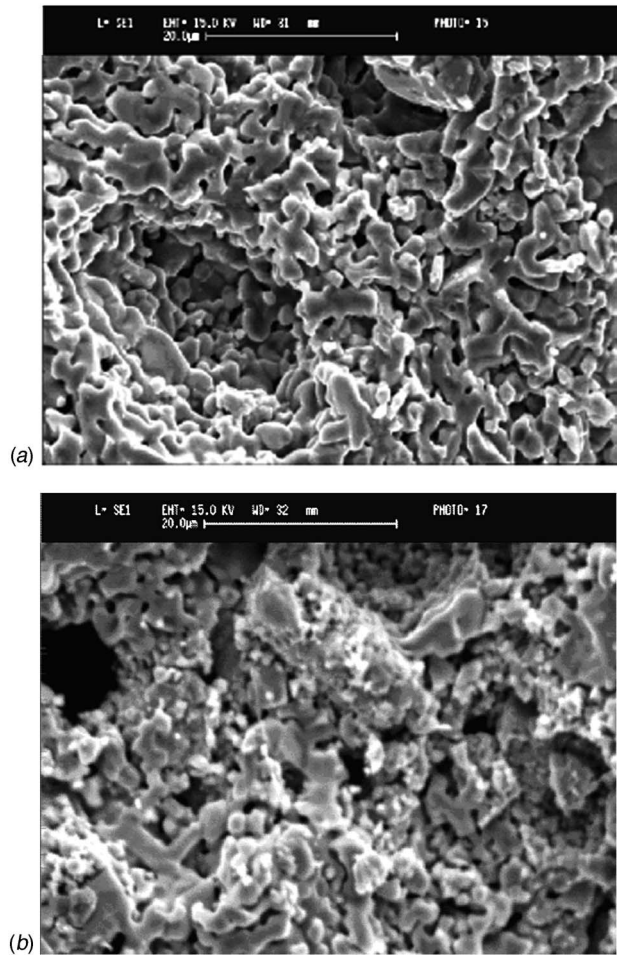


**Fig. 9 Cross-sectional photos of particles (a) before reaction and (b) after reaction**

nol decomposition and CLC combustion, the exergy destruction in the combustion process is decreased, the low-temperature intercooling energy is upgraded, and the $CO_2$ is captured without energy penalty. We have clarified that in the new gas turbine cycle with chemical-looping combustion the exergy losses in combustion and power consumption are much lower than in the reference system. As a result, thermal efficiency in this new cycle with current-technology gas turbines (with a turbine inlet temperature of 1300°C) could be as high as 60.6% with 70% $CO_2$ recovery, increasing efficiency by at least 8 percentage-points higher efficiency compared with that of the reference system with $CO_2$ capture. This new gas turbine cycle with methanol-fueled chemical-looping combustion makes a breakthrough in both the efficient use of alternative fuel and the mitigation of greenhouse gas impact, and can be expected to be a new-generation power plant.

## Acknowledgment

This study is supported by the Natural Science Foundation of China (Contract Nos. 50520140517 and 50836005).

## Nomenclature

$\pi$ = pressure ratio
$\eta$ = thermal efficiency
$\Delta E$ = exergy change
$\Delta H$ = enthalpy change

**Subscripts**

opt = optimal value
ox = oxidation reaction
re = reduction reaction
comp = compressor
GT = gas turbine
ST = steam turbine

## Appendix

Based on the general functions of Gibbs free energy and exergy, Gibbs free energy change $dG$ and exergy change $dE$ in a process of chemical reaction, at a given temperature $T$ and under a pressure $p$, are, respectively, given as

$$dG = dH - TdS \tag{A1}$$

$$dE = dH - T_0 dS \tag{A2}$$

where $dH$ (kJ/mol) is the total enthalpy change in a process, $TdS$ (kJ/mol) is the heat-equivalent energy in a process, and $dS$ (kJ/K mol) is the entropy change in a process, while $T$ refers to the reaction temperature (K), and $T_0$ denotes the environment temperature (K).

For the energy conversion and utilization in a combustion process, Gibbs free energy $\Delta G$ in a combustion reaction cannot produce the work, and the total enthalpy change $\Delta H_f$ is completely transformed into thermal energy. For simplicity, we assumed that a combustion process might be divided into two sections: an exothermic reaction at a given high temperature $T$ and a heat transfer process within the working substance of the thermal cycle. Based on Eqs. (A1) and (A2), exergy of fuel $\Delta E_f$ and Gibbs free energy change $\Delta G$ are, respectively, obtained as follows:

$$\Delta G = \Delta H_f - T\Delta S \tag{A3}$$

$$\Delta E_f = \Delta H_f - T_0 \Delta S \tag{A4}$$

and then, the entropy change $\Delta S$ may be given by Eq. (A3).

$$\Delta S = \frac{\Delta H_f - \Delta G}{T} \tag{A5}$$

Introducing Eq. (A3) into Eq. (A4) yields

$$\Delta E_f = \Delta H_f \left(1 - \frac{T_0}{T}\right) + \Delta G \frac{T_0}{T} \tag{A6}$$

Since $T_0/T = 1-(1-T_0/T) = 1-\eta_c$, Eq. (A6) may be reduced to

$$\Delta E_f = \Delta H_f \eta_c + \Delta G(1-\eta_c) \tag{A7}$$

Equation (A7) states that the exergy of fuel in combustion ($\Delta E_f$) is composed of two parts: work-equivalent energy of $\Delta G(1-\eta_c)$, associated with chemical exergy, and thermal exergy of $\Delta H_f \eta_c$. Traditionally, $\Delta G(1-\eta_c)$ is often regarded as an exergy destruction in the combustion reaction. It is also found from exergy balance that $\Delta E_f$ represents the exergy input, $\Delta H_f \eta_c$ refers to the thermal exergy output, and correspondingly $\Delta G(1-\eta_c)$ stands for the exergy destruction. On the other hand, an important thing we emphasized here is that a part of $\Delta G(1-\eta_c)$ should be taken into account as a usable chemical exergy, which is not simply destroyed as a form of destruction. Hence, Eq. (A7) indicates the interrelationships between exergy of fuel $\Delta E_f$ and Gibbs free energy in combustion reaction, and more importantly, it reveals that the effective use of chemical exergy $\Delta G(1-\eta_c)$ is a key point in reducing exergy destruction in the combustion of fuel.

## References

[1] Abu-Khader, M. M., 2006, "Recent Progress in $CO_2$ Capture/Sequestration: A Review," Energy Sources, **28**(14), pp. 1261–1279.
[2] Assistant Secretary for Fossil Energy, 1993, "Clean Coal Technology Demonstration Program," U.S. Department of Energy, Report No. DOE/FE-0299P.
[3] Gottlicher, G., and Pruschek, R., 1997, "Comparison of $CO_2$ Removal Systems for Fossil-Fuelled Power Plant Processes," Energy Convers. Manage., **38**, (suppl.), pp. S173–S178.

[4] Ishida, M., and Jin, H., 1994, "A New Advanced Power-Generation System Using Chemical-looping Combustion," Energy, **19**(4), pp. 415–422.
[5] Ishida, M., and Jin, H., 1995, "Chemical Looping Combustion Power Generation Plant System," U.S. Patent No. 5447024.
[6] Anheden, M., 1997, "Analysis of Chemical-looping Combustion Systems for Power Generation," Technical Licentiate thesis, Royal Institute of Technology, Stockholm, Sweden.
[7] Consonni, S., Lozza, G., Pelliccia, G., Rossini, S., and Saviano, F., 2006, "Chemical-Looping Combustion for Combined Cycles With $CO_2$ Capture," ASME J. Eng. Gas Turbines Power, **128**, pp. 525–534.
[8] Mattisson, T., and Lyngfelt, A., 2001, "Application of Chemical-looping Combustion With Capture of $CO_2$ ," Second Nordic Mini-Symposium on Carbon Dioxide Capture and Storage, Göteborg, Sweden.
[9] Lee, J. B., Prak, C. S., Choi, S., and Song, Y. W., 2005, "Redox Characteristics of Various Kinds of Oxygen Carriers for Hydrogen Fueled Chemical-Looping Combustion," J. Ind. Eng. Chem. (Seoul, Repub. Korea), **11**(1), pp. 96–102.
[10] Copeland, R. J., Alptekin, G., Cesario, M., Gebhard, S., and Gershanovich, Y., 2001, "A Novel $CO_2$ Separation System," U.S. Department of Energy, Report No. DE-AC26-98FT40421.
[11] Jin, H., and Ishida, M., 2000, "A Novel Gas Turbine Cycle With Hydrogen-Fueled Chemical-Looping Combustion," Int. J. Hydrogen Energy, **25**(12), pp. 1209–1215.
[12] Jin, H., and Ishida, M., 2004, "A New Type of Coal Gas Fueled Chemical-Looping Combustion," Fuel, **83**(17–18), pp. 2411–2417.
[13] Jin, H., Okamoto, T., and Ishida, M., 1999, "Development of a Novel Chemical Looping Combustion: Synthesis of a Solid Looping Material of $NiO/NiAl_2O_4$," Ind. Eng. Chem. Res., **38**(1), pp. 126–132.
[14] Jin, H., Okamoto, T., and Ishida, M., 1998, "Development of a Novel Chemical-Looping Combustion: Synthesis of a Looping Material With a Double Metal Oxide of CoO–NiO," Energy Fuels, **12**(6), pp. 1272–1277.
[15] Jin, H., Hong, H., and Cai, R., 2006, "A Chemically Intercooled Gas Turbine Cycle for Recovery of Low-Temperature Thermal Energy," Energy, **31**, pp. 1554–1566.
[16] Jin, H., Hong, H., Wang, B., Han, W., and Lin, R., 2005, "A New Principle of Synthetic Cascade Utilization of Chemical Energy and Physical Energy," Sci. China, Ser. E: Technol. Sci., **48**(2), pp. 163–179.
[17] Hong, H., Jin, H., and Liu, B., 2006, "A Novel Solar-Hybrid Gas Turbine Combined Cycle With Inherent $CO_2$ Separation Using Chemical-Looping Combustion by Solar Heat Source," ASME J. Sol. Energy Eng., **128**, pp. 275–284.
[18] Riemer, P., 1996, "Greenhouse Gas Mitigation Technologies, an Overview of the $CO_2$ Capture, Storage, and Future Activities of the IEA Greenhouse Gas R&D Program," Energy Convers. Manage., **37**(6–8), pp. 665–670.

# Optimum Planning of Electricity Production

**Giovanni Cerri**
e-mail: cerri@uniroma3.it

**Marco Gazzino**

**Francesca Alessandra Iacobone**

**Ambra Giovannelli**

Dipartimento di Ingegneria Meccanica e Industriale,
Università Roma Tre,
Roma 00146, Italy

*The problem of planning the production of a pool of power plants has been deeply investigated. Maintenance management and load allocation problems have been assumed as crucial aspects for achieving maximum plant profitability. A production-planning approach has been developed, and genetic algorithm techniques have been adopted to implement the developed approach. Life consumption of gas turbines' hot-section components has been considered as a key element required in simulating plants' behaviors. As a result, a deterioration model has been developed and included into the planning algorithm. The developed approach takes market scenarios, as well as actual statuses and performances of plant components into account. The plants' physical models are developed on a modular approach basis and provide the operating parameters required by the planning algorithm. Neural network techniques have been applied to speed up the simulation. Economic implications related to maintenance strategies, including postponement or anticipation of maintenance interventions, are investigated and the results obtained by the numerical simulation are presented and widely discussed.*
[DOI: 10.1115/1.3098429]

## 1 Introduction

The liberalization of electricity market pushes for optimizing efficiencies in power production. Considerable technological efforts have been recently devoted to increasing efficiencies of energy conversion systems, in an attempt to achieve better use of resources within environmental compliance.

Gas turbines (GTs) have had a key role in this process, by dramatically increasing their power and efficiency levels over the past 25 years. Thermal efficiencies of simple-cycle solutions are usually bounded in the 35–40% lower heating value (LHV) range, with a specific power of around 400 kW $kg_{air}^{-1}$ s (50 Hz). Presently, the 60% (LHV) and above efficiencies are practicable with combined-cycle power plants. Specific power easily overcomes the frontier of 600 kW $kg_{air}^{-1}$ s (50 Hz).

The increasing concern for $CO_2$ emissions pushes for further improvements in power plant efficiencies, which are important both for short term and for long term solutions of reducing $CO_2$ [1]. In the short term, efficiency increase is the only way to achieve an immediate reduction in $CO_2$ emissions. In addition, high efficiency allows mitigating energy penalties associated with carbon capture and sequestration (CCS) technologies.

The above considerations suggest developing both methodologies to be able to better exploit resources, as well as tools proficient in increasing the production efficiency of the overall system. In this context, optimization of electricity production can play a key role.

Only a few years ago, the medium term planning of energy production was often obtained through electronic sheets usually set up by the production department. These sheets typically require the manual insertion of fuel costs and power produced by the various units during the different time bands and give as output the power produced by power units and their costs. The optimization is usually performed through manual attempts of step by step approximation, depending on the operator skill.

The main limitations of such a procedure are long computing time; not completed optimization; optimization not based on mathematical algorithms; medium term planning based on monthly mean values calculated on five time bands (and not hourly, as it would be desirable); impossibility to correlate events (stops, programmed maintenance, and so on) during time-intervals lower than 1 month; no transactions and no grid services are considered; variable costs such as start-up, cyclic service, maintenance, and life deterioration can be difficultly considered; necessity of daily planning to verify the power load covering; and difficulty to provide reserve supply and economical risks deriving from the variation in the spinning reserve power availability.

In order to develop a more effective planning methodology, a comprehensive statement of the problem is essential. From a mathematical point of view, the problem of planning and optimum management is referable to the simulation through economic-functional models and to the optimization of a multivariable fitness function respecting a great number of nonlinear constraints. Besides strictly mathematical and numerical aspects, the study of a planning problem should include the following.

(1) *Definition of the fitness function*. The most simple and usual approach is the assumption of the instant profit. This approach may be criticized by different points of view: (i) it does not consider the factors that can influence the income evaluated on longer periods (daily, weekly, and annual); it cannot evaluate the effects of (ii) energy storage (for cogeneration plants, both thermal and electric storage options should be considered), (iii) start/stop cycles, (iv) maintenance related aspects; and (v) it does not consider externalities (pollutant emissions, $CO_2$ and greenhouse gas emissions, etc.). As a result, selection of the fitness function should be based on both simple economical considerations (instant profit) and on more global considerations (energy savings, externalities, etc.), being derived by a mixture of economic, energetic, and environmental considerations and parameters.

(2) *Definition of the functional links between independent variables, constraints, and fitness functions*. Functional links should represent real behavior of power plants, which have their production to be planned. Thus, functional links are established by equality and inequality constraints set by models of plant components. Gathering real-time information about the effective performances of each power plant allows activating automatic correction systems of functional links, such as the introduction [2,3] of actuality func-

Manuscript received January 2, 2009 final manuscript received January 6, 2009; published online July 20, 2009. Review conducted by Dilip R. Ballal. Paper presented at the ASME Turbo Expo 2008: Land, Sea, and Air (GT2008), Berlin, Germany, June 9–13, 2008.

tions (AFs), which provide models with a continuous tuning, according to performance deterioration.

(3) *Definition of the independent variables to be optimized*. The most critical point is to reduce the number of the independent variables, both acting on the number of the temporal intervals which individuate the optimization process and developing a cascaded optimization process where certain groups of "principal" variables are associated with a number of "secondary" variables to be optimized.

4. *Definition of the operating constraints*. It is certainly the most difficult point, because the existence of a huge variety of constraints and its analysis require an accurate insight on the peculiarities of the single power plants.

According to the second point, online solution of production-planning problems requires the application of techniques to be able to speed up procedures. For this purpose, methodologies based on neural networks offer interesting prospects. They got useful application in several fields, showing a good capability to reproduce even the behavior of complex systems. Moreover, artificial neural networks have the peculiarity to be able to interpolate, i.e., to generalize the data presented to it during the training process.

Application of neural modeling coupled with evolutive optimization techniques shows great time saving potentialities. In fact, presently the dispatch technique is based on the combination of consumption curves with the adoption of local linearization techniques to search marginal costs. Neural modeling allows fast solution of problems [4,5], and is error and fault tolerant.

**1.1 The Role of Performance Deterioration in Production Planning.** Operating condition analysis of power plants can be performed through "gas-path analysis" techniques, which allow the determination of geometric and performance characteristic parameters (such as efficiencies, mass flow rates, pressure drops, etc.), which are necessary for operating condition analysis, starting from the processing of measurements taken on the system [6–11].

The number and type of parameters that can be calculated depend on the number and type of the available measurements. Then, the parameters that cannot be calculated have to be kept constant; this implies that the actual (altered) operating state cannot be considered a consequence of their variation. From these considerations, it can be noticed that the reliability of the diagnosis depends on the measurement accuracy, on the reliability of the sensors [11–17], on the number and type of the available measurements, and on the set of characteristic parameters to be determined [6,11,18,19].

Individuation of losses and their different cause assessments are made possible by process monitoring and diagnostics. These are necessary steps to realize an optimum management of energetic systems [20–24].

Several studies have been published concerning maintenance management and investigating possibilities for a better exploitation of gas turbines during their useful life. Cerri et al. [25] proposed an inverse methodology for actual status recognition of GT based power plants from data collected by the plant monitoring system. Benvenuti [26] and Sampath and Singh [27] suggested the application of innovative and advanced fault diagnostic techniques, in order to achieve improved operational availabilities and service performances. Silva et al. [28] showed the benefits related to an optimized scheduling of cleaning time-intervals on GT compressor. Lowden et al. [29] proposed a methodology to predict blade remaining useful life and assess online statuses of components for condition-based maintenance purposes. Cerri et al. [30] developed planning methodologies, including both damage models and factors for continuously tuning plant models according to deterioration of performance.

It is generally recognized that operating a GT over its recommended useful life can be done by rescheduling the maintenance according to the effective life of hot gas-path parts (HGPPs). Thus, life-assessment tools for hot-section components are required. Several life prediction approaches have been proposed in Refs. [31–34]. Since maintenance costs usually include refurbishment and substitution of components, a low accuracy in assessing the actual useful life causes overcosts because components tend to be replaced before having finished their serviceable life. Such considerations become dramatically relevant in the management of a GT, which has hot-section components exposed to severe operating conditions, causing damage rate to depend on the power level exponentially. Hence, the deterioration of high temperature components is one of the most important factors to be considered for an effective maintenance strategy and an optimized production planning.

This paper mainly focuses on the planning algorithm, including plant simulator and deterioration models. It also shows how the application of a reliable damage model in a production-planning problem could lead to improved machine exploitation through an effective maintenance scheduling.

## 2 Simulation Methodology

In order to perform the production planning of a pool of power plants, a planning algorithm has been developed, by adopting genetic algorithm (GA) techniques. Since the planning algorithm needs machine parameters (i.e., thermodynamic variables, fuel consumption, rotating speeds, etc.) to be evaluated at each time instant and for each plant section, a model of the plant has been produced. Such a model is based on a modular description of the components and includes the submodels describing the behavior of each plant component.

Accurate production planning is possible only if plant performance deterioration, as well as accumulated damage of components, is taken into account. As a result, the developed plant model includes dedicated modules taking deterioration of components into account and assessing residual useful life of components. Special attention has been paid to model HGPP deterioration.

Models developed for simulation of plant components, as well as the methodology adopted to account for performance variations related to deterioration of plant components, are briefly discussed in Secs. 2.1 and 2.2. Then, the proposed deterioration model for hot-section life-assessment is described and discussed in detail. Finally, the production-planning algorithm is presented and tested.

**2.1 Plant Model.** The overall plant model is based on a modular description of components. Each module could represent a single component or a group of them. Modules are composed by sets of linear and nonlinear equations, including the conservation of mass, energy, momentum, and entropy, as well as constitutive and auxiliary equations, which describe other phenomena such as heat transfer, pressure loss or equipment specifications, and control rules.

Accordingly, steady state behavior of the plants and the pool is described by a set of equations **F**:

$$\mathbf{F}(\mathbf{u},\mathbf{z},\mathbf{y}) = \mathbf{0} \tag{1}$$

and inequalities **D**:

$$\mathbf{D}(\mathbf{u},\mathbf{z},\mathbf{y}) = \mathbf{0} \tag{2}$$

**u** giving the state of the system (fouling, performance deterioration, etc.), **z** being the vector of the unknown variables, **y** being the vector of degrees of freedom (DOFs). The set of conditions **D** constrains the domain of existence for the solution.

Each module simulates the off-design behavior of the component and carries out the relationship between input and output variables. A simultaneous solution method has been adopted, performing the minimization of a plant *objective function* (Fob) defined as a weighted sum of the partial objective functions given as outputs of modules. A simultaneous solution method developed by

Cerri [35] has been applied to get the solution.

Component models include databases containing geometries, shapes, and architectures with the corresponding related correlations (e.g., profile cascade features and related losses and deviations, finned tube bundles features, and related heat transfer coefficients). Such databases are adopted to select arrangements on the basis of manufacturer information or default choices.

**2.2 Deterioration of Plant Components.** Performance of plant components changes during their life due to phenomena such as fouling, corrosion, erosion of parts, etc., affecting the actual behavior of plant units. As a result, different machines exist at each time instant of the plant operational life. Since characteristic curves of components and performance maps are continuously changing, they need to be continuously re-established within the model if an accurate plant operation management is to be accomplished.

In order to take such changes into account, the plant model contains polynomial AFs, which adapt component models tuned for new and clean (N&C) conditions to the continuously changing actual component behaviors. AFs are established to modify component performance in terms of work transfer or heat transfer, dissipative phenomena, and flow functions.

In the adopted models, the choice of using global AFs has been made. Such functions are necessary to replicate behaviors of plant components and to describe their present performance. More details on the definition and application of AFs are reported by Cerri et al. [2,3].

Besides prediction of performance at every time instant of operating life of components, the development of damage assessment and life prediction technologies is essential. Damage models could be extremely useful as life-assessment tools for the production planning and maintenance scheduling of a pool of power plants.

Since the GT hot section is exposed to extreme operating conditions, the corresponding damage to the hot components plays a key role in maintenance management, cost optimization, and production planning. Accordingly, a deterioration model has been developed and briefly described in Sec. 3.

**2.3 Neural Plant Simulator.** Since direct application of physical models to a problem that requires iterative calculations can lead to quite long calculation times, alternative simulation procedures must be considered. In order to achieve low CPU occupancy and to get the solution in short time, artificial neural network (ANN) techniques have been applied. They allow approximating a stated input-output map representing the behavior of the plant.

The plant model has been utilized to generate the input-output map (database) needed for ANN training and testing. Then, single-layer feed-forward networks have been trained with back-propagation algorithm and a parametric simulator of the plant has been produced. The application of physical models to generate training databases allows providing ANNs with large amount of training data. This made it possible to produce reliable ANNs with one hidden layer only. Cerri et al. [36] extensively discussed neural methodologies applied to heat and power plants.

## 3 Hot Gas-Path Part Deterioration Model

In order to perform hot-section life calculations, a deterioration model has been developed and applied to the first and second stage buckets of the LM-6000 (GE) high-pressure turbine (HPT). The modeled physical system is composed of a row of blades jointed on a rotating disk and surrounded by a hot gas stream, with a bleeding of high-pressure air taken from the compressor and passing through the blade inside cooling passages.

The presented model assumes lumped quantities along the hub-tip centroid line. Actions referred to centrifugal, gas bending, and thermal stresses have been considered as main stress sources. By simulating thermal and mechanical loadings on turbine buckets and calculating the corresponding equivalent stress, the model assesses residual life on the basis of the equivalent uniaxial stress, evaluated by means of the well known von Mises formula [37].

The interaction between creep and corrosion is taken into account by a physical reduction in section areas, which causes a corresponding increase in primary stress levels that occurs as airfoil thickness decreases. Hot corrosion behavior has been assumed to be pseudolinear [38]. The resulting increased stress levels are evaluated by adjusting the equivalent stress according to the reduced cross section areas of buckets at each radial length.

The developed creep model includes databases containing creep rupture properties for the LM6000 blades. They are derived from laboratory tests conduced by the manufacturer on specimens machined from airfoils of the CF6-80C engine [39].

The deterioration model requires gas-path flow conditions (e.g., temperatures, pressures, velocities, flow angles, etc.) as inputs. As a result, a physical-empirical model developed by Cerri et al.[2,3] for the LM6000-PA gas turbine has been applied to provide the deterioration model with such inputs. Component specifications of the LM6000-PA have been properly introduced in the model, and the simulator has been calibrated with empirical data resulting from real plant operations (provided by the electricity producer Fenice S.p.A.).

A complete description of the creep model is reported by Gazzino [40] and by Cerri et al. [2,3]. Some details on the general approach for blade temperature and mechanical load calculation are briefly mentioned in Sec. 3.1.

**3.1 Calculation of Blade Temperature and Mechanical Load.** Blade has been divided into seven finite elements, each one identified by a node. Accordingly, differential equations describing heat transfer were written in terms of one-dimensional finite differences. Since heat transfer related to thermal radiation has been neglected, heat transfer equations associated with each node take only convection and conduction into account.

A simplified cooling scheme has been adopted, with a single cooling passage, so that cooling air goes from root to tip straightforward. A global cooling efficiency $\varepsilon_j$ has been introduced, including all specific cooling aspects (i.e., convection, impingement, film cooling, architecture of the channel, area and spacing of injection holes, and so on),

$$\varepsilon_j = \frac{T_{g,j} - T_{b,j}}{T_{g,j} - T_{c,j+1}} \tag{3}$$

$T_g$ being the gas temperature, $T_b$ being the blade temperature, and $T_c$ being the coolant temperature. All quantities are related to the $j$th section.

Centrifugal, gas bending, and thermal stresses are taken into account by assuming a plane state of stress. Centrifugal actions lead to bending stresses, torsional stresses, and tensile stresses. The bending and torsional stresses arise from centrifugal actions when the centroids of the blade cross sections at different radii do not lie on a radial line, and for the first stages, they are usually small enough to be neglected. Thus, tensile stress contribution is the only one considered.

According to the abovementioned, the value of centrifugal tensile stress $\sigma_{ct}$ at a generic blade cross section is given by

$$\sigma_{ct}(r) = \frac{\rho_b \omega^2}{A(r)} \cdot \int_r^{r_T} (A(r') \cdot r') dr' \tag{4}$$

$\rho_b$ being the blade material density, $\omega$ being the angular velocity, $A$ being the area of blade cross section, $r$ being the radius, $r_T$ being the tip radius, and $r'$ being an integration variable.

Gas-bending stresses have been evaluated as well. These arise from a gas bending moment, which can be resolved into two components, respectively, connected with the change in angular momentum of the flow in the tangential direction and with the pressure drop through the stage. Gas-bending moment $M_a$ about

the axial direction (due to the flow deviation) is the greater contributing moment, and it is responsible for useful torque. This component $M_a$ is a function of the gas flow rate and gas deflection as follows:

$$M_a = \int_{\text{root}}^{\text{tip}} \rho_g c_a \cdot (c_{t,1} - c_{t,2}) \cdot s r dr \tag{5}$$

$\rho_g$ being the gas density, $s$ being the pitch, $r$ being the radius, $c_a$ being the gas axial-velocity, and $c_{t,1}$ and $c_{t,2}$ being the tangential velocities at inlet and outlet sections, respectively.

**3.2 Calibration of the Deterioration Model.** In order to take geometries and shapes into account, the deterioration model has been tuned with maintenance data from real plant operations. The model's calibration has been carried out by introducing reality functions (RFs) into the model

$$\text{RF}_{kj} = \sum_{i=0}^{n} r_{kj,i} \cdot Y_{kj}^{i} \tag{6}$$

$r_{kj,i}$ being the coefficients of the $j$th RF related to the $k$th HGPP component, $Y_{kj}$ being a reference quantity relevant to the deterioration process (i.e., TIT, shaft power, shaft rotating speed, and flow quantities), and $n$ being the order of the polynomial, here fixed equal to 1. The $r_{kj,i}$ coefficients have been set by comparing damage rate predicted by the model before its calibration with those values provided by the real plant owner (Fenice S.p.A.). Matching is reached by minimizing the root mean square (rms) error function, where differences between predicted values and experimental data are taken as terms of the function.

**3.3 Life Consumption Rate.** As reviewed by several authors in Refs. [41,42], different approaches are adopted by O&Ms to determine the life consumption of HGPPs. Some manufactures fix gas turbine maintenance requirements on independent counts of starts and hours; whichever count is first reached determines the maintenance interval. Other manufactures adopt an alternative approach, which converts the firing hours and number of starts in an equivalent amount of operating hours (EOH) and prescribes the maintenance interval when the EOH count reaches the nominal life of components. O&M nominal life $L_n$ sets the time at which the gas turbine is overhauled on nominal load and ISO ambient conditions, which define the baseline operating conditions. EOHs can be used to express the damage occurred on components during actual hours of operation in terms of an equivalent amount of operating time at nominal conditions and load that causes the same life consumption. The recommended interval on baseline conditions for HGPPs inspection is often recommended by the manufacturer, and a typical value for many aeroderivative gas turbines is about 25,000 EOH.

In order to transpose in a concise way outputs produced by the deterioration model introduced above, the concept of EOHs is adopted and applied to define a life consumption rate $f$ as

$$f = \frac{dL_C}{dh} \tag{7}$$

Such a rate is rigorously defined as the derivative of consumed life $L_C$ expressed as EOH, with respect to the operating hours $h$, expressed as fired hours (FHs).

The life consumption rate $f$ expresses how much fast the life consumption of HGPPs is (see Fig. 1). The value of $f$ mainly depends on machine load and duty cycle, firing temperature, shaft speed and vibration levels, compressor fouling, fuel quality, and level of steam/water injection. The life consumption rate $f$ can be applied to relate EOHs to FHs carried out at a particular operating condition.

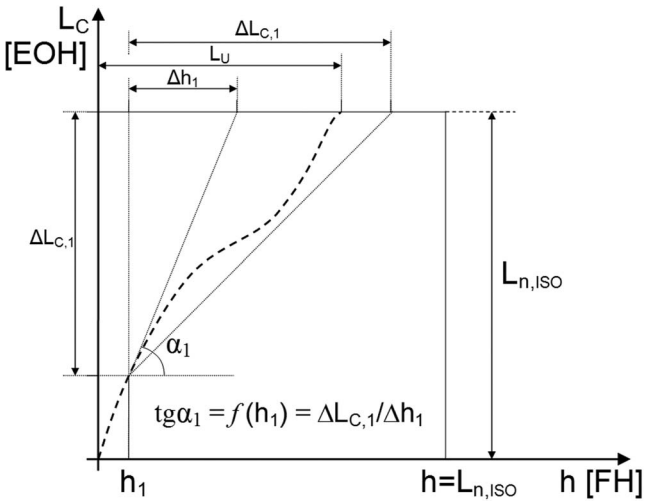


**Fig. 1 Graphic representation of the life consumption rate *f*, evaluated at the operating time instant $h_1$**

After evaluating the deterioration rate $f$, the resulting useful life $L_U$ of HGPPs is assessed solving the following integral equation:

$$L_{n,\text{ISO}} = \int_0^{L_U} f dh \tag{8a}$$

that can be split into two integrals

$$L_{n,\text{ISO}} = \int_0^{h1} f_{\text{in}} dh + \int_{h1}^{L_U} f_{ex} dh \tag{8b}$$

$f_{\text{in}}(h)$ being the life consumption rate $f$ during the production interval since the initial time instant or the last maintenance intervention until the present time instant (i.e., $h_1$ in Fig. 1), while $f_{ex}(h)$ being related to the future forecast time-dependent production.

As a result, $L_U$ is the life predicted according to the past production history, and the expected life consumption distribution is $f_{ex}(h)$. The importance of deterioration models in a production-planning algorithm is due to their capability to relate bi-univocally time distributions of the planning problem's inputs and outputs (e.g., distributions of ambient temperatures at each plant location or net power outputs of each plant unit) to time distributions $f(h)$ of life consumption rates. If $f(h)$ are known, by solving Eq. (8) it becomes possible to evaluate expected life of components $L_U$ for each planning solution and take it into account in the planning problem.

## 4 Power Production Planning

The problem of planning the production of a pool of power plants is stated as determining arrangement of the pool at each characteristic instant $t_k$ and performing allocation of loads to the units, so as to maximize earnings during the whole planning period $T$. Such optimization must be performed according to initial conditions, as well as to time distributions of ambient and economic quantities, such as ambient temperature, pressure and relative humidity distributions, fuel price distribution, distribution of supply costs, and power sale-price distribution.

Statement of a planning problem includes the following:

(a) definition of the fitness function
(b) definition of the functional links between independent variables, constraints and fitness functions
(c) definition of the independent variables to be optimized
(d) definition of the operating constraints

The solution of the problem can be reached by finding the DOF distribution $\xi^*(t)$ that satisfies the fitness function:

$$\xi^*(t)\left|\max\left\{ G = \int_{t_0}^{t_0+T} g(\xi,u,d)dt \right\}\right. \tag{9}$$

which is subject to initial and boundary conditions. Other constraints could be introduced, such as plant availabilities, minimum and maximum power output provided by each unit, requested reservoir level, minimum up/down time, and so on.

*Functional links* between the optimizing variables and the fitness functions are defined by the developed plant models and the corresponding neural simulators. Plant models can represent the actual behavior of components by adjusting AFs according to new statuses of components.

*Independent variables* to be optimized have been properly selected from DOFs. According to the nature of the planning problem, optimization variables are the desired operating statuses of each plant and the loads allocated to each power unit. Hence, the number of DOFs is very high and dependent on the number of plants or power units and the number of planning time-intervals.

The life consumption rate $f$ allows evaluating deterioration costs on components. In addition, a time distribution of life consumption rate also allows assessing expected life of components and predicting maintenance intervals. The fitness function directly takes deterioration costs into account, while maintenance intervals influence the solution by determining availabilities on plants.

**4.1 Planning Algorithm Structure: Supervisor and Operator.** The developed planning algorithm consists of two parts: a supervisor and an operator. Figure 2 shows algorithm's flow diagram.

The *supervisor* is based on a genetic algorithm programming, which allows handling problems with a high number of DOFs. The supervisor generates a "population" of tentative solutions, each one represented by a string composed by sequences of fixed DOFs $\xi_i$. After having fixed DOFs, the supervisor calls the operator, which is constituted by models of plant components or sections.

The *operator* is based on a modular structure, each module simulating the off-design behavior of components or sections. The operator establishes functional links between constraints and independent variables and carries out the relationship between the input and output variables; $x \equiv z \cup \xi$ is the union of the unknown quantities and the DOFs to be established by the optimization procedure. The direct solution of the components' models is obtained by minimizing an appropriate unbalanced objective function. The operator replicates input/output links between quantities related to power plant operations. In order to speed up the computation, physical and empirical plant models have been applied to train ANNs.

**4.2 Genetic Algorithm Encoding.** The GA encoding of information could be quite complex, depending on the problem. A genotype/phenotype approach has been developed, according to requirements of production-planning problems. Such an approach makes it possible to take plant availabilities and other production constraints (e.g., available minimum and maximum power output provided by each unit, requested reservoir level, minimum up/down time, and so on) into account.

The GA routine works as a supervisor of the problem, by searching the DOFs that correspond to fitness function's maximum value. The operator works within the supervisor, providing the operating parameters of plants required to evaluate fitness value. After having fixed DOFs, the operator performs its calculations and then the value of the fitness is evaluated. The principal tasks of the operator routine are provided by plant simulators and deterioration model described in Secs. 2 and 3.

The planning algorithm utilizes integers to account for the nonavailability of a group and for the switching capability to put online or off-line a plant, relating to the convenience. Integers can be equal to 1 or 0, and the system of indices is composed by the following:

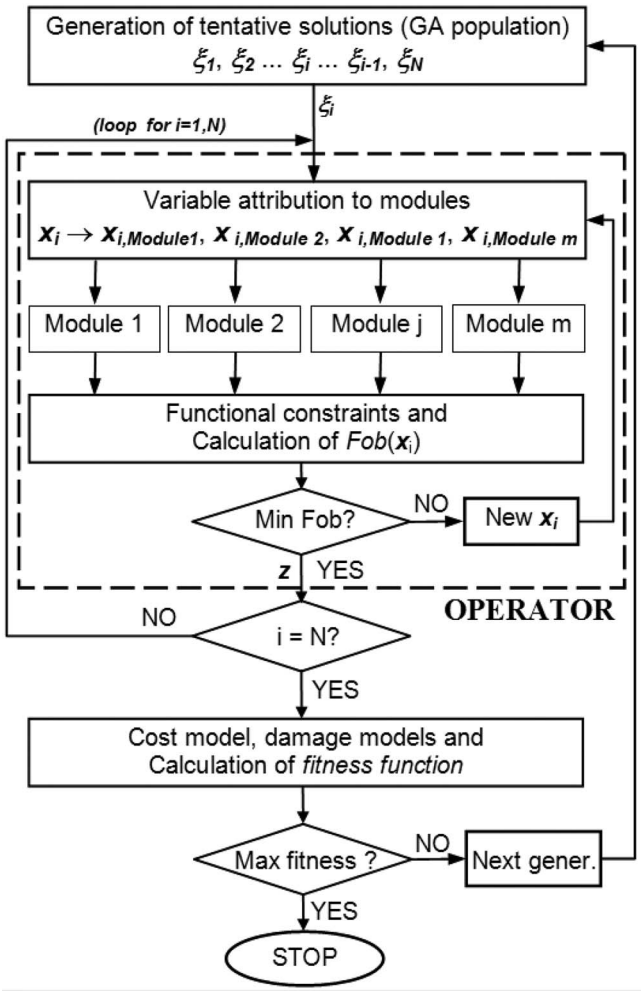


**Fig. 2 Planning algorithm flow diagram, including operator (enclosed in a dotted-line box) and supervisor (other sections)**

(a) desired operating status index $\boldsymbol{ds}_j$ of the $j$th plant
(b) availability status index $\boldsymbol{as}_j$ of the $j$th plant
(c) actual operating status index $\boldsymbol{os}_j$ of the $j$th plant

Desired operating status indices ***ds*** establish what kind of operating status is desired for each plant of the pool at each time instant. Indices ***os*** represent the actual statuses of plants, according to availabilities expressed by ***as*** indices.

The value 1 is associated with the online status, the value 0 is associated with the off-line status. Similarly, regarding to availability statuses, the value 1 is associated with the availability of the plant and the value 0 is associated with the unavailability of

**Table 1 Index relations**

| *ds* desired operating status | *as* availability status | *os* actual operating status |
|---|---|---|
| 0 | 0 | 0 |
| 0 | 1 | 0 |
| 1 | 0 | 0 |
| 1 | 1 | 1 |

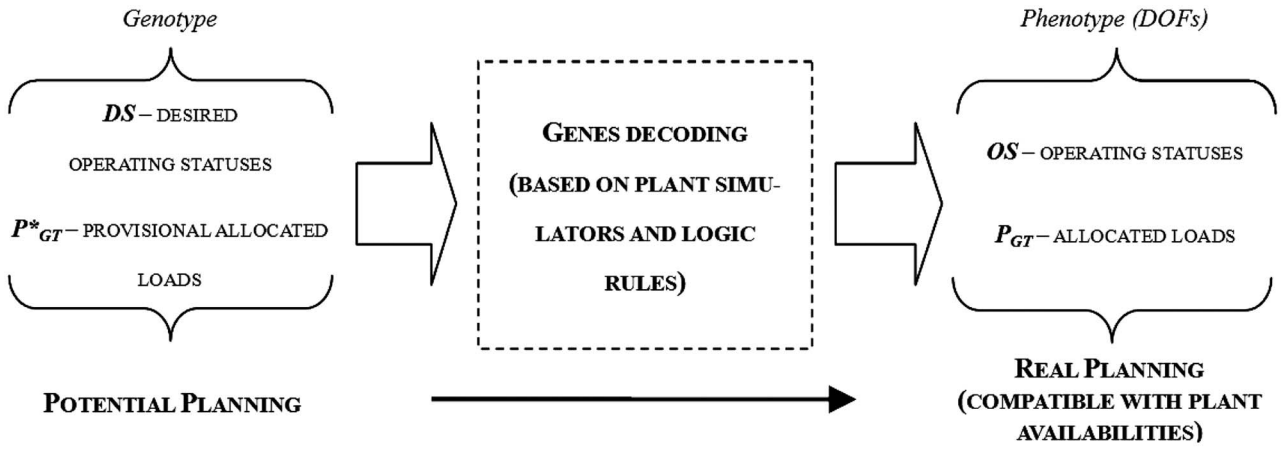


**Fig. 3 Integration of plant simulators within the planning algorithm based on genetic algorithms**

the plant. Table 1 shows how actual operating status indices are evaluated starting by desired operating statuses and availabilities. The corresponding vectors are defined on the basis of the above indices. Desired operating status indices form the vector ***DS*** of the desired operating statuses. Availability status indices form the vector ***AS*** of the availability statuses. Actual operating status indices form the vector ***OS*** of the actual operating statuses.

The vectors introduced above are handled within the planning procedure by the supervisor routine based on genetic algorithm techniques. Figure 3 explains how information involved in a planning problem are elaborated within the planning procedure. A starting random population of individuals is initialized. Each individual is a string of integer numbers, representing tentative values for operating statuses and allocated loads. The first half of the string contains operating status indices, thus appears as a binary sequence of 0s and 1s. The second half of the string is composed by allocated loads, reported as percentages of the nominal load. Values below the technical minimum operating limit are not allowed.

The dimension of the string depends on the number $J$ of plants considered for planning and the number $K$ of time-intervals in which planning period is divided. Thus, the number $DIM$ of elements or genes that composes an individual is given by

$$DIM = 2 \cdot J \cdot K \tag{10}$$

which is valid assuming that the each plant is provided by only a power unit. Of course, the higher the dimension is, the longer the computation time.

Each string or individual forms the genotype, which represents a tentative solution or a potential planning. The phenotype has the same structure of genotype, but it represents an actual planning solution, compatible with availabilities of plant resources. The comparison between desired operating statuses and availability statuses is a part of the decoding process of genotype to phenotype.

As example, it could be considered the simple case of a pool composed by two power plants and a planning period divided into two time-intervals only. In such a case, according to Eq. (10), strings or individuals are eight elements long and a string of the initial population would appear as follows:

| 0 | 1 | 1 | 1 | 80 | 76 | 70 | 95 | genotype |
|---|---|---|---|---|---|---|---|---|

The above string represents a general genotype combination.

According to index relations reported in Table 1, the phenotype is evaluated as follows:

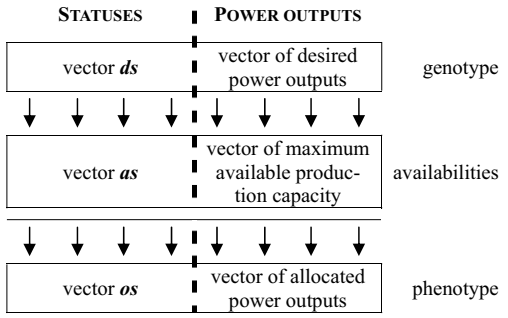


In order to explain the procedure presented earlier, an example case referred to a pool with four power plants is reported as follows. Let us suppose that the first and third plants are unavailable, because of maintenance operations previously started. In addition, suppose that the second plant has passed nominal life for GT hot-section components, but it is still available (the underscored availability).

| STATUSES (binary digits) | | | | POWER OUTPUTS (% of ISO load) | | | | |
|---|---|---|---|---|---|---|---|---|
| 0 | 1 | 1 | 1 | 80 | 104 | 70 | 95 | genotype |
| 0 | 1 | 0 | 1 | 95 | 100 | 90 | 90 | availabilities |
| 0 | 1 | 0 | 1 | 0 | 100 | 0 | 95 | phenotype |

Unavailable plants are put off-line. The fourth plant can be put online, because of no availability limitations. The second plant is kept online, but economic penalties are added to production costs to account for the risk of operating components over their nominal life. Allocated loads are adjusted according to values of actual operating statuses reported in the first half of the string.

**4.3 Fitness Function.** Individual solutions are selected through a fitness-based process and solutions that better satisfy the fitness-function criteria are more likely to be selected. In order to evaluate the fitness function, genotype solutions (provisional) need to be converted to phenotype solutions, which include information on plant availabilities.

Since the solution of the problem is achieved by defining a discrete time-domain and writing Eq. (9) in finite terms, the fitness

function is defined as follows:

$$\text{Fitness} = \sum_{k=1}^{k_{\text{MAX}}} [R(t_k) - C(t_k)] \tag{11}$$

$R(t_k)$ being the income during the time interval $\Delta t_k$,

$$R(t_k) = p_{\text{EL}}(t_k) \cdot \left( \sum_{j=1}^{j_{\max}} P_{\text{GT},j}(t_k) + P_{\text{ST},j}(t_k) \right) \cdot \Delta t_k \tag{12}$$

$C(t_k)$ being the production cost during the time interval $\Delta t_k$,

$$C(t_k) = \left( \sum_{j=1}^{j_{\max}} C_j(t_k) \right) \cdot \Delta t_k \tag{13}$$

and $p_{\text{EL}}$ being the sale-price for power produced, $P_{\text{GT},j}$ being the power produced by the GT of the $j$th plant, $P_{\text{ST},j}$ being the power produced by the steam turbine of the $j$th plant, and $C_j$ being the overall production costs. $\Delta t_k$ is the duration of $k$th time interval $t_k$. Quantities needed for income or production costs evaluation, such as total net power output (comprehensive of steam turbine output level) or fuel consumption flow rate, are calculated by means of plant simulators during the decoding phase of genotype to phenotype.

Equation (11) is the overall fitness function, which is extended to $k_{\max}$ time-intervals and to $j_{\max}$ plants. The fitness function is constrained by the instantaneous behavior of plant groups and by availabilities of each plant of the pool. As proposed by Cerri et al. [43], such constraints can be given by plant simulators.

## 5 Statement of the Production Planning Case

The planning case presented focuses on the capability of managing postponement and anticipation of maintenance intervention to increase production profitability. The effects on production management of applying different damage-assessment techniques have been also investigated in a previous study and report by Cerri et al. [2,3].

A pool of five combined-cycle power plants is chosen as reference for the simulation and adopted for testing the developed planning algorithm. Each plant is based on a twin shaft aeroderivative GT (LM6000-PA), driving an electric generator and discharging exhaust gases through a two-pressure level steam generator, which provides steam to a condensation steam turbine with 10 MW as installed capacity. All units are fed by natural gas and no steam is bled for thermal power production. The steam section of the plant is equipped with an air cooled condenser. Equipments and layouts of each plant of the pool are all the same.

**5.1 Boundary and Initial Conditions.** The solved planning case is defined. The boundary conditions are as follows:

- atmospheric conditions (first, second, third, and fifth plants): $T_{\text{amb}}=10\,^{\circ}\text{C}$, $P_{\text{amb}}=1013$ mbars, and r.u. 60%
- atmospheric conditions (fourth plant): $T_{\text{amb}}=15\,^{\circ}\text{C}$, $P_{\text{amb}}=1013$ mbars, and r.u. 60%
- fuel price is 0.2 €/N m$^3$

The initial HGPPs statuses are as follows:

- first plant: 75% of equivalent life already used
- second plant: 92% of equivalent life already used
- third plant: N&C condition (0%)
- fourth plant: N&C condition (0%)
- fifth plant: N&C condition (0%)

Power sale-price distribution is reported in Fig. 4.

## 6 Results and Discussion

Planning problem solution is reported in Figs. 5–9. Each figure refers to a plant of the pool, starting from Fig. 5 associated with the first plant.

The power sale-price distribution and the initial statuses of first and second plants have been properly chosen so as to highlight the postponement or anticipation capability of the planning algorithm. The power sale-price increases its value before the middle of the planning period and then decreases rapidly at a value lower than the initial one. As a result, if maintenance is needed, it could be preferred to schedule the intervention when the power sale-price has the lowest value of the period $T$, so as to keep the plant running when the price of electricity is high (i.e., between $0.2T$ and $0.6T$).

When a plant is put off-line, a reduced income is suffered because of missing production. Thus, the number of maintenance interventions can actually affect final profit. Providing that service agreements are respected, a maintenance policy that includes postponement of maintenance interventions becomes profitable if costs connected with the risk of operating components over their nominal life are lower than downtime costs on intervals that have power better priced.

Similarly, the anticipation of maintenance intervention becomes profitable if costs connected with prematurely replacing HGPPs are recovered by the subsequent production availability. As an example, such an occurrence can happen when an increase in power sale-price is foreseen. According to the abovementioned, the planning algorithm (1) reduces loads (with respect to the instantaneous optimum), so as to reduce the damage rate and preserve hot components of the first plant; (2) postpones maintenance intervention of the first plant; (3) schedules the maintenance intervention on the first plant when the power sale-price is the lowest of the planning period; (4) anticipates maintenance intervention on the second plant when 96% of nominal life is reached; and (5) fixes loads for the fourth plant lower than the others because of the higher ambient temperature, which causes (at the same load) a higher deterioration on HGPPs.

Maintenance postponement on first plant is profitable because costs connected with the risk of operating units over their nominal life are lower than downtime costs on intervals that have power better priced. The maintenance intervention on the second plant is anticipated because initial status of HGPPs is too close to the nominal limit to allow postponement of maintenance (i.e., risk and costs connected with extended-life operations would be too high). In this case, costs connected with prematurely replacing of components are recovered by the subsequent production availability over the interval with the highest power sale-price.

In order to evaluate time required to achieve the solution, the convergence curve has been drawn, as reported in Fig. 10. The $y$-axes report the ratio between the fitness value at a generic calculation instant and the final value. Such a ratio (fitness ratio) becomes equal to 1 when the solution is achieved.

The simulation and planning procedures have been run on an Intel Pentium IV based personal computer, with 2 GHz of clock frequency, 1 Mbyte of resident cache, and 1 Gbyte of RAM installed. Windows XP has been adopted as operating system. All the routines have been written in FORTRAN 90 and compiled by a commercial developer kit, working at 16–32 bits.

As can be seen in Fig. 10, after 30 min from the start time of the planning routine, the fitness function has reached the 99.6% of its final value. The convergence is very rapid and 9 min after having started the planning routine (700 DOF cases), the fitness function reaches a value close to 96% of the final value.

## 7 Conclusions

Internal and external competition in production and transmission force energy suppliers to create new production behaviors [44]. A context characterized by the liberalization of electricity

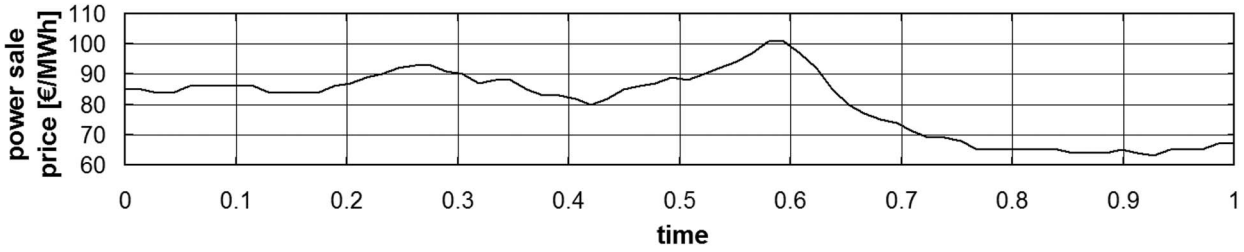


Fig. 4 Sale price for power distribution

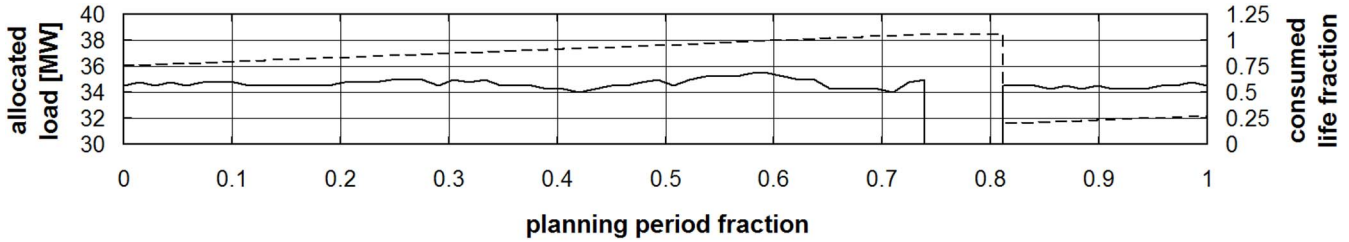


Fig. 5 Allocated load on GT and consumed life fraction of HGPPs with reference to the first plant of the pool

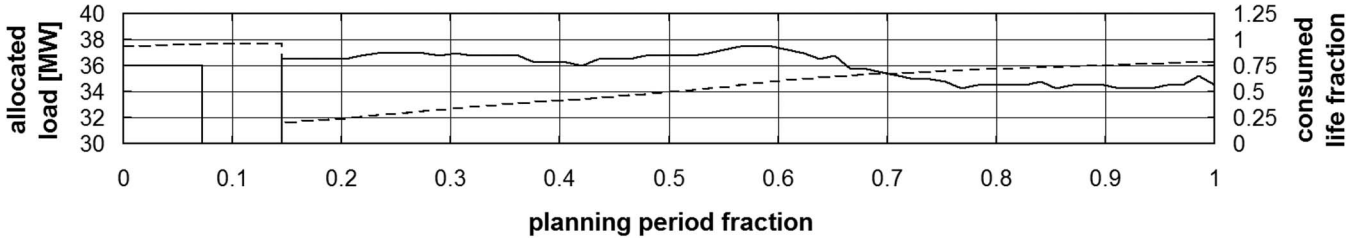


Fig. 6 Allocated load on GT and consumed life fraction of HGPPs with reference to the second plant of the pool

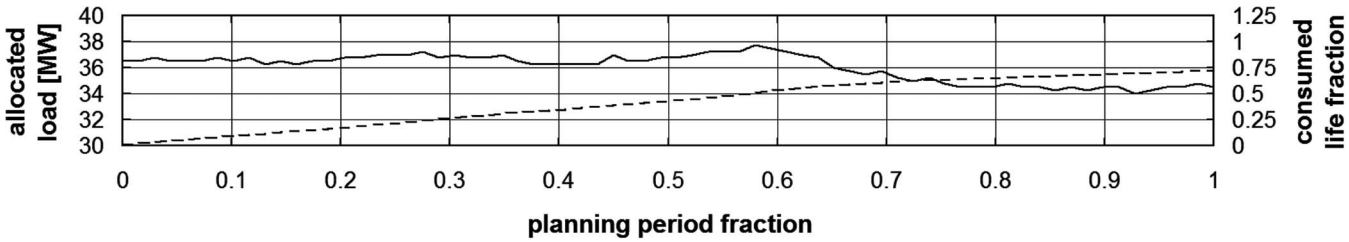


Fig. 7 Allocated load on GT and consumed life fraction of HGPPs with reference to the third plant of the pool

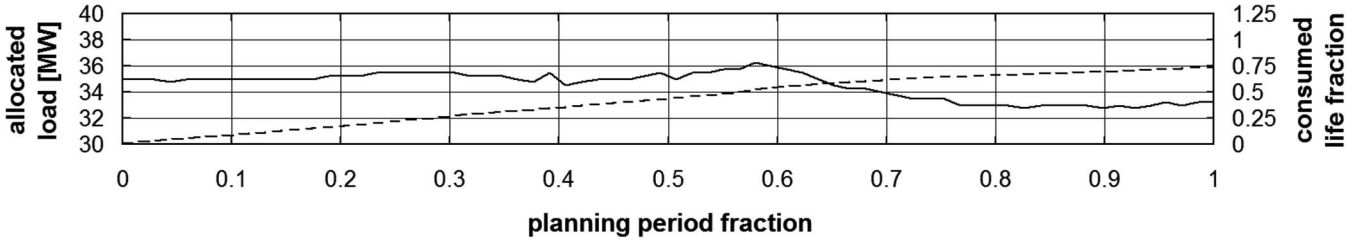


Fig. 8 Allocated load on GT and consumed life fraction of HGPPs with reference to the fourth plant of the pool

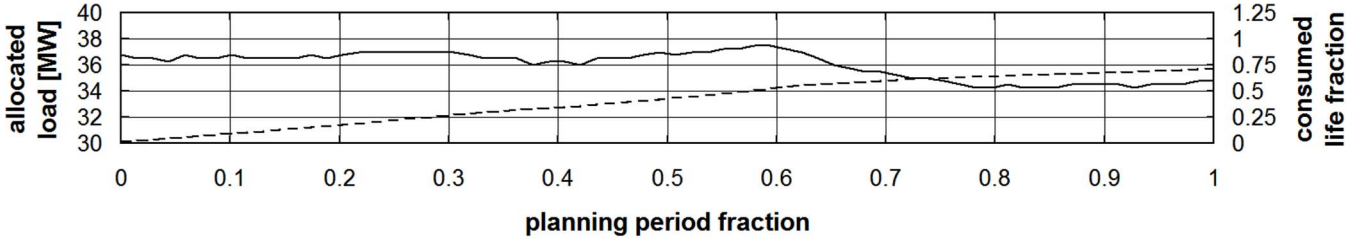


Fig. 9 Allocated load on GT and consumed life fraction of HGPPs with reference to the fifth plant of the pool

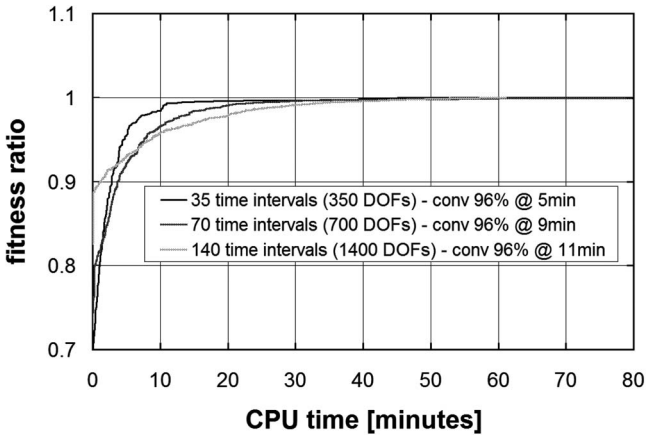


**Fig. 10 Convergence curves (Intel Pentium IV 2 GHz)**

market pushes for optimizing efficiencies in power production. The owner of a pool of power plants feels the necessity to find a trade-off between production levels, maintenance interventions, and plant exploitation, in order to achieve the maximum gain in a certain time period (usually 1 year). Improved maintenance scheduling that takes market scenarios, as well as actual statuses and performances of plant components into account, may play a key role in such a scenario.

A fast and flexible planning tool can allow an established way in which the owner of the pool can approach the market by making the best bid in terms of quantity of electricity produced and selling periods. Development of deterioration assessment and life prediction models resulted as key elements. This paper has pointed out that deterioration models could be extremely influencing if included into production-planning algorithms. Such models can be adopted to establish a bi-univocal correspondence between time distributions typical of a planning problem (e.g., distributions of ambient temperatures at each plant location or net power outputs of each unit of the plant) to the time distributions of life consumption rates of plant components. If those distributions are known, it becomes possible to evaluate expected life of components for a specific planning solution, and as a result, take it into account in the planning problem.

Reliable deterioration models make it possible to estimate when life of plant critical sections ends or maintenance intervention is needed. Such knowledge is essential to evaluate the benefit of planning maintenance, when sale price for power and the corresponding income are lower. In this manner, production resources can be better exploited and downtime costs minimized.

The application of such models along with machine simulators provides with a tool that relates damage directly to the plant operating conditions, such as power level, steam/water injection, and fuel and air quality. The manager of a pool of plants has a basis on which to evaluate consequences of different choices in production management. He can maximize profit, if it is a main concern, or he can tune power output according to a life consumption target, by assessing with models the effect of saving life of components. In this manner, the economic impact of extended-life operations, as well as overdamage costs connected with peaking operations can be easily assessed.

Since CPU occupancy is a main concern for real-time planning, computation times have been measured and reported. Presented cases took about 10 min to converge, with a computation time very short compared with the number of DOFs to be fixed. For planning cases larger than those presented ($>1000$ DOFs), parallel computing techniques are mandatory. Since the amount of solutions to be handled is equal to $2\times$(number of plants) $\times$(number of planning intervals), planning the production of a pool of five power plants over a period of 1 month, with a planning interval of 1 h, would require solving a problem with about 7200 DOFs. This would require calling subroutines and related ANNs 7200 times for each generation and for hundreds of generations.

The application of parallel computing techniques is feasible due to the nature of the proposed planning algorithm. The GA supervisor, after having generated a new set (generation) of tentative solutions (population), calls plant neural models and cost models and then sends economic performance data to the subroutine evaluating fitness value. Such a computation is repeated for each tentative solution (member of the population), and the corresponding data parallelism highlights the applicability of concurrent computing techniques to the proposed planning approach.

## Acknowledgment

Thanks are due to Professor Lorenzo Battisti for his useful advice on methodologies adopted for creep modeling. The authors also wish to express their gratitude to Fenice S.p.A., particularly to S. Salvador and F. Perin for providing this work with data from real plant operations. Support from MIUR is also acknowledged.

## Nomenclature

$C$ = costs
$\mathbf{D}$ = vector of plant model constraints and inequalities
$\Delta t$ = time interval
$f$ = life consumption ratio
$\mathbf{F}$ = vector of plant model equations
$G$ = gain or profit
$h$ = plant's operating time instant (fired hours)
$L_C$ = consumed life
$L_{n,\mathrm{ISO}}$ = nominal life (at nominal load and ISO conditions)
$L_U$ = expected useful life
$M_a$ = gas bending moment
$P$ = power output
$p_{\mathrm{EL}}$ = power sale-price
$R$ = income
$T$ = planning period
$T_b$ = blade temperature
$T_c$ = coolant temperature
$T_g$ = gas temperature
TIT = turbine inlet temperature
$u$ = vector of component's status factors (plant model)
$z$ = vector of plant process and state variables (plant model)

### Greek Letters

$\varepsilon$ = global cooling efficiency
$\xi$ = vector of degrees of freedom (planning problem)
$\sigma$ = stress

## References

[1] Beèr, J. M., 2007, "High Efficiency Electric Power Generation: The Environmental Role," Prog. Energy Combust. Sci., **33**, pp. 107–133.
[2] Cerri, G., Borghetti, S., and Salvini, C., 2006, "Models for Simulation and Diagnosis of Energy Plant Components," ASME Paper No. PWR2006-88146.
[3] Cerri, G., Gazzino, M., and Borghetti, S., 2006, "Hot Section Life Assessment by a Creep Model to Plan Gas Turbine Based Power Plant Electricity Production," The Future of Gas Turbine Technology, Third International Conference, Brussels, Belgium, Oct. 11–12.
[4] Boccaletti, C., Cerri, G., Khatri, D. S., and Seyedan, B., 1999, "An Application of Neural Network in Combustion Processes Evaluations," *Proceedings of the International Conference on Enhancement and Promotion of Computational Methods in Engineering and Science*, Macao, Aug. 2–5.
[5] Boccaletti, C., Cerri, G., Khatri, D. S., and Seyedan, B., 1999, "Neural Network Approach in Gas Expansion Evaluations," 14th International Symposium on Airbreathing Engines, ISABE, Florence, Italy, Sept. 5–10.

[6] Urban, L. A., 1972, "Gas Path Analysis Applied to Turbine Engine Condition Monitoring," AIAA Paper No. 72-1082.
[7] Lensi, R., and Andrenucci, M., 1978, *Designing a Diagnostic Model for Gas Turbine Plants*, Istituto di Macchine, Università di Pisa, Italy.
[8] Stamatis, A., Mathioudakis, K., and Papailiou, K. D., 1990, "Adaptive Simulation of Gas Turbine Performance," ASME J. Eng. Gas Turbines Power, **112**, pp. 168–175.
[9] Doel, D. L., 1994, "TEMPER—A Gas-Path Analysis Tool for Commercial Jet Engines," ASME J. Eng. Gas Turbines Power, **116**, pp. 82–89.
[10] Benvenuti, E., Bettocchi, R., Cantore, G., Negri di Montenegro, G., and Spina, P. R., 1993, "Gas Turbine Cycle Modeling Oriented to Component Performance Evaluation from Limited Design or Test Data," *Proceedings of the Seventh ASME Cogen-Turbo*, Bournemouth, UK, pp. 327–337.
[11] Bettocchi, R., and Spina, P. R., 1999, "A Method for the Diagnosis of Gas Turbine Sensor Faults in Presence of Measurement Noise," ASME Paper No. 99-GT-303.
[12] Patton, R. J., Frank, P., and Clark, R., 1989, *Fault Diagnosis in Dynamic Systems*, Prentice-Hall, Englewood Cliffs, NJ.
[13] Gertler, J., 1988, "Survey of Model-Based Failure Detection and Isolation in Complex Plants," IEEE Control Syst. Mag., **8**(6), pp. 3–11.
[14] Gertler, J., and Singer, D., 1990, "A New Structural Framework for Parity Equation-Based Failure Detection and Isolation," Automatica, **26**(2), pp. 381–388.
[15] Kelly, R. W., 1996, "Application of Analytical Redundancy to the Detection of Sensor Faults on a Turbofan Engine," ASME Paper No. 96-GT-3.
[16] Bettocchi, R., Spina, P. R., and Azzoni, P. M., 1996, "Fault Detection for Gas Turbine Sensors Using I/O Dynamic Linear Models—Methodology of Fault Code Generation," ASME Paper No. 96-TA-002, pp. 1–9.
[17] Bettocchi, R., and Spina, P. R., 1997, "ARX Linear Model Set-Up for Fault Diagnosis of Gas Turbine Sensors," ASME Paper 97-GT-027, pp. 1–9.
[18] Stamatis, A., Mathioudakis, K., and Papailiou, K., 1992, "Optimal Measurement and Health Index Selection for Gas Turbine Performance Status and Fault Diagnosis," ASME J. Eng. Gas Turbines Power, **114**, pp. 209–216.
[19] Pinelli, M., and Spina, P. R., 2000, "Gas Turbine Field Performance Determination: Sources of Uncertainties," ASME Paper No. 2000-GT-0311, pp. 1–8.
[20] Leyse, R. H., Armor, A. F., and Gehl, S. M., 1991, "Fossil Plant Instrumentation and Monitoring," International Joint Power Generation Conference, San Diego, CA.
[21] Mazzarell, G. R., and Chang, P. S., 1991, "Update on the Enhacement of Florida Power and Light 400 MW Steam Generator Program," International Joint Power Generation Conference, San Diego, CA.
[22] Rickli J.P., 1993, "Controls, Monitoring and Performances Measurements," Von Karman Institute for Fluid Dynamics Lecture Series '08.
[23] Lang, F. D., and Lang, A. F., 1999, "Monitoring and Improving Coal-Fired Power plants using the Input/Loss Method," International Joint Power Generation Conference, San Francisco, CA.
[24] Dehil, B., and Lang, F. D., (1999), "Practical Experience With the Input/Loss Method as Applied to a CFB Power Plant," International Joint Power Generation Conference, San Francisco, CA.
[25] Cerri, G., Borghetti, S., and Salvini, C., 2005, "Inverse Methodologies for Actual Status Recognition of Gas Turbine Components," ASME Paper No. PWR2005-50033.
[26] Benvenuti, E., 2001, "Innovative Gas Turbine Performance Diagnostics and Hot Parts Life Assessment Techniques," *Proceedings of the 30th Turbo Machinery Symposium*, Texas A&M University, 2001.
[27] Sampath, S., and Singh, R., 2003, "Managing Maintenance and Operational Availability of Gas Turbine Propelled Naval Ships Through Advanced Engine Fault Diagnostics," ASME Paper GT2003-38456.
[28] Silva, P., Campanari, S., and Macchi, E., 2003, "Optimization of Operating Conditions and Compressor Cleaning Time Intervals of Combined Cycles in a Liberalized Market," *Proceedings of the ASME Turbo Expo*, Atlanta, GA, June 16–19.
[29] Lowden, P., Weber, B., Grant, R., Jin, H., and Pistor, R., 2006, "Prediction of Gas Turbine Blade Life: An Interdisciplinary Engineering Approach for Condition-Based Maintenance," ASME Paper No. GT2006-90037.
[30] Cerri, G., Gazzino, M., Botta, F., and Salvini, C., 2007, "Production Planning With Hot Section Life Prediction for Optimum Gas Turbine Management," *Proceedings of the International Gas Turbine Congress*, Tokyo, Japan, Dec. 2–7, Paper No. IGTC2007-TS-154.
[31] Cunha, F. J., Dahmer, M. T., and Chyu, M. K., 2005, "Thermal-Mechanical Life Prediction System for Anisotropic Turbine Components," ASME Paper No. GT2005-68107.
[32] Beachkofski, B. K., and Grandhi, R. V., 2004, "Probabilistic System Reliability for a Turbine Engine Airfoil," ASME Paper No. GT2004-53381.
[33] Wallace, J. M., and Mavris, D. N., (2003), "Creep Life Uncertainty Assessment of a Gas Turbine Airfoil," *Proceedings of the Fifth AIAA Non-Deterministic Approaches Forum*, Norfolk, VA, April 7–10.
[34] Liu, Z., Mavris, D. N., and Volovoi, V. V., 2001, "Creep Life Prediction of a Gas Turbine Components Under Varying Operating Conditions," *Proceedings of the 2001 ASME International Joint Power Generation Conference*, New Orleans, LA, June 4–7.
[35] Cerri, G., 1996, "A Simultaneous Solution Method Based on a Modular Approach for Power Plant Analyses and Optimized Designs and Operations," ASME Paper No. 96-GT-302.
[36] Cerri, G., Borghetti, S., and Salvini, C., 2005b, "Neural Management for Heat and Power Cogeneration Plants," The Ninth International Conference on Engineering Applications of Neural Networks, Lille, France, Aug. 24–26.
[37] Von Mises, R., 1913, "*Mechanik der Festen Korper im Plastisch Deformablen Zustand*," Göttin. Nachr. Math. Phys., **1**, pp. 582–592.
[38] Ross, E. W., and O'Hara, K. S., 1992, Renè 142: A High Strength, Oxidation Resistant DS Turbine Airfoil Alloy, *Proceedings of the Seventh International Symposium on Superalloys in Champion*, PA, Sept. 20–24, pp. 257–266.
[39] Penny, R. K., and Marriott, D. L., 1995, *Design for Creep*, 2nd ed., Chapman and Hall, London.
[40] Gazzino, M., 2005, "Influenza del Creep dei Componenti ad Alta Temperatura sulla Pianificazione della Produzione Elettrica di un Parco di Centrali Equipaggiate con Turbina a Gas," MS thesis, Roma Tre University.
[41] Diakunchak, I. S., 1992, "Performance Deterioration in Industrial Gas Turbines," ASME J. Eng. Gas Turbines Power, **114**, pp. 161–168.
[42] Hoeft, R., Janawitz, J., and Keck, R., 2003, "Heavy-Duty Gas Turbine Operative and Maintenance Considerations," GE Power Generation Report No. GER3620J.
[43] Cerri, G., Evans, R., Frangopoulos, C. A., Parrella, M., Pitt, R. U., Psychogios, J., Salvador, S., Sepielli, M., and Seyedan, B., 2000, "Optimum Management System With Environmental Monitoring," ASME Paper No. 2000-GT-310.
[44] Kemfert, C., and Tol, R., 2000, "Economic Effects of the Liberalisation of the German Electricity Market-Simulation by a Game Theoretic Modelling Tool," Working Paper No. 89/2000.

# Design Procedure of a Novel Microturbine Low $NO_x$ Conical Wire-Mesh Duct Burner

**Omar B. Ramadan**
e-mail: omarbabr@gmail.com

**J. E. Donald Gauthier**
e-mail: donald_gauthier@carleton.ca

Mechanical and Aerospace Engineering Department,
Carleton University,
Ottawa, ON, K1S 5B6, Canada

**Patrick M. Hughes**
e-mail: phughes@nrcan.gc.ca

**Robert Brandon**
e-mail: rob.brandon@nrcan.gc.ca

CANMET Energy Technology Centre,
Natural Resources Canada,
Nepean, ON, K1A 1M1, Canada

*Nowadays, air pollution and climate change have become a global environmental problem. As a result, government regulations worldwide are becoming increasingly stringent. This has led to an urgent need to develop new designs and methods for improving combustion systems to minimize the production of toxic emissions, such as nitrogen oxides. Microturbine based cogeneration units are one of the interesting alternatives for combined electrical power and heat generation (CHP). Microturbine CHP technology still needs to be developed to increase efficiency and heat-to-power ratio and to improve operating flexibility. This can all be obtained by adding a duct burner to the CHP unit. This paper documents the design process for a novel low $NO_x$ conical wire-mesh duct burner for the development of a more efficient microcogeneration unit. This burner provides the thermal energy necessary to raise the microturbine exhaust gas temperature to increase the heat recovery capability. The duct burner implements both lean premixed and surface combustion techniques to achieve low $NO_x$ and CO emission levels. The design process includes a set of preliminary design procedures relating the use of empirical and semiempirical models. The preliminary design procedures were verified and validated for key components, such as the duct burner premixer, using the laser sheet illumination (LSI) technique. The LSI was used to study the mixing process inside the premixer fitted with different swirlers. The designed duct burner successfully operated in a blue flame mode over a wide range of conditions with $NO_x$ emissions of less than 5 ppmv and CO emissions of less than 10 ppmv (corrected to 15% $O_2$).*
[DOI: 10.1115/1.2968867]

## 1 Introduction

The wire-mesh duct burner (DB) for microturbine (MT) CHP units presented in this paper is a new concept. The design procedure was derived from elements available in the literature and from observations of many previously developed gas turbine combustors and of radiant or conventional burners. The goal of this work was to design a DB to provide the thermal energy necessary to raise the microturbine exhaust gas temperature (MTEGT) to the required temperature while maintaining low $NO_x$ and CO emission levels. The preliminary design procedures involved in the design and construction of the mesh DB are discussed in this paper. At the first stages of the design, the LSI technique was used to verify some of the design procedures implemented, such as the one used to design the DB premixer. The LSI results indicated that the premixer effectively mixed the two fluid streams. After the system was designed and built, it was tested, and successful combustion results were obtained.

## 2 Design Strategies

The overall DB design strategy (Fig. 1) followed in this paper starts by defining and understanding the concept, completing a literature review, and selecting the type of the burner; these parts were covered in a previous publication [1]. Second, the design process, which is the topic of this paper, involves five main components: (1) Design specifications and requirements: these lead to the definition of the design parameters. (2) Preliminary design: In this step the overall dimensions of the DB were determined. (3) Mechanical design: in a coordinated way this step elevates the design concept to production drawing. Solid models (3D drawing) are also needed for a detailed design step (e.g., for thermal analysis and computational fluid dynamics (CFD) modeling). (4) Detailed design: the performance of key components (e.g., DB premixer) was verified and validated using LSI and CFD. (5) DB manufacturing and testing for evaluation. Only the first two steps will be covered in this paper. Part of the experimental testing was covered in previous publications by the same authors [1,2].

## 3 Specifications

The basic requirements for the DB design were (1) low manufacturing cost, (2) simple compact design, (3) easy installation and startup, (4) good ignition and stable and efficient combustion, (5) reliable and safe operation, (6) low burner pressure drop, (7) low gas pressure, (8) operation on natural gas (NG), (9) controlled generation of $NO_x$ to meet environmental regulations, and (10) good load control. During the preliminary design stage, the DB design point was fixed, with the inputs and specification listed in Table 1.

## 4 Preliminary Design

The DB preliminary design procedure is the main topic of this paper in which the design steps were covered and the overall dimensions of the DB were determined. The DB preliminary design was covered by two main tasks referred to in this paper as (1) the combustion problem and (2) the fluid dynamics problem (Fig. 1).

**4.1 The Combustion Problem.** The concept was to design a DB that can produce stable flame and ultralow $NO_x$. To accomplish this, the DB was designed to operate in the lean burn mode, and the combustion process was to be completed over the surface

Contributed by the International Gas Turbine Institute of ASME for publication in the JOURNAL OF ENGINEERING FOR GAS TURBINES AND POWER. Manuscript received April 5, 2008; final manuscript received April 10, 2008; published online July 13, 2009. Review conducted by Dilip R. Ballal. Paper presented at the ASME Turbo Expo 2008: Land, Sea and Air (GT2008), Berlin, Germany, June 9–13, 2008.

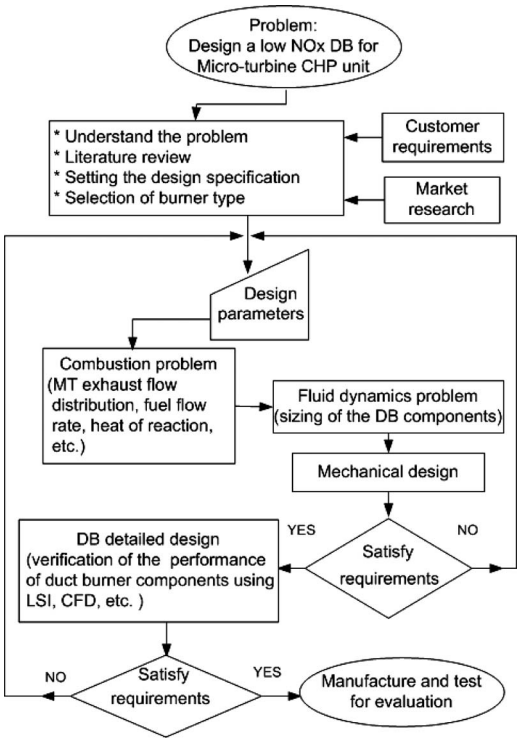


**Fig. 1 Overall duct burner design strategy**

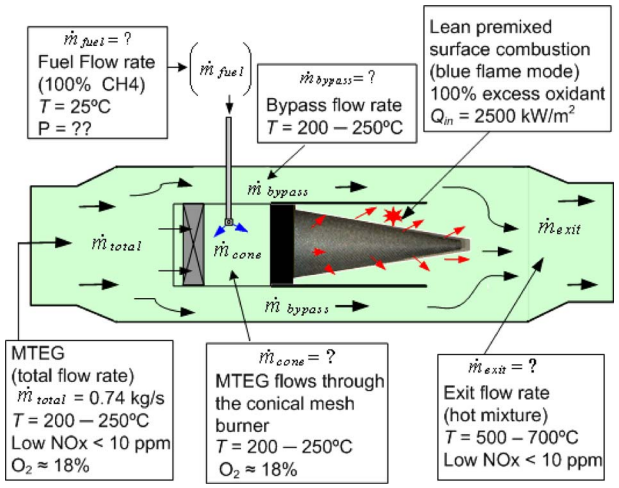


**Fig. 2 DB schematic (combustion problem)**

of a conical wire-mesh burner in the blue flame mode. The combustion calculations based on the concept (lean premixed surface combustion) are briefly presented in this section.

Figure 2 shows the schematic of the DB with the quantities to be calculated during the combustion problem. This problem sought to determine the flows of exhaust gases and fuel needed to obtain the desired mode of operation and final temperature. Calculations were based on the 70 kW MT at its design point (Table 1). Referring to Fig. 2, the oxygen contained in the MTEG from the CHP unit recuperator is split into two streams. One stream bypasses the conical burner, and the other burns with the added fuel inside the DB and over the conical burner. The bypass exhaust stream is then mixed with the hot products of combustion, diluting and cooling these. The DB fuel was natural gas and was assumed to be 100% methane.

*4.1.1 Mass Flow Rate*. Combustion calculations and the determination of the adiabatic flame temperature and heat of reaction were carried out using the JANNAF tables [3]. We assumed perfect mixing, completed combustion reactions, no dissociation, and no heat losses. In addition, it was assumed that the only species present in the product of combustion, for the stoichiometric case, were $CO_2$, $H_2O$, and $N_2$ and, in the lean case, $CO_2$, $H_2O$, $N_2$, and $O_2$. The MTEG were analyzed and used as an oxidant in the DB combustion process. The measured components of $NO_x$, $SO_2$, and CO are of little relevance to the combustion heat release calculation because they are present in very small quantities. Hence, for

**Table 1 Duct burner design point and specifications**

| Parameter | Design values |
|---|---|
| Ambient temperature | 25°C (298 K) |
| Operating pressure | Atmospheric |
| Microturbine used | MT70 kW IR CHP unit |
| Microturbine EGT range | 200–250°C |
| Microturbine exhaust pipe diameter | 0.254 m (10 in.) |
| Microturbine exhaust gases composition (vol %) | $CO_2$ (1.3%), $O_2$ (18%), $N_2$ (78.6%), $H_2O$ (2.35%) |
| Micro-turbine CHP heat recovery system status | Disabled |
| DB exhaust temperature range | 500–700°C |
| DB inlet flow rate | 0.745 kg/s |
| DB combustion efficiency | >99.9% |
| Maximum pressure drop across DB | ≤249 Pa (1 in. $H_2O$) |
| DB fuel type | Natural gas (100% $CH_4$) |
| Energy content of methane (LHV) | 50,050 kJ/kg |
| Methane auto-ignition temperature | 580°C |
| Methane standard flame speed | 0.43 m/s |
| Fuel line pressure | 2–5 psi(gauge) |
| Excess oxidant (in combustion zone) | 100% (Ø=0.5) |
| Combustion concept | Surface combustion |
| Emission limit for $NO_x$ and CO | Less than 10 ppm |
| Type of burner | Porous (wire-mesh) burner |
| Porous burner geometry | Conical shape |
| Operating mode | Blue flame mode |
| Combustion intensity | 2500 kW/m² |
| Material for all the DB components | Stainless steel (SS) |

convenience, they were combined together and presented as CO in the calculation. Therefore the simplified MTEG composition used in the calculation as an oxidant was

$$\text{Oxidant} = (x_1O_2 + x_2CO_2 + x_3CO + x_4H_2O + x_5N_2) \quad (1)$$

The combustion equations (mole basis) used for the stoichiometric case (Eq. (2)) and the lean burn case (Eq. (3)) are

$$aCH_4 + m_{\text{stoich}}(\text{oxidant}) = bCO_2 + cH_2O + dN_2 \quad (2)$$

$$a_1CH_4 + m_{\text{act}}(\text{oxidant}) = b_1CO_2 + c_1H_2O + d_1N_2 + fO_2 \quad (3)$$

where the constants $(a, a_1, x_1, x_2, x_3, x_4, x_5, b, b_1, c, c_1, d, d_1, f)$ are gas mole fractions. The coefficients $(m_{\text{stoich}})$ and $(m_{\text{act}})$ are the stoichiometric and actual mole fractions of the oxidant used in the combustion process.

The atom conservation principle was used to solve the combustion equations for the values of the relative mole fractions of the reactants and products, and then the stoichiometric $((O/F)_{\text{stoich}})$ and actual oxidant-to-fuel ratios (by mass) were computed as follows:

$$(O/F)_{\text{stoich}} = \left(\frac{\dot{m}_{\text{oxid}}}{\dot{m}_{\text{fuel}}}\right)_{\text{stoich}} = \left(\frac{m_{\text{stoich}}}{a}\right)\frac{MW_{\text{oxid}}}{MW_{\text{fuel}}} \quad (4)$$

$$(O/F)_{\text{act}} = \left(\frac{\dot{m}_{\text{oxid}}}{\dot{m}_{\text{fuel}}}\right)_{\text{act}} = \left(\frac{m_{\text{act}}}{a_1}\right)\frac{MW_{\text{oxid}}}{MW_{\text{fuel}}} \quad (5)$$

where $\dot{m}_{\text{oxid}}$, $\dot{m}_{\text{fuel}}$, $MW_{\text{oxid}}$, and $MW_{\text{fuel}}$ are, respectively, the mass flow rate of the oxidant, the fuel flow rate, the molecular weight of the oxidant, and the molecular weight of the fuel. Knowing the total mass flow rate of the MTEG, the design equivalence ratio, and other design parameters listed in Table 1, the fuel flow rate and the amount of oxidant needed for combustion were computed.

This section describes the equations used during the computation. The overall actual oxidant-to-fuel ratio $((O/F)_{\text{ov-actual}})$ was estimated using the following equation:

$$(O/F)_{\text{ov-act}} = \frac{\text{LHV} - (C_P(T_{\text{av}}) \times (T_{\text{exit}}))}{C_P(T_{\text{av}}) \times (T_{\text{exit}} - T_{\text{inlet}})} \quad (6)$$

where $C_p(T_{\text{av}})$ is the constant pressure specific heat of gases at the average temperature between the DB exit $(T_{\text{exit}})$ and inlet temperatures $(T_{\text{inlet}})$.

The equivalence ratio $(\phi)$ is defined as follows:

$$\phi = \frac{(O/F)_{\text{stoich}}}{(O/F)_{\text{act}}} \quad (7)$$

The fuel flow rate was calculated using

$$\dot{m}_{\text{fuel}} = \frac{\dot{m}_{\text{total}}}{(O/F)_{\text{ov-act}}} \quad (8)$$

The amount of oxidant needed for the combustion process to produce blue flame over the conical mesh burner surface was estimated using

$$\dot{m}_{\text{cone}} = \frac{\dot{m}_{\text{fuel}}}{(\phi_{\text{local}}/(O/F)_{\text{stoich}})} \quad (9)$$

where $\phi_{\text{local}}$ is the local equivalence ratio (combustion zone).

*4.1.2 Flame Temperature* $(T_{\text{flame}})$. Assuming a steady flow process, the absence of work interaction, the fact that the oxidant and the combustion gases are ideal gases, and the negligible change in potential and kinetic energies, the steady flow energy equation leads to

$$\sum n_{\text{prod}}\left(\bar{h}_f + \int_{T_{\text{ref}}}^{T} \bar{C}_{Pi}(T)dT\right)_{\text{prod}} = \sum n_{\text{react}}\left(\bar{h}_f + \int_{T_{\text{ref}}}^{T} \bar{C}_{Pi}(T)dT_{\text{react}}\right) \quad (10)$$

where $n_{\text{prod}}$, $n_{\text{react}}$, $\bar{h}_f$, and $\bar{C}_{Pi}(T)$ are, respectively, the products' and the reactants' component mole fractions, the enthalpy of formation, and the constant pressure specific heat (on a molar basis). $T$ and $T_{\text{ref}}$ are the actual and reference (298.15 K) temperatures. The solution for the adiabatic flame temperature is a trial-and-error solution of Eq. (10). The $T_{\text{flame}}$ for nondissociating products of combustion, such as those shown in Eqs. (2) and (3), is usually called the adiabatic frozen-flame temperature [4].

*4.1.3 Burner Heat Release*. The heat of reaction is the heat transferred for a certain chemical reaction, such as that presented in Eq. (3), when the reactants and the products are at the same temperature and the pressure is kept constant. Then the steady flow energy equation leads to

$$Q = \sum n_{\text{prod}}(\bar{h}_f + \bar{h} - \bar{h}^\circ)_{\text{prod}} - \sum n_{\text{react}}(\bar{h}_f + \bar{h} - \bar{h}^\circ)_{\text{react}} \quad (11)$$

where $\bar{h}$ and $\bar{h}^\circ$ are the enthalpy of the gas at the reaction temperature and the reference enthalpy of the reaction (on a molar basis).

Expanding Eq. (11) by replacing the sums with the appropriate terms and their values leads to the solution of the heat release equation.

*4.1.4 Homogeneous Burning Velocity (HBV)*. The burning velocity is an important parameter that must be accounted for in the design of the DB because it is desirable that the velocity of the oxidant through the mesh burner would be equal to the flame speed [5]. If this happens, the flame will be stable on the wire-mesh surface. A simplified form of the Semenov equation [6] was used in the present work for the estimation of the burning velocity during the DB design process,

$$\text{HBV} = \sqrt{\frac{KT_{\text{um}}^2 T_{\text{flame}}^5 \exp\left(\frac{-E}{R_u T_{\text{flame}}}\right)}{(T_{\text{flame}} - T_{\text{um}})^3}} \quad (12)$$

where $K$, $T_{\text{um}}$, $E$, and $R_u$ are, respectively, the constant of proportionality, the unburned mixture temperature, the activation energy, and the universal gas constant.

*4.1.5 Combustion Problem Closing*. The results show that approximately 75% of the MT exhaust had to bypass the combustion zone to achieve the design equivalence ratio of 0.5. The remaining exhaust is the amount of oxidant to be burned with the appropriate amount of methane (it was calculated to be 0.0048 kg/s) over the DB conical mesh surface. This combustion was expected to produce low $NO_x$ combustion products, with a temperature of 1250°C and 235 kW of heat release at the mesh surface. The combustion products were then mixed with bypass exhaust, and the final temperature of the mixture was in the range of 500–700°C.

**4.2 The Fluid Dynamics Problem.** This section discusses the following general topics: (1) the geometry of the DB, (2) the study and design of the proper mixing system, (3) the establishment of a way to deliver the different flows to each zone, and (4) the study of the method to protect the flame from the bypass flow. A concentric-duct-and-conical-burner design was considered (Fig. 3). The different dimensions shown in Fig. 3 were calculated in this phase. The presence of the metal fiber burner and its support structure in an exhaust gas stream contained within an exhaust duct of a MT unit will cause a resistance to the flow and a result-

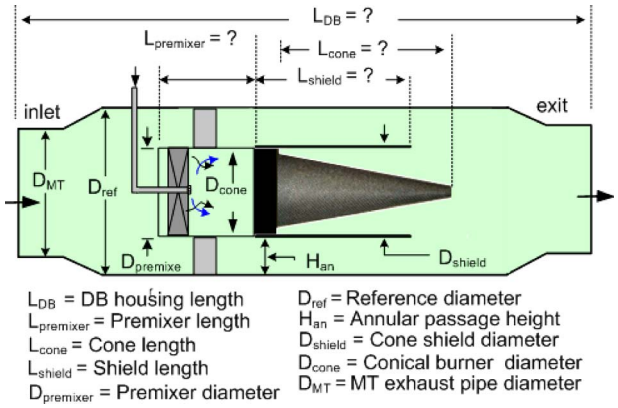


**Fig. 3 DB schematic (fluid dynamics problem)**

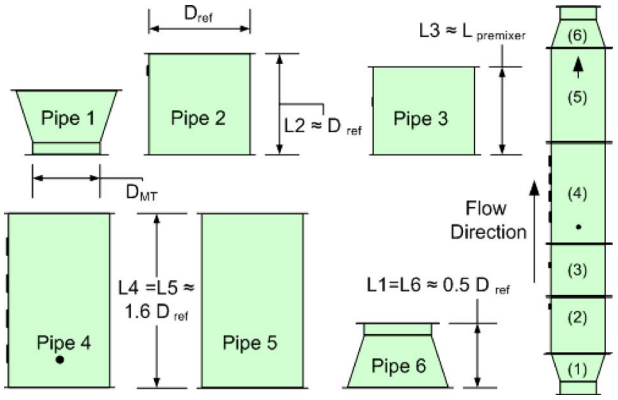


**Fig. 5 DB housing components and assembly (right)**

ing pressure drop. The total pressure drop due to the DB was specified to be no more than 1.0 in. of water to maintain the MT efficiency.

Figure 4 shows the fluid dynamics problem flowchart in which the five main components of the DB are listed. A short description of the geometrical design parameters and design steps used for each component will be provided after a review of some general common design parameters in this section.

*4.2.1 Design Parameters*

*4.2.1.1 DB materials*. Materials appropriate for burners or any combustion system design, which would give the required life and performance for most applications, are available. In the present design, grade 304 stainless steel (SS) was selected as the material for the test DB. Grade 304 SS provides acceptable performance and life. Standard SS pipes, tubes, and sheets were used for the manufacturing of the DB.

*4.2.1.2 DB reference velocity* ($V_{ref}$). Following the approach used by gas turbine combustor designers [7–9], the reference velocity in the present work was defined as the mean velocity across the plane of the maximum cross-sectional area of the DB housing. The DB inlet velocity was measured by traversing the Pitot-static tube across the MT exhaust pipe, and it was measured to be 18 m/s. The $V_{ref}$ was calculated after the expansion at the maximum cross-sectional area using the continuity equation. It was calculated to be 12 m/s.

*4.2.1.3 DB reference diameter* ($D_{ref}$). The DB reference diameter is the maximum diameter of the DB housing where the $V_{ref}$ was defined. The diameter was assigned based on different factors

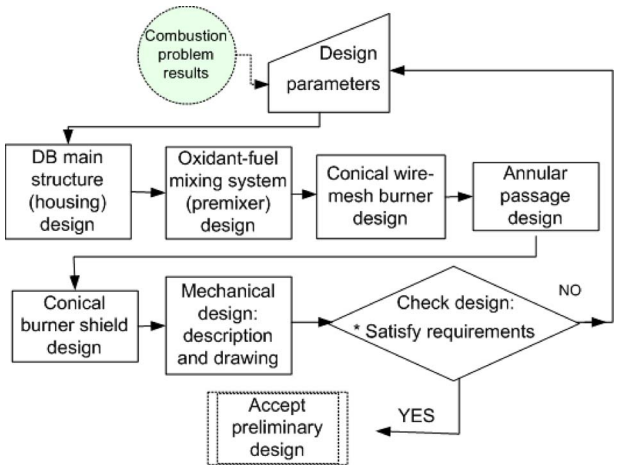


**Fig. 4 Fluid dynamics problem flowchart**

such as DB total pressure drop, flame speed, MT exhaust gas mass flow rate, DB inlet velocity, MT exhaust pipe diameter, and available standard pipe sizing for cost saving. Compromise must be made between the mentioned parameters to select the DB reference diameter. However, the DB size must be adequate to allow the insertion of probes for measurements without sharp disturbance of the flow. At the same time, the DB must be small to be practical for a MT CHP package application. The $D_{ref}$ was selected to be 0.315 m (12.39 in.). The cross-sectional area based on this diameter is the reference area.

*4.2.2 Burner Housing*. The DB housing was composed of sections. The sizing of these sections affects important performance aspects such as pressure drop, mixing, and flow stability. In addition, the size of some of the DB sections was controlled by the internal pieces located inside these sections. As many geometrical parameters were studied in the present work, ease of disassembly was also considered. Figure 5 shows a schematic of the DB housing's main components with their dimensions. SS standard pipe pieces were used for the DB housing. The dimensions of the pipe used were (schedule 10S) 0.315 m (12.39 in.) inner diameter and 4.6 mm (0.18 in.) wall thickness. The DB housing consists of six main pieces. Pipes 1 and 6 are the DB inlet and exit pipes. Both are similar. They connect the DB with the MT exhaust system. The expansion to a larger area is used to reduce the velocity for flame stability reason, to reduce pressure loss, and to gain more space for measurement. Pipe 2 is the premixer inlet pipe, which was made to stabilize the flow after the diffuser. Pipe 3 is the premixer housing pipe. The length of this section was made equal to the premixer length (0.3 m). The premixer via its supports was mounted in this section. Pipe 4 is the conical wire-mesh burner housing, where the visualization ports are located. Pipe 5 is the exhaust pipe, where the hot products mix with the bypassed flow. All the parts of the DB are flanged together to form a 2 m long test rig with 30 probing ports and 4 sight ports.

This section describes the equations used during the computation of the duct housing components. The diffuser design formula used was based on the area ratio [8], which was defined as the ratio between the diffuser exit and inlet cross-sectional areas,

$$\mathrm{AR}_{\mathrm{diff}} = 1 + 4\frac{L_{\mathrm{diff}}}{D_1}(\tan(\alpha)) + \left(\frac{2L_{\mathrm{diff}}}{D_1}(\tan(\alpha))\right)^2 \qquad (13)$$

where $\mathrm{AR}_{\mathrm{diff}}$ is the diffuser area ratio, $D_1$ is the diffuser inlet diameter, $L_{\mathrm{diff}}$ is the diffuser length, and $\alpha$ is the diffuser half angle. The diffuser section pressure drop was estimated by the following equation [8]:

$$\Delta P_{\mathrm{diff}} = \lambda(0.5\rho(V_1)^2)\left[1 - \frac{1}{(\mathrm{AR}_{\mathrm{diff}})^2}\right] \qquad (14)$$

where $\lambda$ is the loss coefficient given by 0.45, $V_1$ is the diffuser inlet velocity, and $\rho$ is the fluid density. For the straight SS pipe

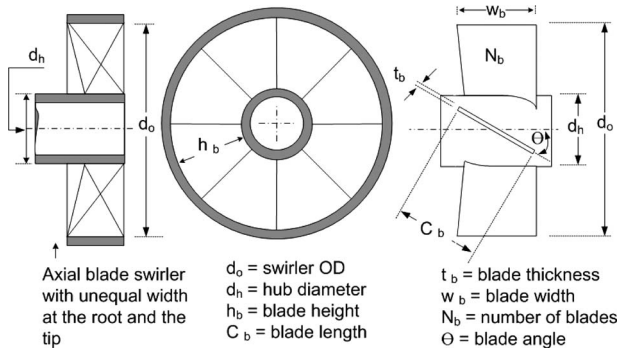


**Fig. 6 Axial blade geometry**

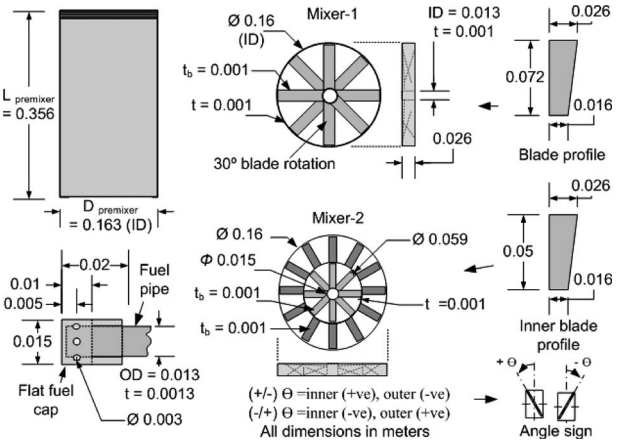


**Fig. 7 DB premixer component dimensions**

sections, the formulations used during the pressure drop calculations are

$$\Delta P_{\text{pipe}} = \frac{\rho V_{\text{ref}}^2}{2} f_{\text{pipe}} \frac{L_{\text{pipe}}}{D_{\text{ref}}} \tag{15}$$

where $f_{\text{pipe}}$ is the friction factor given by

$$f_{\text{pipe}} = \left(1.14 - 2 \times \log\left(\frac{\Psi}{D_{\text{ref}}} + \frac{21.25}{\text{Re}^{0.9}}\right)\right)^{-2} \tag{16}$$

where $\Psi$ is the absolute roughness and Re is the Reynolds number.

*4.2.3 Premixer*. Swirling flow is the method used in this work to rapidly mix the fuel and the oxidant inside the DB premixer. Swirl can be imparted to the flow by different means [10,11]. In the present work the swirling motion of the flow was imported by utilizing a static mixer.

*4.2.3.1 Static mixer (swirler) design*. The goal of the static mixer is to impart sufficient swirl to the flow to thoroughly mix the oxidant and the fuel in the premixer prior to combustion while minimizing the pressure losses. The design procedure followed during the swirler design process was based on Ref. [10]: (1) selecting the model for a tangential velocity, (2) determining the swirl strength, which is characterized by the swirl number ($S$), and (3) developing the swirl vane geometry, which is based on the experimental foundation or other standard rules.

In the present work the axial swirler design of the constant angle model was selected for ease of manufacture. The swirl number is approximated by the ratio of the axial flux of the swirl momentum to the axial flux of the axial momentum times the equivalent nozzle radius [12]. The swirl number was estimated with

$$S = \frac{2}{3} \times \left[\frac{1 - \left(\frac{d_h}{d_o}\right)^3}{1 - \left(\frac{d_h}{d_o}\right)^2}\right] \times \tan(\theta) \tag{17}$$

See Fig. 6 for parameter definitions. The swirl number has a strong impact on recirculation. Little or no axial recirculation occurs below the critical value of 0.6, where the adverse pressure gradient is not enough to cause axial recirculation. Above or equal to this value, a central recirculation zone forms due to the presence of strong radial and axial pressure gradients near the swirler exit [13].

Figure 6 defines all the geometrical design variables for the swirler used. Typical axial swirler designs have blade angles between 30 deg and 70 deg, blade thicknesses between 0.75 mm and 1.5 mm, number of swirler blades between 8 and 16, and blade widths between 0.2 and 0.4 times the outer radius [11,14].

*Swirler pressure drop* ($\Delta P_{\text{sw}}$). Different correlations are available in the literature to estimate the swirler pressure drop (e.g., see Refs. [11,15,16]. The empirical formula used to estimate the pressure drop through the swirl thin blades in this work is given by [16]

$$\Delta P_{\text{sw}} = \rho \frac{V_{\text{ref}}^2}{2}(0.02625\theta^2 - 2.1\theta + 45.5) \quad \text{for} \quad \theta \geq 40 \text{ deg} \tag{18}$$

$$\Delta P_{\text{sw}} = \rho \frac{V_{\text{ref}}^2}{2}(0.0875\theta) \quad \text{for} \quad \theta < 40 \text{ deg} \tag{19}$$

*Swirler effective area* $A\text{sw}_{\text{eff}}$. The effective area, which was used for the computation of the swirler airflow, is defined as the annulus area or the swirler physical area, corrected for swirl and flow blockages and multiplied by the swirler discharge coefficient ($Cd_{\text{sw}}$) [9],

$$A\text{sw}_{\text{eff}} = Cd_{\text{sw}} \times \left(\frac{\pi}{4}(d_o^2 - d_h^2)\cos(\theta) - N_b t_b h_b\right) \tag{20}$$

For thin axial blades, the discharge coefficient could be assumed to be 1.0 [16]. In an axial blade swirler, the width of the flow passage at the blade root is smaller than that at the blade tip. Therefore to avoid and reduce the resistance to the flow at the root of the blades, the blade root is designed as shown in Figs. 6 and 7 [11].

*4.2.3.2 Fuel caps*. A simple plain orifice fuel injector was designed for the DB. In this design Bernoulli's principle was used to compute the fuel velocity at the nozzle exit in terms of the fuel flow rate, fuel pressure, fuel temperature, and discharge coefficient. Treating the gaseous fuel as an ideal gas, the equation of state was used to calculate the fuel density. Then the total nozzle area was calculated by using the continuity equation. To provide a more uniform distribution of the fuel inside the DB premixer and to improve the mixing between the fuel and the oxidizer, the total nozzle area was divided into eight small holes [17]. According to the calculated parameters, the fuel pipe diameter was selected, and hence the premixer inner swirler diameter was fixed (hub diameter) (see Fig. 7). Two types of fuel caps were designed for testing: flat and round caps in which fuel is injected at 90 deg and 45 deg to the main flow direction, respectively. The aim of the present fuel injection technique was to inject the fuel radially from the center into the swirl turbulent region to achieve the maximum utilization of the turbulence for fuel oxidant mixing. Fuel caps with hole diameters of 1.8 mm (Cap-1), 2.3 mm (Cap-2), 2.5 mm (Cap-3), and 3 mm (Cap-4) were tested during the LSI phase to study the affect of the different velocity ratios, fuel injection angles, and fuel jet penetration distances on mixing. For the purpose of initiating the design, the maximum penetration distance of round jets was estimated using the following equation [8]:

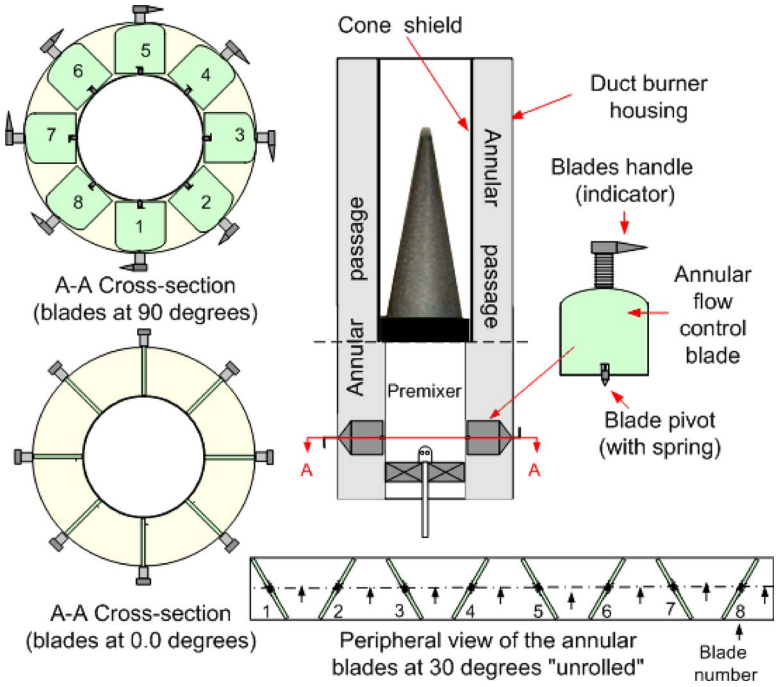


**Fig. 8 Schematic of the annular passage and the blade operation**

$$Y_{\max} = 1.25 D_{\text{jet}} J^{0.5} \frac{\dot{m}_{\text{flow}}}{\dot{m}_{\text{flow}} + \dot{m}_{\text{jet}}} \tag{21}$$

where $D_{\text{jet}}$, $Y_{\max}$, $J$, $\dot{m}_{\text{jet}}$, and $\dot{m}_{\text{flow}}$ are, respectively, the round jet diameter, maximum penetration distance, the momentum flux ratio, the jet mass flow rate, and the main cross flow rate.

*4.2.3.3 Premixer pipe*. The premixer pipe was designed to ensure good mixing at all operating conditions. A SS standard pipe of 0.168 m (6.625 in. pipe Sch-5S) outer diameter was used for the premixer pipe. The size of the premixer pipe was dictated by two parameters: the conical wire-mesh burner dimensions and the best mixing length. The diameter of the premixer pipe was fixed as the conical wire-mesh burner base diameter. The premixer pipe length was selected to be two diameters of the conical wire-mesh burner base diameter to give more mixing time and measurement space (see Fig. 7). The premixer was mounted coaxially in the DB housing by means of two pairs of four supports. One pair was made hollow and used as ports to the temperature measurements made inside the premixer and as support to the cone shield.

*4.2.4 Conical Wire-Mesh Burner Design*. The results of this design process were the dimensions of the cone template and its pressure drop estimation. The base frame of the conical wire-mesh burner design was based on the following parameters: pressure drop assigned to the conical burner, premixer dimensions, and the required combustion intensity. First the conical mesh burner surface area was computed by dividing the previous calculated heat release (Eq. (11)) by the specified combustion intensity (Table 1). Then, the height of the cone ($H_{\text{cone}}$) was geometrically calculated using the formula

$$H_{\text{cone}} = \sqrt{\left(\frac{\left(\frac{Q}{Q_{\text{in}}}\right)}{0.5\pi D_{\text{cone}}}\right)^2 - \left(\frac{D_{\text{cone}}}{2}\right)^2} \tag{22}$$

where $D_{\text{cone}}$ is the cone base diameter, which is equal to the premixer pipe diameter in this case. Correlations from Ref. [18] were used to estimate the pressure drop of the conical burner as a function of the area ratio (open area/total area). The pressure drop estimated was approximately 74.7 Pa (0.3 in. of water). For this value, the results show that the mesh burner must have an area ratio of approximately 95%. The effect of the conical burner pressure drop on the performance of the DB was studied during the combustion test phase of this study. Three conical mesh burners with different nominal pressure drops (Cone-1=74.7 Pa (0.3 in. $H_2O$), Cone-2=149 Pa (0.6 in. $H_2O$), and Cone-3=224 Pa (0.9 in. $H_2O$)) were manufactured and tested. The dimensions and the materials used in the manufacturing of the conical wire-mesh burner were previously reported by Ramadan et al. [1].

*4.2.5 Annular Passage*. The shaded area shown in Fig. 8 represents the annular passage of the DB, which starts from the leading edge of the premixer and ends at the trailing edge of the cone shield. The length and the width of the annular passage depend on the shield length and diameter used in a particular test. During the conceptual design process of the DB, key assumptions were made in both the combustion and the fluid dynamics calculations. Those assumptions lead to some uncertainty. Therefore, eight flat axial manually adjustable blades were introduced 8 cm downstream from the leading edge of the annular passage to provide flexibility and control for stable combustion over a range of operating conditions. Figure 8 shows an overview of the annular flow control blade (AFCB) operation. The blades adjust the MTEG flow split between the conical wire-mesh and the annular passage to achieve a trade-off between emissions, pressure drop. and flame stability. The open cross section, shown in Fig. 8, indicates the way to operate the AFCB between 0 deg and 90 deg. The AFCB are operated in a way that the MTEG flows in convergent and divergent passages to avoid a generation of swirling flow in the annular region for flow measurement reason.

*4.2.6 Mesh Burner Shield (Cone Shield)*. The function of the cone shield is to provide a calm region to ignite and start the combustion until the flame stabilizes at the surface of the mesh burner, providing a continuous source of ignition for the incoming mixture flowing through the wire-mesh burner. In other words, the cone shield was used at this stage to protect or minimize the interaction of the bypass flow with the mesh burner surface to avoid flame quenching. The conical burner shield in the present work has some similar functions as those of a gas turbine combustor liner. It was reported in the literature that for a conventional

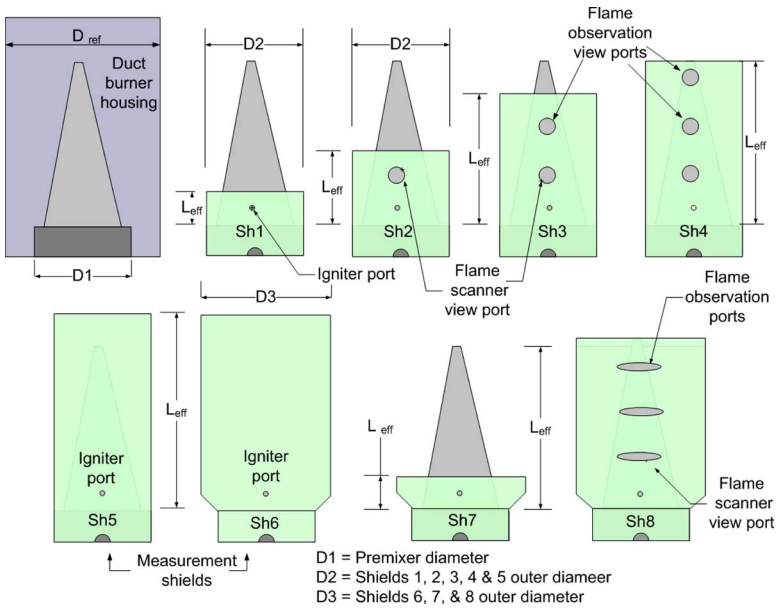


**Fig. 9 Schematic of the shields used**

combustor, the ratio of the liner cross-sectional area to the combustor reference area should be kept within 60–72% [17], and for a tubular combustor with a constant annulus cross section; the area ratio should be in the range of 50–60% for minimum pressure losses [19]. In the present paper the ratio of the burner shield cross-sectional area to the burner reference area was referred to as the blockage ratio (BR). Based on this ratio, two different shield designs were used in this investigation, with blockage ratio values of 0.4 and 0.6. As the blockage ratio increases, the pressure drop across the DB increases, leading to more MTEG entering the combustion zone. To study the effect of shield parameters on the stability of the flame, different shield designs were tested. Shields covering 25%, 50%, 75%, and 100% of the conical mesh burner length with varying BRs were used, and their effect on flame stability and emission levels ($NO_x$ and CO) was measured. In addition to the mentioned shields, two measurement shields were used to provide a smooth uniform flow for the Pitot-static tube measurements performed prior to the combustion test to check the mass flow split between the DB regions. Figure 9 shows the schematics of all the shields used in the present investigation with their parameters. The holes on the shields were aligned to the visualization ports located at the DB outer housing (Pipe 4). One port was used as an igniter port, and the lower semicircular cut was used for setting the shield on the premixer hollow support.

## 5 Combustion Results Sample

A series of extensive parametric tests were conducted in which the effect of varying the different geometries (mixers, fuel caps, cones, annular blade angle setting, and shields) and firing rates (FRs) on the $NO_x$, CO, and flame stability was determined. In previous papers by the present authors [1,2], combustion results were presented for the single-swirl mixer (SM) (30 deg) case only. In this paper sample combustion results from both the SM and the double-swirl mixer (DM) ±30 deg cases will be provided. A HORIBA model PG-250 portable gas analyzer was used for the concentration measurements. All reported $NO_x$ and CO emission values in this paper were for the DB only (total minus MT) corrected to 15% $O_2$. The MT $NO_x$ and CO emissions were reported in Ref. [1].

Figure 10 shows the DB operating in a blue flame mode. The flame images are shown, along with the associated fixed burner parameters and resulting emissions. The $NO_x$ emissions as a function of firing rate for different AFCB angles are presented in Fig. 11. The figure shows lines of constant equivalence ratios. As the equivalence ratio decreases, the $NO_x$ emissions decrease (high excess oxidant). While at a given AFCB angle, the $NO_x$ emissions decrease with the firing rate until the lower stability limit was reached (blow-off limit). During the course of testing, the AFCB angle was found to have a greater effect on the DB overall pressure drop than on the conical wire-mesh burner itself. The two limits used to define the operating range are the blow-off limit and the high $NO_x$ limit (<10 ppm).

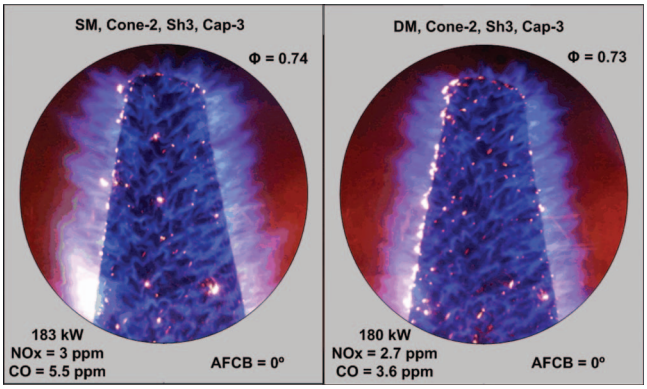


**Fig. 10 DB operating in a blue flame mode (SM, left; DM, right)**

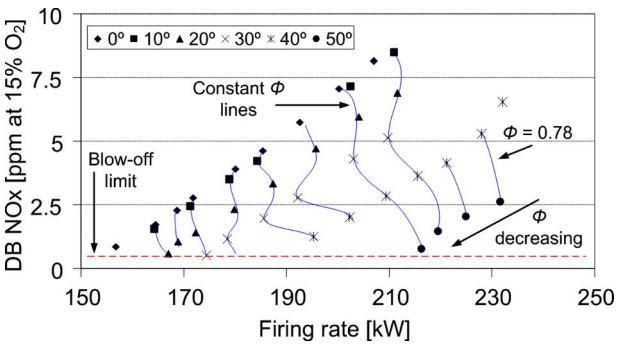


**Fig. 11 Effect of AFCB angles and FR on $NO_x$ emission (SM, Sh2, Cap-2, and Cone-3)**

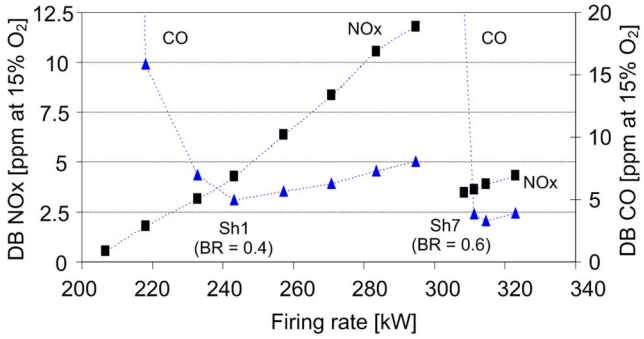


**Fig. 12 Effect of BR and FR on $NO_x$ and CO emissions (SM, Cap-4, Cone-3, and AFCB=0 deg)**

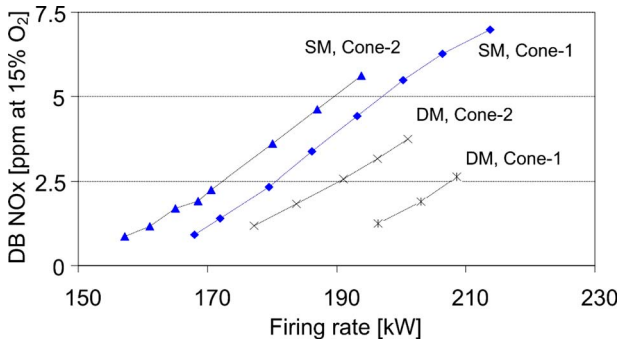


**Fig. 13 Effect of different mixer-cone combinations as a function of FR on $NO_x$ emission (Sh2, Cap-2, and AFCB=0 deg)**

The $NO_x$ and CO emission results as a function of firing rate for different BRs are presented in Fig. 12. The figure shows that as the BR increases to 0.6 (Sh7), the lower emission values were obtained at higher firing rates. The test results also show that the DB operating range is wider with low BR shields. The figure also shows that the CO emissions become excessive at very low firing rates due to incomplete combustion near the blow-off limit. The lower CO ($<5$ ppm) and $NO_x$ ($<5$ ppm) emissions at FR in the range of 250–330 kW were recorded when the DB used Sh7 and Sh8 (BR=0.6), Cap-4, a SM, and both Cone-2 and Cone-3.

Figure 13 shows the effect of four different geometrical combinations on the stability range and $NO_x$ emission levels. The figure shows that for a constant firing rate and a fixed AFCB angle (0 deg), the $NO_x$ emissions decrease as the conical mesh burner pressure drop decreases (higher porosity Cone-1 allows more excess oxidant to flow through the combustion zone, thus reducing $NO_x$). Also at a fixed AFCB angle, the higher conical pressure drop burner extends the lower firing rate range. Hence the operating zone becomes wider (lower porosity Cone-2 increases the local exhaust gas momentum). Using DM shows (Fig. 13) lower $NO_x$ emission due to the better premixing between the oxidant and the fuel. The lower strength mixer, SM, extends the lower firing rate range. Hence the operating zone becomes wider, and the flame stabilizes at leaner fuel/oxidant mixture ratios. Returning to Fig. 10, we can see the effect of using different mixers on the flame structure. The figure shows that the DM provides a better overall flame height uniformity compared with SM.

## 6 Conclusion

The procedures discussed in this paper form a methodology for the preliminary design of a conical wire-mesh DB. The combustion results proved that the design procedures that were used to design this novel MT wire-mesh DB were successful. This DB was verified to operate in the blue flame mode stably with ultralow concentration of pollutants. Sample combustion results were presented, and flame images showing the DB operating in a blue flame mode were provided.

During the course of the evaluation tests, the DB displayed a stable low emission operation throughout the surface firing rate range of 148–328 kW (1574–3489 kW/$m^2$). Emissions of less than 5 ppm for both $NO_x$ and CO emissions were recorded, while the DB successfully raised the MTEGT from about 230°C to as high as 700°C. The DB overall pressure drop throughout all the conducted tests was below the design point of 249 Pa. (1 in. $H_2O$).

## Acknowledgment

This study was supported by the CANMET Energy Technology Centre, Ottawa, ON, Canada.

## Nomenclature

IR = Ingersoll Rand
LHV = lower heating value
LP = lean premixed
MW = molecular weight

## References

[1] Ramadan, O. B., Gauthier, J. E. D., Hughes, P. M., and Brandon, R., 2007, "Experimental Investigation and Evaluation of a Low $NO_x$ Natural Gas-Fired Mesh Duct Burner," ASME Paper No. GT2007-28350.
[2] Ramadan, O. B., Gauthier, J. E. D., Hughes, P. M., and Brandon, R., 2007, "Testing of a Low $NO_x$ Wire-Mesh Duct Burner for Micro-Cogeneration Unit," CANCAM-2007, Toronto, Canada, June 3–7.
[3] Chase, M. W., 1998, *JANNAF Thermochemical Tables*, 3rd ed., American Chemical Society, American Institute of Physics, and National Bureau of Standards, Woodbury, NY, Vol. 14, Pts. I and II.
[4] Kuo, K. K., 2005, *Principles of Combustion*, 2nd ed., Wiley, New York.
[5] Bathie, W., 1996, *Fundamentals of Gas Turbines*, 2nd ed., Wiley, New York.
[6] Gauthier, J. E. D., Bardon, M. F., and Rao, V. K., 1996, "General Flame-Propagation Model for Fuel droplet, Particle and Vapour Mixtures in Air," J. Inst. Energy, **69**, pp. 59–67.
[7] Turns, S. R., 2000, *An Introduction to Combustion: Concepts and Applications*, 2nd ed., McGraw-Hill, New York.
[8] Lefebvre, A. H., 1999, *Gas Turbine Combustion*, 2nd ed., Taylor & Francis, London.
[9] Mellor, A. M., 1990, *Design of Modern Turbine Combustor*, Academic, New York.
[10] Gupta, A. K., Lilley, D. G., and Syred, N., 1984, *Swirl Flows*, Abacus, London.
[11] Basu, P., Kefa, C., and Jestin, L., 1999, *Boilers and Burners Design and Theory*, Springer, New York.
[12] Beer, J. M., and Chigier, N. A., 1972, *Combustion Aerodynamics*, Applied Science, London.
[13] Lilley, D. G., 1977, "Swirl Flows in Combustion: A Review," AIAA J., **15**(8), pp. 1063–1078.
[14] Dodds, W. J., and Bahr, D. W., 1990, *Combustion System Design*, Academic, New York.
[15] Mathur, M. L., and Maccallum, N. R. L., 1967, "Swirling Air Jets Issuing From Vane Swirlers, Part 2: Enclosed Jets," J. Inst. Fuel, **40**, pp. 238–245.
[16] Baukal, C. E., Jr., Gershtein, V., and Jimmyli, X., 2000, *Computational Fluid Dynamics in Industrial Combustion*, CRC Press, Boca Raton, FL.
[17] Sawyer, J. W., 1985, *Sawyer's Gas Turbine Engineering Handbook*, 3rd ed., Turbomachinery International, Norwalk, CT.
[18] Blevins, R. D., 1984, *Applied Fluid Dynamics Handbook*, Van Nostrand Reinhold, New York.
[19] Grobman, J. S., Dittrich, R. T., and Gravs, C. C., 1957, "Pressure Drop and Air Flow Distribution in Gas Turbine Combustors," Trans. ASME, **79**, pp. 1601–1607.

# Experimental Study of Oblong Exhaust Ejectors With Multiring Oblong Entraining Diffusers

**Qi Chen**
e-mail: chenqi@me.queensu.ca

**A. M. Birk**
e-mail: birk@me.queensu.ca

Department of Mechanical and Materials Engineering,
Queen's University,
Kingston, ON, K7L 3N6, Canada

*This paper presents experimental data for the performance of two oblong, straight, air-air ejectors with four-ring oblong entraining diffusers. The effects of inlet swirl angle, nozzle diameter, and flow temperature on the ejector pumping, backpressure, wall pressure distribution, diffuser pressure recovery, and surface film cooling effectiveness were studied. The experiments were carried out on a hot gas wind tunnel that could provide primary mass flow rates up to 2.2 kg/s at ambient temperature and 1.8 kg/s at 500°C. Velocity, pressure, and temperature were measured in the annulus upstream of the primary nozzle, on the mixing tube and diffuser walls, at the diffuser gap inlets, and at the diffuser exit. A comparison between the performance of the oblong ejector and a round ejector indicated that for a short length ejector, the oblong ejector provided better overall performance in terms of pumping and velocity and temperature distributions.*
[DOI: 10.1115/1.2943195]

*Keywords: oblong, ejector, entraining diffuser, hot gas wind tunnel, pumping, wall pressure, velocity distribution, temperature distribution*

## 1 Introduction

Air-air ejectors are simple mechanical devices used to pump a low momentum fluid by mixing it with a higher momentum fluid. Ejectors have no moving parts, and require no power input. Ejectors can be found in many industrial applications for the purposes of entraining air, mixing gases, driving ventilation air, or heating or cooling spaces. Ejectors are widely used in the exhaust systems of gas turbines, for engine space ventilation, particle separation, and exhaust gas cooling. When an ejector is added to the exhaust system of a gas turbine, it may increase the backpressure on the turbine and this affects engine performance (e.g., loss of power for the same fuel consumption). For example, some simple turbomachinery cycle calculations indicate that approximately 1% power loss was realized for every 1% of exhaust duct static backpressure increase [1].

In some gas turbine applications, the exhaust system must be cooled to limit the temperatures inside the structure of the aircraft. The limitation on temperature may be required by structural integrity, space saving, or suppression of infrared signature. The ducts are sometimes cooled by ejectors with entraining diffusers. In many cases, the cooling system must be passive, i.e., without any external power supply. Entraining diffusers typically have poor pressure recovery and as a result, the ejector performance is affected.

The major purpose of a diffuser is to increase flow static pressure by reducing flow dynamic pressure. A diffuser will decrease the pressure at the inlet to the diffuser. The increasing static pressure along the length of diffuser can decelerate the boundary layer in a diffuser and can cause flow separation from the diffuser walls. This separation is called diffuser stall and it results in reduced diffuser pressure recovery. An efficient diffuser should convert as much dynamic pressure into static pressure as possible within a given geometry [2].

Diffuser performance is mainly a function of diffuser geometry, diffuser inlet flow conditions, Reynolds number, and Mach number. Inlet flow properties of interest include the boundary layer thickness, turbulence, swirl, and temperature.

White [3] suggested that the minimum losses for a conical diffuser occurred when the divergence angle ($2\alpha$) was equal to 5 deg. Smaller angles would cause larger frictional loss because of the additional length of the diffuser for the same inlet to exit area ratio. Reneau et al. [4] found that maximum effectiveness, pressure recovery, and minimum loss occurred at $2\alpha$ of about 7 deg for constant area ratios. The important effects of the turbulent boundary layer thickness at the diffuser inlet on the diffuser efficiency were shown by Ackerer and Sprenger [5]. They found that for straight round diffusers, the diffuser efficiency was 0.9 when the inlet blockage factor $B$ ($B=2\delta_{II}/D_I$, where $\delta_{II}$ was the displacement thickness at the diffuser inlet and $D_I$ was the diffuser inlet diameter) was 0.5% and the diffuser efficiency was 0.7 when $B$ was 5%.

Many researchers have reported the important effects of inlet velocity profile on diffuser performance. Shimizu et al. [6] did a study on a straight conical diffuser under five different types of inlet velocity profiles, which were generated by putting several pipe bends in front of the diffuser inlet. The data showed the significant influence of inlet velocity profiles on the diffuser pressure recovery with respect to various area ratios and divergence angles. For example, for the diffuser with 6 deg divergence angle and an area ratio of 4, the pressure recovery coefficient varied in the range of 0.51–0.82. For the diffuser with 12 deg divergence angle, the coefficient changed from 0.32 to 0.7.

Swirling flows include a tangential velocity component. When a swirling flow enters a diffuser, the flow is forced toward the wall by the centrifugal force and the wall boundary layer is less prone to separate even if the divergence angle of diffuser is large. As a result, a higher pressure recovery coefficient can be expected for flows of moderate swirl in simple conical diffusers. However, if the swirl level exceeds a certain amount, core separation is possible. In this case, the axial velocity is decreased to very low levels near the centerline of the diffuser or even a reversed flow region can be induced and diffuser performance is reduced.

The effects of inlet swirl on performance of conical diffusers were experimentally studied by McDonald et al. [7] and Senoo et

Contributed by the International Gas Turbine Institute of ASME for publication in the JOURNAL OF ENGINEERING FOR GAS TURBINES AND POWER. Manuscript received February 23, 2008; final manuscript received March 28, 2008; published online July 13, 2009. Review conducted by Dilip R. Ballal. Paper presented at the ASME Turbo Expo 2008: Land, Sea and Air (GT2008), Berlin, Germany, June 9–13, 2008.

**Table 1 Ejector geometrical parameters**

| Component | | Parameter | Value |
|---|---|---|---|
| Nozzle | ON1 | $A_{annulus}/A_{ne}$ | 1.1 |
| | | $A_{mt}/A_{ne}$ | 2.0 |
| | ON2 | $A_{annulus}/A_{ne}$ | 0.81 |
| | | $A_{mt}/A_{ne}$ | 1.5 |
| Mixing tube (OMT) | | $L_{mt}/D_{mt\text{-}hy}$ | 2.0 |
| Entraining | Gap | $D_{mt\text{-}hy}/h_g$ | 17 |
| Diffuser | Overlap | $L_o/h_g$ | 2.0 |
| (OED) | Length | $L_g/h_g$ | 8.0 |
| ($2\alpha$=20 deg) | Exit | $A_{de}/A_{mt}$ | 2.1 |

al. [8]. The results showed that the pressure recovery of a 20 deg conical diffuser was improved by up to 36% as the diffuser inlet swirl was increased to moderate levels. High swirl had a negative impact on the pressure recovery for some diffuser geometries.

Reneau et al. [4] stated that the flow conditions and performance of unstalled and slightly stalled diffusers were independent of Mach number and Reynolds number when the inlet flow was subsonic and the inlet Reynolds number based on average inlet conditions was greater than approximately $5\times10^4$. Under the above conditions, they cited that the most important inlet conditions were the velocity profile and the turbulence level. McDonald and Fox [9] also concluded that the diffuser performance ($2\alpha$ =4–8 deg, area ratio AR=1.30–4.48) was independent of Reynolds number for incompressible flow if the inlet Reynolds number exceeded $7.5\times10^4$ since the inlet boundary layer was fully turbulent.

In the present work, the primary annulus flow was fully turbulent (hydraulic diameter based Re=$4.7\times10^5$ for the cold flow tests and $2.1\times10^5$ for the hot flow tests) and Mach number was less than 0.3 for both cold and hot flow tests. The present work studied the effects of primary flow swirl and temperature on the performance of simple, oblong air-air ejectors with four-ring entraining diffusers. The study involved a very specific annular to oblong transition in the primary nozzle. This geometry was considered because of its use in certain gas turbine installations.

## 2 Geometry

Oblong is a common shape for gas turbine exhaust ducts in certain platforms. The oblong air-air ejector included a nozzle, which had a round inlet and an oblong exit, an oblong mixing tube and a four-ring, oblong entraining diffuser. The flow transitioned from an annular flow to the nozzle flow with the aid of a bullet shaped center body. The nozzle standoff ratio ($s/(R_{mt}-R_{ne})$) was fixed at 2.25 for all tests. The mixing tube to nozzle exit area ratio ($A_{mt}/A_{ne}$) was fixed at 2.0. A summary of the geometrical parameters used in experiments is given in Table 1.

The full dimensions of the two oblong straight ejector systems, Ejector 4 and Ejector 7, are shown in Figs. 1 and 2, respectively. The main difference between the two ejectors was the size of the nozzle exit. The purpose of Ejector 7 was to study the effects of nozzle size on the ejector performance. Data will also be shown for a round ejector (designated as Ejector 3). The geometrical parameters of Ejector 3 were the same as those of Ejector 4 listed in Table 1. The full dimensions of Ejector 3 are shown in Fig. 3.

## 3 Experimental Approach

The ejector systems were tested under two primary nozzle inlet temperature conditions (cold and hot) and four inlet swirl conditions, using a hot gas wind tunnel (HGWT). This wind tunnel was designed to simulate the flow conditions (mass flow rate, flow temperature, and swirl angle) at the exit of a gas turbine. The 40 hp centrifugal blower could supply airflow up to 2.2 kg/s at ambient temperature and 1.8 kg/s at 500°C with a pressure rise

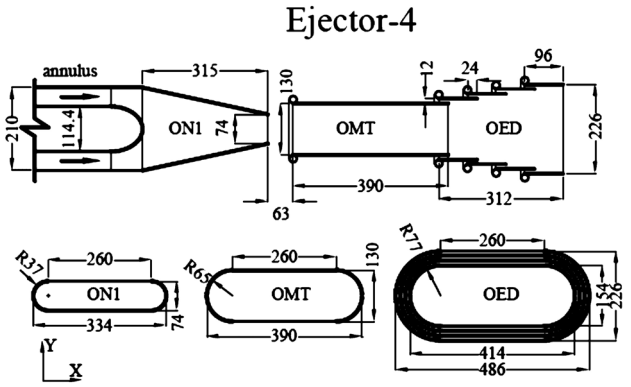


**Fig. 1 Dimensions (in mm) of Ejector 4 (E-4)**

up to 13 kPa. Based on the hydraulic diameter of the annulus and average velocity, the flow at the annulus region had an average Mach number of 0.22 with a Reynolds number of $4.7\times10^5$ for cold flow, and an average Mach number of 0.27 with a Reynolds number of $2.7\times10^5$ for hot flow.

The schematic of the ejector instrumentation is illustrated in Fig. 4. The swirler was mounted at 12 annulus heights upstream from the nozzle inlet. Four seven-hole pressure probes were located at 3.5 annulus heights upstream from the nozzle inlet to measure the inlet flow conditions. The primary mass flow rate ($m_p$) and average backpressure in the annulus were calculated from the seven-hole probe data.

The diffuser rings were connected by 16 struts (see Fig. 5). The rings overlapped by two gap heights and the struts were located in these overlap regions. The four-ring diffuser was also mounted on the mixing tube by 16 struts. Each gap inlet was rounded for smooth entry of the flow.

In total, 160 wall static pressure taps were mounted on the ejector. They were located on the mixing tube wall (16 taps), near the exit of the mixing tube (16 taps), near the exit of each diffuser

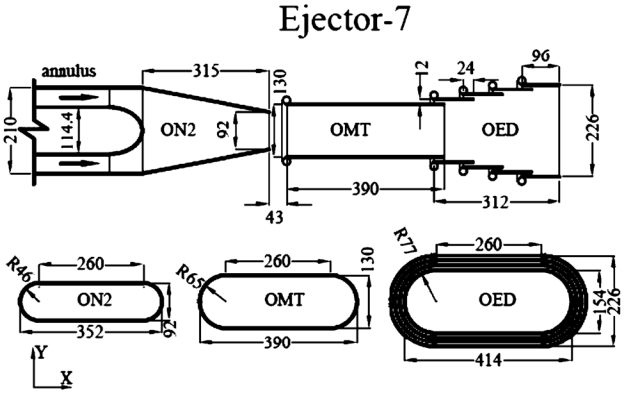


**Fig. 2 Dimensions (in mm) of Ejector 7 (E-7)**

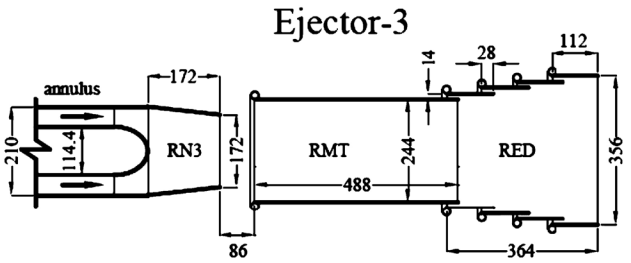


**Fig. 3 Dimensions (in mm) of Ejector 3 (E-3) [10]**

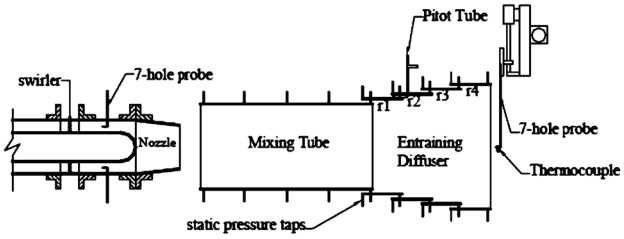


**Fig. 4 Schematic of instrumentation**

ring (16 taps each ring), and near the inlet of the diffuser gaps (16 taps each gap inlet). Wall static pressure was measured by using four pressure transducers. The data were used to calculate the diffuser pressure recovery ($C_p$), diffuser effectiveness ($\eta_d$), and the tertiary mass flow rate ($m_{3rd}$).

As the inlet gap of each diffuser ring was divided into 16 slots by the struts, the measurement of tertiary flow conditions were based on the measured data at each slot.

A Pitot static tube was used to measure the velocity profile at one slot of each diffuser ring. To minimize disturbance to the flow, a very fine tube diameter (2.5 mm) was chosen. The maximum area blockage of each slot caused by placing the Pitot tube (when the Pitot tube tip was at the closest point to the inner wall of the diffuser gap) was in the range of 2.4–3.8% with the average at 3.1%. The measured diffuser inlet gap velocity profile (along radial direction, see Fig. 6) showed a nearly uniform velocity distribution. A dynamic pressure was calculated from the mean velocity obtained from this measured velocity profile and combined with the measured wall static pressure (i.e., wall tap in the same slot) to give a reference total pressure. The mean velocity in the remaining slots was obtained by assuming the same total pressure and subtracting the wall static pressure measurement for each slot. The pumping of the entraining diffuser or tertiary mass flow rate ($m_{3rd}$) was calculated based on the gap inlet velocity measurement.

The velocity profile at the diffuser exit was measured by a seven-hole pressure probe. A thermocouple was mounted near the seven-hole probe tip for measuring the flow temperature distribution at the diffuser exit. A traversing rig was programed to position the seven-hole probe. The total mass flow rate ($m_t$) was calculated from this seven-hole probe data.

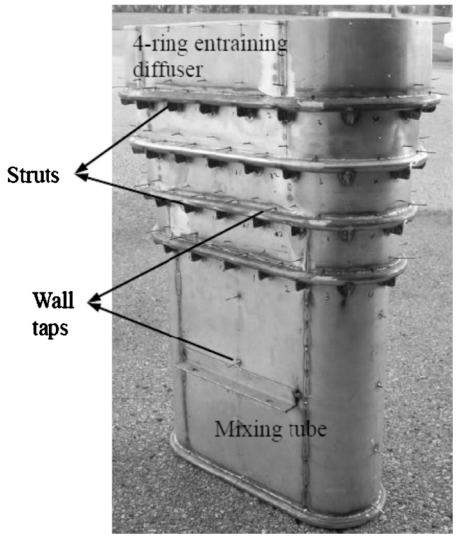


**Fig. 5 Photograph of oblong ejector with four-ring entraining diffuser**

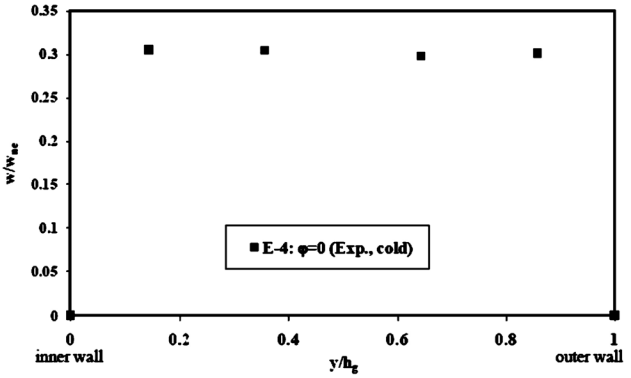


**Fig. 6 Inlet gap velocity profile of the first diffuser ring, flat side, $\varphi$=0 deg, cold flow**

The secondary mass flow rate (i.e., the mass flow entrained at the mixing tube inlet, $m_{2nd}$) was not measured directly. The amount of $m_{2nd}$ was calculated by subtracting the primary mass flow rate ($m_p$) and the tertiary mass flow rate ($m_{3rd}$) from the total mass flow rate ($m_t$) measured at the diffuser exit.

Further details of the HGWT and instrumentation can be found in Chen and Birk [10]. The test matrix is tabulated in Table 2. In total, four different swirl conditions were applied in the annulus upstream of the nozzle inlet using straight vaned swirl generators (16 vanes). Nominal swirl angels were 0 deg, 10 deg, 20 deg, and 30 deg. However, the actual flow angle after the swirler varied from the designed nominal angle due to flow deviation. Actual measured swirl angles before the nozzle inlet are listed in Table 3.

The results of Ejector 4 will be compared to the results of a round ejector (Ejector 3) to show the effects of the oblong shape on the ejector performance. Detailed data for Ejector 3 have been presented in the paper of Chen and Birk [10].

## 4 Uncertainty Analysis

Uncertainties in measured and calculated quantities have been estimated based on calibration results and from instrument manufacturer's data. Analytical methods proposed by Taylor [11] were applied.

In the experimental approach, a calibration was done to find the fixed (bias) and variable (precision) error of the measuring system. The readings of the measuring system were recorded against a known constant input of the variable, e.g., velocity or the temperature. Offset of the mean reading from the known input

**Table 2 Matrix for experiments and simulations**

| | Ejector 4 | | | | Ejector 7 | |
|---|---|---|---|---|---|---|
| | $\varphi$=0 deg | 10 deg | 20 deg | 30 deg | 0 deg | 20 deg |
| Cold | × | × | × | × | × | × |
| Hot (460°C) | × | × | × | × | × | × |

**Table 3 Actual average flow swirl angle in the annulus upstream of the nozzle inlet**

| | Nominal $\varphi$=10 deg | | Nominal $\varphi$=20 deg | | Nominal $\varphi$=30 deg | |
|---|---|---|---|---|---|---|
| | Cold | Hot | Cold | Hot | Cold | Hot |
| E-4 | 13.6 | 14.1 | 19.2 | 19.5 | 32.1 | 32.4 |
| E-7 | | | 18.4 | 18.5 | | |
| E-3 | 11.0 | 12.1 | 18.3 | 18.2 | 30.3 | 32.1 |

**Table 4 Overall uncertainties of the measured values**

| Instrument | Variable/Station | Total uncertainty |
|---|---|---|
| Seven hole probe | Velocity angle | 0.6 deg up to angle of attack of 60 deg |
| | Axial velocity | 1.3 m/s (or 1.5%) |
| | Total velocity | 1.2 m/s (or 1.4%) |
| Thermocouples | Temperature (hot inlet) | 3.6 deg |
| | Temperature (hot exit) | 2.4 deg |
| | Temperature (ambient) | 1.0 deg |
| Wall taps | Wall pressure | 9 Pa |
| Pitot static tube | Velocity | 0.3 m/s (2% up to angle of attack of 30 deg)[a] |

[a]Based on manufacturer's data.

showed the fixed error of the measuring system. Variable error was estimated from the variation in the instrument readings.

The total uncertainty of the measurement was calculated as the root-sum-square (RSS) combination of the bias and precision uncertainties [12]. The uncertainties in the measured values propagated into the calculated results. The total uncertainties in the measured and calculated values are summarized in Table 4.

The uncertainties in the calculated performance parameters were estimated by the method suggested by Kline and McClintock [13]. This method showed that the constant odd combination of the individual uncertainties represents the uncertainty in the result $R$ with good accuracy. The constant odd combination is given as

$$\delta R = \left[ \sum_{1}^{N} \left( \frac{\partial R}{\partial X_i} \delta X_i \right)^2 \right]^{1/2} \quad (1)$$

In the current study, based on Eq. (1), the uncertainties in the flow parameters are tabulated in Table 5. They were calculated based on the cold and hot flow experimental data for Ejector 4 with the 0 deg swirl condition. More details of the uncertainty analysis can be found in Chen [14].

## 5 Results and Discussion

**Flow Swirl.** The swirl level downstream of the swirler can be presented more accurately by using the swirl number $S$. As can be seen from the definition (see Nomenclature), both numerator and denominator are changing when calculating the swirl number at different locations along the length of the ejector. The swirl number calculations for Ejector 4 (oblong) and Ejector 3 (round) are listed in Table 6.

**Table 5 Uncertainties of the flow parameters**

| Parameters | | Condition | Value |
|---|---|---|---|
| Mass flow rate | $m_p$ | Cold | 2% |
| | | Hot | 2% |
| | $m_t$ | Cold | 2% |
| | | Hot | 2% |
| | $m_{3rd}$ | Cold | 2% |
| | | Hot | 2% |
| | $m_{2nd}$ | Cold | 9% |
| | | Hot | 9% |
| Entraining ratio | $\Phi_t$ | Cold | 3% |
| | | Hot | 3% |
| | $\Phi_{3rd}$ | Cold | 3% |
| | | Hot | 3% |
| | $\Phi_{2nd}$ | Cold | 9% |
| | | Hot | 10% |
| Pressure recovery | $C_{pD}$ | Cold | 5% |
| | | Hot | 3% |

**Table 6 Swirl number distribution along Ejector 4 (oblong) and Ejector 3 (round) under various nominal swirl conditions, cold flow**

| | $\varphi$ (deg) | $S$ at nozzle inlet | $S$ at nozzle exit | $S$ at diffuser exit |
|---|---|---|---|---|
| E-4 | 10 | 0.41 | 0.15 | 0.071 |
| | 20 | 0.59 | 0.21 | 0.082 |
| | 30 | 1.1 | 0.24 | 0.080 |
| E-3 | 10 | 0.32 | 0.16 | 0.07 |
| | 20 | 0.56 | 0.29 | 0.14 |
| | 30 | 1.0 | 0.38 | 0.28 |

The degree of swirl can be categorized as very weak swirl ($S \leqslant 0.2$), weak swirl ($S \leqslant 0.4$), and strong swirl ($S \geqslant 0.6$) [15]. As shown in the measured data of the swirl in the annulus, weak swirl was produced by the 10 deg swirler and strong swirl was produced when the swirl angle was greater than 20 deg. The degree of swirl was decreasing along the ejector length. The swirl level at the nozzle exit was reduced by axial flow acceleration in the nozzle and by the shape of the nozzle. The oblong nozzle reduced the swirl more than the round nozzle. The swirl degree at the exit of the diffuser for Ejector 3 (round straight ejector) was around 25% of the swirl at the annulus. For the oblong ejector, Ejector 4, the swirl numbers were reduced to very low levels for all swirl cases. This was probably due to the secondary flows created by the oblong nozzle shape.

### Flow Structure for Ejector 4

*Flow Structure at the Nozzle Exit*. In the oblong nozzle, the flow transitioned from a round annular flow to the oblong exit. With no swirl, this shape transition made the flow move outwards along the horizontal direction (major $x$-axis) and move inwards along vertical direction (minor $y$-axis) (see Fig. 7). This also introduced secondary flows, as shown in Fig. 7. One can also see the effect of the annular to round flow transition at the end of the annulus center body. This appears as a velocity deficit in the middle of the nozzle exit plane.

When swirl was added, the velocity deficit increased due to flow separation behind the annulus center body. For the 30 deg swirl condition, the measured velocity contours at the round nozzle exit of Ejector 3 and at the oblong nozzle exit of Ejector 4 are illustrated in Figs. 8 and 9, respectively. (Flow asymmetry shown in Figs. 7 and 9 was due to the nonideal alignment of the test components along the $z$-axis centerline. Black color in Figs. 8 and 9 indicated a flow separation zone (such as recirculation) in which the velocity information could not be captured by the seven-hole probes because the flow angle was outside of the cali-

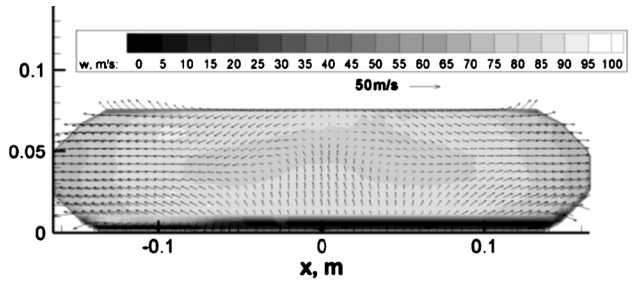


**Fig. 7 Exp. velocity contours of the oblong nozzle exit for Ejector 4, cold flow, $\varphi$=0 deg**

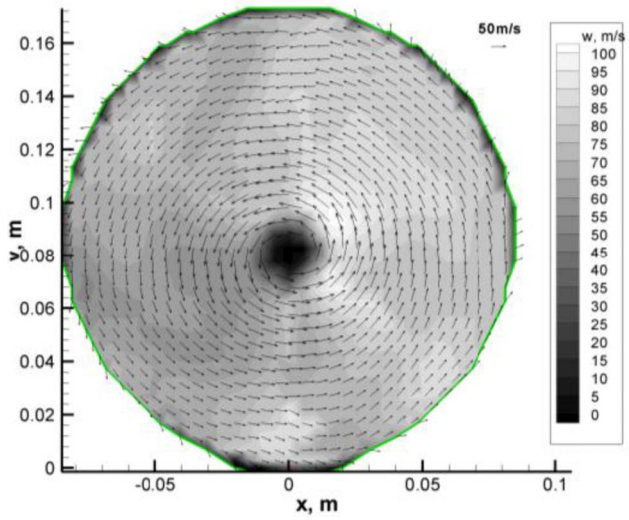


**Fig. 8 Exp. velocity contours of the round nozzle exit for Ejector 3, cold flow, $\varphi$=30 deg**

brated range of the probes.)

As can be seen, the flow at the round nozzle exit was fully rotated by the swirl. However, the oblong shape reduced the swirl, and some of this angular momentum was converted into radial and axial momenta. As a result, the swirl number was reduced more than in the round nozzle case. The swirl numbers at the annulus and the nozzle exit of Ejector 4 and Ejector 3, which were presented in Table 6, clearly pointed out that, at very similar swirl inlet conditions, the swirl number at the oblong nozzle exit was much lower than that of the round nozzle exit.

*Flow Structure at the Diffuser Exit*. Selected axial velocity contours at the diffuser exit for Ejector 4 (hot flow) are illustrated in Fig. 10. As can be seen from the measured data, the increase in swirl from 0 deg to 20 deg reduces the velocity at the diffuser exit and this improves pressure recovery and pumping. It is believed the swirl enhances mixing. At the 20 deg swirl condition, two clockwise vortices were generated at the upper-left and lower-right corners, which were not seen at the 0 deg swirl condition.

The effects of swirl on the uniformity of the velocity and temperature at the diffuser exit for Ejector 4 and Ejector 3 are shown in Table 7. The swirl had a strong effect on the velocity and temperature uniformities for the round Ejector 3. However, this was not the case for the oblong Ejector 4. When the swirl angle was no more than 20 deg, the temperature at the diffuser exit of Ejector 4 was much more uniform than that of Ejector 3.

For these kinds of installations, temperature uniformity and large pumping ratio are desirable. Therefore, for the purpose of generating a uniform exit temperature at the diffuser exit, the oblong ejector was better for all but the highest swirl angle (30 deg).

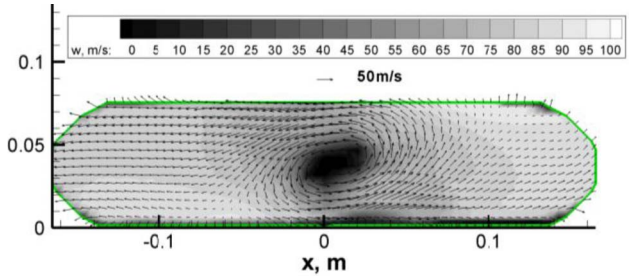


**Fig. 9 Exp. velocity contours of the oblong nozzle exit for Ejector 4, cold flow, $\varphi$=30 deg**

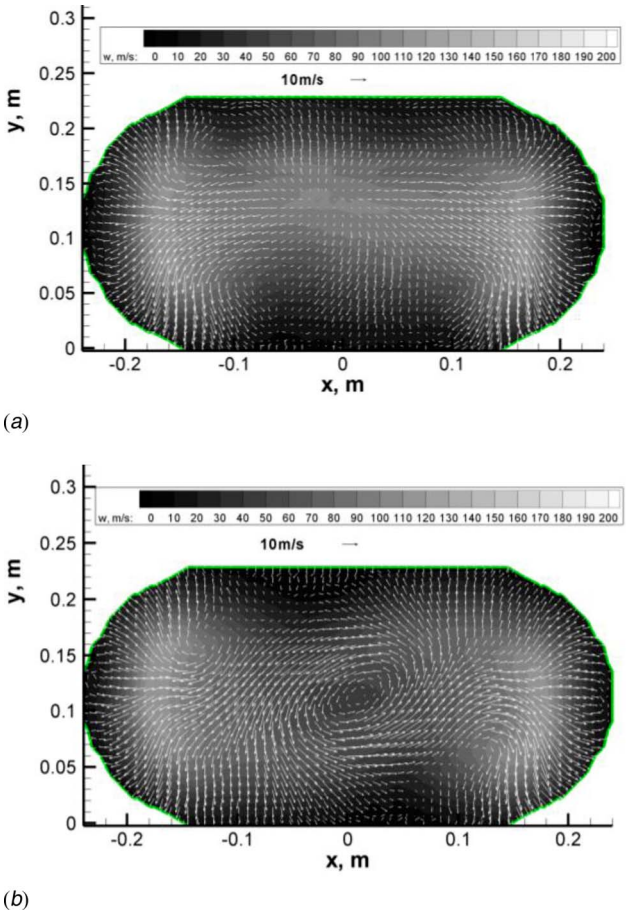


**Fig. 10 Exp. velocity contours at the diffuser exit for Ejector 4, hot flow: (*a*) $\varphi$=0 deg; (*b*) $\varphi$=20 deg**

For the highest swirl angle, the temperature uniformity was quite similar for the round and oblong ejectors. This is of course comparing ejectors to similar area ratios.

**Wall Pressure Distribution.** Wall pressure distribution along the mixing tube and diffuser for Ejector 4 and Ejector 7 are shown in Fig. 11. The mixing tube wall pressure of the curved wall/flat wall was the average of the pressure readings on the two curved/flat walls. The diffuser wall pressure was the average of a large number of pressure samples taken at a given tap.

After the primary flow left the oblong nozzle, it spreads rapidly along the major axis of the nozzle and this spreading jet impinged on the mixing tube curved sides. This resulted in local high pressures in these regions. This rapid spreading was increased by increasing swirl. This characteristic was probably due to the specific shape of our oblong nozzles. This rapid spreading also helped the flow to remain attached to the flat upper and lower walls of the

**Table 7 Velocity uniformity ($f_{ke}$) and temperature uniformity ($f_t$) at the diffuser exit as a function of swirl angle for ejectors, hot flow**

| | | $\varphi$ | | | |
|---|---|---|---|---|---|
| | | 0 deg | 10 deg | 20 deg | 30 deg |
| $f_{ke}$ | E-4 | 1.9 | 1.9 | 2.0 | 1.9 |
| | E-3 | 2.8 | 2.3 | 1.7 | 1.5 |
| $f_t$ | E-4 | 0.53 | 0.53 | 0.61 | 0.55 |
| | E-3 | 0.12 | 0.22 | 0.49 | 0.59 |

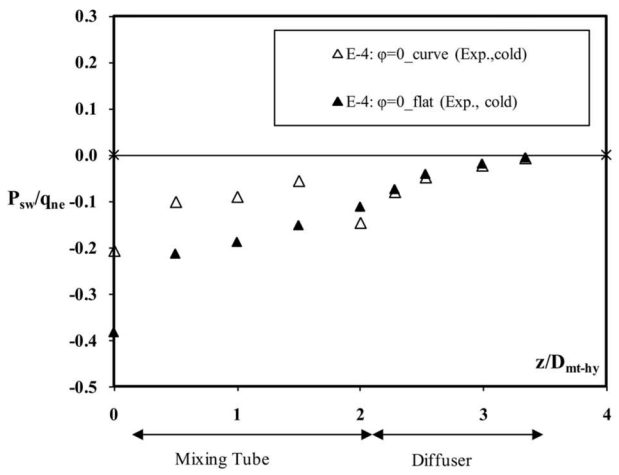


(a) E-4, $\varphi$=0°, cold flow

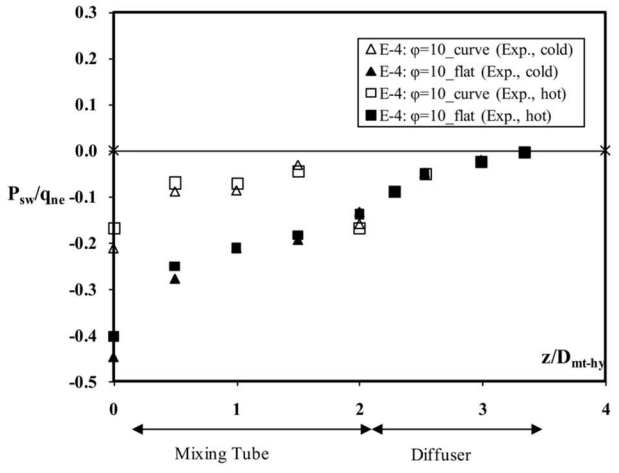


(b) E-4, $\varphi$=10°, cold and hot flow

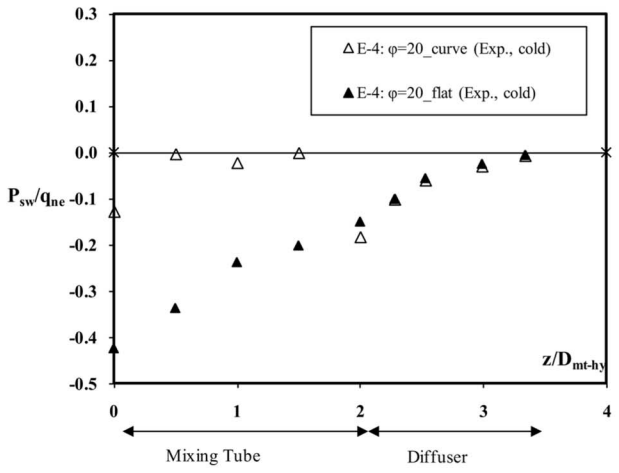


(c) E-4, $\varphi$=20°, cold flow

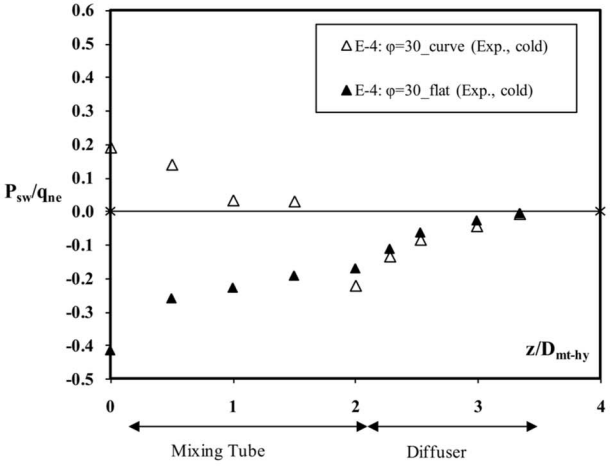


(d) E-4, $\varphi$=30°, cold flow

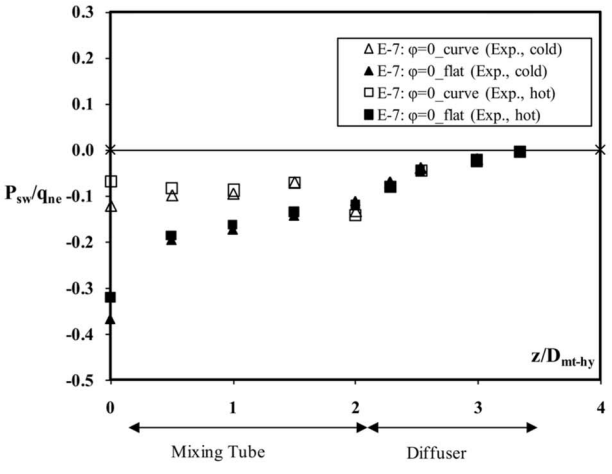


(e) E-7, $\varphi$=0°, cold and hot flow

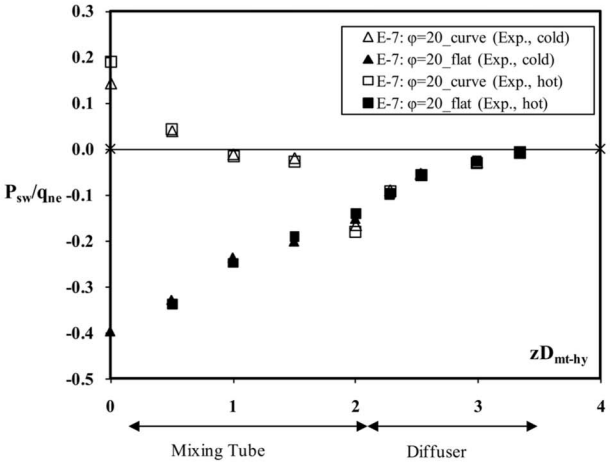


(f) E-7, $\varphi$=20°, cold and hot flow

**Fig. 11 Wall pressure distribution along the mixing tube and diffuser for Ejector 4: (*a*) cold, $\varphi$=0 deg; (*b*) cold and hot, $\varphi$ =10 deg; (*c*) cold, $\varphi$=20 deg; (*d*) cold, $\varphi$=30 deg; For Ejector-7: (*e*) cold and hot, $\varphi$=0 deg; (*f*) cold and hot, $\varphi$=20 deg**

mixing tube. The measured data shown in Fig. 11 clearly presents this tendency. However, higher resolution of the wall pressure taps was needed to find the detailed trend.

For the 30 deg swirl condition, the decreasing pressure trend along the curved wall indicates that there was a rapid decrease in swirl probably due to a core separation at the end of the mixing tube due to the high swirl. When the primary flow transitioned from the annulus region into the nozzle, the flow separated from the ellipsoidal end of the annulus center body. This produced a low velocity wake region behind the center body. When swirl was applied, the flow tended to separate from the center body earlier thus producing a larger wake region. This phenomenon can be

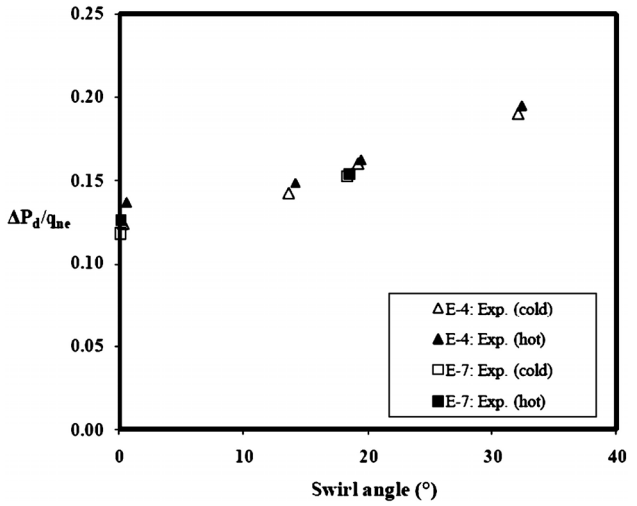


**Fig. 12 Diffuser pressure recovery as a function of swirl angle for Ejector 4 and Ejector 7, cold and hot flows**

seen in the experimental axial velocity contours of the oblong nozzle (ON1) exit at different swirl conditions (see Fig. 7 and 9). At the 30 deg swirl condition, a core separation zone can be clearly seen at the oblong nozzle exit due to the high swirl.

The size of the core separation was further amplified along the flow direction inside the ejector and caused the curved wall pressures to decrease rapidly. The pressure decrease was due to changing velocities and streamline curvature. Swirl did not show obvious effects on the pressure recovery along the flat wall. For Ejector 7, the bigger nozzle size made the flow more prone to impinge the wall (the flow started to hit the mixing tube inlet at the 20 deg swirl condition). Figures 11(*b*), 11(*e*), and 11(*f*) indicate that flow temperature did not present any major effects on the wall pressure distribution.

As can be seen, at each swirl condition, the curved-wall pressure was much higher than the flat-wall pressure. This might imply that most air was entrained at upper and lower flat-wall side and less air was entrained at curved-wall sides.

Since the pressure distribution along the mixing tube wall was completely different on the flat side and curved side, the calculation of pressure recovery in the mixing tube was less meaningful. Only the diffuser pressure recovery, which was calculated based on the average pressure of flat wall and curve wall, is presented in Fig. 12. The pressure recovery in the diffuser increases as the swirl increases. Under similar swirl conditions, Ejector 4 and Ejector 7 had very close pressure recovery. The pressure recovery of the cold flow was also very close to that of the hot flow.

**Pumping.** Pumping ratio, which was defined as the ratio of secondary, tertiary, or total mass flow to the primary mass flow rate, was an important performance parameter to demonstrate how the ejector pumps the air. The pumping ratios of Ejector 4, Ejector 7, and Ejector 3 are shown in Fig. 13. For the pumping of the mixing tube ($\Phi_{2nd}$), instead of a negative effect resulting from the high angle swirl (30 deg) as in Ejector 3 [10], a positive influence was observed from the increasing swirl angle for both oblong ejectors. Under each swirl angle, $\Phi_{2nd}$ of Ejector 4 was higher than that of Ejector 7 for both cold and hot flow tests. This was because Ejector 4 had higher area ratio of $A_{mt}/A_{ne}$ and higher primary flow momentum at the nozzle exit than Ejector 7 had. The pumping ratio of the entraining diffuser ($\Phi_{3rd}$) and the pumping ratio of the whole ejector ($\Phi_t$) showed the similar trend as $\Phi_{2nd}$ did, i.e., the pumping performance was improved by the increasing swirl. Higher pumping of the diffuser of Ejector 4 than Ejector 7 indicated that higher primary flow momentum also had a positive effect on the pumping of the diffuser.

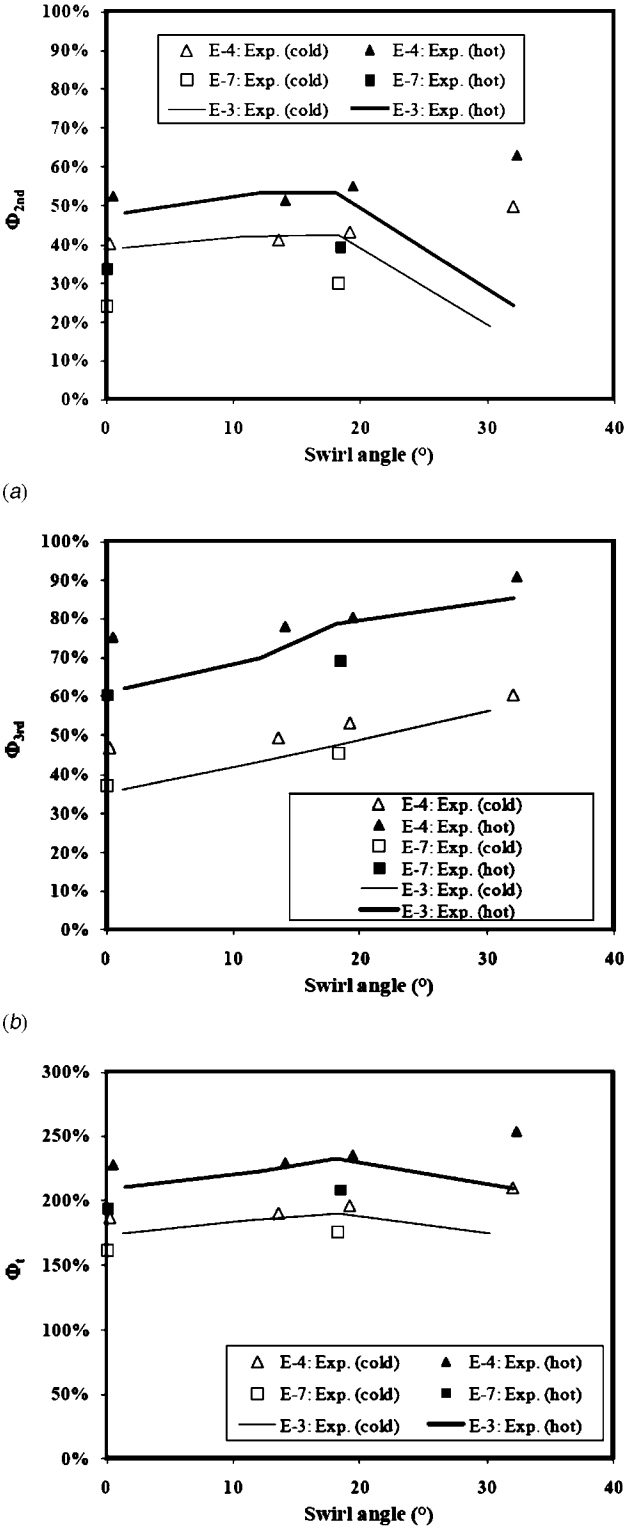


**Fig. 13 Pumping ratios as a function of swirl angle for Ejector 4, Ejector 7 and Ejector 3, cold and hot flows: (*a*) $\Phi_{2nd}$, (*b*) $\Phi_{3rd}$, and (*c*) $\Phi_t$**

As can be seen, the pumping ratios of hot flow were higher than those of cold flow. The higher pumping ability of the hot primary flow could be attributed to two effects, higher primary flow momentum and higher Reynolds stress (turbulent kinetic energy) in

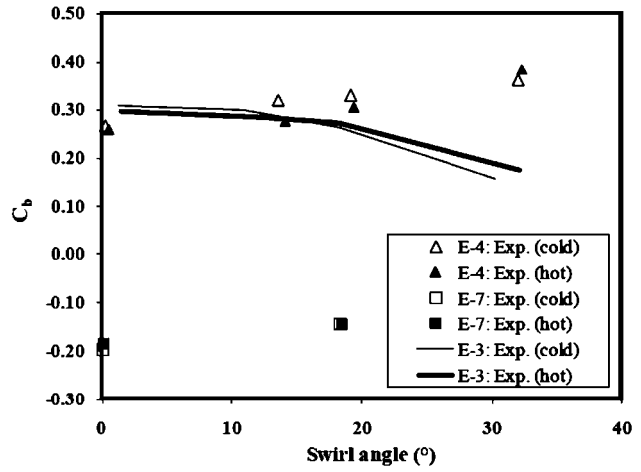


**Fig. 14 Backpressure coefficient as a function of swirl angle for Ejector 4, Ejector 7, and Ejector 3, cold and hot flows**

the mixing boundary (shear) layer, which resulted in faster momentum and energy transfer, due to the higher temperature (density) gradient [16,17].

For both cold and hot flow tests, most of entrained mass flow was contributed by the tertiary entraining at all swirl conditions. The tertiary pumping was more important for the ejector with lower primary jet momentum and smaller area ratio of $A_{mt}/A_{ne}$. In addition, the ratio of $\Phi_{2nd}/\Phi_{3rd}$ was nearly constant for all the swirl conditions, i.e., around 83% for the cold flow of Ejector 4 and around 68% for the hot flow of Ejector 4.

Comparison of entraining ratios between Ejector 4 and Ejector 3 showed that the secondary and total entraining ratios of Ejector 4 were almost equal to those of Ejector 3 when the swirl angle was no more than 20 deg. However, at the 30 deg swirl condition, the oblong ejector had much better performance on the secondary and total entraining. For the tertiary entraining, the advantage of using the oblong shape was maximized at the 0 deg swirl condition.

**Backpressure.** It is desirable to have a low backpressure for these installations. The backpressure coefficient of Ejector 3, Ejector 4, and Ejector 7 are shown in Fig. 14. The backpressure for oblong ejector (E-4) and round ejector (E-3) were quite similar for the no swirl case. As the swirl increased, the backpressure coefficient increased for the oblong ejectors and decreased for the round ejector. Much lower backpressure was observed in Ejector-7 due to its larger nozzle exit.

## 6 Conclusions

An experimental study of oblong air-air ejectors with four-ring oblong entraining diffusers has been carried out. The work has included the investigation of geometric and flow variables on the ejector performance. The following conclusions can be made based on the work done.

1. The swirl number was greatly reduced by the converging oblong nozzle. At the same inlet swirl condition, the swirling degree inside the oblong ejector was much lower than that of the round ejector.
2. Unlike the round ejector, where pumping performance was degraded by 30 deg swirl [10], the pumping of the oblong ejector was improved by the increasing swirl angle up to 30 deg.
3. The swirl did not have a noticeable influence on the velocity and temperature uniformities at the oblong diffuser exit, as it did on the round ejector.
4. At low inlet swirl conditions (swirl angle was no more than 20 deg), the oblong ejector had better mixing performance than the round ejector.
5. At each swirl condition, most of entrained mass flow rate was contributed by tertiary entraining in the entraining diffuser for the specific design tested here. The ratio of $\Phi_{2nd}/\Phi_{3rd}$ was nearly constant for all swirls.
6. As expected, the ejector (Ejector 7) with lower primary flow momentum and smaller area ratio of $A_{mt}/A_{ne}$ presented a lower pumping ability. However, the diffuser pressure recovery of the two oblong ejectors was similar. The backpressure of Ejector 7 was much smaller than that of Ejector 4 because of the larger nozzle area.

CFD analysis has been done and will be published at a later date.

## Acknowledgment

This research was funded by NSERC, DND, and W. R. Davis Engineering Ltd. under the Collaborative Research Partnerships Program administered by NSERC.

The authors would like to acknowledge the colleagues and staff in the Department of Mechanical and Materials Engineering at Queen's University, Kingston, Ontario, Canada.

## Nomenclature

$A$ = area
AR = area ratio
$C_{pD}$ = wall pressure recovery coefficient of diffuser used in this paper $(\overline{P_{sw5}}-\overline{P_{sw4}})/(0.5\rho\overline{w_{ne}}^2)$
$C_b$ = backpressure coefficient $P_{s\_ni}/q_{ni}$
$D$ = diameter
$D_{hy}$ = hydraulic diameter
$f_{ke}$ = kinetic energy flux profile factor $\int(0.5V^2)dm/(0.5m\bar{V}^2)$
$f_t$ = uniform factor of temperature profile $(T_p - T_{max})/(T_p - T_{av})$
gr = gap ratio $h_g/D_m$
$G_\theta$ = axial flux of angular momentum $G_\theta = \int \rho u_\theta w r dA$
$G_z$ = axial flux of axial momentum $G_z = \int \rho w^2 dA$
$h_g$ = the vertical gap space between adjacent plates of ringed diffuser
$L_o$ = overlap between adjacent plates
$m$ = mass flow rate, such as $m_p$, $m_t$, $m_{2nd}$, and $m_{3rd}$
Ma = Mach number
$P_b$ = backpressure
$P_s$ = static pressure
$P_{sw}$ = wall static pressure
$q$ = dynamic pressure $0.5\rho\bar{V}^2$
$R$ = radius
Re = Reynolds number
$s$ = standoff, distance between nozzle exit and mixing tube entrance
$S$ = swirl number $G_\theta/(G_z D_{hy}/2)$
$T_h$ = hot air temperature at nozzle inlet
$T_c$ = entrained cold flow temperature
$u_\theta$ = tangential velocity
$w$ = axial velocity
$V$ = velocity magnitude
$\bar{V}$ = average velocity magnitude

### Greek Symbols

$\alpha$ = diffuser half angle
$\varphi$ = swirl angle
$\Phi$ = pumping ratio $m/m_p$, such as $\Phi_t$, $\Phi_{2nd}$, and $\Phi_{3rd}$

### Subscripts

- 2nd = secondary
- 3rd = tertiary
- am = ambient
- $d$ = diffuser
- de = diffuser exit
- mt = mixing tube
- $n$ = nozzle
- ne = nozzle exit
- ni = nozzle inlet
- $p$ = primary
- $t$ = total

### Acronyms

- OED = oblong straight entraining diffuser
- OMT = oblong mixing tube
- ON = oblong nozzle
- RED = round straight entraining diffuser
- RMT = round mixing tube
- RN = round nozzle

## References


[1] Thompson, J., Birk, A. M., 1999, "Design of an Infrared Signature Suppressor for the Bell 2005 (UH-1H) Helicopter, Part-1: Aerothermal Design," *Proceedings of the 7th CASI Aerodynamics Symposium*.

[2] Blevins, R. D., 1984, *Applied Fluid Dynamics Handbook*, Van Nostrand Reinhold Company, New York.

[3] White, F. M., 2003, *Fluid Mechanics*, 5th ed., McGraw-Hill, New York.

[4] Reneau, L. R., Johnston, J. P., and Kline, S. J., 1967, "Performance and Design of Straight, Two-Dimensional Diffusers," ASME J. Basic Eng., **89**(1), pp. 141–150.

[5] Schlichting, H., 1968, *Boundary-Layer Theory*, 6th ed., McGraw-Hill, New York.

[6] Shimizu, Y., Nagafusa, M., and Kuzuhara, S., 1982, "Effects of Approaching Flow Types on the Performances of Straight Conical Diffusers," Bull. JSME, **25**(208), pp. 1506–1512.

[7] McDonald, A. T., Fox, R. W., and Dewoestine, R. V., 1971, "Effects of Swirling Inter Flow on Pressure Recovery in Conical Diffuser," AIAA J., **9**(10), pp. 2014–2018.

[8] Senoo, Y., Kawaguchi, N., and Nagata, T., 1978, "Swirl Flow in Conical Diffusers," Bull. JSME, **21**(151) pp. 112–119.

[9] McDonald, A. T., Fox, R. W., 1966, "Experimental Investigation of Incompressible Flow in Conical Diffusers," Int. J. Mech. Sci., **8**(2), pp. 125–139.

[10] Chen, Q., and Birk, A. M., 2007, "Experimental and CFD Study of an Exhaust Ejector With Round Entraining Diffuser," *Proceedings of the ASME Turbo Expo 2007*, Vol. 6, Part A, pp. 27–35.

[11] Taylor, J. L., 1986, "Computer-Based Data Acquisition System: Design Techniques," *Instrument Society of America*.

[12] Moffat, R. J., 1988, "Describing the Uncertainties in Experimental Results," Exp. Therm. Fluid Sci., **1**(1), pp. 3–17.

[13] Kline, S. J., and McClintock, F. A., 1953, "Describing Uncertainties in Single Sample Experiments," Mech. Eng. (Am. Soc. Mech. Eng.), **75**(1), pp. 3–8.

[14] Chen, Q., 2008, "Performance of Air-Air Ejectors With Multi-ring Entraining Diffusers," Ph.D. thesis, Department of Mechanical and Materials Engineering, Queen's University at Kingston, Canada.

[15] Gupta, A. K., Lilley, D. G., and Syred, N., 1984, *Swirl Flows*, Abacus, Tunbridge Wells, Kent, England.

[16] Tam, C. K. W., and Ganesan, A., 2004, "Modified k-Epsilon Turbulence Model for Calculating Hot Jet Mean Flows and Noise," AIAA J., **42**(1), pp. 26–34.

[17] Abdol-Hamid, K. S., Pao, S. P., Massey, S. J., and Elmiligui, A., 2004, "Temperature Corrected Turbulence Model for High Temperature Jet Flow," ASME Trans. J. Fluids Eng., **126**(5), pp. 844–850.

**Rainer Kurz**
Solar Turbines Incorporated,
9330 Skypark Court,
San Diego, CA 92123
e-mail: kurz_rainer_x@solarturbines.com

**Klaus Brun**
Southwest Research Institute,
San Antonio, TX 78238
e-mail: klaus.brun@swri.org

**Meron Wollie**
Rotating Equipment Engineer
EPT-Mechanical Engineering,
BP Exploration and Production,
501 Westlake Park Boulevard,
Houston, TX 77079
e-mail: meron.wollie@bp.com

# Degradation Effects on Industrial Gas Turbines

*This paper provides a discussion on how degradation develops and affects the performance of the gas turbine. Because the function of a gas turbine is the result of the fine-tuned cooperation of many different components, the emphasis of this paper is on the gas turbine and its components as a system. Therefore, the interaction of components is studied in detail. An engine model is subjected to various types of degradation, and the effect on operating parameters is studied. The focus is on three areas: How does component degradation impact the operating points of the engine compressor, how does component degradation impact full load and part load gas turbine performance characteristics, and how does component degradation impact measurable engine operating parameters. Experimental data are provided that supports the theoretical conclusion. Parameters that indicate levels of degradation are outlined, thus providing guidance for condition monitoring practice.* [DOI: 10.1115/1.3097135]

## 1 Introduction

Gas turbines are widely used in industrial applications. They usually are either single shaft or two shaft designs. In this paper, we will both consider single shaft designs (i.e., compressor and turbine sections operate on a single shaft at the same speed) and two shaft designs (one shaft for the gas generator (GG), another shaft for the power turbine that powers the driven load and can operate at speeds independent of the gas generator). The key difference is that in two shaft engines, but also in some single shaft engines, the gas generator speed varies with the gas turbine load, while in single shaft engines for generator drives, the speed stays constant even with varying loads.

Any prime mover exhibits the effects of wear and tear over time. Because the function of a gas turbine is the result of the fine-tuned cooperation of many different components, the emphasis of this paper is on the entire gas turbine as a system rather than on isolated components. Treating the gas turbine as a system reveals the effects of degradation on the match of the components.

Several mechanisms cause the degradation of gas turbines. *Fouling* is caused by the adherence of particles to airfoils and annulus surfaces. *Hot corrosion* is the loss or deterioration of material from components exposed to hot combustion gases, caused by chemical reactions between the component and certain contaminants. *Corrosion* is caused both by inlet air contaminants and by fuel and combustion derived contaminants. *Erosion* is the abrasive removal of material from the flow path by hard or incompressible particles impinging on flow surfaces. *Abrasion* is caused when a rotating surface rubs on a stationary surface. Damage may also be caused by *foreign objects* striking the flow path components. While some of these effects can be reversed by cleaning or washing the engine, others require the adjustment, repair, or replacement of components.

The dominant degradation mechanisms for aircraft engines and industrial engines are different. Aircraft engines are operated without the benefit of an inlet air filtration system, and therefore, erosion, especially of the compressor, is one of the key contributors. Industrial engines, assuming an appropriate air filtration system is installed, are probably more subject to fouling caused by smaller particles, corrosion, and possibly lube oil. The exception may be engines subject to water injection in the compressor inlet [1], where an incorrectly sized system can generate water droplets of a size sufficient to cause blade erosion.

Manuscript received October 29, 2008; final manuscript received November 6, 2008; published online July 15, 2009. Review conducted by Dillip R. Ballal. Paper presented at the ASME Turbo Expo: Land, Sea and Air (GT2008), Berlin, Germany, June 9–13, 2008.

## 2 Degradation of Components

Three major effects determine the performance deterioration of the gas turbine compressor: increased tip clearances, changes in airfoil geometry, and changes in airfoil surface quality. While the first two effects typically lead to nonrecoverable degradation, the latter effect can be at least partially reversed by washing the compressor [2]. Stage degradation also has a cumulative effect; a degraded stage will create different exit conditions than a new stage, and each subsequent stage will operate further away from its design point. While in the new machine all stages were working at their optimum efficiency point at design surge margins, the degradation will force all stages after the first one to work at off-optimum surge margins and lower than design efficiency. This will not only lower the overall efficiency and the pressure ratio that can be achieved but also the operating range. Furthermore, increased tip clearances will effectively reduce the flow capacity of the compressor. Careful readjusting variable geometry, where available, could be used to counteract some of the mismatching effects of degradation.

Typically, a degraded compressor also will have a reduced surge or stall margin [3,1]. Graf et al. [4] showed data for an axial compressor, where increased clearances caused reduced surge margin and reduced efficiency. In this case, the clearance was increased from 2.9% (design value) to 4.3%. This lead to an increase in surge flow coefficient of about 20%, a reduction in design pressure coefficient of 12%, and a loss of design point efficiency of 2.5 points. Notably, the loss in pressure coefficient became negligibly closer to choke flow. Similar results are reported by Smith and Cumpsty [5] where an increase in the clearance from 1% to 3.5% reduced the pressure coefficient by 9%. Frith [6] tested a helicopter gas turbine with compressor blades cropped to simulate increased clearances. A 3% crop on the axial compressor stages reduced airflow by 4.6% and pressure ratio by 3%. The compressor discharge temperature is reported to remain unchanged, which indicates a reduction in compressor efficiency by about 2.5%.

The compressor pressure ratio and the compressor flow are not independent, and the compressor efficiency is determined by the resulting compressor operating point. Increases in tip clearance as

well as deteriorated airfoils will shift the pressure ratio-flow relationship for a given operating speed to lower flow rates, as well as to lower efficiencies.

The combustion system is not likely to be the direct cause for performance deterioration. The combustion efficiency will usually not decrease, except for severe cases of combustor distress. However, deterioration could potentially lead to a variation in the combustor exit temperature profile. The problems with a distorted exit temperature distribution are threefold. Local temperature peaks can damage the turbine section. The altered temperature profile will increase secondary flow activity, thus reducing the turbine efficiency. Because the control temperature is measured at discrete circumferential points, the average of these measured temperatures is not the same as the true thermodynamic average temperature in this plane. Therefore, in the factory test, the correlation between the measured average and the true thermodynamic average is established. If the temperature field is altered due to one of the reasons above, this correlation is no longer correct. The engine could therefore be overfired, thus producing more power, but shortening its life, or underfired, thus additionally losing power. Since many engines bleed air from the compressor discharge directly into the exhaust, either for surge avoidance during startup or for emission control purposes, it should be mentioned that leaks in the bleed valves have a significant impact on the engine performance. Leaking valves can be relatively easily detected, and since they are usually external to the engine, easily repaired.

Just as the compressor section, the turbine section experiences the following issues that result in degradation: increased tip clearances, changes in airfoil geometry, and changes in airfoil surface quality. Maintenance of tip clearances is, in particular, a problem in the turbine section, due to the extreme changes in temperature between a cold engine and an engine accelerating to full load. In many designs, the stationary components expand at a different rate than rotating components. Many new turbine designs use abradable seals to minimize these clearances. However, the most severe case, which is usually after a hot restart, will determine the minimum clearance for the engine. In addition to a reduced efficiency, added clearances will also increase the axial flow blockage, and thus will cause reduced flow and increased velocities in the main flow. Radtke and Dibelius [7] reported a reduction in efficiency of a multistage turbine by 0.6% when they increased the radial clearances from 0.5% of the blade height at the rotors and 0.4% of the blade height at the stators to 0.8% of the blade height at rotors and stators.

Corrosion tends to alter the flow path in two ways. It increases the surface roughness, but it may also remove material, in particular, at the leading edges and the trailing edge of the airfoils. Especially the turbine nozzles, operating at or near choked conditions, are very sensitive to changes in the flow area. Furthermore, changes in the flow capacity of the turbine section will subsequently alter the operating points for the engine compressor. Increased surface roughness causes thicker boundary layers on the blades and sidewalls, and thus may reduce the flow capacity, especially near choking conditions. Boyle [8] found for a two stage turbine efficiency losses of 2.5% for a 10.2 $\mu$m surface roughness when compared with smooth blades. He also found that the most pronounced differences appear at the optimum operating point at the turbine, whereas the far off-optimum efficiency was almost the same for rough and smooth blades. It should be noted, that the losses due to clearances were in the same order of magnitude as the profile losses.

However, if the degradation of the turbine section leads to material removal, especially in the nozzle area, we will see the opposite effect: The flow capacity increases for any given pressure ratio. Because the flow capacity of any nozzle is limited by the effective throat area, erosion of the trailing edge causes the throat area to increase and the exit flow angle to become more axial. This means a reduction of turning in the stator and the rotor, which will lead to reduced work extraction for this stage and to an increased flow capacity. Since the turbine nozzles constitute a flow restriction, any change in the flow capacity of the turbine section will also impact the operating points of the engine compressor.

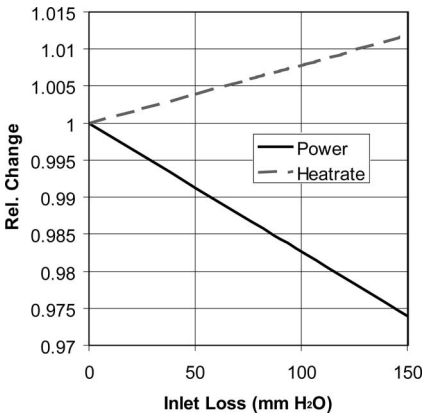


**Fig. 1 Impact of inlet pressure loss on engine power and heat rate**

## 3 Air Filtration System

Fouling of inlet filters occurs progressively over time. This leads to increased pressure drop in the inlet system, and as a result, reduced engine power and efficiency. Figure 1 shows the relative impact of the pressure loss in the inlet system on power and efficiency. Self cleaning filters, where appropriate, or changing of filter pads or cartridges can reverse this pressure loss. It must be noted that air filtration systems are always a compromise between filtration effectiveness, pressure loss, and size or cost of the system. Also, the filtration system has to be appropriate for the type of contamination that is expected. Some types of filters are very effective for small particle sizes, some are specifically designed for high dust loads, and others are effective in keeping droplets (with potentially dissolved contaminants) out of the engine.

## 4 Effect of Degradation on the Gas Turbine

Degradation of engine components has a compounded effect on engine performance, because the change in component performance characteristics leads to a mismatch of these components on the engine level, as well as on the component level. The impact of individual component degradation is also influenced by the control system and the control modes of the engine. Single shaft engines operating at constant speed will show a different degradation behavior than two shaft engines. The impact of degradation on two shaft engines depends on the control mode they are in, e.g., whether the gas generator speed or the firing temperature is the limiting factor. Additionally, the method and location of measuring the control temperature will determine the behavior of the engine in a degraded state. Emission controls may attempt to keep the firing temperature within preset limits.

In the following comparisons, we separate effects that normally occur together. For example, compressor degradation will impact pressure ratio, efficiency, and flow capacity, albeit to various degrees depending on the type of degradation. The engine cycle deck used allows the isolated introduction of degraded components. We can thus study the individual impact of reduced compressor efficiency (predominantly due to fouling), reduced compressor flow capacity (opening of clearances and fouling), altered gas producer turbine flow capacity (corrosion, erosion, fouling), and reduced gas producer turbine efficiency (fouling, erosion) as isolated events. It should be noted that, if we state a change in efficiency, we assume that the component loses that amount of efficiency over its entire operating map. Since in many instances,

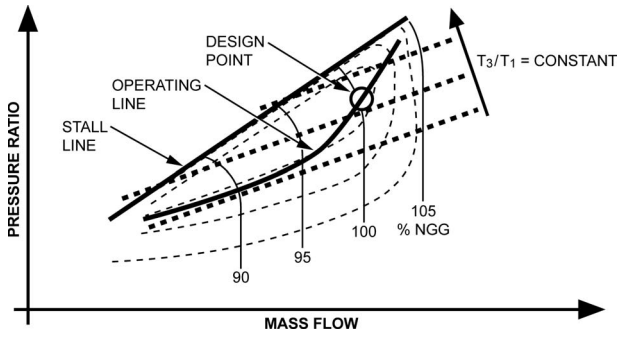


**Fig. 2 Schematic compressor map for a two shaft gas turbine [9]**

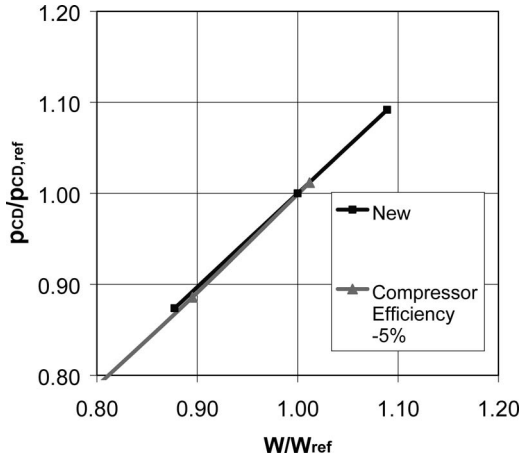


**Fig. 3 Compressor discharge pressure as a function of compressor flow for a new compressor and a compressor with 5% reduced efficiency**

the operating point on the map is different (but not very different) between the new and the degraded engines, the actual efficiency in the cycle calculation is the result of degradation and the move of the operating point. The compressor blockage (i.e., reduced flow capacity) used in this paper is not to be confused with the observed reduction in flow through a degraded engine. The observed reduction in flow is rather a result of a higher power consumption of the compressor (generally related to a deteriorated compressor) or a reduced flow capacity of the turbine section. Frith [6] cropped the blades of the compressor of a two shaft turboprop engine, thus simulating the effect of tip rubs. This crop reduced both airflow and compressor efficiency, but also compressor pressure ratio. This indicates that the increased power consumption of the compressor leads to a reduced pressure ratio. In turn, since the flow capacity of the turbine was not changed, this causes a reduction in air flow.

To make the results of some of the following simulations clearer, Fig. 2 shows the typical map of a gas turbine air compressor. The actual operating point of the compressor is determined by the relationship between flow and compressor discharge pressures, as well as the available and consumed powers to drive that compressor.

## 5 Reduced Compressor Efficiency

Compressor degradation in the overall engine environment will yield different results for single and two shaft engines. Due to the fixed speed of the single shaft machine in combination with a usually choked turbine nozzle, loss of compressor efficiency will mostly affect compressor pressure ratio, but only to a very limited degree the flow through the machine. A two shaft engine with a compressor with reduced efficiency will exhibit significant changes in flow and pressure ratio (Fig. 3). The reduction in flow was observed in several studies [10,11]. Figure 3 reflects the same findings as in Ref. [2]; The pressure ratio-flow relationship of the gas turbine compressor operating points remains unchanged because it is determined by the turbine section, but the engine will have to run faster, and the compressor will consume more power for any point on the pressure-flow line once it deteriorates.

The impact of reduced compressor efficiency on full load power and heat rate (HR) of a two shaft engine depends on the ambient temperature and seems to be more severe at warm ambient temperatures (Figs. 4 and 5). For a temperature topped two shaft engine, the gas producer speed is reduced for the degraded engine (because for a given pressure and flow, the compressor now consumes more power). For single shaft engines, where the compressor speed is kept constant, the impact on power and heat rate is almost the same for all ambient conditions. Also, the reduction in performance is less pronounced than for a two shaft engine. Some of the impact of degradation can be reduced for two shaft engines by re-adjusting the controls to allow the engine to reach full firing temperature.

Both Tarabrin et al. [12] and Meher-Homji and Bromley [13] found that twin spool and three spool engines seem to be particularly susceptible to performance deterioration. For all types, the relative degradation in power is far more pronounced than the degradation in heat rate for a two shaft engine.

For an engine with standard combustion, at constant load, a reduction in compressor efficiency will cause the gas generator speed, and with it the compressor discharge pressure and the airflow, to drop. At the same time, the firing temperature increases (to maintain the required power output) as well as the heat rate (Fig. 6).

Syverrud and co-workers [10,14,15] performed tests on a J-85 gas turbine, where they deteriorated the compressor performance by spraying salt water in the engine inlet. The deposits caused increased surface roughness on the compressor airfoils. They found that the majority of deposits occur on the first stage and become insignificant after about the fourth compressor stage. The deterioration shifted the compressor operating line to both a lower flow rate and a lower pressure ratio, which confirms the simulation results in Fig. 3. The data show further that the degradation not only leads to reduced stage performance, but also to additional losses because individual stages no longer operate at their design flow coefficients. The operating points of the deteriorated engine were consistently at lower flow coefficients than for the clean

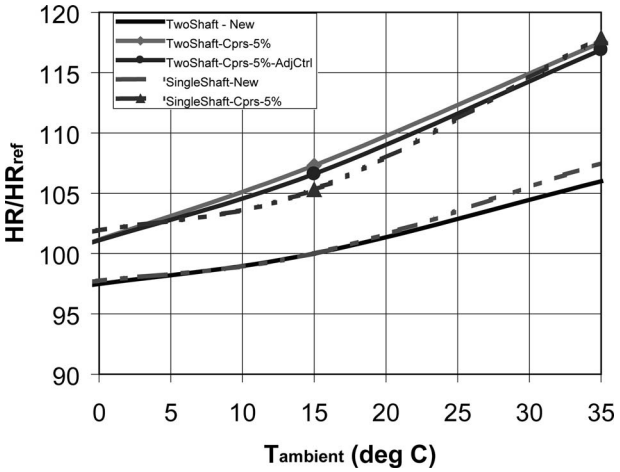


**Fig. 4 Impact of reduced compressor efficiency (reduction of 5%) on the full load heat rate of a single shaft and a two shaft gas turbine for a range of ambient temperatures**

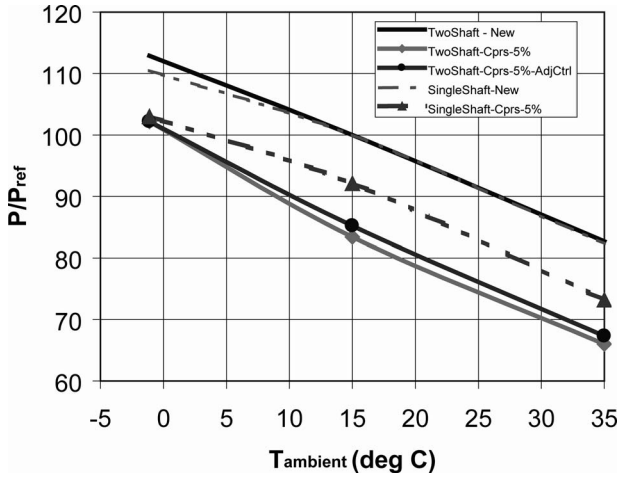


**Fig. 5 Impact of reduced compressor efficiency (reduction of 5%) on the full load power of a single shaft and a two shaft gas turbine for a range of ambient temperatures**

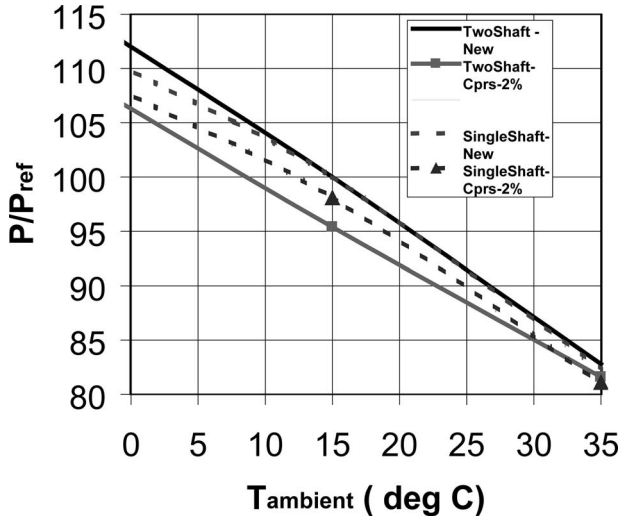


**Fig. 7 Impact of reduced compressor flow capacity (reduction by 2%) on full load power for a single shaft and a two shaft gas turbine at varying ambient temperatures**

engine. This also leads to additional efficiency reductions due to the movement of the stage operating points away from the stage design point.

Syverrud et al. [10] were able to show the direct impact of the blade surface roughness on added profile losses and the increase in sidewall boundary layers due to the deposits on the deteriorated compressor performance. Their data also show that the compressor condition cannot be separated form the turbine section of the engine, since the turbine flow capacity determines the operating point of the compressor.

## 6 Reduced Compressor Flow Capacity

Next, we consider the impact of reduced compressor flow capacity, which can be the result of fouling or increased clearances. Spakovszky et al. [3] and MacLeod et al. [16] related increased rotor clearances to an increase in flow blockage, thus reduced compressor flow capacity. Khalid et al. [17] investigated the effect of component deterioration on overall engine performance on a single shaft turboprop engine (thus operating at a constant speed). Besides the expected loss in engine efficiency, they found a significant reduction in compressor flow capacity with increased compressor clearances, but no significant change in compressor efficiency.

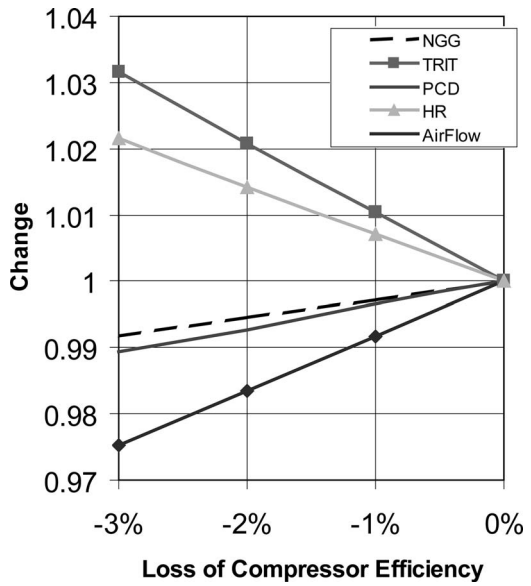


**Fig. 6 Impact of reduced compressor efficiency (at constant gas turbine power) on gas generator speed ($N_{GG}$), firing temperature (turbine rotor inlet temperature (TRIT)), compressor discharge pressure ($p_{cd}$), heat rate, and airflow for a two shaft engine**

We find that the same level of compressor flow blockage leads to more power degradation in a two shaft engine than in a single shaft engine. It is interesting that both for single shaft and for two shaft engines there is a very small increase in heat rate due to the compressor blockage at higher ambient temperatures. Only for temperatures below 10 °C, the heat rate starts to increase slightly at about the same rate for single shaft and two shaft machines.

Also, the loss in available power is more pronounced at low ambient temperatures (Fig. 7). This is probably due to higher Mach numbers at low ambient temperatures, which make the compressor more sensitive to changes in flow capacity. Compressor deterioration by itself will usually cause higher power losses than losses in heat rate, because a higher compressor exit temperature (due to lower efficiency) at a fixed firing temperature will reduce the possible fuel flow. An operating point at part load (i.e., below maximum firing temperature and below maximum gas generator speed) can still be maintained with a degraded engine, albeit at a lower firing temperature and a higher gas generator speed than for the new condition. The relative loss in efficiency is significantly lower than for an engine at full load for the same amount of degradation. Airflow and compressor discharge pressure change very little.

## 7 Changes in Gas Generator Turbine Flow Capacity

Degradation effects on the flow capacity of the gas generator turbine can either increase or reduce the flow capacity: The reduction in the available flow path is either due to added surface roughness or eroded leading edges, both leading to thicker boundary layers and thus a reduced effective throat area [18]. The throat area increases when the nozzle trailing edges erode, thus increasing the flow capacity of the turbine.

Both for single and two shaft engines, changes in gas generator flow capacity lead to a pronounced change in the operating points of the compressor (Fig. 8). Increased gas generator flow capacity moves the engine compressor operating points further into the choke region and thus leads to lower compressor efficiency, whereas a reduced flow area has the opposite effect. The impact on full load power is shown in Fig. 9. It seems that the opening of

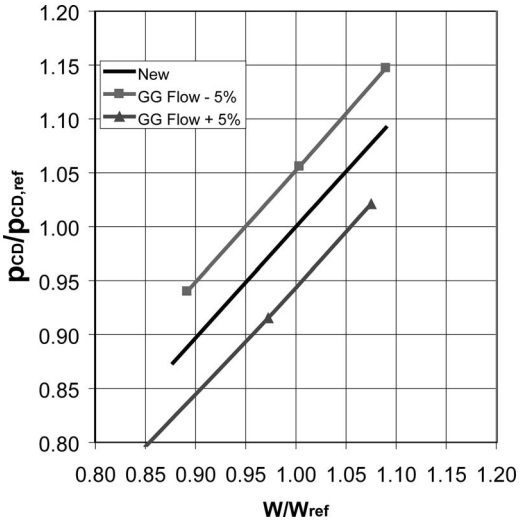


**Fig. 8 Impact of changed gas generator flow capacity (increased by 5% and decreased by 5%, respectively) on the operating lines of the compressor in a two shaft gas turbine**

the throat area in a gas turbine has a larger detrimental effect than a reduction in flow area. This is at least partially due to the fact that increased flow area moves the engine compressor operating points further into the choke region and thus leads to lower compressor efficiency. For a single shaft engine operating at a constant gas generator speed, an increase in gas generator flow capacity will lead to a drop in compressor discharge pressure (that is, the compressor gains in surge margin), while the engine flow stays the same. This is accompanied by a loss in power and efficiency. A reduction in flow area has a higher impact at low ambient temperatures. In a two shaft engine, the reduced flow capacity will cause the gas generator speed to increase, which may actually be beneficial at higher ambient temperatures. Depending on the operating point of the engine relative to its design point, the lower flow area can actually reduce the heat rate at higher ambient temperatures. At lower ambient temperatures, the gas generator speed may already be at its maximum, thus causing higher losses in power and efficiency.

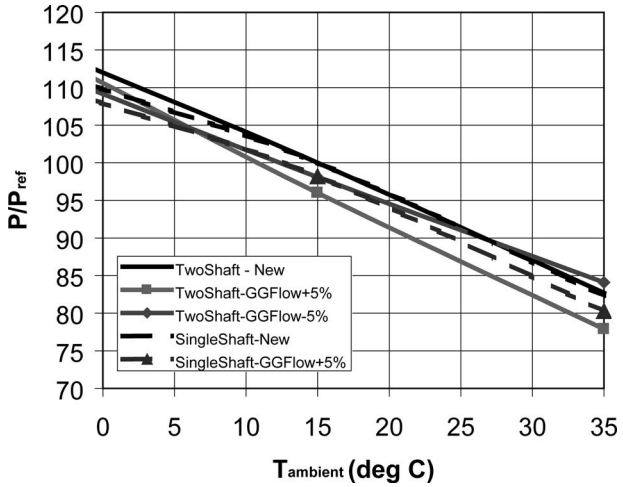


**Fig. 9 Impact of reduced and increased gas generator flow capacities (by 5%, respectively) on full load power at varying ambient temperatures**

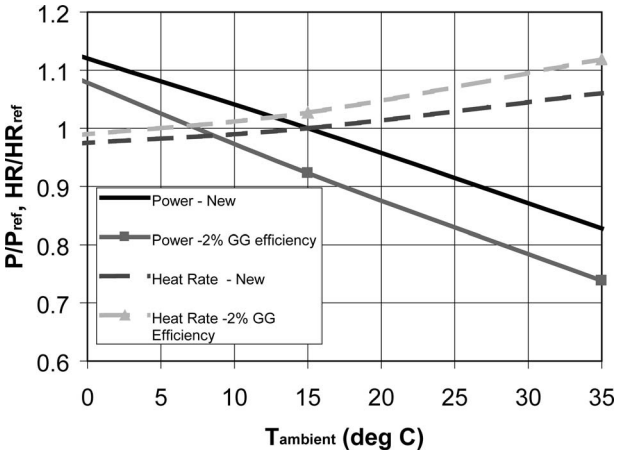


**Fig. 10 Impact of reduced gas generator turbine efficiency (by 2%) on full load power and heat rate for a two shaft gas turbine**

## 8 Reduced Gas Generator Turbine Efficiency

Now we will review the case of an engine with reduced gas generator turbine efficiency due to fouling, or simply due to the fact that a change in nozzle geometry has altered the operating point of the turbine section. Rather severe degradation of the gas producer turbine nozzle occurs when material is removed due to erosion or corrosion. In this case, the turbine efficiency will drop [18], while its flow capacity increases (see above). Both full load power and heat rate deteriorate (Fig. 10), but again, the loss in power is more pronounced than the increase in heat rate. We also find a stronger deterioration at high ambient temperatures.

At a constant load, the increasing drop in gas generator efficiency causes a reduction in air flow, gas generator speed, and compressor discharge pressure. At the same time, heat rate and firing temperature increase (Fig. 11). The decrease in airflow and compressor discharge pressure is at different rates, thus the operating line of the compressor is impacted by this type of degradation mechanism, moving it closer to the surge limit.

A change in gas generator turbine efficiency or flow capacity has a pronounced effect on the engine output and a smaller effect on engine efficiency. It can be shown that a reduction in gas generator turbine efficiency or an increase in flow capacity will lead to the underfiring of a two shaft engine where the firing temperature is indirectly controlled via the power turbine inlet tempera-

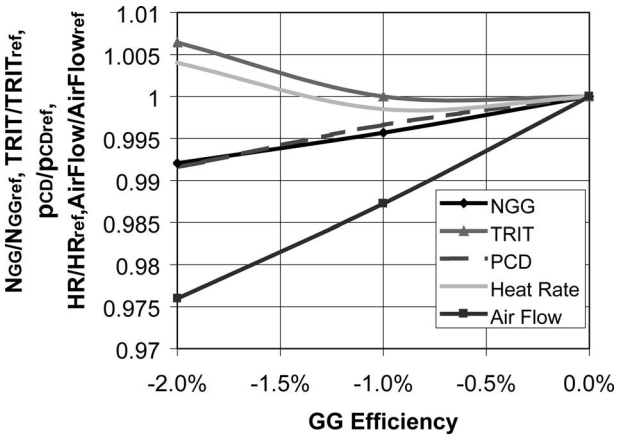


**Fig. 11 Impact of reduced gas generator turbine efficiency gas generator speed, firing temperature, compressor discharge pressure, heat rate, and air flow for a two shaft gas turbine at constant load**

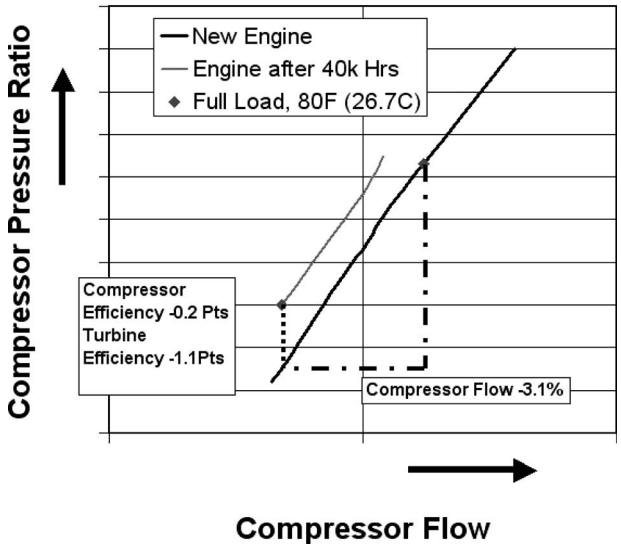


**Fig. 12 Compressor operating line for a gas turbine after 40,000 actual operating hours**

ture. This is one of the positive side effects of this control mode: the engine is not driven into a more damaging over firing situation.

Degradation also affects the optimum power turbine speed, albeit not very much. If a lower engine compressor ratio or deterioration at the gas generator turbine itself leads to a lower gas generator turbine pressure ratio, then the actual flow through the power turbine will increase slightly, thus increasing the optimum speed. However, the effect on the engine output at fixed power turbine speed is rather small (less than 0.1%) for modern power turbines with a relatively wide operating range.

## 9 Combined Effects

The simulations above assume a reduction in compressor efficiency as a cause of engine degradation. However, many industrial engines returning for overhaul after 30–40,000 actual hours of operation show major degradation issues, reduced compressor air flow, and reduced turbine efficiency, but only little deterioration in compressor efficiency. This is particularly true for engines that have been subject to regular condition based water or detergent washing combined with good air filtration and clean fuel. These types of changes lead to a change in the operating line of the engine compressor, as well as a reduction in firing temperature when the engine is controlled by exhaust temperature or power turbine inlet temperature. The actual test data used to create Fig. 12 allow tracing of the individual effects that were reflected in the simulation results: reduction of compressor flow and a reduction in compressor and turbine efficiencies.

Kurz and Brun [19] reported about an industrial gas turbine that was operated for 3500 h without a detergent wash. The environment was laden with jet engine exhaust and salt laden air. Borescope inspections had shown deposits on the compressor and turbine. A detergent wash was recommended. Control system data were recorded at full load before and after detergent washing. The data were taken with the ambient temperature below the design match temperature.

The improvement in compressor pressure ratio, compressor efficiency, power, and heat rate are as expected, because the washing was reported to be very black and dirty. The engine was also underfired, because one of the effects of degradation is the reduction in the $TRIT/T_5$ ratio. These improvements explain the very substantial 9.7% increase in output power. After washing and given the test uncertainties, this engine appears to be performing essentially the same as new. The model exactly predicts this behavior. If we use a 2.1% loss in compressor efficiency, a 5% reduction in airflow and pressure ratio, and a 0.5% reduction in gas generator turbine efficiency, we see a reduction in power of 8.6%, the efficiency drops by 3.5%, while the engine speed stays almost the same, and $T_3$ drops due to a reduction in $TRIT/T_5$ ratio.

**Table 1 Relative impact of component degradation on a two shaft engine at two different ambient temperatures. Normalized to power degradation (at 15°C) due to compressor efficiency. Example: Heat rate degradation at 15°C due to 1% compressor flow degradation is 8% of the power degradation percentage due to 1% compressor efficiency reduction at 15°C.**

| | Power 15 °C | Power 35 °C | Heat rate 15 °C | Heat rate 35 °C |
|---|---|---|---|---|
| Compressor efficiency | 1.00 | 1.71 | 0.49 | 0.66 |
| Compressor flow | 0.77 | 0.25 | 0.08 | −0.007 |
| GG turbine efficiency | 1.30 | 2.04 | 0.46 | 0.88 |
| GG turbine flow increase | 0.27 | 0.42 | 0.08 | 0.02 |
| GG turbine flow reduction | 0.13 | −0.01 | −0.02 | −0.01 |

Interestingly, while Tarabrin et al. [12] indicated that smaller engines may be more susceptible to degradation, the study of Aker and Saravanamuttoo [20] reaches exactly the opposite conclusion. We suspect that the intricate interactions that define the amount of degradation as a function of a certain level of ingested material, or of a certain amount of material removal, are very engine specific and do not lend themselves to simplified rules of thumb. Comparison of emission controlled gas turbines (i.e., lean premix combustion engines) with standard combustion gas turbines reveals different part load behaviors in degraded engines. The behavior of emission controlled engines is usually less linear, as the control algorithm tries to control the temperature conditions in the combustor.

## 10 Insights

While the data indicate that the engine airflow tends to react more distinctly to some degraded components than, for example, compressor discharge pressure (e.g., Figs. 6 and 11), we still believe that monitoring compressor discharge pressure (against a reference) is the correct way to monitor degradation. This is for the practical reason that engine air flow is usually not as easily monitored at site as compressor discharge pressure. Haq and Saravanamuttoo [21] came to a similar conclusion based on their tests on a two shaft industrial gas turbine at high ambient temperature conditions.

Table 1 shows a summary of the relative severity of component degradation for a two shaft industrial engine. It reveals some important facts.

- The amount of power or efficiency lost for a given amount of component degradation differs for different ambient conditions. It is therefore not possible to establish a universal engine degradation that is valid for any condition.
- The impact of any component degradation is more severe on the full load power output than on the full load efficiency or heat rate of the engine.
- Except for a reduction in compressor flow capacity or a reduction in gas generator turbine flow, all other component degradations have a larger impact on engine performance at higher ambient temperatures than at lower temperatures.
- Gas generator turbine efficiency and compressor efficiency have by far the largest impact on degradation.

Degrading a component in an engine will always lead to observable changes in engine parameters due to the impact of altered operating points, not only at the degraded component, but also for all other engine components. In a reverse sense, this finding can

also be used for diagnostic purposes, because different types of degradation on different components will alter the engine in a different way [22]. For example, compressor efficiency deterioration will not change the compressor operating line, but a loss in turbine efficiency will. Conversely, at a given load in a two shaft engine, the reduction in compressor flow capacity will not change the engine airflow, while a reduction in turbine efficiency will lead to a significant change besides a much more distinct change in compressor discharge pressure.

## 11 Protection Against Degradation

While engine degradation cannot entirely be avoided, certain precautions can clearly slow the effects down. These precautions include the careful selection and maintenance of the air filtration equipment and the careful treatment of fuel, steam, or water that are injected into the combustion process. It also includes the observance of manufacturer's recommendations regarding shutdown and restarting procedures. The site location and environment conditions, which dictate airborne contaminants, their size, concentration, and composition, need to be considered in the selection of air filtration. Atmospheric conditions, such as humidity, smog, precipitation, mist, fog, dust, oil fumes, and industrial exhausts, will affect the entire engine. Fuel quality will impact the hot section.

Given all these variables, the rate of degradation is impossible to predict with reasonable accuracy. While the rate of deterioration is slowed by frequent online washing, thorough on-crank washing can yield a more significant recovery [23]. Online washing will usually only clean the first few stages of the compressor, because the increase in air temperature during compression will evaporate the washing fluid. The online washing process therefore can transport contaminants from the front stages of the compressor to the rear stages or the turbine section. No matter how good the washing, the rear stages of the compressor will not get cleaned. If the compressor blades can be accessed with moderate effort, for example, when the compressor casing is horizontally split, hand cleaning of the blades can be very effective.

## 12 Conclusions

The paper covered in detail degradation mechanisms and the impact of component degradation on the overall gas turbine performance. We have attempted to make clear the impact of component interaction, as it plays a crucial role in the understanding of degradation effects. This is key in understanding and using other studies on this subject, which typically only address individual components. It must be understood that the apparent change in efficiency of a component is *both* due to its deterioration and a change in its operating point as a result of component interactions. In particular, the change in the compressor operating point as a result of the degradation of the compressor and turbine section, both in terms of flow and efficiency, has been highlighted.

This study also shows that the impact of a given component degradation on measurable engine performance, such as engine power or engine heat rate, varies for different operating conditions. It further indicates the resulting changes in engine parameters that are often used in the condition monitoring of the engine, such as compressor discharge pressure, gas generator speed, air flow, and firing temperature.

Proper design and selection of inlet systems and fuel treatment systems, together with proper maintenance and operating practices, can significantly affect the level of performance degradation and thus time between repairs or overhauls of a gas turbine. The authors have avoided presenting figures about the rate of degradation, because it is subject to a variety of operational and design factors that typically cannot be controlled entirely. Maintenance and overhaul decisions are ultimately based on economic and safety considerations. Understanding performance degradation, as well as factors that influence degradation, can help in these decisions.

## Nomenclature

Cprs = compressor
$N$ = speed
$p_{CD}$ = compressor discharge pressure
$P$ = power
$T$ = temperature
$T_5$ = power turbine inlet temperature
$T_{ambient}$ = engine inlet temperature
$W$ = mass flow

### Subscripts

ref = reference

## References


[1] Brun, K., Kurz, R., Simmons, H., 2005, "Aerodynamic Instability and Life Limiting Effects of Inlet and Interstage Water Injection into Gas Turbines," ASME Paper No. GT2005-68007.
[2] Stalder, J. P., 1998, "Gas Turbine Compressor Washing State of the Art Field Experiences," ASME Paper No. 98-GT-420.
[3] Spakovszky, Z. S., Gertz, J., Sharma, O. P., Paduano, J. D., Epstein, A. H., Greitzer, E. M., 1999, "Influence of Compressor Deterioration on Engine Dynamic Behavior and Transient Stall Margin," ASME Paper No. 99-GT-439.
[4] Graf, M. B., Wong, T. S., Greitzer, E. M., Marble, F. E., Tan, C. S., Shin, H.-W., and Wisler, D. C., 1998, "Effects of Nonaxisymmetric Tip Clearance on Axial Compressor Performance and Stability," ASME J. Turbomach., **120**(4), pp. 648–661.
[5] Smith, G. D. J., and Cumpsty, N. A., 1984, "Flow Phenomena in Compressor Casing Treatment," ASME J. Eng. Gas Turbines Power, **106**(3), pp. 532–541.
[6] Frith, P. C., 1992, "The Effect of Compressor Rotor Tip Crops on Turboshaft Engine Performance," ASME Paper No. 92-GT-83.
[7] Radtke, F., and Dibelius, G., 1980, "Reynoldszahleinfluss bei hochbelasteten axialen Turbinenbeschaufelungen," VDI-Berichte Nr. 361.
[8] Boyle, R. J., 1994, ""Prediction of Surface Roughness and Incidence Effects on Turbine Performance," ASME J. Turbomach., **116**, pp. 745–751.
[9] Cohen, H., Rogers, G. F. C., and Saravanamuttoo, H. I. H., 1996, *Gas Turbine Theory*, Addison-Wesley, Reading, MA.
[10] Syverrud, E., Brekke, O., and Bakken, L. E., 2005, "Axial Compressor Deterioration," ASME Paper No. GT2005-68701.
[11] Millsaps, K. T., Baker, J., and Patterson, J. S., 2004, "Detection and Localization of Fouling in a Gas Turbine Compressor From Aerothermodynamic Measurements," ASME Paper No. GT2004-54173.
[12] Tarabrin, A. P., Schurovsky, V. A., Bodrov, A. I., and Stalder, J. P., 1998, "Influence of Axial Compressor Fouling on Gas Turbine Unit Performance Based on Different Schemes and With Different Initial Parameters," ASME Paper No. 98-GT-416.
[13] Meher-Homji, C. B., and Bromley, A., 2004, "Gas Turbine Axial Compressor Fouling and Washing," 33rd Turbomachinery Symposium.
[14] Syverrud, E., and Bakken, L. E., 2005, "Online Water Wash Tests of GE J85-13," ASME Paper No. GT2005-68702.
[15] Syvverrud, E., and Bakken, L. E., 2006, "The Impact of Surface Roughness on Axial Compressor Deterioration," ASME Paper GT2006-90004.
[16] MacLeod, J. D., Taylor, V., and Laflamme, J. C. G., 1991, "Implanted Component Faults and Their Effects on Gas Turbine Engine Performance," ASME Paper 91-GT-41.
[17] Khalid, S. A., Khalsa, A. S., Waitz, I. A., Tan, S. C., Greitzer, E. M., Cumpsty, N. A., Adamczyk, J. J., and Marble, F. E., 1998, "Endwall Blockage in Axial Compressors," ASME Paper No. 98-GT-188.
[18] Kurz, R., 1995, "Effects of Nonuniform Blade Pitch on the Flow Through an Annular Turbine Nozzle," Int. J. Rotating Mach., **2**(1), pp. 59–65.
[19] Kurz, R., and Brun, K., 2001, "Degradation in Gas Turbine Systems," ASME J. Eng. Gas Turbines Power, **123**, pp. 70–77.
[20] Aker, G. F., and Saravanamuttoo, H. I. H., 1988, "Predicting the Gas Turbine Performance Degradation Due to Compressor Fouling Using Computer Simulation Techniques," ASME Paper No. 88-GT-206.
[21] Haq, I., and Saravanamuttoo, H. I. H., 1991, "Detection of Axial Compressor Fouling in High Ambient Temperature Conditions," ASME Paper No. 91-GT-67.
[22] Lambiris, B., Mathioudakis, K., Stamatis, A., and Papalliou, K., 1991, "Adaptive Modeling of Jet Engine Performance With Application to Condition Monitoring," ISABE Paper No. 91-7058.
[23] Byington, C. S., Watson, M., Roemer, M. J., Golie, T. R., McGroarty, J. J., and Savage, C., 2003, "Prognostic Enhancements to Gas Turbine Diagnostic Systems," IEEE, Vol. 7, pp. 3247.

# A Viscoplastic Modeling Approach for MCrAlY Protective Coatings for Gas Turbine Applications

**Roland Mücke**
Alstom,
Brown Boveri Strasse 7,
CH-5401 Baden,
Switzerland

*MCrAlY coatings are applied in industrial gas turbines and aircraft engines to protect surfaces of hot gas exposed components from oxidation and corrosion at elevated temperature. Apart from oxidation resistance, coatings have to withstand cracking caused by cyclic deformation since coating cracks might propagate into the substrate material and thus limit the lifetime of the parts. In this context, the prediction of the coating maximum stress and the strain range during cyclic loading is important for the lifetime analysis of coated components. Analyzing the state of stress in the coating requires the application of viscoplastic material models. A coupled full-scale cyclic analysis of substrate and coating, however, is very expensive because of the different flow characteristics of both materials. Therefore, this paper proposes an uncoupled modeling approach, which consists of a full-scale cyclic analysis of the component without coating and a fast postprocessing procedure based on a node-by-node integration of the coating constitutive model. This paper presents different aspects of the coating viscoplastic behavior and their computational modeling. The uncoupled analysis is explained in detail and a validation of the procedure is addressed. Finally, the application of the uncoupled modeling approach to a coated turbine blade exposed to a complex engine start-up and shut-down procedure is shown. Throughout the paper bold symbols denote tensors and vectors, e.g., $\boldsymbol{\sigma}$ stands for the stress tensor with the components $\sigma_{ij}$. The superscripts $(.)^S$ and $(.)^C$ symbolize the substrate and the coating, respectively, e.g., $\boldsymbol{\varepsilon}_{th}^S$ stands for the tensor of substrate thermal strain. Further symbols are explained in the text.* [DOI: 10.1115/1.3094032]

## 1 Introduction

MCrAlY materials are a class of alloys, which consist of a base metal (M) of nickel (Ni), cobalt (Co), and/or iron (Fe), as well as chromium (Cr), aluminum (Al), yttrium (Y), and sometimes other alloying elements. MCrAlY coatings are used in industrial gas turbines and aircraft engines for protecting surfaces of hot gas exposed components from environmental degradation (oxidation and corrosion) [1,2].

The coating is typically applied as a thin overlay on top of a load carrying substrate material, which, for most gas turbine applications, consists of a suitable nickel superalloy (Fig. 1). In this case, the base metal of the applied MCrAlY coating typically consists of nickel or nickel/cobalt, and these coatings are sometimes referred to as NiCrAlY and NiCoCrAlY coatings, respectively.

The protective strength of MCrAlY coatings is achieved by forming an oxide scale on top of the coating surface, which results from the oxidation of the alloying elements Al and Cr (Fig. 2). The protective capability of the coating is used up when the Al and Cr resources are exhausted [3,4].

Apart from oxidation protection, MCrAlY coatings are used as a bondcoat for the application of thermal barrier coatings (TBCs) such as yttrium stabilized $ZrO_2$ (YSZ). In this case, the MCrAlY coating develops an oxide layer beneath the TBC—typically termed as thermally grown oxide (TGO). Besides other criteria, the TGO should not exceed a specific thickness since thick TGO layers are prone to oxide cracking under cyclic loading and can trigger TBC spallation (for details see Refs. [5,6], among others). The presented paper, however, addresses MCrAlY protective coatings applied as overlay only. TBC coated systems are not considered here.

In addition to resistance against environmental degradation, protective coatings have to withstand cracking caused by cyclic deformation (Fig. 2). In particular, coating cracks might propagate into the substrate material and thus limit the lifetime of the parts [7–10]. Moreover, coating cracks might accelerate the rate of oxidation since they destroy the protective oxide scale and enlarge the high temperature exposed surface. In this context, constitutive modeling for predicting the coating maximum stress and strain range in the course of cyclic loading is important, because these data enter the lifetime analysis of the substrate-coating system.

This paper addresses the prediction of the coating constitutive response. In particular, an uncoupled modeling approach is presented, which allows a full-scale (transient viscoplastic) analysis of turbine components followed by a fast postprocessing procedure for predicting the coating response.

This paper is structured as follows. Section 2 addresses different aspects of the coating constitutive behavior. Then the unified viscoplastic model suggested by Robinson is presented and applied to the simulation of coating and substrate materials. The proposed uncoupled analysis approach is explained in detail and a validation of the procedure is demonstrated. Finally, the application of the uncoupled modeling approach to a coated turbine blade exposed to a complex engine start-up and shut-down procedure is shown.

## 2 Constitutive Behavior of MCrAlY Coatings

**2.1 Coating Response to TMF Loading.** Typical load conditions in hot gas exposed components of industrial gas turbines can

Manuscript received October 15, 2008; final manuscript received October 16, 2008; published online July 14, 2009. Review conducted by Dilip R. Ballal. Paper presented at the ASME Turbo Expo 2007: Land, Sea and Air (GT2007), Montreal, QC, Canada, May 14–17 2007.

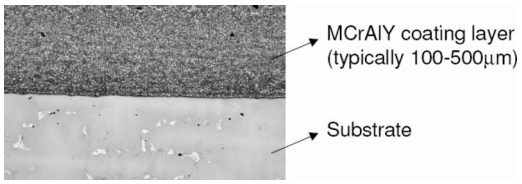


**Fig. 1 Virgin substrate/MCrAlY-coating system**

either be related to out-of-phase (OP) thermomechanical fatigue (TMF) load cycles or in-phase (IP) TMF cycles. OP load cycles are characterized by a decreasing mechanical strain while the temperature increases, whereas in IP cycles both mechanical strain and temperature are increasing. OP load cycles typically occur at leading edges of cooled turbine blades, whereas IP cycles often arise at trailing edges (Fig. 3).

Figure 4 shows the measured material response of a freestanding coating specimen subjected to an OP TMF cycle. The yield strength $R_p$ and the rupture strain $\varepsilon_B$ as functions of temperature are schematically shown in Fig. 5. Note that MCrAlY coatings undergo a typical transition in their mechanical behavior. In particular, the coating is brittle at low and ductile at high temperatures (e.g., $\varepsilon_B(T=20°C)<1.0\%$ and $\varepsilon_B(T>700°C)<20\%$); whereas the yield strength of the coating approaches the yield strength of the substrate at low temperatures, while at high temperatures the yield strength is very low (typically $R_p<50$ MPa).

The transition between both deformation regimes is characterized by the ductile brittle transition temperature (DBTT) (for details, see Refs. [7,10,11]). The DBTT depends on the chemical composition of the coating and the temperature rate during shutdown, whereas the latter effect is a result of the viscoplastic deformation rate sensitivity of the coating in the intermediate temperature regime.

**2.2 Sensitivity of Coating Behavior.** Many parameters affect the constitutive response, the cyclic life, and the protective properties of MCrAlY coatings. Only three of them are mentioned here.

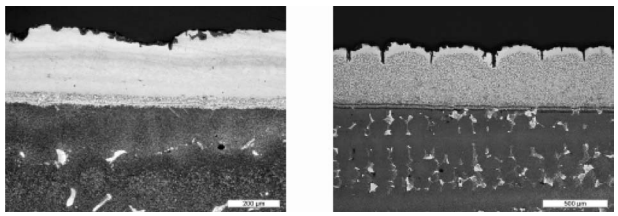

**Fig. 2 MCrAlY coating after service: (left) coating layer intact and aluminum resource exhausted; (right) coating TMF cracks not propagating into the substrate**

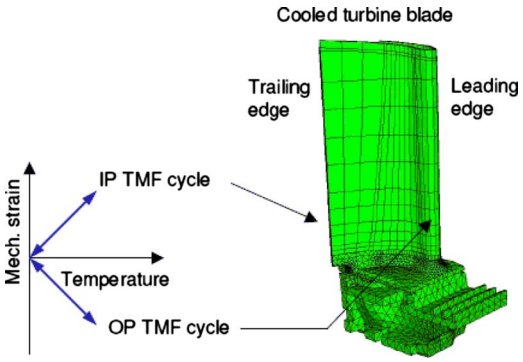


**Fig. 3 Definition of cycle types**

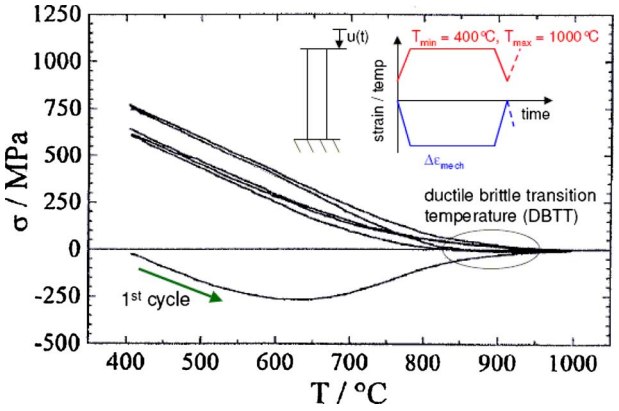


**Fig. 4 Measured stress temperature response of a MCrAlY coating subjected to an OP TMF cycle [7]**

(1) *Chemical composition*. A high amount of Al and/or Cr improves the oxidation resistance of the coating. However, adversely, alloys with a high content of aluminum are brittle at low temperatures because of large amounts of brittle phases such as NiAl. Thus, the development of the coatings always aims for an optimum balance of oxidation resistance and fatigue strength of the substrate-coating system [12]. Moreover, the addition of rhenium (Re) to NiCoCrAlY coatings does not change the DBTT, but it significantly influences the TMF resistance [13].

(2) *Processing*. Besides the chemical composition, the coating application process, the process parameters, and the powder characteristics influence the functionality of the coating. For gas turbine components low pressure plasma spraying (LPPS) is typically used for coating deposition because LPPS produces fine-grained and oxide-free coating layers with high density (low porosity) at competitive cost [14–16].

(3) *Substrate material*. An optimized coated system has to consider the mechanical properties of the substrate. In particular, a low thermal expansion mismatch between coating and substrate—especially at room temperature and in the range of operation temperatures—decreases the maximum strain range in the coating and thus improves the coating cyclic life [1,7,8,12].

## 3 The Robinson Constitutive Model

**3.1 Governing Equations.** The governing equations of structural mechanics consist of the kinetic equation

$$\nabla \cdot \boldsymbol{\sigma} + \bar{\mathbf{p}} = 0 \tag{1}$$

which results from the equilibrium of forces, the kinematic equation

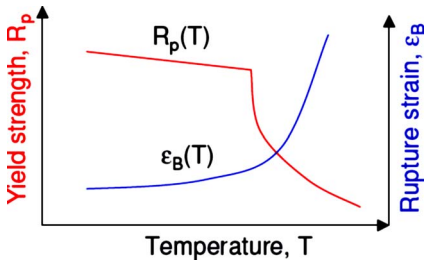


**Fig. 5 Temperature dependence of yield strength and rupture strain of MCrAlY coatings [7]**

**Table 1 Governing equations of the Robinson model**

| | |
|---|---|
| (a) Strain decomposition | $\boldsymbol{\varepsilon}=\boldsymbol{\varepsilon}_{\text{th}}+\boldsymbol{\varepsilon}_{\text{mech}}$ with $\boldsymbol{\varepsilon}_{\text{mech}}=\boldsymbol{\varepsilon}_{\text{el}}+\boldsymbol{\varepsilon}_{\text{in}}$ |
| (b) Thermal strain | $\boldsymbol{\varepsilon}_{\text{th}}=\beta_{\text{th}}(T-T_0)\mathbf{I}$ |
| (c) Elastic strain | $\boldsymbol{\varepsilon}_{\text{el}}=\frac{1+\nu}{E}\boldsymbol{\sigma}^{\text{dev}}+\frac{1-2\nu}{3E}\boldsymbol{\sigma}^{\text{vol}}$ |
| (d) Flow rule | $\dot{\boldsymbol{\varepsilon}}_{\text{in}}=F\mathbf{d}$ for $\boldsymbol{\sigma}^{\text{dev}}:\boldsymbol{\Sigma}>0$ |
| (e) Flow function | $F=\frac{1}{2\mu}\left\langle\frac{J_2(\boldsymbol{\Sigma})}{K^2}-1\right\rangle^n$ |
| (f) Flow direction | $\mathbf{d}=\boldsymbol{\Sigma}$ |
| (g) Effective stress | $\boldsymbol{\Sigma}=\boldsymbol{\sigma}^{\text{dev}}-X$ |
| (h) Rate of back stress | $\dot{\mathbf{X}}=C_1G^{-\beta}\dot{\boldsymbol{\varepsilon}}_{\text{in}}-C_2G^{-m}\mathbf{X}$ with $G=\begin{cases}J_2(\mathbf{X})/K^2 & \text{for } J_2(\mathbf{X})/K^2\geq G_0\\ G_0 & \text{for } J_2(\mathbf{X})/K^2<G_0\end{cases}$ |
| (i) Second invariants | $J_2(\boldsymbol{\Sigma})=\frac{1}{2}\boldsymbol{\Sigma}:\boldsymbol{\Sigma}$ <br> $J_2(\mathbf{X})=\frac{1}{2}\mathbf{X}:\mathbf{X}$ |
| (j) Material parameters | $\mathbf{P}_{\text{el}}=[E,\nu,\beta_{\text{th}}]$ <br> $\mathbf{P}_{\text{in}}=[\mu,n,C_1,C_2,\beta,m,K]$ |

$$\boldsymbol{\varepsilon}=\frac{1}{2}(\nabla\mathbf{u}+\mathbf{u}\nabla) \tag{2}$$

for describing the deformation of the material, and the constitutive function

$$\boldsymbol{\varepsilon}=f(\boldsymbol{\sigma},T,t,\text{etc.}) \tag{3}$$

which defines the relation between the stress and the strain as a function of temperature, time, and material parameters. Moreover, appropriate boundary conditions have to be described for preventing a rigid body movement and to define the loading of the investigated structure.

The complexity of the required constitutive equations depends on the behavior of the material to be modeled. Considering MCrAlY coatings, the following effects have to be taken into account:

- linear-elastic behavior below the temperature dependent yield strength
- time independent plastic deformations for low, medium, and high temperatures
- time dependent viscous deformations above the DBTT
- strain rate dependency
- strong temperature dependence of various material parameters

To consider the above requirements, a viscoplastic modeling approach for MCrAlY coatings is mandatory. The type of constitutive equations is based on the Robinson model since it provides a reasonable compromise between model capability and number of required material parameters.

The Robinson model belongs to the class of unified viscoplastic models. Unified models are characterized by only one strain variable—denoted as inelastic strain—which describes both plastic and viscous effects. Thus, considering small deformations as defined in Eq. (2), the total strain tensor $\boldsymbol{\varepsilon}$ can be expressed by the additive composition of the thermal strain $\boldsymbol{\varepsilon}_{\text{th}}$, the elastic strain $\boldsymbol{\varepsilon}_{\text{el}}$, and the inelastic strain $\boldsymbol{\varepsilon}_{\text{in}}$. Furthermore, the elastic strain and the inelastic strain are considered together as mechanical strain $\boldsymbol{\varepsilon}_{\text{mech}}=\boldsymbol{\varepsilon}_{\text{el}}+\boldsymbol{\varepsilon}_{\text{in}}$, which results from external forces, temperature gradients, and structural constraints, whereas the thermal strain is exclusively produced by the thermal expansion of the material.

Different variants of the Robinson model are reported in Refs. [17–20]. The constitutive equations applied in this work are summarized in Table 1. Apart from the definitions given there, $\boldsymbol{\sigma}^{\text{dev}}=\boldsymbol{\sigma}-\frac{1}{3}\text{tr}(\boldsymbol{\sigma})\mathbf{I}_2$ and $\boldsymbol{\sigma}^{\text{vol}}=\frac{1}{3}\text{tr}(\boldsymbol{\sigma})\mathbf{I}_2$ denote the deviatoric and the volumetric parts of the Cauchy stress tensor $\boldsymbol{\sigma}$, respectively,

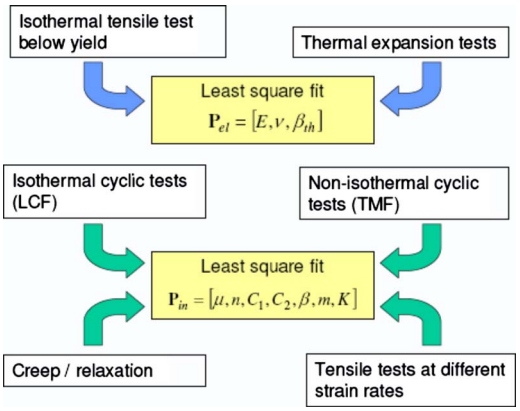


**Fig. 6 Type of material tests for parameter identification**

where $\text{tr}(\boldsymbol{\sigma})=\sigma_{11}+\sigma_{22}+\sigma_{33}$ symbolizes the trace of $\boldsymbol{\sigma}$; $\mathbf{I}$ represents the second order identity tensor; $G_0$ is a cut-off parameter, which prevents the rate of the back stress $\mathbf{X}$ to become singular for small $G$; $T_0$ describes a reference temperature associated with zero thermal strain; and the symbol $\langle . \rangle$ denotes the Macauley bracket

$$\langle x\rangle=\begin{cases}x & \text{for } x\geq 0\\ 0 & \text{for } x<0\end{cases} \tag{4}$$

### 3.2 Remarks.

(1) For modeling MCrAlY coatings we found it sufficient to consider nonlinear kinematic hardening only (see h in Table 1), i.e., the model does not contain an isotropic hardening term.
(2) Compared with the classical Chaboche viscoplastic model described in Refs. [21,22], the Robinson model offers a higher flexibility in the kinematic hardening term by including the hardening exponents $\beta$ and $m$. We noticed that these parameters improve the simulation of ratcheting [23].
(3) For modeling large temperature ranges and fast transients, as they typically occur in gas turbine operation, appropriate temperature rate terms for the hardening parameters $C_1$ and $\beta$ are required (for details, see Ref. [23]). Since temperature rate terms do not affect the methodology of coating modeling shown here, the rate terms are not explicitly described in this paper.

**3.3 Identification of Material Parameters.** The constitutive model involves the material parameters $\mathbf{P}_{\text{el}}=[E,\nu,\beta_{\text{th}}]$ of the thermo-elastic model and the parameters $\mathbf{P}_{\text{in}}=[\mu,n,C_1,C_2,\beta,m,K]$ of the inelastic model. The temperature dependence is considered to have material parameters, which are empirically dependent on temperature. This approach requires the identification of the model parameters at different temperature levels and suitable interpolation schemes for intermediate temperatures.

Figure 6 shows the type of material tests, which are required for full characterization of the constitutive model. Note that the inelastic parameters $\mathbf{P}_{\text{in}}$ are determined independently from the parameters of the thermo-elastic model since the staggered approach simplifies the parameter identification, and thus it improves the stability of the computational parameter identification process.

Nevertheless, the determination of the material parameters for viscoplastic models requires experience and a profound understanding of the material and the material model. For most cases, the model parameters are derived from the minimization of a weighted least square function by using a suitable optimization algorithm. Such fitting, however, is affected by the relative weights of the different types of data used (for details, see Refs.

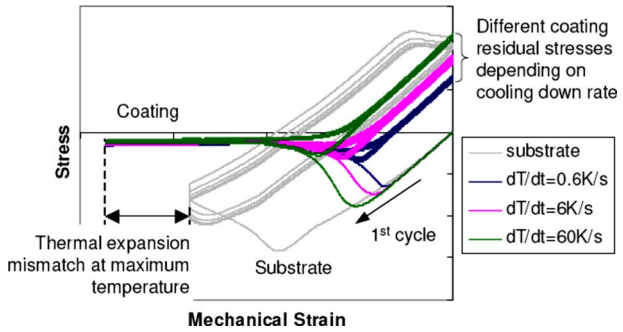


**Fig. 7 Simulation of coating and substrate subjected to TMF OP cycles with different loading rates**

[24,25]). Moreover, gradient methods are not always successful in minimizing the least square function because they have problems to overcome local minima in the objective function space. In this case, either different start parameters are applied or gradient free methods such as evolutionary and genetic algorithms may be used (see, e.g., Refs. [26,27]). For the parameter identification of the models applied in this work, the downhill simplex algorithm described in Refs. [28,29] was applied for minimizing the least square function.

**3.4 Application to Substrate and Coatings.** The parameters of the Robinson viscoplastic model have been determined for different substrate and coating materials. The parameter identification for coatings is based on the testing of coating bulk materials, as described in Refs. [7,8]. Figure 7 shows the simulation results of coating and substrate responses to TMF OP cycles with temperature rates of $dT/dt=0.6$ K/s, 6 K/s, and 60 K/s. Note that the different loading rates during cooling down affect the DBTT, while the loading rate during heating up does not influence the coating residual stress as long as the coating maximum temperature exceeds the DBTT. The rate dependence of the DBTT leads to different residual tensile stresses in the coating, i.e., the higher the rate of temperature and strain during cooling down, the higher the coating residual stress.

## 4 The Uncoupled Modeling Approach for Coatings

**4.1 Outline of the Approach.** The constitutive behavior of coating and substrate differs significantly, as in Fig. 7. Considering a loading—hold time—unloading stabilized cycle of a typical gas turbine component, the substrate behaves nearly elastically during wide ranges of the loading and the unloading phases. At the same time, however, the yield strength of the coating decreases significantly, which requires tight time steps for integrating the coating constitutive equations. Using a full-scale component model including the coating layer, the computation time can be extensive, especially since viscoplastic analyses typically require transient modeling of several load cycles until the stabilized stress-strain hysteresis is reached. In fact, these demands often limit the applicability of viscoplastic analyses to full-scale models with typically $10^5-10^6$ finite element analysis (FEA) nodes. In this context, the paper addresses a modeling approach which decouples the coating from the substrate analysis. This modeling approach is based on the following two assumptions.

(1) The MCrAlY coating and the substrate are completely bonded to each other. Therefore, on the interface the deformations of substrate and coating are equal, i.e., $\mathbf{u}^S(t)=\mathbf{u}^C(t)$ where $\mathbf{u}^S(t)$ and $\mathbf{u}^C(t)$ denote the substrate and the coating deformations on their joint interface.
(2) The stiffness of the coating can be neglected because the thickness of the coating layer is typically small compared with the thickness of the substrate and the coating yield strength at high temperature is very low. The results of a sensitivity analysis are discussed in Sec. 4.2.

**Table 2 Substrate residual stress sensitivity**

| Substrate thickness (mm) | Coating thickness ($\mu$m) | Stiffness ratio $(EA)^C/(EA)^S$ (%) | Residual stress delta (%) |
|---|---|---|---|
| 3.05 | 100 | 5.2 | 3.2 |
| 2.95 | 200 | 10.7 | 6.2 |
| 2.85 | 300 | 16.6 | 9.9 |
| 2.75 | 400 | 22.9 | 17.7 |

As a consequence of assumption 2, the coating does not influence the constitutive response of the substrate. Assumption 1 implies that the loading of the coating is completely described by the mechanical strain $\boldsymbol{\varepsilon}^S_{\text{mech}}(t)$ of the substrate on the coating-substrate interface and the thermal mismatch between coating and substrate $\Delta\boldsymbol{\varepsilon}_{\text{th}}(t)=\boldsymbol{\varepsilon}^S_{\text{th}}(t)-\boldsymbol{\varepsilon}^C_{\text{th}}(t)$. In particular, for the coating mechanical strain it follows that

$$\boldsymbol{\varepsilon}^C_{\text{mech}}(t)=\boldsymbol{\varepsilon}^S_{\text{mech}}(t)+\Delta\boldsymbol{\varepsilon}_{\text{th}}(t) \tag{5}$$

Therefore, the uncoupled modeling approach is characterized by the following three steps:

(1) Calculate the metal temperature and the mechanical strain in the substrate on the substrate-coating interface using a full-scale finite element model *without* coating.
(2) Determine the coating mechanical strain with Eq. (5).
(3) Evaluate the coating stress from an independent node-by-node integration of the coating constitutive model.

This simple modeling approach offers the following advantages over a fully coupled simulation procedure.

(1) The analysis time for coated components is significantly reduced. Thus the modeling of complex transient operation conditions in a maintainable time frame becomes now feasible.
(2) The coating analysis can be performed in a postprocessing step after the analysis of the full-scale uncoated model.
(3) If appropriate, the coating analysis can therefore be restricted to the most critical regions on the component.

Note that although in the uncoupled analysis approach the coating is not explicitly modeled, the effect of the coating mass, of course, needs to be included in the assessment of eigenfrequencies and airfoil mass.

**4.2 Sensitivity Analysis.** The uncoupled modeling approach requires that the substrate constitutive response is independent from the coating. Of course, this assumption is only valid for sufficiently thin coating layers since for cold temperatures the coating residual stress may reach—or even exceed—the stress in the substrate and thus the coating may influence the stiffness of the cold part. Therefore, a sensitivity analysis on internally cooled cylindrical specimens (inner diameter of 6 mm) subjected to TMF cycles has been performed (Table 2). As expected, the delta in substrate residual stress for models with and without coating can be correlated with the stiffness ratio $(EA)^C/(EA)^S$ of both materials where $E$ and $A$ denote Young's modulus and the cross section area, respectively. In addition, the residual stress depends to a lower extend on other parameters such as the ratio of mechanical and thermal loads and therefore the temperature gradient across the wall.

However, considering the airfoil of turbine blades, for example, even for coating layers up to 10% of the wall thickness, the overall stiffness of the part is normally not affected since a large por-

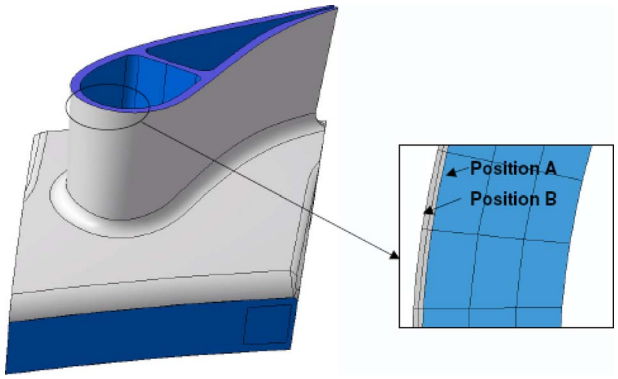


**Fig. 8 Coated turbine component and mesh details**

tion of substrate material belongs to internal load carrying structures such as struts and webs, which essentially increase the stiffness of the part.

## 5 Validation

The proposed methodology is validated by comparing the analysis results of the coupled and the uncoupled modeling approaches. For doing so, a cooled gas turbine vane is investigated (Fig. 8). The simulation model of the vane is subjected to simplified heating up, hold time, and cooling down load conditions whereby five load cycles were evaluated.

For the coupled modeling approach a full-scale analysis of the vane model with coating has been performed. For the uncoupled approach the histories of total strain and temperature on the outer surface of the substrate model (position A in Fig. 8) are extracted from a cyclic analysis of the uncoated turbine component, and this input is then applied for integrating the coating constitutive model.

Figure 9 shows the calculated stress-strain hysteresis in the substrate (position A) and in the coating using the coupled and the uncoupled modeling approaches. Note that both approaches give close analysis results whereby the uncoupled approach was faster by a factor of nearly 2 (Table 3). The reduction in the computational effort using the uncoupled approach is caused by the lower number of iterations with the full-scale uncoated component model and less effort per iteration because of the smaller size of the finite element stiffness matrix. On the other hand, the computational time for the node-by-node integration of the coating model takes only a few seconds. Note that the reduction in computational effort becomes even more pronounced when, in the uncoupled approach, the full-scale cyclic viscoplastic analysis of the uncoated component can be replaced by a transient linear-

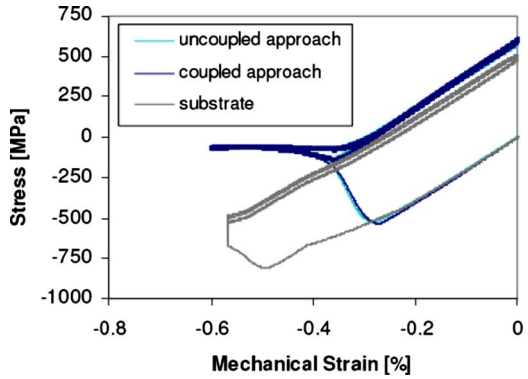


**Fig. 9 Stress-strain results using the coupled modeling approach (substrate at position A and coating at position B) and the uncoupled approach (coating at position B)**

**Table 3 Reduction in CPU time and number of iterations for the uncoupled approach**

| | CPU time (%) | No. of iterations (%) |
|---|---|---|
| Coupled approach | 100 | 100 |
| Uncoupled approach | 57 | 51 |

elastic analysis. Avoiding the cyclic viscoplastic analysis in the coupled approach is not possible because of the complex coating constitutive behavior.

In the presented form, the uncoupled modeling approach does not take the temperature gradient across the coating into account. In the validation example this implies that the coupled analysis considers the outer coating temperature (position B in Fig. 8), whereas in the uncoupled approach the substrate surface temperature (position A in Fig. 8) enters the coating integration procedure. Although in the validation example the temperature gradient across the coating reached only 10 K, the increased temperature affects the coating behavior. In particular, the higher temperature on the coating outer surface results in a higher thermal mismatch between coating and substrate, which increases both the coating maximum strain range and the coating residual stress.

The temperature gradient effect can be avoided when the coating temperature in the uncoupled approach is corrected. The correction can be done by applying an effective heat transfer coefficient onto the substrate surface, which takes the coating thickness, the coating heat conductivity, and, for highly curved surfaces, the radius of curvature into account.

Figure 10 shows the development of the absolute mechanical strain difference between the coupled and the uncoupled modeling approach. Table 4 summarizes the percentage differences of both methods for the coating mechanical strain range and the coating residual stress in the fifth cycle. Note that the uncoupled analysis results are considerably improved when the coating temperature is corrected.

## 6 Application to Engine Start-Up and Shut-Down Analysis of Gas Turbine Blades

In order to avoid coating cracks, the coating response to typical load cycle conditions has to be investigated. The uncoupled simu-

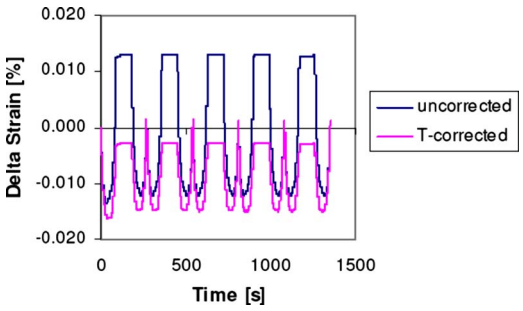


**Fig. 10 Absolute difference in mechanical strain between coupled and uncoupled modeling approaches**

**Table 4 Percentage difference between uncoupled and coupled modeling approaches in the fifth cycle**

| | Difference without *T*-correction (%) | Difference after *T*-correction (%) |
|---|---|---|
| Strain range | 2.1 | 0.5 |
| Residual stress | 3.3 | 2.1 |

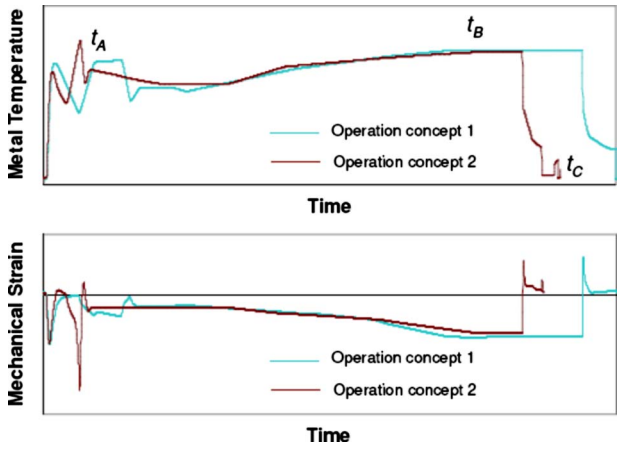


**Fig. 11 History of substrate metal temperature and mechanical strain for different engine start-up and shut-down operation concepts (only one cycle is shown)**

lation approach allows for a fast comparison of different engine operation concepts for start-up, normal shut-down, fast shut-down, gas/oil fuel switch-over including burner lance purging, etc.. As an example, Fig. 11 shows the history of metal temperature and mechanical strain at a specific location of a turbine blade subjected to different start-up and shut-down operation procedures. The data are based on cyclic transient analyses of the full blade model without coating. Applying the proposed uncoupled simulation approach, the metal temperature and the mechanical strain enter the integration procedure of the coating constitutive model.

Figure 12 presents the coating constitutive response. Similar as for standard TMF cycles, the full load condition at time $t_B$ corresponds to the coating minimum mechanical strain at low stress, whereas the coating maximum tensile stress is reached after the unloading at time $t_C$. Moreover, in this case the comparison of coating strain and stress shows that for both operation concepts a similar state of loading in the coating is expected and that in both cases the coating tensile residual stresses are very low.

## 7 Conclusion

An uncoupled modeling approach for MCrAlY protective coatings on top of hot gas exposed gas turbine components has been proposed. The method consists of a full-scale analysis of the component without coating followed by a node-by-node integration of the coating constitutive model in a finite element postprocessing procedure. The validation of the method has shown nearly identical results for the coupled and the uncoupled modeling approaches, in particular, when a temperature correction is used in the uncoupled approach. Finally, the proposed method is applied to the analysis of complex load histories as they typically occur during start-up and shut-down operation conditions of gas turbine engines. This detailed coating analysis would hardly be feasible without using the proposed uncoupled modeling approach for MCrAlY protective coatings.

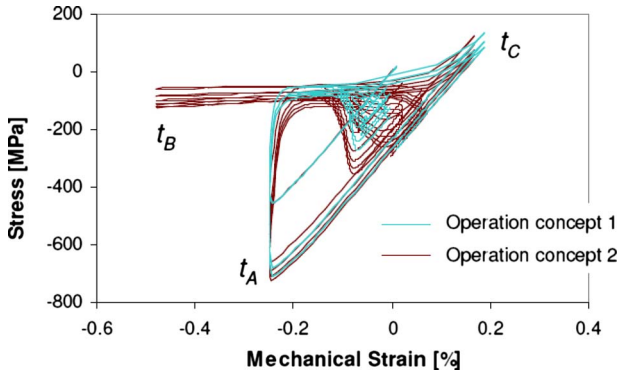


**Fig. 12 Stress-strain response of the coating for different engine start-up and shut-down operation concepts**


## Acknowledgment

The author thanks Alstom for permission to publish.


## Nomenclature

$\boldsymbol{\varepsilon}$ = tensor of total strain
$\boldsymbol{\varepsilon}_{el}$ = tensor of elastic strain
$\boldsymbol{\varepsilon}_{in}$ = tensor of inelastic strain
$\boldsymbol{\varepsilon}_{th}$ = tensor of thermal strain
$\boldsymbol{\varepsilon}_{mech}$ = tensor of mechanical strain, $\boldsymbol{\varepsilon}_{mech}=\boldsymbol{\varepsilon}-\boldsymbol{\varepsilon}_{th}$
$\Delta\boldsymbol{\varepsilon}_{th}$ = tensor of thermal mismatch, $\Delta\boldsymbol{\varepsilon}_{th}(t)=\boldsymbol{\varepsilon}_{th}^{S}(t)-\boldsymbol{\varepsilon}_{th}^{C}(t)$
FEA = finite element analysis
$\boldsymbol{\sigma}$ = Cauchy stress tensor ($N/m^2$)
$T$ = metal temperature (K)
$t$ = time (s)
$\mathbf{P}_{el}$ = parameters of the thermo-elastic model
$\mathbf{P}_{in}$ = parameters of the inelastic model
$\mathbf{u}$ = vector of displacement (m)

## References


[1] Tamarin, Y., 2002, *Protective Coatings for Turbine Blades*, ASM International, Materials Park, OH.
[2] Meetham, G. W., 1986, "Use of Protective Coatings in Aero Gas Turbine Engines," Mater. Sci. Technol., **2**, pp. 290–294.
[3] Schütze, M., 1997, *Protective Oxide Scales and Their Breakdown*, Wiley, New York.
[4] Frances, M., Steinmetz, P., Steinmetz, J., Duret, C., and Mevrel, R., 1985, "Hot Corrosion Behavior of Low Pressure Plasma Sprayed NiCoCrAlY+Ta Coatings on Nickel Base Superalloys," J. Vac. Sci. Technol. A, **3**(6), pp. 2537–2544.
[5] Sjönström, S., Brodin, H., and Jinnestrand, M., 2003, "Prediction of Fatigue Life of Thermal Barrier Coatings in Gas Turbines: Modeling and Experimental Verification," ASME Paper No. GT2003-38285.
[6] Jung, A., 2002, "Experimental Access of Damage Mechanisms of Advanced Thermal Barrier Coatings for Gas Turbine Components," *Proceedings of TurboMat on Advanced TBCs and Titanium Aluminides for Gas Turbines*, Bonn, Germany.
[7] Kowalewski, R., and Mughrabi, H., 1998, "Influence of a Plasma-Sprayed NiCrAlY Coating on the Low-Cycle Fatigue Behavior of a Directionally Solidified Nickel-Base Superalloy," Mater. Sci. Eng., A, **247**, pp. 295–299.
[8] Kowalewski, R., 1997, *Thermo-Mechanical Fatigue of a Coated Columnar Grain Nickel Based Superalloy*, VDI Verlag GmbH, Düsseldorf, Germany, in German.
[9] Cheravu, N. S., Chan, K. S., and Leverant, G. R., 2002, "Condition Assessment and Life Prediction of Diffusion and Overlay Coatings," *Proceedings of EPRI International Conference on Advances in Life Assessment and Optimization of Fossil Power Plants*, Orlando, FL.
[10] Jung, A., and Schnell, A., 2008, "Crack Growth in a Coated Gas Turbine Superalloy Under Thermo-Mechanical Fatigue," Int. J. Fatigue, **30**, pp. 286–291.
[11] Veys, J. M., Rivière, A., and Mèvrel, E., 1988, "Mechanical Properties of LPPS NiCoCrAlYTa Alloy," *Proceedings of First Plasma-Technik-Symposium*, Luzern, Switzerland, Vol. 2, pp. 115–123.
[12] Grünling, H. W., Schneider, K., and Singheiser, L., 1987, "Mechanical Properties of Coated Systems," Mater. Sci. Eng., **88**, pp. 177–189.
[13] Czech, N., Schmitz, F., and Stamm, W., 1995, "Thermal Mechanical Fatigue Behavior of Advanced Overlay Coatings," Mater. Manuf. Processes, **10**(5), pp. 1021–1035.
[14] Irons, G., and Zanchuk, V., 1993, "Comparison of MCrAlY Coatings Sprayed by HVOF and Low Pressure Processes," *Proceedings of National Thermal Spray Conference*, Anaheim, CA.
[15] Guo, X. X., Zheng, X. M., Milidantri, G., and Fenton, R., 1995, "Development and Application of Low Plasma Sprayed Coatings on Gas Turbine Engine Components," *Proceedings of International Thermal Spraying Conference*, Kobe, Japan.
[16] Loch, M., and Barbezat, G., 2002, "Progress in the Area of Low Pressure Plasma Spraying," *Proceedings of the International Thermal Spray Conference*, Essen, Germany, pp. 347–350, in German.
[17] Robinson, D. N., 1978, "A Unified Creep-Plasticity Model for Structural Met-

als at High Temperatures," Oak Ridge National Laboratory, ORNL Report No. TM-5969.
[18] Robinson, D. N., and Swindeman, R. W., 1982, "Unified Creep-Plasticity Constitutive Equations for 2–1/4Cr–1Mo Steel at Elevated Temperature," Oak Ridge National Laboratory, ORNL Report No. TM-8444.
[19] Robinson, D. N., and Bartolotta, P. A., 1985, "Viscoplastic Constitutive Relationships With Dependence on Thermomechanical History," NASA Report No. CR-174836.
[20] Robinson, D. N., 1984, "Constitutive Relationships for Anisotropic High-Temperature Alloys," Nucl. Eng. Des., **83**, pp. 389–396.
[21] Chaboche, J. L., 1989, "Constitutive Equations for Cyclic Plasticity and Cyclic Viscoplasticity," Int. J. Plast., **5**, pp. 247–302.
[22] Lemaitre, J., and Chaboche, J.-L., 1990, *Mechanics of Solid Materials*, Cambridge University Press, Cambridge, England.
[23] Mücke, R., and Bernhardi, O. E., 2006, "On Temperature Rate Terms for Viscoplastic Constitutive Models With Applications to High Temperature Materials," Comput. Methods Appl. Mech. Eng., **195**, pp. 2411–2431.
[24] Bard, Y., 1974, *Nonlinear Parameter Estimation*, Academic, New York.
[25] Norton, J. P., 1986, *An Introduction to Identification*, Academic, London.
[26] Andrade-Campos, A., Thuillier, S., Pilvin, P., and Teixeira-Dias, F., 2007, "On the Determination of Material Parameters for Internal Variable Thermoelastic-Viscoplastic Constitutive Models," Int. J. Plast., **23**(8), pp. 1349–1379.
[27] Lin, J., and Yang, J., 1999, "GA-Based Multiple Objective Optimisation for Determining Viscoplastic Constitutive Equations for Superplastic Alloys," Int. J. Plast., **15**(11), pp. 1181–1196.
[28] Press, W. H., Teukolsky, S. A., Vetterling, W. T., and Flannery, B. P., 1992, *Numerical Recipes*, Cambridge University Press, Cambridge, England.
[29] Nelder, J. A., and Mead, R., 1965, "A Simplex Method for Function Minimization," Comput. J., **7**, pp. 308–313.

# Static Performance Characteristics and Rotordynamic Coefficients for a Four-Pad Ball-in-Socket Tilting Pad Journal Bearing

**Dara Childs**
Mechanical Engineering Department,
3123,
Texas A&M University,
College Station, TX 77845

**Joel Harris**
Entergy Services, Inc.,
Arkansas Support Group,
Little Rock, AR 77201

*Static performance characteristics and rotordynamic coefficients were experimentally determined for a four-pad, ball-in-socket, tilting-pad journal bearing in load-between-pad configuration. Measured static characteristics include journal static equilibrium position, estimated power loss, and trailing-edge pad temperatures. Rotordynamic coefficients were determined from curve-fits of measured complex dynamic-stiffness coefficients as a function of the excitation frequency. Aside from the cross-coupled damping coefficients, a frequency-independent [M]-[C]-[K] model did a good job of fitting the measurements. The added-mass coefficient was frequently dropped, leaving only a frequency-independent stiffness and damping coefficient. Test conditions included speeds from 4000 rpm to 12,000 rpm and unit loads from 0 kPa to 1896 kPa (0–275 psi). The bearing uses cool inlet oil to decrease the pad operating temperatures and increase the bearing's load and speed capacity. The bearing has a nominal radial clearance of 95.3 μm (3.75 mils). However, measurements indicated significant bearing crush with a radial bearing clearance of 99.6 μm (3.92 mils) in the axis 45 deg counterclockwise from the loaded axis and 54.6 μm (2.15 mils) in the axis 45 deg clockwise from the loaded axis (assuming counterclockwise rotation). The pad length is 101.60 mm (4.00 in.), giving L/D = 1.00. The pad arc angle is 73 deg, and the pivot offset ratio is 65%. Testing was performed using a test rig described by Kaul (1999, "Design and Development of a Test Setup for the Experimental Determination of the Rotordynamic and Leakage Characteristics of Annular Bushing Oil Seals," MS thesis, Texas A&M University, College Station, TX), and rotordynamic coefficients were extracted using a procedure adapted from the work of Childs and Hale (1994, "A Test Apparatus and Facility to Identify the Rotordynamic Coefficients of High-Speed Hydrostatic Bearings," ASME J. Tribol., **116**, pp. 337–344). A bulk-flow Navier–Stokes model was used for predictions, using adiabatic conditions for the fluid in the bearing. However, the model assumes constant nominal clearances at all pads, and an average clearance was used based on measured clearances. Measured static eccentricities and attitude angles were significantly higher than predicted. Attitude angles varied from 6 deg to 39 deg and decreased with load. Power loss was underpredicted at low speeds and very well predicted at high speeds, with a maximum value of 25 kW (34 hp). The maximum detected pad temperature was 71°C (160°F) while the temperature increase from inlet to maximum pad temperature location was overpredicted by 10–40%. Direct stiffness and damping coefficients were significantly overpredicted, but the addition of a stiffness-in-series correction vastly improved the agreement between theory and experiment. Direct added masses were zero or negative at low speeds and increased with speed up to a maximum of about 50 kg; they were normally greater in the x (unloaded) direction. Although significant cross-coupled stiffness terms were present, they always had the same sign, and the bearing had a whirl frequency ratio of zero netting unconditional stability over all test conditions.* [DOI: 10.1115/1.3098376]

## 1 Introduction

Lund [1] noted that tilting-pad journal bearings (TPJBs) eliminate oil whip instabilities because they direct the load component of each pad through the journal center, if the effects of pad inertia and pivot friction are neglected. Because of this characteristic, TPJBs are the first choice for high-speed turbomachinery.

The three basic types of pivots used for the pads (or shoes) of TPJBs are cylindrical, spherical, and flexure-pivot. Cylindrical, or rocker-back, pivots have a constant-curvature profile machined into the back of the pads, allowing them to rotate about the axial length of the bearing. Spherical pivots add a degree of freedom to the pads, allowing pitch perpendicular to the bearing's axial length. Spherical pivots can be further divided into sphere-in-cylinder and ball-in-socket types. Sphere-in-cylinder pivots have a spherical curvature machined into the back of the pad with a higher degree of curvature than that of the cylindrical housing, allowing them to roll without slipping about the housing. Ball-in-socket pivots, such as the one under consideration, have a steel hemisphere (ball) affixed to the bearing housing as well as a

Manuscript received November 7, 2008; final manuscript received November 13, 2008; published online July 17, 2009. Review conducted by Dilip R. Ballal. Paper presented at the ASME Turbo Expo 2008: Land, Sea and Air (GT2008), Berlin, Germany, June 9–13, 2008.

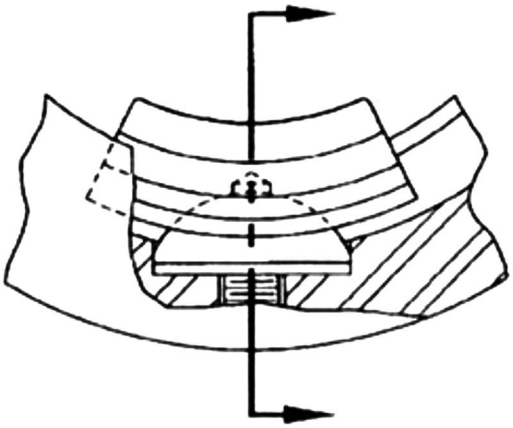

**Fig. 1 Ball-in-socket pivot [3]**

matching socket of slightly lower curvature machined into the back of the pad. This type of pivot is described in detail by Nicholas and Wygant in Ref. [2] and shown in Fig. 1.

Ball-in-socket pivots depend on the slipping motion between the socket and the ball to rotate the pads to their optimum angle. Both types of spherical-seat pivots can accommodate shaft misalignments. Flexure-pivot (FP) bearings use a narrow flexural "web" to support the pad. The web is electron-discharge machined into the bearing's inner diameter [4].

Some important TPJB bearing geometrical parameters are shown in Fig. 2. In Fig. 2(*a*), $R_s$, $R_b$, and $R_p$ represent the respective radii of the shaft, bearing, and pad. The bearing clearance is defined as $C_b=R_b-R_s$ while the pad clearance is defined as $C_p=R_p-R_s$. These clearances combine to give the preload factor $M_p=1-C_b/C_p$. Zero preload would imply that the pad is concentric with the shaft while nonzero positive preload implies a larger pad than the shaft radius and vice versa for a negative preload. Figure 2(*b*) shows the pad angle, or circumferential pad length $\theta_{\text{pad}}$, and the pivot angle $\theta_{\text{pivot}}$. The pivot offset is defined as $\theta_{\text{pivot}}/\theta_{\text{pad}}$. Typical pivot offsets are between 50% and 70% while the highest load capacity is achieved with a 60% offset [3].

Two additional parameters of interest are the length-to-diameter ($L/D$) ratio and the clearance-to-radius ($C_r/R$) ratio. The $L/D$ ratio defines the ratio of the effective axial length of the bearing (axial pad length for TPJBs) while the $C_r/R$ ratio defines the ratio of the nominal radial bearing clearance to nominal bearing radius. For TPJBs, $C_r=C_b$ and $R=R_b$.

**1.1 Theoretical Background.** Many publications consider the prediction of rotordynamic coefficients for TPJBs. Equation (1) is a widely accepted force-displacement model for a bearing.

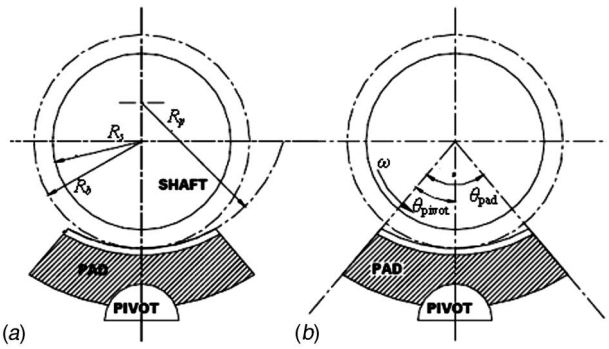


**Fig. 2 (*a*) Radial and (*b*) angular geometrical parameters of the TPJB [5]**

$$-\begin{bmatrix} f_{bx} \\ f_{by} \end{bmatrix} = \begin{bmatrix} K_{xx} & K_{xy} \\ K_{yx} & K_{yy} \end{bmatrix}\begin{bmatrix} \Delta x \\ \Delta y \end{bmatrix} + \begin{bmatrix} C_{xx} & C_{xy} \\ C_{yx} & C_{yy} \end{bmatrix}\begin{bmatrix} \Delta \dot{x} \\ \Delta \dot{y} \end{bmatrix} + \begin{bmatrix} M_{xx} & M_{xy} \\ M_{yx} & M_{yy} \end{bmatrix} \times \begin{bmatrix} \Delta \ddot{x} \\ \Delta \ddot{y} \end{bmatrix} \tag{1}$$

Here, $\Delta x$ and $\Delta y$ define the relative motion between the rotor and the stator. Equation (1) is a "[M]-[C]-[K]" model. Many analysts use only stiffness and damping terms, producing a "[C]-[K]" model.

Lund [1] provided the first predictions for TPJBs in 1964, using the *pad assembly method* that calculates the gradient of the fluid force for each pad independently and makes a summation of the results over all the pads to obtain their net effect. This method produces frequency-independent stiffness and damping coefficients since it neglects fluid inertia while assuming that the pad precession frequency is synchronous with the journal running speed. A 1975 study by Reinhardt and Lund [6] showed that convective and temporal fluid inertia terms can become significant at Reynolds numbers (Re) as low as 100. Inclusion of these terms causes the predicted stiffness coefficients to decrease with increasing frequency, which can be modeled as a frequency-independent added-mass coefficients as shown in Eq. (1).

Parsell et al. [5] extended Lund's original model to include nonsynchronous excitation frequencies. Lund's method requires assumption of a pad rotational frequency to reduce the equations of motion from $(2+N_{\text{pad}})$ to two degrees of freedom. By assuming a range of frequencies (including synchronous), Parsell et al. showed that this "model reduction" imposes a quadratic decrease in stiffness and an increase in damping with increasing excitation frequency.

Neither Lund [1] nor Parsell et al. [5] considered translation pad motion. However, Kirk and Reedy [7] and Childs [8] arrived at identical equations for equivalent stiffness and damping of a support spring with stiffness $K_p$ in series with a parallel combination of film stiffness $K$ and damping $C$ of a single pad. To show the effect of the zeroth and second order frequency terms on the equivalent stiffness and damping ($K_{\text{eq}}, C_{\text{eq}}$), Childs calculated a Taylor series expansion about excitation frequency $\Omega=0$ as follows:

$$K_{\text{eq}}(\Omega) = \frac{KK_p}{K+K_p} + \frac{K_p^2 C^2}{(K+K_p)^3}\Omega^2 + O(\Omega^4)$$
$$C_{\text{eq}}(\Omega) = \frac{CK_p^2}{(K+K_p)^2} - \frac{C^3 K_p^2}{(K+K_p)^4}\Omega^2 + O(\Omega^4) \tag{2}$$

Equation (2) predicts that inclusion of pivot stiffness in a TPJB model has four main effects, which become more pronounced as pivot stiffness decreases: (i) a decrease in the zero-frequency stiffness value, (ii) an increase in stiffness proportional (primarily) to the square of excitation frequency, (iii) a decrease in the zero-frequency damping value, and (iv) a decrease in damping proportional (primarily) to the square of excitation frequency.

Kirk and Reedy [7] provided formulas for predictions of pivot stiffness for several pivot types, based on Hertzian contact stress formulation. When Nicholas and Wygant [2] applied these formulas to correct calculated results for a TPJB with sphere-in-cylinder pivots, a 56% decrease in stiffness and an 82% decrease in damping are predicted.

**1.2 Experimental Background.** In 1999, Wygant et al. [9,10] tested two five-pad TPJBs with $L/D=0.75$, 0.50 offset ratio, 113.0 $\mu$m (4.45 mils) radial clearance, 0.320 preload, and 70 mm (2.76 in.) diameter. One bearing had a rocker-back pivot design while the other had a ball-in-socket design. Test speeds ranged from 900 rpm to 2250 rpm. Unit loads, directed on the pivot, ranged from 60.7 kPa to 727 kPa (8.80–105 psi). Synchronous frequency excitations of 15 Hz, 27.5 Hz, and 37.5 Hz were used to

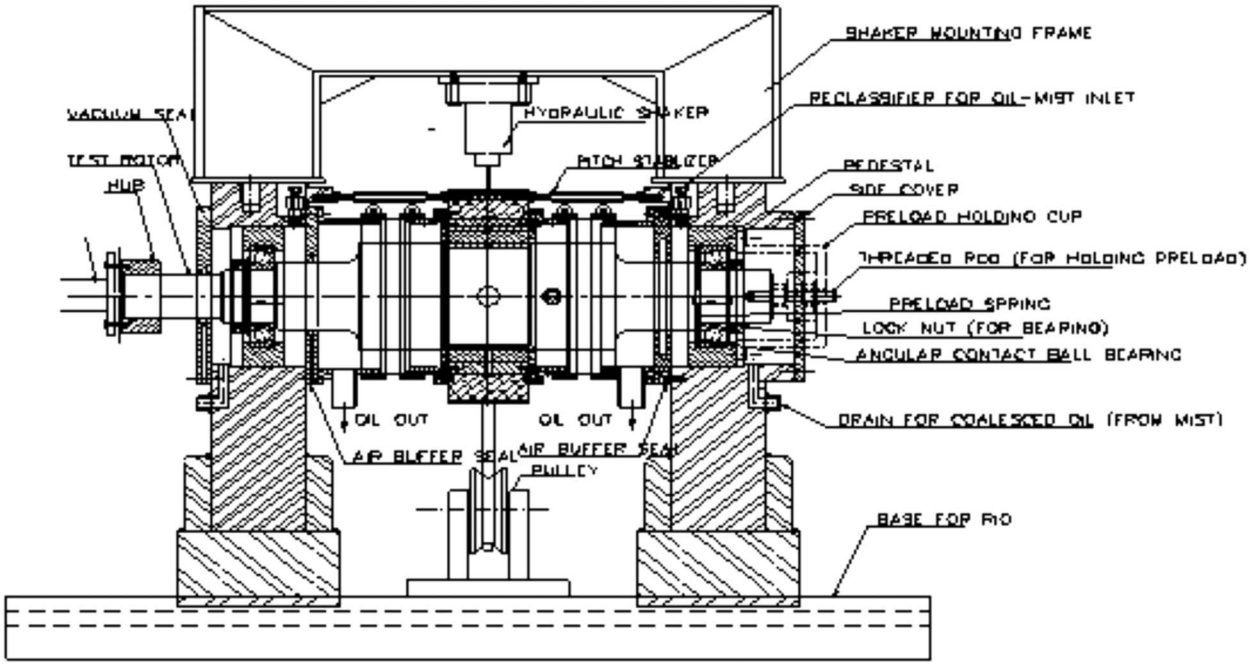


**Fig. 3 Main test section of test rig**

extract dynamic coefficients. While roughly zero cross-coupled stiffnesses were found for the rocker-back design, significant values were found for the ball-in-socket design. The uncertainty in the cross-coupled stiffness measurements ranged from 25% to 270%, but they were typically much less than the range of measured values. Wygant suggested that there should be a much larger friction coefficient for sliding motion of the ball-in-socket pivot (0.4) than for the nominal rolling without slipping of the rocker-back pivot (0.006) and attributes the added cross-coupled stiffness to this difference. If generally confirmed, this "locking up" condition could be a drawback of ball-in-socket pivot designs.

In 2007, Dmochowski [11] obtained the dynamic properties for a five-pad rocker-back pivot TPJB in load-between-pad (LBP) configuration. The bearing had $D=98.5$ mm (3.88 in.), $L/D=0.4$, and an applied load of 4.0 kN (900 lb), netting a bearing unit load of 1.03 MPa (149 psi). The bearing had a 0.3 preload factor and shaft speed was 9000 rpm. Dynamic coefficients for frequencies ranging from 0 Hz to 300 Hz were obtained using the power spectral density method, described in Ref. [12] by Rouvas and Childs. Stiffness terms were approximately constant versus frequency until they began to decrease at the synchronous frequency (150 Hz). The direct damping terms were generally constant and frequency independent.

In 2005, Al-Ghasem and Childs [13] reported test results for a FP-TPJB bearing in LBP configuration with $D=116.8$ mm (4.6 in.) using the test rig described Sec. 2. The bearing was tested at speeds from 4000 rpm to 12,000 rpm and excited at frequencies of up to 300 Hz. The results were compared with theoretical predictions from a bulk-flow Navier–Stokes (NS) model, based on Ref. [14]. The computer code can use either the NS or Reynolds equation (user's choice) and can also use either isothermal or adiabatic conditions for the fluid between the journal and the bearing. It does not account for pivot flexibility but does produce frequency-dependent results due to the inclusion of pad and fluid inertia and (primarily) elimination of the pads' rotational degrees of freedom from the model. The measured real parts of the direct dynamic-stiffness coefficients decreased with excitation frequency as predicted by both the NS and Reynolds models. Measured results were effectively modeled with a frequency-independent mass-spring-damper [M]-[C]-[K] form as opposed to a frequency-dependent spring-damper [C]-[K] form. The decrease in the direct dynamic-stiffness coefficients with excitation frequency produced effective added-mass terms of approximately 32 kg.

In 2006, Rodriguez and Childs [15] reported test results for the same bearing in load-on-pad (LOP) configuration. Similar results were found, with direct added masses around 40 kg. Measured frequency-dependent characteristics for the real direct dynamic-stiffness coefficients produced added-mass coefficients and were well predicted using either the Reynolds equation or the NS solution for frequencies of up to $1x$. Both the NS and the Reynolds equation models began to modestly diverge from measurements above $1x$, predicting lower added-mass terms than measured. However, the NS model predicted the decrease in direct dynamic-stiffness coefficients at frequencies above the $1x$ frequency more accurately, presumably because it accounts for fluid inertia terms.

In 2007, Carter [16] used the same rig to test a five-pad rocker-back TPJB in both LOP and LBP configurations. The bearing and rotor had the following geometrical parameters: 0.282 preload, 60% offset, 57.9 deg pad arc angle, 101.587 mm (3.9995 in.) rotor diameter, 0.1575 (0.0062 in.) diametrical clearance, and 60.325 mm (2.375 in.) axial pad length. This bearing had directed lubrication and spray blockers. Static and dynamic characteristics were reported at speeds from 4000 rpm to 13,000 rpm and loads from 345 kPa to 3101 kPa (50–450 psi). Direct stiffnesses were slightly overpredicted and generally showed a linear increase with load with a (modestly) higher degree of orthotropy in LOP configuration. The cross-coupled stiffnesses were generally less than 10% of their direct counterparts and had opposite signs only in LBP configuration at high speeds. Added-mass terms increased with speed and were as high as 60 kg. They were typically higher in the loaded direction and were overpredicted at high speeds and underpredicted at low speeds. Negative added mass was measured—but not predicted—at 4000 rpm. Direct damping did not vary appreciably with speed or load and was consequently (greatly) overpredicted at low speeds and high loads.

## 2 Test Facility Description

Figure 3 illustrates the test rig that was originally designed by

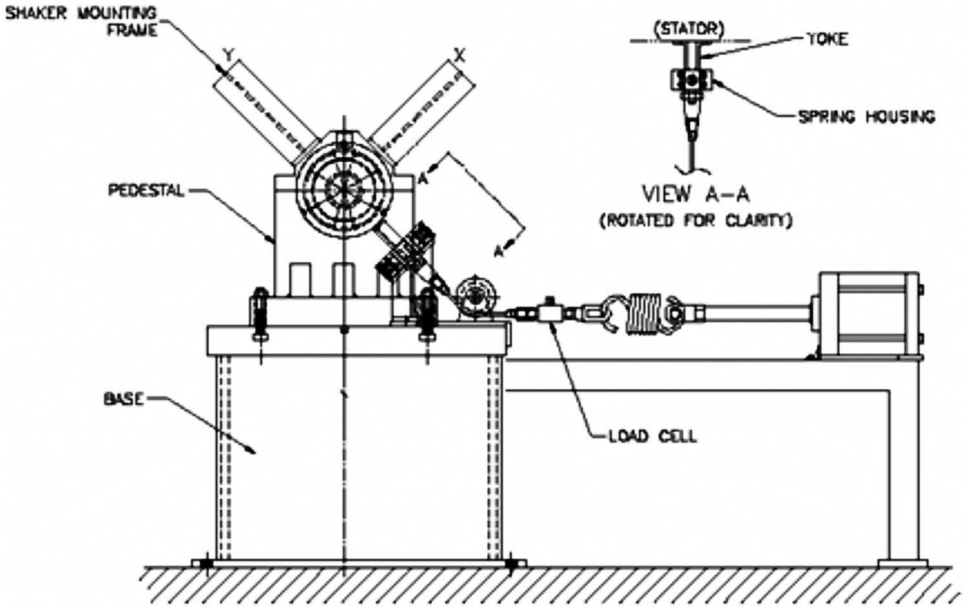


**Fig. 4 Static loader configuration**

Kaul [17] for oil seals and has been modified for testing hydrodynamic bearings.

The rotor is supported by two pedestals spaced approximately 381 mm (15 in.) apart, where it sits on two ball bearings. An oil-mist system supplies lubricant to the ball bearings during operation. An air turbine is coupled to the rotor by a high-speed flexible coupling, and it can provide 65 kW (90 hp) to drive the rotor up to 17,000 rpm. The rotor diameter is measured at 101.587 mm (3.9995 in.).

The stator houses the bearing and the noncontacting eddy current proximity probes that measure the relative stator-to-rotor position in two orthogonal directions at two planes. The planes are located orthogonally to the rotor's axis at the drive end (DE) and nondrive end (NDE). The absolute stator acceleration is measured with piezoelectric accelerometers, which are also located in the stator. Figure 4 shows the static loader assembly as viewed from the NDE of the test rig. The static loader has a 20 kN (4500 lb) capacity.

Shaft speed is measured with a tachometer at the NDE, and inlet/outlet pressure and temperature to the bearing are measured with probes attached to the stator. The shakers can provide dynamic forces with amplitudes approaching 4400 N (1000 lb) at excitation frequencies up to 1 kHz. Figure 5 shows the shaker-stinger configuration as viewed from the NDE.

## 3 Rotordynamic Coefficient Identification

Childs and Hale [18] explained how the rotordynamic coefficients are estimated from the measurements. The following discussion describes how this method was utilized to obtain the coefficients presented in this paper. The equations of motion for the stator mass $M_s$ are given in Eq. (3), where $\ddot{x}_s$, $\ddot{y}_s$ are the stator accelerations components; $f_x$,$f_y$ are the force components induced by the hydraulic shakers; and $f_{bx}$, $f_{by}$ are the bearing reaction force components. $M_s$ is obtained by simply weighing the entire bearing and accompanying instrumentation housing (including the mass of the pads). A very comparable $M_s$ value is obtained from the curvature of the real direct dynamic-stiffness coefficients $\boldsymbol{H}_{ii}$ in the dry-shake mode. The housing assembly is treated as a rigid body, neglecting the relative motion of the pads. This simplification is based on the assumption that the pad natural frequencies are significantly higher than the excitation frequencies. We see no evidence in our tests that the relative pad motion has any perceptible influence on housing acceleration measurements.

$$M_s\begin{bmatrix}\ddot{x}_s\\ \ddot{y}_s\end{bmatrix}=\begin{bmatrix}f_x\\ f_y\end{bmatrix}-\begin{bmatrix}f_{bx}\\ f_{by}\end{bmatrix} \tag{3}$$

Substituting Eq. (1) into Eq. (3) and applying an FFT nets

$$\begin{bmatrix}\boldsymbol{F}_x-M_s\boldsymbol{A}_x\\ \boldsymbol{F}_y-M_s\boldsymbol{A}_y\end{bmatrix}=-\begin{bmatrix}\boldsymbol{H}_{xx} & \boldsymbol{H}_{xy}\\ \boldsymbol{H}_{yx} & \boldsymbol{H}_{yy}\end{bmatrix}\begin{bmatrix}\boldsymbol{D}_x\\ \boldsymbol{D}_y\end{bmatrix} \tag{4}$$

$\boldsymbol{D}_i$ denotes the Fourier transform of the measured displacements in the $i$ direction. $\boldsymbol{H}_{ij}$ coefficients are the direct and cross-coupled dynamic-stiffness coefficients for the bearing. $\boldsymbol{F}_i$ and $\boldsymbol{A}_i$ are the complex Fourier transformed values for the measured force and acceleration components, respectively. The four dynamic-stiffness coefficients $\boldsymbol{H}_{ij}$ in Eq. (4) are the unknowns, but there are only

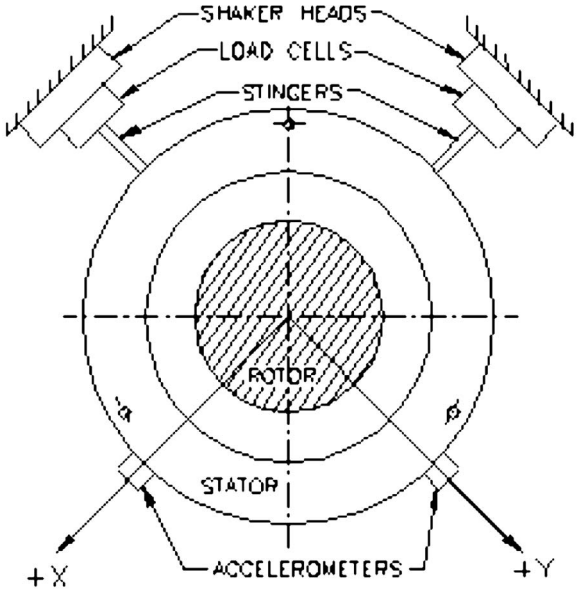


**Fig. 5 Shaker-stinger configuration, viewed from NDE**

two equations. Independent excitation in the $x$ and $y$ directions produces the following four independent equations:

$$\begin{bmatrix} \boldsymbol{F}_{xx} - M_s\boldsymbol{A}_{xx} & \boldsymbol{F}_{xy} - M_s\boldsymbol{A}_{xy} \\ \boldsymbol{F}_{yx} - M_s\boldsymbol{A}_{yx} & \boldsymbol{F}_{yy} - M_s\boldsymbol{A}_{yy} \end{bmatrix} = -\begin{bmatrix} \boldsymbol{H}_{xx} & \boldsymbol{H}_{xy} \\ \boldsymbol{H}_{yx} & \boldsymbol{H}_{yy} \end{bmatrix}\begin{bmatrix} \boldsymbol{D}_{xx} & \boldsymbol{D}_{xy} \\ \boldsymbol{D}_{yx} & \boldsymbol{D}_{yy} \end{bmatrix} \tag{5}$$

The stator was shaken alternately in the $x$ and $y$ directions with a force-versus-time waveform containing components with discrete frequency values ranging from 20 Hz to 260 Hz at intervals of 10 Hz, repeated 32 times with averaging in the frequency domain. Relationships between the dynamic-stiffness $\boldsymbol{H}_{ij}$ coefficients and the rotordynamic coefficients are as follows:

$$\boldsymbol{H}_{ij} = (K_{ij} - \Omega^2 M_{ij}) + \boldsymbol{j}(\Omega C_{ij})$$
$$\mathrm{Re}(\boldsymbol{H}_{ij}) = K_{ij} - \Omega^2 M_{ij}, \quad \mathrm{Im}(\boldsymbol{H}_{ij}) = \Omega C_{ij} \tag{6}$$

where $\Omega$ is the excitation frequency and $\boldsymbol{j} = \sqrt{-1}$. The stator was shaken ten times in each direction, and values for $\boldsymbol{H}_{ij}$ at each of the 25 discrete frequencies were calculated, using Eq. (5). These values were averaged over the ten shakes to produce plots of the real and imaginary parts of dynamic stiffness versus frequency with known uncertainties at each point. The plots were then fit to quadratic and linear curves for the real and imaginary parts, respectively, as in Eq. (6), to determine the rotordynamic coefficients. Error values were based on the correlation of the curve-fits to experimental data.

In many cases, Eq. (6) did not fit the real and/or imaginary parts of the dynamic-stiffness coefficients. For $\mathrm{Re}(\boldsymbol{H}_{ij})$, this could be remedied by dropping the added-mass term and assuming

$$\mathrm{Re}(\boldsymbol{H}_{ij}) = K_{ij} \tag{7}$$

Here, the reported value of $K_{ij}$ is the mean of $\mathrm{Re}(\boldsymbol{H}_{ij})$ over the range of test frequencies, and the error in $K_{ij}$ is proportional to the sample standard deviation. If $\mathrm{Im}(\boldsymbol{H}_{ij})$ could not be fit by a linear regression within a reasonable margin of error, the corresponding damping coefficient was not reported.

## 4 Test Bearing

The test bearing is a four-pad TPJB with ball-in-socket type pivots. The pads are made from C18200 chromium-copper alloy with a Babbitt metal lining. The bearing's parameters are given in Table 1.

The bearing uses patented Spray-Bar Blockers® and By-Pass Cooling®, described by Nicholas in Ref. [19]. These technologies aim to increase load capacity and stability by keeping the oil temperature as close to the inlet temperature as possible. In a conventional "flooded" bearing, hot oil carried over from upstream pads flows onto downstream pads such that the oil temperature increases from pad to pad. Spray-bar blockers reduce this development by blocking hot oil carryover from the upstream pad while spraying cool inlet oil onto the downstream pads. By-pass cooling uses circumferential cooling chambers that direct cool inlet oil through the outside of the pad, cooling the pad metal and decreasing thermal deformation and degradation as well as assisting oil-film cooling on the pad.

The bearing was tested at 1.0 l/s (16 gpm) at 97 kPa (14 psi). The load and speed conditions are summarized in Table 2. "**s**" denotes a test point at which steady state operating characteristics (static data) were collected while "**d**" denotes a test point at which rotordynamic coefficients (dynamic data) were collected. Static data include journal position (expressed as eccentricities about both axes and an attitude angle), estimated power loss, and trailing-edge pad temperatures. Dynamic data include the direct and cross-coupled added masses, stiffnesses, and damping coefficients in the loaded and unloaded direction.

**Table 1 Test bearing parameters**

| | |
|---|---|
| Number of pads | 4 |
| Configuration | LBP |
| Pad arc angle | 73 deg |
| Pivot offset | 65% |
| Rotor diameter | $101.59 \pm 0.01$ mm ($3.9995 \pm 0.0005$ in.) |
| Pad axial length | $101.60 \pm 0.03$ mm ($4.000 \pm 0.001$ in.) |
| Manufacturer-reported radial bearing clearance ($C_b$) | 95.3 $\mu$m (3.75 mils) |
| Radial bearing clearance about $x'$ axis ($C_b$), measured | $99.6 \pm 0.2$ $\mu$m ($3.92 \pm 0.01$ mils) |
| Radial bearing clearance about $y'$ axis ($C_b$), measured | $54.6 \pm 4.5$ $\mu$m ($2.15 \pm 0.18$ mils) |
| Mean loaded pad preload | 0.37 |
| Mean unloaded pad preload | 0.58 |
| Ball radius of curvature (design) | $3.175 + 0.0008 - 0$ cm($1.25 + 0.0003 - 0$ in.) |
| Ball material | 4140 Rc 52 steel w/12L14 steel support shim |
| Socket radius of curvature (design) | $3.175 \pm 0.013$ cm ($1.25 + 0.005$ in.) |
| Socket material | Bronze |
| Lubricant type | ISO VG32 |

## 5 Prediction Model

XLTFPBRG™, a program developed under the direction of Luis San Andrés at Texas A&M University and based on the theoretical model described in Ref. [14], was used to predict the values measured in this study. Although Ref. [14] describes the analysis in terms of the bulk-flow NS equation, the user can also utilize the Reynolds equation. A CFD control-volume algorithm is used to solve the bulk-flow NS equations, and a perturbation analysis is applied to determine the rotordynamic coefficients.

Pad rotations are included as degrees of freedom, yielding $2(4+5N_{\mathrm{pad}})$ total stiffness and damping coefficients. For a specified excitation frequency, the code relates the rotational motion of the pads to translational motion of the shaft and hence, to the bearing forces in the horizontal and vertical directions. This approach eliminates pad rotational degrees of freedom from the bearing-force model, producing eight total reduced stiffness and damping coefficients. Multiple frequencies equal to the excitation frequencies used in testing were input at each load-speed condition. The code does not model the effect of pivot stiffness, but a direct measurement of the entire "pad support structure" stiffness was placed in series with the predicted stiffnesses and damping coefficients using only the zeroth order terms in Eq. (2).

## 6 Measurement of Pad Support Structure Stiffness

While the experimenters were not capable of measuring the pivot stiffness directly, the net stiffness of the pad support structure was measured. The pad support structure includes all elements from the top of the pad to the base of the pivot, including the pad and Babbitt layer, the contact area between the rotor and pad, the ball-in-socket pivot (Hertzian contact area), and the support shims for the ball and socket inserts. Though the addition of elements other than the pivot act to decrease the net stiffness since they are in series with the pivot, the experimenters presume that these elements are significantly stiffer than the pivot and the measured value should only be slightly lower than the pivot stiffness.

The bearing was positioned in the test rig such that the static load acted directly on pivot 4 of Fig. 7. Without rotation or oil flow—and at ambient temperature—pad 4 was pulled into contact with the rotor, and the static load was incrementally increased while recording load and deflection data from the static loader's

**Table 2 Load and speed conditions for test bearing**

| Rotational speed (rpm) | Bearing unit load, kPa (psi) | | | | | | |
|---|---|---|---|---|---|---|---|
| | 0 (0) | 345 (50) | 689 (100) | 1034 (150) | 1379 (200) | 1724 (250) | 1896 (275) |
| 4,000 | s,d | s | s,d | s | s,d | s | s,d |
| 6,000 | s,d | s | s,d | s | s,d | s | s,d |
| 8,000 | s,d | s | s,d | s | s,d | s | s,d |
| 10,000 | s,d | s | s,d | s | s,d | s | s,d |
| 12,000 | s,d | s | s,d | s | s,d | s | s,d |

load cell and the proximity probes. During the procedure, the $y$ direction stinger was disengaged while the $x$ direction stinger was used to statically stabilize the load atop pivot 4.

Although a nonlinear relation between load and deflection was expected from the formulas of Kirk and Reedy [7], the load versus deflection values had a high degree of linear correlation. A linear regression of the data was performed, yielding a $r^2$ value of 0.9995 and the following value for pad support structure stiffness $K_{ps}$:

$$K_{ps} = 350 \pm 13 \ \text{MN/m} = 2000 \pm 75 \ \text{lb/mils} \tag{8}$$

## 7 Stiffness-in-Series Correction of Direct Stiffness and Damping

Since the user of XLTFPBRG™ does not have access to the individual reduced stiffness and damping coefficients of each pad, a definition of "effective pad support structure stiffness" was required in order to analyze the effect of the measured pad support structure stiffness on the equivalent bearing stiffness and damping coefficients. Static and dynamic loads were directed at roughly a 45 deg angle to each pad for static and dynamic testings. In the free-body diagram of Fig. 6, it can be shown that the springs (representing the pivot) will deflect a distance $(\sqrt{2}/2)\delta_r$, where $\delta_r$ is the rotor deflection due to a static force $F$ on the rotor. Also, since the component of the spring reaction force in the axis of the force $F$ is $(\sqrt{2}/2)[(\sqrt{2}/2)K_{ps}\delta_r]$, a net contribution of $2K_{ps}\delta_r$ is required for static equilibrium.

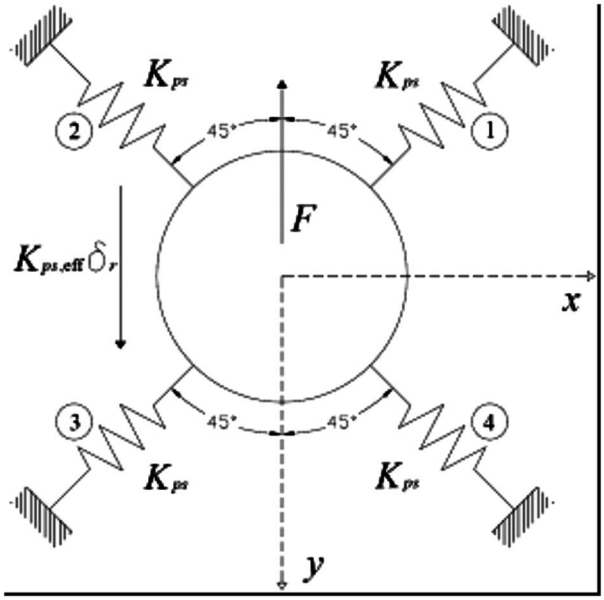


**Fig. 6 Free-body-diagram of rotor connected to pad support structure "springs"**

Extending the static solution to dynamic excitation, the effective value for pad support structure stiffness to be placed in series with the total bearing stiffness and damping is simply $2K_{ps}$.

$$K_{ps,eff} = 2K_{ps} = 700 \ \text{MN/m} = 4000 \ \text{lb/mil} \tag{9}$$

Since the predicted cross-coupled stiffness coefficients for TPJBs are small, accounting for stiffness-in-series has a negligible effect on them. Accordingly, the modification is only applied to the direct stiffness and damping coefficients. Making the substitutions $K \rightarrow K_{ii}$, $K_{eq} \rightarrow K_{ii,eq}$, $C \rightarrow C_{ii}$, $C_{eq} \rightarrow C_{ii,eq}$, $K_p \rightarrow K_{ps,eff}$, the following modification are applied to the predicted values:

$$K_{ii,eq} = \frac{K_{ii}K_{ps,eff}}{K_{ii} + K_{ps,eff}}, \quad C_{ii,eq} = \frac{C_{ii}K_{ps,eff}^2}{(K_{ii} + K_{ps,eff})^2} \tag{10}$$

## 8 Static Performance Characteristics

The static journal position was measured relative to the center of the bearing clearance using the coordinate system shown in Fig. 7. Pads 2–4 and pads 1–3, bearing diametrical clearances, were measured along the $x'$ and $y'$ axes, respectively, with the proximity probes via a "contact" test. The hydraulic shakers were used to push and pull the bearing until rotor contact was established. As shown in Table 1, measured clearances along the $x'$ and $y'$ axes differed significantly. Since the computer model only accepts the same bearing clearance for all pads, the average clearance of 77.1 $\mu$m (3.04 mils) was used for predictions. Eccentricity ratios were not defined in this study due to the large difference in clearance values about the pivot axes.

Figure 8 provides a generally representative comparison between measured and predicted locus plots (eccentricity $e_x$ versus $e_y$). The "bearing clearance" represented by the black line in the figure is based on the definitions $C_x = C_{y'}$ and $C_y = C_{x'}$ because, if the pad preload is disregarded and the pad are not tilted, the dia-

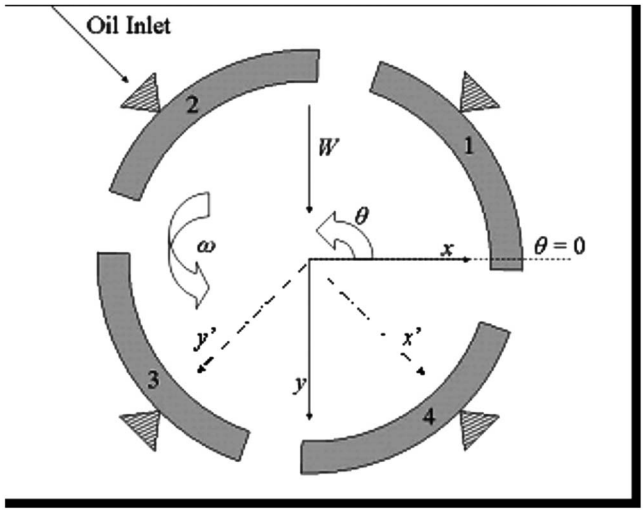


**Fig. 7 Bearing coordinate system**

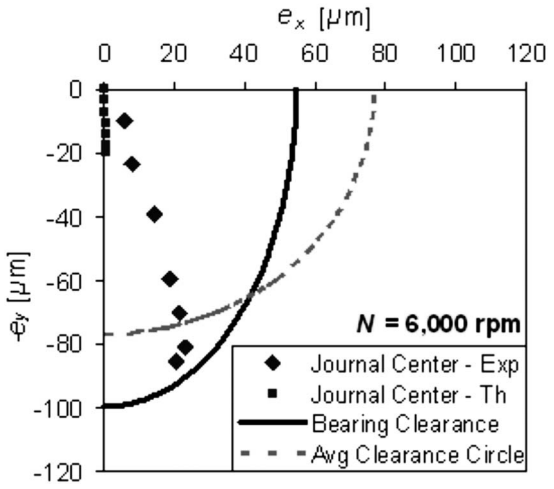


**Fig. 8 Bearing centerline locus plot (eccentricity) at 6000 rpm**

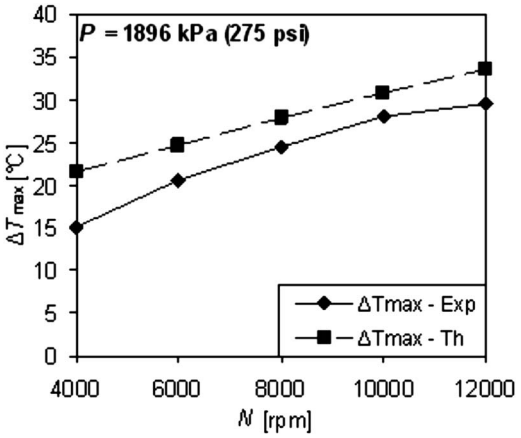


**Fig. 10 Maximum bearing temperature increase at 1896 kPa (275 psi)**

metrical clearance between pads 1 and 3 about the $x$ axis is taken as the measured diametrical clearance about the $y'$ axis while that between pads 2 and 4 about the $y$ axis is taken as the measured diametrical clearance about the $x'$ axis.

Figure 8 shows that eccentricities were substantially underpredicted. At 4000 rpm, the measured eccentricities were outside of the defined bearing clearance ellipse. However, note that (i) the pads are allowed to tilt, (ii) the pad clearance is greater than the bearing clearance at locations away from the pivot, and (iii) the pads and (more notably) the pivots will deflect under load. All three of these factors act to increase the clearance space about the location of the journal center. In fact, according to the measured pad support structure stiffness, the maximum load of 19.6 kN (4400 lb) would increase the clearance of the loaded pads about the pivot axes by 39.1 $\mu$m (1.54 mils), which is a substantial fraction of the measured clearances.

Attitude angles were also generally underpredicted. Predicted values were typically 2 deg or less while measured values were normally 30–39 deg at low loads and then "leveled out" to 6–20 deg at high loads.

Power loss, based on inlet and outlet oil temperatures and assuming all heat was carried away by the fluid, showed negligible load-dependence and a high speed-dependence, both in measurement and predictions. Figure 9 shows power loss versus speed at the highest load, 1896 kPa (275 psi). The maximum value is roughly 25 kW (34 hp). Power loss was underpredicted as much as 50% at low speeds, but exceptionally well predicted at high speeds.

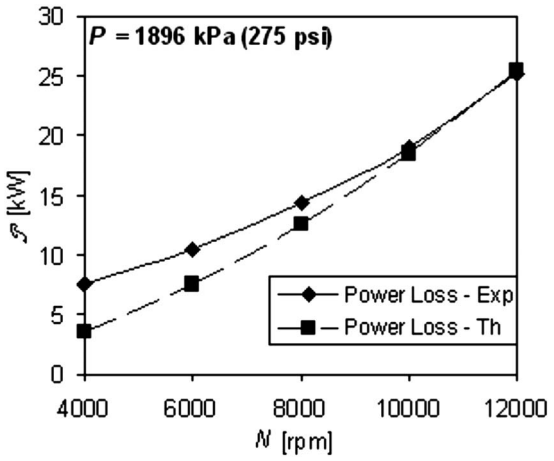


**Fig. 9 Power loss at 1896 kPa (275 psi)**

Two thermocouples at identical circumferential locations and centered axial locations were positioned near the trailing edge of each pad (68 deg), near the expected maximum fluid film temperature. Predicted and measured maximum temperature increases are plotted in Fig. 10 at the highest load. "Maximum temperature rise" is the increase from inlet temperature to maximum bearing temperature. Maximum temperature increase, as opposed to maximum bearing temperature, was plotted since, during testing, there was roughly a 10% variation in the nominal oil temperature control loop, leaving an inlet temperature between 38–43°C (100–110°F). Assuming a constant 38°C inlet temperature, the maximum temperature increase had a trend that was well predicted but values that were overpredicted by 10–40%. Under the said conditions, the maximum trailing-edge pad temperature detected during testing was 71°C (160°F).

## 9 Rotordynamic Coefficients

Figure 11 shows measured and predicted values of the dynamic-stiffness coefficients. $\boldsymbol{H}_{ii}$ and $\boldsymbol{H}_{ik}$ denote direct and cross-coupled coefficients, respectively. The bars in these figures represent twice the sample standard deviation of ten separate tests. The dynamic-stiffnesses were curve-fitted to the quadratic or linear models (Eq. (6)) if the uncertainty of the slope (added mass or damping) was 35% or less. This normally corresponded to $r^2 \geq 0.7$. But this was rarely the case for $\mathrm{Im}(\boldsymbol{H}_{xy})$, $\mathrm{Im}(\boldsymbol{H}_{yx})$; in most cases, these coefficients were not reported due to poor linear correlation. In slightly less than half of the cases for $\mathrm{Re}(\boldsymbol{H}_{xx})$, $\mathrm{Re}(\boldsymbol{H}_{yy})$ and most of the cases for $\mathrm{Re}(\boldsymbol{H}_{xy})$, $\mathrm{Re}(\boldsymbol{H}_{yx})$, the added-mass coefficients were dropped and the stiffness was defined as the average of $\mathrm{Re}(\boldsymbol{H}_{ij})$. $\mathrm{Im}(\boldsymbol{H}_{xx})$, $\mathrm{Im}(\boldsymbol{H}_{yy})$ were modeled very well by a linear regression, with $r^2$ values averaging 0.96. Also, note that the predicted direct dynamic-stiffness coefficients are much larger than the measured values.

Figure 12 shows the direct stiffness coefficients at each unit load versus speed. These coefficients are only load-dependent at low speeds, where they increase modestly with load. Similarly, they are only speed-dependent at low loads, increasing modestly with speed. It is clear that the simple stiffness-in-series correction (denoted as "Mod Th" in the legend) markedly improves agreement between theory and experiment. Uncertainty in direct stiffness was low, averaging only 2%.

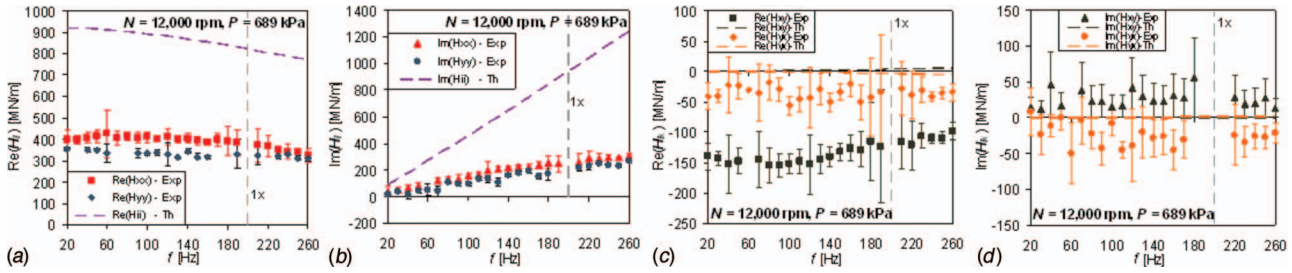


**Fig. 11 Dynamic stiffness coefficients: (*a*) Re($H_{ii}$), (*b*) Im($H_{ii}$), (*c*) Re($H_{iik}$), (*d*) Im($H_{ik}$), and at 12,000 rpm, 689 kPa (100 psi)**

Figures 13 and 14 shows the direct damping coefficients at each unit load versus speed. They showed negligible load-dependence, but dropped modestly with speed. As with the direct stiffness coefficients, the stiffness-in-series modification substantially improved theory-to-prediction agreement. However, the damping is still overpredicted by up to a factor of 2 at low speeds. Uncertainty in the direct damping coefficients was 10% on average.

Figure 15 shows the direct added-mass coefficients, in the cases that they were retained in the model, versus speed. Note that there are cases where these coefficients are negative, indicating a bearing that stiffens with increasing frequency. $M_{xx}$ is typically the higher of the coefficients and they both increase with speed. Theory overpredicts both of these coefficients and does not predict negative added masses. The average uncertainty in direct added mass was 25%.

Figure 16(*a*) shows the cross-coupled stiffness coefficients versus unit load at 6000 rpm. They were neither generally load-dependent nor speed-dependent. They had magnitudes around 35% and 15% of the direct coefficients for $K_{xy}$ and $K_{yx}$, respectively, but always had the same sign, which has no impact on stability. Figures 16(*b*) and 16(*c*)show the cross-coupled added-mass coefficients for most of the cases that they could be retained in the model. This typically only occurred at maximum speed or zero load. While the negative cross-coupled added masses caused

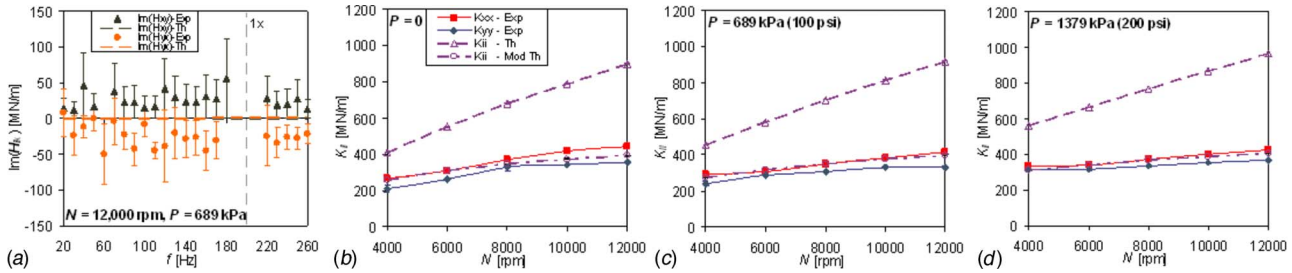


**Fig. 12 $K_{xx}$ and $K_{yy}$ versus speed at (*a*) 0 kPa, (*b*) 689 kPa, (*c*) 1379 kPa, and (*d*) 1896 kPa**

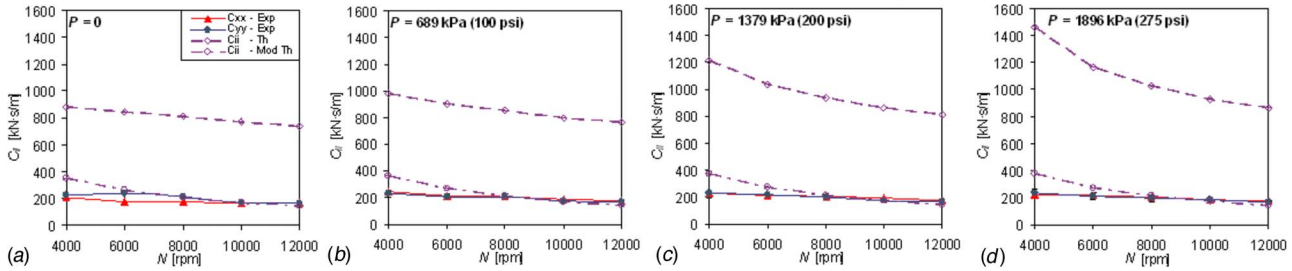


**Fig. 13 $C_{xx}$ and $C_{yy}$ versus speed at (*a*) 0 kPa, (*b*) 689 kPa, (*c*) 1379 kPa, and (*d*) 1896 kPa**

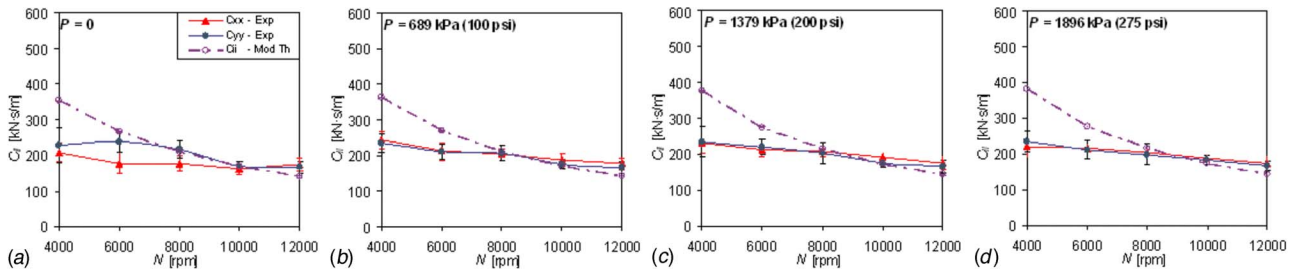


**Fig. 14 $C_{xx}$ and $C_{yy}$ versus speed at (*a*) 0 kPa, (*b*) 689 kPa, (*c*) 1379 kPa, and (*d*) 1896 kPa, with vertical axis zoomed in**

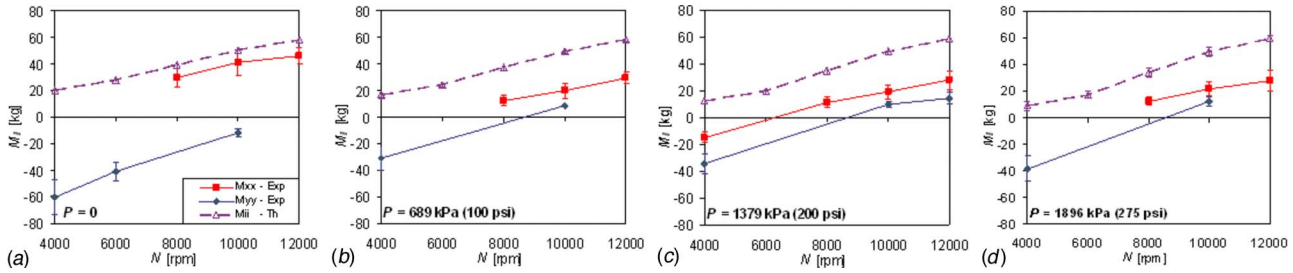


**Fig. 15** $M_{xx}$ **and** $M_{yy}$ **versus speed at (*a*) 0 kPa, (*b*) 689 kPa, (*c*) 1379 kPa, and (*d*) 1896 kPa**

the corresponding dynamic-stiffness curves to trend toward the zero axis (which would make $\mathrm{Re}(\boldsymbol{H}_{xy})$, $\mathrm{Re}(\boldsymbol{H}_{yx})$ opposite in sign), they only became positive above $1x$ frequency.

## 10 Frequency-Dependent Damping

Although $\mathrm{Im}(\boldsymbol{H}_{xx})$, $\mathrm{Im}(\boldsymbol{H}_{yy})$ generally had high $r^2$ values for linear correlation to frequency, there is noticeable curvature in the plots of these values versus frequency when viewed on a smaller scale than in Fig. 11(*b*). Figure 17 shows these values at 12,000 rpm, 689 kPa (100 psi) with the vertical axis zoomed. This load-speed condition is representative of most others.

Using the secant definition of damping, where one assumes that the value of damping at any excitation frequency is the slope of the line connecting (0,0) to the value of $\mathrm{Im}(\boldsymbol{H}_{ig})$ at that frequency $(C_{ij}(\Omega)=\mathrm{Im}(\boldsymbol{H}_{ij})/\Omega)$, a plot of frequency-dependent damping can be deduced from the above values; this is shown in Fig. 18. While there is not a general trend in $C_{yy}(\Omega)$, $C_{xx}(\Omega)$ tends to decrease with frequency.

This is contrary to the common assumption that damping is lower at subsynchronous frequencies for TPJBs (e.g., Ref. [5]). However, one cannot conclusively claim that either curve is frequency-dependent due to high uncertainty at low frequencies.

While Fig. 18 shows subtle evidence that damping decreases with frequency, which more careful testing may corroborate, low uncertainty in the frequency-independent coefficients makes these coefficients suitable for the bearing model.

## 11 Whirl Frequency Ratio

Whirl frequency ratio (WFR) is the ratio of the natural frequency of the rotor-bearing system to the onset speed of instability and characterizes the bearing stability. Since cross-coupled added-mass terms were present, San Andrés' formula [20] was utilized. Note that while cross-coupled damping coefficients were not reported, they are needed for WFR calculations. Rough linear estimates of these coefficients were used for the WFR calculations herein, and little difference was found in using them and assuming them to be zero since these linear estimates were typically 10% or less of the direct coefficients. Both cases resulted in a zero WFR for all test conditions, implying unconditional stability.

## 12 Summary, Conclusions, and Discussion

The eccentricity is notably underpredicted, which could result from pivot flexibility. The attitude angle is also underpredicted. These results are similar to Wygant et al. [9] for the case of their ball-in-socket bearing. Pivot friction induced by the ball-in-socket pivot [2,9] could explain this outcome; however, there is no evidence of Coulomb friction in dynamic tests in terms of hysteresis, including slow cycling of the applied load.

Power loss was generally well predicted at high speeds and underpredicted by as much as 50% at low speeds. However, temperature increase from inlet to maximum bearing temperature was overpredicted by 10–40% in general, suggesting that the special design features to minimize temperature increase are effective in reducing bearing pad temperatures.

Measured dynamic-stiffness coefficients produced a frequency-independent [M]-[C]-[K] model, but many times the added-mass terms were dropped from the model. Note that frequency-independency is not an a priori requirement of the identification method. The same approach has been used extensively for hole-pattern gas annular seals where strongly frequency-dependent dynamic-stiffness coefficients are both predicted and measured [21].

At zero load, the identified $K_{xx}$ and $K_{yy}$ coefficients increase modestly with increasing speed but as load is increased, this dependency is eliminated. The direct stiffness coefficients also increase modestly with increasing load only at low speeds, with the curves flattening out as speed is increased. Carter's results [16] for a rocker-pivot design differ in that these coefficients always increased modestly with speed and briskly with increasing applied load.

Measured $C_{xx}$ and $C_{yy}$ coefficients drop slightly with increasing speed but are insensitive to changes in the applied loads, which is similar to Carter's results [16].

This bearing's striking characteristic is its pronounced flexibility as reflected by much larger measured eccentricity ratios than predicted and correspondingly lower direct stiffness coefficients. The damping coefficients are also much lower than predicted. While these coefficients were greatly overpredicted by the model (neglecting support flexibility), placing the measured pad support structure stiffness in series with the predicted bearing stiffness and

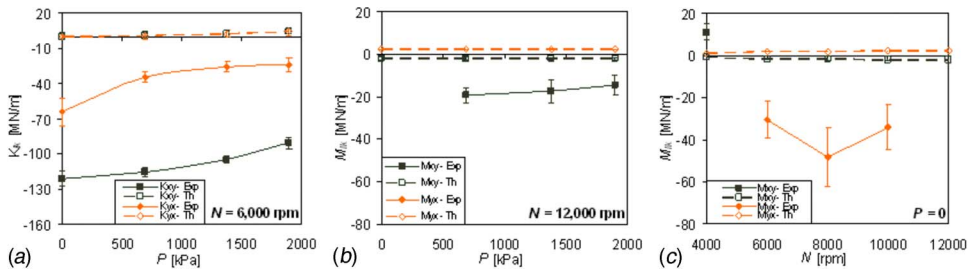


**Fig. 16** (*a*) $K_{xy}$ **and** $K_{yx}$ **at 6000 rpm, (*b*)** $M_{xy}$ **and** $M_{yx}$ **at 12,000 rpm, and (*c*)** $M_{xy}$ **and** $M_{yx}P=0$

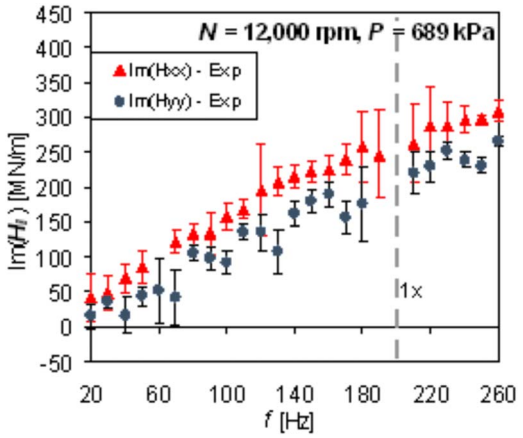


**Fig. 17 Im($H_{xx}$), Im($H_{yy}$) at 12,000 rpm, 689 kPa (100 psi) zoomed to experiment only**

damping improved the agreement profoundly. This is not an outcome that can be repeated on Carter's [16] bearing where the direct stiffness are reasonably predicted, and the damping coefficient is overpredicted at low speeds but reasonably well predicted at high speeds.

At low speeds, $M_{xx}$ and $M_{yy}$ were negative (to a higher degree for $M_{yy}$) in many cases, indicating a bearing that stiffens with increasing excitation frequency. $M_{xx}$ and $M_{yy}$ increased with increasing speed and were overpredicted by the model, which predicted all positive added masses. Carter's [16] results for a rocker-back bearing showed smaller negative added masses at the lowest speed.

Cross-coupled stiffnesses did not show a general dependence on speed or load. They were of significant magnitude, as were the results of Wygant et al. [10]. But unlike the results of Wygant et al. [10], both terms were negative, aiding stability. At maximum speed and zero load conditions, cross-coupled mass terms were negative, which could impact stability; however, the WFR was always positive.

A brisk discussion proceeds in the rotordynamic community regarding the proper way to calculate bearing coefficients for TPJBs in doing stability calculations for compressors, namely: should the coefficients be calculated for precessional motion at the running speed (synchronously reduced) or at the rotor's first natural frequency (subsynchronously reduced)? The current results repeat the results of Refs. [11–13,15,16] in measuring frequency-independent damping coefficients.

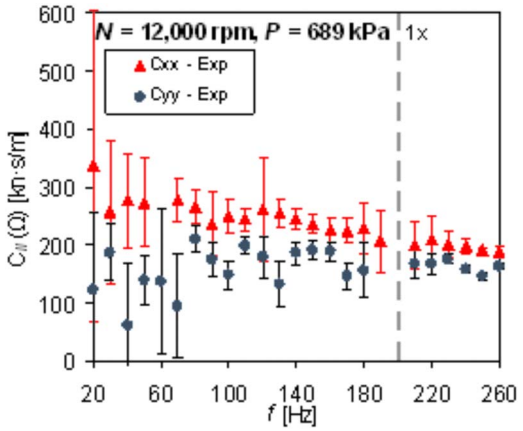


**Fig. 18 Frequency-dependent damping at 12,000 rpm, 689 kPa (100 psi)**

Subsynchronously reduced damping coefficients have historically been assumed smaller than synchronously reduced coefficients, and their advocates frequently state they have obtained better predictions of compressor stability by using the smaller coefficients. However, there is some evidence that damping way even be higher at subsynchronous frequencies. For this bearing as well as those in Refs. [11–13,15,16] direct damping can be approximated as frequency-independent within a low margin of error. A simple explanation for the conflict between (i) measurements that show frequency-independent damping coefficients, and (ii) stability-calculation requirements for lower damping values is: Damping, while approximately frequency independent, is being systematically over predicted by computer models.

## Nomenclature

$\boldsymbol{A}_{ij}$ = Fourier transforms for the measured stator acceleration; e.g., $\boldsymbol{A}_{ij}$ is the acceleration in $j$ direction, due to an excitation force in the $i$ direction $[L/T^2]$

$C$ = damping of a single pad $[M/T]$

$C_{\mathrm{eq}}$ = damping of a single pad $[M/T]$

$C_{ii,\mathrm{eq}}$ = equivalent direct bearing damping $[M/T]$

$C_{ij}$ = direct and cross-coupled damping coefficients $[M/T]$

$C_b$ = radial bearing clearance $[L]$

$C_p$ = pad radius $[L]$

$C_r$ = radial clearance $[L]$

$D$ = bearing diameter $[L]$

$\boldsymbol{D}_{ij}$ = Fourier transform for the measured stator relative motion $[L]$

$e_x$, $e_y$ = journal eccentricity components in the $x$, $y$ directions $[L]$

$F$ = static force applied to rotor $[M|L/T^2]$

$\boldsymbol{F}_{ij}$ = Fourier transforms for the measured stator force $[M|L/T^2]$

$F_s$ = static force applied by pneumatic loader $[M|L/T^2]$

$f_{bx}$, $f_{by}$ = bearing reaction force components in the $x$, $y$ directions, respectively $[M|L/T^2]$

$f_x$, $f_y$ = measured excitation force component in the $x$, $y$ directions $[M|L/T^2]$

$\boldsymbol{H}_{ij}$ = direct and cross-coupled dynamic-stiffness coefficients $[M/T^2]$

$\boldsymbol{j}$ = imaginary unit, $\sqrt{-1}$

$K$ = stiffness of a single pad $[M/T^2]$

$K_{\mathrm{eq}}$ = equivalent stiffness of a single pad $[M/T^2]$

$K_p$ = pivot stiffness $[F/L]$

$K_{\mathrm{ps}}$ = pad support structure stiffness $[M/T^2]$

$K_{\mathrm{ps,eff}}$ = effective pad support structure stiffness $[M/T^2]$

$K_{ii,\mathrm{eq}}$ = equivalent direct bearing stiffness $[M/T^2]$

$K_{ij}$ = direct and cross-coupled stiffness coefficients $[M/T^2]$

$L$ = effective bearing length (pad length for TPJB) $[L]$

$M_{ij}$ = direct and cross-coupled added-mass coefficients $[M]$

$M_p$ = preload factor

$M_s$ = stator mass $[M]$

$N$ = running speed of rotor in rpm $[1/T]$

$N_{\mathrm{pad}}$ = number of pads

$P$ = bearing unit load $(F_s/LD)$ $[M/(L|T^2)]$

$r$ = Pearson product moment correlation coefficient

$R$ = bearing radius $[L]$

$R_b$ = nominal bearing radius $[L]$

$R_p$ = pad radius $[L]$

$R_s$ = shaft radius $[L]$
Re = Reynolds number, $\rho\omega RC_r/\mu$
$\ddot{x}_s, \ddot{y}_s$ = absolute stator acceleration $[L/T^2]$
$\delta_r$ = static rotor deflection in response to force static force $F[L]$
$\Delta T_{\max}$ = maximum temperature rise (inlet to max. bearing) $[\Theta]$
$\Delta x$, $\Delta y$ = relative motion components between the rotor and the stator in the $x$, $y$ directions $[L]$
$\theta_{\text{pad}}$ = pad arc angle
$\theta_{\text{pivot}}$ = pivot angle
$\mu$ = lubricant viscosity $[M/(L|T)]$
$\rho$ = lubricant density $[M/L^3]$
$\omega$ = running speed of rotor in rad/s $[1/T]$
$\Omega$ = excitation frequency of stator in rad/s $[1/T]$

### Subscripts

$i, j$ = arbitrary coordinate directions
$x, y$ = $x$ and $y$ directions

## References


[1] Lund, J. W., 1964, "Spring and Damping Coefficients for the Tilting-Pad Journal Bearing," ASLE Trans., **7**(3), pp. 342–352.
[2] Nicholas, J. C., and Wygant, K. D., 1995, "Tilting Pad Journal Bearing Pivot Design For High Load Applications," *Proceedings of the 24th Turbomachinery Symposium*, Houston, TX, pp. 33–47.
[3] Rotech Engineering Services, 2007, "Tilting Pad Journal Bearings: Principles of Operation," http://www.rotechconsulting.com/bearings_sub2.htm.
[4] Kepple, W. E., Read, D. W., Zeidan, F. Y., Paraskevakos, C., and Dawson, M. P., 1998, "Experience in the Use of Flexure Pivot Tilt Pad Bearings in Boiler Feed Water Pumps," *Proceedings of the 15th International Pump Users Symposium*, Houston, TX, pp. 77–84.
[5] Parsell, J. K., Allaire, P. E., and Barrett, L. E., 1983, "Frequency Effects in Tilting-Pad Journal Bearing Dynamic Coefficients," ASLE Trans., **26**, pp. 222–227.
[6] Reinhardt, E., and Lund, L., 1975, "The Influence of Fluid Inertia on the Dynamic Properties of Journal Bearings," ASME J. Lubr. Technol., **97**, pp. 159–167.
[7] Kirk, R. G., and Reedy, S. W., 1988, "Evaluation of Pivot Stiffness for Typical Tilting-Pad Journal Bearing Designs," ASME J. Vib., Acoust., Stress, Reliab. Des., **110**, pp. 165–171.
[8] Childs, D., 2002, "Rotordynamics of Turbomachinery… Looking Back… Looking Forward," *Proceedings of the Sixth IFToMM International Conference on Rotordynamics*, Sydney, Australia, Sept., pp. 25–27.
[9] Wygant, K. D., Barrett, L. E., and Flack, R. D., 1999, "Influence of Pad Pivot Friction on Tilting-Pad Journal Bearing Measurements—Part I: Steady Operating Position," Tribol. Trans., **42**(1), pp. 210–215.
[10] Wygant, K. D., Barrett, L. E., and Flack, R. D., 1999, "Influence of Pad Pivot Friction on Tilting-Pad Journal Bearing Measurements—Part II: Dynamic Coefficients," Tribol. Trans., **42**(1), pp. 250–256.
[11] Dmochowski, W., 2007, "Dynamic Properties of Tilting-Pad Journal Bearings: Experimental and Theoretical Investigation of Frequency Effects Due to pivot Flexibility," J. Eng. Gas Turbines Power, **129**, pp. 865–869.
[12] Rouvas, C., and Childs, D. W., 1993, "A Parameter Identification Method for the Rotordynamic Coefficients of a High Reynolds Number Hydrostatic Bearing," ASME J. Vibr. Acoust., **115**(3), pp. 264–270.
[13] Al-Ghasem, A., and Childs, D., 2006, "Rotordynamic Coefficients; Measurements versus predictions for a High Speed Flexure-Pivot Tilting-Pad Bearing (Load-Between-Pad Configuration)," ASME J. Eng. Gas Turbines Power, **128**(4), pp. 896–906.
[14] San Andrés, L. A., 1995, "Bulk-Flow Analysis of Flexure and Tilting Pad Fluid Film Bearings," Research Progress Report to the Turbomachinery Research Consortium, Turbomachinery Laboratory, Texas A&M University, College Station, TX, Paper No. TRC-B&C-3-95.
[15] Rodriguez, L., and Childs, D., 2006, "Frequency Dependency of Measured and Predicted Rotordynamic Coefficients for a Load-on-Pad Flexible-Pivot Tilting-Pad Bearing," ASME J. Tribol., **128**, pp. 388–391.
[16] Carter, C. R., 2007, "Measured and Predicted Rotordynamic Coefficients and Static Performance of a Rocker-Pivot, Tilt Pad Bearing in Load-on-Pad and Load-Between-Pad Configurations," MS thesis, Texas A&M University, College Station, TX.
[17] Kaul, A., 1999, "Design and Development of a Test Setup for the Experimental Determination of the Rotordynamic and Leakage Characteristics of Annular Bushing Oil Seals," MS thesis, Texas A&M University, College Station, TX.
[18] Childs, D., and Hale, K., 1994, "A Test Apparatus and Facility to Identify the Rotordynamic Coefficients of High-Speed Hydrostatic Bearings," ASME J. Tribol., **116**, pp. 337–344.
[19] Nicholas, J. C., 2002, "Bearing Assembly with By-Pass Cooling," U.S. Patent No. 6,485,182.
[20] San Andrés, L. A., 1991, "Effect of Eccentricity on the Force Response of a Hybrid Bearing," STLE Tribol. Trans., **34**, pp. 537–544.
[21] Childs, D., and Wade, J., 2004, "Rotordynamic-Coefficient and Leakage Characteristics for Hole-Pattern-Stator Annular Gas Seals—Measurements Versus Predictions," ASME J. Tribol., **126**(2), pp. 326–333.

# Analysis and Customization of Rocker Arm Joint Sliding Velocity

**Bruce K. Geist**[1]
Advance Vehicle Engineering,
Chrysler LLC,
Auburn Hills, MI 48326-2757
e-mail: bg57@chrysler.com

**David Eovaldi**
Performance Parts and Motorsports Division,
Chrysler LLC,
Auburn Hills, MI 48326-2757
e-mail: dme5@chrysler.com

*This paper examines how the sliding motion between a rocker arm and a valve stem tip can be adjusted by reshaping the rocker pad surface. The valve tip is assumed flat, and the rocker arm and valve stem are assumed to lie in a common plane. It is shown that the rubbing velocity between a rocker arm and a valve stem tip, as well as the curvature of the rocker arm pad, may be determined from two features of the contact: (1) the contact point path between the rocker arm and the valve stem tip and (2) the angle that the valve stem tip makes with the line connecting the rocker pivot to the zero-lift point of contact. An algorithm is presented for determining a rocker arm surface from a prescribed contact point path and valve angle. The derived technique enables customization of rocker arm pad curvature and rocker arm joint sliding velocity.* [DOI: 10.1115/1.3078184]

## 1 Introduction

As valve train designs are required to meet the ever higher demands of the market, individual component optimization in the context of overall valve train system optimization becomes crucial to producing the required system durability and performance. Guidelines set forth by Turkish [1] have been widely used for many years to maintain a controllable sliding interface on the valve tip. As the valve lift requirements grow larger and the rocker levers get smaller for packaging and inertia considerations, the contact stress and wear in the interface can quickly exceed the material limits of the mating components. A detailed analysis of the motion at that interface facilitates better control of the velocity and load, which in turn minimizes the stress and wear at that joint.

A rocker arm joint is similar, but not identical, to a planar gear. The similarity is that two surfaces interact for the purpose of transferring motion. A rotating gear driving a translating gear (commonly called a rack) typically involves a translating surface that is *not* perpendicular to the direction of translation. A valve tip, by contrast, is presumed to move parallel to the normal vector that defines the valve tip's plane. This difference necessitates some adjustments to existing planar gear design techniques. In this paper, methodologies useful in determining surfaces for translating planar gears are adapted for rocker arm joint optimization. A new algorithm for producing a rocker pad surface from a prescribed contact point path is developed to aid in optimizing rocker arm joint design.

The discussion to follow identifies the extent to which surface adjustments can influence rocker arm sliding velocity and rocker arm curvature. First, the required theoretical perspective borrowed from Litvin and Fuentes [2] is reviewed. Our assumption is that a valve stem tip is planar and that its plane is orthogonal to valve travel within the valve train. In particular, it is shown below that sliding velocity within a rocker arm joint and the curvature of the rocker pad depend only on the contact point path and the orientation of the valve tip to the rocker arm at zero lift (specified by an angle $\alpha$). Therefore, to determine an alternative rocker arm pad shape that produces a prescribed sliding velocity pattern or satisfies prescribed curvature limits (to manage contact stress), either the contact path or valve stem angle $\alpha$ must be adjusted—there are no other choices. Once a contact point path is defined, which produces a target sliding velocity profile and/or meets curvature requirements, the surface of the rocker arm that generates such a contact pattern (and hence gives rise to a joint that has the desired sliding velocity and contact stress profile) can be determined using Algorithm 1 defined below.

## 2 Relative and Transfer Velocities

Figure 1 shows a diagram of a typical rocker arm. The analysis to follow assumes that the rocker pad cross sections parallel to the plane of the figure are identical. It is therefore sufficient to derive the shape of a single cross section since all cross sections of the rocker arm pad are identical. Consider that there are two surfaces, $\Sigma_1$ and $\Sigma_2$; let $\Sigma_1$ be the valve tip surface, which is just a portion of a plane, and let $\Sigma_2$ be a narrow cross-sectional slice of the rocker arm pad surface.

Following Litvin and Fuentes [2], let each of these surfaces have its own local coordinate system fixed to it. Let $S_1$ be the coordinate system that moves with $\Sigma_1$, and let $S_2$ be the coordinate system that moves with $\Sigma_2$. Suppose also that there is a fixed coordinate system $S_f$. $\Sigma_1$ translates and $\Sigma_2$ rotates about the rocker pivot within this fixed coordinate system $S_f$.

Let $\Sigma_1$ and $\Sigma_2$ meet at point $M$. The velocity of point $M$ on $\Sigma_i$ can be decomposed into two types of motion: the motion due to the surface itself rotating or translating within $S_f$, say, $v_{\text{tr}}^{(i)}$, as well as the motion of the point along, or relative to, the surface $\Sigma_i$ within coordinate system $S_i$, say, $v_r^{(i)}$. The subscripts indicate either *transfer* or *relative* motion associated with surface $\Sigma_1$ or $\Sigma_2$.

The velocity $v$ in $S_f$ of a single contact point common to both surfaces can be expressed in two equivalent ways:

$$v = v_{\text{tr}}^{(1)} + v_r^{(1)} = v_{\text{tr}}^{(2)} + v_r^{(2)} \tag{1}$$

Rewriting the last equation, we have

$$v_r^{(2)} - v_r^{(1)} = v_{\text{tr}}^{(1)} - v_{\text{tr}}^{(2)} \doteq v^{(12)} \tag{2}$$

Suppose that point $M^{(1)}(t)$ represents the point on $\Sigma_1$ that makes contact with surface $\Sigma_2$ at time $t$ in reference frame $S_1$. Suppose $M^{(2)}(t)$ is the corresponding point on $\Sigma_2$ that touches $\Sigma_1$ at time $t$ in reference frame $S_1$. At any given time $t=t_0$, $M^{(1)}(t_0)=M^{(2)}(t_0)$ (because the surfaces are in contact there). The middle equality in Eq. (2) shows that $v^{(12)}$ may be interpreted as the velocity an observer from surface $\Sigma_2$ in coordinate system $S_2$ sees as the direction and magnitude of motion for point $M^{(1)}(t_0)$. On the other hand, the left most equality in Eq. (2) indicates that $v^{(12)}$ is also equal to the speed at which surface $\Sigma_1$ rubs or slides on surface $\Sigma_2$.

[1]Corresponding author.

Manuscript received June 24, 2008; final manuscript received July 9, 2008; published online July 13, 2009. Review conducted by Dilip R. Ballal. Paper presented at the 2008 Spring Conference of the ASME Internal Combustion Engine Division (ICES2008), Chicago, IL, April 27–30, 2008.

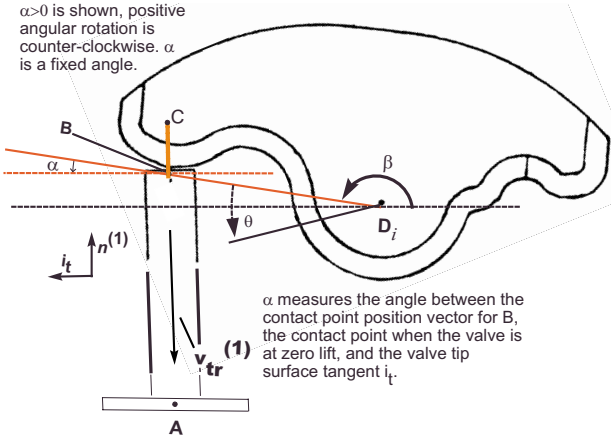


**Fig. 1 Diagram of rocker arm and valve when the valve is at zero lift**

## 3 Unit Normal Relationships

Suppose the surface $\Sigma_1$, parametrized as $r_1(u_1,v_1)$, has unit normal vector $n_1(u_1,v_1)$. Similarly, let $n_2(u_2,v_2)$ represent the unit normal on surface $\Sigma_2$ that is parametrized as $r_2(u_2,v_2)$. The unit normals $n_1(u_1,v_1)$ and $n_2(u_2,v_2)$ identify points on the unit sphere. At contact points, the unit normals coincide.

A unit normal $n$ of a contact point can change direction for two reasons:

1. The whole surface rotates, and hence so does $n$.
2. The point on the surface $\Sigma$ from which the normal emanates changes.

To calculate the rate of change in $n$ due to type 1 motion, suppose a surface rotates about vector $\boldsymbol{\omega}$. Then the location of the tip of the normal vector emanating from position $r$ of the rotating surface is given by

$$\boldsymbol{\omega} \times (r+n) \tag{3}$$

If the velocity of the base of the normal vector is subtracted from this quantity, we find that the type 1 motion of the normal vector along the unit sphere is

$$\boldsymbol{\omega} \times (r+n) - (\boldsymbol{\omega} \times r) = \boldsymbol{\omega} \times n$$

In addition to type 1 motion, as the contact point moves across a surface, $n$ can change because the surface tangent plane changes direction. Define this "type 2" motion to be $\dot{n}_r^{(i)}$, $i=1,2$. This discussion shows that

$$\dot{n}^{(i)} = \dot{n}_r^{(i)} + \boldsymbol{\omega}^{(i)} \times n^{(i)}, \quad i=1,2 \tag{4}$$

Because $n^{(1)}=n^{(2)}$ along a contact path, it follows that $\dot{n}^{(1)}=\dot{n}^{(2)}$ and that

$$\dot{n}_r^{(2)} = \dot{n}_r^{(1)} + (\boldsymbol{\omega}^{(1)} - \boldsymbol{\omega}^{(2)}) \times n \tag{5}$$

Observe that change in the normal vector $n_r^{(2)}$ due to motion along a contact path of surface $\Sigma_2$ is defined entirely in terms independent of surface $\Sigma_2$. This equation therefore offers a way of understanding the features of one surface in terms of the features and motion of the other contacting surface.

## 4 Normal Curvature

Consider the map $n(s)=n\circ r\circ \xi(s)$, where $\xi(s)=(u(s),v(s))$. Observe that $\zeta(s):=r\circ\xi(s)=(x(u(s),v(s)),y(u(s),v(s)),z(u(s),v(s)))$ is a curve on the surface $\Sigma$. Without loss of generality, suppose that the parametrization $s$ measures arc length of the curve $\zeta$ (so that $\zeta'(s)$ is a unit tangent vector to $\zeta$ at $s$). Then

$$\langle n\circ\zeta(s), \zeta'(s)\rangle = 0 \tag{6}$$

Since this is an identity in $s$, we can differentiate both sides of the equation to find that

$$\langle dn\zeta', \zeta'\rangle = -\langle n\circ\zeta(s), \zeta''(s)\rangle = -\langle n\circ\zeta(s), \kappa(s)m(s)\rangle = -\kappa\langle n,m\rangle \tag{7}$$

where $m$ is the normal to the curve $\zeta$ and $n$ is the normal to the surface. Within the right hand side of the last equation, there appears the standard definition for normal curvature—i.e., the magnitude of the projection of $\zeta''(s)=\kappa m$ onto the surface normal $n$.

Equation (7) shows that normal curvature at a point is fully determined once $\zeta'$, a vector in the tangent plane to the surface, is known. As the unit vector $\zeta'$ is allowed to vary through all possible directions, the Rayleigh quotient on the left hand side varies between a maximum and a minimum value corresponding to the maximum and minimum eigenvalues of the linear transformation $dn$. These eigenvalues are the principal curvatures for the surface, and the eigenvectors are the principal directions.

In effect, we have assumed that $\Sigma_2$ has zero normal curvature in a direction corresponding to movement into and out of the plane of Fig. 1. That is, the surface normal is constant as a point moves in this direction on $\Sigma_2$.

Along a contact path, denote normal curvatures of surfaces $\Sigma_1$ and $\Sigma_2$ as $\kappa_1$ and $\kappa_2$, respectively. Let $\zeta_i$ represent the contact path on surface $\Sigma_i$, so that $\zeta_i' \cdot ds_i/dt = v_r^{(i)}$. By definition of the differential $dn$, it follows that $\dot{n}_r^{(i)} = dn\zeta_i' \cdot (ds_i/dt)$ and hence that

$$dn\zeta_i' = \dot{n}_r^{(i)}/(ds_i/dt)$$

Requiring that

$$\kappa_1 v_r^{(1)} = -\dot{n}_r^{(1)} \tag{8}$$

$$\kappa_2 v_r^{(2)} = -\dot{n}_r^{(2)} \tag{9}$$

will imply that $dn\zeta_i' = -\kappa_i v_r^{(i)}/(ds_i/dt) = -\kappa_i\zeta_i'$. Equation (7) then shows that

$$\langle dn\zeta_i', \zeta_i'\rangle = -\langle -\kappa_i\zeta_i', \zeta_i'\rangle = \kappa_i \tag{10}$$

Therefore, enforcing Eqs. (8) and (9) in effect makes $\kappa_i$ the normal curvature of the contact point path on surface $\Sigma_i$. For surface $\Sigma_2$, the normal to the surface is parallel to the normal of the contact point path. This means that the normal curvature is equal to the curvature of the contact path that lies on $\Sigma_2$.

## 5 Rocker Arm Sliding Velocity and Curvature

The contact stress between valve stem and rocker arm, multiplied by sliding velocity $v^{(12)}$ and integrated over time, provides a metric for assessing wear. Reducing sliding velocity where there is high contact stress may enhance rocker arm durability. Formulas developed in this section indicate the extent to which we can manipulate $v^{(12)}$ and $\kappa_2$, both significant factors influencing contact stress and wear.

The formulas for $v^{(12)}$ and for the curvature of $\Sigma_2$, $\kappa_2$, show that both quantities depend only on the contact point path and the positioning of the valve stem relative to the rocker arm. This fact motivates a technique presented in Sec. 5, in which we construct the shape of a rocker arm surface from the contact point path and geometry of the valve train. A contact point path that produces the desired curvature and sliding velocity can be engineered based on the formulas derived below. The surface can then be constructed using the technique defined in Sec. 5.

The rocker arm shown in Fig. 1 makes contact with the valve stem at zero lift at point **B**. The rocker arm shaft axis passes through points $\mathbf{D}_i$, $i=1,2$; this axis is perpendicular to the plane of the page. As discussed in Sec. 1, $\Sigma_2$ is considered to be a narrow cross-sectional slice of the rocker arm pad that is orthogonal to $\mathbf{D}_1\mathbf{D}_2$. The valve tip surface is planar and perpendicular to the direction of valve movement. Define the positive $x$-axis of $S_f$ to be

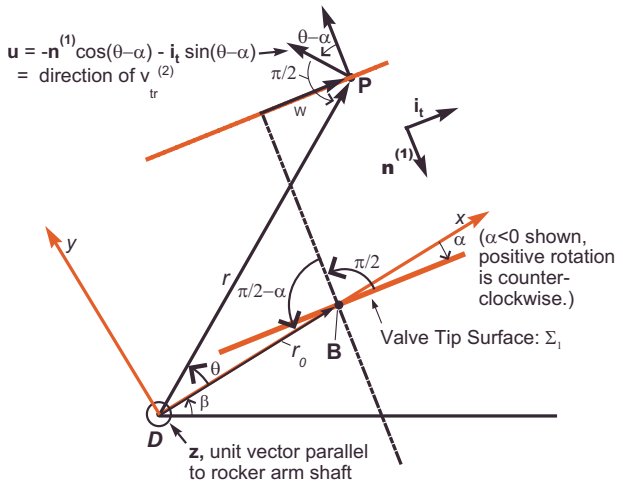


**Fig. 2 Calculating translational velocities $v_{tr}^{(1)}$ and $v_{tr}^{(2)}$**

the ray that is perpendicular to line $\overline{\mathbf{D}_1\mathbf{D}_2}$ that passes through point **B**, the initial contact point of contact between $\Sigma_1$ and $\Sigma_2$ at zero lift. The origin of $S_f$ is **D**, the point where the $x$-axis intersects line $\overline{\mathbf{D}_1\mathbf{D}_2}$. The angle $\alpha$ is that angle between the $x$-axis and the projection of this axis on the valve stem plane.

Because, by definition, the relative movement of two sliding surfaces cannot be directed in a way that causes one surface to puncture the other, the sliding velocity $v^{(12)}$ must lie in the tangent plane. Therefore, for all $t$

$$\langle n, v^{(12)} \rangle = 0 \tag{11}$$

From Eq. (1) it follows that

$$v_r^{(2)} = v_r^{(1)} + v^{(12)} \tag{12}$$

Let $\Sigma_1$ be the valve stem tip, which is a plane that translates without rotation as it is pushed by the rotating rocker arm. Equations (5) and (9) imply that

$$-\kappa_2 v_r^{(2)} = \dot{n}_r^{(1)} + (\boldsymbol{\omega}^{(1)} - \boldsymbol{\omega}^{(2)}) \times n \tag{13}$$

Observe that $\dot{n}_r^{(1)}=0$, $\omega^{(1)}=0$, and $n=n^{(1)}$. If $\boldsymbol{\omega}^{(2)}=\omega\cdot\hat{z}$, where $\hat{z}$ is a unit vector coming out of the page, then positive rotation of the rocker arm is counterclockwise, and

$$\kappa_2 v_r^{(2)} = \omega(\hat{z} \times n^{(1)}) = \omega i_t \tag{14}$$

Angle $\theta$ in Fig. 2 is as indicated, where $t=0$ corresponds to the time when the rocker arm is at its beginning (zero-lift) position. The angular velocity of the rocker arm is $\omega$. Point **B** indicates the contact point at time $t=0$ when the rocker arm and valve are at zero lift. Let $w(\theta)i_t$ indicate the sliding displacement distance from point **B** of the valve tip to the contact point at angle $\theta$. Observe that $\dot{w}i_t=v_r^{(1)}$.

Figure 2 shows that $v_{tr}^{(2)}=r\omega\mathbf{u}$, where $r$ is the distance between the center of rotation (the origin) and the contact point on surface $\Sigma_2$. This follows from the observation that the rocker arm is in pure rotation, and hence a fixed point on the rocker arm can only move in the **u** direction, and its distance from the origin is constant.[2] Here, $\mathbf{u}=-n^{(1)}\cos(\theta-\alpha)-i_t\sin(\theta-\alpha)$ (see Fig. 2).

On the other hand, $v_{tr}^{(1)}$ has only a component in the $n^{(1)}$ direction, since the valve stem translates without rotation in a direction normal to its valve tip surface. (Recall that $v_{tr}^{(1)}$ includes no sliding velocity along the surface of the valve tip.) It follows that

$$\langle v^{(12)}, i_t \rangle = \langle v_{tr}^{(1)} - v_{tr}^{(2)}, i_t \rangle = [r\omega \sin(\theta-\alpha)] \tag{15}$$

Here, $i_t$ is the unit tangent to the initial contact point **B**, as shown in Fig. 2. The normal component of $v^{(12)}$ must be zero (see Eq. (11)). Because the valve tip is planar and does not rotate, $n^{(1)}$ and $i_t$ are constant unit vectors. If $r(\theta(t))$ is the distance to the point of contact at time $t$, it follows that the sliding velocity is

$$v^{(12)} = i_t[r\omega \sin(\theta-\alpha)] \tag{16}$$

We summarize these results in Lemma 1.

LEMMA 1. *Let $(\theta, r(\theta))$ indicate in polar coordinates a continuously differentiable contact point path, showing the sequence of contact points between a rocker arm and valve tip in $S_f$. Let $\alpha$ be the angle that a position vector, pointing from origin D to the point of zero lift B, makes with surface tangent vector $i_t$ (see Fig. 2). Then the velocity of the contact point across the valve tip surface is*

$$v_r^{(1)} = [-r\dot{\theta}\sin(\theta-\alpha) + \dot{r}\cos(\theta-\alpha)]i_t \tag{17}$$

*The sliding velocity between the valve tip and the rocker arm surface is*

$$v^{(12)} = i_t[r\omega \sin(\theta-\alpha)] \tag{18}$$

*Proof.* The unit vector $i_t=(\cos\alpha, \sin\alpha)$ is parallel to the valve tip surface (by definition) and orthogonal to the direction of translation of the valve tip. Project onto $i_t$ the vector formed by connecting point $B$ at $(0, r_0)$ to point $P$ at $(\theta, r(\theta))$ (see Fig. 2) to find the signed distance $w$. We find that

$$\begin{aligned} w &= \langle [r(\theta)\cos\theta - r_0, r(\theta)\sin\theta], [\cos\alpha, \sin\alpha] \rangle \\ &= r\cos\theta\cos\alpha - r_0\cos\alpha + r\sin\theta\sin\alpha \\ &= r\cos(\theta-\alpha) - r_0\cos\alpha \end{aligned} \tag{19}$$

Now $v_r^{(1)}=\dot{\theta}(dw/d\theta)$, which implies that

$$v_r^{(1)} = [-r\dot{\theta}\sin(\theta-\alpha) + \dot{r}\cos(\theta-\alpha)]i_t$$

which proves Eq. (17). Equation (18) follows from the discussion preceding the Lemma 1. □

Lemma 1 shows that sliding velocity can only be reduced by making the difference $\theta-\alpha$ small or by making the radius $r$ small. The radius $r(\theta)$ traces a path of contact points, and those points lie within the region of the plane swept by the valve stem as it translates. Therefore, $r(\theta)$ is highly constrained. In Sec. 5, a process for determining a rocker arm surface for a target contact point path and angle $\alpha$ is defined. Nevertheless, formula ((17)) shows that adjusting angle $\alpha$ offers the most control over sliding velocity. Targeting angular sweeps of near zero sliding velocity can be accomplished by choosing $\alpha$ so that $\theta-\alpha$ is small in the targeted region.

LEMMA 2. *Let $(\theta, r(\theta))$ and $\alpha$ be as defined in Lemma 1 (see Fig. 2). Let $0<|\alpha|<\pi/2$ and let $-\pi/2<\theta-\alpha<\pi/2$. Suppose also that $r>0$ and that $dr/d\theta\neq 0$. Then*

$$v_r^{(2)} = [r(\omega-\dot{\theta})\sin(\theta-\alpha) + \dot{r}\cos(\theta-\alpha)]i_t \tag{20}$$

*When $|\omega-\dot{\theta}|$ is negligibly small (the typical case), then*

$$v_r^{(2)} = [\dot{r}\cos(\theta-\alpha)]i_t \tag{21}$$

*and*

$$\kappa_2(\theta) = \frac{1}{(dr/d\theta)\cos(\theta-\alpha)} \tag{22}$$

*Proof.* Equation (20) follows from the previous lemma and from the fact that $v_r^{(2)}=v_r^{(1)}+v^{(12)}$ (see Eq. (12)) and the fact that $v^{(12)}=r\omega\sin(\theta-\alpha)i_t$ (see Eq. (15)). Equation (21) follows immediately from the assumption that $|\omega-\dot{\theta}|$ is negligibly small. Equation (22) follows from Eqs. (21) and (14). □

[2] $v_{tr}^{(2)}$ is defined as the velocity of a *fixed* point on surface $\Sigma_2$. The velocity $v_{tr}^{(2)}$ does not include any velocity contribution due to sliding motion along the surface of $\Sigma_2$.

For most applications, $|\omega-\dot{\theta}|$ will be small because the rate of change in the angular coordinate of the contact point, $\dot{\theta}$, will typically be nearly equal to the rocker arm rotation speed $\omega$.

Lemma 2 indicates that $dr/d\theta$ controls rocker pad curvature. When the hypothesis of the lemma hold, the curvature of $\Sigma_2$ is roughly proportional to $1/(dr/d\theta)$. The equation for curvature given in Lemma 2 indicates another restriction on the radius function $r(\theta)$. Referring to Fig. 2, observe that the positive unit normal vector at the contact point is directed in the negative $y$ direction. If $\zeta(s)$ represents the contact point path in $S_2$, parametrized in terms of arc length, then by definition $\langle \zeta''(s), n\rangle = \kappa_2$, and hence positive curvature indicates that the unit tangent $\zeta'(s)$ moves toward the unit normal. Therefore, positive curvature ensures that the rocker arm pad will be concave down. Lemma 2 therefore implies that $dr/d\theta > 0$ for a convex rocker pad.

The next lemma will be useful in determining where the contact point path intersects the surface.

LEMMA 3. *Let* $(\theta, r(\theta))$ *and* $\alpha$ *be as defined in Lemma 1 (see Fig. 2). Let* $0 < |\alpha| < \pi/2$ *and let* $-\pi/2 < \theta - \alpha < \pi/2$. *Suppose also that* $r > 0$ *and that* $dr/d\theta \neq 0$, *and let* $|\omega - \dot{\theta}|$ *be negligibly small. Then as the contact point moves from* $(0, r(0))$ *to* $(\theta, r(\theta))$, *the arc length traveled by the contact point along the rocker arm surface is*

$$s(\theta) = \int_0^\theta (dr/d\theta)\cos(\theta - \alpha)d\theta \tag{23}$$

*Proof.* Lemma 2 shows that $v_r^{(2)} = \dot{r}\cos(\theta-\alpha)i_t$, so that the arc length traveled across $\Sigma_2$ as $\theta$ changes from $\theta_0$ at time $t=0$ to time $t=t(\theta)$ at angle $\theta$ is

$$s(\theta) = \int_{t=0}^{t(\theta)} \frac{dr}{dt}\cos(\theta-\alpha)dt = \int_{\theta_0}^{\theta} \frac{dr}{d\theta}\cos(\theta-\alpha)d\theta$$

□

## 6 Approximating a Surface $\Sigma_2$ That Produces a Prescribed Contact Point Path

Lemma 1 shows that $v^{(12)}$ depends only on angle $\alpha$ and $r(\theta)$, the polar radius of the contact point path in $S_f$. The constraints on a contact point path $r(\theta)$ identified earlier—that it generate a rocker pad that is convex, and hence that $dr/d\theta > 0$, and that it fall within the envelope of motion of the valve stem—limit the set of contact point paths that can be considered for a rocker arm joint. However, some customization is possible. For practical applications, $\alpha$ will not be outside the interval $(0, \theta_{\max})$, where $\theta_{\max}$ is the angular rotation of the rocker arm that corresponds to the maximum lift. The formula for $v^{(12)}$ in Lemma 1 shows that when $\theta - \alpha$ is small, the sliding velocity is small. Adjusting $\alpha$ therefore can be utilized to customize the rocker arm sliding velocity profile.

In this section, we define an algorithm for constructing a surface from a prescribed $\alpha$ and contact point path $r(\theta)$, the only two determinants of sliding velocity. Lemma 2 shows that controlling $dr/d\theta$ enables customization of rocker pad curvature. Therefore, the algorithm below can help produce a surface contour that customizes, to the extent possible, where sliding is highest and where it is lowest. It can also help generate a rocker pad with specific curvatures along its profile.

Let the curve $(x(s), y(s))$ define the cross-sectional shape for rocker pad surface $\Sigma_2$ within $S_f$. Let $\Sigma_2$ be placed so that the point of contact between the rocker and valve tip at zero rocker rotation is located a distance $r_0$ from the pivot point of the rocker (see Fig. 3). Suppose the parameter $s$ represents the arc length. Suppose at rocker arm rotation angle $\eta$, the contact point between the rocker arm and valve tip occurs at $x = r(\theta)\cos(\theta)$ and $y = r(\theta)\sin(\theta)$. If

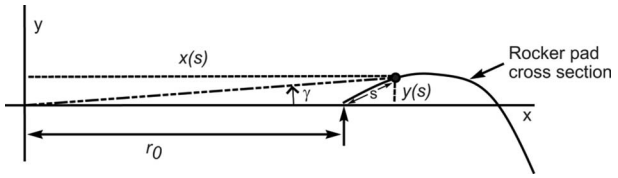


**Fig. 3 Define $\gamma(s) = \arctan(y(s)/x(s))$. To produce an approximate surface reconstruction, assume that $\gamma(s)$ is negligible compared to $\theta(s)$.**

$\gamma(s) = \arctan(y(s)/x(s))$, then it follows that the rocker arm rotation angle $\eta(s)$ is equal to $\theta(s) - \gamma(s)$, where $\theta(s)$ is implicitly defined by Eq. (23) of Lemma 3. That is, $\eta(s)$ is the rocker rotation angle that brings point $(x(s(\eta)), y(s(\eta)))$ into contact with the valve stem at $(r(\theta)\cos(\theta), r(\theta)\sin(\theta))$.

To formulate an approximate technique for constructing a cross-sectional curve for a surface that closely approximates a surface that will generate a given contact point path, we suppose $\gamma(s)$ is small, a reasonable assumption since $x > r_0$ implies that $y/x$ will generally be small. We therefore make the simplifying assumption that $\eta(s) \approx \theta(s)$. We also suppose that $|\omega - \dot{\theta}|$ is negligibly small, making Eqs. (22) and (23) valid approximations to $\kappa_2$ and $s(\theta)$, respectively.

When these assumptions are made, it follows that the tangent vector $(x'(s), y'(s))$ must form an angle of

$$\Psi(s) = \alpha - \theta(s)$$

with the positive $x$-axis. This follows because when the surface, and hence the tangent vector $(x'(s), y'(s))$, is rotated by $\theta(s)$, the unit tangent vector at the contact point $(x(s(\theta))y(s(\theta)))$ must be parallel to the valve tip surface.

The function $\theta(s)$ implicitly defined by Eq. (23) can be determined numerically. That such an inverse function for $s(\theta)$ exists follows from the fact that $dr/d\theta$ is continuous and greater than zero. As a result, $s(\theta)$ as defined in Eq. (23) is strictly monotonic when $\theta \in (-\pi/2 + \alpha, \pi/2 + \alpha)$. A process for determining the rocker arm cross-sectional shape for $\Sigma_2$ is defined as follows.

*Algorithm 1.*

*Inputs.* $N > 50$, $\alpha \in (-\pi/2, \pi/2)$, $\theta_{\max} < \pi/2 + \alpha$, $r_0 = r(0)$, a function representing a target for $(dr/d\theta)(\theta)$ that is positive and continuous for $0 < \theta < \theta_{\max}$. Zero valve lift corresponds to $\theta = 0$, and the maximum valve lift corresponds to $\theta_{\max}$.

*Output.* Parametric equations for a cross-sectional curve of a rocker arm pad. The curve, parametrized in terms of arc length, approximately generates a polar-coordinate specified target contact point path, $(\theta, r(\theta))$, where $r(\theta) = r_0 + \int_0^\theta (dr/d\theta)d\theta$. This contact point path represents the sequence of contact points the rocker arm makes with a valve stem tip $\Sigma_1$ as the rocker pad $\Sigma_2$ is rotated about the pivot location at (0,0).

1. Calculate a mesh $\theta_i$ of $N$ equally spaced points between $\theta = 0$ (zero rocker arm rotation) and $\theta = \theta_{\max}$ (maximum rocker rotation), so that $\theta_i = (i-1)\cdot(\theta_{\max})/(N-1)$. Using a numerical integration scheme, determine

$$s_i = \int_0^{\theta_i} \frac{dr}{d\theta}(u)\cos(u-\alpha)du, \quad i = 1, 2, \ldots, N$$

   The sequence $s_i$ strictly increases.
2. Construct a piecewise polynomial approximation of the function $\theta(s)$ by building a shape preserving spline (see, for example, Ref. [3]) using $s_i$ and $\theta_i$. The values $\theta_i$ define the ordinate. Define $\Psi(s) = \alpha - \theta(s)$.
3. Determine a parametric representation $(x(s), y(s))$ for a cross section of surface $\Sigma_2$ as

$$x(s) = r_0 + \int_0^s \cos \Psi(s) ds \tag{24}$$

$$y(s) = \int_0^s \sin \Psi(s) ds \tag{25}$$

Algorithm 1 generates a cross section to a surface that approximately generates a prescribed contact point path $(\theta, r(\theta))$ [4]. Note that parameter $s$ measures the arc length for this curve because $\sqrt{(x')^2 + (y')^2} \equiv 1$ for all $s$. Note also that for a generated cross-sectional profile, the exact contact point can be determined: for a rocker rotation angle $\theta$, determine the required arc length along the cross section so that the tangent to the curve makes an angle $\alpha - \theta$ at that point. By construction, $s(\theta)$ defines the arc length distance to the point along $\Sigma_2$ such that its tangent there makes an angle $\alpha - \theta$ with the $x$-axis. Upon rotating the surface by angle $\theta$, the rotated point corresponding to $x(s(\theta)), y(s(\theta))$ is now the point of contact because its tangent vector is now parallel to $\Sigma_1$, making an angle $\alpha$ with the $x$-axis. The polar coordinates of such a contact point are $(\eta + \gamma, \sqrt{x^2(s(\theta)) + y^2(s(\theta))})$, where $\gamma \equiv \arctan(y(s)/x(s))$.

The surface constructed approximately follows the prescribed contact point path. It is worth noting, however, that the curvature of the generated surface follows formula (22) exactly. By construction, angle $\Psi(s)$ is the angle the unit tangent makes with the positive $x$-axis in $S_2$. Therefore,

$$\kappa_2 = -\frac{d\Psi}{ds} = \frac{1}{ds/d\theta} = \frac{1}{(dr/d\theta)\cos(\theta - \alpha)}$$

(The minus sign in front of $d\Psi/ds$ applies here because **n** points in the negative $y$ direction.) Equation (22) produces a precise value for $\kappa_2$ when calculated using the $dr/d\theta$ provided as input to Algorithm 1. Contact stress calculations that are highly dependent on the exact knowledge of curvature can be carried out with confidence—the curvature of the generated surface is known accurately.

The exact value of rubbing velocity may be computed as well, using formula (18), except that the input $r(\theta)$ to this formula should be the exact radius determined by reconstructing the exact contact point path as described above. Alternatively, rubbing velocity may be closely approximated by using the target contact point path radius (instead of the reconstructed exact radius function) in formula (18).

The target contact radius $r(\theta)$ (from which the Algorithm 1 input $dr/d\theta$ is calculated) may be thought of as a control curve. In every example tested, the target contact points produced from a prescribed $r(\theta)$ closely matches the locus of actual contact points generated by the Algorithm 1 generated surface. However, even if this were not the case in every instance, iterative modification of $r(\theta)$ and subsequent calculations of the exact contact point path make it possible to converge on a very precise surface that has a closely engineered rubbing velocity or curvature profile.

A convenient way of specifying $r(\theta)$ is by choosing an interpolation point set and building a quadratic shape preserving spline as defined by an algorithm specified in Ref. [3]. The function $r(\theta)$ must strictly increase over the range of $\theta$ between 0 and $\theta_{max}$. Using a shape preserving spline construction ensures that the piecewise polynomial will increase whenever the input interpolation data set increases. In addition, the piecewise polynomial so generated may be differentiated to reliably produce a strictly positive, piecewise linear, continuous, and exact representation of $dr/d\theta$ that is suitable as input to Algorithm 1.

It is also possible to specify $dr/d\theta$ with an input interpolation data set and then derive $r(\theta)$ from this representation. This approach may be preferred especially when rocker arm curvature is the primary objective for a new rocker pad design (see formula (22) for $\kappa_2$). Rocker pad curvature may require close control to prevent excessive contact stress during engine operation. An exact representation of $r(\theta)$ can be produced by calculating the spline that is the antiderivative of $dr/d\theta$ and that satisfies $r(0) = r_0$. Integrations and differentiations of piecewise polynomials can be quickly and conveniently carried out symbolically within an environment such as MATLAB™, using existing MATLAB™ functionality and data structures. The preset data structure within MATLAB™ designed for storing piecewise polynomial objects is also quite convenient for producing and saving splines as inputs for Algorithm 1.

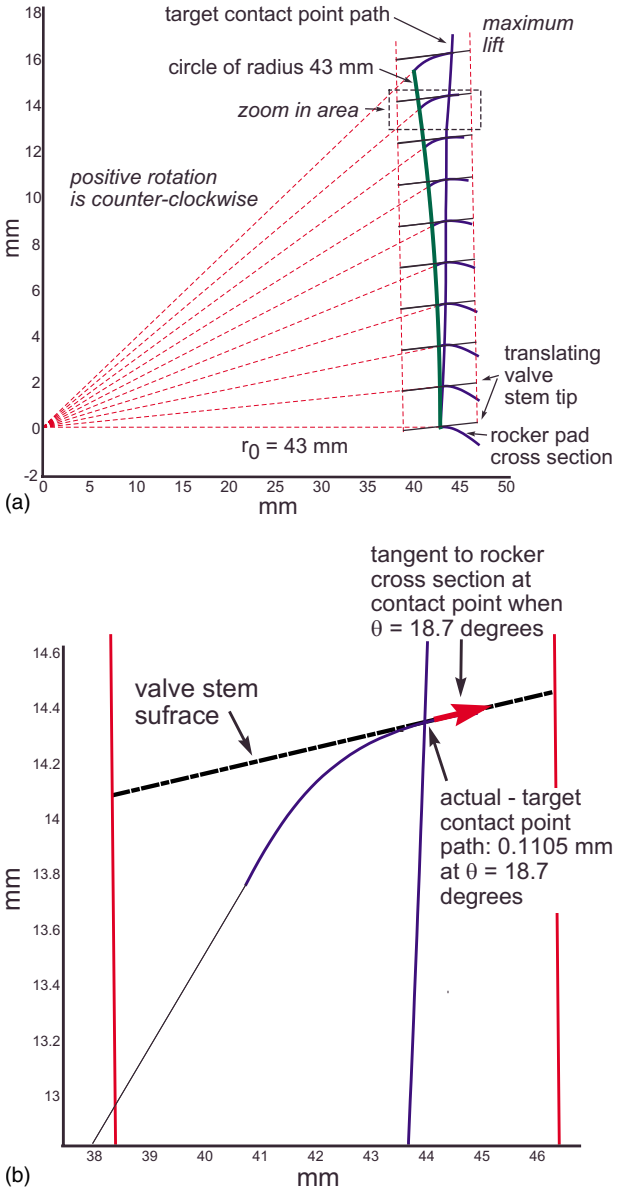


**Fig. 4 First axis: derived rocker arm pad shown rotating about its pivot at the origin. Design parameters are $r_0$=43 mm, $\alpha$ =2.73 deg, and valve radius of 4 mm. The target contact point path is shown to the right of a circular arc of radius 43 mm. Second axis: shows a zoom-in of the indicated area from the first axis.**

## 7 Sample Application of Algorithm 1

Algorithm 1 produced the following rocker pad cross-sectional curve indicated in Fig. 4. The rocker pad profile suggested below

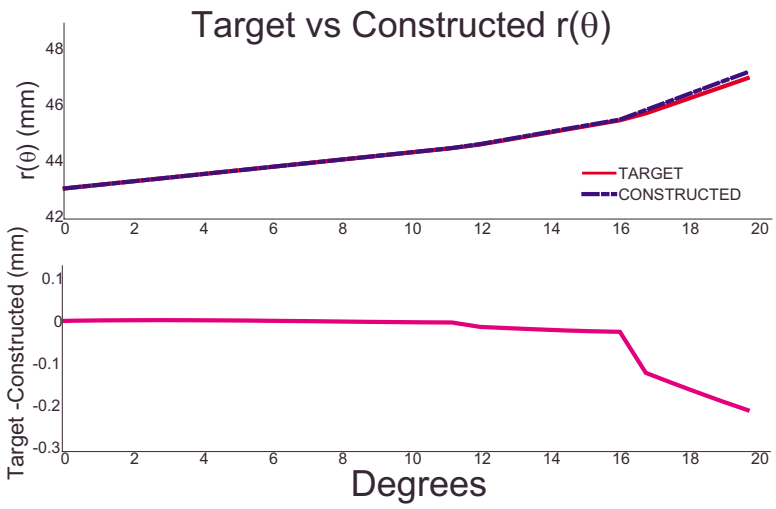


**Fig. 5 Target versus actual: pivot to contact point distance as a function of contact point angle**

is intended for a high speed racing vehicle. At high engine speeds, maximum loads between cam and cam follower, and hence maximum loads within the valve train, tend to occur early in the valve lift cycle. (This is because of the inertias of the various valve train components during high engine speed operation that tend to counteract high spring loads produced as the cam follower rounds the nose of the cam lobe. The inertia loads tend to increase the loading on the flanks of the cam at high speed. This translates to high loading of valve train components early in the valve lift cycle.)

For this particular high speed application, it was determined that peak valve acceleration occurs at about 13% of the maximum valve lift, which for this valve train is 17 mm. The initial point of contact is to be 43 mm from the pivot. To reduce wear and friction during high speed operation, the rubbing velocity between the valve tip and rocker arm pad is minimized at 13% lift. To accomplish this, $\alpha$ is set to be 2.73 deg (0.0476 rad). The path input to Algorithm 1, $dr/d\theta$, is chosen to be small but large enough that the curvature (as computed by formula (22)) is below 0.14 $\text{mm}^{-1}$. This is to ensure that contact stress remains below a prescribed threshold. Finally, $dr/d\theta$ is made larger as $\theta$ approaches $\theta_{\max}$. This is to flatten the rocker pad surface so that at low engine speeds, when forces are high at high lift, contact stress is kept low. Figure 5 shows that Algorithm 1 produced a surface that generates the target contact point path with the maximum error in $r$ of 0.22 mm. Figure 6 shows a comparison of target versus actual sliding velocities, as well as a plot of curvature $\kappa_2$.

## 8 Discussion

Angle $\alpha$ and the contact point path between the rocker pad and valve tip ultimately control curvature (and hence contact stress) and sliding velocity. Lemma 1 shows that sliding velocity is small when $\theta-\alpha$ is small. Therefore, the valve train engineer can choose $\alpha$ to minimize the sliding velocity over a targeted rocker arm angular rotation range by selecting $\alpha$ appropriately. Lemma 2 shows that selecting a contact point path so that $(dr/d\theta)$ is small will produce a rocker pad with a large curvature and possibly unacceptably high contact stress in the operating valve train as a result. Making $(dr/d\theta)$ larger will flatten (reduce curvature), but at the expense of increasing sliding velocity as $r$ increases for larger $\theta$. In short, Lemmas 1 and 2 offer the engineer insight into how to design a rocker pad by controlling the features of contact. After making these design choices, i.e., after choosing $\alpha$ and a

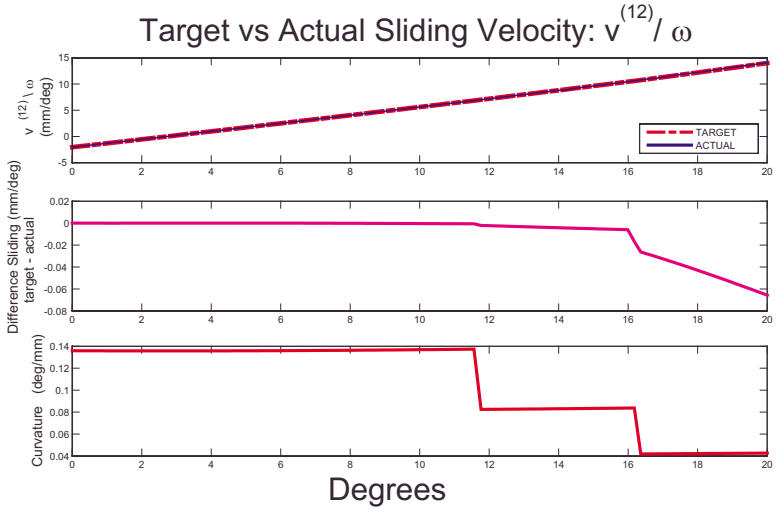


**Fig. 6 First and second axes: target versus actual $v^{(12)}/\omega$ as a function of contact point angle. third axis: curvature of constructed surface, piecewise linear because $r(\theta)$ is piecewise quadratic**

contact point path $(\theta, r(\theta))$, Algorithm 1 offers a new technique for determining a rocker pad surface from these inputs.


## Acknowledgment

The authors would like to thank Professor Zhengfang Zhou, of Michigan State University, for insights and help with this project.


## Nomenclature

- $\beta$ = rocker offset angle, indicating the zero-lift position of the rocker arm with respect to a horizontal axis
- $\Sigma_1$ = valve tip surface, assumed planar
- $\Sigma_2$ = narrow cross-sectional slice of the rocker arm pad surface (the slice lies in the plane of Fig. 1)
- $\vec{\omega}$, $\vec{\omega}^{(i)}$ = angular velocity vector and angular velocity vector for surface $\Sigma_i$
- $\omega$ = angular speed of the rocker arm
- $S_1$ = coordinate system fixed to $\Sigma_1$
- $S_2$ = coordinate system fixed to $\Sigma_2$
- $S_f$ = fixed coordinate system where $\Sigma_2$ rotates and $\Sigma_1$ translates (the origin of $S_f$ is the rocker pivot)
- $\alpha$ = angle between a ray that connects the rocker pivot point to the zero-lift contact point and the valve tip surface
- $v_{\mathrm{tr}}^{(i)}$ = translational velocity of surface $\Sigma_i$
- $v_r^{(i)}$ = relative velocity of the contact point across surface $\Sigma_i$
- $v^{(12)}$ = sliding velocity between $\Sigma_1$ and $\Sigma_2$
- $n_i$ = unit normal to surface $\Sigma_i$
- $r_i(u_i, v_i)$ = parametrizations of surface $\Sigma_i$
- $i_t$ = unit tangent vector to the contact point in the plane of $\Sigma_1$
- $s$ = arc length distance along the contact point path, measured from the zero-lift initial contact point
- $\theta$ = angular polar coordinate, in $S_f$, of the contact point path
- $r(\theta)$ = polar radius from a pivot point of rocker to a contact point at polar angle $\theta$ in $S_f$
- $r_0$ = distance from pivot to initial point of contact, $r(0)$
- $\kappa_i$ = curvature of the contact path on surface $\Sigma_i$ in $S_i$
- $\gamma(s)$ = $\arctan(y(s)/x(s))$
- $\Psi(s)$ = angle that the tangent vector to $\Sigma_2$ at $s$ makes with the positive $x$-axis of $S_f$
- $\mathbf{B}$ = initial point of contact between $\Sigma_2$ and $\Sigma_1$
- $\mathbf{D_i}$, $\mathbf{D}$ = points that lie on the rocker pivot axis
- $x(s)$ = $x$-coordinate of $\Sigma_2$ at $s$, at zero lift, in $S_f$
- $y(s)$ = $y$-coordinate of $\Sigma_2$ at $s$, at zero lift, in $S_f$

## References


[1] Turkish, M. C., 1946, *Valve Gear Design*, 1st ed., Eaton Manufacturing Company Wilcox-Rich Division, Detroit, MI.

[2] Litvin, F. L., and Fuentes, A., 2004, *Gear Geometry and Applied Theory*, 2nd ed., Cambridge University Press, Oxford, UK.

[3] Schumaker, L. L., 1983, "On Shape Preserving Quadratic Spline Interpolation," SIAM (Soc. Ind. Appl. Math.) J. Numer. Anal. **20**, 854.

[4] DoCarmo, M. P., 1976, *Differential Geometry of Curves and Surfaces*, Prentice-Hall, Englewood Cliffs, NJ.

# Measurement of Biodiesel Blend and Conventional Diesel Spray Structure Using X-Ray Radiography

**A. L. Kastengren**[1]
e-mail: akastengren@anl.gov

**C. F. Powell**

Center for Transportation Research,
Argonne National Laboratory,
Argonne, IL 60439

**K.-S. Im**

**Y.-J. Wang**

**J. Wang**

Advanced Photon Source,
Argonne National Laboratory,
Argonne, IL 60439

*The near-nozzle structure of several nonevaporating biodiesel-blend sprays has been studied using X-ray radiography. Radiography allows quantitative measurements of the fuel distribution in sprays to be made with high temporal and spatial resolution. Measurements have been made at different values of injection pressure, ambient density, and with two different nozzle geometries to understand the influences of these parameters on the spray structure of the biodiesel blend. These measurements have been compared with corresponding measurements of Viscor, a diesel calibration fluid, to demonstrate the fuel effects on the spray structure. Generally, the biodiesel-blend spray has a similar structure to the spray of Viscor. For the nonhydroground nozzle used in this study, the biodiesel-blend spray has a slightly slower penetration into the ambient gas than the Viscor spray. The cone angle of the biodiesel-blend spray is generally smaller than that of the Viscor spray, indicating that the biodiesel-blend spray is denser than the Viscor spray. For the hydroground nozzle, both fuels produce sprays with initially wide cone angles that transition to narrow sprays during the steady-state portion of the injection event. These variations in cone angle with time occur later for the biodiesel-blend spray than for the Viscor spray, indicating that the dynamics of the injector needle as it opens are somewhat different for the two fuels.* [DOI: 10.1115/1.3094023]

## 1 Introduction

Recent increases in prices for petroleum and concerns about global climate change have spurred interest in biologically derived alternatives to conventional motor fuels. For compression ignition (diesel) engines, a particularly attractive alternative fuel is biodiesel. Biodiesel is formed from the transesterification of biologically derived fats or oils with an alcohol, usually methanol. Biodiesel has several advantages over conventional diesel fuel, including high cetane number, biodegradability, and low net greenhouse gas emissions [1,2]. Though the exact properties of biodiesel fuel depend on the source of the feedstock oil or fat, biodiesel tends to have a higher density, viscosity, and bulk modulus than conventional diesel fuel [1]. Thus, careful study of the effects of biodiesel when used in diesel engines is needed to achieve optimal use of biodiesel fuels.

Numerous studies have been conducted using biodiesel and biodiesel blends in diesel engines. These studies have generally found that the use of biodiesel decreases the soot, CO, and unburned hydrocarbon emissions from diesel engines, at the expense of higher $NO_x$ emissions [1–9]. The reduction in soot emissions is generally attributed to the oxygen content of the biodiesel fuel [4]. The cause for the increase in $NO_x$ emissions is less well understood [1]. This increase has been attributed to several factors, including a higher oxygen concentration in the spray due to the oxygen content of the biodiesel fuel [5], an increase in flame temperatures, and a decrease in the time delay between the commanded and actual start of injection when using biodiesel [8].

It is well accepted that the performance and emissions of diesel engines are closely tied to the behavior of the fuel spray used to introduce fuel into the engine cylinder. This spray process controls the mixing of fuel and air, which is critical in controlling the combustion process. The changes in physical properties seen when changing from conventional diesel fuel to biodiesel would be expected to significantly alter spray structure. The accepted models for spray breakup depend on the Weber and Reynolds numbers of the spray droplets, which are directly related to the fuel properties [10]. Moreover, previous studies of fuels with different viscosities have shown that higher viscosity fuel tends to produce a spray with a smaller cone angle than a lower viscosity fuel [11].

While many studies of biodiesel combustion in engines have been performed, relatively few studies have been performed to examine biodiesel sprays. Higgins et al. [12] performed liquid-length measurements for several alternative fuels, including biodiesel, in the steady state of injection events under vaporizing conditions. Other studies of sprays under nonvaporizing conditions have shown that biodiesel has a similar or slightly greater penetration at a given time after the start of injection than conventional diesel fuel and that the spray angle is similar between the two fuels [13–15]. A recent study comparing diesel and biodiesel behavior with conical and cylindrical nozzles showed that the fuels responded to changes in nozzle geometry differently, with these differences attributed to differences in the cavitation behavior of the fuels [16].

A limitation of optical diagnostics in the study of diesel sprays is that diesel sprays strongly scatter visible light, particularly in the dense region near the nozzle. This scattering prevents light from entering or leaving the near-nozzle region. For this reason, most extant biodiesel spray data focus on spray leading-edge penetration and the spray angle. An alternative measurement technique for high-density diesel sprays, which has been demonstrated in recent years, is X-ray radiography [17–19]. X-ray radiography provides ensemble-averaged, quantitative measurements of the fuel distribution in diesel sprays, even in high-density regions. As such, it provides data that are difficult or impossible to obtain with other nonintrusive techniques.

[1]Corresponding author.

Manuscript received July 15, 2008; final manuscript received July 15, 2008; published online July 14, 2009. Review conducted by Dilip R. Ballal. Paper presented at the 2008 Spring Conference of the ASME Internal Combustion Engine Division (ICES2008), Chicago, IL, April 27–30, 2008.

This paper will provide detailed measurements of sprays of a 50% blend of biodiesel and diesel calibration fluid. The distribution of fuel in the spray, both during the steady-state portion of the spray and during the opening and closing transient phases of the injection, will be examined. The near-nozzle penetration and cone angle behavior of these sprays will be shown. Measurements will be provided at different injection pressures, ambient pressures, and for different nozzle geometries to allow for a full range of behaviors to be examined. These results will also be compared with those of sprays of a petroleum diesel calibration fluid to show how the use of a biodiesel blend affects spray properties.

## 2 Experimental Method

Detailed discussions of the measurement technique can be found elsewhere [17,20]; thus, only a brief description of the measurement technique will be given in this work. The basis of the X-ray radiography technique is relatively straightforward. At visible light wavelengths, the refractive index of fuel is significantly greater than unity. Hence, light is strongly scattered from fuel droplets, obscuring the high-density regions of the spray. Moreover, multiple scattering effects hinder quantitative measurements in dense regions of the spray. In contrast, at X-ray wavelengths, the refractive index of fuel is very near unity, while absorption of X-rays by the fuel is quite strong. Thus, X-ray energy tends to be absorbed by fuel, rather than scattered.

To determine the fuel distribution in the spray, a narrow beam of monochromatic X-rays is directed through the fuel spray. Over the time scales of the spray, the X-ray intensity is relatively constant. Thus, by recording the transmitted X-ray intensity during the spray event and comparing it to the X-ray intensity before the spray event begins, the projected density of the fuel in the beam path during the spray event can be determined. The absorption is governed by the Beer–Lambert law, which can be written as

$$I = I_0 e^{-\mu M} \tag{1}$$

where $\mu$ is the absorption coefficient of the fuel, $M$ is the projected density of fuel in the beam path, and $I$ and $I_0$ are the X-ray intensity values during and before the spray event, respectively. This equation applies for a single X-ray wavelength. The absorption coefficient is a strong function of the X-ray energy (wavelength), so revision of Eq. (1) would be required if a polychromatic X-ray source were used. For a monochromatic X-ray beam, Eq. (1) can be rewritten to solve for the projected density in terms of mass per unit area.

$$M = \frac{\ln(I_0/I)}{\mu} \tag{2}$$

To obtain sufficient monochromatic X-ray flux to perform these experiments, a synchrotron X-ray source is used. These experiments are performed at the 1-BM beamline of the Advanced Photon Source at Argonne National Laboratory. The beamline consists of a bending magnet X-ray source, a collimating mirror, a double-crystal multilayer monochromator, a focusing mirror, harmonic rejection mirror, and X-ray slits. These components are used to control the beam size, filter out all but a narrow band of X-ray energies (2% bandwidth), and focus the beam to a small spot. The photon energy used in these experiments is 8 keV, which allows for good penetration through the ambient gas while providing sufficient absorption from the fuel.

Once the X-ray beam reaches the experiment station, two pairs of X-ray slits are used to define the vertical and horizontal extents of the beam. For the experiments in this study, the full width at half maximum (FWHM) size of the beam is 160 $\mu$m streamwise and is 13 $\mu$m transverse to the injector axis. The beam passes through a spray chamber with X-ray transparent windows. After passing through the chamber and the spray, the beam illuminates an avalanche photodiode (APD) detector, which records the X-ray beam intensity as a function of time. A Yokogawa DL7480 500 MHz digital oscilloscope is used to record the signal from the APD; data are recorded every 1 ns for a duration of 2 ms for each measurement position. Ionization chambers are used to nonintrusively monitor the time-averaged X-ray intensity.

The raw data from the measurement consist of a series of voltage peaks from the X-ray detector that occur in a cycle that repeats every 3.6825 $\mu$s. To interpret these data, the height of each of these peaks is determined and the values are binned together for every cycle. Thus, the time resolution of the final data is 3.6825 $\mu$s. A time period (typically 100 $\mu$s in duration) before the spray event is used to determine the beam intensity when no spray is present. For the remaining time steps, Eq. (2) is used to determine the projected density of the spray. The data analysis is discussed in greater detail elsewhere [17,20].

This radiography measurement gives the spray density as a function of time integrated along one beam path through the spray flowfield; this measurement is termed the projected density of the spray. To determine the two-dimensional structure of the spray, the spray chamber is translated to many different positions to build a map of the spray behavior. To improve the signal strength in these measurements, the X-ray intensity versus time for every position is recorded as the average of 32 individual spray events. Thus, the measurements show the persistent, repeatable features of the sprays. Recent experiments indicate that the spray is generally quite repeatable [21], so these measurements provide a reasonable representation of the behavior of most individual spray events.

A Bosch light-duty common rail diesel injector was used to produce the sprays in this study. Rail pressures of 500 bar and 1000 bar were used. The sprays issued from two axial single-hole nozzles. One nozzle has been extensively hydroground (24%), with an outlet diameter of 183 $\mu$m and an inlet radius of curvature of 2.0 times the nozzle radius. The second nozzle was not extensively hydroground and has an outlet diameter of 208 $\mu$m, with an inlet radius of curvature of 0.4 times the nozzle radius. Both nozzles have nearly the same steady-state flowrate due to their different diameters and discharge coefficients.

In this study, chamber pressure values of 5 bar and 20 bar have been used. The chamber is filled with $N_2$ gas at ambient temperature (25°C). While these pressure values are far below those seen in operational diesel engines, it is the ambient density, rather than the pressure, that exerts the greatest influence on the spray development [22]. The chamber density values are 5.66 kg/m$^3$ and 22.7 kg/m$^3$, which range from far below typical in-cylinder chamber density values to slightly below the density seen in an operational diesel engine at start of injection (SOI).

Two fuels have been used in these measurements. The biodiesel blend is a mixture of 50% by volume of the cottonseed oil methyl ester with 50% Viscor 1487 diesel calibration fluid. While the discussion will focus on this fuel, corresponding experiments have been performed using Viscor 1487 to simulate conventional diesel fuel. Rhodia DPX9 diesel fuel additive in a 10% volume fraction has been added to both fuels. This additive contains cerium, which improves the X-ray contrast of the spray.

## 3 Results

Sixteen different combinations of fuel, rail pressure, chamber pressure, and nozzle were tested in these experiments. Global quantities will be presented for all of the cases, but for brevity, only selected results will be presented in detail.

**3.1 Projected Density.** Figures 1–4 show the projected density versus time for the spray from the hydroground nozzle at 1000 bar rail pressure and 20 bar ambient pressure. Figure 1 shows the spray behavior early in the injection event. At this stage of the injection event, the fuel jet is narrow, with a high projected density, near the nozzle. A region of particularly high density exists near the leading edge of the spray. This concentrated region

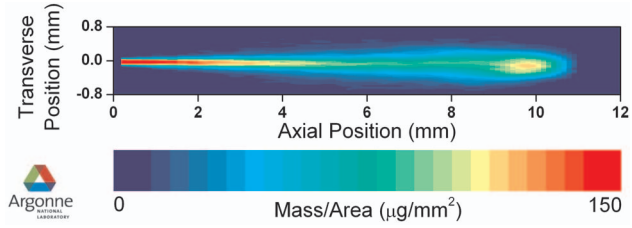


**Fig. 1 Biodiesel-blend spray behavior for the hydroground nozzle 67 $\mu$s after SOI; rail pressure=1000 bar and ambient pressure=20 bar**

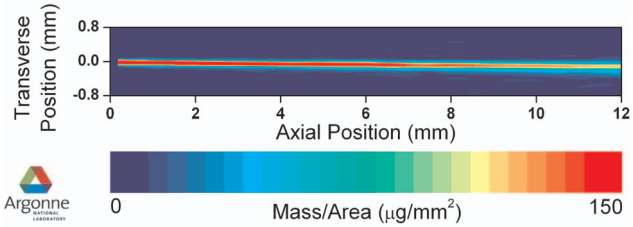


**Fig. 5 Biodiesel-blend spray behavior for the hydroground nozzle 612 $\mu$s after SOI; rail pressure=1000 bar and ambient pressure=5 bar**

has been seen in previous measurements of Viscor sprays [17] and has been referred to as "tip clustering" [23].

Figure 2 shows the spray behavior 182 $\mu$s after SOI. The spray is narrow and dense near the nozzle, but it expands rapidly at more downstream locations. The spray dispersion (rate at which the spray spreads as one moves downstream) at this stage of the injection event is quite large. Soon after this stage of the injection event, the spray transitions to a much narrower structure, as shown in Fig. 3, which is taken 612 $\mu$s after SOI. This behavior has been seen in previous Viscor spray measurements at lower injection pressure [17]. Unlike this previous case, the current spray does still show a significant degree of dispersion. This is due to the higher ambient density for the current case.

The structure of the spray resembles that shown in Fig. 3 for most of the spray event; this appears to be the steady-state behavior of the spray. At the end of the injection event, the projected density rapidly decreases across the entire spray domain at approximately the same time. An example of this behavior is shown in Fig. 4, which is taken 1423 $\mu$s after SOI, as the injector is closing. As has been seen in previous measurements of Viscor sprays [17], the decline in spray density at the end of injection is remarkably rapid and spatially uniform. This makes the definition and tracking of the trailing edge of the spray quite difficult.

The behaviors shown in Figs. 1–4 are present in many of the other biodiesel-blend measurements. As such, only selected images from the other spray cases will be presented. The effect of ambient pressure (and thus density) on the spray structure is shown in Fig. 5, which gives the spray behavior under the same conditions as Fig. 3, but with an ambient pressure of 5 bar rather

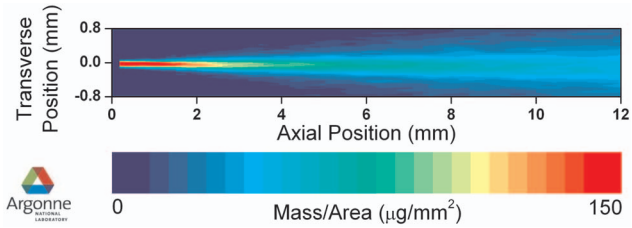


**Fig. 2 Biodiesel-blend spray behavior for the hydroground nozzle 182 $\mu$s after SOI; rail pressure=1000 bar and ambient pressure=20 bar**

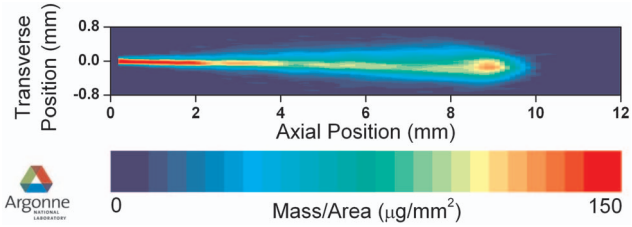


**Fig. 6 Biodiesel-blend spray behavior for the nonhydroground nozzle 67 $\mu$s after SOI; rail pressure=1000 bar and ambient pressure=20 bar**

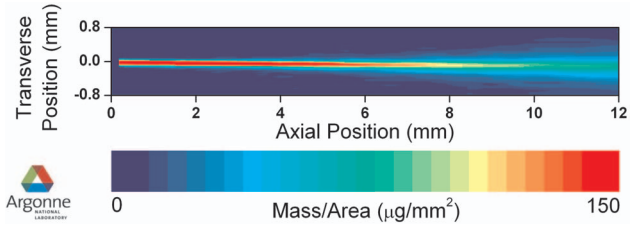


**Fig. 3 Biodiesel-blend spray behavior for the hydroground nozzle 612 $\mu$s after SOI; rail pressure=1000 bar and ambient pressure=20 bar**

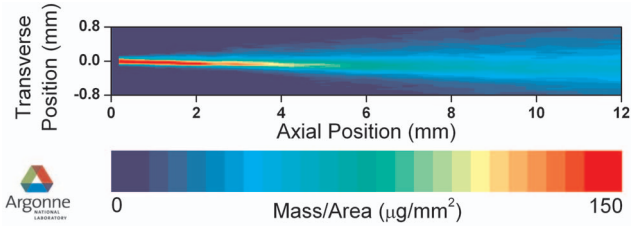


**Fig. 7 Biodiesel-blend spray behavior for the nonhydroground nozzle 612 $\mu$s after SOI; rail pressure=1000 bar and ambient pressure=20 bar**

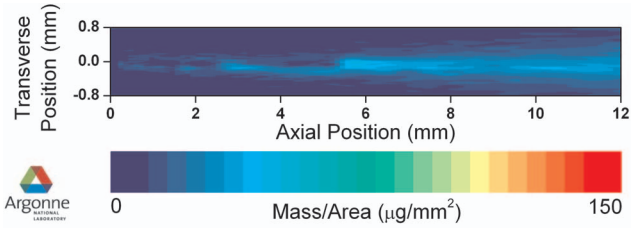


**Fig. 4 Biodiesel-blend spray behavior for the hydroground nozzle 1423 $\mu$s after SOI; rail pressure=1000 bar and ambient pressure=20 bar**

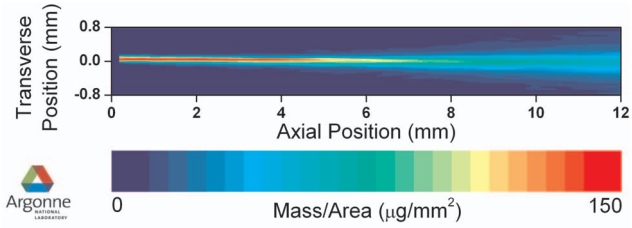


**Fig. 8 Viscor spray behavior for the hydroground nozzle 612 $\mu$s after SOI; rail pressure=1000 bar and ambient pressure=20 bar**

**Table 1 Delay (in microseconds) between the commanded and apparent SOI**

| Nozzle | | $P_{amb}$ | | | |
|---|---|---|---|---|---|
| | | Viscor | | B50 blend | |
| | | 500 bar | 1000 bar | 500 bar | 1000 bar |
| Hydroground | 5 | 338 | 333 | 342 | 328 |
| | 20 | 341 | 331 | 338 | 324 |
| Nonhydroground | 5 | 349 | 310 | 332 | 304 |
| | 20 | 322 | 303 | 327 | 297 |

than 20 bar. The spray dispersion decreases significantly as the ambient density decreases. At 5 bar ambient pressure, the spray appears as a largely uniform core of high-density fuel for the first several millimeters from the nozzle.

All of the results presented thus far were measured with the hydroground nozzle. Figures 6 and 7 show the projected density of the spray from the nonhydroground nozzle 67 $\mu$s and 612 $\mu$s after SOI, respectively. As shown in Fig. 6, the structure of the spray early in the injection event is very similar between the two nozzles. However, the dispersion of the spray has less variation with time for the nonhydroground nozzle than for the hydroground nozzle. The distribution of mass across the spray is also somewhat asymmetric for the spray from the nonhydroground nozzle. This shows that the internal nozzle geometry has a significant impact on the spray structure. The sprays from both nozzles show similar trends with respect to injection pressure and ambient density.

While the trends noted above have been seen in measurements of Viscor sprays, it is of particular interest to determine the differences between biodiesel-blend sprays and Viscor sprays. Figure 8 shows the behavior of Viscor sprays under the same conditions as Fig. 3, during the steady-state part of the spray. The high-density region of the spray extends for a shorter distance downstream in the Viscor sprays, and the spray appears to spread at a greater rate. This trend of larger spray dispersion for Viscor is largely consistent across different ambient density and rail pressure values, as well as with both nozzles. Otherwise, the overall behavior of the biodiesel-blend sprays is remarkably similar to that of Viscor sprays.

**3.2 Injection Timing.** The different properties of biodiesel compared with conventional diesel have been shown in previous studies to affect the injection rate characteristics of the injector, including the timing of the injection event [24]. Differences in the SOI timing of the injection event with respect to the time when current is first applied to the injector (termed the commanded SOI) can change the phasing of the injection event. Previous studies have attributed part of the increased $NO_x$ emissions from engines running biodiesel to an advance in the SOI [25], though these studies were performed with pump-line-nozzle injection systems, in contrast with the common rail system used in this study.

Table 1 gives the injection delay, defined as the time between the commanded SOI and apparent SOI. The values in the table are accurate to within 1 time step of the measurement (i.e., approximately 4 $\mu$s). The major trends are that biodiesel-blend fuel, the hydroground nozzle, and lower ambient pressure all tend to advance the SOI timing, but each of these effects is on average only slightly greater than the accuracy of the SOI measurements. Higher injection pressure advances injection to a somewhat greater degree, although the influence is still relatively minor.

**3.3 Penetration of Spray Leading Edge.** The speed with which the leading edge of the spray advances into the ambient gas, known as penetration speed, is a standard parameter measured in optical spray measurements. Most previous studies of biodiesel penetration have focused on regions relatively far from the nozzle [11,14–16]. The near-nozzle penetration is more significantly influenced by the transient dynamics of the injector. Given that the physical properties of biodiesel are somewhat different than those of conventional diesel fuel, it might be expected that the use of biodiesel fuel will affect the transient injector opening process and hence the near-nozzle spray penetration.

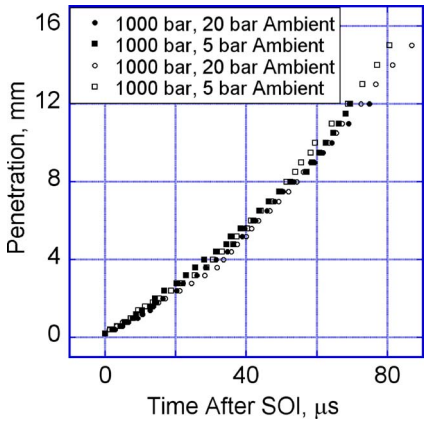


**Fig. 9 Penetration versus time for the hydroground nozzle. The filled symbols represent biodiesel-blend data; the open symbols represent Viscor data.**

To determine the penetration of the leading edge of the spray, the projected density data are integrated in the transverse direction for every measurement position in $x$, yielding the transverse integrated mass (TIM) for each $x$ measurement position. For each $x$ position, the TIM is monitored versus time. When the spray leading edge reaches a particular $x$ position, the TIM rises quite rapidly to a maximum value, usually within a time span of 10 $\mu$s. The leading edge is judged to be present at this $x$ location when the TIM reaches 25% of its maximum value. Tests have shown that the results of this analysis are insensitive to the threshold used; this is due to the sharp gradient in TIM near the leading edge. Moreover, this determination of spray penetration is insensitive to spray targeting.

Figures 9 and 10 show a comparison between the penetration with biodiesel-blend and Viscor fuels for selected measurement conditions. The curvature of these data is opposite of that usually seen in penetration data. Unlike most studies of spray penetration [13–15,22], this study focuses on the near-nozzle region, which is upstream of the area in which strong deceleration from the ambient gas would be expected [22]. Thus, the injector needle is still in the process of opening, and the penetration speed tends to accel-

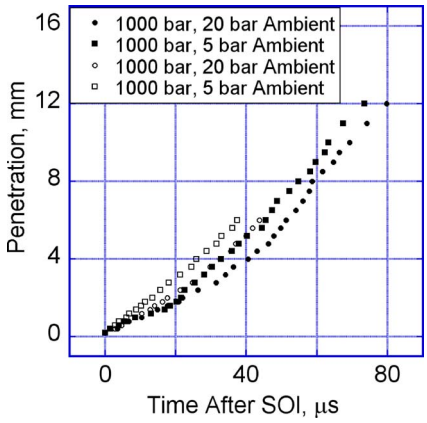


**Fig. 10 Penetration versus time for the nonhydroground nozzle. The filled symbols represent biodiesel-blend data; the open symbols represent Viscor data.**

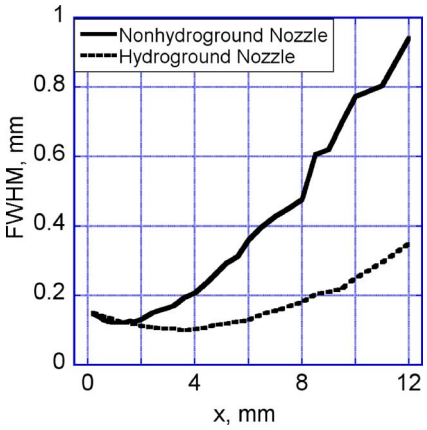


**Fig. 11 Example FWHM data during the steady-state part of the spray for the nonhydroground (1000 bar rail pressure) and hydroground (500 bar rail pressure) nozzles. The ambient pressure in both cases was 20 bar.**

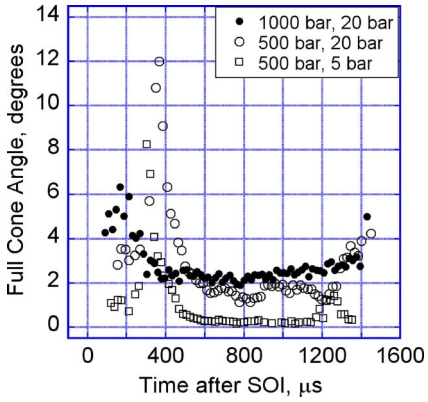


**Fig. 12 Cone angle versus time for selected measurements with the hydroground nozzle. For clarity, only every fifth point is displayed.**

erate for the first few millimeters downstream of the nozzle. As expected from standard correlations, increased injection pressure causes faster spray penetration.

For the hydroground nozzle, there is virtually no difference between the two fuels. For the nonhydroground nozzle, the Viscor spray tends to penetrate faster than the biodiesel-blend spray, especially early in the spray event. The nonhydroground nozzle has relatively sharp inlet corners, which are expected to result in much more cavitation in the nozzle than in the hydroground nozzle. The cavitation behavior of the biodiesel-blend fuel would be expected to be different than that of the Viscor fuel, perhaps explaining why penetration differences appear for only the nonhydroground nozzle.

**3.4 Spray Cone Angle.** A typical spray parameter measured from visible light imaging of sprays is the spray cone angle. This angle is generally defined by applying a threshold to the intensity of a visible light image to define the spray boundary and measuring the angle between these edges. Although such measurements provide insights regarding the dispersion of the spray and allow for comparisons between different spray conditions, the lack of data regarding the internal structure of sprays limits the capability of these cone angle measurements.

The cone angle can be measured from X-ray radiography data using a similar methodology. Unlike in visible light images, however, the projected density in the spray smoothly transitions from a peak value at the center of the spray to lower values near the periphery of the spray. As such, the choice of threshold is arbitrary, but it is based on quantitative data and thus is unambiguous. However, the threshold value significantly affects the final cone angle values.

For this study, the projected density distribution across the spray is examined for each $x$ measurement location. The FWHM of the distribution is recorded for each $x$ position at each time step. Figure 11 shows example trends in the spray FWHM with axial distance for both nozzles. Generally, the FWHM increases with axial distance, as expected from optical measurements. Close to the nozzle, however, the FWHM actually decreases as the axial distance increases. This is tied to changes in the shape of the distribution from a flat-topped distribution near the nozzle to a more Gaussian distribution farther downstream.

A linear fit is performed for each time step on the FWHM versus $x$ trend. Only the region from $x=6$ mm to $x=12$ mm is used in the fit since this region exhibits a reasonably linear trend in FWHM versus $x$. The slope of this line is used to calculate the full cone angle of the spray. The linear fits are deemed acceptable only if appropriate FWHM values are found for most of the $x$ positions and the $R^2$ value of the fit is at least 0.90.

Figures 12 and 13 show the cone angle versus time data for selected biodiesel-blend spray measurements. The uncertainty of the individual values shown is approximately 10–25% above and below the value plotted. There are significant changes in the cone angle during the spray development for the hydroground nozzle. The cone angle has a maximum value early in the injection event, and then it decreases to a small value compared with the nonhydroground nozzle. The timing and magnitude of the peak cone angle seem to depend on the injection pressure and ambient pressure. Higher ambient-pressure values tend to accentuate this peak, while the peak occurs much earlier in the spray development at 1000 bar injection pressure than at 500 bar. For the nonhydroground nozzle, the cone angle is for the most part uniform to within the uncertainty of the measurements for the entire duration of the spray event. The cone angle data generally match the behavior seen in the images of projected density for this nozzle.

Generally, the features of the cone angle versus time data for biodiesel-blend sprays with the hydroground nozzle match those seen for Viscor sprays. There are two interesting differences. The peak in cone angle near the beginning of the spray event for the hydroground nozzle seems to be larger in magnitude and occurs later in time after SOI in the biodiesel-blend spray than in the Viscor spray. In previous studies of Viscor sprays, the dynamics of the cone angle for the hydroground nozzle spray have been attributed to the dynamics of the injector needle as the injector opens and closes [17]. Given the differences in properties between

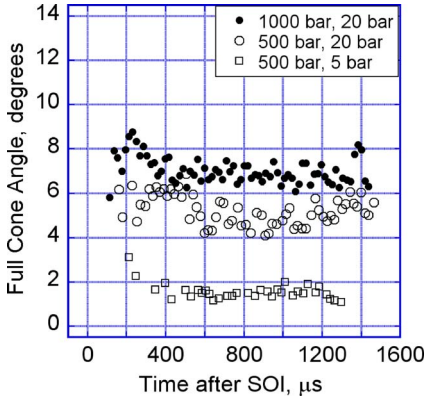


**Fig. 13 Cone angle versus time for selected measurements with the nonhydroground nozzle. For clarity, only every fifth point is displayed.**

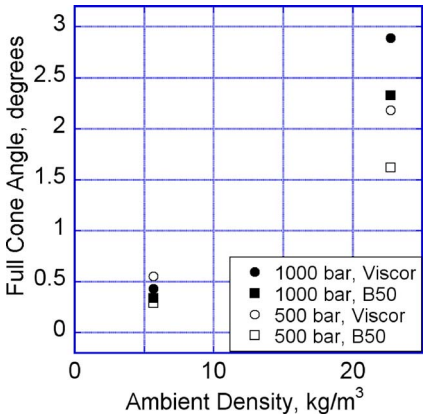


**Fig. 14 Steady-state cone angle versus ambient density for the hydroground nozzle**

biodiesel-blend fuel and Viscor, it is perhaps not surprising that the use of biodiesel-blend fuel would affect the needle lift behavior and hence the spray cone angle dynamics.

Another interesting difference is seen with the nonhydroground nozzle at 500 bar rail pressure and 20 bar ambient pressure. While a peak cone angle is seen early in the injection event when Viscor is used, no such peak is evident when the biodiesel-blend fuel is used.

Given the rather significant uncertainty in the cone angle measurements at any particular time, it is difficult to make meaningful comparisons between different conditions at any single instant in time after SOI. Instead, the cone angle values are averaged for the time from 600 $\mu$s to 1200 $\mu$s after SOI, during which time the cone angle is typically constant. The results are shown in Figs. 14 and 15. Several trends are clearly evident from these plots. For most cases, the biodiesel-blend sprays are narrower than the Viscor sprays. Averaging over the six cases for which comparisons can be made, the biodiesel sprays are on average 13% narrower than the Viscor sprays. Such a difference in the width of the spray may have profound impacts on the evaporation of the spray, the mixing with the ambient air, and ultimately the combustion of biodiesel-blend fuels in diesel engines.

Other trends seen in the steady-state cone angle are similar to those seen with Viscor fuel. Higher ambient density values yield significantly larger cone angles. Injection pressure has only a small effect on cone angle, with higher rail pressure values leading to slightly larger cone angle values.

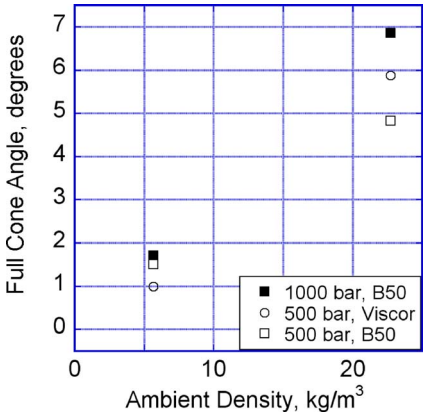


**Fig. 15 Steady-state cone angle versus ambient density for the nonhydroground nozzle**

## 4 Discussion

Overall, the behavior of the biodiesel sprays is quite similar to that of the Viscor sprays; SOI timing, penetration, and overall spray structure show few differences between the two fuels. These results lend confidence that, at least from the perspective of spray structure, biodiesel blends can be applied to existing diesel injection equipment.

An interesting difference between the biodiesel-blend and Viscor sprays is the narrowing of the cone angle when biodiesel blends are used. This finding is in contrast to the findings of Higgins et al. [12], which found no dependence of cone angle on fuel properties for a number of different alternative fuels. This difference in behavior may be caused by the differences in the definitions used in that paper and the current work. The work by Higgins et al. focused on the spray periphery, as determined from schlieren imaging of vaporizing sprays. The current X-ray technique, in contrast, focuses on the core region of nonevaporating sprays. As has been stated elsewhere [17], comparisons between optical and X-ray cone angles must be made with caution.

According to accepted models of diesel combustion [26], the central, fuel-rich region of the diesel spray is responsible for the proliferation of soot in diesel combustion. Had this study found that the fuel density was lower in the central region of the spray with the biodiesel-blend fuel, it would have been tempting to attribute at least part of the soot reduction when biodiesel fuels are used to this change in spray structure. Interestingly, this study shows the opposite trend: Biodiesel-blend sprays tend to have a narrower cone angle and denser central region than conventional diesel calibration fluid. Other effects must be important in causing the soot reduction seen with biodiesel fuels, including fuel chemistry or evaporating spray effects. Unfortunately, it was not possible to study such effects in the current work

## 5 Conclusions

The structure of biodiesel-blend sprays from a common rail injector has been examined with X-ray radiography. Measurements have been performed at different ambient density values, rail pressure values, and nozzle geometry with both biodiesel-blend fuel and Viscor, a diesel calibration fluid. These measurements have been examined to quantify how fuel property changes affect spray structure. The major conclusions are as follows.

- Gross spray structure with biodiesel-blend fuel is quite similar to the structure with Viscor. The tip clustering and spray structure early in the injection event are similar with both fuels. The dynamic transition in spray dispersion with the hydroground nozzle occurs with both fuels.
- The penetration of the spray leading edge near the nozzle is largely unaffected by the use of biodiesel-blend fuel. For the nonhydroground nozzle, the biodiesel-blend fuel slightly slowed the penetration near the nozzle.
- The cone angle when using biodiesel fuels tends to be smaller than the cone angle with Viscor. The cone angle when using biodiesel fuel tends to increase slightly with increased rail pressure and significantly with increased ambient density. These trends are similar to the trends seen with Viscor.
- The timing of the transition in the hydroground nozzle spray behavior for the biodiesel-blend spray seems to occur somewhat later than for the Viscor spray. This suggests that the needle opening transient occurs differently when different fuels are used.

## Acknowledgment

This research was performed at the 1-BM-C beamline of the Advanced Photon Source, Argonne National Laboratory. The Viscor spray measurements described in this work and the use of the APS are supported by the U.S. Department of Energy under Con-

tract No. DE-AC02-06CH11357 and by the Department of Energy Vehicle Technologies Program.

## Nomenclature

EOI = end of injection
$I$ = X-ray intensity during the spray event
$I_0$ = X-ray intensity before the spray event
$M$ = projected density, $\mu g/mm^2$
SOI = star of injection, measured when the spray penetration reaches the measurement position closest to the spray orifice, $\mu s$
$p_{amb}$ = ambient pressure, bar
$x$ = axial distance from the nozzle exit, mm
$y$ = transverse distance from the center of the nozzle exit, mm
$\theta$ = spray full cone angle, deg
$\mu$ = X-ray absorption coefficient, $mm^2/\mu g$

## References

[1] Graboski, M., and McCormick, R., 1998, "Combustion of Fat and Vegetable Oil Derived Fuels in Diesel Engines," Prog. Energy Combust. Sci., **24**(2), pp. 125–164.
[2] Wang, M. Q., 1999, "GREET 1.5 – Transportation Fuel-Cycle Model, Volume 1: Methodology, Development, Use, and Results," Argonne National Laboratory Report No. ANL/ESD-39.
[3] Armas, O., Hernández, J., and Cárdenas, M., 2006, "Reduction of Diesel Smoke Opacity From Vegetable Oil Methyl Esters During Transient Operation," Fuel, **85**(17–18), pp. 2427–2438.
[4] Choi, C., Bower, G., and Reitz, R., 1997, "Effects of Biodiesel Blended Fuels and Multiple Injection on D. I. Diesel Engines," SAE Paper No. 970218.
[5] Corgard, D. and Reitz, R., 2001, "Effects of Alternative Fuels and Intake Port Geometry on HSDI Diesel Engine Performance and Emissions," SAE Paper No. 2001-01-0647.
[6] Grimaldi, C., Postrioti, L., Battistoni, M., and Millo, F., 2002, "Common Rail HSDI Diesel Engine Combustion and Emissions With Fossil/Bio-Derived Fuel Blends," SAE Paper No. 2002-01-0865.
[7] Hashimoto, M., Dan, T., Asano, I., and Arakawa, T., 2002, "Combustion of the Rape-Seed Oil in a Diesel Engine," SAE Paper No. 2002-01-0867.
[8] Parvate-Patil, G., Vasquez, M., and Payne, M., 2006, "Effects of Different Biodiesel Blends on Heat Release and Its [sic] Related Parameters," ASME Paper No. ICEF 2006-1582.
[9] Scholl, K., and Sorenson, S., 1993, "Combustion of Soybean Oil Methyl Ester in a Direct Injection Diesel Engine," SAE Paper No. 930934.
[10] Reitz, R., 1987, "Modeling Atomization Processes in High-Pressure Vaporizing Sprays," Atomisation and Spray Technology, **3**, pp. 309–337.
[11] Chang, C., and Farrell, P., 1997, "A Study on the Effects of Fuel Viscosity and Nozzle Geometry on High Injection Pressure Diesel Spray Characteristics," SAE Paper No. 970353.
[12] Higgins, B., Mueller, C., and Siebers, D., 1999, "Measurements of Fuel Effects on Liquid-Phase Penetration in DI Sprays," SAE Paper No. 1999-01-0519.
[13] Senatore, A., Cardone, M., Allocca, L., Vitolo, S., and Rocco, V., 2005, "Experimental Characterization of a Common Rail Engine Fuelled With Different Biodiesel," SAE Paper No. 2005-01-2207.
[14] Lee, C., Park, S., and Kwon, S., 2005, "An Experimental Study on the Atomization and Combustion Characteristics of Biodiesel-Blended Fuels," Energy Fuels, **19**, pp. 2201–2208.
[15] Grimaldi, C., and Postrioti, L., 2000, "Experimental Comparison Between Conventional and Bio-Derived Fuels Sprays From a Common Rail Injection System," SAE Paper No. 2000-01-1252.
[16] Postrioti, L, Grimaldi, C., Ceccobello, M., and Di Gioia, R., 2004, "Diesel Common Rail Injection System Behavior With Different Fuels," SAE Paper No. 2004-01-0029.
[17] Kastengren, A., Powell, C. F., Riedel, T., Cheong, S.-K., Im, K.-S., Liu, X., Wang, Y.-J., and Wang, J., 2007, "Nozzle Geometry and Injection Duration Effects on Diesel Sprays Measured by X-Ray Radiography," Paper No. 041301.
[18] Cheong, S.-K., Liu, J., Shu, D., Wang, J., and Powell, C.F., 2004, "Effects of Ambient Pressure on Dynamics of Near-Nozzle Diesel Sprays Studied by Ultrafast X-Radiography," SAE Paper No. 2004-01-2026.
[19] Powell, C.F., Ciatti, S., Cheong, S.-K., Liu, J., and Wang, J., 2004, "X-Ray Absorption Measurement of Diesel Sprays and the Effect of Nozzle Geometry," SAE Paper No. 2004-01-2011.
[20] Kastengren, A., and Powell, C. F., 2007, "Spray Density Measurements Using X-Ray Radiography," Proc. Inst. Mech. Eng., Part D (J. Automob. Eng.), **221**(6), pp. 653–662.
[21] Kastengren, A., Powell, C. F., Wang, Y.-J., and Wang, J., "Study of Diesel Jet Variability Using X-Ray Radiography," Paper No. 032811.
[22] Naber, J., and Siebers, D., 1996, "Effects of Gas Density and Vaporization on Penetration and Dispersion of Diesel Sprays," SAE Paper No. 960034.
[23] Tanner, F., and Boulouchos, K., 1996, "A Computational Investigation of the Spray-Induced Flow and Its Influence on the Fuel Distribution for Continuous and Intermittent Di-Diesel Sprays," SAE Paper No. 960631.
[24] Miers, S., Kastengren, A., El-Hannouny, E., and Longman, D., 2007, "An Experimental Investigation of Biodiesel Injection Characteristics Using a Light-Duty Diesel Injector," ASME Paper No. ICEF 2007-1735.
[25] Szybist, J., and Boehman, A., 2003, "Behavior of a Diesel Injection System With Biodiesel Fuel," SAE Paper No. 2003-01-1039.
[26] Flynn, P., Durrett, R., Hunter, G., Loye, A., Akinyemi, O., Dec, J., and Westbrook, C., 1999, "Diesel Combustion: An Integrated View Combining Laser Diagnostics, Chemical Kinetics, and Empirical Validation," SAE Paper No. 1999-01-0509.

# Low-Temperature Combustion Within a HSDI Diesel Engine Using Multiple-Injection Strategies

**Tiegang Fang**[1]
Department of Mechanical and Aerospace Engineering,
North Carolina State University,
3182 Broughton Hall,
Campus Box 7910,
2601 Stinson Drive,
Raleigh, NC 27606
e-mail: tfang2@ncsu.edu

**Robert E. Coverdill**

**Chia-Fon F. Lee**

**Robert A. White**

Department of Mechanical Science and Engineering,
University of Illinois at Urbana–Champaign,
1206 West Green Street,
Urbana, IL 61801

*Low-temperature compression ignition combustion employing multiple-injection strategies in an optical high-speed direct injection diesel engine was investigated. Heat release characteristics were analyzed. The whole cycle combustion process was visualized by imaging the natural flame luminosity. The $NO_x$ emissions were measured in the exhaust pipe. The effects of the pilot injection timing, pilot fuel quantity, main injection timing, operating load, and injection pressure on the combustion and emissions were studied. Low-temperature combustion modes were achieved by using a small pilot injection with an injection timing much earlier than top dead center (TDC) followed by a main injection after TDC. The results were compared with conventional diesel (diffusion) combustion for comparison purposes. A premixed-combustion-dominated heat release rate pattern was seen for all the low-temperature combustion cases, while a typical diffusion flame combustion heat release rate was obtained for the conventional combustion case. A highly luminous flame was observed for the conventional combustion condition while a much less luminous flame was seen for the low-temperature combustion cases. For the higher-load and lower injection pressure cases, liquid fuel being injected into low-temperature premixed flame was observed for certain cases. Compared with the conventional diffusion combustion, simultaneous reductions in soot and $NO_x$ were obtained for the low-temperature combustion mode under similar operating loads. For high-load conditions, higher $NO_x$ emissions were obtained due to higher in-cylinder temperatures. However, compared with the conventional combustion case, a significant reduction in soot was achieved for the high-load conditions, which shows that increasing injection pressure greatly reduces soot emissions.* [DOI: 10.1115/1.3093999]

*Keywords: high-speed direct injection (HSDI) diesel engine, low-temperature combustion, HCCI combustion, combustion visualization*

## 1 Introduction

Direct injection (DI) diesel engines offer higher thermal efficiency and greater reliability than gasoline engines. Because of the limited fossil fuel resources and worldwide environmental concerns, the emission regulations are becoming more and more stringent [1]. Exhaust emissions, for example, oxides of nitrogen ($NO_x$) and particulate matter (PM), must be reduced for diesel engines.

A multiple-injection strategy has been reported for simultaneous reductions in $NO_x$ and PM in both large-bore DI diesel engines [2–4] and small-bore high-speed DI diesel engines [5–7]. Nehmer and Reitz [2] showed that pulsed injection could provide a method to reduce PM and $NO_x$ emissions. Based on the experimental results [3], numerical simulations were performed to explore the mechanism of soot and $NO_x$ reduction using multiple-injection strategies [4]. A multiple-injection strategy had a similar effect on $NO_x$ reduction to a retarded single injection. Reduced soot emissions were due to the fact that the rich soot producing region was not replenished when the injection pulse was terminated and restarted. Zhang [5] experimentally investigated the effect of pilot injection on $NO_x$ and soot emissions as well as on the combustion noise. By optimizing the exhaust gas recirculation (EGR) rate, pilot timing and quantity, main timing, and dwell between the main and pilot injections, simultaneous reductions in $NO_x$ and PM were obtained in a small diesel engine [6]. Simultaneous reductions in combustion noise and emissions were possible by reducing the pilot fuel quantity and advancing the pilot injection timing [7].

New combustion concepts such as homogeneous charge compression ignition (HCCI) concept have been studied with promising potential for $NO_x$ and PM reductions [8–11]. HCCI combustion is a bulky combustion by eliminating local high-temperature regions; therefore, the $NO_x$ emissions are extremely low compared with conventional diesel combustion. In addition, because the air-fuel mixture is premixed, there are less locally rich regions and soot is also greatly reduced. Najt and Foster [10] showed that the ignition process was controlled by low-temperature (950 K) oxidation kinetics and the energy release process was controlled by high-temperature (above 1000 K) oxidation for the HCCI combustion mode.

Because of the flexibility of a multiple-injection strategy in controlling the combustion processes, it was also employed in DI diesel engines for HCCI combustion modes [12–20]. Hashizume et al. [12] proposed an HCCI solution for higher-load operating conditions. The combustion mode was named multiple stage diesel combustion (MULDIC) on the basis of a premixed lean diesel combustion (PREDIC) concept [13]. Smoke and $NO_x$ were reduced by MULDIC even at an excess air ratio of 1.4 for a retarded main injection. A multiple-injection strategy was adopted in a study and the combustion system was named homogeneous

[1]Corresponding author.

Manuscript received October 16, 2008; final manuscript received November 16, 2008; published online July 15, 2009. Review conducted by Dilip R. Ballal. Paper presented at the 2007 Fall Conference of the ASME Internal Combustion Engine Division (ICEF2007), Charleston, SC, October 14–17, 2007.

**Table 1 Specifications of the single-cylinder DIATA research engine**

| | |
|---|---|
| Bore | 70 mm |
| Stroke | 78 mm |
| Displacement/cylinder | 300 cc |
| Compression ratio | 19.5:1 |
| Swirl ratio | 2.5 |
| Valves/cylinder | 4 |
| Intake valve diameter | 24 mm |
| Exhaust valve diameter | 21 mm |
| Maximum valve lift | 7.30/7.67 mm (intake/exhaust) |
| Intake valve opening | 13 CAD ATDC (at 1 mm valve lift) |
| Intake valve closing | 20 CAD ABDC (at 1 mm valve lift) |
| Exhaust valve opening | 33 CAD BBDC (at 1 mm valve lift) |
| Exhaust valve closing | 18 CAD BTDC (at 1 mm valve lift) |

charge intelligent multiple-injection combustion system (HiMICS) [15,16]. Low $NO_x$ and smoke emissions and low fuel consumption were achieved for retarded main injection timings. A study by Hasegawa and Yanagihara [18] employed two injections in the HCCI combustion mode. The combustion concept was named uniform bulky combustion system (UNIBUS). HCCI combustion in a small-bore high-speed direct injection (HSDI) diesel engine was investigated by using early multiple short injection pulses during the compression stroke [19]. Results showed dramatic reduction in $NO_x$. Smoke emissions were also significantly reduced, while HC and CO substantially increased. Two-stage diesel fuel injection HCCI combustion was investigated in a small diesel engine [20]. $NO_x$ was greatly reduced with higher HC, CO, and fuel consumption.

The above-discussed combustion processes belong to HCCI combustion with a premixed lean mixture. A recent work on smokeless rich combustion provided a wider range for low sooting and low $NO_x$ combustion [21]. By reducing temperature, the low sooting and low $NO_x$ combustion range can be expanded to rich mixture. Low-temperature combustion with charge heterogeneity can be used to expand the low emission operating conditions to high-load regimes. Pickett [22] showed that mixing controlled diesel combustion was possible at lower flame temperatures with minimal $NO_x$ formation.

In previous studies, however, the experiments of in-cylinder diagnostics were often carried out with flat windows to attain optical access to the combustion chamber. The replacement of the true piston shape changes the in-cylinder flow field. For this work, a low-temperature combustion mode was studied in an environment with realistic piston geometry. A multiple-injection strategy including an early short injection (pilot) and a late main injection was employed. The influential factors such as injection pressure, pilot injection timing, pilot injection fuel quantity, and operation load were investigated. In-cylinder pressure was used to study the heat release process by calculating the net apparent heat release rate. The procedure of the heat release rate calculation was similar to those used in previous publications [23,24]. $NO_x$ emissions were measured in the exhaust pipe. The whole cycle combustion was visualized using a high-speed digital video camera.

## 2 Optical Engine and Facility

A single-cylinder direct injection aluminum through-bolt assembly (DIATA) research engine supplied by Ford Motor Co. was modified into an optical engine. Key aspects of the DIATA engine are listed in Table 1. The design is similar to the drop-liner design used at Sandia National Laboratories [23]. The optical access to the combustion chamber is attained from the side through a window or from below through a fused silica piston top. The optical engine design maintains the geometry of the ports and combustion chamber of the metal engine. A complete description of the optical engine can be found in a previous publication [25]. A common-rail injection system capable of rail pressures up to 1350 bars was used. A valve-covered-orifice (VCO) injector with six 0.124 mm holes and a spray cone angle of 150 deg was used. The injector is fitted with a needle lift sensor to measure the needle position throughout the injection event. A Phantom v7.1 high-speed digital video camera was used to capture the natural flame luminosity for the whole cycle. National Instruments LABVIEW version 6.0 was used as the data acquisition and timing software. An optical shaft encoder with a resolution of 0.25 crank angles was used to provide the time basis. The engine temperatures and pressures were monitored by using a multifunction data acquisition board. The necessary timing involved in running the engine and cameras was performed with 16 up/down 32 bit counter/timers.

**Table 2 Selected properties of the low-sulfur European diesel fuel**

| | |
|---|---|
| Specific gravity | 0.8352 |
| Cetane No. | 52.9 |
| Sulfur | 27.5 ppm |
| Mid boiling point | 260°C |

## 3 Engine Operating Conditions

The current results were from operating conditions considered typical for this engine under moderate loads. The intake temperatures and pressures were increased to match the top dead center (TDC) conditions that would occur within the metal engine with the same geometry and operating conditions. The engine speed remained constant at 1500 rpm. A multiple-injection strategy was used with a pilot injection and a main injection for each cycle. The injection pressure changed between 600 bars and 1000 bars. Pilot injection fuel quantities of 0.8 $mm^3$ and 1.3 $mm^3$ were selected. Pilot injection timings were set at $-30$ crank angle degrees (CADs) after top dead center (ATDC) and $-40$ CAD ATDC. The main injection timings were retarded to 5 CAD ATDC or 12 CAD ATDC in order to obtain low-temperature combustion modes. The main injection pulse duration was adjusted to match the load at 5.0 bar or 7.0 bar indicated mean effective pressure (IMEP). Fuel used was a low-sulfur European diesel fuel, selected properties of which are shown in Table 2. The relevant operating conditions are summarized in Table 3. Due to the extensive optical access provided by the optical engine, A 3D-like imaging setup was feasible [24,26,27]. The high-speed camera was operated with a resolution of $512 \times 256$ to capture the combustion images from the side window and the bottom of the optical piston simultaneously. The operating frame rate was 12,000 frames/s. This frame rate corresponded to 0.75 (CAD) intervals between two sequential images at the operating speed.

## 4 Results and Discussion

**4.1 In-cylinder Pressure and Heat Release Analysis.** The in-cylinder pressures for the 12 cases are shown in Fig. 1. The data are categorized into three groups. Cases 1–4 are shown in the upper plot, Cases 5–8 are shown in the middle plot, and Cases 9–12 are shown in the bottom plot. Other crank-angle-based data are also grouped in a similar manner. Slightly earlier ignition can be seen for the high-load and low injection pressure cases under similar pilot and main injection timings. The reason for the first situation is believed to be high gas temperature under high-load operating conditions due to high wall temperatures. This higher gas temperature makes the pilot injection combustion of Cases 5–8 more complete than those of Cases 1–4. For Cases 9–12 with lower injection pressure, the pilot injection combusts more completely than the relevant high injection pressure cases. The reason is that early injection timing with high injection pressure leads to a too lean mixture to combust completely.

The ignition delay for the main injection is shorter for a larger

**Table 3 Summary of engine operating conditions**

| Case No. | Rail pressure (bar) | Pilot timing (CAD ATDC) | Pilot quantity ($mm^3$) | Main timing (CAD ATDC) | IMEP (bar) |
|---|---|---|---|---|---|
| 1 | 1000 | −40 | 0.8 | 5 | 5.05 |
| 2 | 1000 | −30 | 0.8 | 12 | 5.09 |
| 3 | 1000 | −40 | 1.3 | 5 | 5.09 |
| 4 | 1000 | −30 | 1.3 | 12 | 5.03 |
| 5 | 1000 | −40 | 0.8 | 5 | 7.00 |
| 6 | 1000 | −30 | 0.8 | 12 | 6.88 |
| 7 | 1000 | −40 | 1.3 | 5 | 6.99 |
| 8 | 1000 | −30 | 1.3 | 12 | 6.99 |
| 9 | 600 | −40 | 0.8 | 5 | 5.00 |
| 10 | 600 | −30 | 0.8 | 12 | 5.00 |
| 11 | 600 | −40 | 1.3 | 5 | 5.07 |
| 12 | 600 | −30 | 1.3 | 12 | 5.08 |
| Con. | 600 | −30 | 1.3 | 0 | 5.01 |

pilot fuel quantity. An earlier pilot injection timing leads to a lower TDC pressure before the main injection due to incomplete combustion for earlier pilot injection timings with a too lean air-fuel mixture. The pressure rising rates for the high injection pressure cases are higher than the low injection pressure cases, which results in more combustion noise. Later main injection timing results in a soft combustion process with lower pressure increasing rates. The needle lift data for these cases are shown in Fig. 2. Based on the needle lift, it is seen that a larger pilot fuel quantity leads to slightly longer injection duration. Lower injection pressures and high-load conditions result in longer injection duration. The main injection duration for Cases 1–4 is about 8.25 CADs, for Cases 5–8 about 9.75 CADs, and for Cases 9–12 about 10.5 CADs. The difference among the four cases under similar injection pressures and loads is less than 0.25 CADs.

The heat release rate curves are shown in Fig. 3. Amplified heat release rate curves for the pilot injections are shown in Fig. 4 to clearly illustrate their heat release patterns. Similar to the observations in the in-cylinder pressure data, slightly shorter ignition delays are observed for higher-load (Cases 5–8) and lower injection pressure cases (Cases 9–12) than Cases 1–4 with the same injection timings and pilot injection fuel quantities. A larger pilot fuel quantity leads to shorter ignition delays. Because of the later main injection timing at 12 CAD ATDC for the even-number cases, their ignition delays are longer than the odd-number cases. A premixed-combustion-dominated heat release pattern is seen for all of the cases in the main injection. Higher loads and higher injection pressures result in higher peak values of the heat release rate. Retarded main injection timing leads to wider heat release rate curves and a lower peak heat release rate.

For the pilot injection, although the heat release rate value is small, a two-stage low-temperature reaction pattern is seen for all of the 12 cases. Referring to the needle lift data for the pilot injection, the heat release starts later than the end of injection for all cases, especially for the earlier pilot injection timing cases. There is sufficient time for the fuel to mix with the ambient air. However, the start of heat release timing is less than the injection timing difference for the two pilot injections, which indicates that the low-temperature combustion requires a certain ambient temperature to initiate the cool flame. The cool flame heat release rate occurs slightly earlier for the earlier pilot injection timing. However, the influence of the pilot fuel quantity on the cool flame occurring timing is rarely seen, showing that the overall equivalence ratio on the cool flame has a relatively less effect than that of the ambient temperature [28]. Ambient temperature plays an important role in determining the start of the cool flame. But a larger pilot fuel quantity does lead to a stronger two-stage heat release process. The dwell time between the cool flame and the second-stage heat release is longer for the earlier injection timing cases. The second-stage heat release is weaker for an earlier pilot

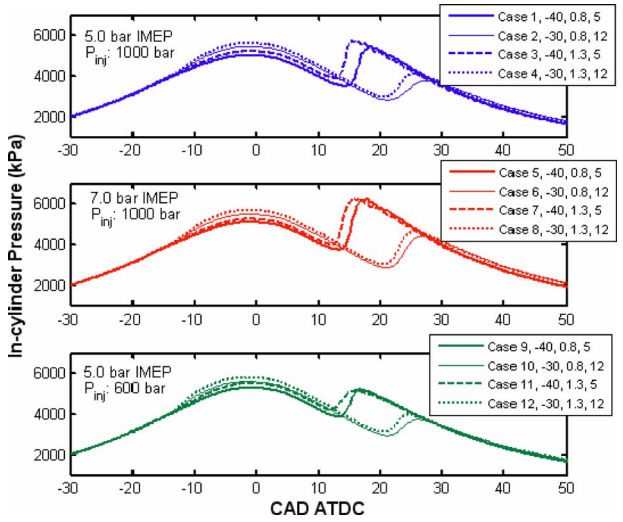


**Fig. 1 In-cylinder pressure for the 12 low-temperature combustion cases**

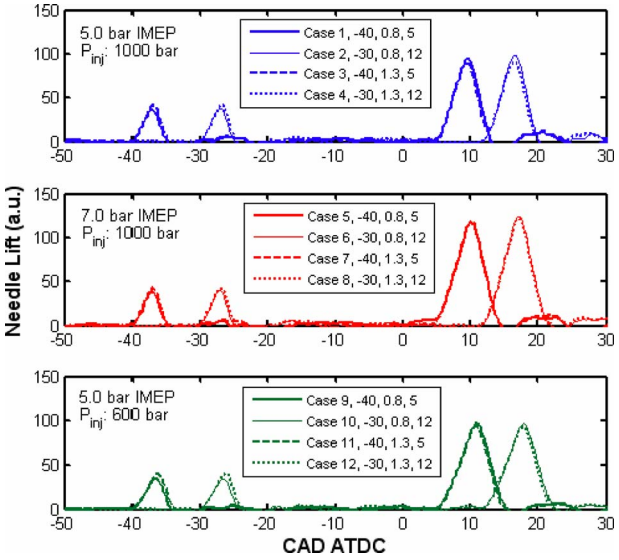


**Fig. 2 Needle-lift data for the 12 low-temperature combustion cases**

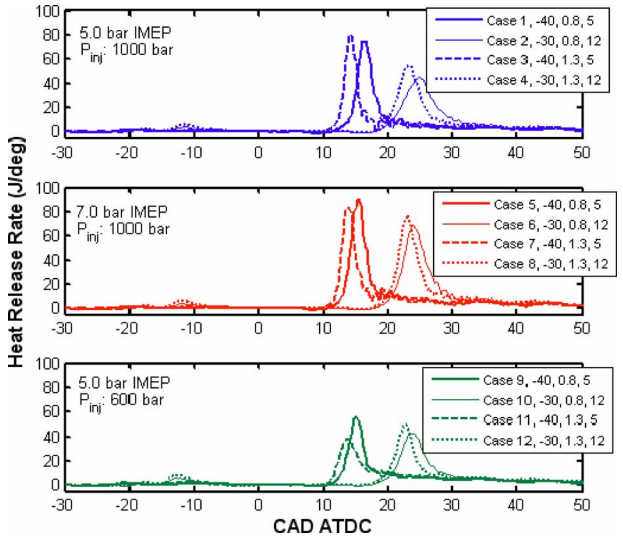


**Fig. 3 Heat release rates for the 12 low-temperature combustion cases**

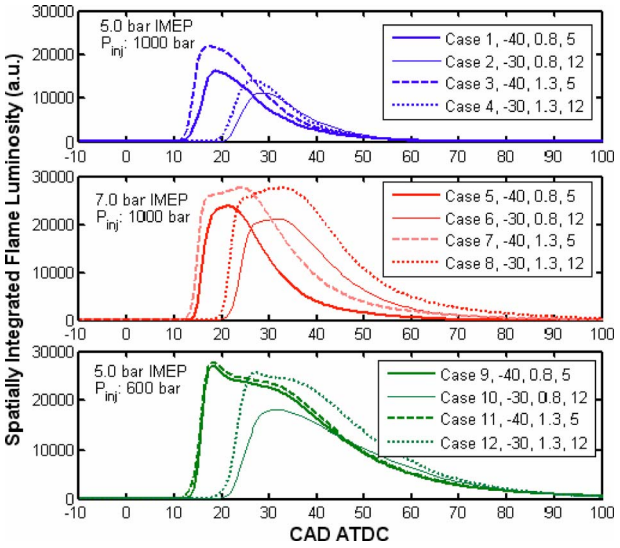


**Fig. 5 Spatially integrated flame luminosity for the 12 low-temperature combustion cases**

injection timing, higher injection pressure, and lower fuel quantity, which leads to lower TDC in-cylinder temperatures and pressures.

**4.2 Flame Luminosity Analysis.** The spatially integrated flame luminosity for the 12 cases is illustrated in Fig. 5. The early flame appearance timings are quite close to the beginning of the main heat release rate stage. Higher peak flame luminosity is observed for higher loads and lower injection pressures under similar injection timings and pilot fuel quantities. A larger pilot fuel quantity leads to early appearance of flame luminosity and higher peak flame luminosity. Higher flame luminosity generally implies higher soot concentration during the combustion processes [29]. For Cases 1–4 with higher injection pressure at 5.0 bar IMEP, the flame luminosity duration is less than the higher-load and lower injection pressure cases. This is due to the fact that high-load conditions with richer mixtures lead to more soot formation and lower injection pressure with less air-fuel mixing results in more soot formation. In addition, for high-load conditions, higher in-cylinder soot concentration requires more time to oxidize the soot particles during late cycle burning and low injection pressure with less air-fuel mixing leads to lower soot oxidation rate making the late cycle oxidation last longer.

The flame luminosity variation rates, or the flame luminosity time derivative curves, are shown in Fig. 6. The flame luminosity variation rate, to some extent, shows the soot formation (positive value) and/or oxidation (negative value) during the combustion process. Under similar load conditions and injection timings, a higher injection pressure leads to lower positive peaks of the flame luminosity variation rates indicating less soot formation and higher negative peaks of the flame luminosity variation rates showing faster soot oxidation process. High-load conditions show higher positive peaks and negative peaks compared with the low-load conditions. It is interesting to note that Cases 2 and 4 show lower positive variation rate peaks and relatively lower negative variation rate peaks, which indicates that these premixed charge compression ignition (PCCI) combustion modes have less soot formation because of less fuel rich regions and less oxidation rates

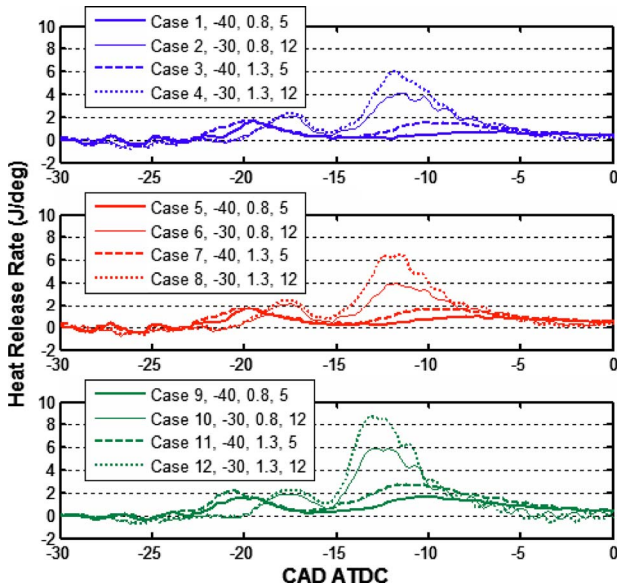


**Fig. 4 Heat release rates of the pilot injections for the 12 low-temperature combustion cases**

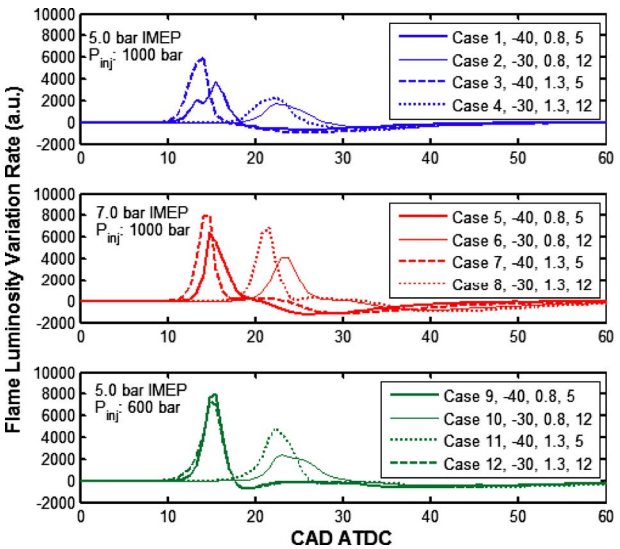


**Fig. 6 The variation rates of spatially integrated flame luminosity for the 12 low-temperature combustion cases**

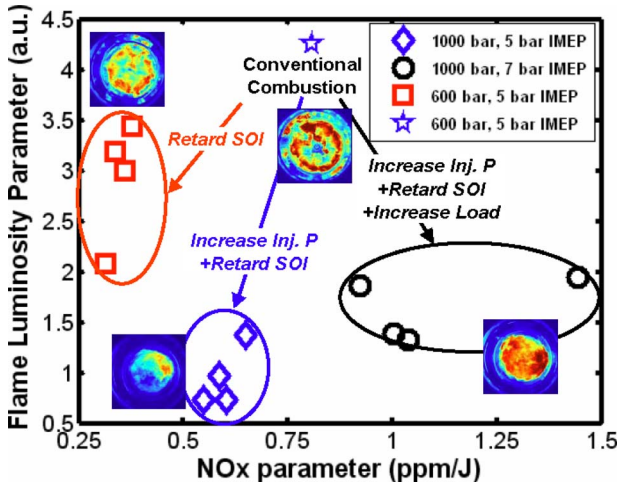


**Fig. 7 The FLP and $NO_x$ parameters for low-temperature combustion conditions with a multiple-injection strategy**

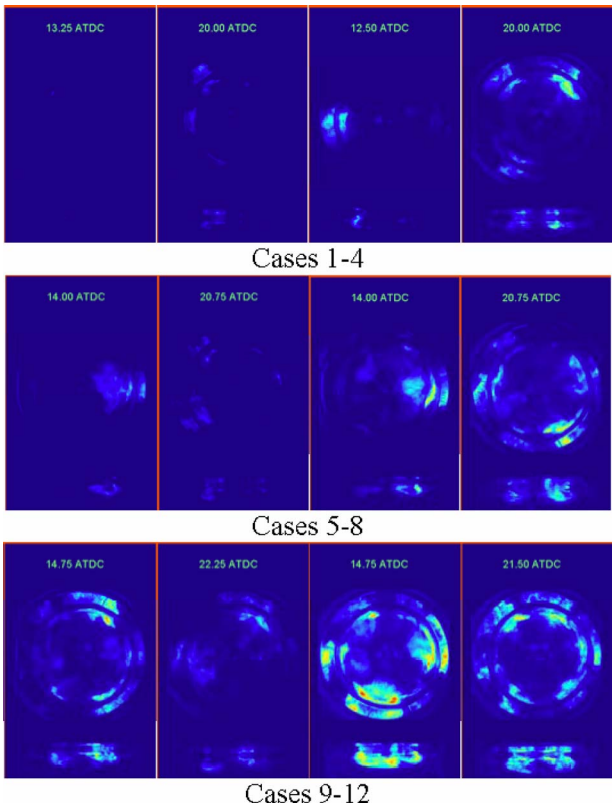


**Fig. 8 Early combustion images at the end of the main injection**

due to lower in-cylinder soot concentration.

Using the same logic as that in previous works, the flame luminosity parameter can be defined as the ratio of the average flame luminosity over the released heat for the main injection [24,26]. In order to compare the $NO_x$ emissions for different loads, a $NO_x$ parameter (NP) was defined as the $NO_x$ emissions divided by the released heat for the combustion process. The unit for the $NO_x$ parameter is ppm/J. A small value indicates a better performance in $NO_x$ emissions during the combustion process. The flame luminosity parameter (FLP) and $NO_x$ parameters for the 12 cases are depicted in Fig. 7. For comparison purposes, the conventional diesel combustion case, namely, Case Con. in Table 3, is also plotted. Under similar injection pressures, by retarding the main injection timing, both FLP and $NO_x$ parameters decrease. The reduction in $NO_x$ parameter is significant while the FLP decrease is moderate. By further increasing the injection pressure as well as retarding the main injection timing, the FLP is greatly reduced indicating a significant soot reduction. However, the $NO_x$ parameter increases. The reason of the $NO_x$ parameter increase is due to the faster combustion under higher injection pressures with high in-cylinder temperatures. Also a higher injection pressure results in a leaner air-fuel mixture, which also contributes to the higher $NO_x$ emissions. But compared with the conventional diesel combustion case, the high injection pressure cases still give us simultaneous reductions in the FLP and $NO_x$ parameters. By increasing the load to 7 bar IMEP under high injection pressures, the FLP increases compared with Cases 1–4. A decent reduction in the FLP is obtained compared with the low injection pressure cases, which shows that increasing injection pressure greatly reduces soot formation. The $NO_x$ parameter, on the other hand, increases due to the higher in-cylinder temperature under high-load conditions.

**4.3 Combustion Images.** The digital combustion images obtained using the high-speed video camera were processed using the same colormap and scales to compare different injection strategies. The image time is processed using CAD after TDC for all of the cases. For each case, five combustion movies were obtained and a typical whole cycle movie was selected for the analysis and presentation. The presented images are from the same cycle.

The combustion images of the 12 low-temperature combustion cases are shown in Fig. 8 at a time near the end of main injection. It is found that the early flames for different conditions are very different. Generally speaking, the combustion flame near the end of injection is weaker than the conventional combustion flame as will be seen later in Fig. 13. Some pieces of local flame can be found for the lower injection pressure cases. High flame luminosity shows that there are more flame spray overlap indicating liquid fuel is injected into early flames for some cases, namely, Cases 2–12. It is seen that higher injection pressure leads to less flame spray overlap with a weaker flame near the end of fuel injection. Earlier pilot injection timings and small pilot fuel quantities have similar effects to high injection pressures. For Case 1, the early flame is so weak and it shows a typical premixed charge combustion mode. Shorter spray and flame overlap time results in less fuel thermal cracking and less soot formation. Different from the conventional diesel combustion shown later in Fig. 13, the early flame occurs in a colder environment for the low-temperature combustion modes.

The combustion images with strong flame luminosity are illustrated in Fig. 9 for the 12 cases. At these crank angles, the flame is mostly confined in the bowl region for most of the cases. Some flames in the squish regions are found for the low injection pressure cases. Overall, the flame luminosity is stronger for low injection pressure and high-load conditions. A larger pilot fuel quantity leads to more luminous flame with more soot formation. The main injection timing plays an important role in soot formation. Even though the pilot injection timing is earlier for the odd-number cases, the main injection timing is also earlier compared with the even-number cases. Therefore, a slightly stronger flame is found for the odd-number cases at these crank angles.

The late cycle flames for the 12 low-temperature combustion cases are shown in Fig. 10. For late cycle flames, the flame temperature is greatly reduced due to volume expansion and the gas temperature becomes more uniform. The late cycle flame intensity is dominantly controlled by the soot concentration because the in-cylinder temperature is quite close for conditions with similar loads. From the images it is seen that the soot concentrations for Cases 1–4 are very low compared with the high-load and low injection pressure cases. Although Cases 5–8 have more fuel burnt, the soot concentration is lower than Cases 9–12, which indicates that increasing injection pressure greatly benefits the

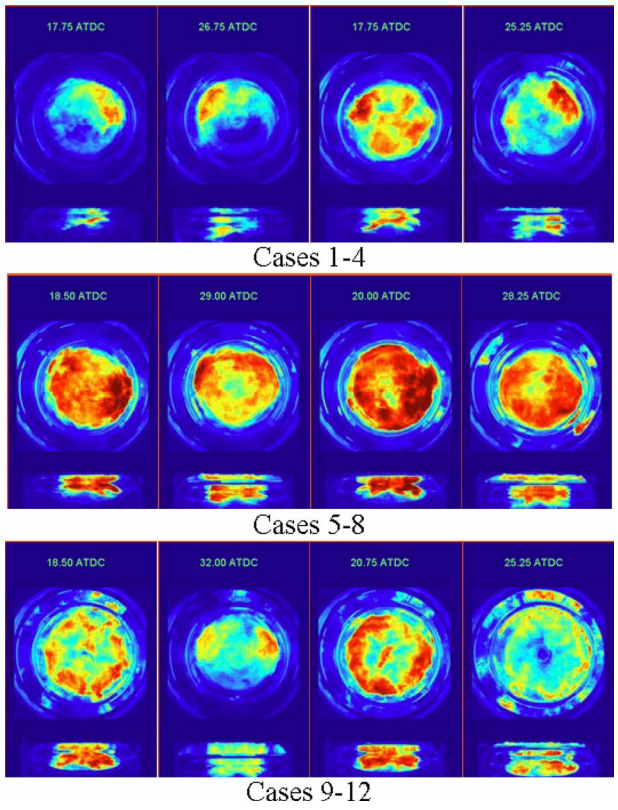


**Fig. 9 Combustion images with strong flame luminosity**

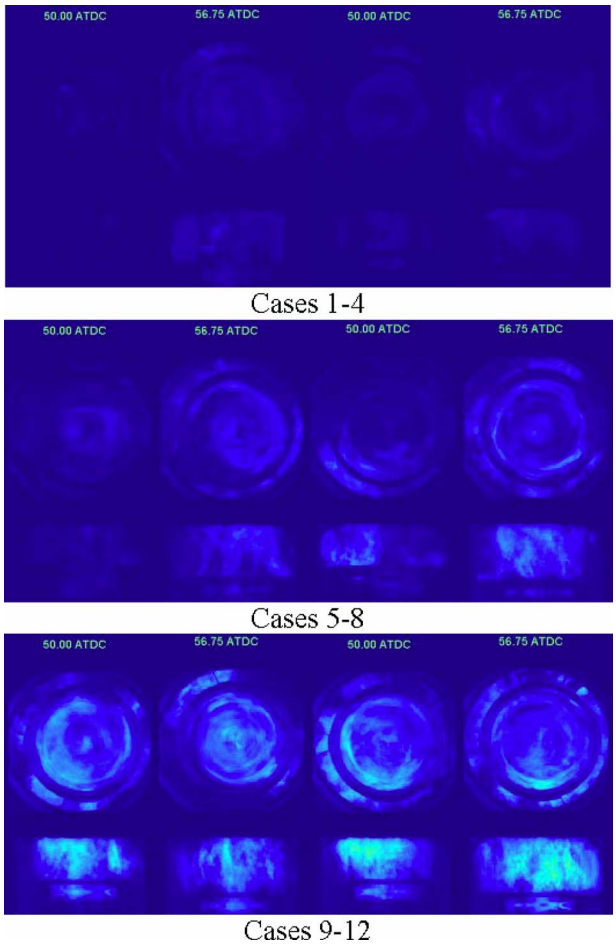


**Fig. 10 Late cycle combustion images**

soot reduction. Compared with flames in Fig. 9 for Cases 5–8, it is expected that the soot oxidation rate for these conditions is higher than Cases 9–12, which has also been shown in the flame luminosity variation rate curves.

**4.4 Comparison With Conventional Diesel Combustion.** In order to show the difference of the low-temperature combustion modes with the conventional diesel combustion mode, a direct comparison is made and the mechanisms for the low soot and low $NO_x$ emissions of the low-temperature combustion mode will be discussed in this section.

For comparison purposes, the in-cylinder pressure and heat release rate for a conventional diesel combustion case as listed in Table 3 are plotted in Fig. 11 together with those of Case 1, where Case 1 shows typical premixed charge low-temperature combustion. The heat release pattern of the main injection for Case 1 is similar to the UNIBUS combustion with shorter combustion duration and little diffusion combustion [18]. This heat release pattern is significantly different from the conventional diesel combustion [30], which includes a premixed phase and a mixing controlled combustion phase with relatively low heat release rate as shown in Fig. 11 for the conventional combustion case. The heat release pattern difference between the current low-temperature combustion and conventional diesel combustion is mainly due to the difference of the in-cylinder environment into which the main injection fuel is injected.

Another interesting point is that for the current study retarding the injection timing does not necessarily result in significantly lower cycle efficiency when the injection pressure is increased. The cycle thermal efficiencies for the 12 low-temperature combustion cases and the conventional case are shown in Fig. 12. It is seen that Cases 1, 3, 5, and 7 have higher or similar thermal efficiency compared with the conventional combustion case. This is attributed to the higher heat release rate peaks during the combustion process. A faster burning process makes the combustion closer to a constant-volume combustion process with higher thermal efficiency. This is why the PCCI-like combustion mode has higher efficiency than the conventional combustion mode under certain conditions. In addition, the radiation heat loss for the low-temperature combustion mode is generally lower than the conventional combustion mode due to lower combustion temperature and lower soot concentration, which also contributes to the higher fuel efficiency. However, it should be noted that based on the current results with the same injection pressure, a retarded injection timing generally leads to a lower cycle thermal efficiency for late

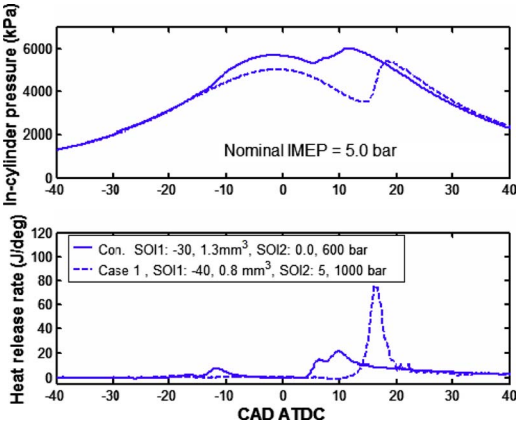


**Fig. 11 In-cylinder pressure and heat release rate for Case 1 and the conventional combustion case**

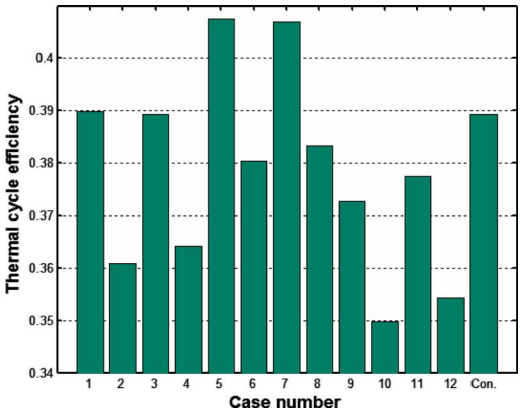


**Fig. 12 Cycle thermal efficiency for Cases 1–12 and the conventional combustion case**

main injection after TDC.

The combustion flame development for the conventional diesel combustion case is shown in Fig. 13. Based on the needle lift data, there is an overlap time between the end of injection and the early flame for most of the 12 low-temperature combustion conditions, showing that the liquid fuel is being injected into the reacted gas mixture during the main injection event. For conventional diesel combustion, it is obviously seen that the early flame occurs during the fuel injection process and the early flame becomes very luminous during the fuel injection process. The fuel injected into such a hot flame has no sufficient time for mixing and undergoes a fast thermal cracking process with a significant amount of soot generated in the flame for the conventional diffusion flame. But for the low-temperature combustion, namely, Cases 1–12, the liquid fuel is being injected into a lower-temperature flame, which is not high enough to accelerate the thermal cracking process but high enough to promote the evaporation process. Hence, even though there are spray-flame overlaps and charge heterogeneity in the combustion chamber, the soot formation process of the early combustion stage is greatly impeded by lowering the early flame temperature with a retarded main injection timing.

For conventional combustion mode, the flame fills both the combustion chamber and the squish region. With the interaction with air motion, the flame is most confined in the bowl after it burns out the flames in the squish region. However, late cycle flame would also fill the squish region due to the piston downward motion with flames coming out of the piston bowl. Compared with the low-temperature combustion modes, the soot formation is significantly higher for the conventional diffusion flame. In addition, the larger diffusion flame region also leads to more $NO_x$ formation due to high flame temperatures in the diffusion flame layers [31].

## 5 Conclusions

The low-temperature compression ignition (LTCI) combustion employing multiple-injection strategies was investigated in an optical HSDI diesel engine. Some important findings are summarized as follows.

1. A premixed-combustion-dominated heat release rate pattern

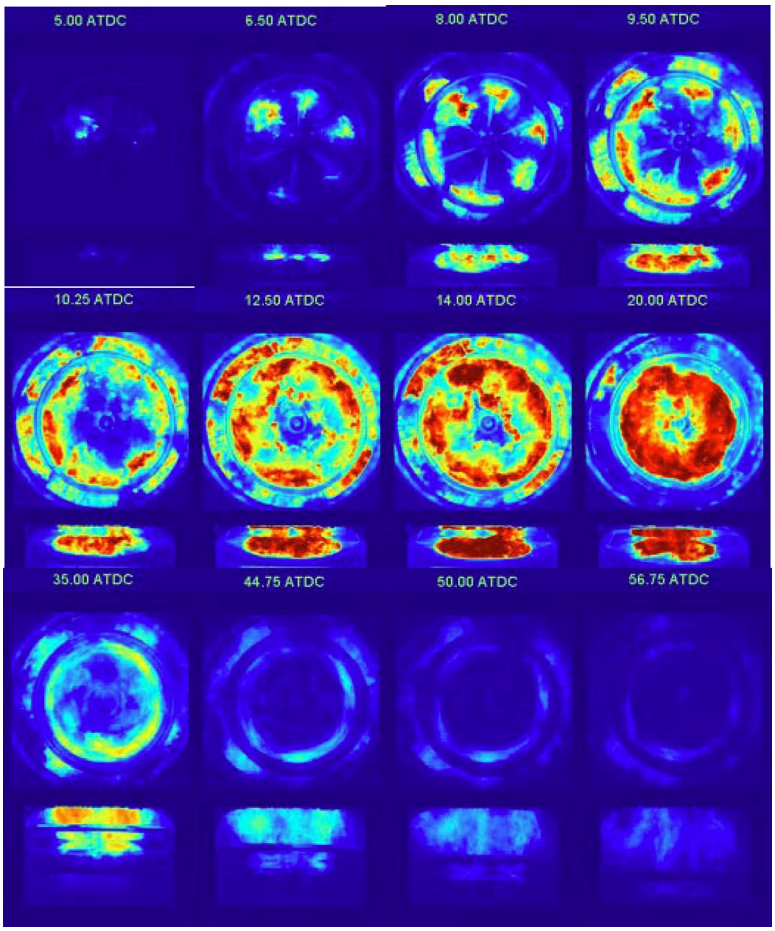


**Fig. 13 Combustion flame images of the conventional combustion condition**

was seen for all the low-temperature combustion cases, while a typical diffusion combustion heat release rate was obtained for the conventional diesel combustion case.
2. A highly luminous flame was observed for the conventional combustion case while a much less luminous flame was seen for the low-temperature combustion cases even with higher operating loads.
3. For some of the LTCI conditions, no liquid fuel is found when the early flame appears, which indicates low-temperature premixed combustion. For the higher-load and lower injection pressure cases, liquid fuel being injected into low-temperature early flames was observed, which was different from the conventional diesel combustion with liquid fuel injected into highly luminous flames.
4. Simultaneous reductions in the FLP and $NO_x$ were obtained for the low-temperature combustion mode under similar operating loads compared with the conventional diesel combustion case. For high-load conditions, higher $NO_x$ emissions were obtained due to the higher in-cylinder temperatures. However, compared with the conventional combustion mode with a lower load and a lower injection pressure, a significant reduction in soot was achieved for the high-load conditions.
5. A fast combustion process for the PCCI combustion helps recover the thermal cycle efficiency loss due to retarded main injection timing.
6. The low-temperature combustion mode greatly impedes the soot formation with significantly less soot generation than the conventional diffusion combustion. By reducing high-temperature diffusion combustion flame regions, the $NO_x$ emissions are also reduced under similar operating loads.

## Acknowledgment

This work was supported in part by the Department of Energy Grant No. DE-FC26-05NT42634, by Department of Energy GATE Centers of Excellence Grant No. DE-FG26-05NT42622, and by the Ford Motor Co. under University Research Program. We also thank Paul Miles of Sandia National Laboratories, and Evangelos Karvounis and Werner Willems of Ford for their assistance on the design of the optical engine and on the setup of the experiments.

## References

[1] Environmental Protection Agency, 2000, "Control of Air Pollution From New Motor Vehicles: Tier 2 Motor Vehicle Emissions Standards and Gasoline Sulfur Control Requirements; Final Rule," Fed. Regist., **65**(28), pp. 6697–6870.
[2] Nehmer, D. A., and Reitz, R. D., 1994, "Measurement of the Effect of Injection Rate and Split Injections on Diesel Engine Soot and $NO_x$ Emissions," SAE Paper No. 940668.
[3] Tow, T. C., Pierpont, D. A., and Reitz, R. D., 1994, "Reducing Particulate and $NO_x$ Emissions by Using Multiple Injections in a Heavy Duty DI Diesel Engine," SAE Paper No. 940897.
[4] Han, Z., Uludogan, A., Hampson, G. J., and Reitz, R. D., 1996, "Mechanism of Soot and $NO_x$ Emission Reduction Using Multiple Injection in a Diesel Engine," SAE Paper No. 960633.
[5] Zhang, L., 1999, "A Study of Pilot Injection in a DI Diesel Engine," SAE Paper No. 1999-01-3493.
[6] Chen, S. K., 2000, "Simultaneous Reduction of $NO_x$ and Particulate Emissions by Using Multiple Injections in a Small Diesel Engine," SAE Paper No. 2000-01-3084.
[7] Tanaka, T., Ando, A., and Ishizaka, K., 2002, "Study on Pilot Injection of DI Diesel Engine Using Common Rail Injection System," JSAE Rev., **23**, pp. 297–302.
[8] Onishi, S., Hong Jo, S., Shoda, K., Do Jo, P., and Kato, S., 1979, "Active Thermo-Atmosphere Combustion (ATAC)—A New Combustion Process for Internal Combustion Engines," SAE Paper No. 790501.
[9] Noguchi, M., Tanaka, Y., Tanaka, T., and Takeuchi, Y., 1979, "A Study on Gasoline Engine Combustion by Observation of Intermediate Reactive Products During Combustion," SAE Paper No. 790840.
[10] Najt, P. M., and Foster, D. E., 1983, "Compression Ignition Homogeneous Charge Combustion," SAE Paper No. 830264.
[11] Thring, R. H., 1989, "Homogeneous Charge Compression Ignition (HCCI) Engine," SAE Paper No. 892068.
[12] Hashizume, T., Miyamoto, T., Akagawa, H., and Tsujimura, K., 1998, "Combustion and Emission Characteristics of Multiple Stage Diesel Combustion," SAE Paper No. 980505.
[13] Takeda, Y., Keiichi, Na., and Keiichi, Ni., 1996, "Emission Characteristics of Premixed Lean Diesel Combustion With Extremely Early Staged Fuel Injection," SAE Paper No. 961163.
[14] Akagawa, H., Miyamoto, T., Harada, A., Sasaki, S., Shimazaki, N., Hashizume, T., and Tsujimura, K., 1999, "Approaches to Solve Problems of the Premixed Lean Diesel Combustion," SAE Paper No. 1999-01-0183.
[15] Yokota, H., Kudo, Y., Nakajima, H., Kakegawa, T., and Suzuki, T., 1997, "A New Concept for Low Emission Diesel Combustion," SAE Paper No. 970891.
[16] Yokota, H., Nakajima, H., and Kakegawa, T., 1998, "A New Concept for Low Emission Diesel Combustion (2nd Rep.: Reduction of HC and CO Emission, and Improvement of Fuel Consumption by EGR and MTBE Blended Fuel)," SAE Paper No. 981933.
[17] Su, W., Lin, T., and Pei, Y., 2003, "A Compound Technology for HCCI Combustion in a DI Diesel Engine Based on the Multi-Pulse Injection and the BUMP Combustion Chamber," SAE Paper No. 2003-01-0741.
[18] Hasegawa, R., and Yanagihara, H., 2003, "HCCI Combustion in DI Diesel Engines," SAE Paper No. 2003-01-0745.
[19] Helmantel, A., and Denbratt, I., 2004, "HCCI Operation of a Passenger Car Common Rail DI Diesel Engine With Early Injection of Conventional Diesel Fuel," SAE Paper No. 2004-01-0935.
[20] Kook, S., and Bae, C., 2004, "Combustion Control Using Two-Stage Diesel Fuel Injection in a Single Cylinder PCCI Engine," SAE Paper No. 2004-01-0938.
[21] Akihama, K., Takatori, Y., Inagaki, K., Sasaki, S., and Dean, A. M., 2001, "Mechanism of the Smokeless Rich Diesel Combustion by Reducing Temperature," SAE Paper No. 2001-01-0655.
[22] Pickett, L. M., 2005, "Low Flame Temperature Limits for Mixing-Controlled Diesel Combustion," Proc. Combust. Inst., **30**, pp. 2727–2735.
[23] Miles, P. C., 2000, "The Influence of Swirl on HSDI Diesel Combustion at Moderate Speed and Load," SAE Paper No. 2000-01-1829.
[24] Fang, T., Coverdill, R. E., Lee, C. F., and White, R. A., 2005, "Low Temperature Combustion Within a Small Bore High Speed Direct Injection (HSDI) Diesel Engine," SAE Paper No. 2005-01-0919.
[25] Mathews, W. S., Coverdill, R. E., Lee, C. F., and White, R. A., 2002, "Liquid and Vapor Fuel Distributions in a Small-Bore High-Speed Direct-Injection Diesel Engine," SAE Trans.: J. Fuels Lubr., **111**(4), pp. 1059–1071 (Also SAE Paper No. 2002-01-2666).
[26] Fang, T., Coverdill, R. E., Lee, C. F., and White, R. A., 2006, "Combustion and Soot Visualization of Low Temperature Combustion in an HSDI Diesel Engine Using Multiple Injection Strategy," SAE Paper No. 2006-01-0078.
[27] Fang, T., Coverdill, R. E., Lee, C. F., and White, R. A., 2007, "Smokeless Combustion Within a Small-Bore HSDI Diesel Engine Using a Narrow Angle Injector," SAE Paper No. 2007-01-0203.
[28] Fang, T., Coverdill, R. E., Lee, C. F., and White, R. A., 2005, "Liquid and Vapor Fuel Distributions Within a High Speed Direct Injection (HSDI) Diesel Engine Operating in HCCI and Conventional Combustion Modes," SAE Paper No. 2005-01-3838.
[29] Mueller, C. J., Pitz, W. J., Pickett, L. M., Martin, G. C., Siebers, D. L., and Westbrook, C. K., 2003, "Effects of Oxygenates on Soot Processes in DI Diesel Engines: Experiments and Numerical Simulations," SAE Paper No. 2003-01-1791.
[30] Dec, J. E., and Espey, C., 1998, "Chemiluminescence Imaging of Autoignition in a DI Diesel Engine," SAE Paper No. 982685.
[31] Dec, J. E., 1997, "A Conceptual Model of DI Diesel Combustion Based on Laser-Sheet Imaging," SAE Paper No. 970873.

# Chromium Activity Measurements in Nickel Based Alloys for Very High Temperature Reactors: Inconel 617, Haynes 230, and Model Alloys

**Stéphane Gossé**
**Thierry Alpettaz**
**Sylvie Chatain**
**Christine Guéneau**

Laboratoire de Modélisation, de Thermodynamique et de Thermochimie, CEA Saclay-DEN/DANS/DPC/SCP, 91191 Gif-sur-Yvette Cedex, France

*The alloys Haynes 230 and Inconel 617 are potential candidates for the intermediate heat exchangers (IHXs) of (very) high temperature reactors ((V)-HTRs). The behavior under corrosion of these alloys by the (V)-HTR coolant (impure helium) is an important selection criterion because it defines the service life of these components. At high temperature, the Haynes 230 is likely to develop a chromium oxide on the surface. This layer protects from the exchanges with the surrounding medium and thus confers certain passivity on metal. At very high temperature, the initial microstructure made up of austenitic grains and coarse intra- and intergranular $M_6C$ carbide grains rich in W will evolve. The $M_6C$ carbides remain and some $M_{23}C_6$ richer in Cr appear. Then, carbon can reduce the protective oxide layer. The alloy loses its protective coating and can corrode quickly. Experimental investigations were performed on these nickel based alloys under an impure helium flow (Rouillard, F., 2007, "Mécanismes de formation et de destruction de la couche d'oxyde sur un alliage chrominoformeur en milieu HTR," Ph.D. thesis, Ecole des Mines de Saint-Etienne, France). To predict the surface reactivity of chromium under impure helium, it is necessary to determine its chemical activity in a temperature range close to the operating conditions of the heat exchangers ($T \approx 1273$ K). For that, high temperature mass spectrometry measurements coupled to multiple effusion Knudsen cells are carried out on several samples: Haynes 230, Inconel 617, and model alloys 1178, 1181, and 1201. This coupling makes it possible for the thermodynamic equilibrium to be obtained between the vapor phase and the condensed phase of the sample. The measurement of the chromium ionic intensity (I) of the molecular beam resulting from a cell containing an alloy provides the values of partial pressure according to the temperature. This value is compared with that of the pure substance (Cr) at the same temperature. These calculations provide thermodynamic data characteristic of the chromium behavior in these alloys. These activity results call into question those previously measured by Hilpert and Ali-Khan (1978, "Mass Spectrometric Studies of Alloys Proposed for High-Temperature Reactor Systems: I. Alloy IN-643," J. Nucl. Mater., **78**, pp. 265–271; 1979, "Mass Spectrometric Studies of Alloys Proposed for High-Temperature Reactor Systems: II. Inconel Alloy 617 and Nimomic Alloy PE 13," J. Nucl. Mater., **80**, pp. 126–131), largely used in the literature.* [DOI: 10.1115/1.3094017]

## 1 Introduction

Haynes 230 and Inconel 617 have been successfully used for high temperature applications for years. They are, respectively, strengthened by the addition of tungsten and molybdenum plus cobalt in the nickel based. Their good oxidation resistance is provided by a high chromium content that allows the development of a protective surface chromia scale in most atmospheres.

These alloys are under consideration as structural materials for the primary circuit and the intermediate heat exchangers of (very) high temperature reactors ((V)-HTRs). Although both alloys contain the same percentage of chromium 22 wt %, differences were evidenced in the corrosion resistance in the reactor specific environment, namely, diluted impure helium up to 950°C [1,2].

On the one hand, the minor alloying elements, especially manganese in Haynes 230 and titanium and aluminum in Inconel 617, take part to the surface oxide layer and can significantly modify its growth rate and properties.

On the other hand, it is known that regarding thermodynamics, the activity in the metallic phase plays the major role in the chromium behavior. It is especially true in the HTR atmosphere for which a specific interaction was evidenced [3–7], which damages the surface layer.

Above a given temperature, the carbon from the alloy is indeed able to reduce chromia following the global process:

$$Cr_2O_3 + 3C_{sol} = 3CO_{(g)} + 2Cr \quad (1)$$

where $C_{sol}$ is the carbon from the alloy.

As discussed elsewhere [7–11], the chromium activity is a key factor to understand the previous reaction (Eq. (1)). Due to the difficulty of the experimental measurements, few data were published about the chromium activity in commercial nickel based alloys. Hilpert and Ali-Khan [10,12] studied the vaporization of three commercial alloys by mass spectroscopy, In-643, Nimonic PE 13, and Inconel 617. Together with nickel and cobalt, the

Manuscript received October 20, 2008; final manuscript received November 28, 2008; published online July 15, 2009. Review conducted by Dilip R. Ballal. Paper presented at the Fourth International Topical Meeting on High Temperature Reactor Technology (HTR2008), Washington, DC, September 28–October 1, 2008.

partial pressure of chromium was determined in the range 1350–1500 K and their chemical activities were calculated. In the 1355–1527 K temperature range, Hilpert and Ali-Khan [10,12] reported that the chromium activity in Inconel 617 is given by the following law (with an uncertainty estimated at ±15%):

$$\ln(a_{Cr}^{IN\text{-}617}) = 0.143 \times \frac{10^4}{T} - 2.259 \quad (2)$$

Considering the lack of data on Haynes 230 and the uncertainty on the results on Inconel 617, it was decided to measure the chromium activity in the (V)HTR candidate materials—Haynes 230 and Inconel 617—like in model alloys: 1178, 1181, and 1201.

The model alloys have a simplified composition in comparison with the commercial ones. These materials were synthesized in order to make possible the understanding of the corrosion phenomena of nickel based alloys.

The model alloys were synthesized by an electromagnetic field fusion process in a cold crucible. Pure nickel balls and tungsten bars were added to a Ni–30Cr ingot to obtain the required nickel, chromium, and tungsten compositions. Carbon as a minor element was added to this mixture to obtain the final composition of the alloys. Then, mechanical and thermal treatments were applied to these alloys to obtain the final materials [3].

The chromium activity measurements in the Ni based alloys were performed by high temperature mass spectrometry (HTMS) coupled to multiple effusion Knudsen cells [8,13–15] in the 1423–1548 K temperature range. In this paper, the experimental apparatus and method are described. New developments in the technique allow reaching a high accuracy on the results, which are compared with published data [10,12]. The values of the chromium activity have been used in other papers [3,7] to ascribe the role of chromium activities in the high temperature surface reactivity of the alloys in impure helium regarding Eq. (1).

## 2 Experiment

High temperature mass spectrometry, coupled with Knudsen effusion cells, is an accurate experimental method well suitable to perform gas release, partial pressure measurements, and high temperature thermodynamic properties [12,14,15].

A condensed-phase system is heated in a Knudsen cell to vaporize at a known temperature. The vapors evaporate and form a molecular beam, which is properly collimated. The effused flux of each vapor species is related to the partial pressure of the atom or molecule in the condensed phase.

Using a mass spectrometer, the mass-to-charge ratio for each atomic or molecular ion is determined and the associated intensities are measured. By appropriate calibration, the ion intensities can be converted into partial pressures in the vapor phase under investigation at high temperature [14–16].

**2.1 Experimental Apparatus.** A schematic view of the apparatus is presented in Fig. 1. The Knudsen cell is a closed container whose lid is bored of an orifice (2 mm diameter) whose dimensions remain small with respect to the surface of the sample (Fig. 2).

The mean free path of the gaseous species within the cell should remain larger than the diameter of the effusion orifice [13,14]. The collimated molecular beam goes through a diaphragm and is submitted to ionization in the source of the mass spectrometer.

Several materials were tested for the effusion cell block and for the four Knudsen cells (crucible and lid). Pure tungsten was chosen for its low chemical reactivity with regard to both pure chromium and nickel based alloys.

In this geometry, no collision occurs in the rarefied evaporating gas flow. The molecular beam goes through a diaphragm directly in the ionization chamber of a mass spectrometer maintained under high vacuum. Inside the mass spectrometer, the gas ionization will generate positive charged ions, which are extracted from the ionization chamber, accelerated by an electric field. Then, the molecules are separated according to their mass/charge ratio by a high frequency electric field.

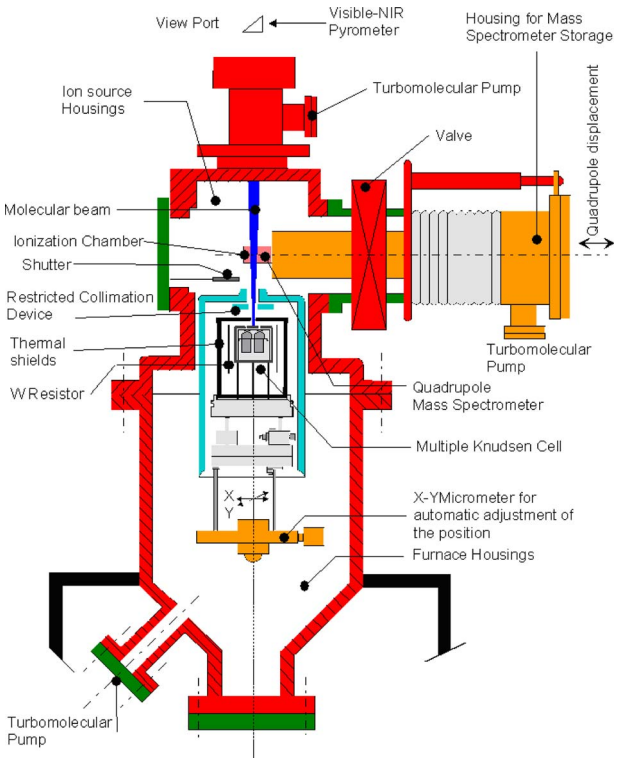


**Fig. 1 HTMS with multiple effusion Knudsen cells**

The furnace temperature is regulated using a W–Re thermocouple placed inside the cell block. The temperature is in situ calibrated by measuring the ionic intensities of silver around the melting point of the pure element. Furthermore, the temperature is measured using an optical pyrometer through the orifice of each effusion cell during the ionic intensity measurements. The results obtained by these two methods differ from ±5 K. This allows estimating the uncertainty on the temperature.

The specific characteristics of the apparatus have been described in several previous studies [8,16,17]. In particular, a restricted collimation device has been developed by Baïchi et al. [16] in order to improve the accuracy of the intensity measurements. The geometry has been modified to reduce surface revaporization, which may cause detection of parasitic signal [16].

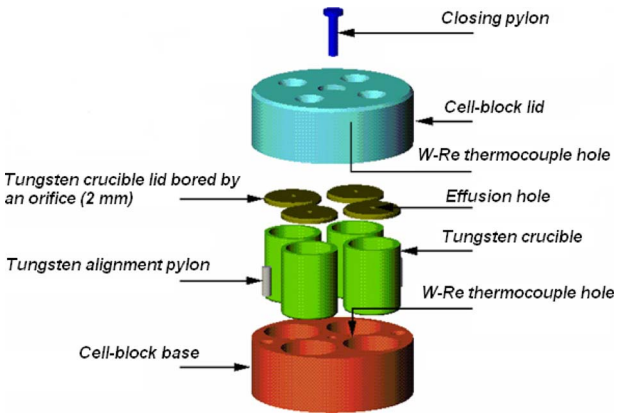


**Fig. 2 Cell block with multiple effusion Knudsen cells**

**2.2 Experimental Method.** The application of the Beer–Lambert [14] law to the absorption of the electrons in a diluted medium leads to the basic mass spectrometric relation. In this relation, the vapor pressure ($p_i$) is directly linked to the measured ionic intensity ($I_i$) of a gaseous species $i$:

$$p_i S_i = I_i T \tag{3}$$

where $T$ is the temperature and $S_i$ is the sensitivity of the instrumental assembly and the ionization process.

In the molecular flow regime, which corresponds to a pressure in the cell lower than $10^{-4}$ bar, the gaseous phase is in equilibrium with the condensed phase. This rarefied vapor phase can be considered as ideal. Thus the thermodynamic activity $a_i$ of the component $i$ in an alloy can be defined as the ratio of the vapor partial pressure of the component $i$ over the alloy (printed $m$) to the vapor pressure over the pure element (printed 0) at the same temperature:

$$a_i = \frac{p_i^{\mathrm{al}}}{p_i^0} \tag{4}$$

The ionic intensity $I_i$ of the component $i$ is measured using the mass spectrometer and the temperature is measured using both the thermocouple and the pyrometer. With the restricted collimation device [16], the sensitivity $S_i$ relative to the component $i$ remains constant whatever the considered cell. For a constant temperature, the activity of the component is equal to the ratio of its ionic intensity, successively measured over the alloy and over the pure substance.

$$a_i = \frac{p_i^{\mathrm{al}}}{p_i^0} = \frac{I_i^{\mathrm{al}}}{I_i^0} \tag{5}$$

The activity determinations of chromium were performed using a pure chromium reference (99.99 wt %). The main mass peak, i.e., $^{52}$Cr (83.8%) was analyzed at 25 eV. This ionization energy produces only ($Cr^+$) ions. No other molecular chromium vapor species ($Cr^{2+}$, $CrO^+$, $CrO_2^+$, $Cr_2O_3^+$) was detected with a significant intensity in comparison with the background noise of the spectrometer. The only important interfering signal came from manganese ($Mn^+$), which even if present at a small content in the Haynes 230 demonstrated a high volatility.

The detection limit of the chromium intensity determined the lower experimental temperature $T_{\min} \approx 1423$ K. The upper temperature $T_{\max} \approx 1553$ K was determined by the threshold of the molecular regime ($p < 10^{-4}$ bar) calculated from the pressure law of pure chromium according to Eq. (6). $T_{\max}$ must be lower than the temperature at which chemical interactions occur between sample and crucible.

$$\ln(p_{\mathrm{Cr}}) = 28.550 - 4.740 \times \frac{10^4}{T} \quad (p \text{ in Pa}, \quad T \text{ in K}) \tag{6}$$

**2.3 Validation of the Chemical Stability.** Postmortem analyses were performed by energy dispersive spectroscopy (EDS) in a scanning electron microscope on some metallic specimens heated up to 1573 K in tungsten crucibles. No interaction was never evidenced. Furthermore, the samples were weighted after experiment. The mass loss did not exceed 0.3% of the total mass meaning that the composition of samples is constant over the whole test runs.

**2.4 Validation of the Spatial Alignment.** Effect of micrometric moves of the cell block around its original position where cell and ionization chamber of the spectrometer are aligned have been checked using a graphite crucible containing pure silver (about 2 g) close to its melting point ($T = 1235$ K). With the restricted collimation device, the profile of the ionic intensity signals exhibits a window response [4,8]. Thanks to this geometry, no significant difference was detected in the signal amplitude when the cell block was slightly displaced in both $X$ and $Y$ directions. Therefore, this configuration ensures a good reproducibility of the measurements.

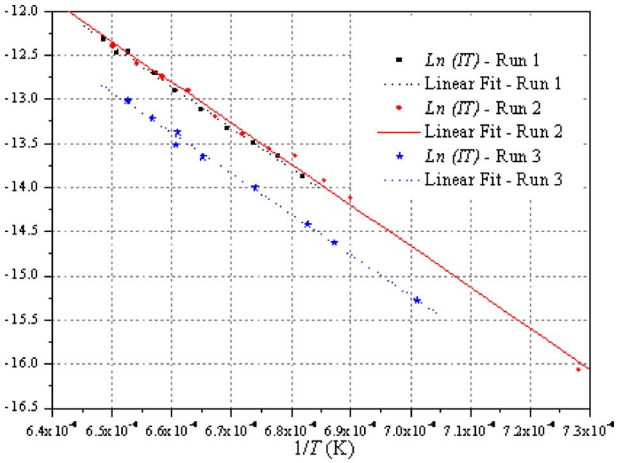


**Fig. 3 Logarithm of the chromium ionic intensity and temperature product (ln *IT*) versus reciprocal temperature for pure Cr in the 1423–1538 K temperature range**

**2.5 Validation of the Spectrometer Response.** The sublimation reaction of pure chromium (Eq. (7)) was used as a reference standard to validate the sensitivity of the mass spectrometer for chromium activity measurements [17]:

$$\mathrm{Cr}_{(s)} = \mathrm{Cr}_{(g)} \tag{7}$$

Eq. (7) is characterized by a specific heat of evaporation $\Delta H_T^0$, which, according to the second law of the thermodynamics (Eq. (8)), verifies

$$\Delta H_T^0 = -R \frac{\partial \ln p_{\mathrm{Cr}}}{\partial \frac{1}{T}} \tag{8}$$

where $R$ is the gas constant. Using Eq. (3), Eq. (8) gives a new relation

$$\Delta H_T^0 = -R \frac{\partial \ln(I_{\mathrm{Cr}} T)}{\partial \frac{1}{T}} \tag{9}$$

After Eq. (9), the slope of the experimental line is proportional to $\Delta H_T^0$ for pure chromium. At 1415 K, which corresponds to the mean of the experimental temperature range, the measured heat of evaporation $\Delta H_{1415,\mathrm{ex}}$ is, respectively, equal to 385.7, 386.4 and 382.8 kJ/mol for the three runs (Fig. 3). The experimental technique showed thus a good reproducibility and the experimental values are in excellent agreement with the specific heat of evaporation from the NIST JANAF tables for pure chromium: $\Delta H_{1415,\mathrm{theo}}^0 = 386.5 \pm 4.2$ kJ/mol [18]. Thus, the experimental error is less than 1%.

It is worth noticing that no hysteresis took place due to mass spectrometer instability. Indeed, ($I_{\mathrm{Cr}}T$), no significant shift was observed during heating and cooling monitoring. Thus, the high temperature mass spectrometer allows a high experimental accuracy to be reached for the measurement of the chromium activity in metallic materials.

**2.6 Systematic Error Due to Temperature Determination.** According to the calibration procedure and to the specifications of the manufacturer, the error on the measured temperature is equal to $\pm 5$ K within the experimental range. This error directly gives a relative uncertainty of $\pm 1\%$ on the reciprocal temperature, which in turn has an impact on the HTMS measurements. The uncer-

**Table 1 Major elements and impurities in nickel based alloys in wt % (nickel is considered as the base)**

| | C | Cr | W | Co | Mo | Fe | Al | Mn | Ti | Si |
|---|---|---|---|---|---|---|---|---|---|---|
| H 230 | 0.105 | 22 | 14.7 | 0.2 | 1.3 | 1.3 | 0.4 | 0.5 | 0.1 | 0.4 |
| 1178 | 0.001 | 22 | 14 | | | | | | | |
| 1181 | 0.101 | 22 | 14 | | | | | | | |
| 1201 | 0.103 | 18 | 14 | | | | | | | |
| In 617 | 0.060 | 22 | – | 12.0 | 9.2 | 1.0 | 1.0 | 0.1 | 0.4 | 0.2 |

tainty on the experimental enthalpies of sublimation is estimated to ±1%. It is necessary to add to this systematic error, another uncertainty equal to three times the average standard deviation on the measurements of ionic intensity, that is to say, roughly ±1.5%. The total relative error on the $(I_{Cr}T)$ product is thus about 2.5%. This value must be doubled in case the activity is calculated from the $(I_{Cr}T)$ over an alloy surface, that is to say, ±5%.

**2.7 In Situ Calibration on Pure Chromium.** The activity of chromium was determined at a given temperature based on successive measurements of $(I_{Cr}T)$ for the pure chromium and then for each alloy. Each run provides approximately ten points from which the activities are calculated. For each set of data, $a_{Cr}$ in the alloys refers to the linear fit of ionic intensities measured over pure chromium during the same test at the same temperature. This method of in situ calibration suppresses any error related to a slight variation in the sensitivity of the mass spectrometer from one test to the other.

## 3 Materials

The two commercial alloys, Haynes 230 and Inconel 617, and three model alloys were analyzed [3]. Table 1 reports the chemical composition of the materials. Cylindrical specimens (mass: about 4 g) were machined in the as-received alloys.

## 4 Results: Chromium Activity in Nickel Based Alloys in the 1423–1538 K Range

The same procedure was applied for the measurement of the chromium activity in all the nickel based alloys. The results are given in Secs. 4.1–4.3.

**4.1 Inconel 617.** Three runs were performed in the 1423–1538 K range. The measurements were reproducible with a 5% accuracy The results are compared with Hilpert's values (Fig. 4).

For Inconel 617, the best fit on the experimental data (three runs) leads to the following equation:

$$\ln(a_{Cr}^{In\text{-}617}) = \frac{3810}{T} - 3.673 \tag{10}$$

**4.2 Haynes 230.** Haynes 230 exhibits a slightly different behavior with higher chromium activity than in Inconel 617 (Fig. 5). The chromium activity in this alloy can be written as

$$\ln(a_{Cr}^{H\text{-}230}) = \frac{4340}{T} - 3.897 \tag{11}$$

**4.3 Model Alloys: 1178, 1181, and 1201.** The chromium activities were also measured in three model alloys (Fig. 6). Three sets of measurements were performed in the 1423–1573 K range. All these alloys are nickel based. Their respective mass compositions are

Alloy 1178:Ni(base) + 22%Cr + 0.001%C

Alloy 1181:Ni(base) + 22%Cr + 0.101%C

Alloy 1201:Ni(base) + 18%Cr + 0.103%C

## 5 Discussion

The results obtained for all alloys are listed in Table 2. The values of the chromium activities for the Haynes 230 alloy show a larger deviation from ideality in comparison with the Inconel 617 alloy. For Inconel 617, the high temperature mass spectrometry measurements are higher than the data of Hilpert and Ali-Khan [10], although these authors also used a mass spectrometric technique. Both sets of data are compared in Fig. 4.

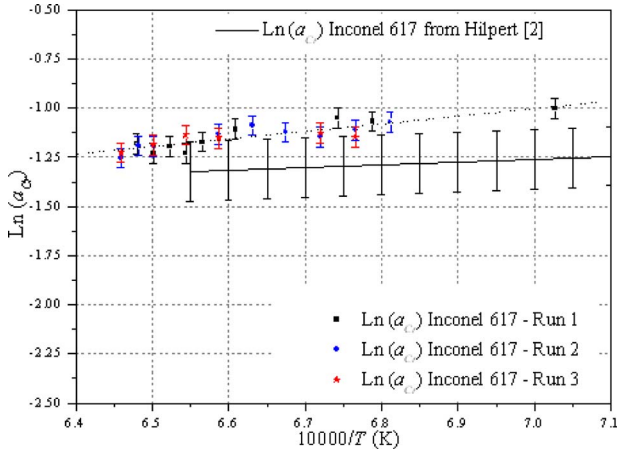


**Fig. 4 Measurements of the chromium activity in the Inconel 617 alloy (three runs) compared with Hilpert and Ali-Khan [10,12] results**

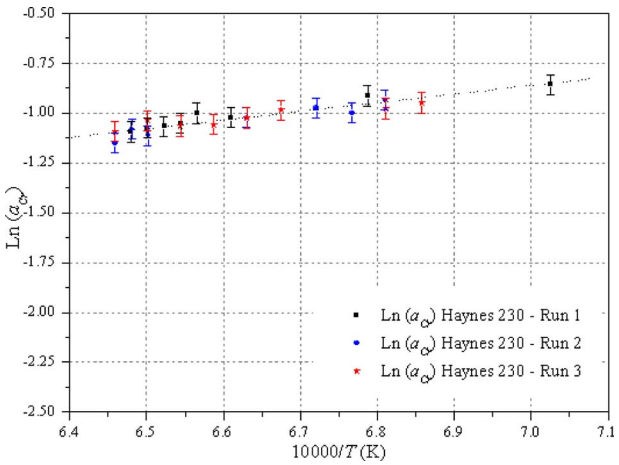


**Fig. 5 Measurements of the chromium activity in the Haynes 230 alloy (three runs)**

**Table 2 Chromium activity laws for the alloys, calculated chromium activity value at 1423 K**

| Alloy | Chromium activity | $a_{Cr}$ at 1423 K |
|---|---|---|
| H 230 | $\ln(a_{Cr}^{H\text{-}230}) = 4340/T - 3.897$ | 0.429 |
| 1178 | $\ln(a_{Cr}^{1178}) = 3470/T - 3.368$ | 0.395 |
| 1181 | $\ln(a_{Cr}^{1181}) = 4940/T - 4.406$ | 0.398 |
| 1201 | $\ln(a_{Cr}^{1201}) = 2670/T - 3.148$ | 0.280 |
| In 617 | $\ln(a_{Cr}^{In\text{-}617}) = 3810/T - 3.673$ | 0.369 |
| In 617 [13] | $\ln(a_{Cr}^{In\text{-}617}) = 1430/T - 2.259$ | 0.285 |

Several reasons could account for such a discrepancy. In their early work, Hilpert and Ali-Khan [10,12] estimated the systematic error on their results at ±15%, that is to say, $a(Cr)^{1423\ K} = 0.242 - 0.328$.

In this study, the multiple Knudsen cells coupled with a restricted collimation device allows to reach a far better accuracy, about 5%. But this difference of uncertainty cannot justify the whole shift between the two sets of data.

Other reasons can be considered such as the choice of the crucible material. In our work, we used tungsten and we experimentally checked that tungsten and specimens are stable in the test conditions. In Ref [13], the crucible is made of molybdenum that could lead to the formation of a solid solution at low temperature as observed in the phase diagram of the binary Mo–Cr system [19]. Furthermore, the paper does not report any post-test observations to ensure if such a chemical interaction had occurred between specimens and molybdenum during the experiment (Fig. 6).

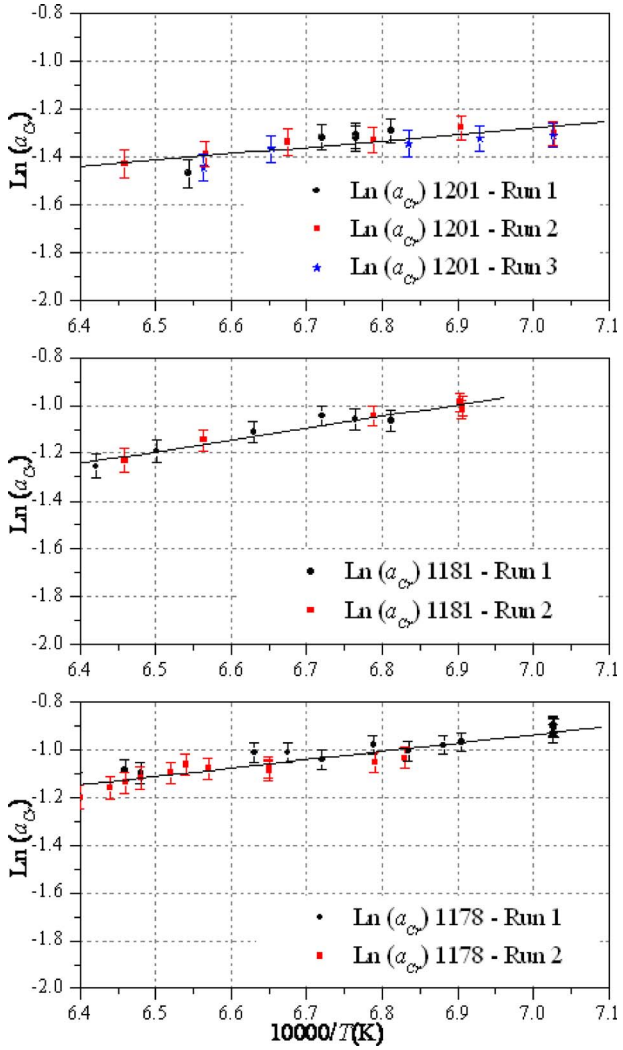


**Fig. 6 Measurements of the chromium activity in the model alloys 1201, 1181, and 1178**

Moreover, in this study we measured that the mass loss is negligible after exposure at high temperature and we concluded that the composition of the specimens remained stable over the whole test procedure. Such a validation was not presented in Ref. [13].

Finally, we also checked that the specimens did not undergo any oxidation during experiments at high temperature. We would have expected this kind of analysis in the paper by Hilpert and Ali-Khan [10,12]. Indeed, if some oxide scale had formed on the specimen surface due to the residual oxygen content in vacuum, the volatilization of chromium would have been strongly lowered.

## 6 Conclusion

High temperature mass spectrometry coupled to a multiple effusion Knudsen cell was used to measure the activity of chromium in several nickel based alloys: Haynes 230, Inconel 617, and three model alloys (1178, 1181, and 1201) in the 1423–1573 K temperature range (Table 2).

Although the alloys have almost the same chromium content (about 22 wt % except alloy 1201), the experimental results show that the chromium activity is higher in Haynes 230 alloy than in Inconel 617 and model alloys.

The measured chromium activity for Inconel 617 was compared with the data of Hilpert and Ali-Khan [10]. The lower values obtained by these authors may be attributed to the use of a molybdenum crucible, to possible changes in the specimen chemical composition, or to oxidation during their test.

These validated HTMS results give new insight in the surface kinetics of Haynes 230 and Inconel 617 [7,11] especially regarding the damaging reaction between chromia and carbon from the alloys (Eq. (1)).

## Nomenclature

$a_{Cr}^{i}$ = chromium chemical activity in the $i$ material
$\Delta H_T^0$ = heat of evaporation at $T$(kJ/mol)
$I_i$ = measured ionic intensity of the $i$ species
$p_i^{al}$ = partial pressure of the $i$ species over the alloy
$p_i^0$ = partial pressure of the $i$ species over the pure substance
$R$ = perfect gas constant
$S_i$ = sensitivity of spectrometer for the $i$ species
$T$ = temperature (K)

## References


[1] Venkatraman, M., and Neumann, J. P., 1990, *Binary Alloy Phase Diagrams*, 2nd ed., T. B. Massalski, H. Okamoto, P. B. Subramanian, L. Kacprzak, and W.W. Scott, Jr., eds., ASM International, Materials Park, OH, p. 1293.

[2] Cabet, C., Terlain, A., Lett, P., Guétaz, L., and Gentzbittel, J.-M., 2006, "High Temperature Corrosion of Structural Materials Under Gas-Cooled Reactor Helium," Mater. Corros., **57**, pp. 147–153.

[3] Rouillard, F., 2007, "Mécanismes de formation et de destruction de la couche d'oxyde sur un alliage chrominoformeur en milieu HTR," Ph.D. thesis, Ecole des Mines de Saint-Etienne, France.

[4] Quadakkers, W. J., and Schuster, H., 1985, "Corrosion of High Temperature Alloys in the Primary Circuit Helium of High Temperature Gas Cooled Reactors.-Part I: Theoretical Background, Werkst. Korros., **36**(4), pp. 141–150.

[5] Brenner, K. G. E., and Graham, L. W., 1984, "The Development and Application of a Unified Corrosion Model for High-Temperature Gas-Cooled Reactor Systems," Nucl. Technol., **66**(2), pp. 404–414.

[6] Warren, M. R., 1986, "Rapid Decarburization and Carburization in High Temperature Alloys in Impure Helium Environments," High Temp. Technol., **4**, pp. 119–130.

[7] Rouillard, F., Cabet, C., Wolski, K., and Pijolat, M., 2008, "Thermodynamic Modeling of the Oxide Destruction on a Nickel Base Alloy in Impure Helium of Gas Cooled Reactors," *Proceedings of the High Temperature Corrosion and Protection of Materials*, Les Embiez, France.

[8] Chatain, S., Gonella, C., Bordier, G., and Le Ny, J., 1995, "Thermodynamic

Activity Measurements of the Liquid Cu–Gd Alloy by High Temperature Mass Spectrometry," J. Alloys Compd., **228**, pp. 112–118.
[9] Rouillard, F., Cabet, C., Wolski, K., Terlain, A., Tabarant, M., Pijolat, M., and Valdivieso, F., 2007, "High Temperature Corrosion of a Nickel Base Alloy by Helium Impurities," J. Nucl. Mater., **362**, pp. 248–252.
[10] Hilpert, K., and Ali-Khan, I., 1979, "Mass Spectrometric Studies of Alloys Proposed for High-Temperature Reactor Systems: II. Inconel Alloy 617 and Nimomic Alloy PE 13," J. Nucl. Mater., **80**, pp. 126–131.
[11] Rouillard, F., Cabet, C., Gossé, S., Girardin, G., and Blat, M., 2008 "Corrosion Issues of HTR Structural Metallic Materials," *Proceedings of the Fourth HTR Technology Conference*, Washington, DC.
[12] Hilpert, K., and Ali-Khan, I., 1978, "Mass Spectrometric Studies of Alloys Proposed for High-Temperature Reactor Systems: I. Alloy IN-643," J. Nucl. Mater., **78**, pp. 265–271.
[13] Chatillon, C., Pattoret, A., and Drowart, J., 1975, "Thermodynamic Studies of Condensed Phases by Mass Spectrometry at High Temperature: Analysis of the Method and Review of the Results," High Temp. - High Press., **7**, pp. 119–148.
[14] Chatillon, C., 1998, "La Spectrométrie de Masse à Haute Température: Données Accessibles et Développements Récents," La Revue de Métallurgie-CIT/Science et Génie des Matériaux, pp. 1077–1099.
[15] Heyrman, M., 2004, "Etude par Spectrométrie de Masse à Haute Température du Système $Al_2O_3$–C: Application aux Fours d'Elaboration sous Vide," Ph.D. thesis, INPG, Grenoble.
[16] Baïchi, M., Chatillon, C., Guéneau, C., and Chatain, S., 2001, "Mass Spectrometry Study of $UO_2$–$ZrO_2$ Pseudo-Binary System," J. Nucl. Mater., **294**, pp. 84–87.
[17] Chatain, S., Larousse, B., Maillault, C., Guéneau, C., and Chatillon, C., 2008, "Thermodynamic Activity Measurements of Iron in Fe–Zr Alloys by High Temperature Mass Spectrometry," J. Alloys Compd., **457**, pp. 157–163.
[18] Cabet, C., and Terlain, A., 2005, "High Temperature Corrosion of Structural Materials Under Gas-Cooled Reactor Helium," *Proceedings of the Eurocorr 2005*, Lisbon, Portugal, Paper No. O-355.
[19] Chase, M. W., Jr., 1998, *NIST-JANAF Thermochemical Tables Journal of Physical and Chemical Reference Data*, 4th ed., American Chemical Society, Washington, DC/American Institute of Physics, New York, Pt. II.

# Corrosion Issues of High Temperature Reactor Structural Metallic Materials

**Celine Cabet**
e-mail: celine.cabet@cea.fr

**Fabien Rouillard**
e-mail: fabien.rouillard@cea.fr

CEA, DEN, DPC, SCCME,
Laboratoire d'Etude de la Corrosion
Non Aqueuse,
F-91191 Gif-sur-Yvette, France

*Cooling helium of high temperature reactors (HTRs) is expected to contain a low level of impurities: oxidizing gases and carbon-bearing species. Reference structural materials for pipes and heat exchangers are chromia former nickel base alloys, typically alloys 617 and 230. And as is generally the case in any high temperature process, their long term corrosion resistance relies on the growth of a surface chromium oxide that can act as a barrier against corrosive species. This implies that the HTR environment must allow for oxidation of these alloys to occur, while it remains not too oxidizing against in-core graphite. First, studies on the surface reactivity under various impure helium containing low partial pressures of $H_2$, $H_2O$, CO, and $CH_4$ show that alloys 617 and 230 oxidize in many atmosphere at intermediate temperatures (up to 890–970°C, depending on the exact gas composition). However when heated above a critical temperature, the surface oxide becomes unstable. It was demonstrated that at the scale/alloy interface, the surface oxide interacts with the carbon from the material. These investigations have established an environmental area that promotes oxidation. When exposed in oxidizing HTR helium, alloys 617 and 230 actually develop a sustainable surface scale over thousands of hours. On the other hand, if the scale is destabilized by reaction with the carbon, the oxide is not protective anymore, and the alloy surface interacts with gaseous impurities. In the case of $CH_4$-containg atmospheres, this causes rapid carburization in the form of precipitation of coarse carbides on the surface and in the bulk. Carburization was shown to induce an extensive embrittlement of the alloys. In $CH_4$-free helium mixtures, alloys decarburize with a global loss of carbon and dissolution of the pre-existing carbides. As carbides take part in the alloy strengthening at high temperature, it is expected that decarburization impacts the creep properties. Carburization and decarburization degrade rapidly the alloy properties, and thus result in an unacceptably high risk on the material integrity at high temperature. Therefore, the purification system shall control the gas composition in order to make this unique helium atmosphere compatible with the in-core graphite, as well as with structural materials. This paper reviews the data on the corrosion behavior of structural materials in HTRs and draws some conclusions on the appropriate helium chemistry regarding the material compatibility at high temperature.*
[DOI: 10.1115/1.3098377]

## 1 Introduction

AREVA NP has launched the ANTARES program [1] to develop a high temperature reactor/very high temperature reactor (HTR/VHTR). This HTR/VHTR is a modular helium-cooled reactor operating at (very) high temperature in the indirect cycle. It offers the possibility to coproduce electricity and process heat which shall be used for massive hydrogen production or for any other high temperature industrial application.

Helium reaches 850–950°C at the outlet of the reactor pressure vessel and diverts its calories to a secondary fluid within the intermediate heat exchanger (IHX). Use of compact IHX, such as plate-stamped heat exchanger, shall reduce the overall reactor size and thus increase competitiveness. However such compact components are highly demanding toward structural materials, as very thin metallic sheets shall provide for mechanical resistance, as well as gas tightness at elevated temperatures (up to 850–950°C) and under a pressure differential of about 5 MPa in off-normal situations (accidents). Moreover, the IHX lifetime shall be 20 years or so.

Manuscript received: November 3, 2008; final manuscript received November 28, 2008; published online July 16, 2009. Review conducted by Dilip R. Ballal. Paper presented at the Fourth International Topical Meeting on High Temperature Reactor Technology (HTR2008), Washington, DC, September 28–October 1, 2008.

### 1.1 High Temperature Metallic Materials.

Considering the high temperature, high pressure, and long service time, IHX materials must meet high level requirements, especially for the VHTR variant at the highest temperatures. In support of the ANTARES program, R&D is performed in France to select and qualify IHX materials [2–4]. Candidate alloys for such temperature levels are Inconel 617 and Haynes 230®, which are nickel based, rich in chromium (approximately 22 wt %) for the oxidation resistance, and strengthened by addition of molybdenum, cobalt, tungsten, etc.

The joint materials program mostly investigates the structural stability, the mechanical properties at low and high temperature, and the compatibility with the coolant. Regarding corrosion, this program mainly has aimed at understanding then comparing the resistance of the candidate alloys for medium durations in representative service conditions.

### 1.2 Specific VHTR Helium.

It is expected that the VHTR cooling gas will be polluted. The impurity content may be estimated based on the gas analyses that were performed in experimental helium-cooled reactors [5–7]. Few tens to few hundreds of ppm (volume parts per million) are expected for $H_2$, CO, $CO_2$, $CH_4$, and $N_2$, and few tenths of ppm for water vapor content. Such a medium is reactive toward metallic materials at high temperature [8–10].

The high temperature resistance of chromia former alloys relies

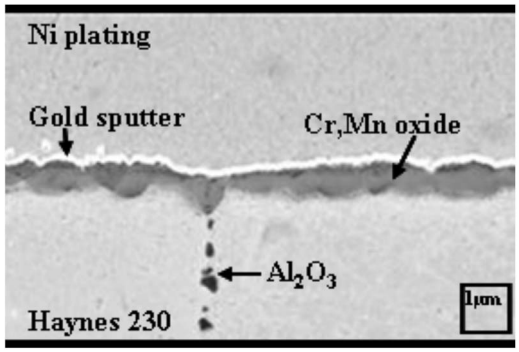


**Fig. 1 Haynes 230® after 25 h at 900°C in helium with 193 ppm $H_2$, 49 ppm CO, 18 ppm $CH_4$, and 1.6 ppm $H_2O$**

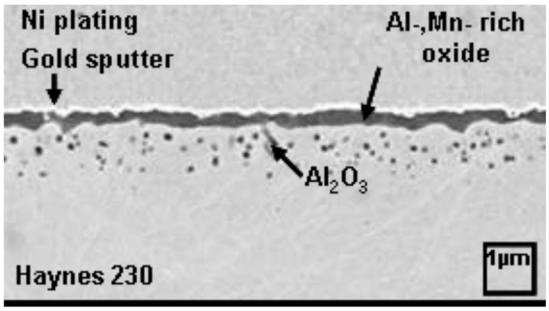


**Fig. 2 Haynes 230® after 25 h at 900°C, then 20 h at 980°C in helium with 193 ppm $H_2$, 49 ppm CO, 18 ppm $CH_4$, and 1.6 ppm $H_2O$**

on the formation of a continuous self-healing surface oxide that acts as a barrier against gases. The scale must be adherent, dense, and slow growing. In order to enable the development of the protective chromia, oxidation must be the major corrosion process of candidate alloys in the VHTR atmosphere.

**1.3 High Temperature Reactivity of Alloys in Impure Helium.** Studies on the surface reactivity of Haynes 230® and Inconel 617 in impure helium at high temperature [11–17] show that two oxidants are likely to react with the metallic surface at intermediate temperature: water vapor and carbon monoxide, following Eqs. (1) and (2)

$$\mathrm{Me} + x\mathrm{H_2O} \rightarrow \mathrm{MeO}_x + x\mathrm{H_2} \quad (1)$$

$$\mathrm{Me} + x\mathrm{CO} \rightarrow \mathrm{MeO}_x + x\mathrm{C}_{(s)} \quad (2)$$

Me is a metal from the alloy Al, Si, Ti, Mn and especially Cr, but $C_{(s)}$ is elementary carbon at the surface.

Gas phase analysis shows that after some hours water vapor is the only impurity that takes part in oxidation. Oxidation results in the formation of a continuous surface oxide scale, rich in chromium. After 25 h at 900°C in helium with 193 ppm $H_2$, 49 ppm CO, 18 ppm $CH_4$, 1.6 ppm $H_2O$, the scale on Haynes 230® is approximately 1 $\mu$m thick (see Fig. 1). Protective oxidation should thus be achievable in the VHTR coolant.

However at higher temperatures a specific process has been evidenced to damage the surface oxide. When passivated at 900°C and further heated under the same gas mixture, a Haynes 230® specimen releases a significant amount of carbon monoxide. As already discussed in the literature [18,19], the whole amount of CO cannot be explained by a reaction involving water vapor or methane. As a matter of fact, the CO production can be ten times higher than the total content of water vapor in the gas and is much higher than the methane consumption. Besides, CO is released in $CH_4$-free atmospheres as well. The production of CO goes with specimen mass loss and decrease in the surface scale thickness (see Fig. 2).

It was shown that the surface oxide is reduced at the scale/alloy interface by the carbon from the alloy according to

$$\mathrm{Cr_2O_3} + 3\mathrm{C}_{(s)} \xrightarrow{T>T_a} 3\mathrm{CO} + 2\mathrm{Cr} \quad (3)$$

Chromia is first reduced; eventually manganese oxides are also reduced. According to Eq. (3) the surface oxide reacts with the carbon from the alloy to produce gaseous carbon monoxide and chromium. The equilibrium temperature for Eq. (3) was called $T_A$ by Brenner and Graham [9]. At temperature below $T_A$, the reaction is on the left hand side and is equivalent to Eq. (2) with Me=Cr.

$T_A$ appears to largely depend on the gas chemistry, mainly on $P$(CO). Figure 3 plots evolutions of $T_A$ as a function of $P$(CO) in helium for Haynes 230. It is clear that the higher the level of carbon monoxide, the higher the $T_A$ value. Quadakkers and coworker [8,20], Brenner and Graham [9] and Graham [21], Warren [18], Cook et al. [19], and Chapovaloff et al. [14,15] observed that Inconel 617 suffers from a similar reduction in the chromium-rich surface oxide. The comparison of our results for Haynes 230® to the data from Ref. [20] for Inconel 617 in Fig. 3 shows that both alloys exhibit similar dependence of $T_A$ versus $P$(CO).

In Fig. 3, the area locates at intermediate temperatures and higher carbon monoxide partial pressures will induce oxidation of chromium into chromia, while the area above the curve at higher temperature and lower $P$(CO) corresponds to instability of the surface chromia because it is irreversibly reduced by the carbon from the alloy. By destabilizing the oxide scale, Eq. (3) can expose chromia former alloys to an active corrosion mode, and thus can significantly question the material integrity.

**1.4 Aim of the Work.** In this paper, the medium term corrosion behavior of VHTR candidate alloys, Inconel 617, and Haynes 230® is investigated at 950°C. The test gases are selected according to data in Fig. 3, in order to be either in the area for chromia formation or to promote chromia instability. Effect of increasing partial pressures of methane is also studied.

## 2 Experimental Setup

**2.1 Materials.** Haynes 230® was manufactured by Haynes International® as a 2.03 mm thick sheet. Inconel 617 specimens were taken from a 2 mm sheet purchased at Special Metals®. Table 1 reports the chemical composition of the tested alloys. Rectangular specimens of about 6 $cm^2$ and 2 mm thick were ma-

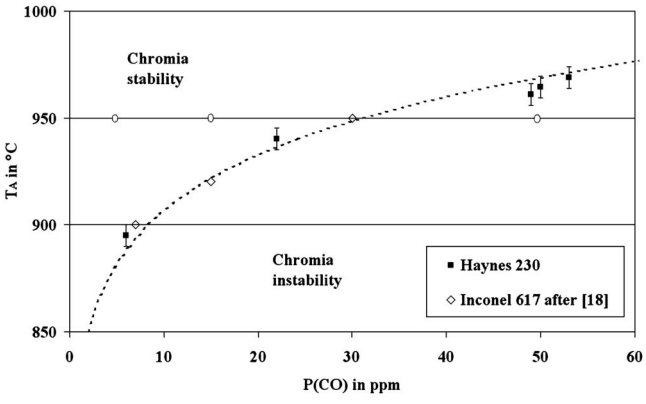


**Fig. 3 Critical temperature $T_A$ as a function of $P$(CO) in the gas phase; squares: measured data for Haynes 230® in impure helium with ~200 ppm $H_2$, ~20 ppm $CH_4$, and ~1 ppm $H_2O$ and diamonds: published data for Inconel 617 from Ref. [20] in helium containing 500 ppm $H_2$, 22 ppm $CH_4$, and ~1.5 ppm $H_2O$**

Table 1 Chemical composition (in wt %) of Inconel 617 and Haynes 230®

| | Ni | C | Cr | Mo | Co | W | Fe | Al | Si | Mn | Ti |
|---|---|---|---|---|---|---|---|---|---|---|---|
| Inconel 617 | Base | 0.06 | 21.6 | 9.2 | 12.0 | | 1.0 | 1.0 | 0.2 | 0.1 | 0.4 |
| Haynes 230® | Base | 0.1 | 22.0 | 1.3 | 0.2 | 14.0 | 1.3 | 0.4 | 0.4 | 0.5 | 0.1 |

chined in the as-received materials, ground to 1200 grit, and then ultrasonically cleaned in an acetone/ethanol mixture.

**2.2 Test Conditions.** Test facilities are elsewhere described [4]. Four to six specimens are exposed to flowing impure helium at high temperature and atmospheric pressure. Purposely added impurities are $H_2$, CO, $CH_4$, and $H_2O$. A cryogenic trap coupled to a system for water vapor injection enables accurate adjustment of $P(H_2O)$ in the order of ppm. Concentrations of impurities are analyzed at the test section inlet and outlet by gas phase chromatography. In any case, oxygen, nitrogen, and carbon dioxide partial pressures were below the chromatography detection limit (about 0.1 ppm). Moisture is on-line monitored via a capacitive-probe hygrometer coupled to high-sensitivity chilled-mirror dew point analyzer. Blank tests were carried out without any specimen in order to check that the loop and specimen-holder materials do not significantly react with gaseous impurities, or influence the gas composition.

Corrosion tests are isothermal at 950°C for different durations up to approximately 1000 h; specimens were heated up at 1°C/min and cooled down at 7.5°C/min in pure helium. The gas flow rate was about 0.15 ml/s per $cm^2$ of metallic surface. It was validated that downstream effect—depletion of impurities causing interference between materials—was negligible throughout the test section.

Table 2 reports the impurity concentration in test helium.

Composition of the test helium mixtures was determined considering the results presented in Fig. 3 with the following characteristics at 950°C:

i) *He-1* should be oxidizing
ii) *He-2*, *He-3* and *He-4* should promote active corrosion modes as chromium oxide is not stable (cf. reaction (3)); increasing $P(CH_4)$ is tested from 0 in He-2 to 300 ppm in He-4.

**2.3 Specimen Observations and Analyses.** After exposure, the metallic specimens were weighted. Surface is directly characterized by X-ray diffraction (XRD) (with Cu-$K\alpha$ radiation). The global carbon content was analyzed by the LECO analyzer. Coupons were mounted in a conducting resin, ground to 2400 grit, and finished with a 1 $\mu$m alumina powder for observations by scanning electron microscopy (SEM) and analysis by energy-dispersive X-ray (EDX) spectroscopy.

## 3 High Temperature Corrosion of Alloys in VHTR Helium

**3.1 Corrosion in "Oxidizing" VHTR Helium.** Figure 4 shows SEM cross-sectional pictures of Haynes 230® and Inconel 617 tested for 813 h at 950°C in oxidizing helium He-1. As expected in the oxidizing conditions, alloys exhibit a surface scale that is made of chromium-rich oxide.

Table 2 Composition (in ppm) of the test helium mixtures

| | $H_2$ | $H_2O$ | CO | $CH_4$ |
|---|---|---|---|---|
| He-1 | 200 | 1.5 | 50 | 20 |
| He-2 | 200 | 0.5–12 | 5 | |
| He-3 | 200 | 0.7 | 5 | 20 |
| He-4 | 500 | 0.5 | 15 | 300 |

Main corrosion features are as follows.

(i) *Growth of the chromia scale.* After a couple of hours, the reaction of CO(g) following Eq. (2) becomes negligible and water vapor becomes the only oxidant of importance. Equation (1) thus occurs and chromium oxidizes into chromia; other minor oxidizable elements react as well. Long duration tests in impure oxidizing helium show that specimens still exhibit a surface oxide. This means that oxidation is a sustainable behavior for at least 5000 h. As exemplified in Fig. 5, all specimens gain mass in these conditions. Moreover, the longer the exposure, the higher the mass gain and the thicker the surface scale in agreement with parabolic kinetics limited by diffusion phenomena throughout the scale as observed by Cook et al. [19] for Inconel 617.

Haynes 230® exhibits slower oxidation rate than Inconel 617 (see the smaller mass gains in Fig. 5). This lesser oxidation can mainly be ascribed to a thinner surface scale. Difference in the scale growth kinetics can be attributed to incorporation of minor elements in the surface chromia. In the case of Haynes 230®, manganese exhibits a strong tendency to diffuse into chromia and to form a spinel phase with chromium in the outer part of the scale. Incorporation of manganese into chromia globally improves the oxidation behavior up to 950°C [22]. For Inconel 617, the surface chromia is doped with titanium. Incorporation of titanium in chromia is known to increase its oxidation rate [23].

(ii) *Internal oxidation of aluminum.* Some internal oxides containing Al, Ti, or Si are evidenced close to the oxide/alloy interface. They may have segregated at the very beginning of the oxidation test and further formed because the oxygen pressure prevailing at the alloy/chromia interface (set by the dissociation of chromia) enables them to be oxidized. However, minor Si and Al

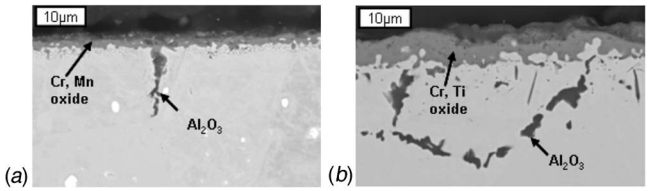


Fig. 4 Haynes 230® (*a*) and Inconel 617 (*b*) after 813 h at 950°C in He-1

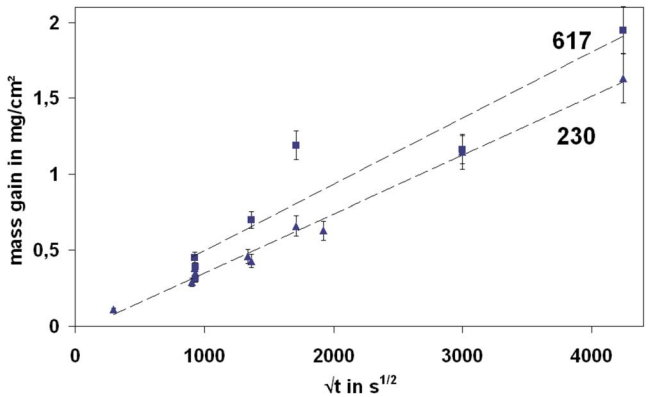


Fig. 5 Mass gains of Inconel 617 and Haynes 230® after exposure at 950°C in He-1 versus square root of time

**Table 3 Global carbon weight percentage analyzed by LECO® in the as-received and corroded alloys (for 500 h at 950°C)**

| | As-received | He-1 | He-2 | He-3 | He-4 |
|---|---|---|---|---|---|
| Inconel 617 | $0.067 \pm 0.03$ | $0.097 \pm 0.02$ | $0.035 \pm 0.02$ | | $0.56 \pm 0.20$ |
| Haynes® 230 | $0.101 \pm 0.05$ | $0.075 \pm 0.03$ | $0.075 \pm 0.03$ | $0.170 \pm 0.08$ | $1.78 \pm 0.90$ |

should stop reacting because of their progressive depletion in the surface vicinity.

Aluminum oxide is formed deeper in the alloy. Internal oxidation is observed at grain boundaries in Haynes 230® (as grain boundaries represent high diffusion paths) but is inter- and intragranular in Inconel 617. It is deeper and more intense when the test time increases. Cook and Graham [24] showed that the degree of internal oxidation of alloy 800 H decreases with reduction in the Al content.

(iii) *Development of a carbide-free zone.* Due to thermal aging, significant precipitation of secondary carbides—mainly of the $M_{23}C_6$ type and rich in Cr—occurs at grain boundaries in the alloy bulk after treatment at 950 °C [2,12], but these secondary intergranular carbides do not form in a subsurface zone, which penetrates somewhat deeper than the internal oxidation. It is observed that the depth of this zone is related to the chromia thickness. One possible cause could be depletion of Cr beneath the growing oxide scale leading to increased solubility of carbon in the depleted substrate.

(iv) *Slight increase in carbon content.* Table 3 gives the total carbon content measured by the LECO analyzer in specimens exposed for 500 h in various test helium mixtures. The carbon weight percentage has slightly increased after treatment in oxidizing helium. An increase in carbon corresponds to a deposition in the alloy by carbon-bearing gases $CO_{(g)}$ or $CH_{4(g)}$. The environment actually carburizes the structural alloys [20], but the formation of the surface oxide effectively minimizes carburization by forming a barrier between the gas and the material. In the case of oxidizing helium, reactivity of carbon monoxide and methane according to Eqs. (2) and (4) is thus limited

$$CH_4 = C_{(s)} + 2H_2 \tag{4}$$

The higher oxidation rate of Inconel 617 can thus be attributed to its rather high titanium and aluminum contents that, respectively, promote higher chromia growth rate and internal oxidation.

As chromia scale effectively protects the surface from exchange with the gas phase, the inner composition and microstructure of alloys do not significantly change. The bulk properties, such as tensile and creep strengths, are thus expected to be maintained [25].

**3.2 Corrosion in "Decarburizing" VHTR Helium.** Figure 6 shows Haynes 230® after exposure at 950°C in test helium He-2 that falls within the area for chromia instability ($P(CO)=5$ ppm in Fig. 3) and without methane. As expected in the "reducing" conditions, alloys do not exhibit any surface oxide.

Main corrosion features are as follows.

(i) *Absence of chromia scale.* Due to reduced $P(CO)$ in the test gas He-2, Eq. (3) is driven to the right hand side. Cr-rich oxide is then reduced by the carbon from the alloy to give some chromium back. In the mean time, water vapor can still react with reactive elements, first of all Cr, following Eq. (1). This regenerates surface chromia and sustains the corrosion. It is worth noticing that a kinetic competition occurs between Eqs. (1) and (3). The relative reaction rates, depending on environmental factors, such as temperature, $P(H_2O)$, etc., determine whether $Cr_2O_3$ is fully removed from the surface, as in Fig. 6 (Eq. (3) plus possibly Eq. (5) faster than Eq. (1)) or not (Eq. (1) faster than Eq. (3)). In this later case, a highly porous chromia scale is formed on the surface [9] that is totally pervious to gas transport toward the alloy

$$H_2O + C_{(s)} = CO + H_2 \tag{5}$$

(ii) *Internal oxidation of aluminum.* Even though He-2 corresponds to the area for chromia instability, Eq. (3) does not involve Al or Si oxides. Internal oxidation of Al can thus proceed.

(iii) *Decrease in the carbon content.* System of equations (Eqs. (1) and (3)) leads to consumption of the dissolved carbon that is removed from the alloy surface in the form of CO(g). Table 3 shows that within 500 h at 950°C, Inconel 617 loses about 50% of its initial carbon.

(iv) *Dissolution of primary carbides and development of a deep secondary carbide-free zone.* As carbon is removed by Eq. (3) from the surface to the gas phase, it will diffuse from the bulk to the surface. Along the concentration gradient, carbides are destabilized, as shown by the global process

$$\text{carbides} \rightarrow C + \text{metal} \tag{6}$$

Degree of dissolution will depend on the carbide stability, as well as on kinetic factors. Figure 6 shows partial dissolution of primary carbides in the surface vicinity, as well as a deep zone free of secondary carbides. The global carbon loss, as well as the depth of the carbide-free zone, increases with exposure time.

It is expected that dissolution of secondary carbides, which participates in the alloy strengthening at high temperature by limiting the grain boundary glide, will have a dramatic effect on the creep rupture life [26].

**3.3 Corrosion in "Carburizing" VHTR Helium.** Exposure to reducing test helium mixtures ($P(CO)=5$ ppm and 15 ppm in Fig. 3) with methane (20 ppm and 300 ppm) has produced carburization of chromia former alloys. Figure 7 shows pictures of Haynes 230® and Inconel 617 after 240 h at 950°C in the highly carburizing conditions.

Main corrosion features are as follows.

(i) *Absence of chromia scale.* As expected in the reducing conditions, Eq. (3) is initiated and surface chromia is unstable versus

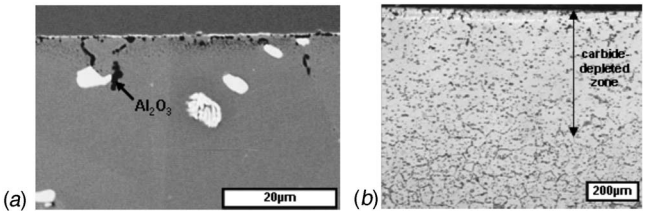


**Fig. 6 Haynes 230® after exposure at 950°C in He-2 for 240 h (*a*) and for 1000 h (*b*)**

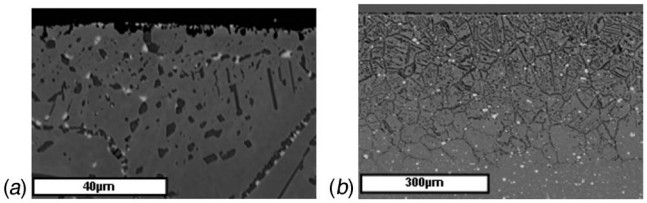


**Fig. 7 Inconel 617 (*a*) and Haynes 230® (*b*) after 240 h at 950°C in He-4**

dissolved carbon.

(ii) *Internal oxidation of aluminum.* As explained in Sec. 2, Eq. (1) can still proceed, regenerating surface chromia and causing internal oxidation of aluminum.

(iii) *Precipitation of surface and internal carbides*. In the mean time cracking of methane on the alloy—following Eq. (4)—deposes carbon on the surface. Part of the carbon can, in turn, participate in the chromia reduction, and the carbon excess will either precipitate as surface carbides (mainly of the $Cr_2C_3$ and $Cr_{23}C_6$ types) or diffuse into the bulk; as the local carbon solubility limit is reached, coarse internal carbides will develop following the global process:

$$C + \text{metal} \rightarrow \text{carbides} \quad (7)$$

In Fig. 7 surface carbides, as well as coarse inter- and intragranular carbides, have formed. The front of coarse carbides goes deeper in the bulk when exposure time increases.

(iv) *Increase in the carbon content.* Table 3 shows an increase in the global carbon concentration of alloys after exposure to test gases He-3 and He-4; the carbon uptake is moderate for He-3 but high for He-4. Besides the longer the exposure time, the higher the carbon uptake.

Precipitation of coarse internal carbides is known to be associated with low temperature embrittlement of metallic materials. Ennis and Lupton [27] showed a dramatic decrease in the room temperature impact energy, the tensile strength, and the elongation rupture of carburized Inconel 617. An increase of 0.4 wt % carbon induces full embrittlement of the alloy.

**3.4 Specific Transitory Behavior of Inconel 617 in Very Dry Helium.** Mention should be made of the ability for Inconel 617 to form alumina scales in very dry conditions [28]. This has been observed in reducing helium, He-2 and He-3, with partial pressure of about 0.5 ppm. Under these circumstances chromia cannot form; instead aluminum is oxidized at the surface to form a thin film of $Al_2O_3$ following Eq. (1). The presence of this film prevents internal oxidation, as well as decarburization and carburization. As already discussed by Graham [21], this specific behavior cannot be a reliable technological solution to the prevention of corrosion in VHTR systems. It is actually considered that the water vapor level during reactor start-up would always lead to the formation of chromia-based surface layer and to consumption of the aluminum reservoir as internal oxidation.

## 4 Conclusion

VHTR helium coolant is expected to contain impurities, which can interact with metallic materials at high temperature, especially with structural chromia-former nickel base alloys. Interplay between the alloy surface, temperature, and gas composition determines whether corrosive oxidation, carburization, or decarburization occurs. Corrosion phenomena, which can significantly affect the mechanical stability, are carburization—associated with low temperature embrittlement—and decarburization—causing a reduced creep rupture time. Within the primary circuit of a VHTR, the atmosphere must thus in any circumstances sustain chromium oxidation because a continuous self-healing chromia-based surface scale is needed to act as a barrier against the reactive gases. However, a specific process occurs at high temperature, which irreversibly destroys chromia; this reaction can be suppressed by increasing the CO partial pressure. A first approach that must be considered to mitigate high temperature corrosion of VHTR alloys is thus the control of the helium chemistry, especially in terms of CO partial pressure. However, the atmosphere must also be compatible with other high temperature materials in particular carbon-based in-core structures.

## Acknowledgment

Studies presented were performed in cooperation with AREVA NP and EDF. Works of S. Guillou, A. Monnier, P. Lett, F. Thieblemont, A. Thomazic, and L. Lemort; S. Gossé and M. Tabarant (CEA, DEN, DPC, SCP); H. Burlet and J. M. Gentzbittel (CEA, DRT, LITEN) are acknowledged.

## References

[1] Gauthier, J.-C., Brinkmann, G., Copsey, B., and Lecomte, M., 2006, "ANTARES: The HTR/VHTR Project at Framatome ANP," Nucl. Eng. Des., **236**, pp. 526–533.

[2] Burlet, H., Gentzbittel, J.-M., Cabet, C., Lamagnere, P., Blat, M., Renaud, D., Dubiez-Le Goff, S., and Pierron, D., 2008, "Evaluation of Nickel-Base Materials for VHTR Heat Exchanger," *Proceedings of the Workshop Structural Materials for Innovative Nuclear Systems (SIMS)*, OECD.

[3] Séran, J. L., Lamagnere, P., Cabet, C., Guetaz, L., Walle, E., and Riou, B., 2005, "Selection and Qualification of Materials for the Primary Circuit and Intermediate Heat Exchanger of Very High Temperature Reactor (VHTR)," *Proceedings of the ICAPP'05*, Paper No. 5419.

[4] Wallé, E., Blat, M., Kaczorowski, D., Cabet, C., Lamagnere, P., Combrade, P., Terlain, A., Dubiez-Le Goff, S., Billot, P., and Boursier, J.-M., 2005, "Concerted Program and Development of New Test Facilities to Address High Temperature Corrosion Issues of Ni Based Alloys in Impure Helium Environment for Applications in Very High Temperature Reactors," *Proceedings of the GLOBAL 2005*, Paper No. 183.

[5] Graham, L. W., Everett, M. R., Lupton, D., Ridealgh, F., Sturge, D. W., and Wagner-Löffler, M., 1976, "Environmental Conditions in HTRs and the Selection and Development of Primary Circuit Materials," *Proceedings of the Symposium on Gas-Cooled Reactors With Emphasis on Advanced Systems*, IAEA, ed., pp. 319–352.

[6] Yao, M. S., Wang, R. P., Liu, Z. Y., He, X. D., and Li, J., 2002, "The Helium Purification System of the HTR-10," Nucl. Eng. Des., **218**(1–3), pp. 163–167.

[7] Sakaba, N., and Hirayama, Y., 2005, "Helium Chemistry in High-Temperature Gas-Cooled Reactors—Chemistry Control for Avoiding Hastelloy XR Corrosion in the HTTRIS System," *Proceedings of the GLOBAL 2005*, Paper No. 263.

[8] Quadakkers, W. J., and Schuster, H., 1984, "Thermodynamic and Kinetic Aspects of the Corrosion of High-Temperature Alloys in High-Temperature Gas-Cooled Reactor Helium," Nucl. Technol., **66**(2), pp. 383–391.

[9] Brenner, K. G. E., and Graham, L. W., 1984, "Development and Application of a Unified Corrosion Model for High-Temperature Gas-Cooled Reactor Systems," Nucl. Technol., **66**(2), pp. 404–414.

[10] Bates, H. G. A., 1984, "The Corrosion Behavior of High-Temperature Alloys During Exposure for Times Up to 10000 h in Prototype Nuclear Process Helium at 700 to 900°C," Nucl. Technol., **66**(2), pp. 415–428.

[11] Rouillard, F., Cabet, C., Wolski, K., Terlain, A., Tabarant, M., Pijolat, M., and Valdivieso, F., 2007, "High Temperature Corrosion of a Nickel Base Alloy by Helium Impurities," J. Nucl. Mater., **362**, pp. 248–252.

[12] Rouillard, F., Cabet, C., Wolski, K., and Pijolat, M., 2007, "Oxide-Layer Formation and Stability on a Nickel-Base Alloy in Impure Helium at High Temperature," Oxid. Met., **68**, pp. 133–148.

[13] Rouillard, F., Cabet, C., Terlain, A. and Wolski, K., 2005, "Gas Cooled Reactors: Corrosion Behavior of a High Strength Nickel Base Alloy," *Proceedings of the Eurocorr 2005*, Paper No. O-358-8.

[14] Chapovaloff, J., Kaczorowski, D., and Girardin, G., 2008, "Parameters Governing the Reduction of Oxide Layers on Inconel 617 in Impure VHTR He Atmosphere," Mater. Corros., **59**(7), pp. 584–590.

[15] Chapovaloff, J., Girardin, G., Kaczorowski, D., Wolski, K., and Pijolat, M., 2008, "Influence of Al on the High temperature Corrosion Behaviour of Inconel 617 in VHTR Primary Coolant Atmosphere," Mater. Sci. Forum, **595–598**(1), pp. 491–500.

[16] Cabet, C., Chapovaloff, J., Rouillard, F., Girardin, G., Kaczorowski, D., Wolski, K., and Pijolat, M., 2008, "High Temperature Reactivity of Two Chromium-Containing Alloys in Impure Helium," J. Nucl. Mater., **375**, pp. 173–184.

[17] Cabet, C., Girardin, G., Rouillard, F., Chapovaloff, J., Wolski, K., and Pijolat, M., 2008, "Comparison of the High Temperature Surface Reactivity of Two Materials for Gas Cooled Reactors," Mater. Sci. Forum, **595–598**, pp. 439–448.

[18] Warren, M. R., 1986, "Rapid Decarburization and Carburization in High Temperature Alloys in Impure Helium Environments," High Temp. Technol., **4**(3), pp. 119–130.

[19] Cook, R. H., Exner, R., and Graham, L. W., 1988, "Post-Service Examination of a 10 MW Helium-Helium Heat Exchanger and Comparison With Long Term Behaviour in Laboratory Tests," *Proceedings of the Specialists' Meeting on High-Temperature Metallic Materials for Gas-Cooled Reactors*, pp. 129–135.

[20] Quadakkers, W. J., 1985, "Corrosion of High Temperature Alloys in the Primary Circuit Helium of High Temperature Gas Cooled Reactors—Part II: Experimental Results," Werkst. Korros., **36**, pp. 335–347.

[21] Graham, L. W., 1990, "Corrosion of Metallic Materials in HTR-Helium Environments," J. Nucl. Mater., **171**, pp. 76–82.

[22] Shindo, M., and Kondo, T., 1982, "Studies on Improving Compatibility of Nickel-Base Alloys With High-Temperature Helium-Cooled Reactor (VHTR) Environment," *Proceedings of the Gas-Cooled Reactors Today*, BNES, ed., Vol. 2, pp. 179–184.

[23] Shida, Y., and Moroishi, T., 1992, "Effect of Aluminium and Titanium Additions to Fe-21%Cr-32%Ni on the Oxidation Behavior in an Impure Helium

Atmosphere at High Temperatures," Oxid. Met., **37**(5/6), pp. 327–348.
[24] Cook, R. H., and Graham, L. W., 1978, "Chemical Behavior and Mechanical Performance in HTR-Helium at High Temperatures," *Alloy 800*, W. Betteridge et al., eds., pp. 309–326.
[25] Shindo, M., Quaddakers, W. J., and Schuster, H., 1986, "Corrosion Behaviour of High Temperature Alloys in Impure Helium Environments," J. Nucl. Mater., **140**, pp. 94–105.
[26] Kurata, Y., Ogawa, Y., Nakajima, H., and Kondo, T., 1989, "Creep Rupture Characteristics in the HTGR Simulated Helium Gas Environment and Their Relevance to Structural Design," *Proceedings of the Workshop on Structural Design Criteria for HTR*, pp. 275–291.
[27] Ennis, P. J., and Lupton, D. F., 1980, "The Relationship Between Carburisation and Ductility Loss," *Proceedings of the Petten International Conference on Behaviour of High Temperature Alloys in Aggressive Environments*, The Metals Society, ed., pp. 979–991.
[28] Menken, G., Nieder, R., Graham, W. L., Schuster, H., and Thiele, W., 1982, "Review of the Gas/Metal Interactions in HTR Helium Up to 950°C," *Proceedings of the Gas-Cooled Reactors Today*, BNES, ed., Vol. 2, pp. 185–190.

# Mixing Conditions in the Lower Plenum and Core Inlet of a Boiling Water Reactor

**Hernan Tinoco**[1]
e-mail: htb@forsmark.vattenfall.se

**Stefan Ahlinder**[2]
e-mail: ahl@forsmark.vattenfall.se

Forsmarks Kraftgrupp AB,
SE-742 03 Östhammar, Sweden

*A thermal mixing analysis of the downcomer, main recirculation pumps (MRPs) and lower plenum of Forsmark's Unit 3 has been carried out with three separate computational fluid dynamics models. Several difficulties with the boundary conditions have been encountered, particularly with the MRP model. The results obtained predict stable temperature differences of around 8 K at the core inlet. Such large temperature differences have never been observed at Forsmark nuclear power plant (NPP). Temperature measurements at four positions above the reactor pressure vessel (RPV) bottom give the mean value used as the core inlet temperature for core analyses. Even if the temperature transmitters used are rather slow and inaccurate, they should be able to detect such large temperature differences that may lead to fuel damage. The only damage reported at Forsmark NPP since the implementation of liner cladding in fuel design is that caused by mechanically induced debris fretting (threadlike particles). Also, the difficulties with the connection of the models throw some doubt on the accuracy of these predictions. A completely connected model of the same RPV volume covered by the separate models predicts temperature differences at core inlet that are almost one-fourth of those mentioned above, i.e., approximately 2.5 K. Most of the mixing occurs downstream of the MRP diffusers, at the lower plenum "inlet." This prediction divergence seems to arise from an impossibility of a correct transfer of complete three-dimensional flow field properties by means of boundary conditions defined at a two-dimensional inlet section.*
[DOI: 10.1115/1.3097130]

*Keywords: thermal mixing, turbulent transport, pumps, core temperature, CFD*

## 1 Introduction

Industrial processes generally involve regions of mixing between fluids with different properties. The direct-cycle boiling water reactor (BWR) is no exception since colder heavier feed water has to mix with warmer lighter reactor water exiting the steam separators. This mixing region is located at the upper part of the downcomer, in the vicinity of the feed water sparger.

According to Dimotakis [1], "turbulent mixing can be viewed as a three-stage process of entrainment, dispersion (or stirring), and diffusion, spanning the full spectrum of space-time scales of the flow." An estimate of the mixing level may be given through two quantities [2]. The first is the scale of segregation, being a measure of the size of the unmixed lumps of the original components. The second is the intensity of segregation, being a measure of the concentration difference between neighboring clumps of fluid, i.e., it describes the effect of molecular diffusion on the mixing process. A small scale of segregation and a low intensity of segregation characterize good mixing.

A high degree of mixing between two streams of a fluid with different properties, such as temperature and density, may be a hard task. Depending on the mixing process space and time scales, complete mixing may even be impossible without special mixing devices. An example is the use of specially designed spacers in the nuclear fuel to enhance the turbulent heat transport. Another is the use of mixers to avoid the problem of thermal fatigue caused by temperature fluctuations at a mixing point constituted by a tee-junction of a pipe net.

The approach of the present work for modeling the mixing process is that of FLUENT [3], i.e., turbulent heat transport and mixing are treated using the concept of Reynolds' analogy to turbulent momentum transfer. It uses an effective thermal conductivity, i.e., the sum of the molecular thermal conductivity and the thermal conductivity of turbulence (see Sec. 3.2).

The operating reactor pressure of the simulations is 7 MPa. Temperature dependent water data at that pressure, based on standard steam table data [4], have been implemented in FLUENT. The temperature dependence of water density allows for buoyancy effects to be included in the simulations. Turbulence is modeled by means of the shear-stress transport (SST) model of Menter [5], (see Sec. 3.2). Second-order discretization schemes in space and time have been used for all momentum and scalar equations. In spite of a large number of cells, the typical value of $y^+$ for the cells adjacent to the wall is of the order of $3 \times 10^3$ due to the high prevailing Reynolds number of the order of $10^7$ or higher. The high $y^+$ values lead to an overestimation of the wall friction losses.

The simulations of the present study using separated models of the downcomer, main recirculation pumps (MRPs), and lower plenum, corresponding to Unit 3 of Forsmark nuclear power plant, are reported in Sec. 2. The results obtained with a completely connected model of the same region of the reactor pressure vessel (RPV) covered by the separate models are presented in Sec. 3. An analysis of the cause leading to this deviation in core temperature predictions using these two approaches is given in Sec. 3.

## 2 The Separate Models

Three separate models, i.e., downcomer, MRP, and lower plenum (see, e.g., Ref. [6] for a view of the reactor vessel), have been

[1]Corresponding author.
[2]Present address: AREVA NP GmbH, Abteilung NEPR-G, Paul-Gossen-Strasse 100, 91052 Erlangen, Germany.

Manuscript received October 31, 2008; final manuscript received November 10, 2008; published online July 17, 2009. Review conducted by Dillip R. Ballal. Paper presented at the 16th International Conference on Nuclear Engineering (ICONE 16), Orlando, FL, May 12–15, 2008.

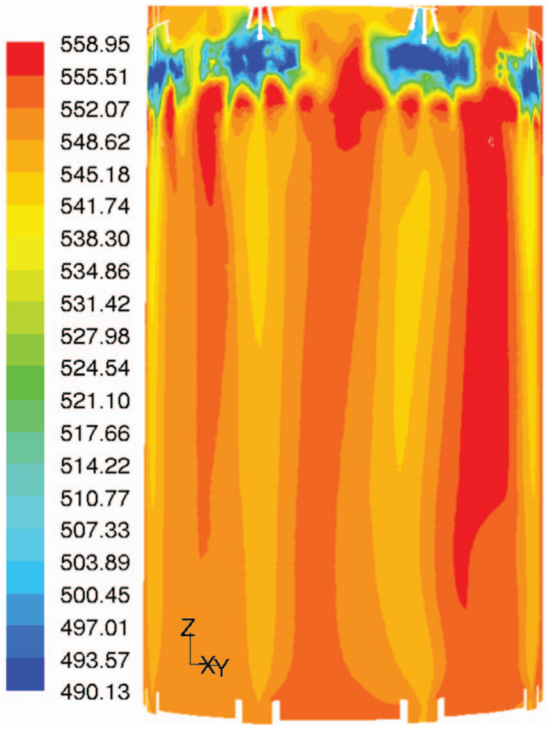


**Fig. 1 Temperature (in kelvin) at the downcomer center**

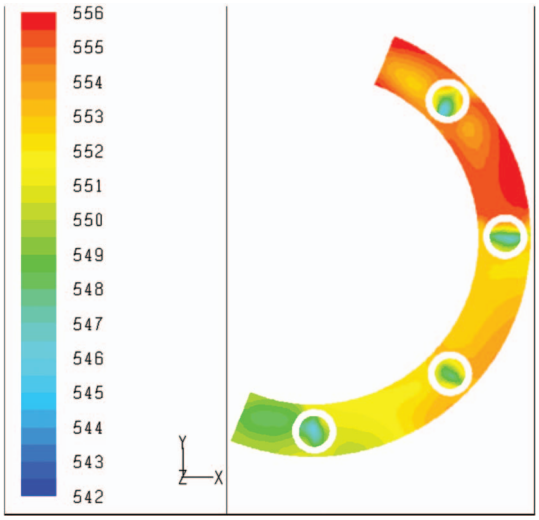


**Fig. 2 Temperature distribution (in kelvin) at the MPR inlets at a level close to the pump deck**

coupled together to simulate of the temperature distribution of the main recirculation flow at the core inlet. The coupling of the models has been carried out by adopting what has been considered to be suitable boundary conditions. But the geometry influenced choice of spatial limits of each model may complicate and limit the options to define appropriate boundary conditions. For example, the MRP model has to include a part of the downcomer due to the upstream vortex generated by the impeller rotation. Also the region downstream of the pump must have the right extension in order to allow for the outlet flow and possible recirculation regions to develop properly. However, the actual geometry of what may be denoted as "inlet" to the lower plenum might prevent this development and might hinder correct definitions of the boundary conditions. Therefore, it is impossible to avoid some degree of arbitrariness in the definitions of the models, which may to a noticeable extent characterize the associated boundary conditions. Consequently, the solution for avoiding the aforementioned deficiencies associated with the separate models seems to be the development of a completely connected model, to be described in Sec. 2.1.

**2.1 Downcomer Model.** The first doubts about the quality of the mixing between feed water and reactor water in the downcomer of Forsmark reactors aroused at the end of the 1980s when the implementation of hydrogen water chemistry (HWC), i.e., the addition of hydrogen gas to recombine the oxygen in the reactor water, did not produce the expected results. Later, very rough simulations by means of the PHOENIX code were carried out, revealing the presence of large downcomer regions with unmixed reactor water between feed water spargers [7]. Consequently, the addition of hydrogen to the feed water was discontinued. Additional numerical analyses have been carried out later with a geometrically more advanced model containing 6,070,935 tetrahedral cells, in order to study how the mixing conditions in the downcomer may be improved to make recombination of hydrogen and oxygen possible by means of HWC [8,9]. Recently, an analysis of boron injection and mixing in the downcomer has been accomplished with the same numerical model [6].

Vertically, the model extends from the water surface to the MRP inlets, where normal operation of the MRPs has been simulated through software based rotation by momentum sources (see Ref. [6]). This rough simulation of the MRPs seems to capture the upstream vortex of the pumps affecting the flow in the downcomer. Figure 1 shows the temperature distribution in the downcomer for normal operation conditions along a cylindrical surface passing through the center of the downcomer. As Fig. 1 shows, mixing in the downcomer is incomplete, and several temperature streaks form due mainly to two reasons. First, the reactor water coming from the steam separators flows below the feed water flow coming from the spargers and pushes up the colder water. A larger part of this water finds its way down to the pump deck through the region between each sparger and the reactor vessel. Second, the reactor water flows down practically unmixed to a substantial part of the downcomer region between spargers. The temperature distribution results indicate maximum temperature differences of the order of 10 K in one and the same MRP inlet (see Fig. 2).

Figure 3 shows the velocity field along the aforementioned cylindrical surface and some streamlines in the downcomer. This flow is primarily vertical but contains some eddylike structures, making it more three-dimensional. This complicates the boundary conditions associated with the single pump model given in Sec. 2.2.

**2.2 Pump Model.** The single pump computational fluid dynamics (CFD) model corresponds to that of an axial PSR600 pump designed by KSB (Germany). Due to the refusal of the manufacturing company to provide suitable drawings, the impeller geometry was measured using a laser technique. Figure 4 shows a view of the simplified geometry used to create the grid of the CFD model. As this figure shows, one-eighth of the downcomer is included in the model (in green in Fig. 4), a rather arbitrary partition from a flow viewpoint. Also a part of what is denominated here as the lower plenum inlet (lower part in purple in Fig. 4) is included in this model. The simulation grid contains 2,473,622 elements. The limiting vertical radial planes of the pump model are symmetry planes, neglecting any transport normal to the planes caused by the eddy structures mentioned above.

In FLUENT 6.3.26 [3], there are two main approaches for dealing with models containing single or multiple moving parts. The multiple reference frame (MRF) model, being the simpler approach, is a steady state approximation in which individual regions move at different rotational and/or translational speeds. The flow in each moving region is solved using moving reference frame equations. The sliding mesh model (SMM) accounts for the relative motion of stationary and moving components and the unsteady interac-

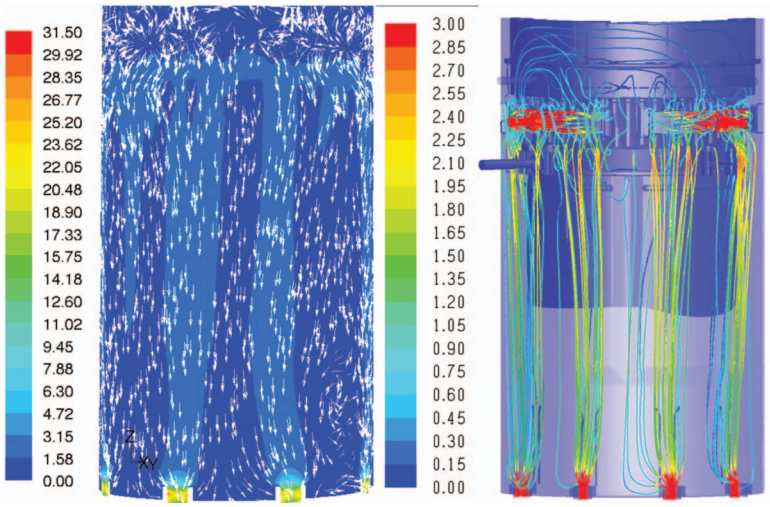


**Fig. 3 Velocity distribution (in m/s) at the downcomer center (left view) and streamlines (right view)**

tions due to this motion are included. Both methods have been used to compute the flow through a single MRP. Since the boundary conditions are time independent, both the head and the main features of the flow and mixing conditions downstream of the pump are similar. In this case, the unsteady interactions captured by the SMM are negligible. However, the computer effort needed is an order of magnitude larger than that needed with the MRF model.

Owing to simplified boundary conditions, the simulations re-

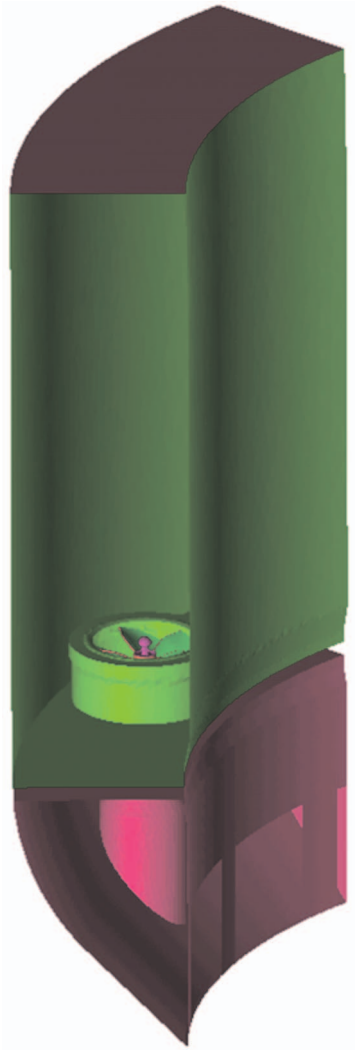

**Fig. 4 Simplified geometry of CFD model MR pump**

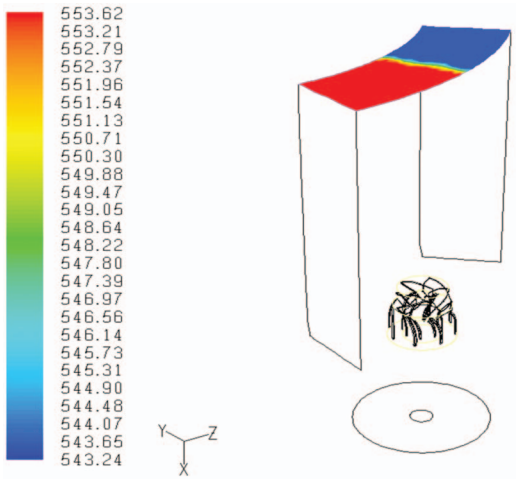


**Fig. 5 View of downcomer temperature boundary conditions (in kelvin) for MR pump test flow**

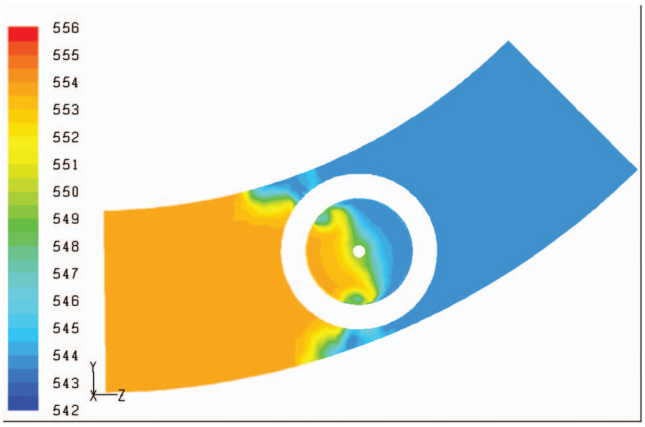


**Fig. 6 Temperature distribution (in kelvin) at the MRP inlet at a level close to the pump deck**

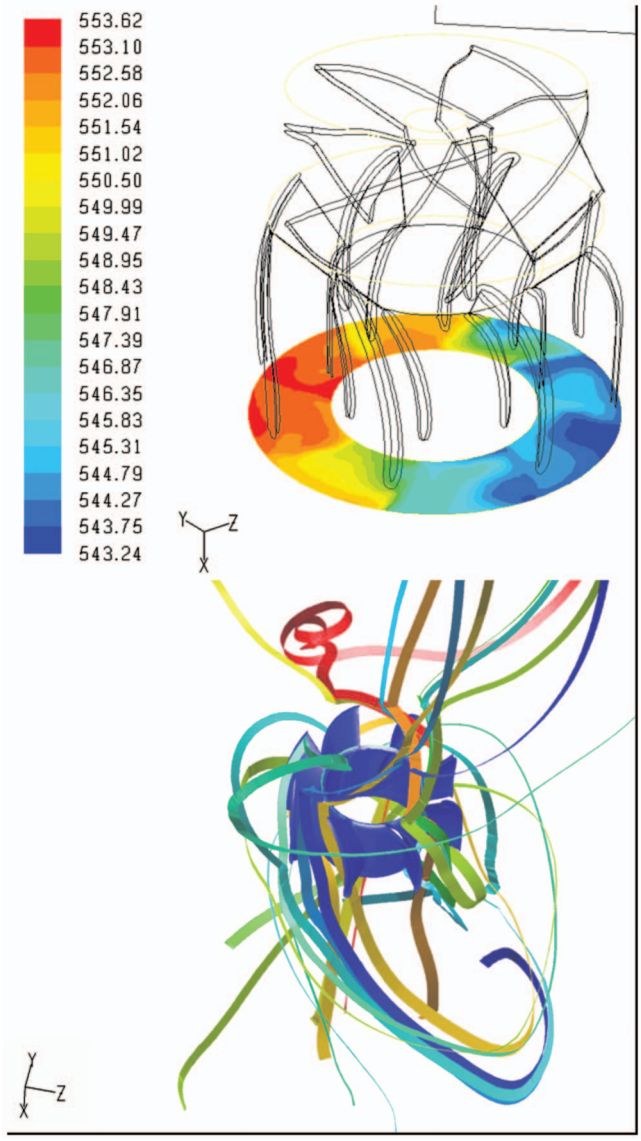


**Fig. 7 Diffuser outlet temperature (in kelvin) for MR pump test flow (upper view) and streamlines through the pump**

ported in this section are only a test of the pump model and of the mixing conditions. Figure 6 shows the temperature boundary condition at the model inlet. The mass flow rate and the pressure head are determined by the rotation speed of the pump, i.e., 1325 rpm.

Figure 5 shows the temperature distribution at the MRP inlet in a horizontal plane at the same vertical position, as in the case of Fig. 2. Figure 7 shows the pump outlet temperature distribution using the MRF model. Here, the mixing through the pump is relatively limited, maintaining regions with the maximum and minimum inlet temperatures, i.e., a difference of 10 K. Thus, the pump works as a device transforming into flow energy, mainly as a pressure head, the external work put into the system. Yet, depending on the pump efficiency, some work is lost to mixing. But the MRF approach might not be suitable for describing thermal mixing. Figure 8 shows a comparison between the temperature distributions over the impeller blades obtained with both approaches. The pattern given by the SMM is less regular and more complex than that given by the MRF method but, at large, the thermal distributions are similar. Indeed, both distributions preserve large regions with the extreme temperature values and a mixing region in between. Yet, the MRF is slightly more conservative, since it maintains larger temperature gradients and generates less mixing.

Figure 9 shows a comparison of the temperature distribution at the pump outlet obtained with the MRF and with SMM. The SMM case differs from the MRF case in two ways, namely, a solid body rotation of the temperature pattern accompanied by an increase in mixing of the region of higher temperatures. The pattern rotation is due to the sliding mesh rotating at a speed of 1325 rpm. But both distributions still have regions containing the extreme temperature values, with a more reduced region of maximum temperature for the SMM case.

Both methods are considered equivalent for thermal mixing in the bulk since they give similar answers regarding the extreme values of the temperature distribution. The advantages of the MRF method, i.e., low computer effort and conservative results, have facilitated the simulations of the single pump and the completely connected models. The SMM has only been used for the comparisons reported in this section. When used with the completely connected model, it has evidenced communication problems similar to those explained in Ref. [10].

The outlet boundary condition of the CFD model is known as "outlet vent." It consists of an infinitely thin surface vent with an associated pressure drop proportional to the dynamic head based on the normal velocity. Usually, this condition stabilizes the outflow and suppresses spurious recirculation regions. Here, recirculation regions are present at the model outlet due to the geometry

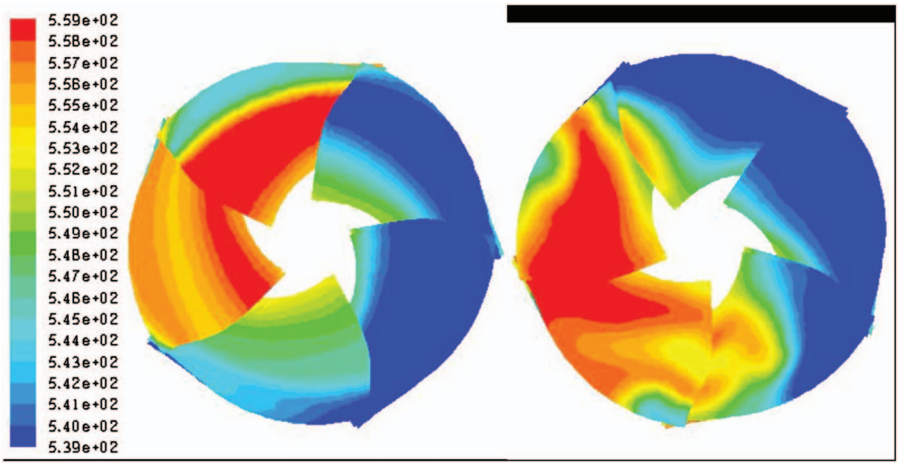


**Fig. 8 Comparison of mixing in a MR pump with MRF (left) and SMM (right) approaches (impeller blades)**

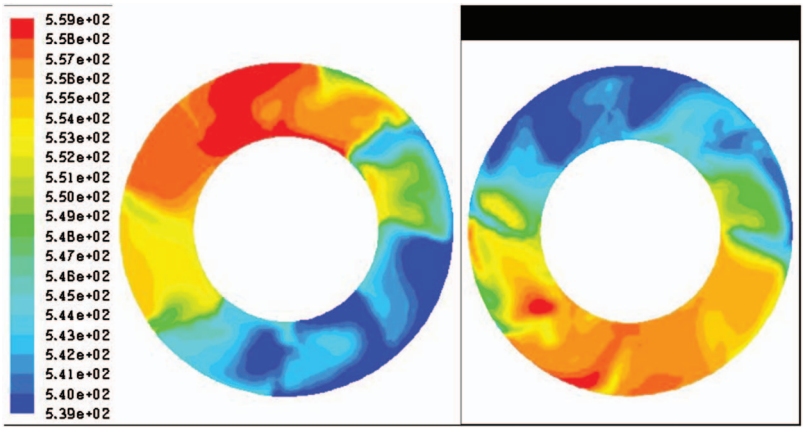


**Fig. 9 Comparison of mixing in a MR pump with MRF (left) and SMM (right) approaches (pump outlet)**

of the lower plenum inlet. These regions close in the part of the lower plenum external to the model and give convergence difficulties to the computations due to an undetermined inflow. These problems suggest the incorporation of a larger part of the lower plenum into the pump model. As the core inlet is the only "natural" geometrical limit suitable for a horizontal cut, the entire lower plenum should be built in. Azimuthally, half of the RPV leads to more suitable symmetry conditions. Therefore, the model has to include four MRPs and a part of the downcomer. To extend it to the complete downcomer seems appropriate because of better defined inlet boundary conditions. However, the size of the CFD model sets some conditions on the computer resources needed.

**2.3 Lower Plenum Model.** The flow in the lower plenum of a BWR has been investigated to an even lesser extent. A limited description of this flow in an advanced boiling water reactor (ABWR) has been done by Hisajima et al. [11].

The separate CFD model of the lower plenum consists of the lower plenum inlet (lower part in purple in Fig. 4) and of the proper lower plenum, i.e., the lower part of the reactor vessel including all the guide tubes of the control rods up to the level of the core inlet. Figure 10 shows a view of the simplified geometry used to create the computational grid of the CFD model. The MRP outlets constitute the inlet boundaries of the computational domain. The outlet boundaries are located in two different regions. The first is the core bypass inlet consisting of a number of holes located at the lower part of the control rod guide tubes (CRGTs), above the control rod (CR) drive penetration nozzles at the bottom RPV (see left picture in Fig. 11). To save computational elements, the round holes have been replaced by square holes with the same sectional area (see Fig. 11), since local effects in the immediate neighborhood of the holes are neglected. The second is the core inlet placed above the upper end of the CR guide tubes, at the level of the core plate.

The core bypass inlet boundary condition is a mass outflow equal to half of the total bypass flow of 1588.8 kg/s, i.e., 13.14% of the main recirculation flow of 12,087 kg/s according to POLCA computations, a code for core analysis at normal operation, [12]. The outlet boundary condition of the core inlet is an "outlet vent" with an associated pressure drop adjusted to give resistance corresponding to the core pressure losses. Thus, the pressure reference level is that of the upper plenum, assumed to be homogeneous and constant.

The aforementioned test run with the MRP model has been coupled to flow simulations of the lower plenum. Figure 12 shows the temperature at the four MR pump outlets constituting the CFD model inlet. The temperature distribution is that of the MRP model run with the MRF approach, i.e., the left picture in Fig. 9. In addition, the velocity field at the MRP outlet has also been prescribed at the inlet of the lower plenum model.

Figure 13 shows the resultant temperature distribution at the inner bottom wall of the RPV. Regions of low and high tempera-

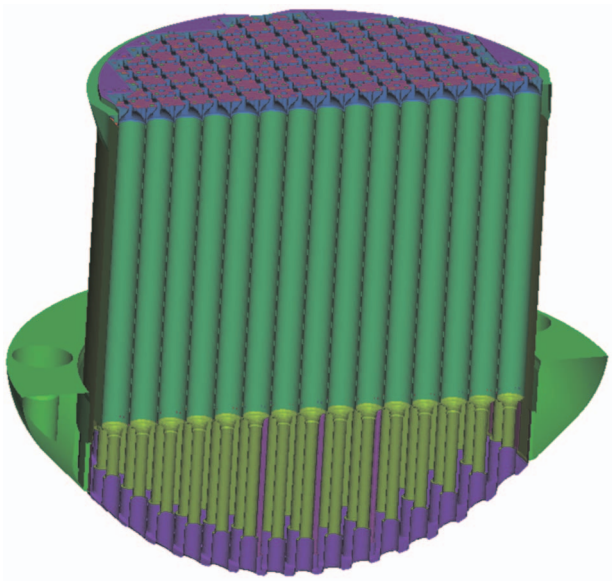

**Fig. 10 Geometry of CFD model of lower plenum**

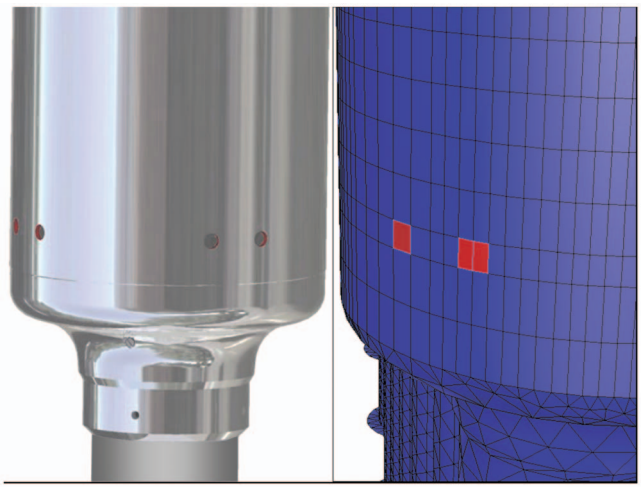

**Fig. 11 CR guide tube holes constituting the core bypass inlet (left) and corresponding grid (right)**

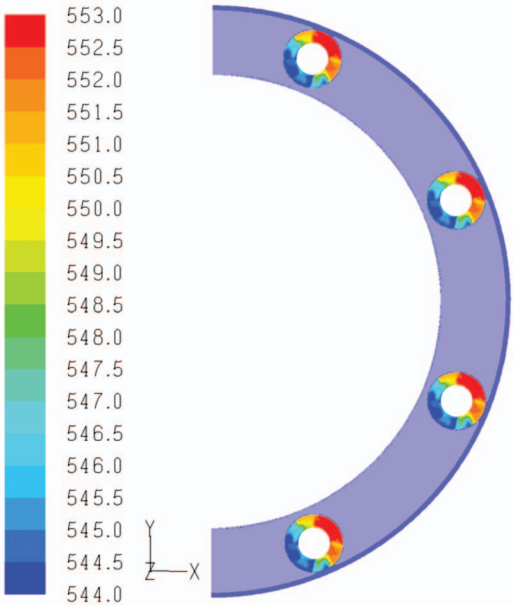


**Fig. 12 View of inlet temperature distribution (in kelvin) for lower plenum test flow**

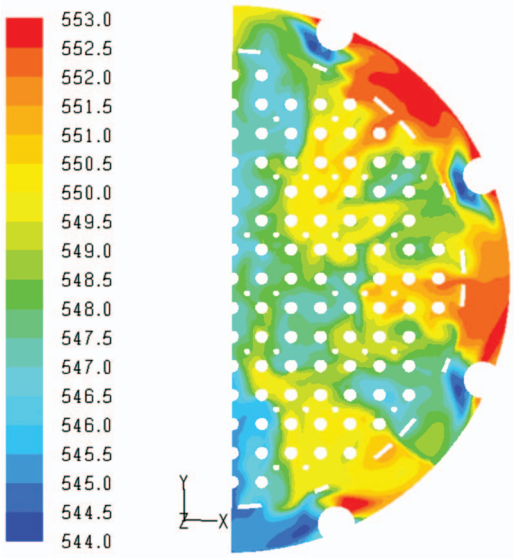


**Fig. 14 Water temperature (in kelvin) at a horizontal plane 1.58 m above the bottom of the RPV**

tures are roughly distributed along radial streaks. Coupling of the two CFD models results in a relatively low mixing at the bottom of the lower plenum and in a reduction in the maximum temperature difference by only 2 K, i.e., 7 K. Figure 14 shows the water temperature distribution along a horizontal plane located 1.58 m above the RPV bottom. This temperature distribution exhibits a radial streak structure, which is less defined than that over the RPV bottom. The maximum temperature difference here is still the same as that of the inlet temperature distribution. Due to the geometry of the lower plenum inlet combined with buoyancy effects, less mixed water, i.e., with larger temperature differences, may end up flowing above more mixed water, i.e., with smaller temperature differences.

The water temperature distribution in a horizontal plane located 4.08 m above the RPV bottom is depicted in Fig. 15. The flow reaching this level has experienced some mixing since the maximum temperature difference has decreased to about 7 K. Still, a temperature pattern similar to that in Fig. 16 can be perceived despite the flow area reduction caused by the CRGT.

Finally, Fig. 16 gives the water temperature distribution at the core inlet. The maximum water temperature difference there is still about 7 K, implying that the narrow channel geometry of the CR guide tube forest is an important obstacle for any crosswise mixing. The results reported in this section and in Sec. 2.2 suggest that a temperature difference of around 10 K at the MRP inlets may survive to a considerable extent all the way to the core inlet. No clear mixing mechanism for the MR flow appears to exist for the coupled MRP and lower plenum models through seemingly suitable boundary conditions. The completely connected model shows the opposite. A well defined mixing mechanism exists for reducing temperature differences of the order of 10 K at the MRP inlets to those of the order of a couple of degrees at the core inlet.

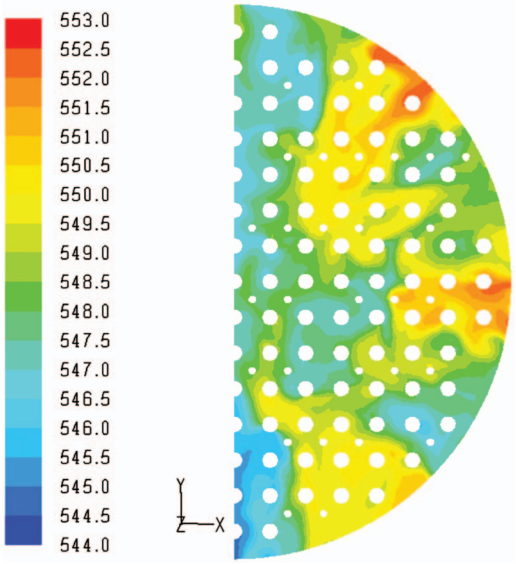


**Fig. 13 Temperature distribution (in kelvin) at the bottom inner wall of the reactor vessel**

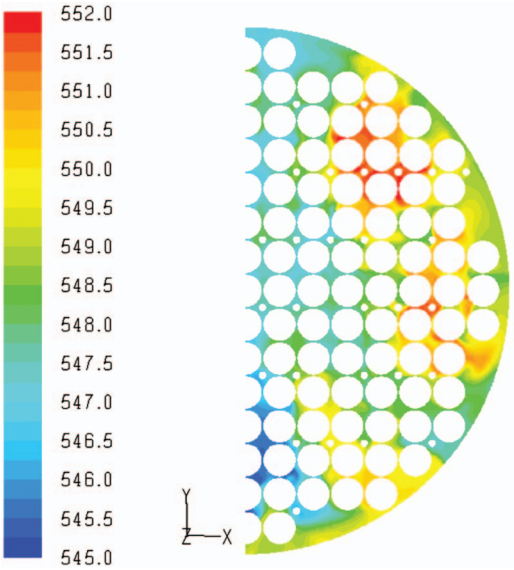


**Fig. 15 Water temperature (in kelvin) at a horizontal plane 4.08 m above the bottom of the RPV**

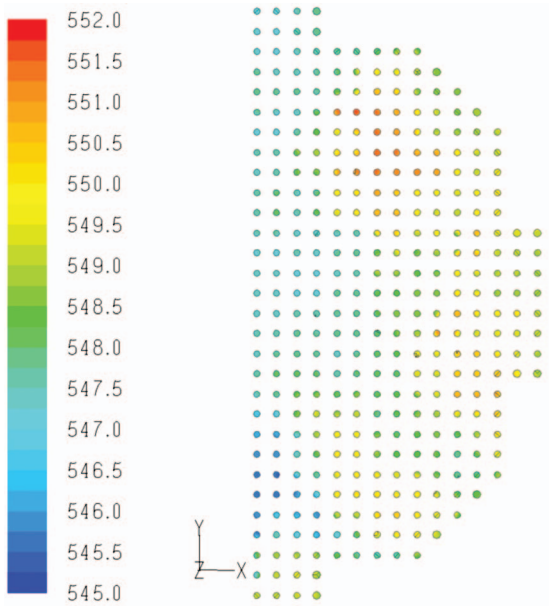


**Fig. 16 Core inlet temperature distribution (in kelvin)**

## 3 The Completely Connected Model

This model comprises the three aforementioned models, i.e., the downcomer, four MRPs, and the lower plenum, fully connected in one continuous grid containing 25,204,026 cells. Figure 17 shows a view of the simplified geometry used to generate the computational grid of the CFD model.

The inlet boundaries of the completely connected model equal those of the downcomer model (see Ref. [6] for details). The boundary conditions for normal operation related to the feed water system are unchanged, i.e., an inflow of 444 kg/s with 490.15 K (217°C) in temperature for the sparger at 45 deg and an inflow of 464 kg/s with the same temperature for the sparger at 135 deg. However, the boundary condition at the reactor water inlet changes from mass inflow with given flow rate to pressure inlet. Now, the MRP pressure head gives the correct mass inflow through this boundary by comprising the pressure losses associated with parts of the reactor not included in the model, i.e., core, upper plenum, steam separators, and steam dryer. The outlet boundaries are a sum of one boundary equaling that of the downcomer model, i.e., the 135 deg nozzle of the reactor water cleanup system (System 321), and two boundaries equaling those of the lower plenum model, the CRGT holes of the core bypass inlet and the core inlet. The boundary condition associated with System 321 still is an outflow of 16 kg/s. The boundary condition of the core bypass inlet is an outflow equal to 794.4 kg/s (see Sec. 2.3 and Ref. [12]). The outlet boundary condition of the core inlet is an "outlet vent," with a pressure drop corresponding to the pressure losses of the parts not included in the model, as mentioned before. In the case of transient operation of the reactor, the boundary conditions may change, and other help systems may start up with specific conditions (see Ref. [6]). In the present study, only normal operation conditions have been considered.

**3.1 Results of Beginning of Cycle Normal Operation.** In this case, the MRPs are run at 1325 rpm, using the MRF approach. Considering the estimate of the pressure drops, the MRPs give a flow rate of 5874.4 kg/s, being only 2.8% lower than half of the nominal MR flow rate of 6043.5 kg/s. The total resulting pressure head is 195.97 kPa, comparing well with that measured in Unit 3 of 212 kPa. The difference is mainly due to the relatively coarse grid that overestimates the losses.

Figure 18 gives a temperature distribution (same surface as Fig. 1), which is similar to that obtained with the downcomer model,

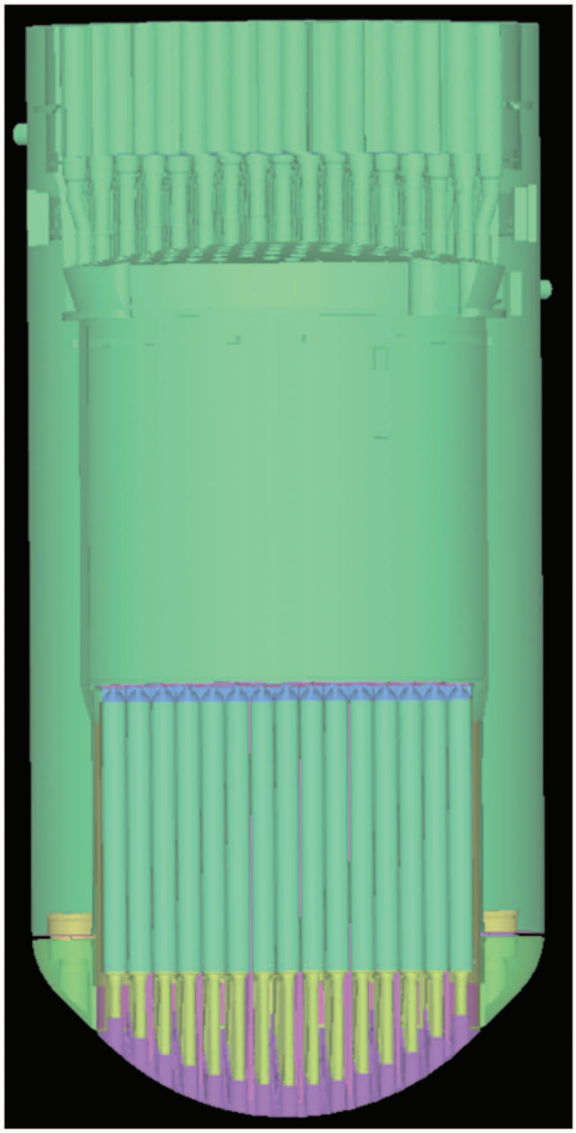

**Fig. 17 Frontal view of the simplified geometry of the completely connected CFD model**

despite different inlet boundary conditions for the reactor water. The mixing is still incomplete and contains vertical streaks with different temperatures. The maximum temperature difference at a MRP inlet is still of the order of 10 K. This picture agrees with results from simulation tests carried out with modifications of the downcomer to improve mixing (see, e.g., Ref. [9]). The flow field and the mixing are almost exclusively dependent on the downcomer geometry. For instance, the blockage of the reactor water flow by plates attached to the steam dryer support in the region between spargers improves the mixing and reduces the maximum temperature difference at MRP inlets to half of the differences shown in Figs. 2 and 19.

Figure 19 shows the temperature at the MRP inlets in the same horizontal plane of Fig. 2. The distribution compares well with that the downcomer model (Fig. 2). Yet, the inlet temperature distribution of the MRP model (Fig. 5) has a similar maximum temperature difference, but reduced regions with intermediate temperatures. This is a result of the simplified inlet boundary conditions of the test mentioned in Sec. 2.2.

Figure 20 depicts the temperature distribution at the same horizontal section in Fig. 12. Now, each section in Fig. 20 has its own temperature distribution. Depending on the section, the maximum

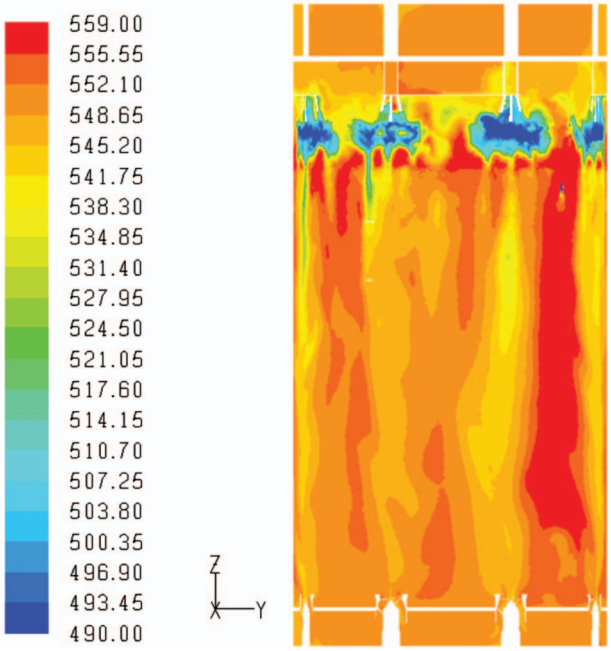


**Fig. 18 Temperature distribution (in kelvin) along a vertical cylindrical surface at the center of the downcomer**

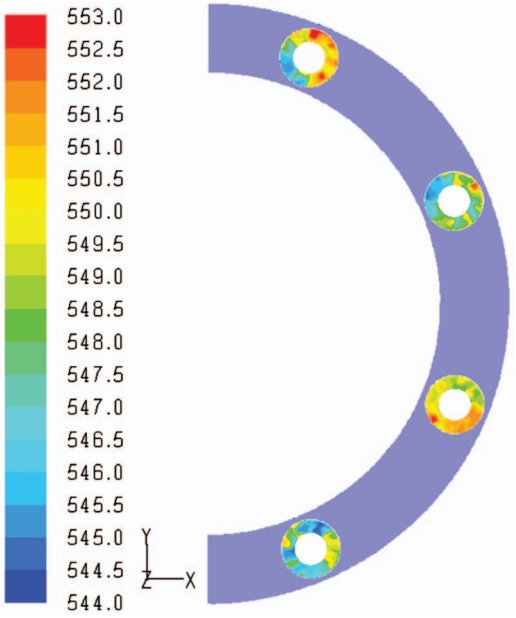


**Fig. 20 Temperature distribution (in kelvin) at MRP diffuser outlets**

temperature difference ranges from 6 K to 10 K. As mentioned before, the regions of intermediate temperatures are larger than the corresponding regions in Fig. 12.

The temperature distribution at the bottom of the RPV is shown by Fig. 21. It shows a maximum temperature difference of only 4 K, almost half of that obtained using the lower plenum model. An increase in mixing downstream of the MRPs of this magnitude was not observed when using the separate MRP and lower plenum models. Yet, the results obtained with the coupled models correspond to a test with simplified boundary conditions at the pump inlet (Fig. 6). Anyhow, the mechanism leading to the aforementioned mixing seems to be absent in the case of the coupled models.

The mixing mentioned above leads to a temperature distribution at the core inlet, having a maximum temperature difference of around 2.6 K shown in Fig. 22.

**3.2 The Mixing in the Inlet to the Lower Plenum.** The main difference in mixing between models seems to arise within the lower plenum inlet. Therefore, results from the two models, hereinafter referred to as LPM for the lower plenum model and CCM for the completely connected model, will be compared in this section. Figures, or pictures, will be considered in pairs, with the first mentioned belonging to the LPM.

A crucial part in this comparison is the turbulence model, being here the SST model of Menter [5]. It is a zonal model, since the near-wall flow is solved by a turbulence/frequency-based $k$-$\omega$ model and the bulk flow by the $k$-$\varepsilon$. Through a smooth transition, the $k$-$\varepsilon$ model matches the $k$-$\omega$ formulation using blending functions (see, e.g., Ref. [3]).

The SST model of turbulence defines turbulent viscosity as

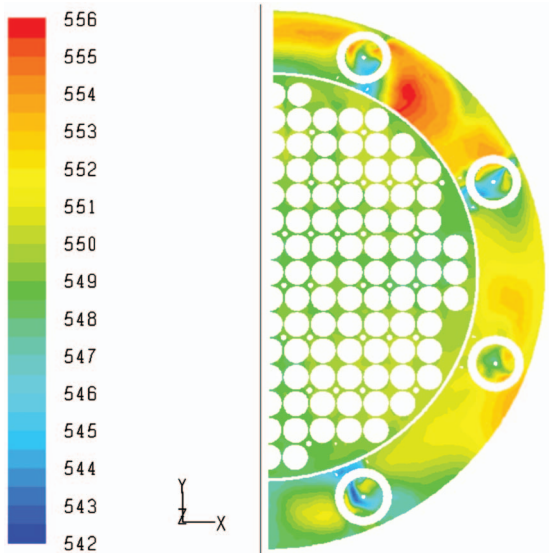


**Fig. 19 Temperature distribution (in kelvin) at the MRP inlets at a level close to the pump deck**

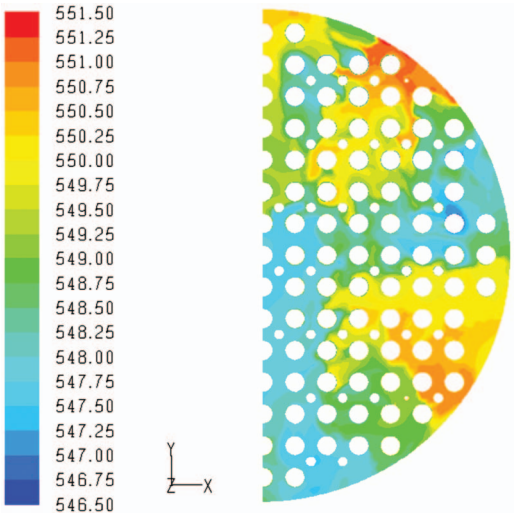


**Fig. 21 Temperature distribution (in kelvin) at the bottom inner wall of the reactor vessel**

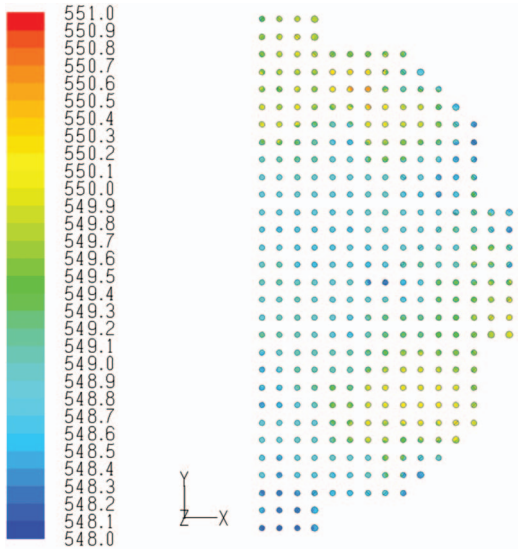


**Fig. 22 Water temperature distribution (in kelvin) at the core inlet**

$$\mu_t = \frac{\rho k}{\omega} \frac{1}{\max\left[\frac{1}{\alpha^*}, \frac{SF_2}{\alpha_1 \omega}\right]} \tag{1}$$

where $\rho$ is density, $k$ is turbulent kinetic energy, and $\omega$ is specific dissipation rate. $S$ is the mean strain rate magnitude given by

$$S = \sqrt{\left(\frac{\partial U_i}{\partial x_j} + \frac{\partial U_j}{\partial x_i}\right)^2} \tag{2}$$

where $U_i$ is the mean velocity field. The other functions in this definition, i.e., $\alpha^*$, $F_2$, and $\alpha_1$, contain low-Reynolds-number corrections and/or blending formulations (see Ref. [3]).

Figures 23 and 24 show the turbulent kinetic energy in a radial vertical plane at 22.5 deg. Figure 24 shows in the upper right corner details not included in the LPM that correspond to the MRP. A comparison between figures reveals a maximum of turbulent kinetic energy for the CCM, which is four times that of the LPM. Also, the overall values of the turbulent kinetic energy throughout the lower plenum inlet are much higher.

Figures 25 and 26 show the turbulent kinetic energy in a radial vertical plane at an azimuthal position of 45 deg. As before, the maximum and the overall values of this field throughout the lower plenum inlet are much higher for the CCM.

Figure 27 shows the turbulent kinetic energy in a horizontal plane 1.58 m from the RPV bottom, i.e., at the center of the lower plenum inlet. The results of the CCM (right view) show a field that has higher maximum and higher and more extended overall values. Figure 28 shows the turbulent viscosity in the same horizontal plane, as in the preceding figure. Also for this magnitude, the results of the CCM (right view) exhibit a field that has higher maximum and higher and more extended overall values, everywhere in the lower plenum inlet.

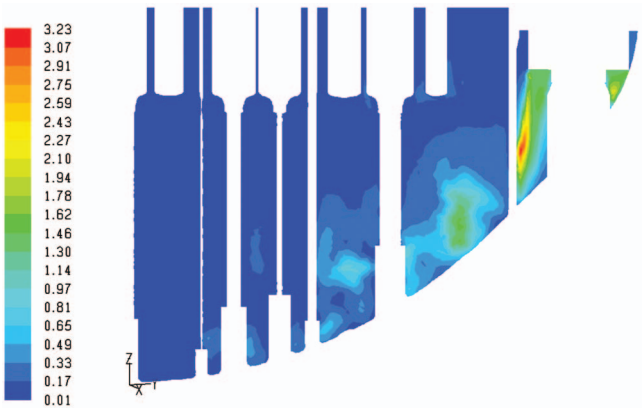


**Fig. 23 Turbulent kinetic energy (in $m^2/s^2$) in a vertical radial plane at 22.5 deg in lower plenum inlet (LPM)**

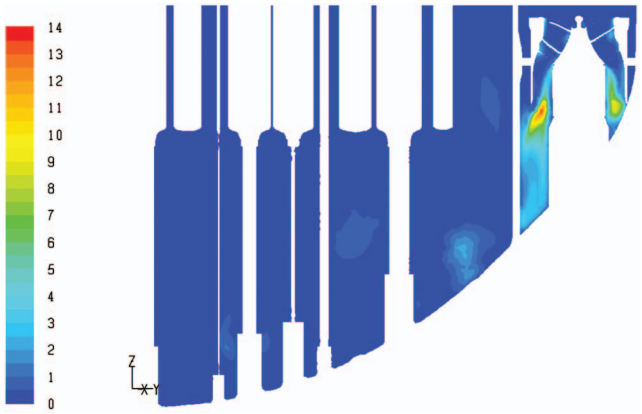


**Fig. 24 Turbulent kinetic energy (in $m^2/s^2$) in a vertical radial plane at 22.5 deg in lower plenum inlet (CCM)**

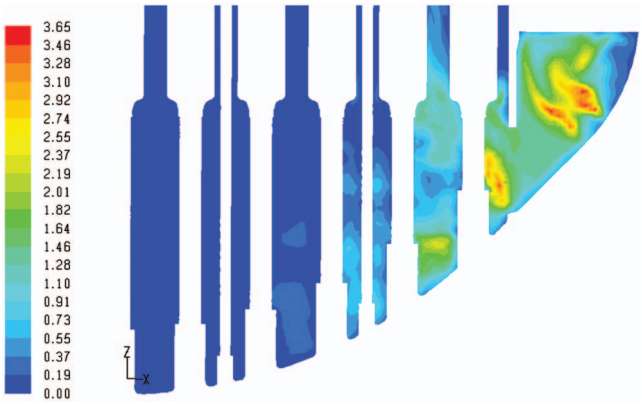


**Fig. 25 Turbulent kinetic energy (in $m^2/s^2$) in a vertical radial plane at 45 deg in lower plenum inlet (LPM)**

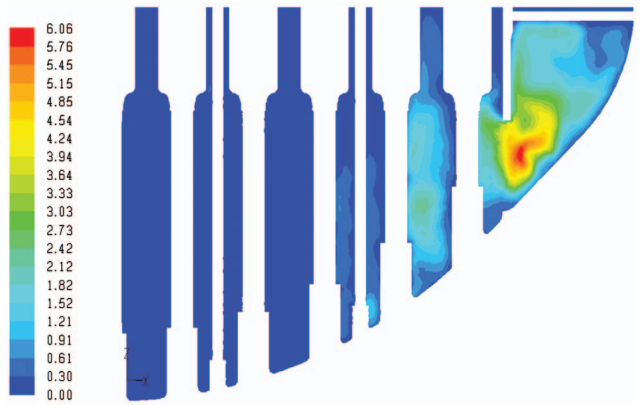


**Fig. 26 Turbulent kinetic energy (in $m^2/s^2$) in a vertical radial plane at 45 deg in lower plenum inlet (CCM)**

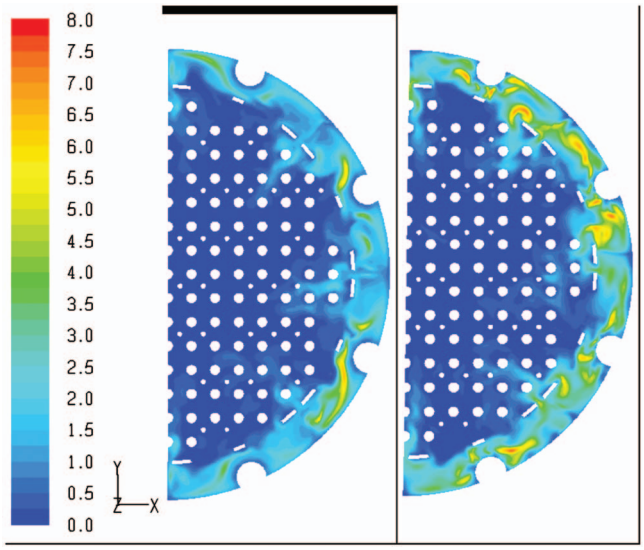


**Fig. 27 Turbulent kinetic energy (in $m^2/s^2$) at the plane in Fig. 16, left LPM and right CCM**

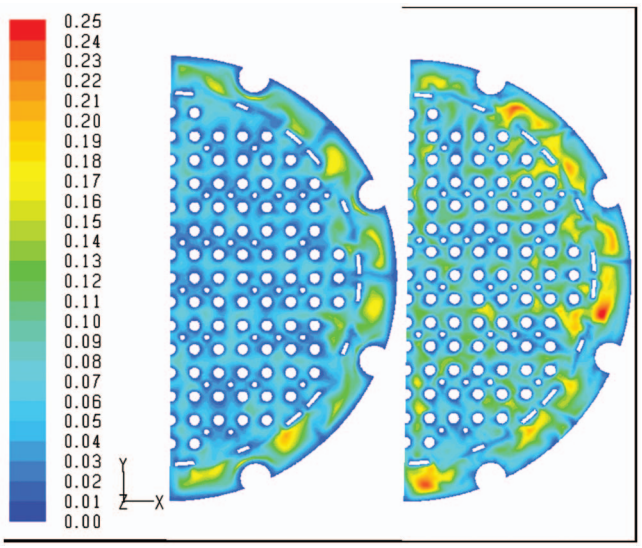


**Fig. 29 Taylor macroscale (in meters) at the plane in Fig. 16, left LPM and right CCM**

In FLUENT, turbulent heat transport is modeled using the concept of Reynolds' analogy to turbulent momentum transfer. Therefore, the turbulent thermal conductivity, $D_t$, is given by

$$D_t = \frac{c_p \mu_t}{\mathrm{Pr}_t} \tag{3}$$

with $c_p$ as the constant pressure specific heat and $\mathrm{Pr}_t$ as the turbulent Prandtl number, its default value being 0.85. According to penetration theory (see, e.g., Ref. [13]), the time, $t_{\mathrm{mix}}$, to mix two species due to turbulent transport is inversely proportional to the turbulent diffusivity, i.e.,

$$t_{\mathrm{mix}} \propto \frac{1}{D_t} \tag{4}$$

Moreover, the distance $\ell_{\mathrm{mix}}$ needed to mix the species is proportional to this time and may be estimated using the length scale characterizing the large eddies, designated as the Taylor macroscale, $L_t$, as follows (see, e.g., Ref. [13])

$$\ell_{\mathrm{mix}} \propto \frac{1}{L_t^{4/3}} \tag{5}$$

where

$$L_t = \frac{k^{3/2}}{\varepsilon} \tag{6}$$

$\varepsilon$ is the dissipation rate of turbulent kinetic energy given by

$$\varepsilon = \beta^* k \omega \tag{7}$$

where $\beta^*$ is a function with low-Reynolds-number corrections [3]. The Taylor macroscale, $L_t$, may not be accurately resolved everywhere in the two cases discussed here, but because it is the scale characterizing the large eddies, its relevance for estimating mixing at large is important only away from the walls.

Figure 29 shows the distribution of the Taylor macroscale, in the same horizontal plane as before. Even in this case, the results of the CCM (right view) exhibit a field that has higher maximum and higher and more extended overall values. Figure 30 confirms

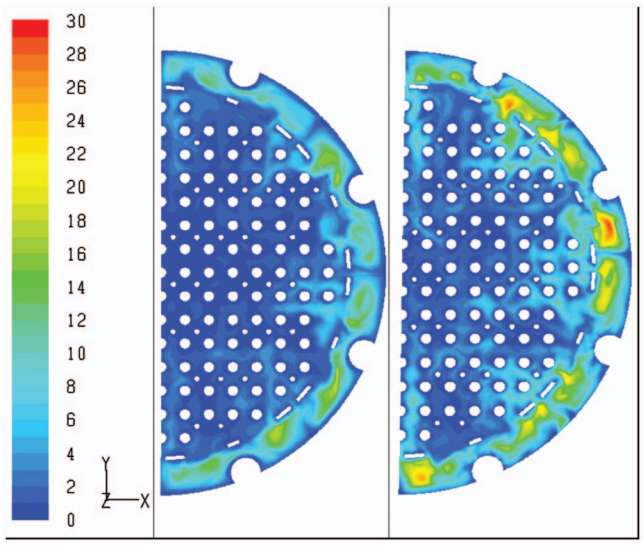


**Fig. 28 Turbulent viscosity (in kg/m s) at the plane in Fig. 16, left LPM and right CCM**

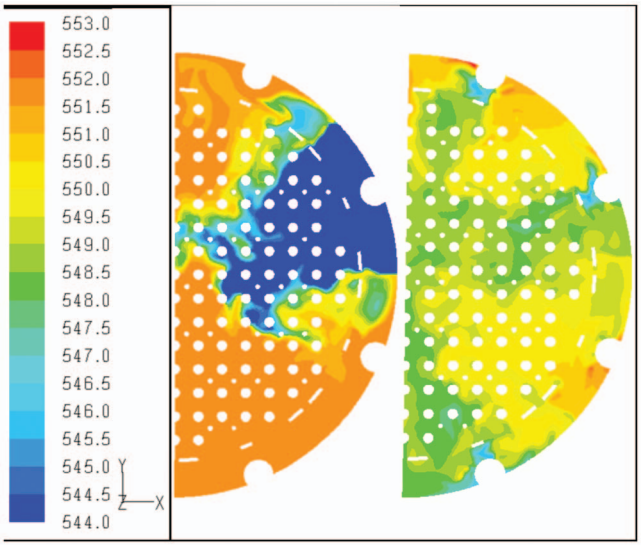


**Fig. 30 Temperature (in kelvin) at the plane in Fig. 16, left LPM and right CCM**

the difference in mixing between the LPM and the CCM. In spite of the similitude in temperature differences at the diffuser outlet (Figs. 12 and 19), the right view in Fig. 30 shows a much larger temperature homogenization at the level of the center of the lower plenum inlet. If mixing is not overpredicted here, the temperature differences at the core inlet are of the order of magnitude of the uncertainty of the temperature gauges used to measure the core inlet temperature.

## 4 Discussion and Conclusions

An analysis of the thermal mixing in the downcomer, MRPs, and lower plenum has been carried out with three separate CFD models. Due to the partition of the RPV volume involved, difficulties with the boundary conditions have been found, particularly with the MRP model. The results of these models indicate that temperature differences of the order of 10 K at the MRP inlets are, to a large extent, conserved and conveyed by flow up to the core inlet. Neither the MRPs nor the lower plenum significantly modifies this thermal inhomogeneity. Thus, temperature differences of around 8 K are predicted to exist at the core inlet. The time dependent computations indicate a stable temperature pattern at the core inlet. Such large temperature differences have not been observed at the Forsmark nuclear power plant (NPP). Temperature measurements at four positions above the RPV bottom give the mean value for the core inlet temperature of core analyses [12]. Even if the temperature transmitters used are rather slow, with a time constant of the order of 300 s, and inaccurate, with an uncertainty of $\pm 2$ K, they should be able to detect such large stable temperature differences that may lead to fuel damage. Incidentally, a temperature decrease of 1 K was registered by one of the transmitters after the core spray removal [14,15], that caused a deterioration in the mixing conditions in the downcomer. The only damage reported at Forsmark NPP since the implementation of liner cladding in fuel design is that caused by mechanically induced debris fretting (threadlike particles).

To decide this issue avoiding unsuitable model connections, a completely connected model of the same RPV volume was developed. The maximum temperature difference at the core inlet predicted by this model is one-fourth of those mentioned above. Most of the mixing takes place downstream of the MRPs, at the lower plenum inlet. The boxlike form of this region slows down the flow and generates more turbulent kinetic energy, enhancing the temperature homogenization. Also the unavoidable swirl component of the flow exiting the pumps substantially contributes to this mixing process. With all probability, the prediction disagreement is due to an impossibility of correctly transferring three-dimensional flow properties through boundary conditions defined at a two-dimensional section. In a case like this, the pressure field may develop so that the swirling part of the flow is not sustained and is damped out. A more correct coupling of the models may be achieved by defining the different magnitudes and their gradients over a volume rather than over a two-dimensional surface.

The $k$-$\varepsilon$ and $k$-$\omega$ approaches are known to overpredict the generation of turbulent kinetic energy as the flow is retarded. In regions dominated by normal strain rates, these models fail due to calibration with respect to shear strain. The SST approach [5] includes a modification of the production term depending on vorticity that avoids the overprediction of kinetic energy production. Some improvement of the turbulence modeling may still be achieved by using Reynolds averaged Navier–Stokes (RANS) second-order closures, such as that in Ref. [16]. An approach, such as large eddy simulation (LES), will need much larger computational resources than those needed for the present simulations.

The MRF approach may not give a totally correct representation of the flow exiting the pumps, especially the swirl component of the velocity. Here, this is not crucial since the same approach is used in both cases, but for more absolute mixing predictions, the SMM approach may be preferable. Yet, the model size seems to cause trouble with parallelization like that encountered with a similar code [10,17]. Also the accuracy of simulations is affected by the precision of the algorithm, of the different models used for turbulence, heat transfer, etc., together with the employed user-developed grid. Mainly, the present computations follow the advices of Menter [18] and Casey and Wintergerste [19]. Still, when dealing with complex geometries like those of a BWR, limitations in software license and/or available computer power rule out an analysis for grid independence of the type proposed by them. Yet, Höhne [20] obtained good agreement with thermal mixing experiments using a coarser grid. For turbulence, the SST model, LES, and detached eddy simulation (DES) are used, the later approach being the most successful.

Also, Moretti et al. [21] showed that meaningful conservative results may be obtained for boron mixing processes with such grids. The difference between these conservative results and experiments is assumed to be caused by limitations of the two-equation turbulence models, standard $k$-$\varepsilon$, and SST model, in taking care of anisotropy effects. Höhne et al. [22], using a Reynolds stress turbulence model and LES, obtained good predictions of thermal mixing with two different CFD codes. These references indicate that more advanced turbulence models may improve the quality of the present results.


## Acknowledgment

The authors want to acknowledge here the help received from P. Hedberg with the grid generation and from B. Hemström with the production of a number of figures.


## Nomenclature

- $c_p$ = constant pressure specific heat (kJ/kg K)
- $D_t$ = turbulent thermal conductivity (W/m K)
- $F_2$ = blending function of SST model of turbulence [3]
- $k$ = turbulent kinetic energy ($m^2/s^2$)
- $\ell_{\mathrm{mix}}$ = distance of mixing (m)
- $L_t$ = Taylor macroscale (m)
- $\mathrm{Pr}_t$ = turbulent Prandtl number
- $S$ = mean strain rate magnitude ($s^{-1}$)
- $t_{\mathrm{mix}}$ = mixing time (s)
- $U_i$ = mean velocity field (m/s)
- $x_i$ = Cartesian coordinates (m)
- $\alpha_1$ = blending function of SST model of turbulence [3]
- $\alpha^*$ = low-Reynolds-number correction, turbulent viscosity [3]
- $\beta^*$ = low-Reynolds-number correction, dissipation rate [3]
- $\varepsilon$ = dissipation rate of turbulent kinetic energy ($m^2/s^3$)
- $\mu_t$ = turbulent viscosity (kg/m s)
- $\rho$ = water density ($kg/m^3$)
- $\omega$ = specific dissipation rate ($s^{-1}$)

## References


[1] Dimotakis, P. E., 2005, "Turbulent Mixing," Annu. Rev. Fluid Mech., **37**, pp. 329–56.
[2] Brodkey, R. S., 1967, *The Phenomena of Fluid Motions*, Dover, New York.
[3] ANSYS FLUENT, 2006, "FLUENT 6.3 Documentation," Fluent Inc., Lebanon, NH.
[4] Schmidt, E., and Grigull, U., 1989, *Properties of Water and Steam in SI-Units*, Springer-Verlag, Berlin, Germany.
[5] Menter, F. R., 1994, "Two-Equation Eddy-Viscosity Turbulence Models for Engineering Applications," AIAA J., **32**(8), pp. 1598–1605.
[6] Tinoco, H., Buchwald, P., and Frid, W., 2007, "Numerical Simulation of Boron Injection in a BWR," 12th International Topical Meeting on Nuclear Reactor Thermal-Hydraulics, NURETH 12, Pittsburgh, PA, Sept. 30–Oct. 4.
[7] Hemström, B., Lundström, A., Tinoco, H., and Ullberg, M., 1992, "Flow Field Dependence of Reactor Water Chemistry in BWR," Sixth International Conference on Water Chemistry of Nuclear Reactor Systems, Bournemouth, UK, Oct. 12–15.

[8] Tinoco, H., and Einarsson, T., 1997, "Numerical Analysis of the Mixing and Recombination in the Downcomer of an Internal Pump BWR," Eighth International Topical Meeting on Nuclear Reactor Thermal-Hydraulics, NURETH 8, Kyoto, Japan, Sept. 30–Oct. 4, pp. 806–816.
[9] Ahlinder, S., Tinoco, H., and Ullberg, M., 2007, "CFD Analysis of Recombination by HWC in the Downcomer of a BWR," 12th International Topical Meeting on Nuclear Reactor Thermal-Hydraulics, NURETH 12, Pittsburgh, PA, Sept. 30–Oct. 4.
[10] Tinoco, H., Ahlinder, S., and Hedberg, P., 2007, "Estimate of Core Shroud Temperature by Means of a CFD-Model of Core Bypass," 15th International Conference on Nuclear Engineering, ICONE 15, Nagoya, Japan, Apr. 22–26.
[11] Hisajima, K., Uchida, K., Matsumoto, K., Kondo, K., Yokoyama, S., and Miyagawa, T., 2006, "Development of 1000 MWE Advanced Boiling Water Reactor," 14th International Conference on Nuclear Engineering, ICONE 14, Miami, FL, Jul. 17–20.
[12] ABB Atom AB, 1994, "Core Master Documentation," POLCA User's Manual, Västerås, Sweden, Vol. 6.
[13] Bakker, A., and LaRoche, R. D., 2000, "Modeling of the Turbulent Flow in HEV Static Mixers," The Online CFM Book, http://www.bakker.org/cfm.
[14] Tinoco, H., 2003, "Two-Phase Flow in the Upper Plenum of a Boiling Nuclear Water Reactor," Tenth International Topical Meeting on Nuclear Reactor Thermal Hydraulics, NURETH 10, Seoul, Korea, Oct. 5–9.
[15] Tinoco, H., Adolfsson, E., Baltyn, W., and Marcinkiewicz, J., 2005, "BWR ECCS—Thermal Loading Analysis of Internals Related to Spray System Removal," 13th International Conference on Nuclear Engineering, ICONE 13, Beijing, China, May 16–20.
[16] Launder, B. E., Reece, G. J., and Rodi, W., 1975, "Progress in the Development of Reynolds-Stress Turbulence Closure," J. Fluid Mech., **68**(3), pp. 537–566.
[17] CFD Online, 2007, "Parallel Computing," http://www.cfd-online.com/Wiki/Parallel_computing/.
[18] Menter, F., 2002, "CFD Best Practice Guidelines for CFD Code Validation for Reactor-Safety Applications," UE/FP5 ECORA Project "Evaluation of Computational Fluid Dynamic Methods for Reactor Safety Analysis," Germany, Paper No. EVOL-ECORA-D01.
[19] 2000, "Best Practice Guidelines," ERCOFTAC Special Interest Group on "Quality and Trust in Industrial CFD," M. Casey and T. Wintergerste, eds., Sulzer Innotec, Version 1.0, Switzerland.
[20] Höhne, T., 2007, "CFD-Simulations of Thermal Hydraulic Benchmark V1000CT-2 Using ANSYS CFX," *Proceedings of the 15th International Conference on Nuclear Engineering, ICONE 15*, Nagoya, Japan, Apr. 22–26.
[21] Moretti, F., Melideo, D., D'Auria, F., Höhne, T., and Kliem, S., 2007, "CFX Simulations of ROCOM Slug Mixing Experiments," *Proceedings of the 15th International Conference on Nuclear Engineering, ICONE 15*, Nagoya, Japan, Apr. 22–26.
[22] Höhne, T., Kliem, S., and Bieder, U., 2006, "Modeling of a Buoyancy-Driven Flow Experiment at the ROCOM Test Facility Using the CFD Codes CFX-5 and TRIO-U," Nucl. Eng. Des., **236**, pp. 1309–1325.

# Evaluation of the Phase Composition, Crystallinity, and Trace Isotope Variation of SiC in Experimental TRISO Coated Particles

**Johan P. R. de Villiers**
**James Roberts**
**Noko Ngoepe**
**Alison S. Tuling**

University of Pretoria,
Pretoria 0002, South Africa

*The SiC layers in experimental tristructural-isotropic (TRISO) coated particles with zirconia kernels were evaluated for their phase composition, impurity levels, crystal perfection, and twinning of the crystallites in the layers. This evaluation was necessary to compare the different SiC layers and relate these properties to various quality tests and ultimately to manufacturing parameters in the chemical vapor deposition (CVD) coater. Identification of the various polytypes was done using electron diffraction methods. This is the only method for the unequivocal identification of the different polytypes. The 3C and 6H polytypes were positively identified. The SiC in some samples is disordered. This is characterized by planar defects, of different widths and periodicities, giving rise to streaking in the diffraction pattern along the [111] direction of the 3C polytype. Polarized light microscopy in transmission easily distinguishes between the cubic (beta) and noncubic (alpha) SiC in the layers and provides valuable information about the distribution of these phases in the layers. Raman spectroscopy was used to examine the distribution of Si in the SiC layers of the different samples. Two samples contain elevated levels of Si (~50%), with the highest levels on the inside of the layers. The elevated Si levels also occur in most of the other samples, albeit at lower Si levels. This was also confirmed by the use of scanning electron microscope (SEM) electron backscatter analysis. Rietveld analysis using X-ray diffraction is presently the only reliable method to quantify the polytypes in the SiC layer. It was found that the SiC layer consists predominantly (82–94%) of the 3C polytype, with minor amounts of the 6H and 8H polytypes. Impurities in the SiC and PyC could be measured with sufficient sensitivity using laser ablation inductively coupled mass spectrometry (LA-ICP-MS). The SiC and PyC layers are easily located from the intensity of the $C^{13}$ and $Si^{29}$ signals. In most cases the absolute values are less important than the variation of impurities in the samples. Elevated levels of the transition elements Cu, Ni, Co, Cr, and Zn are present erratically in some samples. These elements, together with $Ag^{107}$ and $Ag^{109}$, correlate positively, indicating impurities, even metallic particles. Elevated levels of these transition elements are also present at the SiC/outer pyrolytic carbon (OPyC) interface. The reasons for this are unknown at this stage. NIST standards were used to calibrate the impurity levels in the coated particles. These average from 1 ppm to 18 ppm for some isotopes.*
[DOI: 10.1115/1.3098426]

## 1 Introduction

This investigation was initiated to evaluate the polytype distribution, the crystallinity, and the trace element levels in experimentally produced TRISO coated particles produced by Pebble Bed Modular Reactor (Pty) Limited (PBMR). These particles were manufactured with zirconia kernels instead of $UO_2$.

The aim of the study was to compare the silicon carbide layers in different batches of particles manufactured under different conditions in the CVD coater. In addition, the properties measured here can be related also to different quality parameters measured on the same batches of particles. During the investigation some analytical methods proved to be better suited for the analysis than others. This also is useful for the choice of instrumentation necessary for the adequate characterization of TRISO nuclear fuel on a more routine basis. Lastly, these methods are used to compare PBMR fuel with known superior material produced elsewhere.

From the beginning of the development of coated particle fuel, their characterization formed an integral part of the evaluation of their suitability and effectiveness as a container for fission products. This is summarized in various reviews [1–3]. There is however scarce detailed information on the various methods used, their applicability, and the results obtained. Recent studies dealing with the distribution of different polytypes in the coated particles were done mainly on irradiated cubic SiC [4] and the evolution of various defects was discussed. Transmission electron microscopy was also used in the discussion of the microstructure of SiC in TRISO particles by Hélary et al. [5]. It was decided to do a more detailed study on the occurrence of the different polytypes, their disorder, and twinning.

The polytype distribution of TRISO particles was examined by Krautwasser et al. [6] using Raman spectroscopy, who showed

Manuscript received November 27, 2008; final manuscript received December 1, 2008; published online July 17, 2009. Review conducted by Dilip R. Ballal. Paper presented at the Fourth International Topical Meeting on High Temperature Reactor Technology (HTR2008), Washington, DC, September 28–October 1, 2008.

that the predominant phase is the cubic 3C polytype. Other Raman studies of SiC [7,8] also discussed the characteristic spectra of the various polytypes.

The distribution of the impurities in the SIC layers in nuclear fuel was studied using X-ray fluorescence microtomography using a synchrotron source by Naghedolfeizi et al. [9]. This study is of particular relevance to the findings of the LA-ICP-MS study in that similar impurities are found. The application of the latter method to TRISO particle studies was examined in detail.

This study examines the SiC polytypes, the presence of Si in the SiC layer, and the distribution of impurity isotopes in the various layers. To achieve this, electron microscopy, selected area electron diffraction analysis, Raman spectrometry, energy-dispersive microanalysis, Rietveld analysis and laser ablation ICP mass spectrometry was used.

## 2 Sample Preparation and Measurement Procedures

Experimental samples PO-1–PO-10, prepared under variable coating conditions, were obtained from PBMR [10].

**2.1 Optical and Transmission Microscopies.** The coated particles are mounted in a Technovit™ acetone soluble resin, sectioned to ~30 $\mu$m, and polished [11].

After optical microscopic examination, the sample is used for transmission electron microscopy (TEM) studies. The particle is ion thinned using a Gatan precision ion polishing system and studied with a Philips CM200 transmission electron microscope equipped with a Gatan Erlangshen model 782 digital imaging camera and an EDAX DX Prime energy-dispersive analyzer at 160 kV. For the electron diffraction analysis a double tilt holder is used. The experimental diffraction patterns are compared with the patterns calculated by the JEMS software [12]. A one-to-one correspondence is sought for both spot positions and intensities to recognize the correct polytypes and zone axis orientations.

**2.2 Raman Spectrometry.** The same samples that are used for energy-dispersive x-ray spectrometry (EDS) analysis by SEM are used for Raman spectroscopy. For calibration, weighed mixtures of Si and the three SiC polytypes (3C, 4H, and 6H) are prepared by prolonged milling to the desired particle size. Because it is not always possible to sample the surface representatively, the averages of several measurements should be done routinely if reliable calibration is desired.

Most of the samples were analyzed with the 514.5 nm excitation line of the Ar-ion laser; alternatively, the excitation line of the 647.1 nm Kr-ion laser was used. The laser beam was formed to a spot diameter of ~1 $\mu$m, with an objective lens of 50× magnification. The presence and concentration of Si in the SiC layers is measured in the various coated particles. Also the presence of the various polytypes is established, with some uncertainty.

**2.3 Scanning Electron Microscopy.** The coated particles are sectioned and polished close to their equatorial positions. This was also done to minimize charging of the samples in the electron beam. These samples are examined both with scanning electron microscopy and Raman spectroscopy. The polished samples are examined using a JEOL JSM-6300 scanning electron microscope operating at 5 kV and $6\times10^{-8}$ A beam current. The spot size for EDS analysis is 50 $nm^2$. For quantitative analysis a 300 s counting time is used and a single crystal SiC–4H is used as a standard. Both coated particles (CPs) and standards are uncoated. A line scan across the SiC layers is also done to check for variations in the Si and carbon contents.

**2.4 X-ray Diffraction Analysis.** The untreated coated particles are loaded in a standard sample holder and analyzed using a PANalytical X'Pert PRO powder diffractometer with X'Celerator detector and variable divergence and receiving slits each set at 10 mm width, scanned from 5–120 deg $2\theta$. The X-radiation used is Fe filtered Co-$K\alpha$ radiation.

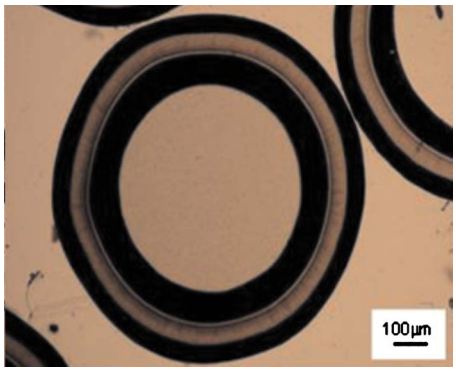


**Fig. 1 Thin section of a coated particle in plane polarized light**

Oxidizing the outer pyrolytic carbon layer gives superior peak to background signals for the examination of the SiC polytype distributions. The small quantities of the 2H, 4H, 6H, and 8H polytypes and peak overlap do not allow for unequivocal identification of these.

The relative amounts are estimated by the Rietveld method using the AUTOQUAN–BGMN Rietveld program [13], employing the fundamental parameter approach. The crystal structure data of the SiC polytypes are obtained from Shaffer [14] and from Ramsdell and Kohn [15] for the 8H polytype. With regard to the minor polytypes, the crystallite sizes are constrained to be similar to that of the 3C polytype.

In this study, and to treat all samples consistently, the following phases and polytypes are quantified in the Rietveld refinement: graphite, SiC–3C, SiC–2H, SiC–4H, SiC–6H, SiC–8H, Si, and $SiO_2$. The $R_{wp}$ parameter is used as a figure of merit for the least-squares refinement [16].

**2.5 LA-ICP-MS.** Several coated particles were ablated using a 266 nm laser and analyzed using a Leco Renaissance time-of-flight ICP-MS. Accurate quantitative analyses are not feasible, owing to the lack of matrix-matched standards at this stage in the project, but a semiquantitative data set has been obtained.

The data from the laser ablation of the CPs are presented as a series of time slices, each time slice comprising 70 ms of signal from the mass spectrometry (MS) so that several of these profiles can be portrayed on the same graph. $C^{12}$ was abundant in the samples and outside the upper analytical range for the MS, thus the detection for this element was blocked out.

The laser does not ablate perfect flat-bottomed holes, and so a limited volume of the outer layers is ablated along with the silicon carbide in each of the profiles. Thus, the carbon signal only drops off after the silicon carbide has started to be eroded.

The raw laser ablation data are collected together with a NIST glass standard, NIST 610. The accepted trace element data are taken from Ref. [17]. Unfortunately, not all elements of interest are present in the standard and other standards need to be found or prepared for the purpose. Because of the absence of accepted standards with the same ablation characteristics, i.e., silicon carbide, the results are at best semiquantitative and must be accepted as such. Suitable standards need to be found so that more accurate quantification can be achieved.

The isotopic composition of the silicon carbide was measured to develop the methodology for analyzing the ration of Si/C after irradiation; this is necessary for the determination of the rate of *P* formation from $Si^{30}$.

## 3 Results and Discussion

**3.1 Optical Microscopy.** Figure 1 shows a thin section of a coated particle in plane polarized light. At higher magnification, the growth layers of different compositions can be seen as differences in color and the radial growth of crystallites can be seen as

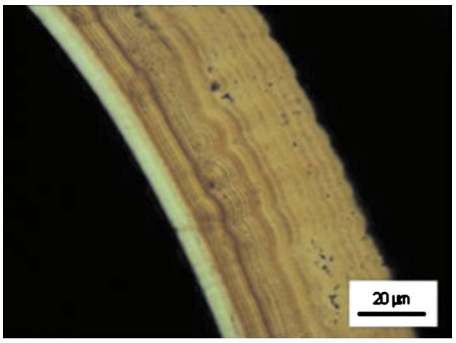


(*a*)

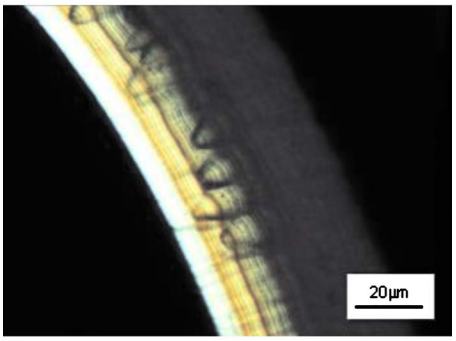


(*b*)

**Fig. 2 (a) Enlarged section of a SiC layer in plane polarized light; (*b*) SiC layer in crossed polarized light. The cubic polytype remains dark when the microscope table is rotated.**

widening domains in crossed polarized light in Figs. 2(*a*) and 2(*b*). The inner almost colorless layer represents pure noncubic $\alpha$-SiC, which, in contrast to the cubic $\beta$-SiC, does not stay dark under crossed polarized light, when the sample is rotated. The cusping is due to crystallites growing radially outwards from a seed point.

### 3.2 Transmission Electron Microscopy.

*3.2.1 Identification of the Polytypes*. The predominant polytype of SiC is the 3C cubic one. Its identity is verified by its electron diffraction patterns in different crystallographic directions. Figure 3 shows a typical selected area diffraction pattern (SADP) of cubic SiC–3C, with its calculated diffraction pattern.

The 6H polytype has also been identified. Figure 4 shows its experimental diffraction pattern compared with the calculated pattern.

*3.2.2 Disorder in SiC*. Disorder is present to a variable extent and it is manifested as streaking in the electron diffraction patterns along the [111] direction in the cubic polytype and the [001] direction in the hexagonal polytypes. Figure 5 shows the streaking

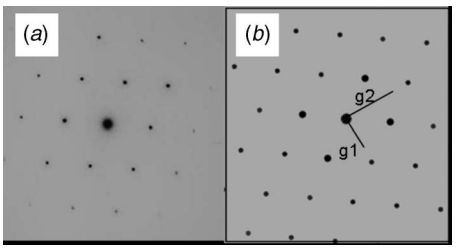


**Fig. 3 (a) Typical SADP of ordered 3C SiC along the [110] zone axis; (*b*) the calculated SADP. G1=[110], G2=[001]. The stacking direction is [111].**

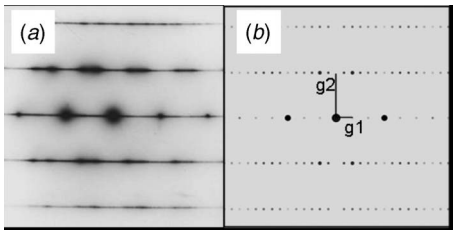


**Fig. 4 (*a*) Experimental and (*b*) calculated SADP of the 6H SiC polytype. G1=[001], G2=[110]. The streaking along [111] is due to disorder.**

in a disordered crystallite compared with an ordered polytype.

The dark field image indicates the cause for the streaking and it is generated by placing the objective aperture on the streak and obtaining an image from this. This dark field image obtained from the aperture in Fig. 5 is shown in Fig. 6. The variable stacking periodicity can be seen.

Under low magnification, this sample is characterized by numerous crystallites that show disorder. This is shown in Fig. 7. The figure also shows the orientation of the crystallites in relation to a growth layer. The [111] direction is perpendicular to the layering. Where the crystals are homogeneous, the 3C polytype is the dominant one, but in most cases the stacking is random. The interface between subparallel crystallites is accentuated by the ion milling. The spotted appearance is due to sputtered copper from the microscope grid.

*3.2.3 Twinning*. A common type of twinning occurring in these samples is shown in the electron diffraction pattern shown in

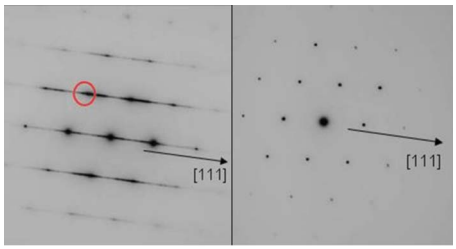


(*a*) (*b*)

**Fig. 5 SADP of (*a*) a disordered crystallite and (*b*) an ordered crystallite of the 3C polytype. Streaking occurs along the [111] direction. The position of the objective aperture for the dark field image in Fig. 6 is shown in (*a*).**

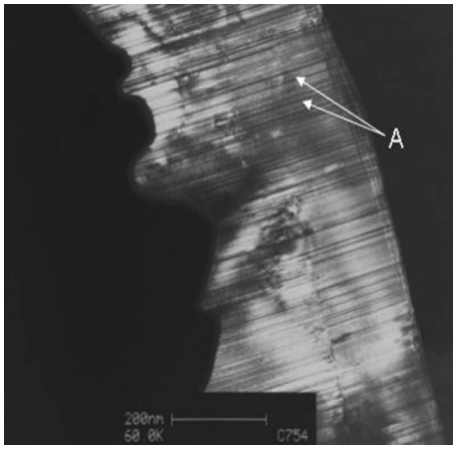


**Fig. 6 Dark field image from the (002) diffraction spot, marked in Fig. 5. The disorder with variable periodicity is present, indicated by arrows A.**

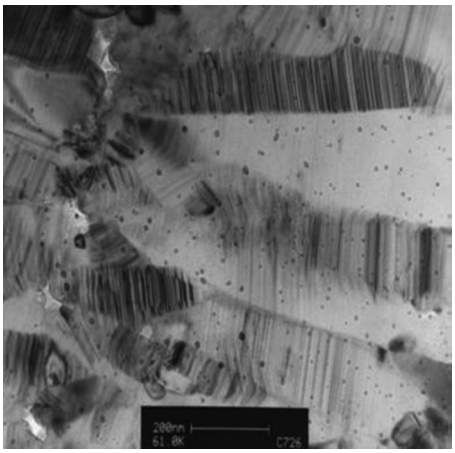

**Fig. 7 Transmission electron micrograph showing elongated disordered crystallites**

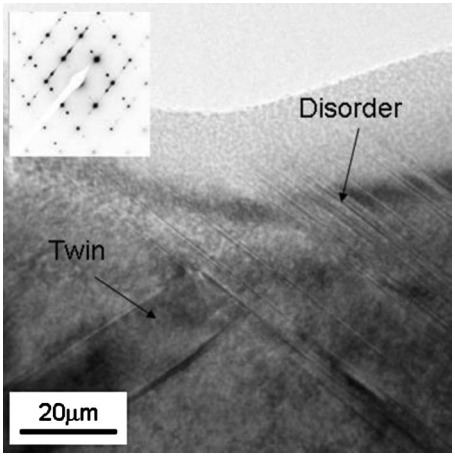


**Fig. 10 Image showing both twinning and stacking disorder; the diffraction pattern also shows the presence in two different directions**

Fig. 8.

The diffraction spots can all be accounted for by a twin plane separating rotational twin domains situated at 71 deg from each other. This can be seen in Fig. 9. The weak spots can be accounted for by multiple diffraction.

In contrast, some samples contain very few disordered crystallites, but twinning is much more prevalent. This is shown in Fig. 10, together with some disorder in the right hand part of the micrograph. The diffraction pattern is aligned with the features in the micrograph and is included to show the extra spots due to twinning and the streaks due to disorder.

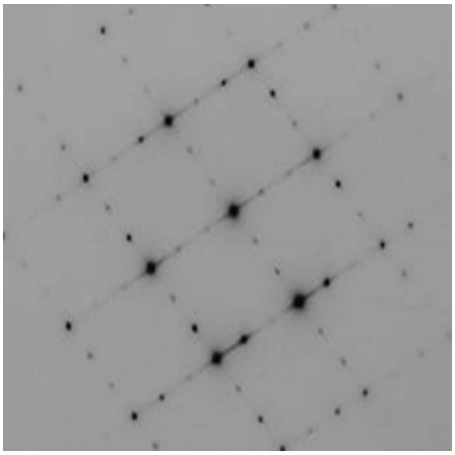

**Fig. 8 SADP of a twinned SiC–3C crystal. Some disorder is visible, and both twinning and multiple diffraction spots are present.**

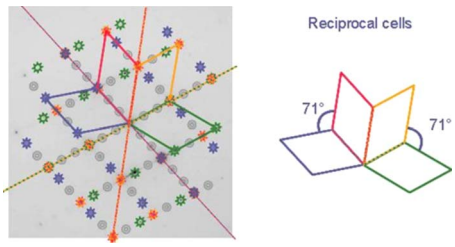


**Fig. 9 Interpretation of the twinning shown in Fig. 8 with the different domains contributing to the SADP**

**3.3 Raman Spectroscopy.** Samples were analyzed in several spots in a straight line along the cross section from the innermost part of the SiC layer to the outermost part. The sample positions were located with an optical microscope in the beam path of the spectrometer.

The polytype identification was done using the data given by Nakashima et al. [8] and Krautwasser et al. [6]. Calibration of the relative Si and SiC contents has been done for the 3C, 4H, and 6H polytypes. The quantification of the various common polytypes has also been attempted, but this is not practical due to the extensive overlap of the definitive peaks of these polytypes.

*3.3.1 Calibration Results.* The 3C material produced by PBMR for silver diffusion experiments was used as the best material. It however contains only 80% of the 3C polytype. The rest of the sample consists of quartz, silicon, carbon, and other minor polytypes. Due to particle size effects, a low magnification lens (10×) was used for the calibration. However, a high magnification for adequate resolution to measure the SiC layers in coated particles is required.

*3.3.2 Distribution of Polytypes and Si in the SiC layers.* Many samples also contain a Si peak at 520 $cm^{-1}$, especially on the inside of the SiC layers. This is a significant finding as the presence of elemental silicon is detrimental to the quality of the coated particles. Figure 11 shows the distribution of silicon as well as the SiC polytypes in sample PO-6. The Si peak is located at 520 $cm^{-1}$ and the SiC–3C peak at ~800 $cm^{-1}$.

Other samples contain no Si in the SiC layer. This is shown in Fig. 12.

From the Raman study we can determine that the main SiC

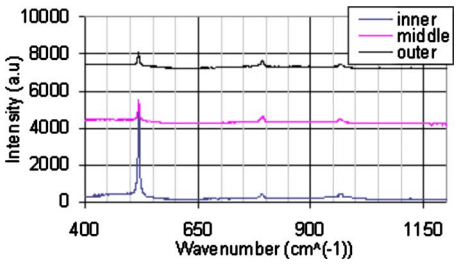


**Fig. 11 Successive Raman spectra of sample PO-6 taken from the inside of the SiC layer to the outside. Si is the predominant phase on the inside and gradually diminishes outwards.**

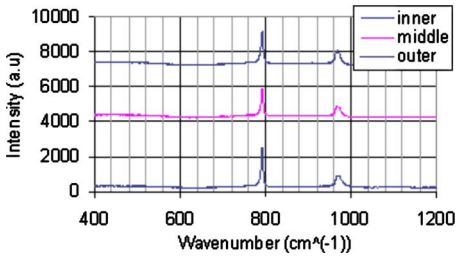


**Fig. 12 Successive Raman spectra of sample PO-5 taken from the inside of the SiC layer to the outside. The main phase is SiC–3C. No Si is present in the SiC layer.**

polytypes are the 3C and 6H varieties with minor 2H, together with sometimes major crystalline Si. The broad enhanced background of some samples is due to amorphous Si.

It must be mentioned that the unequivocal identification of the different polytypes is complicated by extensive peak overlap. However, the micro-Raman method is especially useful for the micro-analysis of individual SiC layers, and it is ideally suited for detecting silicon, which is an unwanted phase. Variations in deposition conditions can easily be detected using this method, which has a resolution of 1 $\mu$m.

Quantification of the Si and SiC contents is the next step and calibration of the method is in progress. Single crystal 4H and 6H polytypes are available, but suitable pure 3C material is not available. An impure sample containing ~80% SiC (3C) was used as a standard to prepare known mixtures in order to prepare a calibration curve for Raman analysis. The Si fraction in the SiC layers of the various samples is given in Fig. 13.

**3.4 Bulk Composition of the SiC layer, EDS.** The concentration of Si and C in the SiC layer was measured by EDS analysis. The compositions of the layers in samples PO-1–PO-10 are given in mass percent and normalized atom percent in Table 1. Single crystal 4H SiC was used as a standard. A microprobe analysis, in contrast to the SEM analysis, shows an excess of carbon, the values for PO-9 being 48.4 at % Si, 51.6 at % C.

The EDS analysis shows most layers to contain excess carbon. This result must be treated with caution since it is known that there is a carbon buildup at the analysis spot as a result of the interaction of the beam with hydrocarbons from the diffusion pump oil. This is however also true for the standard and the carbon buildup is included in the standardization. Also, some samples are prone to charging, which has an effect on the analysis.

Line scans showing the compositional variation in the layers of all the samples in Table 1 were also recorded as element intensities across the layers. An example of a SiC layer containing Si within the layer is shown on the electron backscatter image in Fig. 14. The discontinuous Si layer can clearly be seen.

A line scan running across this Si layer, from the inside outwards is shown in Fig. 15. No significant variation in Si content

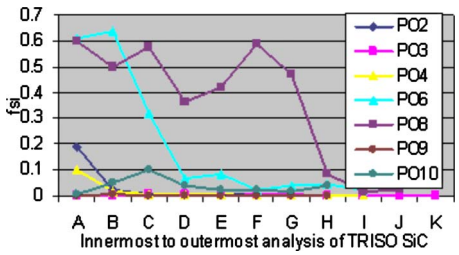


**Fig. 13 The Si fraction in the SiC layers of coated particles of samples PO-1–PO-10. Samples PO-6 and PO-8 have excessive amounts of Si in the layer.**

**Table 1 Compositions of the SiC layers in the samples. The errors are shown as 3$\sigma$ values.**

| Sample | Si (3$\sigma$) (wt %) | C (3$\sigma$) (wt %) | Total (wt %) | Si (at %) | C (at %) |
|---|---|---|---|---|---|
| SiC–4H | 70.1(1.1) | 30.3(1.4) | 100.4 | 49.7 | 50.3 |
| PO-1 | 61.7(1.0) | 46.2(2) | 107.9 | 36.3 | 63.7 |
| PO-2 | 68.1(1.1) | 31(1.4) | 99.1 | 48.4 | 51.6 |
| PO-3 | 65.6(1.1) | 39.8(1.8) | 105.5 | 41.3 | 58.7 |
| PO-4 | 67.5(1.1) | 36.1(1.6) | 103.6 | 44.4 | 55.6 |
| PO-5 | 68.5(1.1) | 32.7(1.5) | 101.2 | 47.3 | 52.7 |
| PO-6 | 68.2(1.1) | 31.5(1.4) | 99.6 | 48.1 | 51.9 |
| PO-8 | 65.4(1.1) | 40.8(1.8) | 106.2 | 40.7 | 59.3 |
| PO-9 | 74.8(2) | 31.8(2.6) | 106.6 | 50.2 | 49.8 |
| PO-10 | 74.4(1.9) | 33.2(2.8) | 107.6 | 48.9 | 51.1 |

can be seen. This means that the interaction volume arising from the electron beam-sample interaction is too large to show the presence of thin Si layers in the SiC.

**3.5 X-ray Diffraction Analysis.** The SiC layers consist of various polytypes of SiC together with Si and carbon. To determine and quantify these, the CPs were examined as such without treatment using powder x-ray diffraction (XRD) methods. To reduce the intensity of the poorly crystalline carbon peaks and to increase the accuracy of the SiC polytype quantification, the CPs were also oxidized in air by heating at 800°C for 8 h. The results are shown in Table 2, and the presence of silicon is only detected in one sample, CPT-T-B2. This finding is supported by the Raman

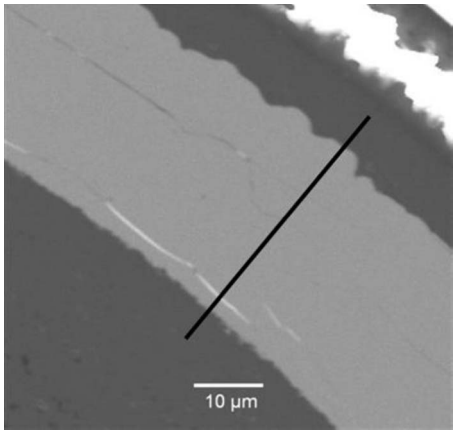


**Fig. 14 Electron backscatter image of the SiC layer in sample PO-2 (CPT-T-B8). The presence of a discontinuous Si layer with a higher backscatter intensity can be seen. The position of the line scan across the SiC layer, shown in Fig. 15, is also shown.**

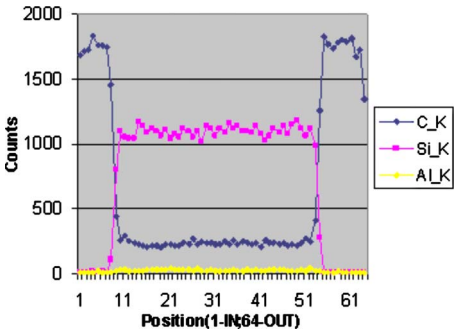


**Fig. 15 Variation of Si, C, and Al counts across a SiC layer shown in Fig. 14; analysis 14 corresponds to the position of the Si layer.**

**Table 2 Phase composition of the SiC layers in original and oxidized samples. SiC is not present in Sample PO-7. The 3C polytype is predominant.**

| Samples | SiC–3C (%) | SiC–6H (%) | SiC–8H (%) | SiC–2H (%) | SiC–4H (%) | Si (%) |
|---|---|---|---|---|---|---|
| PO-$1_{unox}$ | 87.7 | 5.8 | 3.4 | 1.2 | 2.0 | 0.0 |
| PO-$1_{ox}$ | 90.7 | 5.9 | 1.9 | 0.5 | 0.8 | 0.2 |
| PO-$2_{unox}$ | 85.1 | 5.9 | 5.7 | 0.8 | 2.5 | 0.0 |
| PO-$2_{ox}$ | 86.7 | 7.0 | 4.6 | 0.5 | 1.1 | 0.0 |
| PO-$3_{unox}$ | 81.8 | 7.0 | 6.3 | 2.5 | 2.4 | 0.0 |
| PO-$3_{ox}$ | 84.2 | 6.1 | 5.9 | 2.5 | 1.3 | 0.0 |
| PO-$4_{unox}$ | 89.8 | 3.2 | 3.2 | 1.8 | 1.9 | 0.0 |
| PO-$4_{ox}$ | 92.8 | 2.7 | 2.9 | 0.7 | 0.9 | 0.0 |
| PO-$5_{unox}$ | 92.4 | 2.0 | 2.6 | 1.7 | 1.4 | 0.0 |
| PO-$5_{ox}$ | 94.1 | 2.4 | 2.1 | 1.0 | 0.4 | 0.0 |
| PO-$6_{unox}$ | 87.3 | 4.5 | 3.9 | 2.5 | 1.8 | 0.0 |
| PO-$6_{ox}$ | 90.1 | 3.8 | 3.4 | 2.2 | 0.0 | 0.5 |
| PO-$8_{unox}$ | 86.8 | 4.2 | 4.6 | 3.4 | 0.0 | 0.9 |
| PO-$8_{ox}$ | 87.8 | 3.6 | 4.2 | 2.5 | 0.7 | 1.2 |
| PO-$9_{unox}$ | 93.7 | 0.0 | 2.7 | 3.0 | 0.6 | 0.0 |
| PO-$9_{ox}$ | 93.6 | 2.1 | 2.6 | 1.2 | 0.5 | 0.0 |
| PO-$10_{unox}$ | 91.3 | 3.5 | 2.0 | 2.5 | 0.8 | 0.0 |
| PO-$10_{ox}$ | 94.6 | 1.0 | 2.5 | 1.1 | 0.6 | 0.1 |
| 18C$1_{unox}$ | 94.8 | 3.9 | 1.0 | 0.0 | 0.3 | 0.0 |

data. On the other hand, the Raman data reveal that more samples contain silicon. The XRD data are, however, a bulk measurement in comparison with the Raman and micro-analytical measurements.

### 3.6 LA-ICP-MS Results.

*3.6.1 Impurities in the SiC layer.* The coated particles that were analyzed by laser ablation ICP-MS are shown in Fig. 16. The craters produced by laser ablation are clearly visible.

Figure 17 shows the distribution of some of the elements in one of the samples, as the laser ablates deeper into the coated particle.

A second investigation involved the examination of five coated particles each from five sample batches, together with the NIST 610 and a SiC single crystal sample. This enabled the determination of the impurity levels in the SiC layers.

Figure 18 shows the distribution of Ni and Cu in three particles from the same sample. The positions of the carbon layers are indicated by the elevated $C^{13}$ values. The erratic distribution of the impurities indicates that in many cases these impurities could be due to entrainment of foreign particles in the coated particles. The levels of the impurities are positively correlated. In some cases the elevated levels are present at the SiC–PyC interfaces, which points to a different mode of occurrence or mechanism of

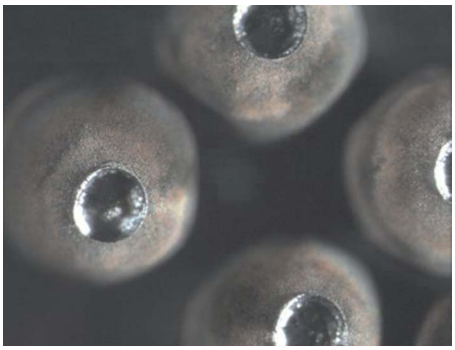

**Fig. 16 Coated particles after examination by LA-ICP-MS. The holes drilled by the laser ablation are shown, (particle diameter ~700 $\mu$M).**

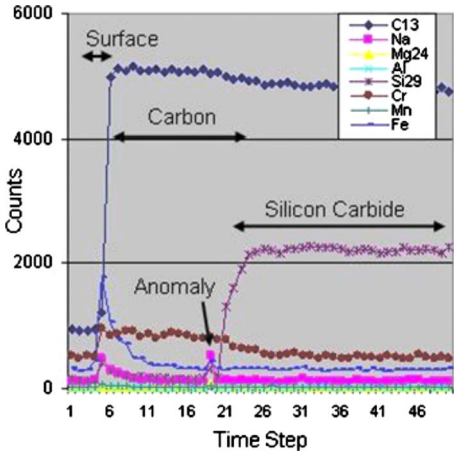


**Fig. 17 Distribution of impurities and major isotopes in the coated particles. The C13 and Si29 distributions show the position of the SiC and outer pyrolytic carbon layers. A contamination layer exists at the particle edge and at the SiC and OPyC interfaces.**

contamination. There are higher levels of Cr in the OPyC layer. Similar results were found independently by Naghedolfeizi et al. [9] using X-ray fluorescence microtomography with a synchrotron source. They also found localized regions of Zn, Cu, Ni, Cr, and Fe in the coated particles, pointing to a similar distribution and chemical signature of the impurities.

## 4 Summary

**4.1 Phase Composition of SiC in the CP.** Identification of the various polytypes was done using electron diffraction methods. The 3C and 6H polytypes were positively identified.

A feature of the SiC in some samples is the disordered nature of the phase. The disorder is characterized by planar defects of different widths and periodicities, giving rise to streaking in the diffraction pattern along the cubic [111] direction.

In some samples disorder is present only in isolated crystals, together with twinning. This can also be deduced from the diffraction patterns.

Rietveld analysis using X-ray diffraction found that the SiC layer consists predominantly (82–94%) of the 3C polytype, with minor amounts of the 6H and 8H polytypes. Very minor amounts of the 2H and 4H polytypes could also be present.

**4.2 Composition of the SiC layer.** The Si contents of the SiC layer was quantified using Raman spectrometry. In most layers elevated Si contents were encountered on the inner boundary of

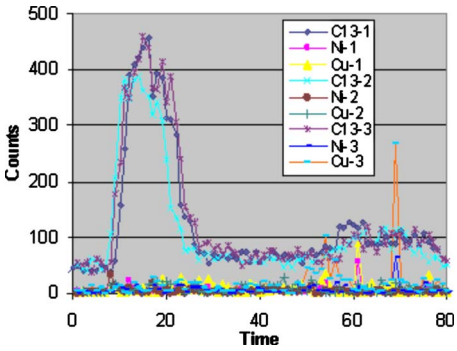


**Fig. 18 Distribution of C13 and Ni and Cu in three particles from the same sample. The erratic distribution of the Ni and Cu is an indication of a possible contribution by contaminant particles.**

the layer with the inner pyrolytic carbon. Two samples (PO-6 and PO-8) contain elevated levels of Si, of the order of 50%, with the highest levels on the inside of the layers. This is also true for most of the other samples, albeit at much lower Si levels.

Measurement of the carbon and Si contents of the SiC layer in the coated particles was attempted using energy-dispersive X-ray analysis of polished areas. The SiC layers in the various samples were found to be carbon-rich, ranging from 50 at % to 59 at % carbon. Sample PO-9 was re-analyzed with an electron microprobe and this contained 51.6 at % carbon.

**4.3 Impurities in SiC/PyC.** Impurities in the SiC and PyC could be measured with sufficient sensitivity. In most cases the absolute values are of less concern than the variation of impurities in the samples. The findings can be summarized as follows.

Elevated levels of the transition elements Cu, Ni, Co, Cr, and Zn are present erratically in the samples. These elements, together with the two isotopes of silver, correlate positively, pointing to the presence of impurities, possibly metallic particles of brass.

Elevated levels of the above transition elements are also present at the SiC/OPyC interface. The reasons for this are not known at this stage.

In some samples there are higher levels of Cr in the OPyC layer.

The NIST standards were used to calibrate the impurity levels in the coated particles. These average from 1 ppm to 18 ppm.

## Acknowledgment

The authors would like to thank Dr. N. vdBerg for the sample preparation, Dr. S. Verryn for the XRD analysis, and C. Coetzee for the SEM analysis.

## References

[1] Snead, L. L., Nozawa, T., Katoh, Y., Byun, T.-S., Kondo, S., and Petti, D. A., 2007, "Handbook of SiC Properties for Fuel Performance Modelling," J. Nucl. Mater., **371**, pp. 329–377.

[2] Sawa, K., Suzuki, S., and Shiozawa, S., 2001, "Safety Criteria and Quality Control of HTTR Fuel," Nucl. Eng. Des., **208**, pp. 305–313.

[3] Petti, D. A., Buongiorno, J., Maki, J. T., and Miller, G. K., 2003, "Key Differences in the Fabrication of US and German TRISO-Coated Particle Fuel, and Their Implications on Fuel Performance," Nucl. Eng. Des., **222**, pp. 281–297.

[4] Katoh, Y., Hashimoto, N., Kondo, S., Snead, L. L., and Kohyama, A., 2006, "Microstructural Development in Cubic Silicon Carbide During Irradiation at Elevated Temperatures," J. Nucl. Mater., **351**, pp. 228–240.

[5] Hélary, D., Bourrat, X., Dugne, O., Maveyraud, G., Perez, M., and Guillermier, P., 2004, "Microstructures of Silicon Carbide and Pyrocarbon Coatings for Fuel Particles for High Temperature Reactors (HTR)," Second International Topical Meeting on High Temperature Technology, Beijing, China, Paper No. B07.

[6] Krautwasser, P., Begun, G. M., and Angelini, P., 1983, "Raman Spectral Characterization of Silicon Carbide Nuclear Fuel Coatings," J. Am. Ceram. Soc., **66**(6), pp. 424–434.

[7] Nakashima, S., and Harima, H., 1997, "Raman Investigation of SiC Polytypes," Phys. Status Solidi A, **162**, pp. 39–64.

[8] Nakashima, S., Higashihira, M., and Maeda, K., 2003, "Raman Scattering Characterization of Polytype in Silicon Carbide Ceramics: Comparison With X-Ray Diffraction," J. Am. Ceram. Soc., **86**(5), pp. 823–829.

[9] Naghedolfeizi, M., Chung, J.-S., Morris, R., Ice, G. E., Yun, W. B., Cai, Z., and Lai, B., 2003, "X-Ray Fluorescence Microtomography Study of Trace Elements in a SiC Nuclear Fuel Shell," J. Nucl. Mater., **312**, pp. 146–155.

[10] van Rooyen, I. J., 2006, private communication.

[11] van der Berg, N., 2007, private communication.

[12] Stadelmann, P., JEMS, I2M-EPFL, Lausanne, Switzerland.

[13] Kleeberg, R., and Bergmann, J., 1998, "Quantitative Röntgenphasenanalyse mit den Rietveldprogrammen BGMN und AUTOQUANT in der täglichen Laborpraxis," Ber. DTTG Greifswald, **6**, pp. 237–250.

[14] Shaffer, P. T., 1969, "A Review of the Structure of Silicon Carbide," Acta Crystallogr., Sect. B: Struct. Crystallogr. Cryst. Chem., **25**, pp. 477–488.

[15] Ramsdell, L. S., and Kohn, J. A., 1952, "Developments in Silicon Carbide Research," Acta Crystallogr., **5**, pp. 215–224.

[16] Pecharsky, V. K., and Zavalij, P. Y., 2005, *Fundamentals of Powder Diffraction and Structural Characterization of Materials*, Springer, New York.

[17] Coursey, J. S., Schwab, D. J., and Dragoset, R. A., 2005, "Atomic Weights and Isotopic Compositions (Version 2.4.1)," http://physics.nist.gov/Comp.

# Investigation of High-Temperature Printed Circuit Heat Exchangers for Very High Temperature Reactors

**Sai Mylavarapu**
**Xiaodong Sun**
**Justin Figley**
**Noah Needler**
**Richard Christensen**

Nuclear Engineering Program,
The Ohio State University,
Columbus, OH 43210

*Very high-temperature reactors require high-temperature (900–950°C) and high-integrity heat exchangers with high effectiveness during normal and off-normal conditions. A class of compact heat exchangers, namely, the printed circuit heat exchangers (PCHEs), made of high-temperature materials and found to have these above characteristics, are being increasingly pursued for heavy duty applications. A high-temperature helium test facility, primarily aimed at investigating the heat transfer and pressure drop characteristics of the PCHEs, was designed and is being built at Ohio State University. The test facility was designed to facilitate operation at temperatures and pressures up to 900°C and 3 MPa, respectively. Owing to the high operating conditions, a detailed investigation on various high-temperature materials was carried out to aid in the design of the test facility and the heat exchangers. The study showed that alloys 617 and 230 are the leading candidate materials for high-temperature heat exchangers. Two PCHEs, each having 10 hot plates and 10 cold plates, with 12 channels in each plate, were fabricated from alloy 617 plates and will be tested once the test facility is constructed. Simultaneously, computational fluid dynamics calculations have been performed on a simplified PCHE model, and the results for three flow rate cases of 15, 40, and 80 kg/h at a system pressure of 3 MPa are discussed. In summary, this paper focuses on the study of the high-temperature materials, the design of the helium test facility, the design and fabrication of the PCHEs, and the computational modeling of a simplified PCHE model.*
[DOI: 10.1115/1.3098425]

*Keywords: PCHE, high-temperature materials, compact heat exchanger, photochemical machining, diffusion bonding, alloy 617, heat exchanger modeling*

## 1 Introduction

The United States Department of Energy's Generation IV Program has generated considerable interest for high-temperature gas-cooled reactors (HTGRs), in particular, the very high-temperature reactor (VHTR). VHTR is one of the six reactor concepts selected by the Generation IV International Forum and is anticipated to be the reactor type for the Next Generation Nuclear Plant (NGNP) Project. VHTRs require high-temperature (900–950°C) and high-integrity heat exchangers with high effectiveness for use as nuclear reactor-hydrogen production process interface, as recuperators in loop heat transport subsystems, or for electricity generation via an indirect Brayton or Rankine cycle [1]. Compact printed circuit heat exchangers (PCHEs) are expected to help realize high efficiency in the power conversion and hydrogen production cycles during normal operation and to provide enhanced and reliable decay heat removal capability in off-normal scenarios.

In the literature, some research work has been performed with the PCHEs. Nikitin et al. [2] and Ishizuka et al. [3] investigated, both numerically and experimentally, the thermal-hydraulic performance of a 3 kW PCHE in a supercritical $CO_2$ loop. Their experimental operating temperatures reached 300°C, which is far from high-temperature reactor (HTR) requirements. Recently, Pra et al. [4] carried out steady and transient tests on a PCHE recuperator mock-up and investigated their thermal-mechanical behavior in an air test loop for temperature conditions as high as 510°C. Their results showed that PCHEs are potential candidate heat exchangers for high-temperature applications. Notwithstanding the above few works on PCHEs, to the authors' knowledge, however, a detailed thermal-hydraulic performance of the PCHEs with helium as the working fluid has not been investigated thoroughly for the temperatures typical of VHTRs. In an effort to realize these conditions, a high-temperature helium experimental test facility was designed and is being built to investigate the heat transfer and pressure drop characteristics of PCHEs for potential applications in the VHTRs. The current test facility design facilitates operation at temperatures and pressures up to 900°C and 3 MPa, respectively, with flow rates ranging from 10 to 80 kg/h. This range of mass flow rates enables the PCHEs fabricated to be operated in the laminar and laminar-to-turbulent transition flow regimes.

Pressure and temperature conditions mandated judicious material selection for the helium test facility and the PCHEs. In the present study, eight high-temperature alloys were reviewed for their high-temperature mechanical properties (creep and creep-fatigue properties), physical properties, environmental resistance, fabricability, availability, and cost. The study indicated that either alloy 617 or alloy 230 would be the most suitable material for high-temperature and high-pressure (up to 7.0 MPa) applications. However, alloy 617 was preferred over alloy 230 for the PCHEs in this study due to its better mechanical properties and creep resistance at elevated temperatures. In the current study, two PCHEs, configured for countercurrent flow with cross flow at entry and exit regions, were fabricated using alloy 617 plates. In what follows, studies on various high-temperature resistant mate-

Manuscript received November 30, 2008; final manuscript received December 7, 2008; published online July 17, 2009. Review conducted by Dilip R. Ballal. Paper presented at the Fourth International Topical Meeting on High Temperature Reactor Technology (HTR2008), Washington, DC, September 28–October 1, 2008.

Table 1 High-temperature resistant materials [5–7]

| Alloy | UNS No. | Nominal chemical composition (wt %) |
|---|---|---|
| 617 | N06617 | 52Ni–22Cr–13Co–9Mo |
| 230 | N06230 | 57Ni–22Cr–14W–2Mo–La |
| HR-160 | N12160 | 37Ni–30Co–28Cr–2.7Si |
| HX | N06002 | 47Ni–22Cr–9M0–18Fe |
| 556 | R30556 | 21Ni–30Fe–22Cr–18Co–3Mo–3W |
| 800 HT | N08811 | 33Ni–42Fe–21Cr |
| 800 H | N08810 | 33Ni–42Fe–21Cr |
| 625 | N06625 | 60Ni–22Cr–9Mo–3.5Cb |

rials, design of the helium test facility, design and construction of PCHEs, and a computational fluid dynamics (CFD) modeling of a simplified PCHE model are presented.

## 2 Review of High-Temperature Materials

**2.1 ASME Allowable Design Stresses for Materials.** High operating temperatures and pressures of VHTRs call for components with high mechanical integrity, which can only be realized by appropriate selection of high-temperature resistant materials. Eight high-temperature alloys were reviewed for their high-temperature mechanical properties (creep and creep-fatigue properties), physical properties (thermal conductivity and thermal expansion), environmental resistance, fabrication and joining technology, availability, and economics. Table 1 lists these alloys along with their unified numbering system (UNS) numbers and nominal chemical compositions. This review was carried out to identify a suitable high-temperature material for the helium test facility and heat exchangers.

The high-temperature helium test facility that is designed and being built at Ohio State University is not intended for direct nuclear applications, i.e., Section III, Subsection NH of the ASME Boiler and Pressure Vessel Code (B&PVC) [5] was not invoked in the design. The material selection for the test facility and heat exchangers is primarily based on allowable stresses from the ASME B&PVC Section II, Part D approved for ASME Section VIII, Division I construction. Figure 1 compares the ASME allowable design stresses at different temperatures for the materials listed in Table 1 and is applicable for both seamless pipe and plate product forms. These allowable design stresses are found in Table 1B of Section II, Part D of the ASME B&PVC [5]. The ASME stress allowables are based on the average stress to cause rupture

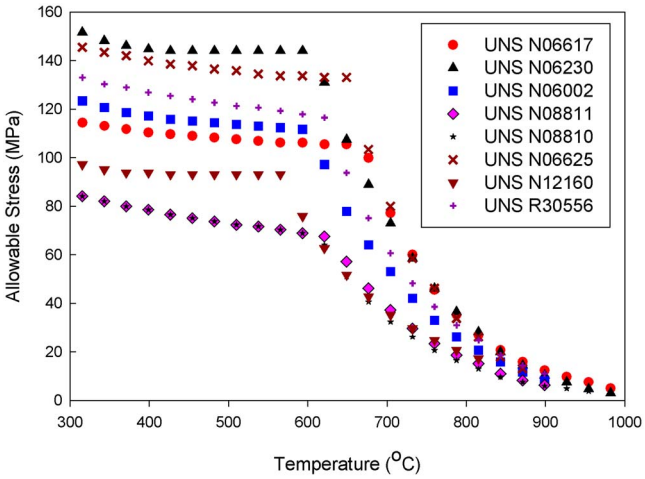


Fig. 1 ASME allowable design stresses for different materials [5]

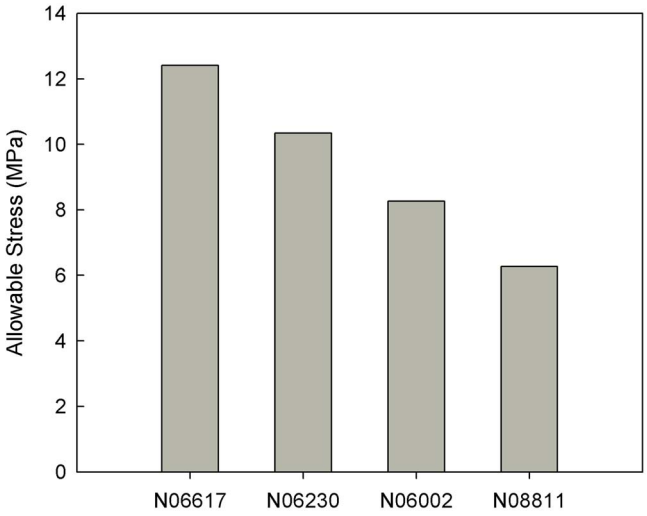


Fig. 2 Comparison of allowable design stresses at 900°C [5]

in a 100,000 h operation (about 11.4 years). The code uses 0.67 times this average stress at each temperature to define the allowable stress.

From Fig. 1, it is evident that only alloys 617, 230, and 800 H are approved for temperatures up to 982°C. With the exception of alloys HR160 and 625, which are approved for up to 815°C and 871°C, respectively, all other alloys are approved for up to 900°C. Although alloy 556 is approved for temperatures up to 900°C, its resistance to nitriding environments is relatively poor. Furthermore, alloy 800 HT has slightly different chemical composition from alloy 800 H, which gives alloy 800 HT higher maximum allowable design stresses. Therefore, further discussion is restricted to alloys 617, 230, HX, and 800 HT.

**2.2 Candidate Materials.** The candidate materials identified in the current study for applications in high-temperature environments are as follows:

- alloy 617
- alloy 230
- alloy 800 HT
- alloy HX

Figure 2 compares the allowable design stresses at 900°C for the above candidate materials. Our study, based on the material's high-temperature strength, fabricability, and corrosion resistance, indicated that either alloy 617 or alloy 230 is the most suitable material for the high-temperature and high-pressure (up to 7.0 MPa) applications. However, alloy 617's higher allowable design stress at high temperatures (12.42 MPa at 900°C), along with its better physical properties (low thermal expansion and high thermal conductivity) and good microstructure stability, made it an ideal choice for the heat exchanger plates. Furthermore, the photochemical etchability of alloy 617 plates and the diffusion bonding procedures employed for joining alloy 617 plates were successfully confirmed during this study.

Table 2 compares the thermal conductivity and mean coefficient of thermal expansion for different candidate materials. Clearly, alloy 617 has a low mean thermal expansion coefficient (lower thermal stresses in service) and a slightly better thermal conductivity among the candidate materials.

At the time when this study on materials was carried out, alloys 617 and 230 were available only in plate form (and not in tube or pipe form), which precluded their usage for the construction of the test facility. Therefore, from the considerations of availability and economics, alloy 800 HT was the only viable alternative for the test facility piping. This dictated the design operating temperature

**Table 2 Thermal conductivity and mean thermal expansion coefficient for various candidate materials at 900°C [6,7]**

| Alloy UNS No. | Thermal conductivity ($W\ m^{-1}\ K^{-1}$) | Thermal expansion coefficient ($\mu m\ m^{-1}\ K^{-1}$) |
|---|---|---|
| N06617 | 27.1 | 15.8 |
| N06230 | 26.4 | 15.7 |
| N08811 | 27.1 | 18.5 |
| N06002 | 26.3 | 16.3 |

and pressure for the helium test facility. As mentioned earlier, ASME Section VIII, Division I construction only approves alloy 800 HT usage for temperatures up to 900°C, which precludes the test facility from being used for operating temperatures beyond 900°C. Figure 3 provides a rationale for designing the test facility for a maximum working pressure and temperature of 3 MPa and 900°C, respectively. Noting the fact that the maximum wall thickness for a commercially available 1 in. (nominal pipe size) alloy 800 HT pipe is 6.35 mm (corresponding to a pipe schedule of 160), it can be observed from Fig. 3 that the required pressure design thickness corresponding to 3 MPa and 900°C is close to 6.35 mm. The pressure design thickness required for operating pressures greater than 3 MPa exceeds the commercially available wall thicknesses. The pressure design thickness in Fig. 3 was estimated based on the Boardman expression from ASME B31.3 Process Piping Code [8] and is given as

$$t = \frac{PD}{2(SE + PY)} \tag{1}$$

where $t$, $P$, $D$, $S$, $E$, and $Y$ are the pressure design thickness, the internal design gauge pressure, the pipe outer diameter, the allowable design stress, the allowable pressure stress penalty factor, and the coefficient to account for nonlinear reduction in allowable stress at design temperatures above 482°C, respectively.

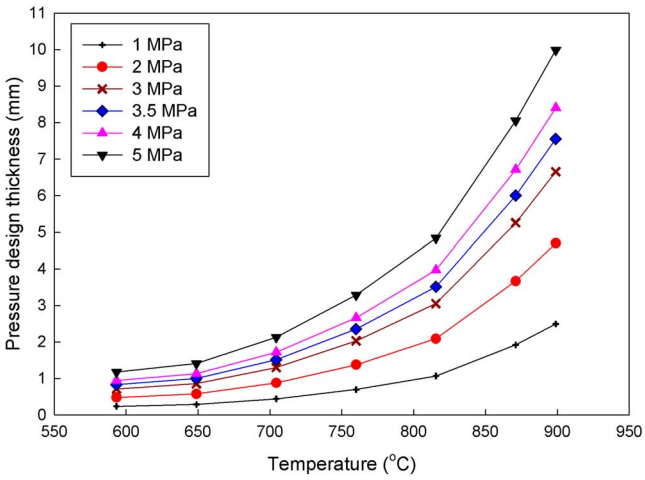


**Fig. 3 Pressure design thickness requirement for a nominal 1 in. seamless alloy 800 HT pipe at different pressures**

## 3 Experimental Facility

**3.1 Printed Circuit Heat Exchanger.** A printed circuit heat exchanger is a high-efficiency plate type compact heat exchanger in which fluid flow channels are photochemically etched on flat metal plates. Photochemical machining is a nonconventional machining technique that utilizes chemical etchants to corrosively oxidize selected areas of metal. The etched plates are then stacked in a single or a double banking configuration and diffusion bonded together to form a heat exchanger block. Diffusion bonding is a solid state joining process in which the plate stack is subjected to thermal soaking for a certain period of time allowing for grain growth, and thus enabling an interface-free joint between the plates. This process offers close to parent metal strength and very high-pressure containment capability. During the course of this research, both photochemical machining and diffusion bonding were successfully confirmed for alloy 617 plates.

**3.2 High-Temperature Helium Test Facility.** Figure 4

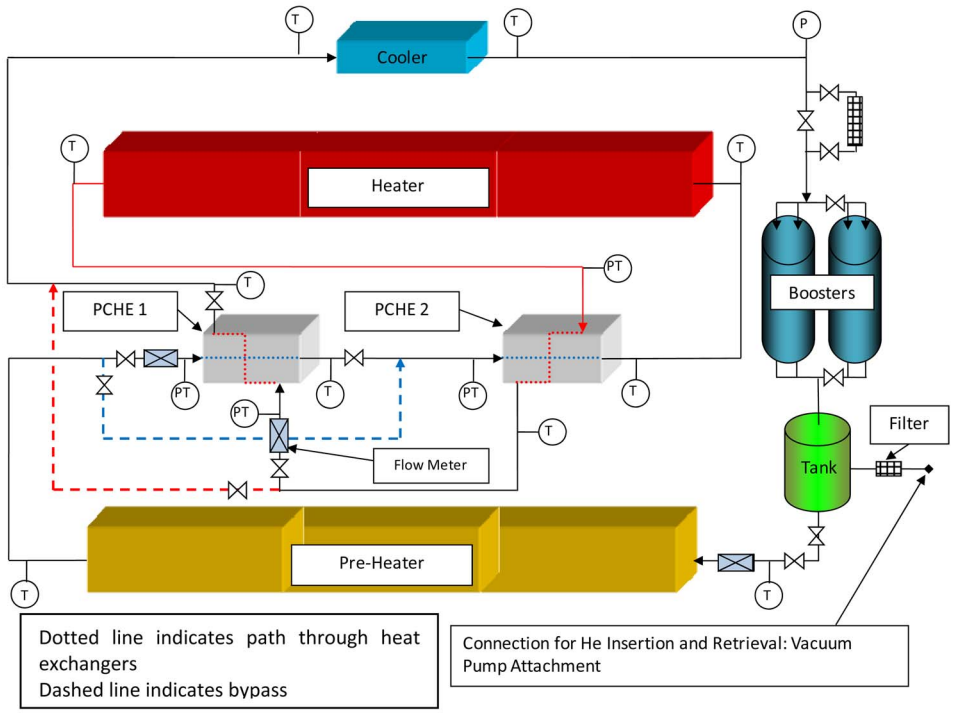


**Fig. 4 High-temperature helium test facility**

**Table 3 PCHE geometric details**

| | Hot side | Cold side |
|---|---|---|
| Plate thickness (mm) | 1.63 | 1.63 |
| Number of plates | 10 | 10 |
| Number of channels in each plate | 12 | 12 |
| Channel pitch (mm) | 2.5 | 2.5 |
| Channel width (mm) | 2 | 2 |
| Channel depth (mm) | 1 | 1 |
| Channel hydraulic diameter (mm) | 1.22 | 1.22 |
| Channel travel length (m) | 0.305 | 0.272 |
| Heat transfer area ($m^2$) | 0.188 | 0.168 |
| Channel cross section ($mm^2$) | 1.57 | 1.57 |
| Free flow area ($mm^2$) | 188 | 188 |

shows the layout of the high-temperature helium test facility that is currently being constructed at Ohio State University. Two gas boosters in parallel provide the necessary head for circulating helium gas in the loop. Originally, a gas compressor was used in the design; however, it was not adopted in this design due to economic considerations. After exiting the gas boosters, helium gas is heated by a preheater with a maximum heating capacity of 23 kW, and then forwarded to the cold side of the PCHEs. The loop is designed such that the fluid exiting the cold side enters the hot side of the PCHE, after flowing through a main heater that heats the helium up to 900°C. After exchanging energy with the cold side of the PCHEs, the helium gas enters a cooler that cools it down to the inlet temperature of the gas booster, i.e., around 120°C. The bypass on the hot and cold sides of PCHE 1 in the loop helps to realize different flow rates on the hot and the cold sides of the PCHE. The piping fittings, such as the elbows, tees, and flanges, used for the high-temperature port of the facility between the preheater and the cooler were custom made from 800 HT material. K-type standard duty socket weld thermowells of alloy 800 HT construction with a nominal accuracy of ±2°C in the measurement range of 100–900°C are used for measuring temperature at various locations in the loop. Three venturi type flow meters with NIST traceable certification measure the volumetric flow rate of helium gas with an accuracy of ±0.20% of reading. Honeywell smart pressure transducers with a 4–20 mA dc output are used for measuring the pressure and pressure differential across the PCHEs. For measuring the pressure and pressure differential in the loop at temperatures above the operating range of the transducer, a coiled section of tubing is added between the transducer and the corresponding pressure tap to reduce the temperature of helium in contact with the transducer.

The present design facilitates operation at temperatures up to 900°C and a wide range of pressures (0.5–3 MPa) and flow rates (10–80 kg/h). This range of mass flow rates corresponds to channel Reynolds numbers ranging from 400 to 4500 for the PCHEs being fabricated, and thus enables the PCHEs to be operated in the laminar flow and laminar-to-turbulent flow transition regimes. In addition, research grade helium with 99.9999% purity will be used as the working fluid. A mass spectrometer or a gas chromatography was considered in the design stage to provide a means of monitoring the helium environment during testing. However, due to economic considerations, neither of them was used in the current design.

**3.3 PCHE Design and Construction.** In the current study, two PCHEs, configured for countercurrent flow with cross flow at entry and exit regions, are being fabricated from alloy 617 plates. Each PCHE has 10 hot plates and 10 cold plates with 12 straight (noncorrugated) channels in each plate. The fluid passages are approximately semicircular with a diameter of 2 mm and a pitch of 2.5 mm. The plates are diffusion bonded in a single banking configuration to form a block. Table 3 lists the geometric details of dimensions of the PCHEs being fabricated.

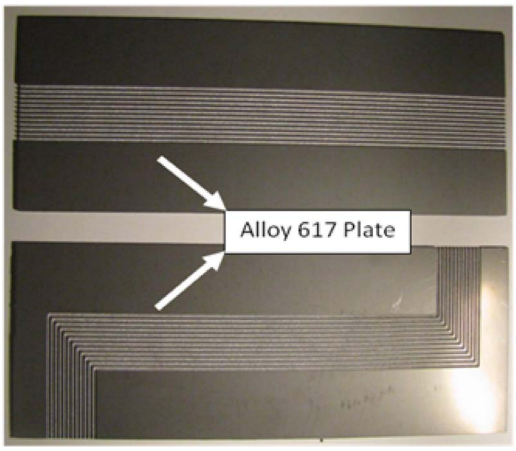


**Fig. 5 Flow passages photochemically etched on alloy 617 plates**

Figures 5 shows the PCHE plate channel configuration on two photochemically etched alloy 617 plates, while Fig. 6 shows the channel profile on one of these plates as approximately semicircular. In the current design, the shape of the flow passage may be described as straight. Figure 7 shows a PCHE header fabricated from an alloy 800 HT solid rod. Figure 8(*a*) shows two diffusion bonded blocks fabricated by stacking alloy 617 plates in a single banking configuration. Currently, these blocks are being machined to facilitate welding of headers. Figure 8(*b*) shows a pictorial schematic of a complete PCHE assembly with the headers. In the current design, straight channels were employed, since its geometry is relatively well understood and the heat transfer and pressure drop correlations for different flow regimes are available in the literature. Based on the experience gained with the straight channel design, additional PCHEs with wavy (herringbone pattern) channels and other channel geometrical configurations will

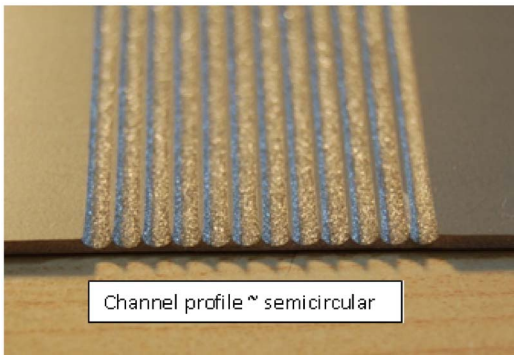


**Fig. 6 PCHE channel profile (close to semicircular)**

**Fig. 7 A PCHE header of alloy 800 HT construction**

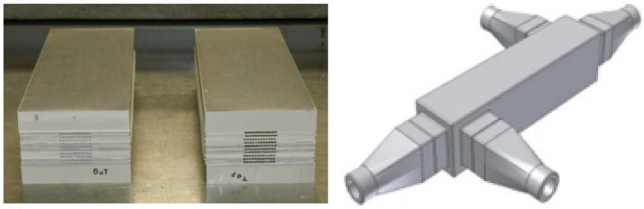

(a) (b)

**Fig. 8 (*a*) Diffusion bonded alloy 617 blocks and (*b*) a complete PCHE assembly with headers**

be fabricated in the future and the performance improvement of these PCHEs in relation to the PCHEs with the straight channels will be examined.

**3.4 Surface Roughness Measurement.** Information of the surface roughness of flow channel is required in the estimation of the channel frictional pressure drop. The surface roughness of the flow channel interior was measured using a Veeco-Wyko NT3300 noncontact optical profilometer. The profilometer was calibrated in vertical scanning interferometry (VSI) mode, and a 2.5× objective lens was used. In the framework of this technique, a substrate was illuminated by white or monochromatic light through a beam splitter. Image processing was carried out by means of a Wyko Vision 32® software package. Figure 9 shows a three-dimensional image of the surface data of a representative channel interior surface. Table 4 lists the basic surface statistics of the same channel. Various surface roughness indicators, *Ra*, *Rq*, *Rt*, and *Rz* represent average roughness, root mean square roughness, maximum height of the surface, and the average maximum height of the profile, respectively. The average surface roughness of the interior surface of the channel, *Ra*, is less than 1 $\mu$m. In our study, a total of 12 roughness measurements were made at random locations on three different channels, which resulted in an average roughness of 0.4 $\mu$m. As a comparison, Ishizuka et al. [3] measured an average surface roughness value of 2–3 $\mu$m in the flow channels of their diffusion bonded compact heat exchanger.

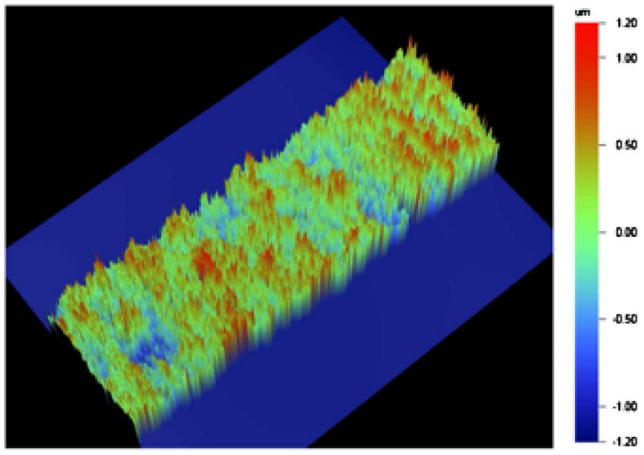


**Fig. 9 Three-dimensional contour map of the interior surface of the channel**

**Table 4 Surface roughness of the interior surface of a representative flow channel**

| *Ra* (nm) | *Rq* (nm) | *Rt* ($\mu$m) | *Rz* ($\mu$m) |
|---|---|---|---|
| 242.6 | 311.7 | 3.2 | 4.0 |

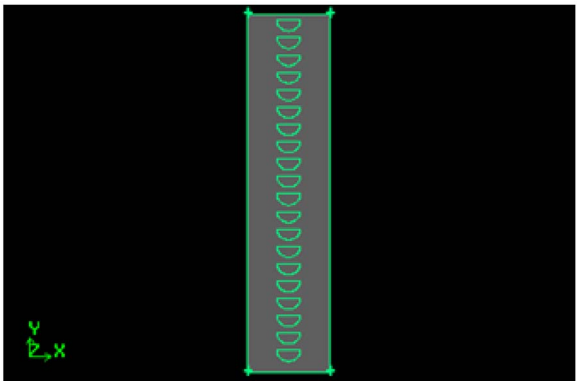


**Fig. 10 A simplified model of the current PCHEs**

## 4 Computational Modeling of PCHE

**4.1 Simplified PCHE Model.** A simplified model of the currently fabricated PCHEs has been constructed using the FLUENT™ commercial CFD package [9]. Figure 10 shows the side view of the PCHE model. The model consists of a vertical arrangement of 20 plates with each containing a single straight channel. The channels are configured for countercurrent flow and are arranged in a single banking configuration, alternating between hot and cold with each plate. This model does not account for the cross flow at the entry and exit regions present on one side of the heat exchangers being fabricated or the effect of multiple channels present on each plate.

For the initial modeling and comparison purpose, only frictional and accelerational pressure drops are considered (entry and exit pressure losses due to flow path sudden expansion and contraction are neglected). As the PCHE channel closely approximates a semicircle, correlations for fully-developed laminar flow in straight semicircular channels were employed for the Fanning friction factor, $f$, and convective heat transfer coefficient, $h$, and are given as [10]

$$f\,\mathrm{Re} = 15.78 \tag{2}$$

$$\mathrm{Nu}_{H1} = 4.089 \tag{3}$$

where the Reynolds and Nusselt numbers are defined as

$$\mathrm{Re} = \rho v D_h/\mu \tag{4}$$

$$\mathrm{Nu}_{H1} = hD_h/k_f \tag{5}$$

From the assumption of fully-developed laminar flow and the knowledge of the Nusselt number, the local convective heat transfer coefficient at various locations in the channel (hot or cold side) is estimated theoretically as

$$h_{\mathrm{theory}} = \mathrm{Nu}_{H1}\ \ k_f/D_h \tag{6}$$

For an incremental length $l_i$, the frictional and accelerational pressure drops are computed as [11]

$$\Delta p_{f,i} = \frac{4f_i l_i}{D_h}\frac{\rho_i v_i^2}{2} = \frac{2}{D_h}(fl\rho v^2)_i \tag{7}$$

$$\Delta p_{a,i} = \rho_{i+1} v_{i+1}^2 - \rho_i v_i^2 \tag{8}$$

where $D_h$, $l_i$, $v_i$, $k_f$, and $\rho_i$ are the channel hydraulic diameter, the $i$th channel incremental length, mean channel fluid velocity for the $i$th incremental length, fluid thermal conductivity, and fluid density, respectively. The total channel (hot or cold side) pressure drop is estimated theoretically by integrating the incremental frictional and acceleration pressure drops along the channel length as

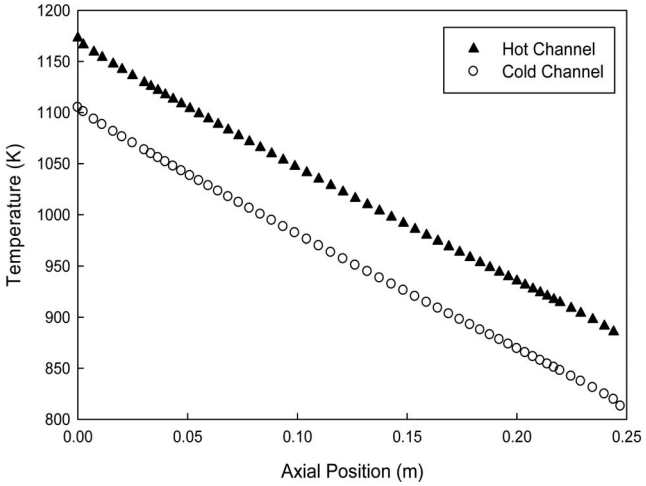


**Fig. 11 Average temperature profiles for hot and cold channels**

$$\Delta p = \sum_i (\Delta p_{f,i} + \Delta p_{a,i}) \tag{9}$$

The thermal entrance length is around 20% of the total channel length, and its effect was accounted for by considering the appropriate local Nusselt number in estimating the local theoretical convective heat transfer coefficient. The local Nusselt numbers for the thermal entrance region of a semicircular duct are interpolated from the data of Hong and Bergles [12]. On the other hand, the local convective heat transfer coefficient for either side of the heat exchanger is numerically computed in FLUENT using data from various positions in the channel as

$$h_{\text{fluent}} = q''/(|T_{\text{bulk}} - T_{\text{wall}}|) \tag{10}$$

**4.2 PCHE Model Assumptions.** In the simplified FLUENT model, the following assumptions have been made:

- uniform entrance velocity for each channel
- property curve fits for helium are obtained as a function of temperature at 3 MPa pressure from NIST data, i.e., the property variations due to pressure drop are neglected because of the relatively high system pressure
- inlet temperatures of 900°C and 540°C are assumed for the hot and the cold sides, respectively
- outlet gauge pressures with respect to 3 MPa are specified as zero on both hot and cold sides, allowing inlet pressure to be calculated by the code
- the length of the hot and cold channels is taken as 0.25 m
- fluid-solid interface is set as a coupled wall allowing for conjugate heat transfer to be calculated by flow field gradients

**4.3 Results and Discussion.** Three initial test cases were devised for a system pressure of 3 MPa and flow rates of 15, 40, and 80 kg/h, respectively. The flow rates on the hot and cold sides are assumed to be the same, i.e., a balanced countercurrent flow PCHE is considered for the modeling. Figure 11 shows the variations in the average helium temperatures for the hot and cold channels of the PCHE at a mass flow rate of 15 kg/h. Figures 12 and 13 show comparisons of the cold and hot side local convective heat transfer coefficients between the theoretical predictions and FLUENT calculations for the mass flow rate of 15 kg/h. This flow rate corresponds to the laminar flow regime in the PCHE with the entrance Reynolds numbers of 520 and 650 on the hot and cold sides, respectively. For a fully-developed laminar flow, the Nusselt number is a constant and independent of the Reynolds

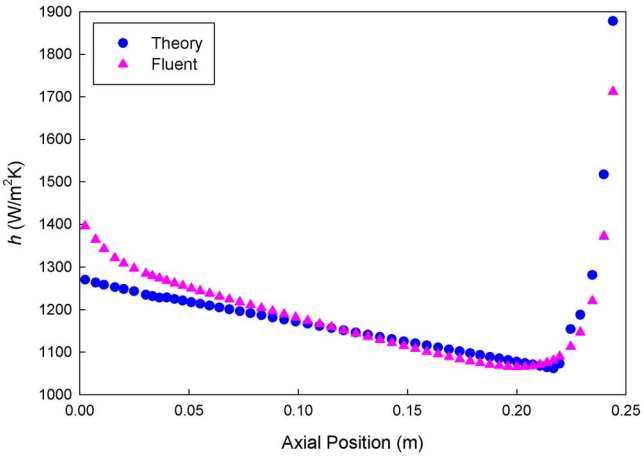


**Fig. 12 Cold channel local convective heat transfer coefficient**

number, therefore the local heat transfer coefficient is just a function of the thermal conductivity of the fluid. Since the thermal conductivity of helium increases with increasing its temperature, the local convective heat transfer coefficient shows an increasing trend from the point reaching a fully-developed flow to the exit of the cold channel (from $z \sim 0.22-0$ m). The relatively high local heat transfer coefficient at and near the inlet for both the numerical and theoretical cases can be attributed to the developing region, where higher convective heat transfer coefficients are expected. A similar argument can be made to explain the trend of the local convective heat transfer coefficient on the hot side of the PCHE, as shown in Fig. 13.

Table 5 compares the theoretical and numerical values of the average convective heat transfer coefficient and the total pressure drop on both sides for a mass flow rate of 15 kg/h and a system pressure of 3 MPa. In addition, Table 6 shows the overall heat transfer coefficients for all the three cases considered in the cur-

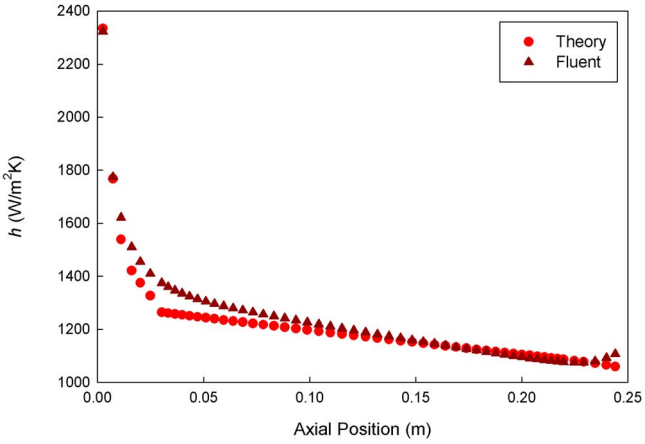


**Fig. 13 Hot channel local convective heat transfer coefficient**

**Table 5 Numerical and theoretical comparison of average convective heat transfer coefficient and pressure drop on the hot and cold sides (mass flow of 15 kg/h)**

| | Cold | | Hot | |
|---|---|---|---|---|
| | Theory | FLUENT | Theory | FLUENT |
| $h_{\text{avg}}$ (W/m² K) | 1215 | 1193 | 1271 | 1252 |
| $\Delta p$ (Pa) | 3678 | 3816 | 3969 | 3863 |

**Table 6 Overall heat transfer coefficients for three different mass flow rates (at 3 MPa system pressure)**

| Case | Flow rate (kg/h) | Flow regime | Overall heat transfer coefficient ($W/m^2$ K) |
|---|---|---|---|
| 1 | 15 | Laminar | 584 |
| 2 | 40 | Laminar | 644 |
| 3 | 80 | Transition | 1697 |

rent study. As the modeled PCHE is a balanced countercurrent flow heat exchanger, the effectiveness is defined as

$$\varepsilon = (T_{hi} - T_{ho})/(T_{hi} - T_{ci}) \tag{11}$$

where $T_{ci}$, $T_{hi}$, and $T_{ho}$ are the helium temperatures at the cold inlet, hot inlet, and hot outlet, respectively. The overall heat transfer coefficient is estimated as

$$U = Q/(A\Delta T_m) \tag{12}$$

where $U$, $A$, and $Q$ are the overall heat transfer coefficient, hot side heat transfer area, and heat load of the PCHE, respectively. $\Delta T_m$ represents the log-mean temperature difference and is expressed as

$$\Delta T_m = \frac{(T_{hi} - T_{co}) - (T_{ho} - T_{ci})}{\ln\left(\frac{T_{hi} - T_{co}}{T_{ho} - T_{ci}}\right)} \tag{13}$$

## 5 Conclusions

A study of high-temperature materials indicated that alloys 617 and 230 are currently the leading candidate materials for the high-temperature applications of interest to the VHTRs. Alloy 617 is the most creep resistant among all the alloys reviewed in the current study. A high-temperature helium test facility that can facilitate experiments at temperatures and pressures up to 900°C and 3 MPa, respectively, was designed and is currently being constructed. The test facility is expected to be commissioned and in full operation by the end of winter 2009. Two PCHEs were successfully fabricated using alloy 617 plates. Furthermore, during the course of this research, both photochemical machining and diffusion bonding techniques were successfully confirmed for alloy 617 plates. Computational modeling of a simplified PCHE model for the PCHEs fabricated is complete, and efforts are currently underway to model the entire heat exchanger core by incorporating the effects of cross flow at the entry and exit regions present on one side of the PCHEs. The computational results of the convective heat transfer coefficient and pressure drop from the simplified PCHE model agree well with the available models in the literature.

## Acknowledgment

This project has been sponsored by the U.S. Department of Energy, Office of Nuclear Energy, Science, and Technology through the Junior Faculty Award Program, administered by Medical University of South Carolina. In addition, the support from the Idaho National Laboratory through the nuclear hydrogen interface program is also greatly appreciated. The authors would like to thank M.W. Patterson and L. Zirker of Idaho National Laboratory and S. Sherman of Savannah River National Laboratory for their invaluable support. D. Lee of the Department of Materials Science and Engineering at the Ohio State University helped with the optical profilometry tests. Finally, the computing resources provided by the Ohio Supercomputer Center are acknowledged.

## Nomenclature

$A$ = heat transfer area on hot side ($m^2$)
$D_h$ = channel hydraulic diameter (m)
$D$ = pipe outer diameter (m)
$E$ = quality factor
$f$ = Fanning friction factor
$h$ = local convective heat transfer coefficient ($W\ m^{-2}\ K^{-1}$)
$h_{avg}$ = average convective heat transfer coefficient ($W\ m^{-2}\ K^{-1}$)
$k_f$ = fluid thermal conductivity ($W\ m^{-1}\ K^{-1}$)
$l$ = incremental length of flow channel (m)
Nu = Nusselt number
$P$ = internal design gauge pressure (MPa)
$Q$ = channel heat transfer rate (W)
$q''$ = heat flux ($W\ m^{-2}$)
Re = Reynolds number
$S$ = allowable stress (MPa)
$T$ = temperature (K)
$\Delta T_m$ = log-mean temperature difference (K)
$v$ = velocity ($m\ s^{-1}$)
$\rho$ = density ($kg\ m^{-3}$)
$\varepsilon$ = heat exchanger effectiveness
$\Delta p_f$ = frictional pressure drop (Pa)
$\Delta p_a$ = acceleration pressure drop (Pa)
$\Delta p$ = total channel pressure drop (Pa)
$Y$ = coefficient from Table 304.1.1 of ASME code [8]
$z$ = axial distance (m)

### Subscripts

avg = average
bulk = refers to bulk fluid
$ci$ = cold inlet
$co$ = cold outlet
fluent = refers to numerically computed value
$H1$ = refers to axially constant wall heat flux with circumferentially constant wall temperature
$hi$ = hot inlet
$ho$ = hot outlet
theory = refers to value computed from analytical expression
wall = refers to metal wall

## References

[1] Idaho National Engineering and Environmental Laboratory, 2005, "Next Generation Nuclear Plant Research and Development Program Plan," Technical Report No. INEEL/EXT-05-02581.
[2] Nikitin, K., Kato, Y., and Ngo, L., 2006, "Printed Circuit Heat Exchanger Thermal-Hydraulic Performance in Supercritical $CO_2$ Experimental Loop," Int. J. Refrig., **29**, pp. 807–814.
[3] Ishizuka, T., Kato, Y., Muto, Y., Nikitin, K., and Ngo, L., 2005, "Thermal-Hydraulic Characteristics of a Printed Circuit Heat Exchanger in a Supercritical $CO_2$ Loop ," *Proceedings of the 11th International Topical Meeting on Nuclear Reactor Thermal Hydraulics (NURETH-11)*, Avignon, France.
[4] Pra, F., Tochon, P., Mauget, C., Fokkens, J., and Willemsen, S., 2008, "Promising Designs of Compact Heat Exchangers for Modular HTRs Using the Brayton Cycle," Nucl. Eng. Des., **238**, pp. 3160–3173.
[5] American Society of Mechanical Engineers, Boiler and Pressure Vessel Committee, 2007, *ASME Boiler & Pressure Vessel Code: An International Code*, American Society of Mechanical Engineers, New York, NY.
[6] Special Metals, 2008, available online at http://www.specialmetals.com, accessed Mar. 24.
[7] Haynes International, 2008, available online at http://www.haynesintl.com, accessed Mar. 24.
[8] American Society of Mechanical Engineers and American National Standards Institute, 2007, *Process Piping: ASME Code for Pressure Piping, B31*, American Society of Mechanical Engineers, New York, NY.
[9] Fluent Inc, 2006, *Fluent 6.3 User's Guide*, Fluent Inc., Lebanon, NH.
[10] Hesselgreaves, J. E., 2001, *Compact Heat Exchangers, Selection, Design, and Operation*, Pergamon, New York.
[11] Todreas, N. E., and Kazimi, M. S., 1990, *Nuclear Systems I: Thermal Hydraulic Fundamentals*, Hemisphere, New York.
[12] Hong, S. W., and Bergles, A. E., 1974 "Augmentation of Laminar Flow Heat Transfer in Tubes by Means of Twisted-Tape Inserts," Technical Report No. ISU-ERI-AMES-75011 HTL-5.

# Design and Technology Development Status and Design Considerations for Innovative Small and Medium Sized Reactors

**Vladimir Kuznetsov**
International Atomic Energy Agency,
Vienna A1400, Austria

*There is continuing interest in Member States in the development and application of small and medium sized reactors (SMRs), i.e., the reactors with an equivalent electric power of less than 700 MW. In 2006–2007, several distinct "families" of innovative SMRs comprising more than 50 innovative concepts and designs have been analyzed or developed by national or international programs involving Argentina, Brazil, China, Croatia, France, India, Indonesia, Italy, Japan, Republic of Korea, Lithuania, Morocco, Russian Federation, South Africa, Turkey, USA, and Vietnam. Innovative SMRs are under development for all principal reactor lines. The target dates when they could be ready for deployment protrude from 2010 to 2030. The designers of innovative small and medium sized reactors pursue new design and deployment strategies making use of certain advantages provided by smaller reactor size and capacity to achieve reduced design complexity and simplified operation and maintenance requirements and to provide for incremental capacity increase through multiple plant clustering or multimodule plant construction. Competitiveness of SMRs depends on the incorporated strategies to overcome loss of economies of scale but equally it depends on finding appropriate market niches for such reactors, which generically include markets with limited investment capability potentially benefiting from reaching the targeted nuclear power station capacity incrementally, small electrical grids, off-grid locations, and nonelectrical applications of nuclear power.* [DOI: 10.1115/1.3078786]

## 1 Introduction

There is an ongoing interest in Member States in the development and application of small and medium sized reactors (SMRs[1]). In the near term, most new nuclear power plants (NPPs) are likely to be evolutionary water cooled reactor designs building on proven systems while incorporating technological advances and often the economics of scale, resulting from the reactor outputs of up to 1600 MW(e). For a longer term, the focus is on innovative designs aiming to provide increased benefits in the areas of safety and security, nonproliferation, waste management, resource utilization, and economy, as well as to offer a variety of energy products and flexibility in design, siting, and fuel cycle options. Many innovative designs are reactors within the small-to-medium sized range, having an equivalent electric power of less than 700 MW(e) or even less than 300 MW(e).

In most of the cases, deployment potential of innovative SMRs is supported by their ability to fill niches in which they would address markets or market situations different from those of currently operated large-capacity nuclear power plants, e.g., more distributed electrical supply, limited investment capability, matching the energy demand growth rate, remoteness and complicated transportation routes, siting flexibility, potable water production or district heating, advanced energy products such as hydrogen, etc. [1–4].

It is important that a small or medium sized reactor does not necessarily mean a small or medium sized nuclear power plant. The majority of innovative SMR concepts and designs [3,4] provide for power station configurations with several units at a site or for NPP configurations with two, four, or even more reactor modules. In many cases, the units or modules could be added incrementally, spreading the investments in time and minimizing the capital at risk.

Also, sometimes it is perceived that SMRs address the users in those countries that currently either do not have or have a small size nuclear infrastructure and are contemplating either induction or significant expansion of nuclear power for the first time. However, this is not the case—most of the innovative SMR designs are meant for a broad variety of applications in the developed and developing countries alike, no matter whether they have already embarked on a nuclear power program or are only planning to do so [3,4].

Finally, it should be emphasized that SMRs are not the only prospective nuclear option; nearly all designers recognize that a diverse portfolio of reactors of different capacity and applications would be needed if nuclear power is to make a meaningful contribution to global sustainable development. Especially, we have in mind that primary energy (in developed countries) is utilized in three roughly equal fractions [4].

- A third is used to generate electricity.
- A third is used in the transportation sector.
- A third is used for domestic and industrial heating.

The role of SMRs in a global nuclear energy system could then be to increase the availability of clean energy in a variety of usable forms for all regions of the world, to broaden the access to clean and affordable and diverse energy products, and, in this way, to contribute to the eradication of poverty and, subsequently, to peace and stability in the world.

## 2 State of the Art in Design and Technology Development for SMRs

**2.1 Safety.** Protection of population from consequences of accidents resulting from internal and external initiators and combinations thereof relies on traditional defense in depth strategies [5,6]. However, in addition to active safety systems, nearly all SMR designs reinforce the first and subsequent levels of the defense in depth by broad incorporation of inherent and passive safety features into design concept. The goal is to eliminate as many accident initiators as possible by design, with the remaining part then being dealt with by appropriate combinations of active and passive systems. The prerequisites are certain common features of smaller reactors, such as larger reactor surface-to-volume ratio and smaller core power density facilitating passive decay heat removal, and smaller reactor size enabling the minimization of the piping and reactor vessel penetrations via integral or compact modular primary circuit layout. The expected outcome is greater plant simplicity with a highly assured level of passive safety response to enable near-urban plant siting with enhanced protection against natural and human-induced external events [2].

Designers of innovative water cooled SMRs pursue an enhanced prevention or elimination of abnormal operation and failures by design. For example, they use integral layout of the primary circuit incorporating the steam generators and the pressurizer, providing for the elimination of large-diameter piping and large-diameter reactor vessel penetrations in order to prevent large-break loss of coolant accidents. They also apply the in-vessel location of control rod drives to eliminate inadvertent control rod ejection and to prevent transient overpower accidents as

[1]According to the classification used by IAEA, small reactors are reactors with an equivalent electric power of less than 300 MW and medium sized reactors are reactors with an equivalent electric power between 300 MW and 700 MW.

Manuscript received August 14, 2008; final manuscript received August 26, 2008; published online July 16, 2009. Review conducted by Dilip R. Ballal.

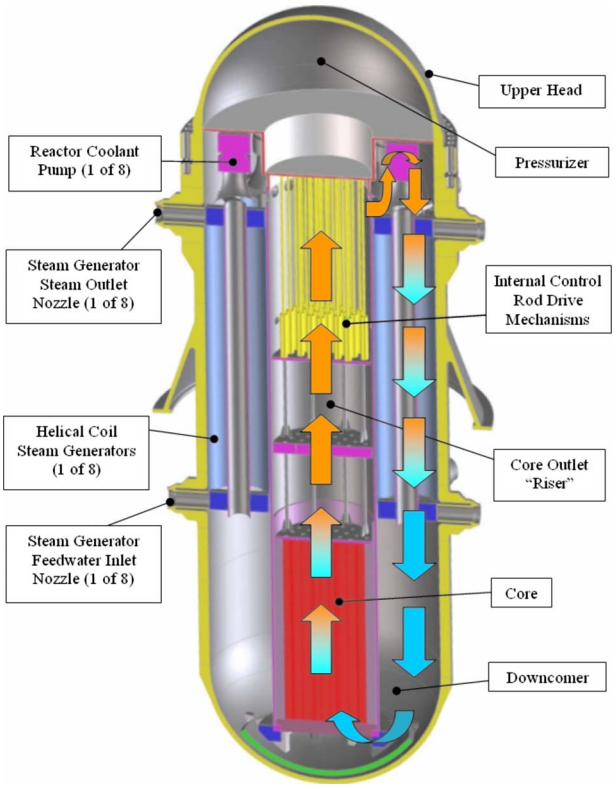


**Fig. 1 Layout of the IRIS integral primary coolant system (international consortium led by Westinghouse, Pittsburgh)**

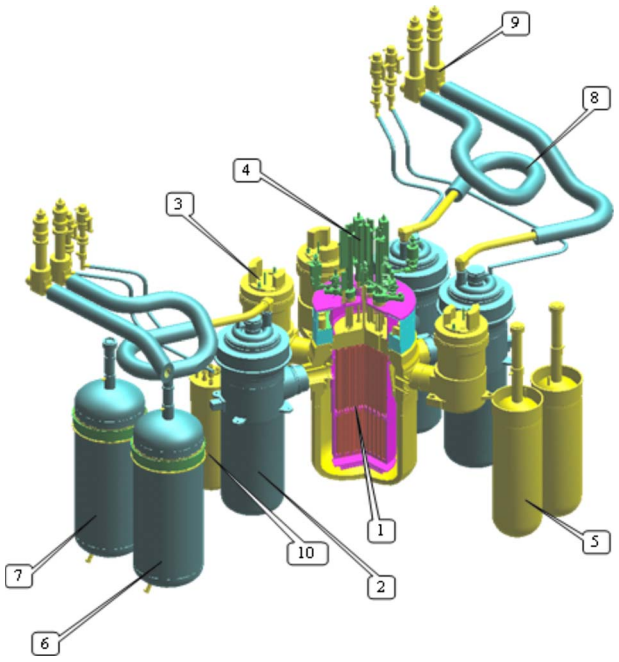


**Fig. 2 Modular layout of the KLT-40S reactor plant (OKBM, Russian Federation): (1) reactor, (2) steam generator, (3) main circulating pump, (4) control and protection system drives, (5) emergency core cooling system accumulator, (6) and (7) pressurizers, (8) steam lines, (9) localizing valves, and (10) heat exchanger of the purification and cooldown system**

well as to reduce the number of reactor vessel penetrations, see Fig. 1.

Alternately, compact loop-type designs with short piping and reduced physical connections between main equipment are applied for the enhanced prevention of loss of coolant accidents, see Fig. 2. SMRs of such design are proven by more than 8000 reactor years of operating experience of the Russian marine-propulsion reactors and have a high potential of being deployed in the very near term.

The designers of high temperature gas cooled reactors (HTGRs) (see Fig. 3) exploit the outstanding fission product confinement capability of tri-isotropic (TRISO) coated particle fuel at high temperatures—an inherent safety feature making a very important contribution to the overall defense in depth concept of such reactors. Proven in previous tests and operation, this capability is definitive for the prevention of consequences of certain accidents that might be severe in reactors of other types and also allows reducing the mitigation measures. Essentially, it may be important to release helium at an early stage of an accident, and only natural processes of conduction, convection, and radiation in the static structures and media then effectively accomplish passive decay heat removal. This feature is complemented by slow and stable response to transients caused by both internal and external initiating events due to large heat capacity of core graphite. It should be noted that, with presently available materials for the reactor vessel, passive decay heat removal capability in the absence of the primary helium could be ensured only at the reactor thermal power of less than ~600 MW(th).

All fast reactors offer extended possibilities to "build" the desired combinations of reactivity coefficients and effects by an appropriate selection of the design parameters of the core and reactor internals at the design stage. This possibility, resulting from a larger leakage rate of fast neutrons as well as from high core conversion ratio, can be effectively used to eliminate transient overpower accidents by design, to ensure the reactor self-control in a variety of anticipated transients without scram, to enable passive load follow capability of the plant, or to allow power control executed only via freed water flow rate adjustment in the steam-turbine circuit [2]. Essentially, a single failure criterion applied in the currently established Safety Standards [5] could be challenged by the design approaches applied in such reactors.

The general consideration for safety of SMRs could be as follows. While with the larger size reactor with adequate implementation of inherent and passive safety features it may be possible to bring down core damage frequency to levels consistent with those in any SMRs with appropriate safety features, the consequences of an accident of the same probability occurring in a large size reactor are likely to be high on account of potentially larger source term, larger quantity of stored heat, and also larger decay heat generation rates.

**2.2 Economics.** To meet the needs of targeted customer groups, the designers of innovative SMRs all over the world examine new design approaches making use of certain advantages provided by smaller reactor capacity to achieve reduced design and operational complexity, simplified maintenance, and to incorporate higher overall energy conversion efficiency [2,3].

The common strategies to improve the economic performance of SMRs are [2,3] as follows:

- to reduce plant complexity by eliminating as many possible accident initiators and/or consequences as possible by design
- to reduce site construction time and/or construction cost and achieve an early start of investment return by

(i) sizing the reactor for transportability (or transportability of modules) and
(ii) targeting a standardized prelicensed design with no site-specific modifications provided for

- to benefit from factory mass production through serial

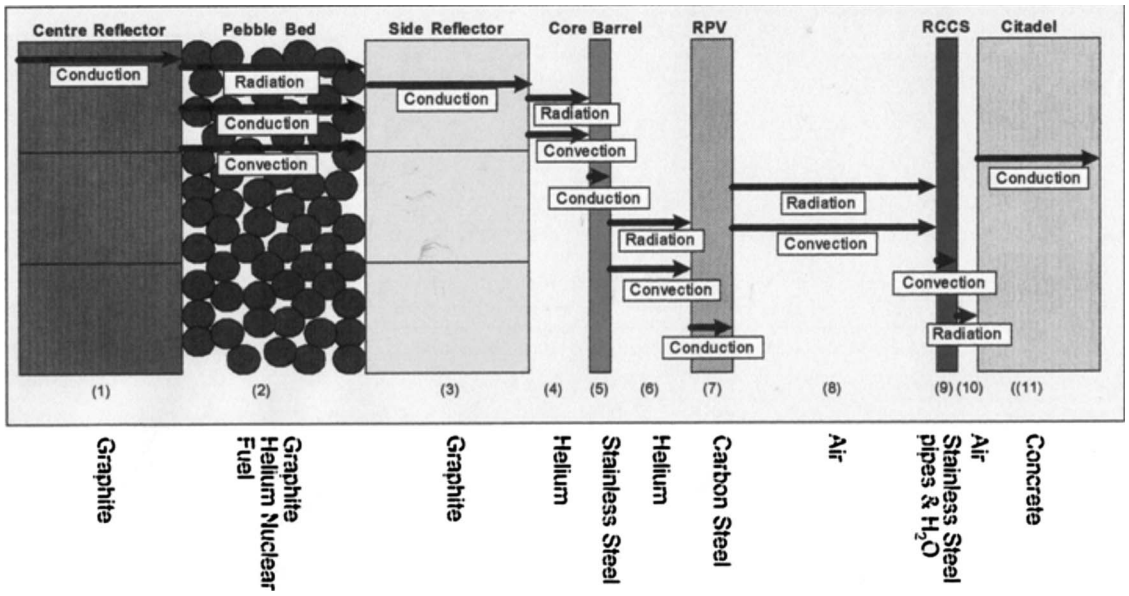


**Fig. 3 Passive heat removal paths of PBMR (PBMR Ltd., South Africa)**

manufacture of standardized plant modules, incorporating unified structures, systems, and components and

- to incorporate an option of incremental capacity increase to achieve economic benefits of "just-in-time" incremental capacity additions, taking a benefit of smaller module sizes to

(i) achieve learning curve acceleration and interest rate savings per total capacity installed and
(ii) to minimize investment risks

SMR designers also target to reduce operation and maintenance (O&M) costs by reducing the number of structures, systems, and components that require maintenance and, in some cases, by targeting a passive load follow or autonomous operation. The examples are small reactors without on-site refueling that require no refueling equipment or fresh and spent fuel storages at the site. Such reactors could also offer an attractive decommissioning strategy.

Bottoming cogeneration cycles, incorporated in many SMRs to produce potable water, heat for district heating, or process heat applications, and in some cases based on the use of heat otherwise rejected in the thermodynamic cycle, provide another option to increase the overall plant efficiency.

**2.3 Small Reactors Without On-Site Refueling.** Small reactors without on-site refueling are the reactors designed for infrequent replacement of well-contained fuel cassette(s) in a manner that impedes clandestine diversion of nuclear fuel material [1,4]. Small reactors without on-site refueling incorporate increased refueling interval (from 5 to 15 years and more), consistent with plant economy and considerations of energy security. Small reactors without on-site refueling are either factory fabricated and fueled or undergo a once-at-a-time core reloading performed at the site by a dedicated service team provided by the vendor; such team is assumed to bring in and take away the fresh and spent fuel load and the refueling equipment.

About 30 concepts of small reactors without on-site refueling are being analyzed or developed within national and international programs in Brazil, India, Indonesia, Japan, Morocco, Russian Federation, Turkey, USA, and Vietnam [1,4]. Small reactor designs without on-site refueling are being considered for both nearer-term and longer-term water cooled, liquid metal cooled, and molten salt cooled reactor lines and some nonconventional fuel/coolant combinations.

Whether for fast or for thermal neutron spectrum concepts of such reactors, the fuel discharge burn-up and the irradiation of core structures never exceed standard practice from the conventional or typically projected designs. The refueling interval is then extended by derating core specific power, and the power densities never significantly exceed ~100 kW(th)/l and often are much lower. Burn-up reactivity loss is mitigated by using burnable poisons and active control rods in thermal systems and by designing for internal breeding in fast systems. Although the specific inventories of fissile materials (per unit of power and energy produced) are higher than for reactors with conventional refueling schemes, some concepts of fast spectrum reactors without on-site refueling are capable of self-sustainable operation on fissile materials (breeding ratio ~1) within a closed nuclear fuel cycle. With this, breeding option is typically excluded owing to a restricted neutron economy.

## 3 Opportunities for SMRs

The deployment progress of innovative SMRs is in many ways defined by their ability to meet the needs of those diverse categories of users that cannot benefit from the economy of scale plant deployments. Notwithstanding the fact that SMRs may still have higher specific costs, they offer other features that could be of importance for certain categories of users, such as

- countries with small and medium electricity grids, insufficient infrastructure, and/or limited investment capability
- villages, towns, and energy intensive industrial sites in off-grid and remote locations and
- in both developed and developing countries, future plants for nonelectric/cogeneration energy services, such as seawater desalination, district heating, and hydrogen production

As an example, in some developing countries, local grids can be small as the development starts and the investment capabilities may be insufficient to import a large economy of scale plant. To accommodate rapid growth but shortage of initial financing, a just-in-time capacity growth plan would be appropriate, with incremental additions deployed as population grows, as energy input per capita increases and as the country becomes wealthier. SMRs could meet the needs of such emerging energy markets where

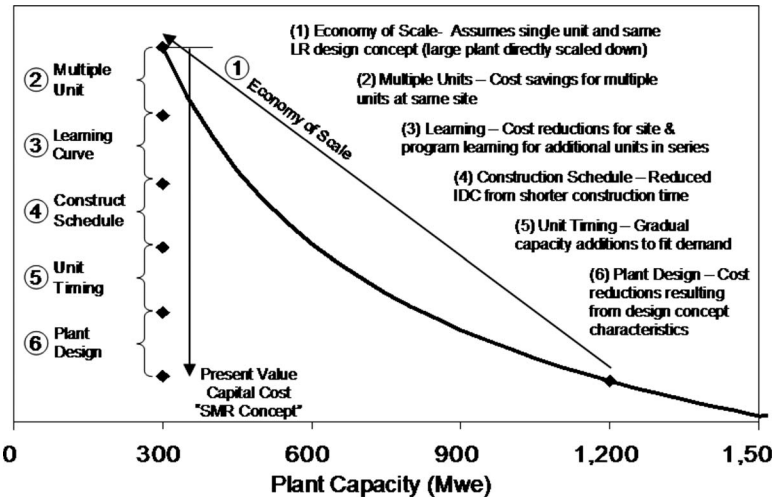


**Fig. 4 A generic scheme illustrating potential SMR economic factor advantages (Westinghouse, Pittsburgh).**

industrial/technical infrastructure is generally poor if they are designed to be easily expandable into clusters comprising ever-larger power installations.

Regarding the second category, much of the world's land mass supports sparse populations and is unsupportable by an electric grid [7]. The examples could be northern extremes of North American and Eurasian continents that are sparsely populated and where the villages and towns and industrial sites are widely separated are unserviced by road, rail, or electrical grid. Island countries face a similar challenge for electricity delivery to widely dispersed population centers located on scattered islands separated by miles of ocean. For users of this category, the difficulties attendant to fuel supply cause busbar energy cost to significantly exceed the rates experienced on well-developed urban grids.

For example, across Alaska the rates vary between 9.3 US$ cent/kW(e) h and 45 US$ cent/kW(e) h [7]; these exceed typical costs in the US contiguous 48 states by factors of 3–10. Many users in this category will require more than electricity to support residential loads and industrial applications—desalinated water or district heating often comprises an additional necessary energy service.

In the future, as fossil fuel resources become depleted and as the share of nuclear power increases in both developed and developing countries, the advantages of incremental addition of small or medium generating capacity to match the demand growth "perfectly" might become more attractive to the utilities operating in the deregulated competitive markets. These advantages may become even more important if nuclear energy broadly enters the nonelectric markets for seawater desalination, district heating, low temperature process heat, and high temperature heat, including hydrogen manufacture by thermochemical processes. These markets are likely to be served by commercial entities, which are separated from electric utilities, and for which financing relies on commercial bank loan rates or usual rates of return on investor equity. For such entities to succeed, payback period must be short, internal rate of return on investment must be high, and financial risk minimization would be at a premium. Design requirements for extreme levels of reliability and safety apply to the nonelectric applications because of the necessity to site process heat sources close to industrial centers [1,4].

A possibility of local participation and gradual technology transfer to the user-country are features commonly mentioned by many potential users in developing countries; with them, nuclear power plants are viewed not only as energy sources but as vehicles of the overall national economy development. Design features that support this request could also contribute to better economy of the plant, e.g., if certain parts of a NPP could be built to local standards by local constructors using local labor with financing denominated in local currency. In the meantime, several developing countries have matured their nuclear industries to offer domestically produced or even domestically designed SMRs to world markets in the very near term.[2]

## 4 Challenges for SMRs

As it was already mentioned, innovative SMRs in many cases do not attempt to compete with large economy of scale plants in the established markets; they rather attempt to meet the needs of those users to whom large economy of scale deployments are not suited. To be competitive in anticipated alternative markets, innovative SMRs rely on approaches alternative to economy of scale. Such approaches include the economy of multiple prefabricated reactor or equipment modules, reduced design complexity resulting from the application of those design features that are most appropriate for the reactor of a given capacity, an option of incremental capacity increase with possible benefits resulting from just-in-time capacity addition and learning curve factors, shorter construction period, and, possibly, greater involvement of local labor, as illustrated by a generic scheme in Fig. 4. The effectiveness of all these approaches for the conditions of targeted markets should be demonstrated, which is a challenge of prime importance for all innovative SMRs.

Many of the innovative SMR concepts incorporate design features and system configurations that are not proven in operating practice of reactors for civil nuclear power; also, many innovative SMRs are just nonwater cooled reactors. Licensing of such reactors within current light water reactor based and sometimes overly prescriptive regulatory frameworks will pose a challenge, and adjustments of regulatory rules toward a risk-informed approach may be required on many occasions [4]. In addition to incorporating many inherent safety features, some innovative SMR concepts suggest stronger reliance on passive systems of innovative design. Reliability of such systems needs to be proven to enable risk-informed qualification and licensing.

Many potential applications of SMRs may require them to be located in proximity to the users.

- In industrial cogeneration applications, such as hydrogen production, they must be sited adjacent to the industrial site for delivery of process heat.

[2]The examples are the Republic of Korea, India, and Argentina.

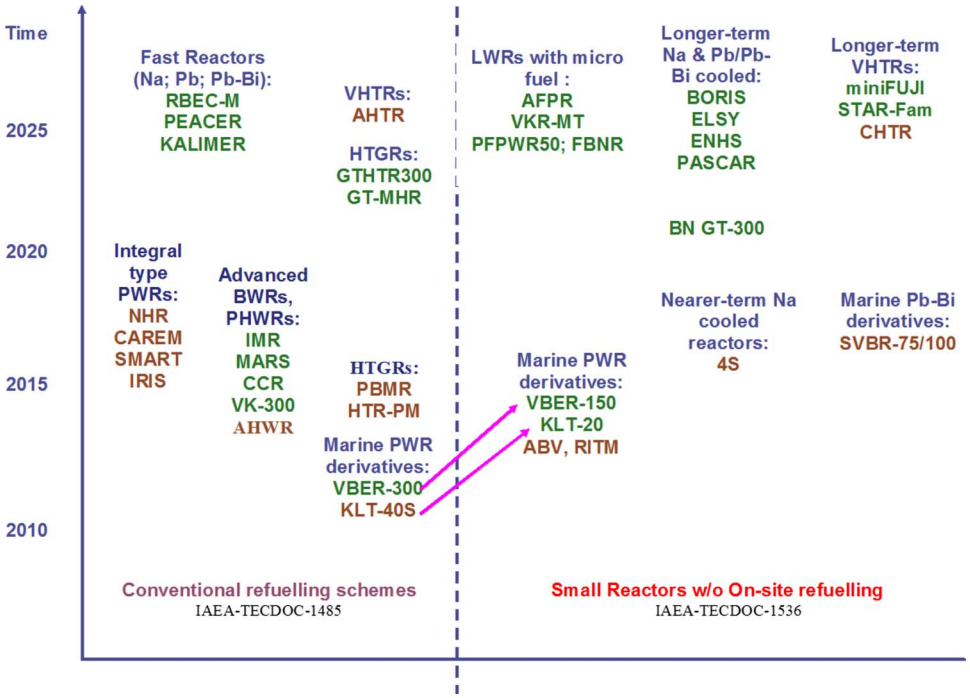


**Fig. 5 A generic scheme illustrating deployment potential of some innovative SMRs. Concepts to the left are described in detail in Ref. [3] and to the right in Ref. [4]. The abbreviations for the SMR designs that currently show good progress toward advanced design stage or deployment are decrypted as follows: ABV—Russian abbreviation for water cooled modular power reactor, OKBM, Russian Federation; AHTR—advanced high temperature reactor, ORNL; AHWR—advanced heavy water reactor, BARC, India; CAREM—Central Argentina de Elementos Modulares, CNEA, Argentina; CHTR—compact high temperature reactor, BARC, India; HTR-PM—high temperature reactor—pebble bed module, INET, Tsinghua University, China; IRIS—International Reactor Innovative and Secure, international team led by Westinghouse; KLT-40S—Russian Federation—icebreaker type reactor 35 MW(e), OKBM, Russian Federation, a floating plant with two such reactors is under construction currently; NHR—nuclear heating reactor, INET, Tsinghua University, China; PBMR—pebble bed modular reactor, PBMR Pty., South Africa; RITM—Russian abbreviation—reactor integral type modular, OKB, Russian Federation (note that the first version will be an icebreaker propulsion reactor); SMART—system integrated modular advanced reactor, KAERI, Republic of Korea; 4S—super-safe small and simple reactor, Toshiba Corporation—CRIEPI, Japan; and SVBR-75/100—Russian abbreviation for lead bismuth fast reactor 75/100 MW(e), IPPE, Russian Federation.**

- They could supply energy to cities in regions where only a local electrical grid exists.
- They could produce energy products such as potable water and district heat, which cannot be transported to significant distances without a significant economic penalty.

These siting considerations lead to a requirement for very high levels of safety and reliability. Colocating a nuclear and a chemical plant on a single site will require developing new safety rules and regulations to be applied to both of them. Licensing of a nuclear power plant with a reduced or eliminated emergency planning zone, which is aimed by the designers of many innovative SMRs, will require that risk-informed regulations be emplaced.

Many small reactors without on-site refueling incorporate substantially increased refueling interval, ranging from ~5 years to 20–25 years and beyond. The operating experience for such elongated refueling intervals is generally unavailable in civil nuclear power [4]. The known experience of marine reactors confirms the possibility of a 7–8 year continuous operation of small reactors. Therefore, the construction of a prototype would be a must for many small reactors without on-site refueling.

Once built, the prototype could be subjected to a pre-agreed set of anticipated transient without scram (ATWS) and other accident initiators. By demonstrating safety based on passive response on the prototype, the licensing authority might be able to certify the design, permitting the manufacture of many tens (or hundreds) of replicate plants to the set of prints and design specifications used for the prototype [4]. In order to assure that aging effects do not degrade the passive safety features of deployed plants, the licensing authority could prescribe the performance of periodic in situ tests on the plant to confirm continued presence of reactivity feedbacks in the required range and of passive decay heat removal continuously operating at the required rate. Such an approach, referred to as "license-by-test," needs to be further examined and established, which is a challenge for many small reactors without on-site refueling.

## 5 Design Considerations for SMRs

Continued operation, construction of new power plants, and progress in design and technology development for future SMRs indicate the continued interest of many countries in the development and application of such reactors. The observed multiplicity of design approaches and user-related features of SMRs suggest that further progress in their development and deployment could benefit from a continued dialog among possible vendors and potential users and the international community. To support such a dialog, certain framework needs to be established to help interested stakeholders re-examine and assess the need for SMRs in countries or certain regions of countries. A useful tool in fostering the dialogs might be design considerations for SMRs, highlighting

specific advantages that could be gained with NPPs based on such reactors and identifying certain design and technology development goals that need to be pursued to achieve such advantages, for example, as brought out in the recent status reports on innovative SMRs produced by the IAEA [3,4]. Such considerations, partly highlighted in the present paper, will be refined and presented by the IAEA in a systematic way in the near future.

## 6 Concluding Remarks

Of the world's 442 operating nuclear power plants, 28 are small, 111 are medium sized, and 303 are large. Of the 31 reactors under construction 7 are small, 4 are medium sized, and 20 are large. In the near term, most new nuclear power reactors are likely to be evolutionary large units. But particularly in the event of a nuclear renaissance, the nuclear industry can expect an increasing diversity of customers and thus an increasing number of customers with needs potentially best met by one or more of the innovative SMR designs now under development.

A generic scheme illustrating an "optimistic" deployment potential of innovative SMRs is given in Fig. 5. The caption of Fig. 5 indicates concepts that show noticeable progress toward advanced design stages, licensing, or deployment.

## References


[1] International Atomic Energy Agency, 2005, "Innovative Small and Medium Sized Reactors: Design Features, Safety Approaches and R&D Trends," Report No. IAEA-TECDOC-1451.

[2] International Atomic Energy Agency, 2006, "Advanced Nuclear Plant Design Options to Cope With External Events," Report No. IAEA-TECDOC-1487.

[3] International Atomic Energy Agency, 2006, "Status of Innovative Small and Medium Sized Reactor Designs 2005: Reactors With Conventional Refuelling Schemes," Report No. IAEA-TECDOC-1485.

[4] International Atomic Energy Agency, 2007, "Status of Small Reactor Designs Without On-Site Refuelling," Report No. IAEA-TECDOC-1536.

[5] International Atomic Energy Agency, 2000, "Safety of Nuclear Power Plants: Design, Safety Standards Series," Report No. NS-R-1, IAEA.

[6] International Atomic Energy Agency, 2003, "External Events Excluding Earthquakes in the Design of Nuclear Power Plants," Report No. NSG-1.5.

[7] US-DOE-NE Report to Congress, 2002, "Small Modular Nuclear Reactors," Available at DOE Web Site, http://www.doe.gov.

# High-Temperature Properties of Nuclear Graphite

**Tracy L. Albers**
GrafTech International Holdings Inc.,
12900 Snow Road,
Parma, OH 44130

*The unique combination of physical properties inherent to graphite makes it an attractive material for use as a moderator in high-temperature nuclear reactors. High-temperature physical properties of three nuclear-grade graphites manufactured by GrafTech International Holdings Inc. (GrafTech, Parma, OH), PCEA™, PCIB-SFG™, and PPEA™, have been determined experimentally and are presented here. Tensile strength, Young's modulus, thermal conductivity, specific resistance, and coefficient of thermal expansion (CTE) data are collected at temperatures from 25°C to as high as 2000°C, and are found to be consistent with classical graphite behavior.* [DOI: 10.1115/1.3093995]

## 1 Introduction

Graphite was used as the moderator for the first nuclear reactor in 1942 because neutrons can travel a great distance in graphite without being captured, while having multiple collisions with carbon atoms that slow down the neutrons. Graphite's thermal stability in inert atmospheres, ease of machining, relatively low cost, and high purity make it a good moderator for nuclear reactors [1,2].

GrafTech has provided nuclear graphite to the industry for more than 60 years and today leverages more than 125 years of manufacturing expertise to provide a wide product offering to the nuclear graphite industry. GrafTech nuclear graphite is specially produced for the desired strength, isotropy, and purity, using raw materials that are expected to be stable in their chemical composition and readily available in large quantities into the distant future. Three different nuclear graphite grades are presented here: PCEA, PCIB-SFG, and PPEA [3]. These grades differ in both their forming methods and raw material base.

The unique high-temperature properties of graphite also make it well suited for the future construction of highly efficient, inherently stable, high-temperature reactors (HTRs). These reactors will operate at temperatures of up to 1200°C, and must be mechanically stable up to 2000°C [4]. Thus, HTR designers must understand the behavior of nuclear-grade graphite at elevated temperatures, in addition to understanding the irradiation effects on graphite.

This paper will highlight some of the strength, thermal, and electrical properties that have been measured for these grades at high temperatures. These nuclear graphites are undergoing irradiation testing as well.[1] The data presented here for "as-manufactured" graphite will later be combined with postirradiation measurements to give HTR designers a complete picture of the high-temperature performance of these three nuclear graphite grades.

[1]Controlled irradiation experiments are currently being performed at NRG Petten as part of the RAPHAEL program.

Manuscript received October 21, 2008; final manuscript received October 27, 2008; published online July 15, 2009. Review conducted by Dilip R. Ballal. Paper presented at the Fourth International Topical Meeting on High Temperature Reactor Technology (HTR2008), Washington, DC, September 28–October 1, 2008.

## 2 High-Temperature Properties

The focus of this paper is to present elevated temperature data of standard graphite samples of grades PCEA, PPEA, and PCIB-SFG, as determined by the modified ASTM test methods summarized below in Table 1 [5,6].

High-temperature tensile strength properties are presented in Table 2. Tensile strengths are 4–9% higher in the with-grain (wg) direction than against-grain (ag) at 25°C, and 1–3% higher at 1600°C. All three grades tested demonstrated significant improvement in tensile strengths (with-grain) at the higher temperature, with increases ranging from 25% to 63%.

Young's modulus was also determined for the three grades of nuclear graphite, over the temperature range 25–2000°C. Selected results are shown in Table 3. As in the case of tensile strength, the moduli are somewhat stronger in the with-grain direction, increasing with temperature for each grade tested. Each value shown in the table is an average of a measurement made during heating and one made during cooling.

Thermal conductivity values were measured for PCEA, PCIB, and PPEA over the temperature range of 25–900°C. The data, shown in Fig. 1 illustrate that thermal conductivity decreases by roughly 50% over this temperature range for each grade tested.

The specific resistance of the nuclear graphite grades was also measured over the temperature range 25–2000°C (Table 4). The against-grain resistances were generally higher than with-grain values, up to 8% greater. For all three grades, resistances reached a minimum between 500°C and 1000°C and increased steadily all the way up to 2000°C.

Coefficient of thermal expansion (CTE) measurements were recorded over the temperature range of 25–2000°C (Fig. 2). All three grades showed a steady increase in with-grain CTE over the entire temperature range, between 65% and 75%. The behavior of these materials is consistent with calculations made from predictive models [7].

**Table 1 High-temperature testing methods for nuclear graphite grades**

| Property | Temperature range (°C) | Test notes |
|---|---|---|
| | | GrafTech design: |
| Young's modulus | 25–2000 | Modified ASTM C747 |
| | 25–100 | GrafTech Design: PATE |
| CTE | 25–2000 | GrafTech design |
| | | GrafTech design: |
| Specific resistance (SR) | 25–2000 | Modified ASTM C611 |
| Thermal diffusivity | | ASTM C714 (TD) |
| and specific heat | 25–900 | ASTM C781 (SH) |
| Tensile strength | 25–2000 | ASTM C565, C749 |

**Table 2 High-temperature tensile strength**

| | 25°C (MPa, wg/ag) | 1600°C (MPa, wg/ag) | % increase (wg) |
|---|---|---|---|
| PCEA | 23.5/21.6 | 31.5/31.2 | 34% |
| PCIB | 41.8/39.9 | 52.1/50.6 | 25% |
| PPEA | 18.3/17.5 | 29.9/29.1 | 63% |

**Table 3 High-temperature Young's modulus**

| | 25°C (GPa, wg/ag) | 1000°C (GPa, wg/ag) | 2000°C (GPa, wg/ag) |
|---|---|---|---|
| PCEA | 11.8/11.3 | 13.5/12.8 | 16.5/15.9 |
| PCIB | 12.8/11.7 | 15.1/13.7 | 17.3/15.8 |
| PPEA | 10.8/10.4 | 12.2/11.9 | 16.3/15.6 |

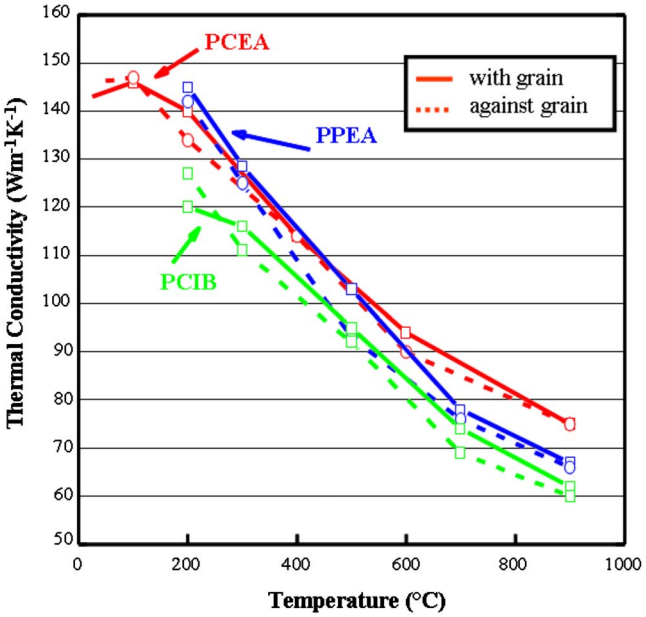


**Fig. 1 High-temperature thermal conductivity**

## 3 Conclusions

High-temperature test results of these three nuclear graphite grades confirm classical predictions of how temperature affects strength, electrical, and thermal properties of graphite.

- Mechanical properties such as tensile strength and Young's modulus increase with temperature.

**Table 4 High-temperature specific resistance**

| | 25°C ($\mu\Omega$ m, wg/ag) | 1000°C ($\mu\Omega$ m, wg/ag) | 2000°C ($\mu\Omega$ m, wg/ag) |
|---|---|---|---|
| PCEA | 7.7/7.9 | 6.6/6.6 | 8.5/8.4 |
| PCIB | 10.4/11.1 | 7.8/8.2 | 9.5/9.9 |
| PPEA | 8.8/9.2 | 6.8/7.4 | 8.6/9.1 |

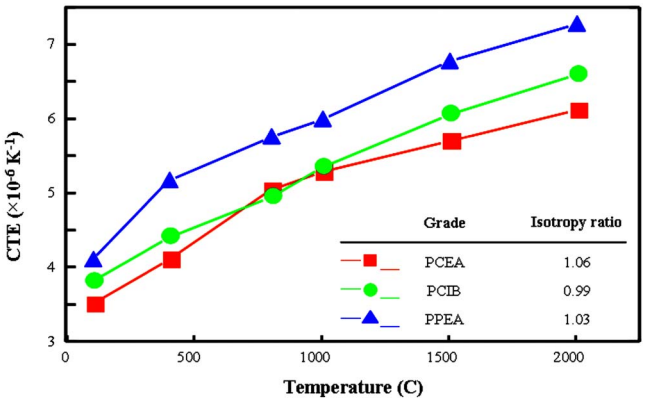


**Fig. 2 High-temperature with-grain CTE. Isotropy ratio is ag/wg value for RT –2000°C.**

- Thermal conductivity decreases by approximately 50% as temperature is increased from RT to 900°C.
- Specific resistance reaches a minimum between 500°C and 1000°C and increases at higher temperatures.
- CTE increases 65–75% upon heating from RT to 900°C, following established predictive models.

These data are part of the extensive characterization effort by academic, government, and industrial partners needed to complete the design of a modern HTR.

## References

[1] Currie, L. M., Hamister, V. C., and MacPherson, H. G., 1955, "The Production and Properties of Graphite for Reactors," UN International Conference on Peaceful Uses of Atomic Energy, Geneva.
[2] Nightingale, R. E., ed., 1962, *Nuclear Graphite*, Academic, London.
[3] PCEA, PCIB-SFG, and PPEA are trademarks of GrafTech International Holdings, Inc. for grades of nuclear graphite.
[4] Parme, L. L., 2001, "Regulatory Challenges for Future Nuclear Power Plants," ACRS Workshop.
[5] ASTM, *2008 Annual Book of ASTM Standards*, 2008, Vol. 05.05, ASTM, West Conshohocken, PA, pp. 191–290.
[6] Wagoner, G., Sprogis, G., and Proctor, D. G., 1986, "Capacitance Bridge Measurement of Thermal Expansion," *Carbon Proceedings*, pp. 234–236.
[7] Tsang, D. K. L., Marsden, B. J., Fok, S. L., and Hall, G., 2005, "Graphite Thermal Expansion Relationship for Different Temperature Ranges," Carbon, **43**, pp. 2902–2906.

# Flow Visualization in the Scaled Up Pebble Bed of High Temperature Gas-Cooled Reactor Using Particle Image Velocimetry Method

**Jae-Young Lee**
e-mail: jylee7@handong.edu

**Sa-Ya Lee**
e-mail: sayalee@seed.handong.edu

School of Mechanical and Control System Engineering,
Handong Global University,
Pohang, Gyeongbuk 791-708, Korea

*The flow visualization in the complicated flow geometry of the pebble bed of the high temperature gas-cooled reactor is investigated to identify the stagnation points at which internal hot spots are expected. A particle image velocimetry method was employed to visualize flow for the pebble bed in the structure of the face centered cubic. The wind tunnel was designed to provide the same Reynolds number of $2.1614 \times 10^4$ as the pebble bed nuclear reactor. Scaling law determined the diameter of the pebble as 120 mm, which is two times bigger than the reference when we use air as a coolant rather than helium. The present scaled up design reduces the load of high speed imaged acquisition and the flow field measured by 4000 frames/s. It was found that the present method identified flow field successfully, including the stagnation points suspected to produce hot spots on the surface of the pebble bed. The present data are useful in evaluating the three-dimensional computational fluid dynamics analysis.*
[DOI: 10.1115/1.3098417]

## 1 Introduction

A pebble bed reactor (PBR) is one type of a very high temperature reactor (VHTR) for a Gen-IV reactor core [1]. High temperature reactor (HTR) is known to have inherent safety, and the inherent safety can be explained by a passive concept. The first passive safety system concept was proposed by Reutler and Lohnert [2]. In PBR, the trisocoated fuel particles cause fission in a graphite pebble. Such a reaction in pebble has low power density, and the reactor core is designed to have a maximum fuel element temperature under 1600°C during any accident. Despite these characteristics, in the view of nuclear safety, the heat transfer in the reactor, the maximum fuel temperature, and the location must be predicted. Therefore, the flow field analysis in the reactor is needed, especially the local flow field analysis, which is important for accident prediction. Such a need for the local flow field analysis is discussed by many other researchers. In computational analysis, it is not practical to create mesh for total flow field, so computer simulation can only cover part of the flow field. If someone increases the calculating power of the computer and simulates the total flow field, the simulation result still must be verified with a local experimental result. Like this, there is much necessity for local analysis; however, the critical investigation is not enough, and the experimental data are not sufficient. This is due to the complications of the high temperature gas-cooled reactor (HTGR) geometry. HTGR has hundreds of thousand pebbles inside the reactor, and those pebbles are stacked with a very complicated geometry. This geometry makes it difficult to measure the local flow field in narrow gaps between pebbles. In the study of Lee et al. [3], flow field measurement was taken in a two-dimensional wind tunnel by a hot-wire system. Hassan [4] measured local velocity field with particle tracking velocimetry (PTV) in a small sized packed bed using refractive index matching liquid. In spite of these efforts, it is still hard to say that the local flow field analysis is completely understood experimentally. Therefore, in this study, we have focused on the experimentalal result. Based on the previous researchers' measurement methods, we designed the experimental system to be more reasonable. A wind tunnel was built, and a three-dimensional pebble bed test section was equipped. The particle image velocimetry (PIV) was developed to measure the velocity field without interruption in the very narrow flow channel between the pebbles.

Manuscript received November 26, 2008; final manuscript received December 1, 2008; published online July 17, 2009. Review conducted by Dilip R. Ballal. Paper presented at the Fourth International Topical Meeting on High Temperature Reactor Technology (HTR2008), Washington, DC, September 28–October 1, 2008.

## 2 Dimensional Analysis

It is hard to find an experimental observation of the flow field in the pebble bed due to its complicated geometry. Hassan [4] provided pioneering observation in the scaled down system from 60 mm of reference pebble to around 5 mm diameter pebble in the liquid medium. However, in the present study, we tried to develop an air-cooled system by scaling up the reference pebble to 120 mm in diameter. The key scaling parameter is determined as the Reynolds number, and the physical properties such as the density and viscosity are calculated from the real HTGR condition (see Table 1) to the room temperature and atmospheric pressure [5].

By applying those values in Table 1, the velocity of the air can be determined as

$$\mathrm{Re}_{\mathrm{He}} = \frac{5.36 \times 2.48 \times D_{h(\mathrm{He})}}{3.69 \times 10^{-5}} = \mathrm{Re}_{\mathrm{air}} = \frac{1.20 \times V_{\mathrm{air}} \times D_{h(\mathrm{air})}}{1.80 \times 10^{-5}} = 2.1614 \times 10^4 \quad (1)$$

In Eq. (1), we just use the ratio of $D_{h(\mathrm{He})}$ and $D_{h(\mathrm{air})}$. In the case of the same size pebble as 60 mm diameter, the $D_{h(\mathrm{He})}$ and $D_{h(\mathrm{air})}$ are the same, and in the double sized case, the ratio of $D_{h(\mathrm{He})}:D_{h(\mathrm{air})}$ is 1:2. Helium gas inlet speed is calculated as 2.48 m/s with the density, mass flow rate, and core diameter in Table 1. By applying the result in Eq. (1), we can obtain the air inlet velocity of 5.4 m/s. If the pebble size is doubled, the air inlet velocity can be 2.7 m/s by the relation of the effective diameter and velocity in Reynolds number. The result of similarity research is shown in Table 2.

## 3 Experiments

**3.1 Wind Tunnel Design.** An open circuit wind tunnel is designed and constructed in the study to equip the pebbles in the face-centered-cubic (fcc) way. The wind tunnel system is constructed with 1.97 m of wind tunnel part and 22 m of ventilation part. The maximum velocity is 5.85 m/s with the pebble bed test section. The wind tunnel was tested to confirm the uniformity of flow with Dwyer-Instrument Series 477 digital manometer, and the maximum nonuniformity was 2.49%.

**3.2 Pebble Bed Test Section.** The pebble bed test section consists of a $170 \times 170 \times 505$ mm$^3$ duct and a fcc stack geometry pebble bed model, as shown in Fig. 1. Transparent acryl spheres were used for the pebble bed model. Two holes for watching inside pebble bed stacks and beam projection were made on the test section wall, as shown in Fig. 2. After pebble bed stack installation in the wind tunnel, in order to check the air flow, we measured the outlet velocity once again with Lutron YK-2004AH (hot-wire anemometer) and verified that the flow velocity is almost same as the inlet velocity.

**3.3 PIV Equipment Setting.** We have developed PIV of less than 5% error. The test pictures and comparison data were taken

Table 1 Specification of PBMR-250 $MW_{th}$

| | | |
|---|---|---|
| Thermal power | 250 | $MW_{th}$ |
| Core height/diameter | 9.0/3.7 | m |
| Helium inlet/outlet temperature | 500/900 | °C |
| Total inlet mass flow rate | 120 | kg/s |
| Primary system pressure | 8.5 | MPa |
| Pebble bed packing fraction | 61 | % |
| Number of fuel pebble | 380,000 | EA |
| Number of graphite pebble | 150,000 | EA |
| Helium gas density | 5.36 | $kg/m^3$ |
| Helium gas viscosity | $3.69\times10^{-5}$ | $N\,s/m^2$ |

from Okamoto et al. [6]. The PIV system is supported by the high speed camera and high power light source. In the present study, we made a 1 mm slit beam source with 14 power light emitting diode (LED) (3 W/615–635 nm) connected module. The high speed camera is Photron FASTCAM Ultima-512. It can take a picture of 4000 fps (frames/s) with $512\times256$ resolution or 8000 fps with $512\times128$ resolution. The PIV system is set with those equipments, as shown in Fig. 2.

## 4 Results and Analysis

The velocity field measurement has to be carried out with a 2.7 m/s inlet speed, but the inlet speed was a half level as 1.3 m/s for the clearer images. Table 3 shows the condition of velocity measurement.

**4.1 Velocity Analysis Near the Pebble Surface.** Figure 4 shows the average velocity field of 40 images within 0.01 s using the PIV algorithm. A velocity graph 1.5 mm away from the pebble surface is presented in Fig. 3. When analyzing the flow pattern along the points in Figs. 3 and 4, velocity increases from 1, then decreases at 5 rapidly, and increases again from 6 to 13. The 1.0 m/s velocity point on 1 is the error caused by the boundary limitation of the PIV system, and it was eliminated in Fig. 4. The velocity rapidly decreases at 14 and reaches a very low level at 15. After this point, flow gets faster and loses the speed at 19. The velocity difference between points 5 and 15 is caused by the contact point. Before the contact point, the vortex is not found, but after the point, vortex makes the stagnation region. This low speed region is also found in the simulation result of Lee et al. [3]. In this observation, we can easily identify the suspected points as the stagnation points. Also, we can see the effect of the contacting point of the pebbles and the effect of the back flow between points 18 and 19.

Considering that the cooling efficiency is proportional to the flow velocity, pebble surface temperature will be highest at the contact point and average temperature will be high within points 15–19 region. We found some flow oscillation in the gap as noted by Hassan [4]; it will be discussed later after accumulating enough experimental data.

Table 2 Result of the dimensional analysis

| | |
|---|---|
| Gas | Air |
| Pressure | 0.1 MPa |
| Temperature | 25°C |
| Density | $1.20\ kg/m^3$ |
| Viscosity | $1.80\times10^{-5}\ N\,s/m^2$ |
| Inlet velocity | 2.7 m/s |

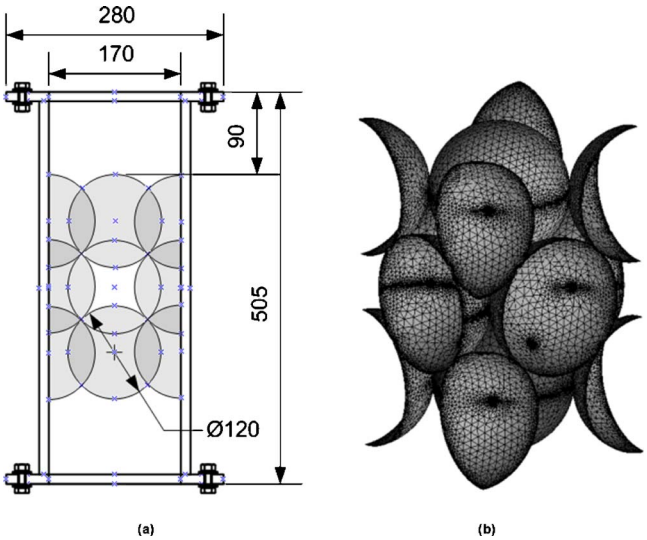


Fig. 1 Structure of the pebble bed test section in the fcc stack geometry: (*a*) test section configuration and (*b*) pebbles stacked in the face-centered-cubic stacked pebbles

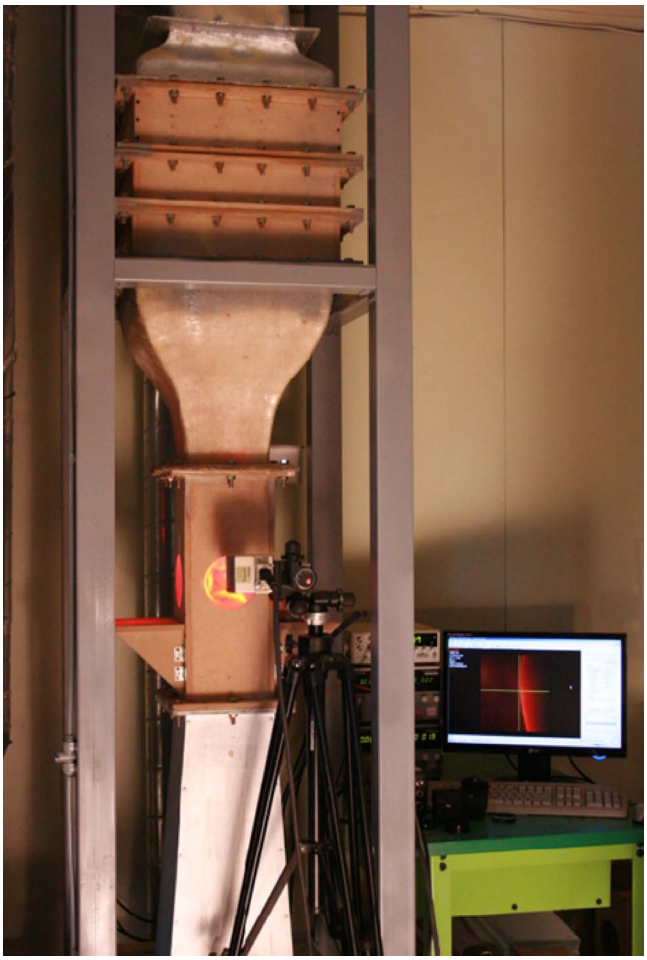

Fig. 2 Picture of the wind tunnel with the test section and the PIV system

Table 3 Velocity measurement condition

| | |
|---|---|
| Inlet velocity | 1.3 m/s |
| Shutter speed | 1/8000 s |
| Frames per second | 4000 fps |
| Image resolution | $256\times512$ pixel$\times$pixel |
| Test section size | $38.5\times77\ mm^2$ |

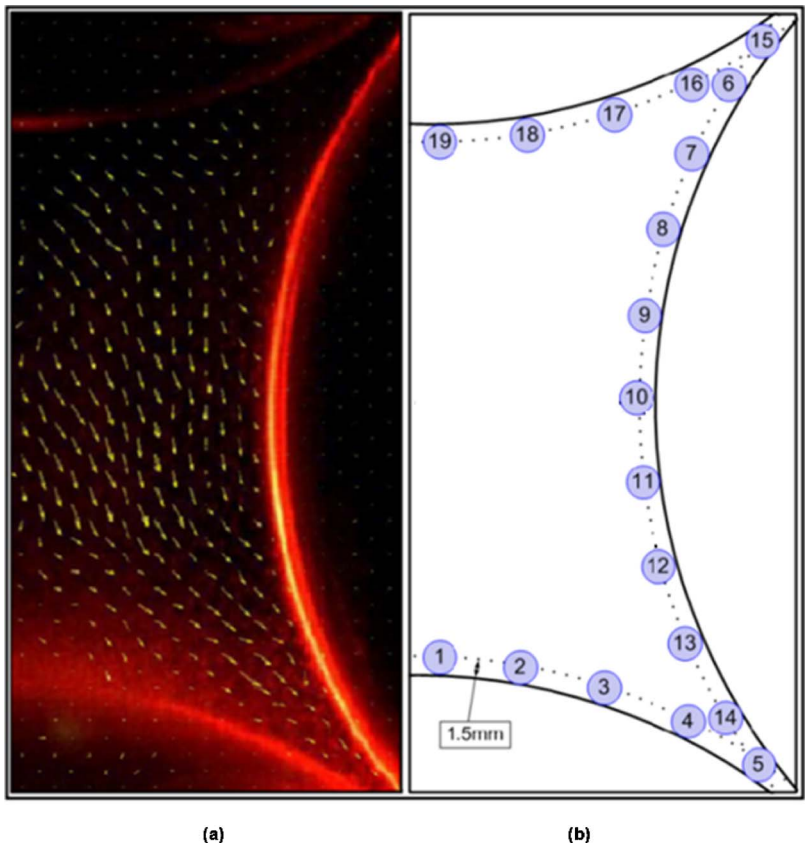


**Fig. 3 Velocity vector field in the gap of pebble: (*a*) velocity vectors and (*b*) the representative points of velocity near the wall**

**4.2 Velocity Analysis Along the Distance From the Pebble Surface.** In Fig. 3, the velocity near the pebble surface is faster than that near the center, and this is caused by fcc stack geometry. As shown in Fig. 1(*b*), all the flow space is covered with top and bottom pebbles in the fcc structure. Flow comes from upper corners and flows out to lower corners. It makes the center velocity slow. In the simulation result of Hassan [4], the body-centered-cubic (bcc) structure has space where the flow can run through directly, and the velocity vector field shows that the velocity at the center of space is faster than on the side of the center. This is not about the velocity magnitude but about the different flow tendencies between the fcc and bcc. If both pressure drops for the fcc and bcc structures are the same, then the fcc structure is more efficient in cooling pebbles, but we can know that those pressure drops are not the same by intuition. Still now, we do not have the experimental result of bcc. Therefore, additional study of which stack structure is more efficient in the same pressure condition is needed.

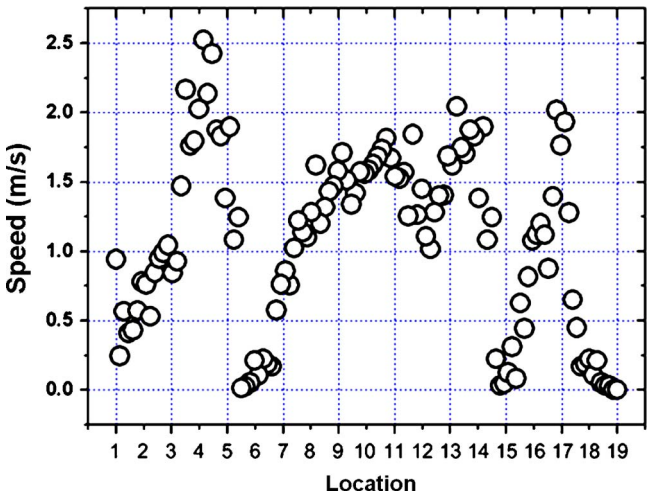


**Fig. 4 The speed ($\sqrt{v_x^2+v_y^2}$) of the cooling gas at the representative points indicated in Fig. 3**

## 5 Conclusion

Considering the importance of the nuclear fuel integrity in the high temperature field of high temperature gas-cooled reactor, the study of the flow field in the complicated flow structure from the packed pebbles is imperative. In the present study, a wind tunnel, with the pebbles scaled up to two times bigger than the reference in the air cooling, is designed with the similarity rule of Reynolds number. Flow was visualized using the high speed particle image velocimetry method with 4000 fps. The present method successfully captured the velocity field and identified the stagnation points. For the fcc geometry, the stagnation points were found at the bottom of the pebble. Also, the present method identified the back flow, which is generated by the contact points between pebbles.

It is expected that the present experimental data are useful for the evaluation of the simulating results of computational fluid dynamics, which will be used for the design and analysis of the nuclear power plant.

## Acknowledgment

The present work is supported by the program of the Basic Atomic Energy Research Institute (BAERI) of the Ministry of Education and Science and Technology (MEST) of Korea.

## References

[1] Driscoll, M. J., and Hejzlar, P., 2005, "Reactor Physics Challenges in Gen-IV Reactor Design," Nuclear Engineering and Technology: an international journal of the Korean Nuclear Society, **37**(1), pp. 1–10.

[2] Reutler, H., and Lohnert, G. H., 1984, "Advantages of Going Modular in HTRs," Nucl. Eng. Des., **78**, pp. 129–136.

[3] Lee, J. J., Kang, S. K., Yoon, S. J., and Park, G. C., 2005, "Assessment of Turbulence Models in CFD Code and Its Application to Pebble Bed Reactor," *Proceedings of the Fourth International Conference on Heat Transfer, Fluid Mechanics, and Thermodynamics*, Cairo, Egypt.

[4] Hassan, Y. A., 2008, "Large Eddy Simulation in Pebble Bed Gas Cooled Core Reactors," Nucl. Eng. Des., **238**, pp. 530–537.

[5] Lee, J. Y., "Experimental Study of Thermal Hydraulic Analysis of Pebble Bed Reactor Core of HTGR," Basic Atomic Energy Research Institute (BAERI), MEST (in preparation).

[6] Okamoto, K., Nishio, S., Saga, T., and Kobayashi, T., 2000, "Standard Images for Particle-Image Velocimetry," Meas. Sci. Technol., **11**, pp. 685–691.